ANNUAL REPORT

University Research Initiative

Contract No.: N00014-92-J-1808

March 1993 - April 1994

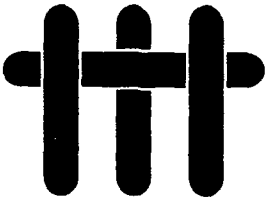

The Processing and Mechanical Properties of High Temperature/ High Performance Composites

by

A.G. Evans & F. Leckie
University of California,
Santa Barbara

University of Pennsylvania
Harvard University
Washington State University
Carnegie Mellon University
University of Virginia

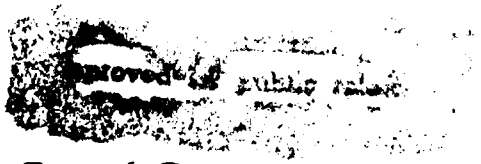

Book 1 of 7:

Mechanism-Based Constitutive Laws and Design

REPORT DOCUMENTATION PAGE

Form Approved
OMB No. 0705–0188

1. AGENCY USE ONLY (Leave blank)	2. REPORT DATE	3. REPORT TYPE AND DATES COVERED
	940301	ANNUAL REPORT 920301 TO 940228

4. TITLE AND SUBTITLE

The Processing and Mechanical Properties of High Temperature/High Performance Composites

5. FUNDING NUMBERS

N00014-92-J-1808

6. AUTHOR(S)

Evans, Anthony G.
Leckie, Frederick A.

7. PERFORMING ORGANIZATION NAME(S) AND ADDRESS(ES)

MATERIALS DEPARTMENT
COLLEGE OF ENGINEERING
UNIVERSITY OF CALIFORNIA
SANTA BARBARA, CA 93106-5050

8. PERFORMING ORGANIZATION REPORT NUMBER

9. SPONSORING/MONITORING AGENCY NAME(S) AND ADDRESS(ES)

OFFICE OF NAVAL RESEARCH
MATERIALS DIVISION
800 NORTH QUINCY STREET
ARLINGTON, VA 22217-5000

DEF. ADV. RESEARCH PROJ. AGENCY
1400 WILSON BLVD..
ARLINGTON, VA 22209

10. SPONSORING/MONITORING AGENCY REPORT NUMBER

11. SUPPLEMENTARY NOTES

12A. DISTRIBUTION/AVAILABILITY STATEMENT

See Distribution List

12B. DISTRIBUTION CODE

13. ABSTRACT (Maximum 200 words)

The annual report of the University Research Initiative project at UCSB on High Temperature, High Performance Composites consists of seven books. The books are entitled as follows: 1-Mechanism-Based Constitutive Laws and Design, 2-Stress Redistribution and Notch Properties, 3-Fatigue and Creep, 4-Processing/Property Correlations, 5-Interface Effects 6-Delamination and Compressive Behavior, and 7-In-Situ Measurements of Stress and Damage

14. SUBJECT TERM

Design, Stress, Fatigue, Creep, Interfaces, Delamination, Compressive, Toughening, Processing, Mechanisms, Composites, Ceramics, In-Situ, Damage

15. NUMBER OF PAGES

2846

16. PRICE CODE

17. SECURITY CLASSIFICATION OF REPORT	18. SECURITY CLASSIFICATION OF THIS PAGE	19. SECURITY CLASSIFICATION OF ABSTRACT	20. LIMITATION OF ABSTRACT
UNCLASSIFIED	UNCLASSIFIED	UNCLASSIFIED	

SUMMARY

OF

TABLE OF CONTENTS

KJS 4/27/94

KJS 4/27/94

BOOK 1

MECHANISM-BASED CONSTITUTIVE LAWS AND DESIGN

KJS 4/27/94

11.	The Mechanisms of Deformation and Failure in Carbon Matrix Composites Subject to Tensile and Shear Loading	K. R. Turner J. S. Speck A. G. Evans
12.	Uncoupled and Coupled Approaches to Predict Crack-Initiation in Fiber-Reinforced Ceramic-Matrix Composites	F. Hild P.-L. Larsson F. A. Leckie
13.	Stress Corrosion Cracking in a Unidirectional Ceramic-Matrix Composite	S. M. Spearing F. W. Zok A. G. Evans
14.	Effects of Gauge Length on the Tensile Strength of SiC Fibers	F. W. Zok X. Chen C. H. Weber
15.	Tunneling Cracks in Constrained Layers	S. Ho Z. Suo
16.	The Effect of Interfacial Properties on the Flow Strength of Discontinuous Reinforced Metal Matrix Composites	D. B. Zahl R. M. McMeeking
17.	On Dislocation Storage and the Mechanical Response of Fine Scale Microstructures	J. D. Embury J. P. Hirth
18.	Effect of Microstructural Parameters on the Yield Strength of Al-4%Mg/Al_2O_3p Composites	R. H. Pestes S. V. Kamat J. P. Hirth

KJS 4/27/94

BOOK 2

STRESS REDISTRIBUTION AND NOTCH PROPERTIES

28.	On the Strength of Fiber Reinforced Ceramic Composites Containing an Elliptic Hole	Y. L. Cui
29.	On the Theoretical Toughness and Strength of Ceramic Composites	B. Budiansky
30.	Microlaminated High Temperature Intermetallic Composites	R. G. Rowe D. W. Skelly M. Larsen J. Heathcote G. R. Odette G. E. Lucas
31.	Fracture Toughness of Al-4%Mg/Al_2O_3p Composites	R. H. Pestes S. V. Kamat J. P. Hirth

KJS 4/27/94

BOOK 3

FATIGUE AND CREEP

43.	The Creep Anisotropy of a Continuous-Fiber-Reinforced SiC/CAS Composite	C. Weber J. Löfvander A. G. Evans
44.	Power Law Creep of a Composite Material Containing Discontinuous Rigid Aligned Fibers	R. M. McMeeking
45.	Diffusive Void Bifurcation in Stressed Solid	Z. Suo W. Wang

BOOK 4

PROCESSING/PROPERTY CORRELATIONS

KJS 4/27/94

54.	Liquid Precursor Infiltration and Pyrolysis of Powder Compacts, I: Kinetic Studies and Microstructure Development	W. C. Tu F. F. Lange
55.	Liquid Precursor Infiltration and Pyrolysis of Powder Compacts: II, Fracture Toughness and Strength	W. C. Tu F. F. Lange
56.	Influence of Interparticle Forces on the Rheological Behavior of Pressure-Consolidated Alumina Particle Slurries	B. V. Velamakanni F. F. Lange F. W. Zok D. S. Pearson
57.	Evolution of a Metastable FCC Solid Solution during Sputter Deposition of Ti-Al-B Alloys	J. P. A. Löfvander U. Ruschewitz C. G. Levi
58.	Novel ODS Copper Alloys from Rapidly-Solidified Precursors—I: Microstructural Development	M. S. Nagorka C. G. Levi G. E. Lucas
59.	Novel ODS Copper Alloys from Rapidly-Solidified Precursors—II: Creep Behavior	M. S. Nagorka G. E. Lucas C. G. Levi
60.	Mechanical Properties of Partially Dense Alumina Produced from Powder Compacts	D. C. C. Lam F. F. Lange A. G. Evans

KJS 4/27/94

BOOK 5

INTERFACE EFFECTS

70.	A Theory for Cleavage Cracking in the Presence of Plastic Flow	Z. Suo C. F. Shih A. G. Varias
71.	Dislocation Nucleation from a Crack Tip: A Formulation Based on Anisotropic Elasticity	Y. Sun G. E. Beltz

KJS 4/27/94

BOOK 6

DELAMINATION AND COMPRESSIVE BEHAVIOR

72.	Compressive Failure of Ceramic Matrix Composites	D. A. W. Kaute M. F. Ashby
73.	Compressive Kinking of Fiber Composites: A Topical Review	B. Budiansky N. Fleck
74.	Delamination of Beams Under Transverse Shear and Bending	T. J. Lu Z. C. Xia J. W. Hutchinson
75.	Mode I Delamination in Ceramic Matrix Composites with 2-Dimensional Reinforcement	D. A. W. Kaute M. F. Ashby H. R. Shercliff
76.	Mode II Delamination in Ceramic Matrix Composites with Unidirectional Reinforcement	D. A. W. Kaute M. F. Ashby H. R. Shercliff
77.	Delamination, Fibre Bridging, and Toughness of Ceramic Matrix Composites	D. A. W. Kaute H. R. Shercliff M. F. Ashby
78.	Bending and Shear Failure of Ceramic Matrix Composites: An Experimental Study	D. A. W. Kaute K. White M. F. Ashby
79.	Mechanics of Splitting in Orthotropic Materials	Y. L. Cui
80.	Transverse Strength of Metal Matrix Composites Reinforced with Strongly Bonded Continuous Fibers in Regular Arrangements	D. B. Zahl S. Schmauder R. M. McMeeking
81.	Contact Damage of Ceramic Matrix Composites	D. A. W. Kaute K. White M. F. Ashby

BOOK 7

IN-SITU MEASUREMENTS OF STRESS AND DAMAGE

82.	Residual Stress Measurement in Sapphire Fiber Composites: Through-Focus and Transmission Fluorescence Spectroscopy	D. Lipkin D. R. Clarke
83.	Measurement of Residual Stresses in Sapphire Fiber Composites Using Optical Fluorescence	Q. Ma D. R. Clarke
84.	Luminescence Sensing of Stress in Ti/Al_2O_3 Fiber Reinforced Composites	H. Hough M. Demas T. O. Williams H. N. G. Wadley
85.	Optical Fluorescence from Chromium Ions in Sapphire: A Probe of the Image Stress	Q. Ma D. Clarke
86.	Residual Stresses in Al_2O_3-ZrO_2 Composites: A Test of Stochastic Stress Models	Q. Ma W. Pompe D. R. Clarke
87.	Stress Measurement Using Optical Fluorescence	Q. Ma D. Clarke

KJS 4/27/94

KJS 4/27/94

EXECUTIVE SUMMARY

The general emphasis for 1994 would be on increased software development, testing of subelements and design calculations. For these purposes, the constitutive law coding and development would be coordinated by Nick Aravas, and implemented in ABAQUS. The initial implementation would be the elastic/plastic model for MMCs with interface debonding developed in 1993 (Leckie). This would be extended in 1994 to include creep and some aspects of thermomechanical cycling. The code would be used for design calculations concerned with MMC rotors, actuators and vanes (Leckie). A plan is being formulated to collaborate with Pratt and Whitney to acquire MMC sub-elements representative of these components during 1994. Experimental tests on these subelements would be capable of providing a direct validation of the code capabilities.

Constitutive law and fatigue lifing software would be created for CMCs using continuum damage mechanics (CDM) approaches (Leckie, McMeeking). The approach has been motivated by micromechanics models developed in 1993 (Hutchinson, Zok, Evans). These codes would be used to calculate stress redistribution effects and fatigue life on simple sub-elements, such as center notched and pin-loaded plates. Comparison with experimental measurements needed to test the fidelity of the models will be based on moiré interferometry and thermoelastic emission. This effort is coordinated with the NASA EPM program through both General Electric and Pratt and Whitney. A plan for acquiring sub-elements from DuPont Lanxide is being formulated.

A new emphasis for 1994 would be on the transverse properties of CMCs. The measurements and calculations performed in 1993 have indicated a strategy for curved sections and junctions that would establish a consistent design approach. The basic approach for resisting failures from combinations of interlaminar shear and transverse tension involves the use of stitching and angle ply weaving patterns that inhibit major reductions in stiffness when matrix cracks are induced by transverse loads and bending moments. For this purpose, calculations would be performed that combine

the mechanics of delamination cracks with models of bridging by inclined fiber bundles (Hutchinson, Ashby, Evans, McMeeking). The insight gained from these calculations would be used to design and acquire sub-elements, such as C sections and T junctions.

Additional software development will be for creep and creep rupture (McMeeking). The models devised in 1993 and test data relevant to MMCs will be combined into a code that predicts the creep and rupture of unidirectional MMCs subject to multiaxial loads. Some aspects of this code will also be applicable to CMCs.

Two new activities will be introduced in 1994: thermal properties and damping. The thermal properties will be studied on both CMCs and MMCs (Ashby, Hutchinson). Measurements of thermal diffusivity will be made by the laser flash method and related to the properties of the interface and the density of matrix damage in the material. Thermal expansion measurements will also be performed with emphasis on determining hysteresis effects, which can be related to the temperature dependence of the interfaces properties, through cell models. The latter might evolve into a diagnostic for establishing relationships between the interface properties and thermomechanical fatigue.

The processing activities in the program will have newly established goals in 1994. The principal emphasis will be on concepts for affordable manufacturing. The issues selected for investigation will be consistent with manufacturing processes that allow near-net shape consolidation while still yielding reasonable combinations of longitudinal and transverse properties. Performance models developed in the program would be used as an initial test of concept viability.

Beyond these general trends, specific activities are planned for 1994. These are elaborated below. The status of understanding and development in each of these areas is summarized in Table I. Increasing magnitudes between 0 and 1 designate a knowledge range from limited to comprehensive.

TABLE 1A

Status of Design Knowledge for MMCs

	$[0°]_n$ MMC				$[0°/90°]_n$	
	LONG.		TRANS.			
	P	S	P	S	P	S
Tensile Strength	3/4	1	1	1/2	1/4	~ 0
Creep and Creep Rupture	3/4	0	1	0	0	0
Cyclic Flow (Isothermal, TMF)	1/4	0	1	1/2	0	0
Crack Growth (Isothermal Fatigue)	1	1	0	1/2	0	0
Crack Growth (TMF)	1/2	1/2	0	0	0	0
Compressive Strength	3/4	0	0	0	0	0

TABLE 1B

Status of Design Knowledge for CMCs

	[0/90]		[45/45]	
	P	S	P	S
Stress/Strain	3/4	1/4	1/2	0
Fatigue	3/4	0	0	0
TMF	1/4	0	0	0
Creep and Rupture	1/2	0	0	0
Compression Strength	3/4	1/4	0	0
Transverse Properties	3/4	1/2	—	—
Thermal Properties	1/4	0	—	—

P Primary Structure

S Secondary Structure

2. CONSTITUTIVE LAWS

Two approaches will be used to create a formulation capable of representing the in-plane properties of CMCs. One would be based on Continuum Damage Mechanics (CDM) (Leckie). The other would use concepts analogous to those used in plasticity theory (Hutchinson). The CDM approach uses damage parameters that relate explicitly to micromechanics models. A potential function has already been identified as the state variable which separately represents the strain from the elastic compliance change caused by the matrix cracks and the inelastic strains associated with the debonding and sliding interfaces. Derivatives of the potential with regard to strain and damage give the relationships between variables, such as stress, interface sliding resistance, matrix crack density, etc.

The first version of the CDM model would use the minimum number of damage variables potentially capable of representing the behavior of laminated or woven composites. Cross terms between the damage variables would not be considered at this stage. Moreover, matrix cracks would be introduced normal to the maximum principal tensile stress, consistent with the experimental observations.

The plasticity theory approach would seek a formulation based on matrix cracks occurring normal to the maximum principal tension. It would introduce parameters that reflect the inelastic strain caused by interface sliding upon off-axis loading which would be calibrated from tests performed in tension in 0/90 and 45/45 orientations.

The insight needed to characterize off-axis loading effects will be gained from cell models (Hutchinson) in a manner analogous to that previously used for axial loads. The principal objective will be to understand trends in matrix crack opening and interface debonding/sliding with applied loads. The stress on the fibers will be calculated with the intent of predicting effects of loading orientation on fiber failure. The models will be compared with measurements made in 45/45 tension, using various CMCs (Evans).

Calibration of the damage parameters for each material would be made from hysteresis loop measurements in accordance with procedures developed in 1993. Experimental results obtained in 0/90 tension, 45/45

tension and in-plane shear will be used. In future work, it is hoped that shear tests will not be necessary.

The validation of the constitutive laws will be achieved by comparing calculations with measurements made on sub-elements, especially pin-loaded holes (Evans). The experimental results include residual strains obtained by Moiré interferometry (Fig. 2.1), ultimate loads for either tensile or shear failure and principal strain trajectories delineated by matrix cracking patterns. Acoustic methods will also be developed to probe the local values of the elastic modulus (Clarke, Wadley) which could be compared directly with the CDM predictions.

3. FATIGUE LIFING

3.1 CMCs

A software program for isothermal low cycle fatigue (LCF) of CMCs, developed in 1993 (Fig. 3.1) will be extended in 1994. The present program asserts that fatigue is associated with cyclic degradation of the interface sliding resistance, τ, which can be characterized by analyzing hysteresis loops measured periodically during a fatigue test. With this methodology, S-N curves have been predicted for both unidirectional and woven 0/90 composites tested in cyclic tension as well as changes in compliance and permanent strain. Some additional effort is required to analyze data on 0/90 laminates in order to validate the model predictions. The extensions envisaged for 1994 include thermomechanical fatigue (TMF), strain controlled LCF and off-axis fatigue (Zok, Evans). Experiments are planned which would assess the effects of temperature cycling and of inclined fibers on τ degradation, measured from hysteresis loops. Various cell model calculations (Hutchinson) will be used to interpret the experiments. The results will be used to establish general *rules* for interface degradation in CMCs.

The off-axis experiments will also give insight into the fiber failure criterion that replaces the global load sharing (GLS) results successfully used for 0/90 loadings. This study will coordinate with the cell calculations described above, and the 45/45 tensile experiments.

Notch fatigue studies will be initiated. These will examine cyclic stress redistribution and notch sensitivity (Evans).

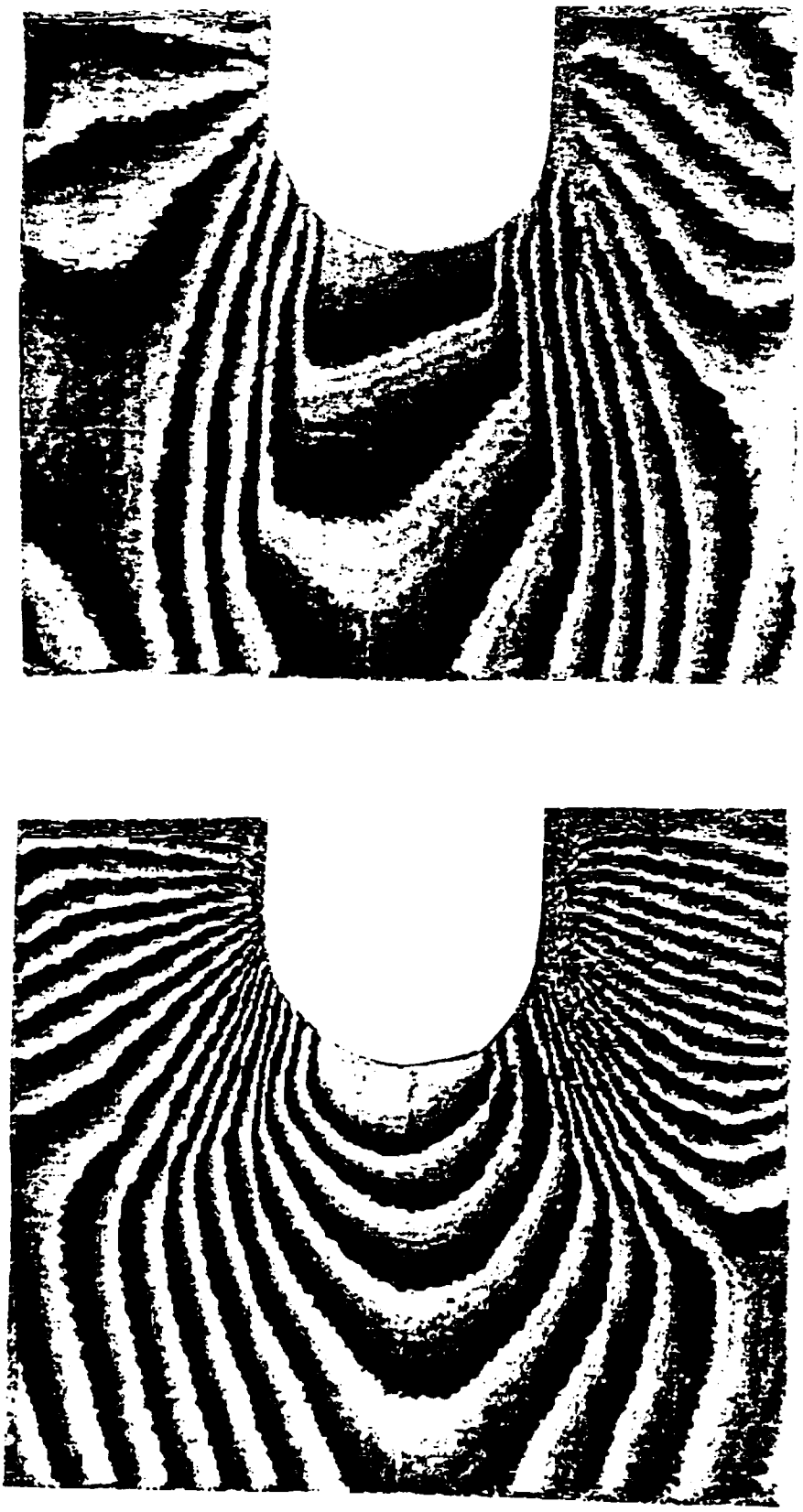

Figure 2.1

Fatigue Methodology

CMC Life Program

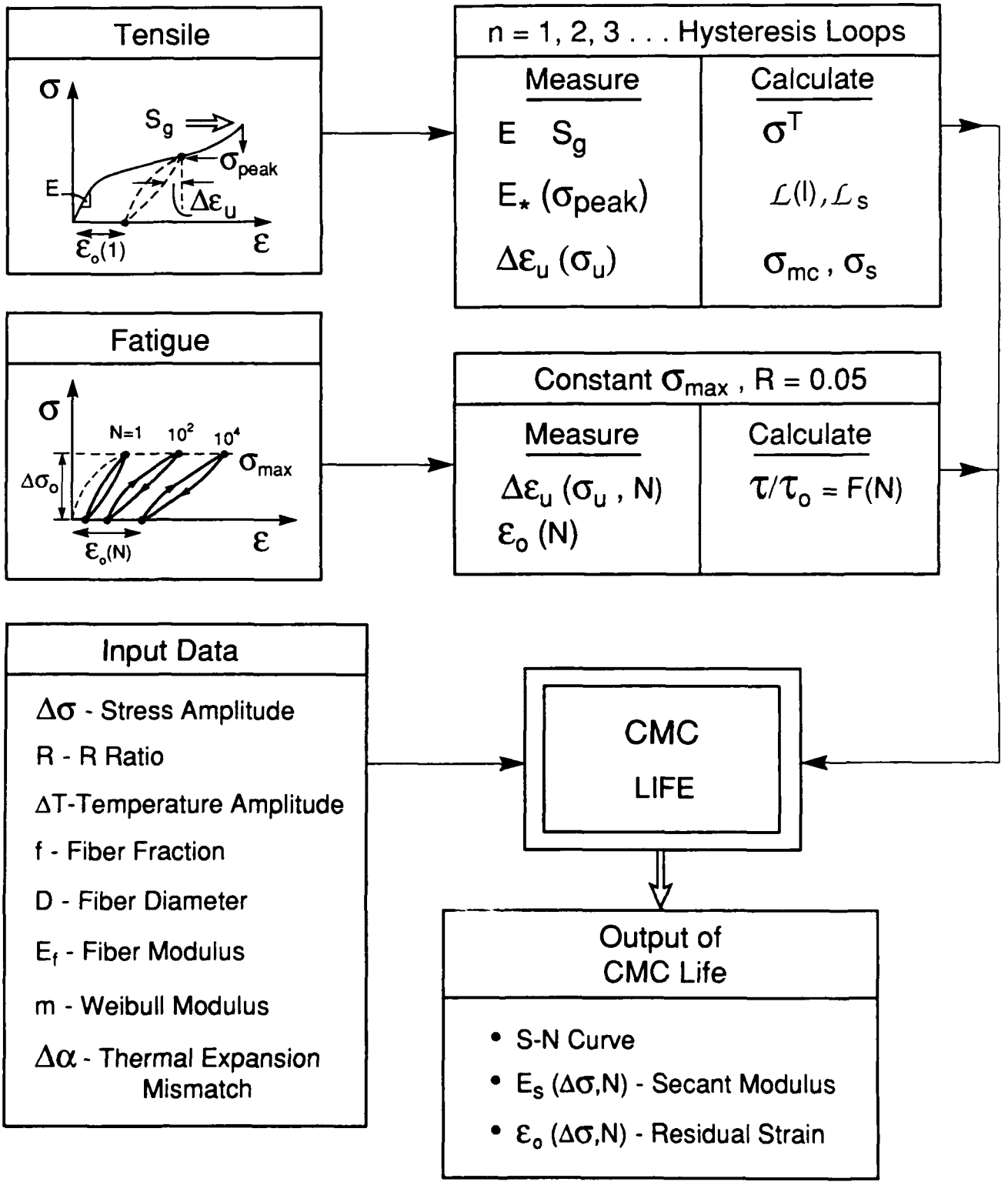

Figure 3.1

3.2 MMCs

Fatigue crack growth and notch strength studies in MMCs will be extended to 0/90 laminates (Zok, Suo). The experiments concerned with crack growth will be interpreted using crack bridging models. The utility of such models has been validated in previous years through studies on unidirectional MMCs. It is envisaged that the fatigue crack growth characteristics of the unidirectional and 0/90 configurations will be related through the volume fraction of fibers aligned with the loading direction. The notch strength behavior will also be interpreted using crack bridging models. Such models have been developed in 1993 and found to be useful in rationalizing the behavior of unidirectional materials (Zok, Suo). In all cases, the mechanical measurements will be augmented by *in-situ* observations to identify changes in damage mechanisms with temperature, fiber architecture, etc. Plans to study the influence of panel thickness on fatigue and fracture resistance are also being developed, as well as tests to understand the potential for crack growth in mixed mode loadings (Hirth, Zok).

Studies of the TMF response of MMCs loaded parallel to the fiber axis will be initiated (Zok, Leckie). Experiments will evaluate both in-phase and out-of-phase loadings. Models of load shedding (matrix-fibers) will be used to interpret the hysteresis loops and to develop fatigue life models applicable to low cycle, high strain TMF.

4. CREEP AND RUPTURE

4.1 MMCs

The considerable progress made in 1993 towards identifying and understanding the mechanisms of creep and rupture in unidirectional MMCs containing non-creeping fibers (McMeeking, Zok) will be used to develop creep rupture software. The longitudinal creep model to be used incorporates stochastic fiber fracture and interface sliding in a format amenable to the prediction of primary and tertiary creep in terms of matrix creep strength, interface sliding resistance, fiber strength, Weibull modulus, etc. The concepts would be visualized in a rupture mechanisms map

(Fig. 4.1). The transverse creep behavior would include interface debonding, which greatly accelerates the creep, leading to marked anisotropy. A constitutive law for creep that includes these effects will be developed (Aravas, McMeeking).

Additional experiments and calculations will be conducted to assess the effects of notches and holes on creep rupture (Zok, Suo). Experience with MMCs at ambient temperature indicates that the notch sensitivity is largely dictated by matrix properties (i.e., strength and ductility). The reduction in matrix properties at elevated temperatures may lead to a substantial elevation in notch sensitivity. However, this behavior may be complicated by the development of alternate damage processes, such as shear bands.

4.2 CMCs

Studies of the creep and rupture of CMCs will continue with emphasis on materials containing creeping fibers. A particular emphasis will be on matrix cracking that arises as fiber creep relaxes fiber bridging tractions (McMeeking, Evans). The experimental studies will be performed on SiC/SiC composites. Hysteresis loop measurements will be used to monitor matrix damage during composite creep, using procedures devised in 1993. Models will be developed based on time dependent fiber bridging concepts (McMeeking, Cox).

It is envisioned that the lifetime of some CMCs will be dictated by time-dependent rupture of the fibers. A lifetime prediction tool for such a composite *must* incorporate the knowledge of fiber strength degradation over time. A new activity will be initiated to address this problem (Suo, Evans). The initial work will involve a survey of data in the existing literature, and a comparison with available models. A new model is being developed for single crystal fibers. This model involves a residual pore inside a fiber which changes shape, under stress, via surface diffusion, to become a crack. These issues will be viewed in the broad context of fiber and composite manufacture.

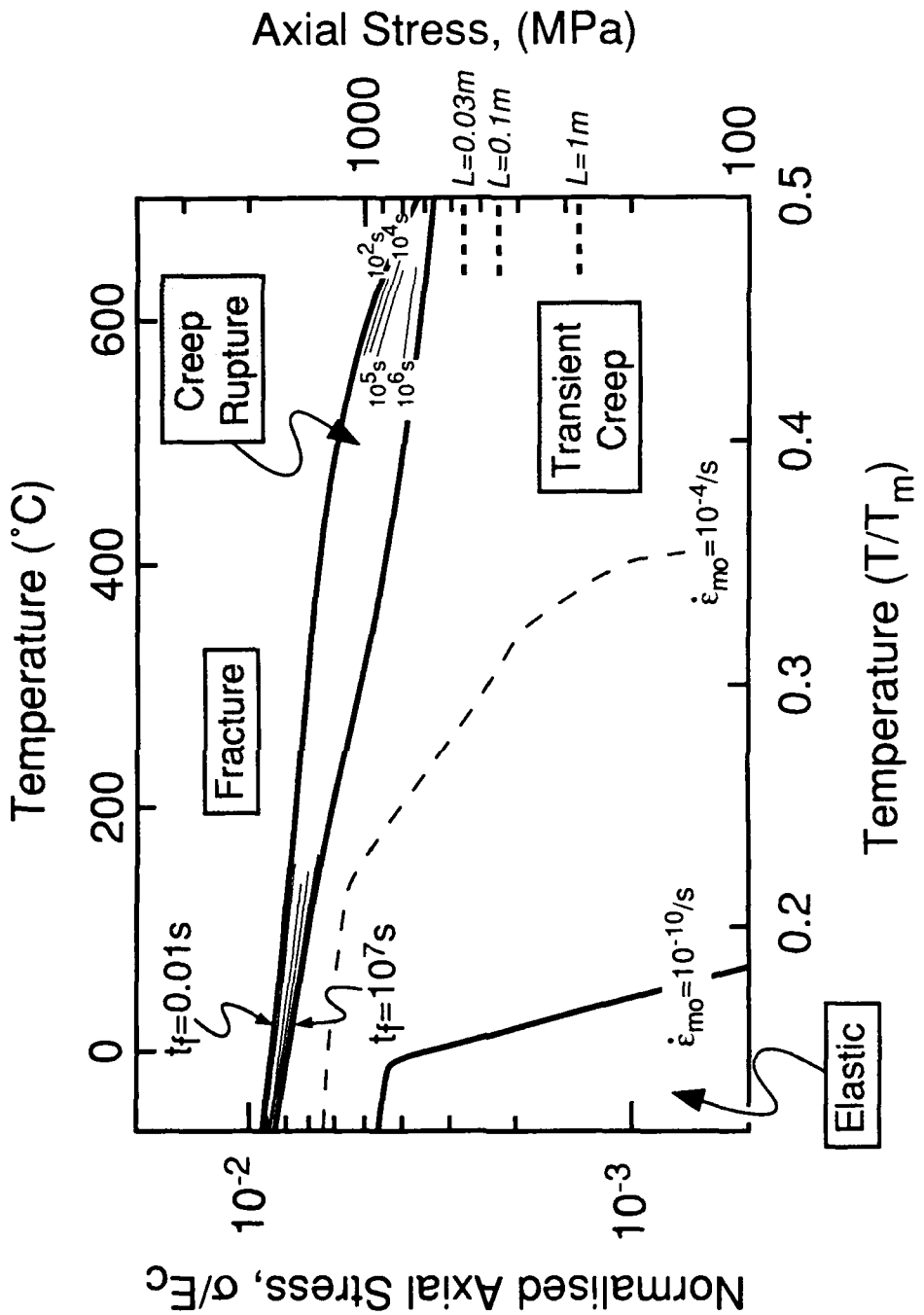
Axial Stress, (MPa)
Temperature (°C)
Temperature (T/T_m)
Normalised Axial Stress, σ/E_C
Creep Rupture
Fracture
Transient Creep
Elastic
L=0.03m
L=0.1m
L=1m
10^2s
10^4s
10^5s
10^6s
t_f=0.01s
t_f=10^7s
ε̇_mo=10^-4/s
ε̇_mo=10^-10/s
0
200
400
600
1000
100
0.2
0.3
0.4
0.5
10^-2
10^-3

Figure 4.1

5. TRANSVERSE PERFORMANCE OF CMCs

Analyses and tests performed in 1993 (Ashby, Hutchinson, Bao) have highlighted the essential issues related to components that experience combinations of transverse tension and interlaminar shear. In both loadings, matrix cracks form at manufacturing flaws at low stresses, of order 10-100 MPa. These cracks extend across the plies and interact minimally with the fibers. Although the crack configurations differ for transverse tension and interlaminar shear loadings, multiple cracks always form. This multiplicity of cracking causes a major reduction in stiffness, which can cause unacceptably large displacements and also redistribute stress into other areas. The formation of the matrix cracks is probabilistic in nature and governed by the size distribution of manufacturing flaws. Design based on the prevention of such transverse cracks must rely on weakest link statistics, usually with a low Weibull modulus. Alternatively, it may be assumed that cracks *inevitably* form and, instead, reliance is placed on *controlling* the diminished modulus of the material, after matrix cracking has occurred. This approach relies on having 3-D architectures, with transverse fibers introduced locally either by stitching or by using angle plies. To explore this possibility, calculations will be performed (Hutchinson, Evans) to examine fiber architectures that lead to minimum stiffness loss, subject to acceptable in-plane properties. Based on these calculations, sub-elements will be designed that test out the concepts.

6. COMPRESSIVE BEHAVIOR

The studies completed in 1993 on the compressive failure of polymer matrix composites by the growth of kink bands (Budiansky, Fleck) will be extended to metal matrix composites, through a coordination with 3M. Compressive failure of Al and Ti MMCs with small diameter fibers has been observed by 3M to occur in accordance with the same kink band mechanism known to operate in PMCs and in C/C composites. The theory should thus extend to the MMCs, with the fiber misalignment, the shear yield strength of the matrix and its work hardening coefficient as the principal variables. A comparison between the theory and experimental

results would provide the basis for specifying the compressive properties of MMCs.

Compression failure of CMCs occurs by different mechanisms (Ashby). The dominant failure modes are similar to those that operate in porous brittle solids such as monolithic ceramics, concrete and rocks. The theory is well established and validated for these materials. Applications of the theory to various CMCs will be made and applied to the understanding of a behavior of pin-loaded holes (Evans, Ashby).

7. THERMAL PROPERTIES

A new focus on the thermal properties of CMCs and MMCs will be initiated in 1994. Calculations of the effects of matrix cracks in the thermal expansion of CMCs will be made (Hutchinson). These will be compared with data obtained from TMF testing (Zok). The effects of such cracks on the in-plane thermal conductivity will also be calculated (Hutchinson). Measurements will be performed using the laser flash method (Ashby).

Thermal conductivity measurements will be initiated on Ti MMCs (Ashby). These will be used to understand the effects of the fiber/matrix interphases and of matrix damage on the transverse and in-plane thermal conduction.

8. MATERIALS SELECTION

The Cambridge Materials Selector software will be expanded in 1994 to include high temperature creep design with the corresponding data base (Ashby). This expanded version will permit estimates to be made of temperature limits for MMCs based on creep controlled TMF and on the transverse creep of components with unidirectional reinforcements.

9. DESIGN CALCULATIONS AND SUB-ELEMENT TESTS

A larger fraction of the effort in 1994 will be on design and sub-element testing, particularly for MMCs. Discussions are now in progress with Pratt and Whitney, Textron and 3M to perform design calculations using the

constitutive equations developed at UCSB and to produce sub-elements for testing.

The design emphasis for MMCs will be on various diffusion bonded joints with Ti matrices and monolithic Ti attachments. Two specific subelements are envisaged. The first involves unidirectionally reinforced rods (or plates), clad with monolithic metal. The purpose of the cladding is to prevent exposure of the fibers to the environment and to mechanical abrasion. The design of clad MMC structures requires consideration of (i) the residual stresses resulting from thermal mismatch between the cladding and the composites section, (ii) the potential for fatigue cracks to initiate and grow through the monolithic material, and (iii) the interaction of such cracks with the composite section and their influence on the strength and life of the structure. The design and testing of such subelements (Zok, Leckie) will be augmented by calculations of crack growth and fracture, incorporating the effects of thermal and elastic mismatch between the cladding and the composite (McMeeking). The clad structures will also be used to initiate studies on the reinforcement of holes in composite sections with monolithic metal patches, as drawn in Fig. 9.1 (Zok, Suo). The second subelement involves the attachment of a MMC actuator rod to a pin-loaded monolithic section (Fig. 9.2). The critical design issues relate to the strength and fatigue resistance of the interfaces between the composite and monolithic matrices. Design studies shall also be completed on rotor rings with special efforts made to produce rule-based design procedures which would be used by industry at the conceptual level of design to determine sizes and the efficient disposition of material.

For CMCs, the sub-element studies would be based on the calculations described above in Section 5. These would include C sections and T junctions (Fig. 9.3) Negotiations for manufacturing these sub-elements will be initiated and tests performed at UCSB.

10. AFFORDABLE MANUFACTURING

As our understanding of composite mechanics and its interplay with design and performance has evolved, it has become increasingly evident that *cost* and *reproducibility*, are major constraints. Even as processing

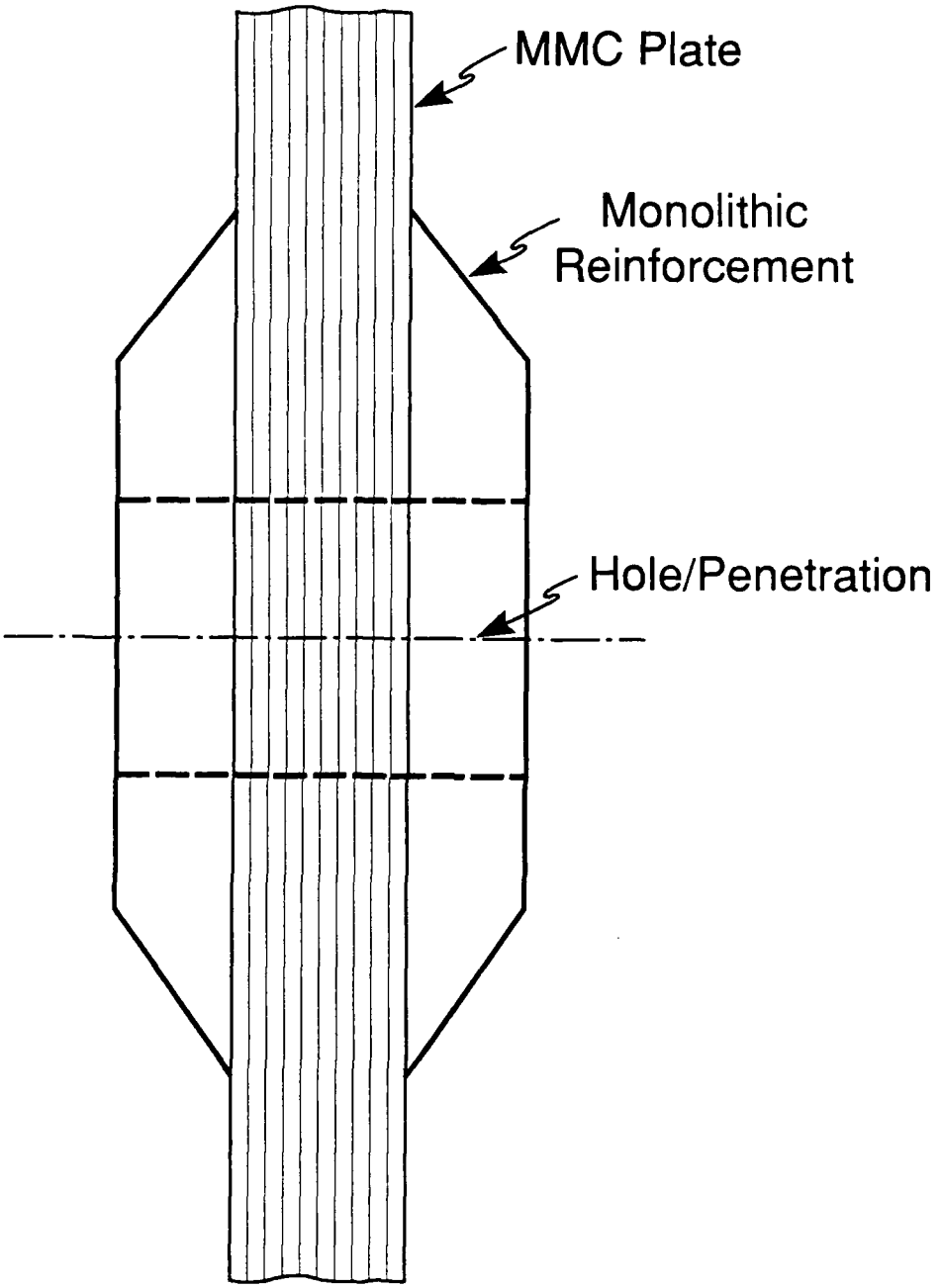

Figure 9.1

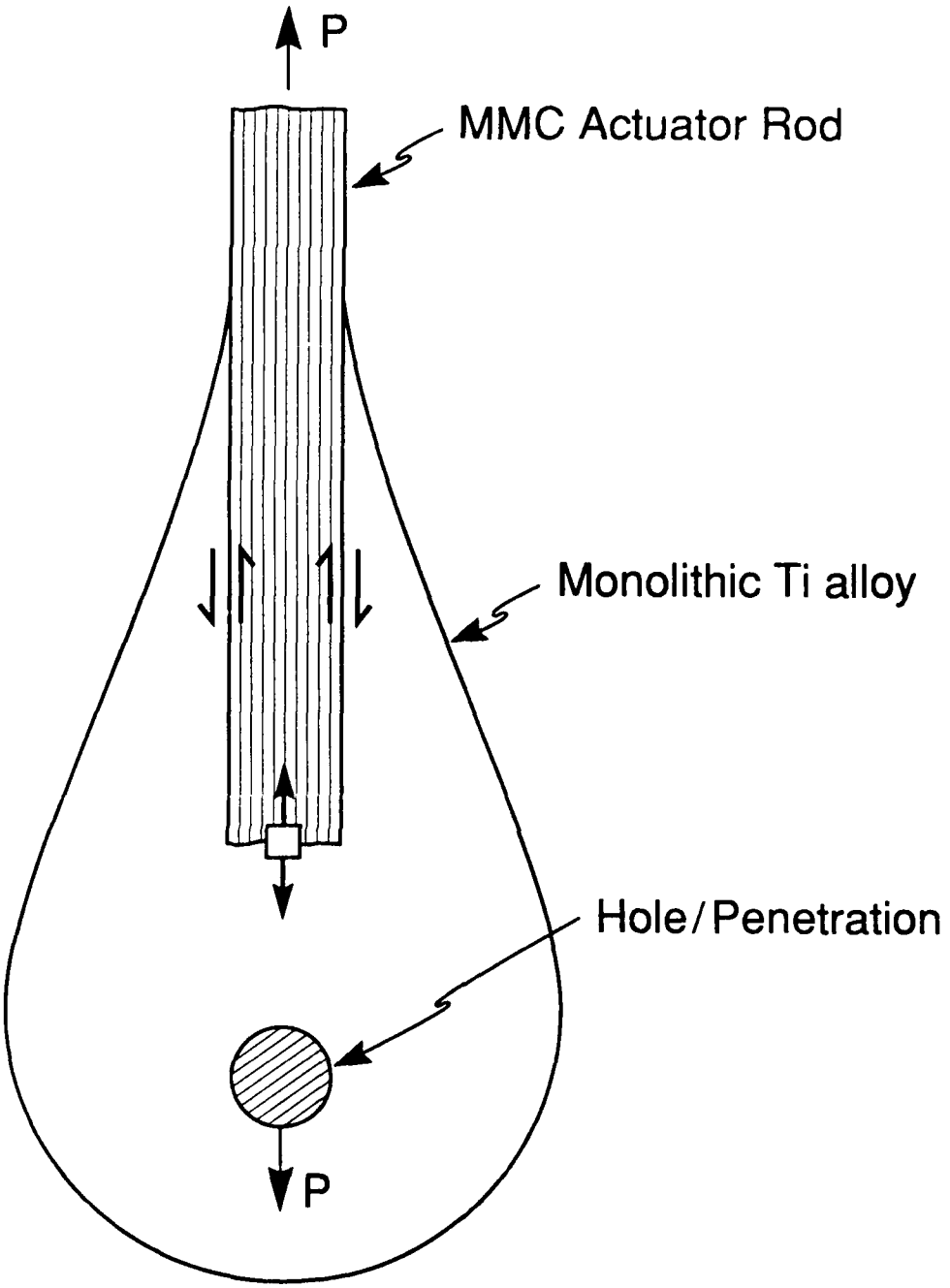

Figure 9.2

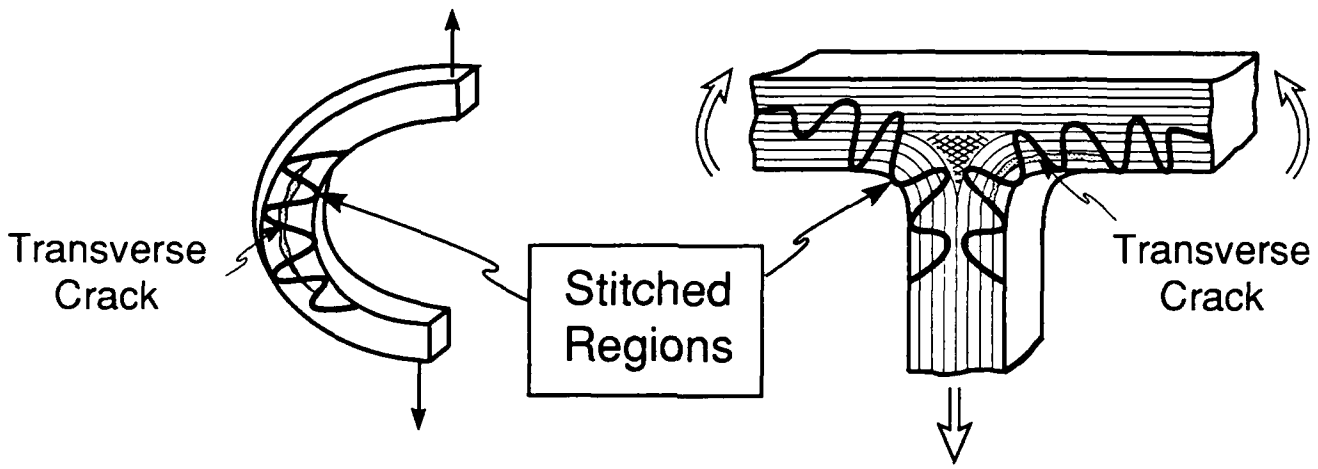
Transverse
Crack
Stitched
Regions
Transverse
Crack
a) C-Specimen
b) T - Junction

Figure 9.3

developments make the prospect of affordable high temperature fibers more realistic, evolving knowledge on the mechanical and thermochemical functions of interfaces have led to design concepts involving carefully tailored interphase layers, with unfavorable impact on cost. Moreover, if affordable coated fibers were available today, fabrication costs associated with consolidation and pressure densification would often remain prohibitive. Future processing and manufacturing activities are predicated on these issues, especially the need for new ideas, and the related knowledge base.

10.1 MMCs

Melt processing methods provide the more affordable options in composite synthesis with the added benefit of near-net shape capability. For continuous fiber composites melt infiltration also enables full density while minimizing the consolidation stresses that typically cause premature reinforcement failure in solid state processes. However, melt processing requires a high degree of thermochemical compatibility between matrix and reinforcement since deleterious diffusional interactions would be accelerated by the liquid phase. Conventional melt processing also exhibits limited ability to control the volume fraction and spatial uniformity of the reinforcements.

Among metal matrices, Ti alloys epitomize unsuitability for direct melt infiltration owing to aggressive reactivity. Fiber clustering is also a concern, even in solid state processes based on powder or foil matrices. Composite consolidation by vapor deposition (PVD) of the matrix on the fibers provides an avenue for improving *homogeneity of fiber spacing*. However, present schemes require expensive pressure densification with its many problems. A potential solution involves a hybrid manufacturing route wherein part of the matrix is first applied to the fibers by PVD. The pre-metallized fibers are then assembled into a preform having the desired shape and then infiltrated with the remaining matrix in liquid form.

Direct infiltration with Ti alloys could be feasible owing to the protection of the fiber by the PVD layer, but the high temperatures involved would exacerbate the diffusional interactions at the fiber-matrix interface. An alternate approach involves depositing the more refractory constituents of

the matrix (e.g., Ti, Nb, Mo, etc.) by PVD and then infiltrating with the lower melting point constituents (e.g. Al). Based on stoichiometric considerations, the latter approach would be suitable for matrices with $\geq$ 25 at.% Al, notably the orthorhombic and α_2 alloys. The obvious problem with this approach is the homogenization of the matrix after consolidation, which may require lengthy high temperature treatments in the solid state. However, a significant part of the matrix synthesis reaction could be effected in the presence of molten Al, followed by a final heat treatment in the solid state. While this lower temperature infiltration approach is evidently desirable from a manufacturing viewpoint, it is not clear that matrix homogenization can be achieved.

A program involving modeling and experimental work will be initiated in 1994 to generate the knowledge base appropriate to hybrid approaches for Ti matrix composites (Levi, Evans). Cell models (single fiber environment) would be developed to study diffusional interactions and remelting/solidification phenomena as a function of processing cycle (temperature-time history). Experiments would be performed to elucidate the relevant aspects of microstructural evolution and provide the reaction and interdiffusion kinetics needed to calibrate the models. Initial experiments would be performed by infiltrating pure Ti-wire preforms with molten Al and subjecting the "composite" to different treatments in the semi-solid state. Subsequent experiments would focus on developing a metallization route for Ti-Nb alloys on SiC fibers and on the relevant interactions with infiltrated Al. Larger scale modeling issues would be tackled in 1995 if the proposed approach appears promising.

Ongoing activities on the understanding of microstructure evolution and its relationship to properties in *in-situ* TMC systems based on TiB reinforcements would be continued (Levi). These are by nature affordable composites which exhibit inherent thermochemical stability and may be cast into shapes using conventional Ti processing techniques. A potential application of these materials would be in joints with unidirectionally reinforced composites, wherein their higher modulus and creep resistance combined with acceptable toughness and isotropic properties could be advantageous. It is also anticipated that these materials could be used for cladding in PVD or plasma-sprayed form, thereby reducing the potential for fatigue crack initiation in the cladding. Since TiB is thermochemically stable

with practically all Ti matrices of interest in fiber composites, such strengthening concepts may be readily implemented.

10.2 CMCs

Measurements and observations in 1993 have shown that strong, high strain to failure CMCs can be fabricated using an inexpensive method that involves a) packing a powder around fibers within a fiber preform using pressure filtration and b) making the powder matrix strong by heat treatment followed by infiltration with a liquid precursor that decomposes to an inorganic material. A composite made this way, with polycrystalline alumina fibers in a silicon nitride matrix, demonstrated that the *matrix* deflects the crack. This observation is significant since it suggest that a class of CMCs can be processed without needing weak fiber/matrix interfaces. The potential of this observation will be explored (Lange, Evans), by processing a composite with strong, polycrystalline alumina fibers in a mullite matrix because the thermomechanical properties of mullite minimize thermal stresses and resist creep. In addition, the thermal expansion mismatch is relatively small. Mixed Al, Si metal alkoxide precursors which can be gelled *in-situ*, prior to decomposition, will be used to strengthen the matrix.

Manufacturing studies would initiate with understanding the precursor infiltration into mullite power compacts. The densification of the matrix would be determined as a function of the cyclic infiltration. Microstructure changes would be controlled to avoid flaw populations during densification. The fracture toughness and the strength of the matrix would be determined as a function of the number of precursor infiltration cycles. Composite processing would initiate with precursor infiltration into alumina fiber preforms by pressure filtration, with emphasis on the colloidal aspects of this processing step. The goal would be to determine the processing conditions needed to produce a matrix that optimizes the ability to deflect cracks without degrading fiber strength. To optimize composite processing, panels for testing under conditions of both strain and stress control would be manufactured.

11. STRESS AND DAMAGE SENSORS

The extensive exploitation of the optical fluorescence method of measuring stresses in sapphire fiber and alumina-containing ceramic composites begun in 1993 will be continued in 1994 (Clarke, Wadley). The emphasis is on using the method to understand basic, unresolved issues in stress redistribution in composites by the direct measurement, with high spatial resolution, of the stresses themselves. Particular attention will be paid to determining the stress distribution associated with interfacial sliding. One of the problems to be addressed relates to new concepts for oxidation resistant interfaces within MMCs and CMCs, particularly the concomitant roles of fiber roughness and sintering on interface sliding and debonding, after exposure to high temperatures and cyclic loadings. For this purpose, fibers with fugitive, low modulus coatings will be explored and fluorescence measurements used to understand stress evolution and its connection with fiber durability within the composite. A second problem relates to the distinction between the line spring and large scale sliding models for fiber bridging (Budiansky, Hutchinson), so as to determine the range of applicability of the two models. The two competing models predict different distributions of stresses in the fibers within the bridging zone and hence are amenable to validation on the basis of the measured stress distribution.

Two approaches to measuring local damage are under development and will be the focus of the sensor activities. One is the use of acoustic methods (Wadley) to probe local variations in the elastic modulus of CMCs as a function of load. This should provide a means of mapping the distribution of damage which can be compared directly with the predictions of continuum damage mechanics models. The second approach (Clarke) is to detect the third harmonic signal generated by the presence of local damage. Preliminary experimental results obtained in 1993 concerned with the detection of crack-like voids in thin metal lines, together with computer simulation studies, have demonstrated the viability of the technique. This work will be extended in order to detect damage accumulation in CMCs and MMCs.

MATERIALS SELECTION AND INNOVATION IN DESIGN

Daniel A.W. Kaute and Michael F. Ashby

Cambridge University Engineering Department
Cambridge, England, European Union

CUED/C-MATS/TR 218

Materials Selection and Innovation in Design

Daniel A.W. Kaute and Michael F. Ashby

Cambridge University Engineering Department, Materials Engineering,
Trumpington Street, Cambridge, England, CB2 1PZ, European Union

CUED/C-MATS/TR 218

Abstract—There is an intrinsic barrier to the adoption of new materials in engineering design—of which ceramic matrix composites are certainly an example. Designers are conservative, wishing to avoid costly mistakes; and the evolution of new design methods to exploit the new materials to the full are slow to develop. Here we review the importance of materials selection in design. The ideas are deployed in a case study to show how design methods might change to utilise ceramic matrix composites.

1. INTRODUCTION

The following is a first attempt to assess the interactions between materials characterisation, processing and design necessary in order to achieve an innovative and successful use of new materials. The focus is on design. To research the topic in depth would be to go beyond the scope of this thesis, but certain conclusions—applicable to the case of ceramic matrix composites—can nonetheless be drawn. The consequences for design with ceramic matrix composites are illustrated in a case study.

Design can be defined as the creative act of finding and establishing a technical solution to a recognised need of society. In *original design* the engineer starts from scratch, whereas *incremental design* is the adaptive development of an existing technical solution. Both involve the following basic steps: first, the *need*, often called *market need* has to be defined as clearly as possible. Then existing and new technical concepts have to be developed to meet the perceived need, and analysed for their physical and economic viability. A full concept outlines a system, divided into subsystems and components, each of which has to fulfil one or more specific functions.

One important factor for the feasibility of a concept is the availability and cost of the materials that are to be used. This is the point at which materials selection comes in.

Historically, materials selection has taken place at a late stage of the design process—once the function and working conditions of each component have been determined. This means that a desired *material property profile* is defined, which gives a rough outline of strength, toughness, temperature range etc. of the materials to be used. As long as the range of available materials was small, the design engineer knew what he could reasonably expect, and he normally defined a component with a specific material in mind. This approach to design with a known or a new material the engineer intuitively feels is right has certainly shown to be viable. However, the advent of a multitude of new materials and grades with unusual and promising property profiles makes it more and more difficult for the design engineer to rely on his intuition for the right choice of material. And, in many cases, the consequences of the materials choice for the performance and competitiveness of a product have become too important for it to rely solely on intuition.

This is the reason why a more rational approach to materials selection in design has been a focus of research in recent years. Dieter [1991] outlines the important aspects in materials selection, one of which is the definition of a detailed materials property profile. Ashby [1992a] has delivered a methodology for translating design performance objectives into materials indices that need to be optimised. These indices are based on condensed material properties like stiffness, strength and toughness. All authors agree that materials selection at an early stage of the design process is important for innovative design—in consequence the classical design methodology with materials selection only late in the design process needs to be changed. Especially when new materials with unusual performance characteristics are needed, the design engineer must be in close contact with materials characterisation and processing right from the beginning in order to achieve optimal materials selection and design. Some of these interactions are depicted in the schematic of Figure 1.

The following sections focus on the way in which a materials property profile is drawn up, and the interactions between design, processing and materials characterisation necessary for an optimal design with the most promising materials.

2. THE MATERIAL PROPERTY PROFILE

One of the crucial points for materials selection is the definition of a material property

profile derived from the envisaged function and operating conditions of the component under consideration. Generally a differentiation between materials indices (e.g. specific strength and stiffness in light weight design) which optimise specific design performance objectives (e.g. maximum strength at minimum weight), and constraints (like maximum load, allowable deflections, particular dimensions, working temperature etc.) is made [Ashby, 1992a]. Some of the constraints are go- no go criteria, for example a working temperature capability of 400°C will exclude most polymers *a priori*. The materials indices are treated as discriminators between those materials that meet all of the constraints. Rare are the cases where one single materials index has to be optimised. Often different indices are contradictory and compromise has to be struck, which is nearly always the case when physical performance and cost have to be brought together. The task of materials selection is then to find the material which fulfils all the constraints while presenting an optimal profile with respect to the various performance objectives expressed in form of materials indices.

The definition of objectives and constraints is not as straight forward as it may seem from the discussion so far. Often it is difficult to tell constraints and objectives apart. What is a constraint in one design, may be an objective in another. Much depends on a precise definition of the function and working conditions of the component. However, this precise definition is difficult in the early stages of design. As a result, constraints are frequently drawn up more from habit than necessity (e.g. a certain minimum strength and toughness), and this may exclude some otherwise promising material candidates *a priori*.

From this short description it becomes clear that materials selection is sensitive with respect to the definition of both objectives and constraints. Frequently certain minimum or maximum numerical values are set which have to be met. However, it is questionable to reject a material which has a testified working range up to 380°C if 400°C has been specified and the material performs best in all other criteria. This example shows that the setting of absolute constraints may present an unnecessary innovation barrier. A first requirement for materials selection must therefore be to restrict absolute (hard) constraints to a minimum in order to keep the mind open for all materials that have a close but not perfect match with the desired performance profile. The aim is therefore the definition of target values for most materials indices, and for the constraints—the definition of fuzzy constraints, so to say. How a candidate material can be best selected will be subject of the following sections. Before, the material property profile for the turbine blade of a gas turbine shall be considered in order to illustrate the way in which material selection enters design.

Case study—part 1: a material property profile for the turbine blade of a gas turbine

The gas turbine is one of the key subsystems of the jet engine with great influence on its overall performance. If we want to redesign the jet engine as a whole, and the gas turbine in particular, our analysis needs to be based on the market need. However, this market need is not as straight forward as in the case of simple consumer goods, because the jet engine is not directly bought by the end user. It is bought by an airline which uses the engine in conjunction with an aircraft to offer a service at its customers—the passengers. The main interests of the end user are relatively simple—safety, low cost, comfort and good service. Only the first two of these needs are directly relevant for the jet engine. However, several further factors are also important, arising from government and airport regulations. These are, for instance restrictions on certain emissions, especially NO_x, and on noise emissions, and act as design constraints.

Concerning the design of the next generation of a jet engine, these rather vague market needs take more concrete forms, because in the sales negotiations of the jet engine manufacturer with the airliner, the specifications of the next generation of jet engines are precisely fixed. The task of the design team is to meet these specifications, which fix engine attributes like

- Thrust
- Specific fuel consumption
- Overall weight
- Ease of maintenance
- Life of the engine
- Life of key components like the turbine blades, which influences both safety and maintenance intervals
- Noise and NO_x emissions
- Price

All of the above attributes translate into specific performance needs for the gas turbine. However, with regard to long term innovation it is simpler to identify the two key driving forces in the jet engine. They are:

- Reduction of cost. This concerns the running cost—much of it in form of fuel consumption—which lies at around 70% of the overall running cost, and the capital cost, that is the cost of the jet engine itself, which is about 30% of the overall cost of an aircraft.

- Maximum possible safety.

To give an example of how important specific fuel consumption is: a gain of one percent point would result in annual savings of the order of 1 million dollars for each of the major airlines [Forster, 1986, p. 189]. Let us now examine how the two driving forces listed above translate into performance objectives for the gas turbine, and in particular the turbine blade, and identify the main material indices and constraints required to meet these objectives.

- Specific fuel consumption is very important for cost. With respect to the gas turbine, it is mainly determined by maximum turbine entry temperature and the blade tip speed [Rolls-Royce, 1986]. Concerning turbine entry temperature, a long-term goal is a blade material *temperature capability* of 2000°C and beyond. Blade tip speed is limited by the *specific strength* of the blade material, as has been illustrated by Ashby [1992a, p. 80 ff.] in the case of a high flow fan for a vacuum cleaner. Note, though, that it is linked to the rotational speed of the compressor and cannot be fixed independently. Another performance limiting factor is the tolerance between blades and casing, which leads to losses due to leaks in the air flow. High *specific stiffness*, a low *thermal expansion coefficient* and high *creep resistance* are probably the main material property targets here. Other design variables are the aerodynamic *shape* of the blades, their *surface finish*, and their *trail edge radius*.
- An indirect but important running cost factor is the *weight* of the blades, because a reduction in blade weight has a knock-on effect. This is independent of the turbine entry temperature. Lower weight of the blade, measured in grams, will make a weight reduction in the disk holding the blades possible, perhaps also in the shaft transmitting the power to the compressor, and ultimately in the pins fixing the engine to the wings, and the wings themselves. This can substantially increase the power to weight ratio and thus the payload and profitability of the aircraft. The driving force to lower weight is therefore considerable. Even more weight, and money, could be saved through materials with higher temperature capability, if they can make the omission of part of the complex cooling system possible.
- The importance of the capital cost of the engine itself means a turbine design must not substantially increase cost. This cost includes material cost, machining and assembly cost.
- The second condition listed above, safety, is important for any jet engine producer because sales are quite sensitive to this issue. For the turbine blades this means they must be *damage tolerant*, which is equivalent to the development of subcritical damage before failure. Much of this damage tolerance must be effective at room

temperature, because the risk for the equipment is highest while it is being handled for instance during maintenance. The damage must be able to survive until the next maintenance check, and it must be detectable by methods of *non-destructive testing*.

This list is far from complete and shows the complexity of designing a gas turbine. The importance for the overall engineering system, the jet engine, is considerable. It is evident, that a key to increasing the efficiency of the jet engine are the temperature capability and specific strength of the turbine blade materials. Ceramic materials are currently the only material class which can combine these features, and large efforts have been made to introduce them into the gas turbine [Devendra, 1990]. Of all ceramic materials, ceramic matrix composites are the only ones which have the potential to fulfil the additional requirement of damage tolerance. However, the hurdles for their introduction in the gas turbine are still high. This will be further discussed below.

3. MATERIAL PROPERTY PROFILES AND DESIGN

The previous section has described and illustrated the way in which a property profile can be established. At the conceptual design phase, this profile may be quite crude, and may have to be refined and completed in further iterations. Nevertheless, any set of material indices and constraints with target values allocated to them can serve as a basis for screening available materials and making a preliminary selection. A computerised materials data bank is best suited for this task. At the conceptual level the Cambridge Materials Selector can serve this function [Cebon and Ashby, 1992].

The result is a set of materials which fulfil the requirements of the performance profile. However, rare are the cases when an ideal material candidate appears, most have one or several severe draw-backs. For example, high physical performance targets nearly always result in high cost. And sometimes, no appropriate material which fulfils all requirements is found. In such a case, a natural approach is to revise the design concept and with it the property profile.

Value analysis

One of the well-known methods used to revise a design concept is value analysis [Dieter, 1991]. All functions of a given component are analysed with respect to their contribution to the overall value of the system and the satisfaction of the underlying market need. This may lead to a critical revision of the required material property profile, e.g. by allocating different functions to separate components, or by using different

materials in one component. A classical example for the latter case is the separation of required surface characteristics like wear resistance and hardness, and bulk characteristics which are not as stringent, but where better machinability and thus a softer material would considerably lower manufacturing cost. A simple solution is the application of coatings or of surface heat treatments after manufacture of such a component.

Matching property profiles

Another approach for finding the appropriate material to fulfil the needs of a particular design concept is to think over carefully all targets for material indices, and the constraints, and relax targets and especially hard constraints wherever possible. However, going through all the targets and constraints and questioning their value may be tedious and long. A more efficient methodology would be useful.

A better approach is to find one or several materials which match the target profile closely and look most promising for the design, and try to revise those constraints or targets which are not met by the particular candidate material(s).

Are these targets really indispensable for the function of the component? Can they be relaxed by changing the design of the component itself or that of other components in the system? If shape restricts the selected material, can the shape be adapted to a feasible one for the chosen material? Is the constraint necessary for bulk or surface properties?

In a way, this is value analysis targeted on a specific material. Let us give an example how this methodology can lead to an innovative design concept in the case of the gas turbine.

Case study—part 2: matching property profiles between SiC-SiC and the turbine blade

The case study of the previous section has given an outline of the material performance objectives for the turbine blades of future gas turbines. At first glance, ceramic matrix composites look like the ideal candidates with respect to the main required material properties—even currently available silicon carbide reinforced silicon carbide (SiC-SiC) looks promising with a *temperature capability* up to 1400°C, an excellent *specific stiffness*, low *thermal expansion coefficient*, and good *creep resistance*, respectable *specific strength*, and an acceptable *room temperature toughness*—all in comparison to the nickel-based superalloys currently used (Table 1).

COMPARISON OF PROPERTIES		
	SiC-SiC[a,b]	Ni-based Superalloy[c]
Density (g/cm^3)	2.5	7.9
Modulus (GPa)	230	214
Specific modulus ($GPa/(g/cm^3)$)	92	27
Tensile strength (MPa)	250	1300
Specific tensile strength ($MPa/(g/cm^3)$)	100	165
Usable (matrix cracking/yield) strength (MPa)	100	800
Specific usable strength ($MPa/(g/cm^3)$)	40	100
Usable compressive (onset of damage/yield) strength (MPa)	300	800
Specific usable compressive strength ($MPa/(g/cm^3)$)	120	100
Fracture toughness ($MPa\ m^{1/2}$)	30	>100
Temperature capability °C	1400	950
Oxidation resistance	up to 1400°C	protection needed
Coefficient of thermal expansion ($10^{-6}\ K^{-1}$)	3	12
Thermal diffusivity ($10^{-6}\ m^2 s^{-1}$)	12	-
Fatigue resistance	good	acceptable
Creep resistance	good	acceptable
Thermal shock resistance	good	good
Impact resistance	?	good

a. Supplier's data; b. Lackey and Starr[1990]; c. Ashby and Jones [1986].

Table 1. Approximate properties of SiC-SiC and nickel based superalloys.

The one fundamental drawback of ceramic matrix composites is that toughness—an indispensable requirement for its aerospace application—is linked to a high amount of damage prior to failure. High toughness and a low threshold for the onset of this damage in the form of matrix cracking are fundamentally connected. To be effective, the threshold for the onset of matrix cracking needs to lie far below ultimate tensile strength, it is at about 40% in the case of SiC-SiC. And as soon as matrix cracks appear, gases of a hot, corrosive environment can penetrate into the interior of the mate-

rial and attack fibres as well as the fibre-matrix interface. Both are not oxidation resistant at the high working temperatures at which ceramics unfold their full potential. This leads to embrittlement in use. In other words, the potentially high toughness of ceramic matrix composites can only be used for stopping fast fracture. It cannot be used in fatigue and creep applications because any damage will quickly lead to embrittlement of the material in a high temperature oxidative environment. Much attention is currently directed towards this problem, solutions are sought especially by developing better fibres and temperature and oxidation resistant fibre-coatings to serve as the interface. Yet, a fundamental physical limit of protecting small diameter fibres exists: because of their high surface to volume ratio they will always be susceptible to embrittlement under oxidative attack. Effective and reliable component coatings—another option—do not yet seem to be in reach. In consequence, if used in high-temperature applications, the design stress for a ceramic matrix composite like SiC-SiC will have to be below the matrix cracking stress [Raj, 1993]. This imposes a serious restriction on the application of ceramic matrix composites to hot section structural components, because their usable specific strength falls far below that of currently used superalloys (Table 1).

The other main drawback of today's ceramic matrix composites is cost. At a price of up to £10,000 per kilogram for SiC-SiC any application has to lead to a substantial improvement in performance to justify the high expenditure. However, much of this high price is due to the high development cost of the material at a very low volume of sales. A long term limit for the price is seen at a much more reasonable £300 per kilogram, double the current price of carbon-carbon composites which are produced by the same method [P.J. Lamicq, private communication]. Alternative processing routes like liquid melt oxidation may bring the price down even further.

Table 1 also reveals a very promising property of SiC-SiC, that of its specific usable compressive strength. Already today it is above that of nickel-base superalloys. As a result of the work presented elsewhere [Kaute and Ashby, 1994], it is known how subcritical damage in compression develops. Most of it emanates from internal macropores, so that, contrary to tensile matrix microcracking, no path into the specimen is created for the hot corrosive gases. Moreover, should accidental matrix cracking occur, compressive stresses tend to close these cracks up and this will slow degradation down. So there is much to be said for the use of ceramic matrix composites like SiC-SiC in compression.

And there is yet another great advantage of ceramic matrix composites—their high potential for improvement. Currently used metals and intermetallics are being pushed to

their physical limits. This is achieved by applying state of the art materials science to its full—from precision alloying and control of crystalline structure to the projected use of fibre reinforcements. However, there are absolute physical limits at about 1200°C. Further scope for engine performance is gained by extensive cooling of the blades: at present this permits a maximum turbine entry temperature of 1500°C while the maximum temperature of the nickel-based superalloys in use is kept at 950°C. But also here, there are limits, and the design is very complicated.

In conclusion, the main advantage of ceramic matrix composites over bulk ceramics, damage tolerance, is not degradation resistant and brings down usable specific strength to uncompetitive levels. The question then is this: how can this weakness in the property profile of ceramic matrix composites be overcome by adapting the design?

4. REVISING THE DESIGN

Case study—part 3: a new design approach with two materials for two different functions

By analysing the working of a turbine blade, it can be seen that there are two main functions:

- The transmission of impulse from the hot corrosive gases (coming out of the combustion chamber) to the shaft in order to power the compressor.
- The safe retention of its own weight due to the high centrifugal forces stemming from high rotational speeds.

The first function does not imply high tensile stresses for the component. The principal mode of loading is bending, but the loads are low. Here, the potential advantages of ceramic matrix composites could be fully exploited.

It is the second function—withstanding the centrifugal force—which causes the main problems. A confinement ring designed to support the centrifugal forces exerted by the blades could solve the problem. This would mean that the two functions combined in the turbine blade would be separated and allocated to two different components, turbine blade and confinement ring, which would surround the shroud, already part of some current design solutions (Figure 2). While the turbine is in use, compressive stresses would build up in the blade, and thus exploit one of the competitive performance char-

acteristics of ceramic matrix composites.

One of the principal difficulties for such a design solution is to find a suitable material for the confinement ring which mainly has to have one quality: high tensile strength at low weight. The choice is practically independent from the choice of material for the turbine blade. It is at this point that the conceptual design method described by Ashby [1992a], can be helpful: the goal is to choose the best suitable material for a confinement ring, and than to check whether it could actually withstand the loads under current operational conditions. This then shows if the design approach is potentially feasible.

Good thermal conductivity, and a relatively high temperature resistance are also important design requirements. However, for the moment it will be assumed that the confinement ring can be protected from the immediate heat of the gases through a protective layer similar to that of the shroud in current turbine blade design, and can be sufficiently cooled to cope with the heat flow emanating from that shroud. Such secondary requirements can be part of a second step in conceptual design. The aim here is to find a material which is strong enough to contain ceramic matrix turbine blades under current operating conditions.

Case study—part 4: a new and independent materials selection

As a turbine is spun up, the stresses exerted on the confinement ring start building up, leading to a large hoop stress. This hoop stress is due to two contributions: the pressure exerted by the blades attached to it and the pressure due to its own mass. The contribution of the rotational weight of the confinement ring to hoop stress cannot be neglected because of the high rotational speeds of up to 10,000 rpm (for typical civil gas turbines). In other words, the mass of the confinement ring reduces the strength available for containing the turbine blades. An efficient confinement ring therefore has a high tensile strength at minimum weight. Think of it as a cylindrical ring of radius r thickness t, and width b. Assuming a small thickness t, the mass of the confinement ring is

$$M = \rho \cdot 2 \cdot \pi \cdot r \cdot b \cdot t \qquad (1)$$

where ρ is the density of the confinement ring material. The mass is the quantity we want to minimise.

TYPICAL GAS TURBINE WORKING CONDITIONS					
Turbines	ω (rpm)	T (K)	D (cm)	Number of Blades	Weight of Blade (g)
High Pressure	10,000	1522	65 - 87.5	102	227
Middle Pressure	6,500	1208	67.5 - 100	92 - 102	>227
Low Pressure	4,500	1068	67.5 - 110	92 - 102	>>227

Table 2. Typical data for working conditions of civil engine turbines.

Let us now analyse the stresses owing to the turbine blades. They push onto the ring due to centrifugal forces. Let us call f the centrifugal force exerted by one turbine blade. It is determined by the geometrical requirements of the turbine blade, the density of its material, as well as the working conditions of the turbine (Table 2 gives typical working conditions for a current civil aircraft jet engine). Taken together, the forces exerted by all n turbine blades lead to an average radial stress $\sigma_{tb,r}$ exerted on the inner surface of the confinement ring

$$\sigma_{tb,r} = \frac{n \cdot f}{2 \cdot \pi \cdot r \cdot b} \tag{2}$$

It in turn contributes with hoop stress $\sigma_{tb,h}$ due to the turbine blades to the overall hoop stress

$$\sigma_{tb,h} = \sigma_{tb,r} \cdot \frac{r}{t} = \frac{n \cdot f}{2 \cdot \pi \cdot b \cdot t} \tag{3}$$

The hoop stress due to centrifugal forces acting on the confinement ring is (again assuming a small thickness t)

$$\sigma_{cr,h} = \rho \cdot \omega^2 \cdot r^2 \tag{4}$$

where ω is the angular velocity of the turbine disk. The section bt of the confinement ring must be sufficient to carry the load due to both contributing factors. This means that the sum of the two stresses above (equations (3) and (4)) must not exceed the failure stress σ_f of the confinement ring material. In other words, the available stress σ_{use} for containing the turbine blades must be equal to

$$\sigma_{use} = \frac{\sigma_f}{S_f} - \rho \cdot \omega^2 \cdot r^2 = \frac{n \cdot f}{2 \cdot \pi \cdot b \cdot t} \tag{5}$$

where S_f is a safety factor. Eliminating the section bt between equations (1) and (5) leads to

$$M = \left(S_f \cdot n \cdot f\right)\left(\frac{r}{\left(\frac{\sigma_f}{\rho}\right) - S_f \cdot \omega^2 \cdot r^2}\right) \tag{6}$$

The first bracket contains the functional requirement that the load due to the turbine blades is safely supported. The second bracket contains the specified geometry, the working conditions of the turbine, as well as the material properties, neither of which can be separated mathematically (in this particular case). As can be seen, the best materials for minimising M in the confinement ring are those with high values of the material index P

$$P = \frac{\sigma_f}{\rho} \tag{7}$$

Any material chosen must fulfil the minimum requirement that it does not fail due to its own centrifugal forces

$$\frac{\sigma_f}{S_f} > \rho \cdot \omega^2 \cdot r^2 \tag{8}$$

Figure 3 shows a chart of strength versus density. Values of P correspond to a grid of lines of slope 1. One such line is shown at the value $P = 100\ kJ/kg$. Candidate materials with high values of P lie in the search region towards the top left. The best choice are engineering composites, particularly carbon fibre reinforced polymers (CFRP), because they combine high performance with high modulus, which is important for tolerances (Data for CFRP: Density–1.5 g/cm^3. Modulus–189 GPa. Strength–1050 MPa [Weeton *et al.*, 1992]).

In the next section we will analyse, whether carbon fibre reinforced polymers as currently available would be suitable for supporting ceramic matrix composite turbine blades under the current working conditions and geometrical specifications of a typical high pressure gas turbine (see Table 2). Of course, it is not assumed that carbon fibre reinforced polymers will actually be used in this application. What could be used is a

strong, stiff fibre, perhaps carbon, probably ceramic, which is embedded in a light, temperature resistant matrix to transfer shear loads in case of single fibre failure. Carbon carbon may be an option using the right fibres. Such a material would probably have to be tailor made. As data are difficult to come by, carbon fibre reinforced polymer data are used to show feasibility with respect to the principal requirement, sufficient tensile strength.

Case study—part 5: verifying practicability under current operating conditions

In a first very simple approach we will assume that the design of the blades has the following form (Figure 2):

- The turbine blade has a similar shape to that of its present day counterparts. However, the conventional—and bulky—fir tree arrangement for fixing the blades to the disk can be avoided, because the weight of the blade is supported by the confinement ring.
- The blades lead into a cylindrical ring section of ceramic matrix composite which shields the actual confinement ring from the hot gases, evenly distributes the centrifugal forces onto it and serves for fixing the position of the blades. We will call it a shroud because it is similar in shape to the shroud of current turbine blades.

Let us first calculate the pressure exerted by ceramic matrix composite turbine blades on the confinement ring under current operating conditions (Table 2). There are two separate contributions—acting at different radial distances: the stresses exerted by the blade itself with mass m_{blade} and mean radial distance $\bar{r}_{blade}$ and those of the shroud with mass m_{shroud} and radial distance r (taken to be the same as that of the confinement ring. The two parts exert the force

$$f = m_{blade} \cdot \omega^2 \cdot \bar{r}_{blade} + m_{shroud} \cdot \omega^2 \cdot r \qquad (9)$$

Taking the dimensions of the turbine blade to be the same as those of a present-day turbine blade, the mass of the blade can be estimated as

$$m_{blade} = \rho_{cmc} \cdot l \cdot b_{blade} \cdot t_{blade} \qquad (10)$$

where l is the length (100 mm), b_{blade} the width (35 mm) of the turbine blade—slightly larger than the width b of the confinement ring—and t_{blade} is a reasonable mean thickness (3 mm). The values given in the brackets are those taken in the calculations which

follow. Taking the density of commercial SiC-SiC (Table 1), this leads to a mass of $m_{blade} = 31.0$ g. Similarly, the mass of the ring section can be estimated as

$$m_{shroud} = \rho_{cmc} \cdot \frac{2 \cdot \pi \cdot r}{n} \cdot b \cdot t_{shroud} \qquad (11)$$

where n is the number of turbine blades, t_{shroud} is the thickness of the ring section. This leads to a mass of $m_{shroud} = 7.4$ g. Note that the overall mass per turbine blade (38.4 g) is far below that of a current design (up to 225 g)—so the potential for weight savings, discussed in Section 2, is substantial.

Inserting the masses calculated from equations (10) and (11) in equations (9), then (2) leads to an average radial stress of 20.9 MPa acting on the confinement ring. This, transformed into hoop stress (equation (3)), must be equal to the available strength σ_{use} (equation (5)). The maximum compressive stress in the turbine blade is 130 MPa—far below its usable compressive strength.

Let us now calculate the available strength σ_{use}, choosing commercially available unidirectional CFRP as our preliminary confinement ring material. The hoop stress due to centrifugal forces acting on the confinement ring is equal to 335 MPa. Taking a safety factor S_f of 1.1, this leads to an available strength of 619 MPa—always assuming operating conditions similar to those of a current gas turbine. The resulting required thickness of the confinement ring is 15.1 mm, which is still a reasonable value—taking into account that there is scope for improvement. Figure 4 shows the technical realisation of such a design with a carbon-carbon confinement ring.

It has to be emphasised again, that the calculations above based on carbon fibre reinforced plastics are only used to see whether the proposed new gas turbine design is conceptually feasible—taking into account only the principal performance index, strength over density. Clearly, such a confinement ring is feasible. A more refined approach, taking into account further design requirements must now follow.

Thus far, it has been shown that the considerable obstacles in the way of an introduction of ceramic matrix composites into the gas turbine can be reduced by rethinking the current design functions of turbine blades and isolating the one function that prevents their application—the task to withstand their own centrifugal forces. In a second step, it has been shown that such a design is potentially feasible.

Case study—part 6: finding a confinement ring material to cope with further performance requirements

Although the shroud may initially shield off the direct heat of the hot gases from the confinement ring, the confinement ring will ultimately have to cope with a combination of relatively high working temperature and/or very high heat conduction—implying cooling from outside (of course without diminishing strength to weight ratio). The by far best solution seems to be a material that can take very high temperatures and does not need any cooling at all. A solution to this material selection/composites design problem seems to be the second major design hurdle. The material taken in the design shown in Figure 4, carbon-carbon, may be a viable solution if the confinement ring can be protected from attack by the hot corrosive gases.

Other questions also have to be addressed, for instance:

- The influence of differences in stiffness and thermal expansion coefficients between the ceramic matrix composite turbine blade and the confinement ring material and the importance of radial expansion due to the high centrifugal forces and changes in temperature.
- Differences in stress between inner and outer surface of confinement ring, influence of thermal gradients.
- The influence of possible stress concentrations at the T-junction between blade and shroud on the stress distribution inside the confinement ring (this would mean a non-evenly distributed-or sinusoidal—radial stress acting on the inner surface of the confinement ring)
- The importance of oxidation resistance at the relatively high working temperatures, and possibly choice of suitable coatings.

Many of these questions have already been solved in similar engineering applications and the answers need not be invented anew. Others may lead to further performance indices that have to be maximised. Ashby [1992c] has set out a methodology of how to find possible composites candidates if currently available materials do not have the required combination of properties. It may well turn out that the project has to be abandoned after this stage because a suitable material to fulfil all the criteria can neither found nor potentially created. This would still be a relevant result.

In the last section of this report, the importance of materials processing and materials characterisation in the design process is discussed and illustrated in the last part of our case study.

5. THE ROLE OF MATERIALS PROCESSING AND CHARACTERISATION

So far, only one way to tackle the mismatch between the required materials profile and that of a promising candidate material has been discussed—changing the design and with it the required material profile to fit that of existing materials. Usually, this is the most economic approach.

Another possibility to tackle the mismatch between required material property profile and the actual properties of a candidate material is to adjust its properties due to better processing and microstructural control of a material. This is especially true for new materials with unusual profiles which need development to maturity in any case. An example is the better control of interface properties in ceramic matrix composites, or the adaptation of reinforcement architecture and lay-up of composites in general [see for instance Ige, 1992]. It is, however, always an expensive way of designing and the potential gains in must therefore be substantial.

New materials face yet another challenge. Because of their more complex internal structure, new and unusual failure modes may occur, which are sometimes only detected after a product has been launched. This danger is especially acute in the case of fibre reinforced composites with their directional properties. Their off-axis mechanical properties must therefore be established beforehand and converted into design specifications, especially if they are to be used in safety sensitive applications.

In both of the tasks described above, improvement of materials and definition of design specifications, the materials engineer is needed for translating understanding on the atomistic and microstructural level into information that can be used by both design and processing. The property profile used by the design engineer necessarily consists of condensed information, ideally easily measurable quantities like stiffness, strength, and toughness, or relations between fatigue life, creep rates, stress levels and temperature. With the creation of a new material, the goal of the materials engineer is not only to supply these condensed data, but to understand their origin, so as to be able to predict behaviour under changed circumstances, like different stress states, and temperature range. The best models are based on an understanding of the underlying physical mech-

anism and relate macroscopic behaviour to constituent material properties [Ashby, 1992c]. Advances in formalising the way in which both design and materials engineers can be brought to speak the same language have been achieved recently by Ashby [1992a]. However, in the case of processing, the basis for common understanding between materials and processing engineers is still limited and needs to be developed.

Case study—part 7: generating the required knowledge for ceramic matrix composites–outline of a testing programme

By introducing an innovative design approach using a separate confinement ring around the blades, we have taken away the main obstacle concerning the application of ceramic matrix composites as gas turbine blade materials—the high sensitivity to tensile loading. It has been shown that the main design constraint on the confinement ring—the high tensile loading in a rotational field—can be overcome in principle. From this point on a design solution for the two now separated functions—transmitting the load on one side, and containing the weight on the other—can be pursued independently. We have laid out the conceptual path for designing the confinement ring in the last section. Let us now take a look at further steps concerning ceramic matrix composites.

The task of the materials engineer is to analyse the modes of loading in the new potential design and find critical failure-prone points. The goal is, first, to generate understanding of material behaviour under these critical, loads, and—perhaps—show ways to improve material behaviour under these loads (via better processing). The second goal is to engender a clear set of criteria within which the designer can safely design his component. Also in this case, not all has to be invented anew. Polymer matrix composite blades of a similar shape have now for long been contemplated for application in the compressor, some of the results may well apply here.

Finite element analysis may be the right tool for identifying critical loads at this preliminary stage. A good understanding of purely aerodynamic requirements concerning the optimum aerofoil shape of the turbine blade (without having to serve for the secondary function of bringing in its own cooling air) is necessary prior to such a FE analysis.

Notwithstanding, intuition may help identify the main modes of loading even without elaborate numerical analysis. Figure 5 shows a schematic of the proposed turbine blade including the shroud and identifies potential trouble spots. They would lead to the following three areas of principal interest for materials testing and modelling:

- Mode I and mixed mode delamination in curved section of the T-bent.
- Compression, and compressive bending, possibly buckling. The gas pressure acting on the blade both at start and during cruise conditions would have to be known.
- Influence of contact stresses at the blade root where the forces are transmitted to the shaft (possible shear failure).
- Note that the design does not necessitate either notches or bolts, which are a known source of trouble in design with brittle materials.

Knowledge about the high temperature behaviour under these same conditions is also vital, because the use of ceramic matrix composites without cooling was one of the important assumptions in evaluating their innovation potential in the jet engine (e.g. use at 1250°C).

6. CONCLUSIONS

The discussion of design in this report is not claimed to be original, it rather reflects current thinking—taken up because of important consequences for ceramic matrix composites, which are illustrated in a case study. Materials selection is shown to play an important role in design and, if used properly, can be used as a tool for guiding innovation. A methodology has been sketched out generating options for innovation based on promising candidate materials. It has been applied to the gas turbine and a novel conceptual approach for its design to make advantageous use of ceramic matrix composites has been outlined—exploiting their good compressive characteristics and their light weight. It shows that best design results can be achieved in an interactive process between processing, materials selection and design. This does not lead to an automated selection of the best material and design, but is one of several tools in the hand of the engineer, pointing the way, but not relieving him of the actual creative act of design.

Acknowledgements—One of us (DK) wishes to acknowledge financial support through a Brite Euram bursary from the Commission of the European Union.

REFERENCES

ASHBY, M.F. (1992a) Materials selection in mechanical design. Pergamon Press, Oxford, England, E.U.

ASHBY, M.F. (1992b) Physical modelling materials problems. *Materials Science and Technology*, **8** [2] pp. 102-111.

ASHBY, M.F. (1992c) Criteria for selecting the components of composites. *Acta Metallurgica et Materialia*, **41** [5] pp. 1313-1335.

ASHBY, M.F., JONES, D.R.H. (1986) Engineering materials 2. Pergamon Press, GB-Oxford, E.C.

CEBON, D., ASHBY, M.F. (1992) Computer-based materials selection for mechanical design. In *Computerization and Networking of Materials Databases,* **ASTM STP 1140**, American Society for Testing and Materials, Philadelphia.

DEVENDRA, K., SYERS, G. (1990) Application of Engineering Ceramics in Gas Turbines. In *Advanced Engineering with Ceramics, British Ceramic Proceedings*, MORRELL, R. editor, The Institute of Ceramics, Shelton, Stoke-on-Trent, England, European Union, pp. 93-112.

DIETER, G.E. (1991) Engineering design, a materials and processing approach, second edition. McGraw-Hill Inc., New York.

FITZER, E. (1987) The future of carbon-carbon composites. *Carbon*, 25 [2] pp. 163-190.

FORSTER, R. (1986) Innovation. Summit Books, New York.

IGE, D.O. (1992) Rationalisation of design with composite materials. *PhD Thesis*, Cambridge University Engineering Department.

KAUTE, D.A.W., ASHBY, M.F. (1994) Compressive failure of ceramic matrix composites. *Cambridge University Engineering Department Report*, **CUED/C-MATS/TR 213**.

LACKEY, W.J., STARR, T.L. (1990) Fabrication of fiber-reinforced ceramic composites by chemical vapor infiltration: processing, structure and properties. In *Fiber Reinforced Ceramic Composites, Materials, Processing and Technology*, MAZDIYASNI, K.S. editor, Noyes Publications, Park Ridge, New Jersey, U.S.A., pp. 397-450.

RAJ, R. (1993) Fundamenteal research in structural ceramics for service near 2000° C. *Journal of the American Ceramic Society*, **76** [9] pp. 2147-2174.

ROLLS-ROYCE PLC (1986) The jet engine. The Technical Publications Department, GB-Derby.

WEETON, J.W., PETERS, D.M., THOMAS, K.L. (1992) Engineer's guide to composite materials. American Society for Metals, Metals Park, Ohio.

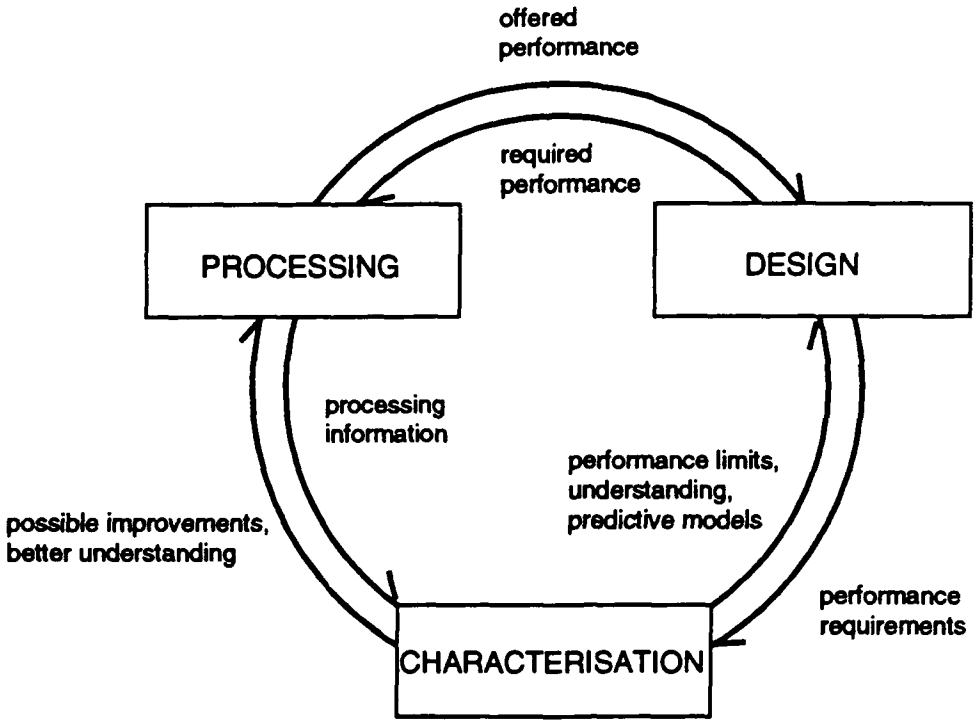

Figure 1. Interactions necessary between processing, characterisation and design for designing with new materials like ceramic matrix composites.

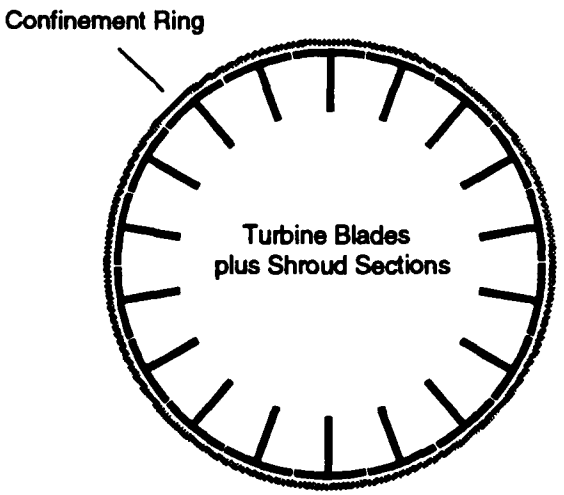

Figure 2. Schematic of proposed geometry for turbine blades and confinement ring.

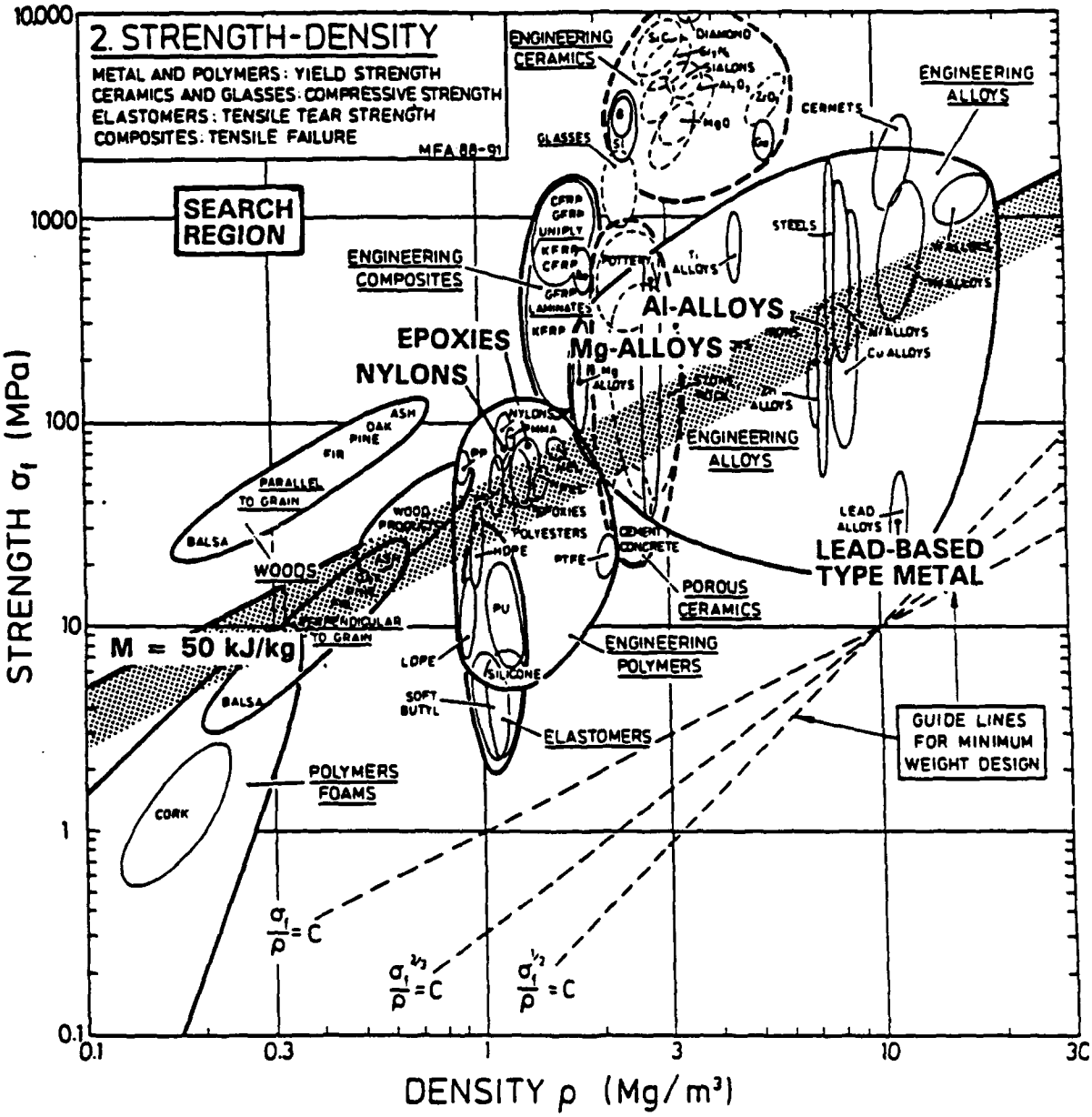

Figure 3. Materials for a confinement ring. *Engineering composites are the best choice* [Ashby, 1992b].

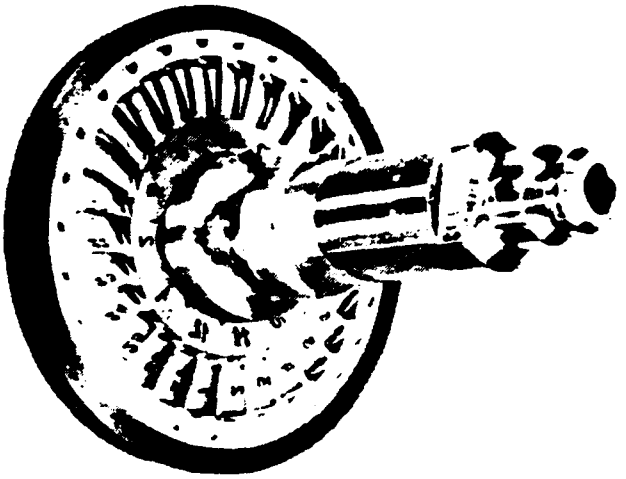

Figure 4. Turbine rotor made with ceramic blades and a carbon-carbon confinement ring to withstand tensile stresses [Fitzer, 1987].

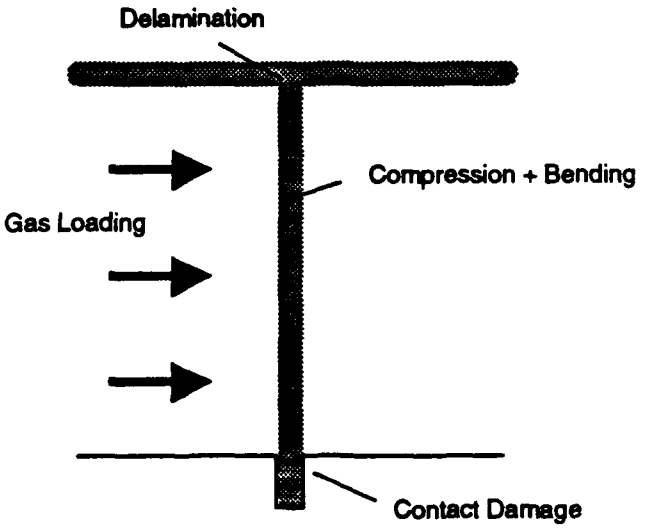

Figure 5. Intuitive analysis of critical loading and failure modes in new turbine blade design.

Composites Science and Technology **51** (1994) 63–74

ELASTO-PLASTIC ANALYSIS OF INTERFACE LAYERS FOR FIBER-REINFORCED METAL-MATRIX COMPOSITES

I. Doghri* & F. A. Leckie

Department of Mechanical and Environmental Engineering, University of California, Santa Barbara, California 93106, USA

(Received 15 October 1990; revised version received 13 July 1993; accepted 10 August 1993)

Abstract

The mismatch of coefficients of thermal expansion (CTE) of fiber and matrix in metal-matrix composites reinforced with ceramic fibers induces high thermal stresses in the matrix. Elasto-plastic analyses—with different degrees of simplification and modeling—show that an interface layer with a sufficiently high CTE can reduce the tensile hoop stress in the matrix substantially.

Keywords: thermal mismatch, metal matrix, ceramic fiber, coating layer, elasto-plasticity

NOTATION

E_j, ν_j	Young's modulus, Poisson's ratio of j
f	Fiber
j	f, l, m
l	Layer
m	Matrix
R_j	External radius of j
t_l	Layer thickness ($=R_l - R_f$)
α_j	CTE of j
ΔT	Change in temperature
λ_j, μ_j	Lamé coefficients of j ($\lambda_j = E_j\nu_j/(1-2\nu_j)(1+\nu_j)$ and $\mu_j = E_j/2(1+\nu_j)$)
σ_{yj}	Initial yield stress in j
σ_{rj}	Radial stress (σ_{rr}) in j
$\sigma_{\theta j}$	Hoop stress ($\sigma_{\theta\theta}$) in j
σ_{zj}	Axial stress (σ_{zz}) in j

In the same manner, we define the total strains, ε_{rj}, $\varepsilon_{\theta j}$, ε_{zj} and the plastic strains, ε^p_{rj}, $\varepsilon^p_{\theta j}$, ε^p_{zj}

$\tilde{\sigma}_j$	von Mises equivalent stress in j

In the same way that the von Mises equivalent stress is related to the distortion energy, a so-called damage equivalent stress[1] is related to the total elastic energy and defined by

$$\sigma_j^* = \tilde{\sigma}_j\left[\frac{1}{2}(1+\nu_j) + 3(1-2\nu_j)\left(\frac{\sigma_{Hj}}{\tilde{\sigma}_j}\right)^2\right]^{1/2}$$

where $\sigma_{Hj} = (\sigma_{rj} + \sigma_{\theta j} + \sigma_{zj})/3$.

1 INTRODUCTION

Metal-matrix composites reinforced with ceramic fibers have attractive properties for engineering applications. These composites have a high strength associated with a low density. The ceramic fibers provide high-temperature resistance, and their brittle behavior is compensated to some extent by the ductility of the metal matrix. However, because ceramics have a lower coefficient of thermal expansion (CTE) than metals, a thermal mismatch is induced which is responsible for thermal stresses in composites subjected to a change in temperature.

Cracking in the matrix has been observed after cooling down from processing temperature to room temperature for brittle matrix materials.[2] It has been proposed that the insertion of an adequate interface layer between the fiber and the matrix can reduce the tensile stresses in the matrix to a level which prevents matrix cracking.

Some numerical parametric studies[3,4] suggested that the optimum interface layer should have a CTE between those of the matrix and the fiber, a low Young's modulus, and a high thickness. However, these conclusions were based on a questionable optimization procedure[3] or on limited numerical results and did not provide an understanding of the problem.

Recently, Jansson and Leckie[5] conducted a simplified analysis assuming a rigid fiber and a very thin layer. They concluded that a compensating layer with a sufficiently high CTE can reduce the residual stresses in the matrix significantly. A complete elastic analysis was performed by Doghri *et al.*,[6] who proposed an optimization procedure offering a window of candidate layer materials. Both of these

*Present address: Centric Engineering Systems Inc., 3801 East Bayshore Road, Palo Alto, CA 94303, USA.

Composites Science and Technology 0266-3538/94/$07.00

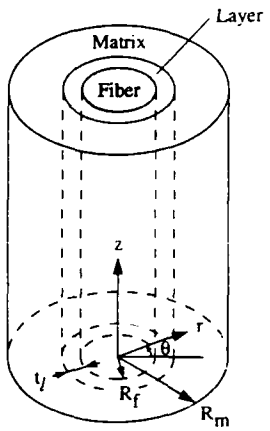

Fig. 1. Concentric three cylinder model.

studies showed that, while the hoop stress in the matrix can be reduced substantially, the axial stress in the matrix is less affected by a layer. They also pointed out that plastic yielding may occur in the interface layer.

In this paper, plasticity is taken into account. The first part of the study is based on a three cylinder model, isolating one fiber with an interface layer and a matrix layer (Fig. 1). The interface layer is elastic-perfectly plastic while the matrix is considered elastic. The material properties are assumed to be constant. A remarkably accurate and efficient numerical procedure is developed allowing one to have approximations of the stress and strain fields everywhere in the composite.

In the second part of this study, finite element computations are performed. Both the coating layer and the matrix are assumed to be elastic-perfectly plastic, and the temperature dependence of material properties is taken into account. The accuracy of the three cylinder model is investigated by studying the response of a unit cell of a hexagonal array of the fibrous composite.

2 DEVELOPMENT OF THE STRESS–STRAIN ANALYSIS FOR THE AXISYMMETRIC THERMAL PROBLEM

The composite is not subjected to transverse loading and the outer surface of the compound cylinder is traction free. The thermal loading is assumed to be axisymmetric with respect to the z-axis, so that the displacement in the transverse plane is radial: $U_l(r)$. The fibers are long and the strain and stress distributions are uniform in the z-direction except at the end regions which are not studied here. A generalized plane strain assumption is made so that $\varepsilon_{zl} = \text{constant} = e_z$. The other strains are given by

$$\varepsilon_{rl} = \frac{dU_l}{dr} \quad \text{and} \quad \varepsilon_{\theta l} = \frac{U_l}{r} \tag{1}$$

and there are no shear strains.

One may use the finite element method (FEM) to solve this problem. But the problem being axisymmetric, we developed a procedure which proved to be more flexible and much less computer time consuming than the FEM. The interface layer is assumed to be elasto-plastic while the fiber and the matrix are elastic.

A solution is sought which will satisfy the following conditions:

C1. The constitutive equations everywhere.
C2. The exact static equilibrium equations with no body forces in (f) and (m).
C3. The continuity of displacement between (f) and (l): $U_f = U_l$ at $r = R_f$.
C4. The continuity of displacement between (l) and (m): $U_l = U_m$ at $r = R_l$.
C5. The stress-free condition at the outer surface of the compound cylinder $\sigma_{rm} = 0$ at $r = R_m$.
C6. A weak form of the equilibrium in (l).
C7. The axial equilibrium condition associated with a generalized plane strain assumption:

$$\int_0^{R_m} \sigma_{zl} r \, dr = 0$$

This solution will not satisfy the continuity of the stress vector at the interfaces (f)/(l) and (l)/(m). However, it was found that the resulting jumps are small. The iterative procedure adopted is the following:

(i) Propose ΔT, a temperature increment.
(ii) For the given ΔT, propose $\Delta\varepsilon_l$, a total strain increment in (l).
—Find stresses in (l) which satisfy the constitutive equations.
—Find strains and stresses in (f) and (m) which satisfy the conditions (C1)–(C5).
—Check the satisfaction of the equilibrium conditions (C6) and (C7).
• If not satisfied, propose another $\Delta\varepsilon_l$, i.e. go to (ii).
• If satisfied, for this temperature, the solution is accepted.

2.1 Equilibrium conditions C6 and C7

Any form of the total strain field in (l) may be assumed, provided that the compatibility conditions are satisfied. For example, the following form of the total strains in (l) is assumed

$$\varepsilon_{rl} = c_l - \left(\frac{R_l}{r}\right)^2 d_l$$
$$\varepsilon_{\theta l} = c_l + \left(\frac{R_l}{r}\right)^2 d_l \tag{2}$$

where c_l and d_l are dimensionless constants to be found.

We have used the present form of the total strain field in (l) because it has a uniform trace; hence, the stress field has a uniform trace also, and since $\varepsilon_{zl} = \text{constant} = e_z$, the stresses σ_{zl} are likely to be almost uniform, which is in agreement with a generalized plane strain assumption.

The radial displacement is given as

$$U_l = c_l r + d_l \frac{R_l^2}{r} \tag{3}$$

The local equations of equilibrium in the layer are

$$\frac{\partial \sigma_{rr}}{\partial r} + \frac{1}{r}(\sigma_{rr} - \sigma_{\theta\theta}) = 0 \tag{4}$$

We use the same procedure by which the local equations of equilibrium are extended to the global ones. We multiply the local equations by U_l and integrate over the domain of (l) to give:

$$\int_{R_l}^{R_l} \left[\frac{\partial \sigma_{rr}}{\partial r} + \frac{1}{r}(\sigma_{rr} - \sigma_{\theta\theta})\right] \left[c_l r + d_l \frac{R_l^2}{r}\right] r \, dr = 0 \quad (\forall c_l, \forall d_l) \tag{5}$$

This is a weak form of the equilibrium because we assume only a particular form of the displacement field.

The previous equation leads to the following system

$$\begin{aligned} &\int_{R_l}^{R_l} \left[r^2 \frac{\partial \sigma_{rr}}{\partial r} + r(\sigma_{rr} - \sigma_{\theta\theta})\right] dr = 0 \\ &\int_{R_l}^{R_l} \left[R_l^2 \frac{\partial \sigma_{rr}}{\partial r} + \frac{R_l^2}{r}(\sigma_{rr} - \sigma_{\theta\theta})\right] dr = 0 \end{aligned} \tag{6}$$

By partial integration this system becomes

$$\begin{aligned} &-\int_{R_l}^{R_l} r(\sigma_{rr} + \sigma_{\theta\theta}) \, dr + [r^2 \sigma_{rr}]\Big|_{R_l}^{R_l} = 0 \\ &\int_{R_l}^{R_l} \frac{R_l^2}{r}(\sigma_{rr} - \sigma_{\theta\theta}) \, dr + R_l^2 [\sigma_{rr}]\Big|_{R_l}^{R_l} = 0 \end{aligned} \tag{7}$$

This system represents the equilibrium condition C6. To this system we add the equilibrium condition in the z-direction, i.e. the equation of condition C7. Since σ_{zf} and σ_{zm} are uniform, we obtain:

$$\int_{R_l}^{R_l} \sigma_{zz} r \, dr + \frac{R_l^2}{2}\sigma_{zf} + \left(\frac{R_m^2}{2} - \frac{R_l^2}{2}\right)\sigma_{zm} = 0 \tag{8}$$

We now define the following matrix notations, which are suitable for numerical analysis:

$$\{\varepsilon_l\} = \begin{Bmatrix} \varepsilon_{rl} \\ \varepsilon_{\theta l} \\ e_z \end{Bmatrix} = \begin{bmatrix} 1 & -(R_l/r)^2 & 0 \\ 1 & (R_l/r)^2 & 0 \\ 0 & 0 & 1 \end{bmatrix} \times \begin{Bmatrix} c_l \\ d_l \\ e_z \end{Bmatrix} = [\mathbf{B}]\{\mathbf{e}\} \tag{9}$$

and

$$\{\sigma_l\} = \begin{Bmatrix} \sigma_{rl} \\ \sigma_{\theta l} \\ \sigma_{zl} \end{Bmatrix} \tag{10}$$

The system of three equations of equilibrium can be rewritten as:

$$\{\mathcal{F}(\mathbf{e})\} = \int_{R_l}^{R_l} [\mathbf{B}]^T \{\sigma_l\} r \, dr + \begin{Bmatrix} R_l^2 \sigma_{rf} - R_l^2 \sigma_{rm}(R_l) \\ R_l^2 \sigma_{rf} - R_l^2 \sigma_{rm}(R_l) \\ \dfrac{R_l^2}{2}\sigma_{zf} + \left(\dfrac{R_m^2}{2} - \dfrac{R_l^2}{2}\right)\sigma_{zm} \end{Bmatrix} = \{\mathbf{0}\} \tag{11}$$

where the superior index T denotes transposition. Note that all the stresses in (f) are uniform and that the axial stress in (m) is also uniform (see Ref. 6 for details).

The stresses $\{\sigma_l\}$ are implicit functions of $\{\mathbf{e}\}$ and the stresses σ_{rf}, σ_{zf}, σ_{rm} and σ_{zm} are explicit functions of $\{\mathbf{e}\}$. Then, the last system is a nonlinear system of three equations and three unknowns, which are the components of $\{\mathbf{e}\}$. This method looks like a FEM with *only three* DOFs (degrees of freedom), which makes it a particularly efficient tool.

2.2 Iterative approximation of the total strain increment in the layer

Keeping the previous notation, we have $\{\Delta\varepsilon_l\} = [\mathbf{B}]\{\Delta\mathbf{e}\}$.

For the starting iteration, $\{\Delta\mathbf{e}\} = \{\mathbf{0}\}$ is proposed.

If the solution found in (f), (l) and (m) does not satisfy the equilibrium equations, Newton's method is used in order to propose another approximation for $\{\Delta\mathbf{e}\}$:

$$\{\mathcal{F}(\mathbf{e})\} + \left[\frac{\partial \mathcal{F}}{\partial \mathbf{e}}\right]\{\mathbf{C}_c\} = \{\mathbf{0}\} \tag{12}$$

where $\{\mathbf{C}_c\}$ represents a 'correction' to $\{\Delta\mathbf{e}\}$ and

$$\left[\frac{\partial \mathcal{F}}{\partial \mathbf{e}}\right] = \int_{R_l}^{R_l} [\mathbf{B}]^T [\mathbf{H}][\mathbf{B}] r \, dr + [\mathbf{h}^*] \tag{13}$$

Here $[\mathbf{H}]$ is the 'tangent' matrix at each point of (l). If perfect plasticity associated with a von Mises yield surface is considered, and if the material properties are assumed not to change with temperature, then the 'continuum' expression for $[\mathbf{H}]$ during plastic yielding is (see Doghri[7] for details)

$$[\mathbf{H}] = [\mathbf{E}_l] - \frac{3\mu_l}{\sigma_{el}^2}\{\sigma_l^D\}\{\sigma_l^D\}^T \tag{14}$$

where $\mathbf{E}_l$ is the Hooke's operator in (l) and σ_l^D is the deviatoric stress in (l).

The details of the computation of the matrix $[\mathbf{h}^*]$

are given in Appendix 1. This matrix takes into account the fact that the external loads applied to (l) are not given as constant, but depend on $\{\mathbf{e}\}$. Its matrix form is as follows:

$$[\mathbf{h}^+] = \begin{bmatrix} R_f^2 \frac{\partial \sigma_{rf}}{\partial c_l} - R_l^2 \frac{\partial \sigma_{rm}}{\partial c_l}(R_l) & R_f^2 \frac{\partial \sigma_{rf}}{\partial d_l} - R_l^2 \frac{\partial \sigma_{rm}}{\partial d_l}(R_l) & R_f^2 \frac{\partial \sigma_{rf}}{\partial e_z} - R_l^2 \frac{\partial \sigma_{rm}}{\partial e_z}(R_l) \\ R_f^2 \frac{\partial \sigma_{rf}}{\partial c_l} - R_l^2 \frac{\partial \sigma_{rm}}{\partial c_l}(R_l) & R_f^2 \frac{\partial \sigma_{rf}}{\partial d_l} - R_l^2 \frac{\partial \sigma_{rm}}{\partial d_l}(R_l) & R_f^2 \frac{\partial \sigma_{rf}}{\partial e_z} - R_l^2 \frac{\partial \sigma_{rm}}{\partial e_z}(R_l) \\ \frac{R_f^2}{2}\frac{\partial \sigma_{zf}}{\partial c_l} + \left(\frac{R_m^2}{2} - \frac{R_l^2}{2}\right)\frac{\partial \sigma_{zm}}{\partial c_l} & \frac{R_f^2}{2}\frac{\partial \sigma_{zf}}{\partial d_l} + \left(\frac{R_m^2}{2} - \frac{R_l^2}{2}\right)\frac{\partial \sigma_{zm}}{\partial d_l} & \frac{R_f^2}{2}\frac{\partial \sigma_{zf}}{\partial e_z} + \left(\frac{R_m^2}{2} - \frac{R_l^2}{2}\right)\frac{\partial \sigma_{zm}}{\partial e_z} \end{bmatrix} \quad (15)$$

2.3 Stresses in the layer

Once $\{\Delta\mathbf{e}\}$ is given, one knows $\{\Delta\varepsilon_l\}$ everywhere in (l). The stresses (and the plastic strains) are then computed by integrating the constitutive equations. An elastic predictor/plastic corrector method is used. A fully implicit integration scheme is adopted and the nonlinear equations are solved by a Newton method. It can be shown that the corrections are found explicitly (see Doghri[7] for details).

3 NUMERICAL RESULTS OF THE THERMAL PROBLEM

We first recall and compare elastic solutions developed by Benveniste *et al.*[8] and Doghri *et al.*[6] Benveniste *et al.* evaluated local fields and the overall thermomechanical properties of composites reinforced by coated fibers or particles. The local strain fields in each inclusion of phase (f) or (l) were assumed to be equal to the fields in a single inclusion of phase (f) or (l) which is embedded in an unbounded matrix (m) and subjected to remotely applied strains which are equal to the average strain in the matrix, and also to a uniform temperature change. After deriving general results for arbitrary shapes, the authors applied their method to a three-phase composite containing coated cylindrical fibers of circular cross-section. They considered six loading cases, the sixth one corresponding to a uniform change in temperature. Doghri *et al.* considered this last case only. However, they tried to solve the optimization problem: for a given (f) and a given (m), find the best (l). In other words, which material properties and what thickness should (l) have in order to minimize the tensile stresses in (m)?

For the thermal loading case, the solutions in Refs 8 and 6 both satisfy the following conditions:

- Linear thermoelastic behavior in (f), (l) and (m).
- Static equilibrium equations with no body forces in (f), (l) and (m).
- Continuity of the displacement at the interfaces (f)/(l) and (l)/(m).
- Continuity of the stress vector at the interfaces (f)/(l) and (l)/(m).
- Zero stress vector at the outer boundary.
- Generalized plane strain assumption.

Since for the thermal loading case, Refs 6 and 8 both make the same assumptions, one expects that they would obtain the same results in that case. This was checked numerically with the data corresponding to system 4 of Table 1 in Ref. 8.

Fiber: SiC		
$E_f = 431$ GPa	$\nu_f = 0.25$	$\alpha_f = 4.86 \times 10^{-6}$/°C
Matrix: titanium aluminate		
$E_m = 96.5$ GPa	$\nu_m = 0.30$	$\alpha_m = 9.25 \times 10^{-6}$/°C
Layer: Carbon		
$E_l = 34.48$ GPa	$\nu_l = 0.20$	$\alpha_l = 3.3 \times 10^{-6}$/°C

The volume fractions for (f), (l), and (m) were 0.4, 0.0107 and 0.5893, respectively. They were simulated using the following data:

$$R_f = 69.57\ \mu\text{m} \quad R_m = 110\ \mu\text{m} \quad t_l = 0.92\ \mu\text{m}$$

Figure 2 shows the stress distributions in (f), (l) and (m) obtained by the method developed in Ref. 6. It is *identical* to Fig. 8 in Ref. 8.

3.1 Coating layer candidates

The elastic studies of Jansson and Leckie[5] and Doghri *et al.*[6] proved that a compensating layer with a sufficiently high CTE can significantly reduce the residual stress in the matrix. They also showed that the hoop stress in the matrix can be reduced substantially but the axial stress in the matrix is less affected by a layer. These studies pointed out that the stresses in the layer can be high enough to induce plastic yielding.

A practical optimization procedure is proposed in Ref. 6 offering a list of candidate layer materials. According to this procedure, silver, for example, seems to be a good candidate since the matrix stresses are considerably reduced; but one may question the selection of silver as a coating material. The answer

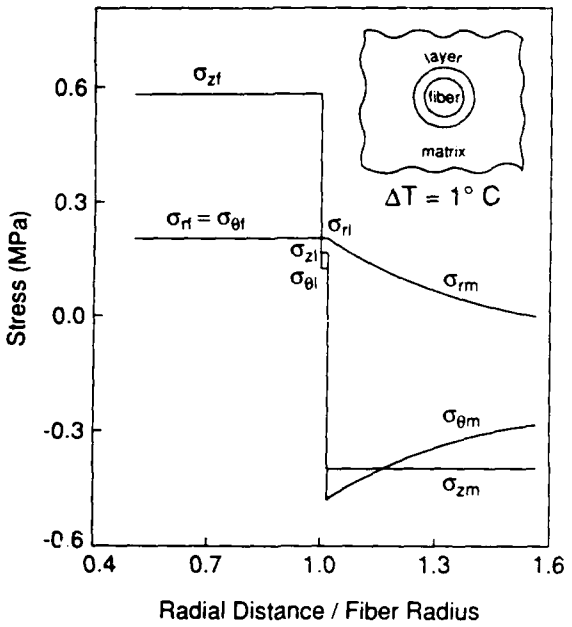

Fig. 2. Stress distributions in System 4 (Table 1) of Ref. 8 in the case of a uniform temperature increase of 1°C. Fiber: SiC; layer: carbon; matrix: titanium aluminate.

is that this material has properties that are needed for this concept to work. In a real situation, however, several other considerations have to be taken into account (cost, chemical compatibility, melting point, etc.). One may use the optimization charts in Ref. 6 to choose other coating materials. For example, copper seems to be a possible candidate.

In this section, we will study the effect of a plastic layer to complement the previously obtained elastic results. All the numerical applications which follow correspond to a monotonic cooling of $\Delta T = -800°C$. The results are always compared to a *reference* case (fiber and matrix, without layer).

3.2 Constant material properties

The fiber and the matrix are defined by the following data:

Fiber: SiC (SCS6)

$E_f = 360$ GPa $\quad \nu_f = 0{\cdot}17 \quad \alpha_f = 4{\cdot}9 \times 10^{-6}$/°C $\quad R_f = 70\ \mu$m

Matrix: Ti3Al

$E_m = 75{\cdot}2$ GPa $\quad \nu_m = 0{\cdot}25 \quad \alpha_m = 11{\cdot}7 \times 10^{-6}$/°C $\quad \sigma_{ym} = 380$ MPa $\quad R_m = 110\ \mu$m

The radii R_f and R_m are related to the fiber volume fraction, C_f, by

$$C_f = \left(\frac{R_f}{R_m}\right)^2 \approx 40{\cdot}5\%$$

The Ag layer is defined by the following data:

$E_l = 71$ GPa, $\nu_l = 0{\cdot}30$, $\alpha_l = 25{\cdot}9 \times 10^{-6}$/°C,

$\sigma_{yl} = 100$ MPa, $t_l = 10\ \mu$m.

In this section, both (f) and (m) are elastic, while (l) is elastic-perfectly plastic. The results were found using the method developed in Section 2.

3.2.1 Monotonic cooling

The final values of stresses and strains at the inner radii are given in Tables 1 and 2, respectively. Analyzing the results, the following observations can be made:

- The reductions of the maximum $\bar{\sigma}_m$ or σ_m^* are important: $\bar{\sigma}_m/\bar{\sigma}_{ref} \cong 0{\cdot}50$ if (l) is elastic and $\bar{\sigma}_m/\bar{\sigma}_{ref} \cong 0{\cdot}55$ if (l) is plastic.
- The reduction of the maximum $\sigma_{\theta m}$ is even more important: $\sigma_{\theta m}/\sigma_{\theta ref} = 0{\cdot}37$ if (l) is elastic and $\sigma_{\theta m}/\sigma_{\theta ref} = 0{\cdot}22$ if (l) is plastic.
- When the layer is added, all the stresses in (m) are reduced; however:
- Without the layer, the maximum tensile stress in the matrix is the hoop stress: $\sigma_{zm}/\sigma_{\theta m} = 0{\cdot}84$

Table 1. Stresses in the compound cylinder after monotonic cooling

		σ_{rr}	$\sigma_{\theta\theta}$	σ_{zz}	$\bar{\sigma}$	σ^*
Stresses in matrix						
Reference	σ(MPa)	−187·3	422·2	372·0	597·5	602·5
(l) elastic	σ(MPa)	−50·4	163·5	292·8	300·2	320·3
	σ/σ_{ref}	0·27	0·37	0·79	0·50	0·53
(l) plastic	σ(MPa)	−30·4	98·7	342·0	327·5	342·7
	σ/σ_{ref}	0·16	0·22	0·92	0·55	0·57
Stresses in layer						
(l) elastic	σ(MPa)	−260·1	1529·5	1437·1	1745·2	1901·7
(l) plastic	σ(MPa)	−36·3	64·9	62·5	100·0	98·8
Stresses in fiber						
Reference	σ(MPa)	−187·3	−187·3	−546·5	359·3	536·0
(l) elastic	σ(MPa)	−260·1	−260·1	−780·5	520·4	763·8
(l) plastic	σ(MPa)	−43·6	−43·6	−417·8	374·2	406·6

Stresses are given at the inner radii of (m) and (l). Stresses are uniform in (f).
Constant material properties.

Table 2. Strains in the compound cylinder after monotonic cooling

		ε_{rr}	$\varepsilon_{\theta\theta}$	ε_{zz}
Strains in matrix				
Reference	$\varepsilon(\%)$	−1·45	−0·41	−0·52
(l) elastic	$\varepsilon(\%)$	−1·15	−0·80	−0·58
(l) plastic	$\varepsilon(\%)$	−1·12	−0·90	−0·50
Thermal strains: $\alpha_m \Delta T = -0{\cdot}94\%$				
Strains in layer				
(l) elastic	$\varepsilon(\%)$	−3·69	−0·41	−0·58
(l) plastic	$\varepsilon(\%)$	−5·27	−0·38	−0·50
	$\varepsilon^p(\%)$	3·10	1·60	1·50
Thermal strains: $\alpha_l \Delta T = -2{\cdot}07\%$				
Strains in fiber				
Reference	$\varepsilon(\%)$	−0·41	−0·41	−0·53
(l) elastic	$\varepsilon(\%)$	−0·41	−0·41	−0·58
(l) plastic	$\varepsilon(\%)$	−0·38	−0·38	−0·50
Thermal strains: $\alpha_l \Delta T = -0{\cdot}39\%$				

Strains are given at the inner radii of (m) and (l). Strains are uniform in (f). Constant material properties.

- With the layer, σ_{zm} exceeds the maximum $\sigma_{\theta m}$ and this trend is accentuated when (l) is plastic: $\sigma_{zm}/\sigma_{\theta m} = 1{\cdot}79$ if (l) is elastic and $\sigma_{zm}/\sigma_{\theta m} = 3{\cdot}46$ if (l) is plastic.
- Since the stresses in (l) are reduced when plastic yielding is considered, there must be an increase in stresses elsewhere. We see that the stresses in (f) decrease and that σ_{rm} and $\sigma_{\theta m}$ decrease; then it is to be expected that σ_{zm} increases, by comparison with the elastic layer situation.
- One observes in Table 1 that the matrix does not yield. So the assumption which was made in Section 2 (elastic matrix) is legitimate.
- We have mentioned at the beginning of Section 2 that our solution does not satisfy the continuity of the stress vector at the interfaces (f)/(l) and (l)/(m). But the following results show that the jumps in σ_{rr} are not too large:

$$\begin{cases} \sigma_{rf}(R_1) = -43{\cdot}57\ \text{MPa} \\ \sigma_{rl}(R_1) = -36{\cdot}27\ \text{MPa} \end{cases} \qquad \begin{cases} \sigma_{rl}(R_1) = -36{\cdot}03\ \text{MPa} \\ \sigma_{rm}(R_1) = -30{\cdot}41\ \text{MPa} \end{cases}$$

- Table 2 gives the strains in (f), (l) and (m). It can be noticed that even when (l) is considered elastic, the strains in (l) are important (due to high thermal strains). When we consider plasticity in (l), the trend becomes accentuated (because the stresses in (l) are reduced).

3.2.2 Sensitivity study

(a) With all other parameters kept constant, the influence of t_l was studied. Figure 3 shows that if $(t_l/R_1) \leq 0{\cdot}11$, the two cases (l) elastic and (l) plastic give the same values for the maximum $\bar{\sigma}_m$. If $(t_l/R_1) > 0{\cdot}11$, then for a given t_l, the maximum $\bar{\sigma}_m$ is higher when (l) is plastic. The same conclusions apply

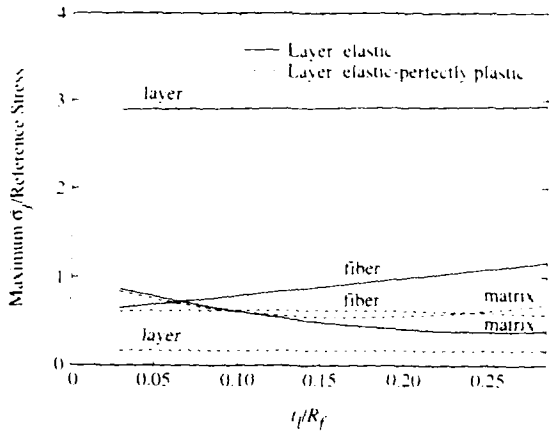

Fig. 3. Influence of the layer thickness on the maximum von Mises equivalent stress in the matrix.

for σ_m^*. The best reductions in the maximum $\bar{\sigma}_m$ are:

$$\frac{\bar{\sigma}_m}{\bar{\sigma}_{ref}} \cong$$

$$\begin{cases} 0{\cdot}5 \text{ when (l) is plastic, and it is obtained for } \dfrac{t_l}{R_1} \cong 0{\cdot}16 \\ 0{\cdot}4 \text{ when (l) is elastic, and it is obtained for } \dfrac{t_l}{R_1} \cong 0{\cdot}23 \end{cases}$$

(b) With all other parameters kept constant, the influence of σ_{yl} was studied. Since $\bar{\sigma}_l = \sigma_{yl}$ (perfect plasticity), one knows that if σ_{yl} increases then the stresses in (l) increase, and one expects that this may reduce the stresses in (m). Figure 4, however, shows that the value of σ_{yl} does not affect $\bar{\sigma}_m$. This result leads to another interesting prediction: if the temperature dependence of properties is taken into account, plasticity in (l) will indeed occur sooner (since σ_{yl} will be smaller) but (m) will not yield and the results will not change too much. This will be checked in Section 3.3.1.

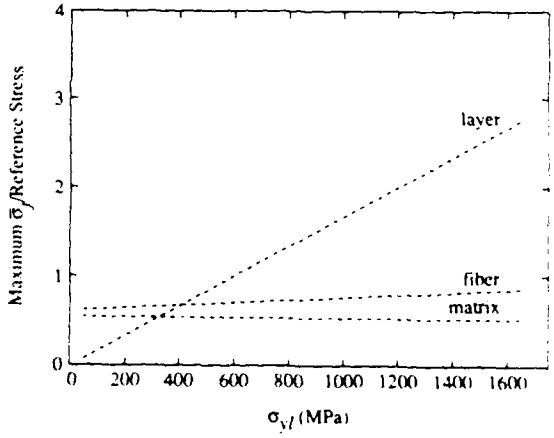

Fig. 4. Influence of the layer yield stress on the maximum von Mises equivalent stress in the matrix.

3.3 Temperature-dependent material properties

In this part of the study, the temperature dependence of the material properties is taken into account.

The following materials were considered:

Fiber: SCS6 Matrix: Ti_3Al Layer: Ag

The material properties were compiled from Refs 9–13. The data are given in Figs 5(a)–5(d). The fiber is elastic and the layer and the matrix are assumed to be elastic-perfectly plastic. Finite element computations were performed with ABAQUS.[14] A generalized plane strain assumption was made. More details about the boundary conditions and the modeling are given in Appendix 2.

3.3.1 Concentric cylinder models

The FE mesh used for the three (or two) cylinder models is given in Fig. 6a. The temperature variation of the stresses in (m) at the inner radius are given in Figs 7(a) and 7(b). The final values of the stresses and the strains at the inner radii of each material are given in Tables 3 and 4. These results show that:

- In the reference case, (m) yields. The layer prevents yielding from occurring in (*m*).
- The layer reduces the maximum $\sigma_{\theta m}$ significantly, while σ_{zm} is increased:

$$\frac{\sigma_{\theta m}}{\sigma_{\theta ref}} = 0{\cdot}23 \quad \text{and} \quad \frac{\sigma_{zm}}{\sigma_{zref}} = 1{\cdot}42$$

It is interesting to note that we made the same remarks in Section 3.2.1 when the material properties were assumed to be constant. One also notices that the strain values are almost identical to those obtained in that section. We may conclude that, from a qualitative point of view, taking into account plasticity

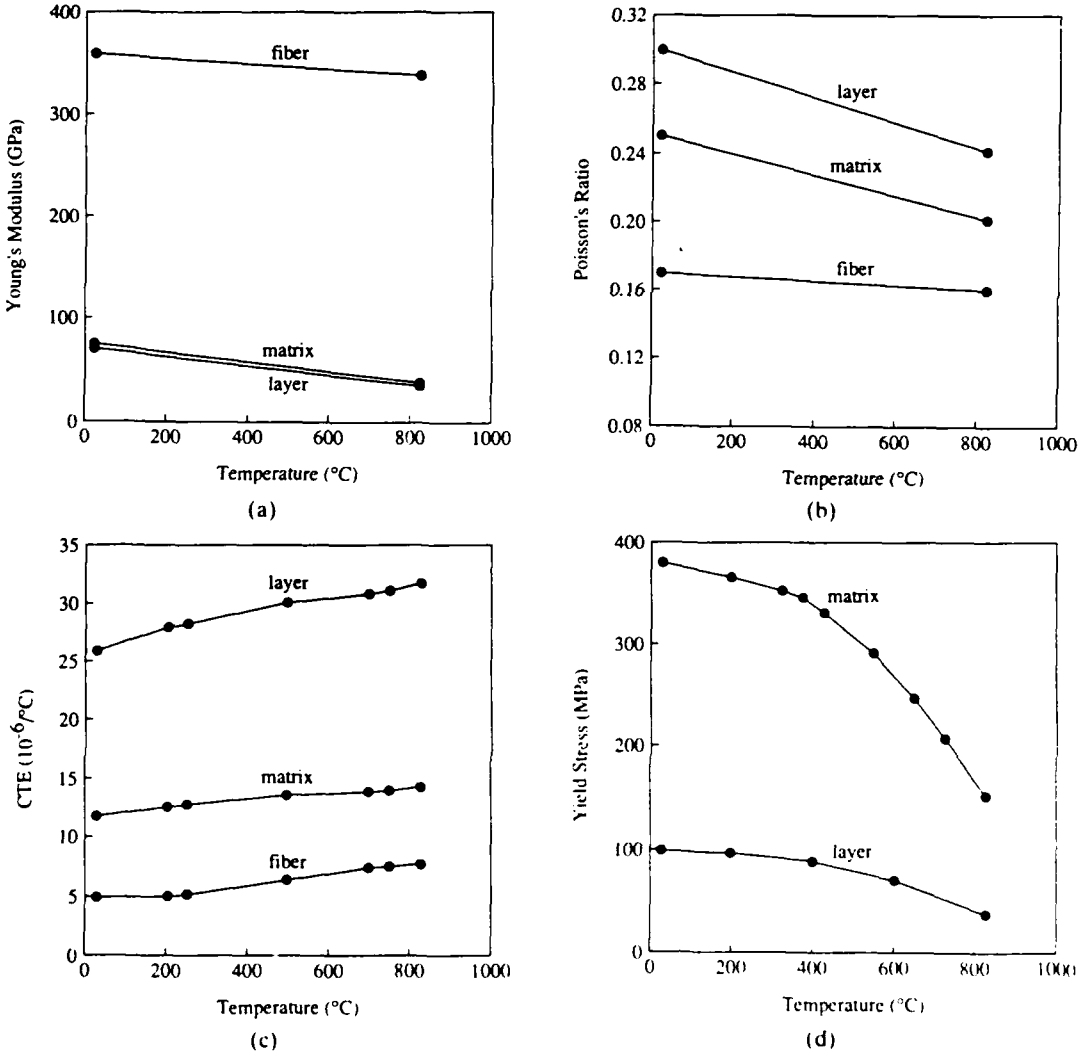

Fig. 5. Temperature dependence of the material properties. Fiber: SiC (SCS6); layer: Ag; matrix: Ti_3Al. (a) Young's modulus; (b) Poisson's ratio; (c) CTE; (d) initial yield stress.

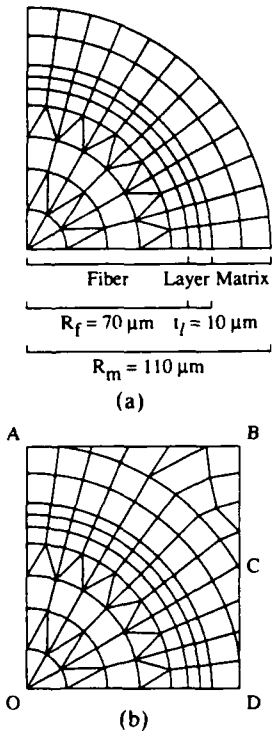

Fig. 6. Finite element meshes: (a) three cylinder model; (b) unit cell of a hexagonal array.

in the layer is more important than the temperature dependence of the material properties.

3.3.2 Unit cell of a hexagonal array

The manufacture and testing of composite materials is demanding in time and effort so that there is special need for procedures that can help determine the macroscopic properties of the materials from the properties of the constituents. Success in this endeavor would mean that prediction of composite properties would bypass expensive and time-consuming manufacture and test procedures.

The so-called homogenization procedure is used to predict the macroscopic properties of the composite from the properties of the individual constituents.

The composite under consideration is composed of a hexagonal array of SCS6 fibers coated with the interface layer, in a Ti_3Al matrix (Fig. 8). A hexagonal array presents more symmetries than a square array. Taking into account the structure periodicity, the problem can be reduced, for symmetric loading, to the study of a single unit cell (ODBA), shown in Fig. 8, with the appropriate boundary conditions, as detailed in Appendix 2. The F E mesh for the cell is shown in Fig. 6(b).

The stress and strain values were found to be almost identical to those obtained for the three cylinder model (presented in Section 3.3.1). Thus, for

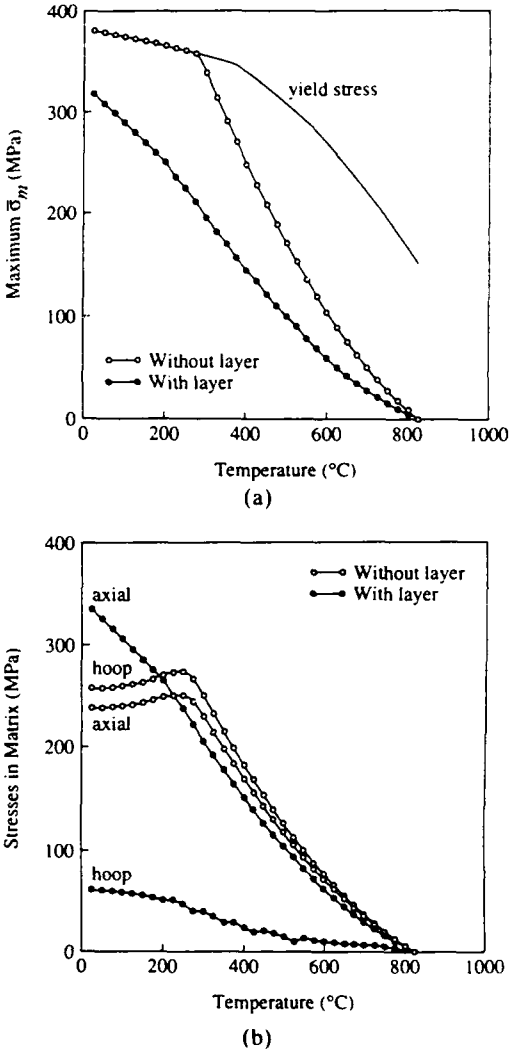

Fig. 7. Temperature variation of the stresses at the inner radius of the matrix cylinder: (a) von Mises equivalent stress; (b) tensile stresses.

axisymmetric problems, the three cylinder model seems to be a simple but accurate representation. However, with the unit cell, it will be possible to study the composite behavior under transverse mechanical loading since the three cylinder model is clearly not adequate for non-symmetric problems.

4 CONCLUSIONS

The optimization procedure proposed in Ref. 6 on the basis of an elastic study allows a choice of good candidate layer materials. The elasto-plastic analysis conducted here confirms that such interface layers can reduce the hoop stress and the von Mises equivalent stress in the matrix significantly. However, the axial stress in the matrix is less affected by a layer (and it may even increase). This implies that these layers

Table 3. Stresses in the compound cylinder after monotonic cooling

		σ_{rr}	$\sigma_{\theta\theta}$	σ_{zz}	$\bar{\sigma}$	σ^*
Stresses in matrix						
Reference	σ(MPa)	−130·8	261·7	235·4	380·0	377·7
(l) plastic	σ(MPa)	−15·43	61·82	335·0	317·5	329·3
	σ/σ_{ref}	0·10	0·23	1·42	0·83	0·87
Stresses in layer						
(l) plastic	σ(MPa)	−1·40	98·13	99·07	100·0	117·4
Stresses in fiber						
Reference	σ(MPa)	−159·7	−159·7	−503·7	344·0	491·3
(l) plastic	σ(MPa)	−41·18	−41·18	−426·7	385·5	415·8
	σ/σ_{ref}	0·26	0·26	0·85	1·12	0·84

Stresses are given at the inner radii of (m) and (l). Stresses are uniform in (f). Temperature-dependent material properties.

Table 4. Strains in the compound cylinder after monotonic cooling

Strains in matrix (%)	ε_{rr}	$\varepsilon_{\theta\theta}$	ε_{zz}	Accumulated plastic strain
Reference	−1·61	−0·437	−0·517	0·34
(l) plastic	−1·08	−0·961	0·506	0
Strains in layer (%)				
(l) plastic	−5·00	−0·594	−0·506	2·94
Strains in fiber (%)				
Reference	−0·405	−0·405	−0·517	
(l) plastic	−0·381	−0·381	−0·506	

Strains are given at the inner radii of (m) and (l). Strains are uniform in (f). Temperature-dependent material properties.

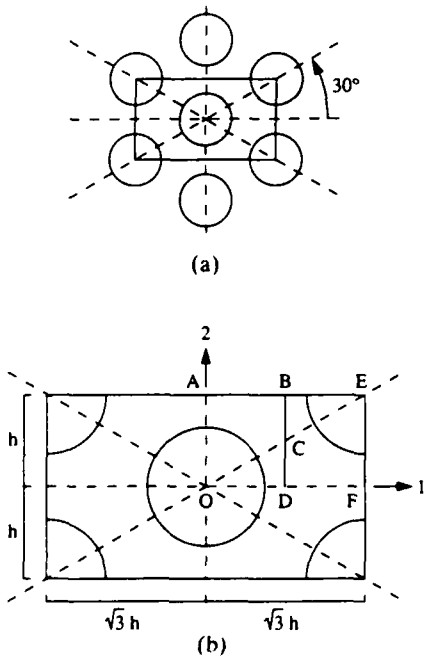

Fig. 8. Fibrous composite: (a) hexagonal array; (b) region of analysis. Unit cell parameter: $h = R_f(\pi/2C_1\sqrt{3})^{1/2} = 104.8\,\mu m$.

could be successful in composites where predominantly radial cracking is observed in the matrix. The interface layer should be ductile enough to sustain relatively high strains. It should also have a yield stress high enough to improve the range of shake down of the composite.

It appears that taking into account plasticity is much more important than the temperature dependence of the material properties. Comparison between the results given by the three cylinder model and a unit cell of a hexagonal array shows that for axisymmetric problems the concentric cylinder is a simple but accurate model.

ACKNOWLEDGEMENTS

The work was supported by a grant from the NASA-Lewis Research Center. The authors wish to express their gratidude to Dr Steve Arnold for the encouragement and support.

REFERENCES

1. Lemaitre, J. & Chaboche, J. L., *Mechanics of Solid Materials*. Cambridge University Press, Cambridge, 1990.

2. Brindley, P. K., Bartolotta, P. A. & MacKay, R. A., *Thermal and Mechanical Fatigue of SiC/Ti3Al + Nb*. 2nd HITEMP Review, NASA CP-10039, paper 52, 1989.
3. Ghosn, L. J. & Bradley, A. L., *Optimum Interface Properties for Metal Matrix Composites*. NASA TM-102295, 1989.
4. Caruso, J. J., Chamis, C. C. & Brown, H. C., *Parametric Studies to Determine the Effects of Compliant Layers on Metal Matrix Composite Systems*. NASA TM-102465, 1990.
5. Jansson, S. & Leckie, F. A., Reduction of thermal stresses in continuous fiber reinforced metal matrix composites with interface layers. *J. Comp. Mater.*, **26** (10) (1992) 1474–86.
6. Doghri, I., Jansson, S., Leckie, F. A. & Lemaitre, J., Optimization of coating layers in the design of ceramic fiber reinforced metal matrix composites. *J. Comp. Mater.* (in press).
7. Doghri, I., Fully Implicit integration and consistent tangent modulus in elasto-plasticity. *Int. J. Eng.* (in press).
8. Benveniste, Y., Dvorak, G. J. & Chen, T., Stress fields in composites with coated inclusions. *Mech. Mater.*, **7** (1989) 305–17.
9. Brindley, P. K., Draper, S. L., Nathal, M. V. & Eldridge, J. I., *Factors which Influence Tensile Strength of SiC/Ti3Al + Nb*. 2nd HITEMP Review, NASA CP-10039, paper 51, 1989.
10. Shafrik, R. E., Dynamic elastic moduli for the titanium aluminides. *Metall. Trans. A*, **8A** (June 1977) 1003–6.
11. Dicarlo, J. A., High temperature properties of CVD silicon carbide fibers. *Int. Conf. of Whisker-and Fiber-Toughened Ceramics*, Oak Ridge, TN, June 7–9, 1988.
12. Jansson, S., Deve, H. E. & Evans, A. G., The anisotropic mechanical properties of a Ti matrix composite reinforced with SiC fibers. *Metall. Trans. A*, **22A** (December 1991) 2975–84.
13. Boyer, H. E. & Gall, T. L., *Metals Handbook, Desk Edition*. ASM, Metals Park, Ohio, 1985.
14. ABAQUS, version 4.7. Hibbitt, Karlsson and Sorensen, Inc.
15. Ranaweera, M. P., Finite element analysis of a metal matrix composite under mechanical and thermal loading. Report, UC Santa Barbara, Department of Mechanical and Environmental Engineering, June, 1989.

APPENDIX 1: CONTRIBUTIONS OF (f) AND (m) TO THE RESIDUAL FORCE VECTOR AND INCREMENTAL STIFFNESS MATRIX (SECTIONS 2.1 AND 2.2)

Here, the fiber and the matrix are assumed to be elastic, their stress and strain fields are completely defined by the acknowledge of three constants: c_f, c_m, d_m (see Ref. 6).

Condition C3, i.e. the continuity of the displacement between (f) and (l), gives:

$$c_f R_f = c_l R_l + d_l \frac{R_l^2}{R_f} \Rightarrow c_f = c_l + \left(\frac{R_l}{R_f}\right)^2 d_l$$

The radial and longitudinal stresses in (f) are then:

$$\sigma_{rf} = 2(\lambda_f + \mu_f)c_f + \lambda_f e_z - (3\lambda_f + 2\mu_f)\alpha_f \Delta T$$
$$\sigma_{zf} = 2\lambda_f c_f + (\lambda_f + 2\mu_f)e_z - (3\lambda_f + 2\mu_f)\alpha_f \Delta T$$

Condition C4, i.e. the continuity of the displacement between (l) and (m), gives:

$$c_m R_l + \frac{R_m^2}{R_l} d_m = c_l R_l + d_l R_l \quad \Rightarrow$$
$$c_m + \left(\frac{R_m}{R_l}\right)^2 d_m = c_l + d_l$$

Condition C5, i.e. the stress free condition at $r = R_m$, gives:

$$2(\lambda_m + \mu_m)c_m + \lambda_m e_z - 2\mu_m d_m - (3\lambda_m + 2\mu_m)\alpha_m \Delta T = 0$$

This gives

$$d_m = \frac{\lambda_m e_z + 2(\lambda_m + \mu_m)(c_l + d_l) - (3\lambda_m + 2\mu_m)\alpha_m \Delta T}{2\mu_m + 2(\lambda_m + \mu_m)\left(\frac{R_m}{R_l}\right)^2}$$

and

$$c_m = c_l + d_l - \left(\frac{R_m}{R_l}\right)^2 d_m$$

Then, the radial and longitudinal stresses in (m) at $r = R_l$ are

$$\sigma_{rm} = 2(\lambda_m + \mu_m)c_m + \lambda_m e_z - 2\mu_m\left(\frac{R_m}{R_l}\right)^2 \times d_m - (3\lambda_m + 2\mu_m)\alpha_m \Delta T$$
$$\sigma_{zm} = 2\lambda_m c_m + (\lambda_m + 2\mu_m)e_z - (3\lambda_m + 2\mu_m)\alpha_m \Delta T$$

Computation of $[\mathbf{h}^+]$

The matrix $[\mathbf{h}^+]$ contains the partial derivatives of the stresses σ_{rf}, $\sigma_{rm}(R_l)$, σ_{zf} and σ_{zm} with respect to the components c_l, d_l and e_z of $\{\mathbf{e}\}$ (see Section 2.2).

- Fiber contribution

We have

$$\frac{\partial c_f}{\partial c_l} = 1, \quad \frac{\partial c_f}{\partial d_l} = \left(\frac{R_l}{R_f}\right)^2 \quad \text{and} \quad \frac{\partial c_f}{\partial e_z} = 0$$
$$\frac{\partial \sigma_{rf}}{\partial c_l} = 2(\lambda_f + \mu_f)\frac{\partial c_f}{\partial c_l}, \quad \frac{\partial \sigma_{rf}}{\partial d_l} = 2(\lambda_f + \mu_f)\frac{\partial c_f}{\partial d_l}$$
$$\frac{\partial \sigma_{rf}}{\partial e_z} = 2(\lambda_f + \mu_f)\frac{\partial c_f}{\partial e_z} + \lambda_f$$
$$\frac{\partial \sigma_{zf}}{\partial c_l} = 2\lambda_f \frac{\partial c_f}{\partial c_l}, \quad \frac{\partial \sigma_{zf}}{\partial d_l} = 2\lambda_f \frac{\partial c_f}{\partial d_l}$$
$$\frac{\partial \sigma_{zf}}{\partial e_z} = 2\lambda_f \frac{\partial c_f}{\partial e_z} + (\lambda_f + 2\mu_f)$$

• Matrix contribution
We have

$$\frac{\partial d_m}{\partial c_1} = \frac{2(\lambda_m + \mu_m)}{2\mu_m + 2(\lambda_m + \mu_m)\left(\frac{R_m}{R_1}\right)^2} = \frac{\partial d_m}{\partial d_1}$$

$$\frac{\partial d_m}{\partial e_z} = \frac{\lambda_m}{2\mu_m + 2(\lambda_m + \mu_m)\left(\frac{R_m}{R_1}\right)^2}$$

$$\frac{\partial c_m}{\partial c_1} = 1 - \left(\frac{R_m}{R_1}\right)^2 \frac{\partial d_m}{\partial c_1} = \frac{\partial c_m}{\partial d_1},$$

$$\frac{\partial c_m}{\partial e_z} = -\left(\frac{R_m}{R_1}\right)^2 \frac{\partial d_m}{\partial e_z}$$

$$\frac{\partial \sigma_{rm}}{\partial c_1} = 2(\lambda_m + \mu_m)\frac{\partial c_m}{\partial c_1} - 2\mu_m \times \left(\frac{R_m}{R_1}\right)^2 \frac{\partial d_m}{\partial c_1} = \frac{\partial \sigma_{rm}}{\partial d_1}$$

$$\frac{\partial \sigma_{rm}}{\partial e_z} = 2(\lambda_m + \mu_m)\frac{\partial c_m}{\partial e_z} - 2\mu_m\left(\frac{R_m}{R_1}\right)^2 \frac{\partial d_m}{\partial c_1} + \lambda_m$$

$$\frac{\partial \sigma_{zm}}{\partial c_1} = 2\lambda_m \frac{\partial c_m}{\partial c_1} = \frac{\partial \sigma_{zm}}{\partial d_1}$$

$$\frac{\partial \sigma_{zm}}{\partial e_z} = 2\lambda_m \frac{\partial c_m}{\partial e_z} + (\lambda_m + 2\mu_m)$$

APPENDIX 2: MODELING AND FINITE ELEMENT DISCRETIZATION

ABAQUS generalized plane strain elements CGPE5 and CGPE6 were used, two extra nodes (EX1 and EX2) were needed to impose the generalized plane strain condition. The node EX1 has one DOF representing the longitudinal displacement which is the increase in thickness of the model. The node EX2 takes care of the rotations at the end planes, and these are prescribed to be zero. A unit thickness is assumed.

(a) Two and three cylinder models

Because of the symmetry of the problem, only a quarter of the cross-section is considered. The dimensions and the mesh used are shown in Fig. 6(a). The normal displacements of the nodes of the two straight edges of the section in Fig. 6(a) are imposed to be zero. The two cylinder model (fiber and matrix) is simply obtained by saying that the layer material is identical to the matrix one.

(b) Unit cell

The composite is composed of a hexagonal array of SCS6 fibers coated with the layer, in a Ti_3Al matrix. The transverse section is given in Fig. 8. We adopt the same approach as in Ref. 15.

Edge effects will not be considered, and hence the analysis can be done using the theory of homogenization. We consider symmetric loading so that the edges of the unit cell as well as the axes O1 and O2, will remain straight during deformation. Hence only a quarter of the unit cell need to be considered for analysis, and this is taken to be the positive quadrant of the O1, 2 axes.

If this quarter cell (OFEA) is isolated and allowed to deform symmetrically, it will undergo displacements as shown in Fig. A1(a). The centerline DCB, about which the region is skew-symmetric, will displace as shown. If (u_1^C, u_2^C) are the displacements of C, (u_1^P, u_2^P) are the displacements of a point P on CB, and (u_1^Q, u_2^Q) are the displacements of a point Q on DC such that QC = CP, then:

$$u_1^C = u_2^C = 0$$
$$u_1^P + u_1^Q = 0$$
$$u_2^P + u_2^Q = 0$$

If this skew-symmetry is taken into account, only the half (ODBA) of the quarter cell need to be analyzed. The deformed shape of (ODBA) is shown in Fig. A1(b), after giving it a rigid body translation so that points in the side OD do not undergo u_2 displacements. In analyzing region ODBA, the boundary conditions to be used are:

(i) Along OD, $u_2 = 0$
(ii) Along OA, $u_1 = u_1^A$

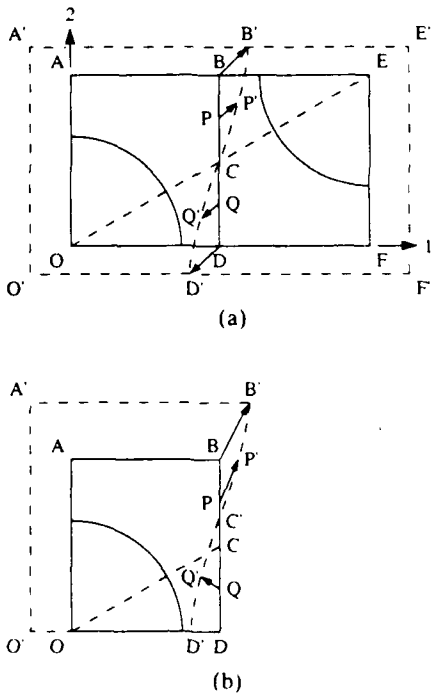

Fig. A1. Unit cell definition: (a) region of analysis and boundary conditions; (b) unit cell and boundary conditions.

(iii) Along BA, $u_2 = u_2^{\mathrm{A}}$

(iv) Along DB, for points such as P and Q,

$$u_1^{\mathrm{P}} + u_1^{\mathrm{Q}} = 0$$
$$u_2^{\mathrm{P}} + u_2^{\mathrm{Q}} = u_2^{\mathrm{A}}$$

The FE mesh used is given in Fig. 6(b). With the boundary conditions given earlier, the key displacements of the FE model are the u_1 and u_2 displacements of the node A and the u_3 displacement of the extra node EX1. In terms of these nodal displacements, the average (macroscopic) direct strains in the composite are given by:

$$\varepsilon_{11} = -\frac{u_1^{\mathrm{A}}}{\frac{\sqrt{3}}{2}h}, \quad \varepsilon_{22} = \frac{u_2^{\mathrm{A}}}{h}, \quad \varepsilon_{33} = \frac{u_3^{\mathrm{EX1}}}{1}$$

Acta metall. mater. Vol. 41, No. 11, pp. 3147–3156, 1993
Printed in Great Britain.

0956-7151/93 $6.00 + 0.00

MODELING OF ANISOTROPIC BEHAVIOR OF WEAKLY BONDED FIBER REINFORCED MMC's

S. R. GUNAWARDENA, S. JANSSON and F. A. LECKIE

Department of Mechanical and Environmental Engineering, University of California at Santa Barbara, Santa Barbara, CA 93106, U.S.A.

(Received 26 March 1993)

Abstract—The anisotropic mechanical behavior of a continuous fiber reinforced Ti alloy matrix composite which possesses a weak fiber matrix interface is modeled numerically. Effects of interface properties and residual stresses incurred during the fabrication are addressed in detail. The computational modeling is guided by comparison with experimental data. The study provides an understanding which will be used to model the multiaxial behavior of weakly bonded composites and to provide a tool for predicting the failure of composite structures.

1. INTRODUCTION

Continuous fiber reinforced metal matrix composites (MMC's) are attractive because of excellent longitudinal properties and relatively high transverse strength and stiffness. The MMC's can be utilized effectively when the loading is predominantly uniaxial with primary stresses in the longitudinal direction and only secondary stresses in transverse directions. However, many structural components and joints are subjected to complex multiaxial stress states. The efficient use of composite materials in such situations requires an understanding of the overall anisotropic mechanical behavior of the MMC systems. MMC's are presently available in restricted quantities and shapes which limit the data that can be produced experimentally. This implies that for the present, numerical models are useful supplements and provide estimates of mechanical responses that cannot be determined experimentally. The models also provide insight which helps establish the failure conditions of the composite.

Experimental and numerical procedures have been applied in a previous study [1], to establish the anisotropic behavior of an FP/Al system which features a strong interface. The present study focuses on the anisotropic mechanical behavior of SCS6/Ti 15-3 which is a candidate for moderately high temperature application. The composite features a weak interface designed to maintain the fiber strength in the fabricated composite.

Single deformation modes such as the transverse tensile behavior of the similar system SCS6/Ti-6V-4Al has been studied by Nimmer *et al.* [2, 3]. Experiments [7] established that the fiber matrix interface plays a major role on the transverse and in-plane shear behavior of the composite. For a system featuring a perfect bond, the constraints induced by the fibers cause the transverse strength to be higher than the matrix strength. The use of a weak interface in the SCS6/Ti 15-3 system results in a transverse strength that is substantially lower than the matrix strength.

A detailed micro-mechanical model is developed that determines the influence of weak interface, residual stresses from fabrication and the matrix plasticity. The model is verified by comparing the computations with experimental data obtained from longitudinal tension, transverse tension and in-plane shear tests performed on specimens manufactured from the composite plate. The different failure modes are also investigated so that failure criteria can be established.

2. COMPOSITE MATERIAL

The material used in this study is SCS6/Ti 15-3 made by Textron. It consists of SiC fibers with a carbon and a SiC coating in a uniaxial lay-up. The fiber volume fraction is 35% and the average fiber diameter 140 mm. The matrix is a β-Ti alloy, Ti–15V–3Cr–3Al–3Sn. The composite is fabricated by vacuum hot pressing a fiber-matrix foil lay-up. Detailed information of the processing is not available, but the composite is consolidated at approximately 900°C. In the subsequent cool down, the mismatch in coefficients of thermal expansion of fibers and the matrix causes residual stresses.

Tensile properties of the matrix were obtained from tests on matrix foil extracted from the composite. The fiber modulus was determined from the average of 50 bend tests [1]. The remaining properties have been extracted from the literature and the elastic properties are summarized in Table 1. The matrix and fiber stress–strain curves are shown in Fig. 1.

The longitudinal and transverse behavior [7] were determined using dog-bone specimens for longitudinal and transverse tension. Specimens of the

Table 1. Matrix and fiber properties at ambient temperature

	Matrix	Fiber
Young's modulus (GPa)	115	360
Poisson's ratio	0.33	0.17
Tensile strength (MPa)	950	4300
Strain to failure in tension (%)	3	1.2
Coefficient of thermal expansion (1/C)	$9.7 \cdot 10^{-6}$	$4.5 \cdot 10^{-6}$

Iosipescu type were used to determine the in-plane shear response.

3. MICRO MECHANICAL STUDY

Numerical simulations were performed using homogenization techniques in conjunction with the general purpose finite element package ABAQUS [4]. In the computations the fibers are assumed to be long parallel cylinders arranged in a hexagonal array (Fig. 3). This is the simplest periodic array for which the linear properties are transversely isotropic. The nonlinear response of the array has a slight deviation from transverse isotropy. It was demonstrated by Jansson [1] that the array can be used to predict the properties of a transversely isotropic system with randomly distribute fibers, if care is exercised when selecting the loading directions. For a system with randomly distributed fibers the matrix area fraction on any plane cut through the composite is equal to the matrix volume fraction, cf. Underwood [5]. However the matrix area fraction is strongly dependent on the orientation and location for a periodic array. The present system has some form of arrangement resulting from the fiber-foil consolidation process, but is difficult to identify any definite simple array type, since the distribution pattern differs from point to point. However it was found that an important feature of the weakly bonded systems for transverse tension is the matrix area fraction on the weakest planes. It was determined to be 40%, which is substantially lower than the value of 65% for randomly distributed fibers. The corresponding value for the hexagonal array is 38% when loaded in the 1-direction, Fig. 2. The hexagonal array was selected in this case because it models the correct volume fraction and matrix area fraction on the weak planes that dictates the transverse strength.

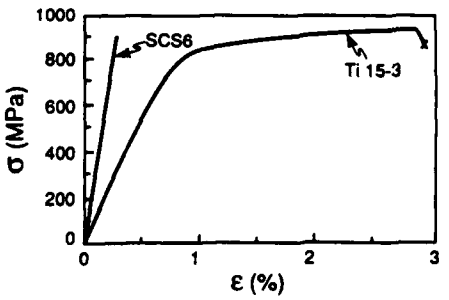

Fig. 1. Uniaxial stress–strain behaviors of Ti 15-3 matrix and SCS6 fibers.

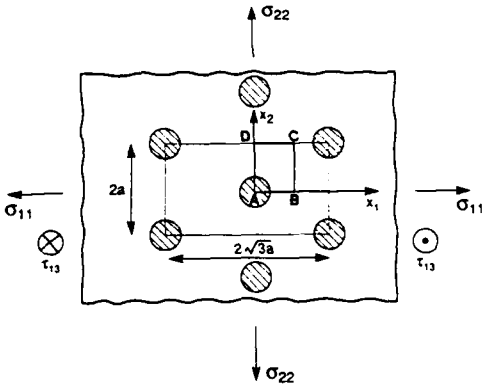

Fig. 2. Hexagonal array with unit cell indicated.

In the homogenization technique, cf. Jansson [6], the displacement field is assumed to have the form

$$u_i = u_i^0 + \langle \epsilon_{ij} \rangle x_j + u_i^p \tag{1}$$

where u_i^0 is an arbitrary constant displacement, $\langle \epsilon_{ij} \rangle$ is the average strain in the composite and u_i^p is an unknown displacement field which is periodic on the unit cell. The average stress $\langle \sigma_{ij} \rangle$ can be determined from the traction T_i on surface S on the unit cell by use of the mean stress theorem as

$$\langle \sigma_{ij} \rangle = \int_s T_i x_j \, ds. \tag{2}$$

All the loading cases considered are symmetric with respect to the x_1 and x_2 axes in Fig. 2 and the displacement field has an inversion symmetry about the point $(x_1 = a\sqrt{3}/2, x_2 = a/2)$. This implies that only the unit cell A–B–C–D in Fig. 2 need be analyzed. Ten node quadratic generalized plane strain elements with reduced integration were used to model the longitudinal and transverse behavior. The boundary conditions at the interface were selected to satisfy the interface bond characteristics. A fully bonded interface was modeled by enforcement of displacement continuity across the interface. The weak interface was modeled by a 3-node sliding interface element available in ABAQUS. The interface is assumed to debond when the normal stresses become tensile and the interface is thereafter traction free. Normal compressive stresses can be accompanied by shear stresses given by Coulomb's law of friction. Restrictions of the code meant that the modeling of the in-plane shear response required a 3-dimensional analysis using a 20 node brick element. Boundary conditions which ensured generalized plane strain behavior and the symmetries on the unit cell were imposed. These conditions reduce the degrees of freedom in the model substantially and results in reasonable solution times. Numerical difficulties were encountered when calculating residual stresses using available 3-dimensional interface elements. This difficulty was overcome by modeling the interface as a thin elastic-perfectly plastic solid

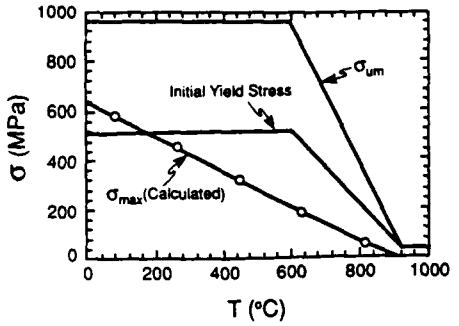

Fig. 3. Temperature dependence of matrix the yield strength and highest calculate equivalent matrix stress for a consolidation temperature of 900°C.

layer whose yield strength was selected to be equal to the sliding resistance of the interface.

The fibers were assumed to be isotropic and linear elastic and the matrix is assumed to be elastic-plastic with isotropic hardening. The influence of different temperature dependence of moduli and matrix yield strength were studied. It was found that the simplified temperature dependence of the yield stress given in Fig. 3 together with temperature independent moduli gave the same residual stress distribution as more refined models. The elastic properties of fiber and matrix given in Table 1 and the temperature dependence of the matrix yield strength given in Fig. 3 were used in the computations.

3.1. *Residual stresses after fabrication*

The residual stresses following fabrication are likely to influence the mechanical behavior of weakly bonded composites. When calculating the residual stress fields the composite is assumed to be stress free at the consolidation temperature before it is subsequently cooled down to room temperature. The exact details of the processing are unknown and consequently no time-dependent viscous behavior was included in the analysis. The residual stress distribution in the matrix is shown in Fig. 4 for the consolidation temperature 900°C. The residual stress in the fiber consists of a compressive axial stress of 720 MPa and almost uniform compressive radial and hoop stresses of 220 MPa. The residual hoop and radial stresses in the matrix vary substantially. The highest magnitudes are found near the interface with a compressive radial stress of 200 MPa and a tensile hoop stress of 500 MPa. The axial stress is tensile and is almost constant, varying between 390 and 420 MPa. No matrix cracking was observed in the as received composite [7] which suggests that the matrix toughness and ductility are sufficiently high to sustain the tensile stresses induced during processing.

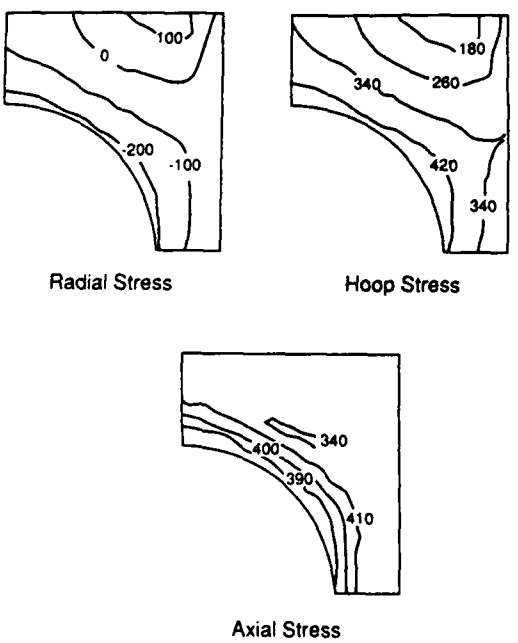

Fig. 4. Calculated residual stress distribution after consolidation at 900°C.

3.2. *Longitudinal tension*

The computed stress–strain curves following the different assumed consolidation temperatures of 0, 600 and 900°C are shown in Fig. 5. The difference in response for different consolidation temperatures is modest which indicates that the magnitude of residual stress has only a weak effect on the longitudinal behavior. The calculated longitudinal modulus E_{33} and Poisson's ratio ν_{31} are close to the experimental values given in Table 2. A slight sample to sample variation in the longitudinal tensile response was observed in experiments, as shown in Fig. 5. The variation is equivalent to a variation in the consolidation temperatures of 600°C. This is unlikely and the observed variation is most likely caused by handling of the panels after fabrication.

Since the longitudinal response is only weakly affected by the constraint in the transverse direction the longitudinal stress strain relationship can be estimated closely using the simple parallel bar model to give

$$\sigma_{33} = fE_f\epsilon_{33} + (1-f)\left[\sigma_m\left(\epsilon_{33} + \frac{\sigma_{rm}}{E_m}\right) - \sigma_{rm}\right] \quad (3)$$

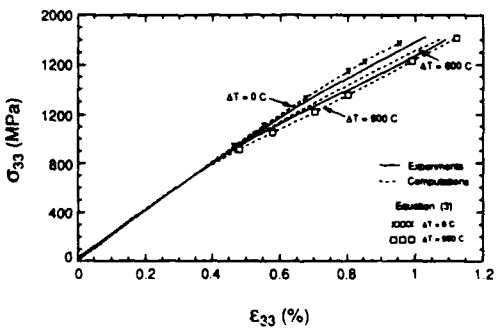

Fig. 5. Longitudinal stress–strain behavior for different consolidation temperatures.

Table 2. Comparison of computed and experimental elastic properties

	E_{11} (GPa)	ν_{13}	E_{11} (GPa)	ν_{12}	ν_{13}	σ_{11u} (MPa)	G^{a}_{13} (GPa)	τ^{a}_{13u} (MPa)	G^{b}_{13} (GPa)	τ^{b}_{13u} (MPa)
Experimental	196	0.25	129	0.34	0.2	420	62	300	62	400
Computed	202	0.27	133	0.48	0.17	420	64	300	73	400

[a]Longitudinal loading.
[b]Transverse loading.

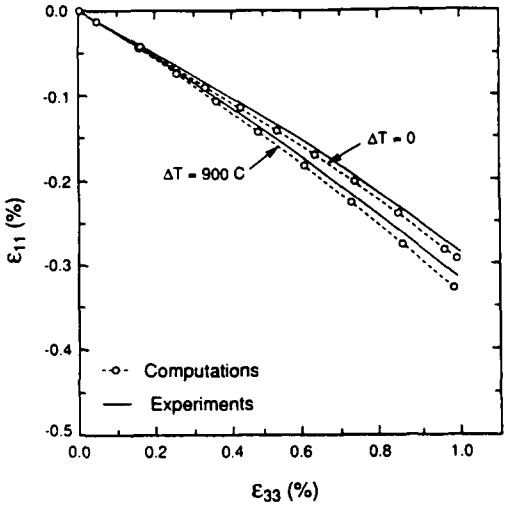

Fig. 6. Transverse contraction for longitudinal loading.

where, f is the volume fraction, E_f is the fiber modulus, E_m is the matrix modulus, σ_{rm} is the longitudinal residual stress in the matrix after consolidation and σ_m is the longitudinal stress in the matrix. This relation agrees well with the corresponding calculations when the longitudinal residual stress used is that determined by computation.

The calculated transverse contractions following consolidation temperatures of 0 and 900°C are compared with the experimental data in Fig. 6. The experimental and calculated curves exhibit the same behavior with an initial linear response followed by increased contraction after matrix yielding. The difference in the calculated responses for the two consolidation temperatures is modest and is of the same order as the sample to sample variation.

3.3. *Transverse tension*

The effect of interface bond conditions on the transverse tensile behavior was first investigated by computing responses for an initially stress free state. Calculations were performed for a fully bonded and for a weak frictionless interface. As illustrated in Fig. 7(a), the stress–strain curve for the fully bonded interface has an initial transverse elastic modulus of 167 GPa and a limit strength of 1195 MPa. These values are higher than the experimentally observed values of 129 GPa and 420 MPa respectively. For a weak frictionless interface the calculated elastic modulus is 48 GPa and the limit strength 380 MPa. For this case the predicted elastic modulus is much lower than the experimental value, while the limit strength is in close agreement with experiment.

When a residual stress state corresponding to the consolidation temperature of 900 C is included in the analysis for the weakly bonded interface, it was found that the elastic properties, Table 2, and the strength agree very well with experiment. The influence of the coefficient of friction at the interface on the stress–strain relationship is negligible as is shown in Fig. 7(b) for the values of $\mu = 0$ and 0.8. The calculations predict that debond initiates when $\sigma_{11} = 140$ MPa at the pole of the fiber and the angle of debond increases rapidly with applied stress until it subtends an angle of 90°. Matrix yielding was predicted to occur in a small confined region on first loading but the effect of plasticity on the transverse

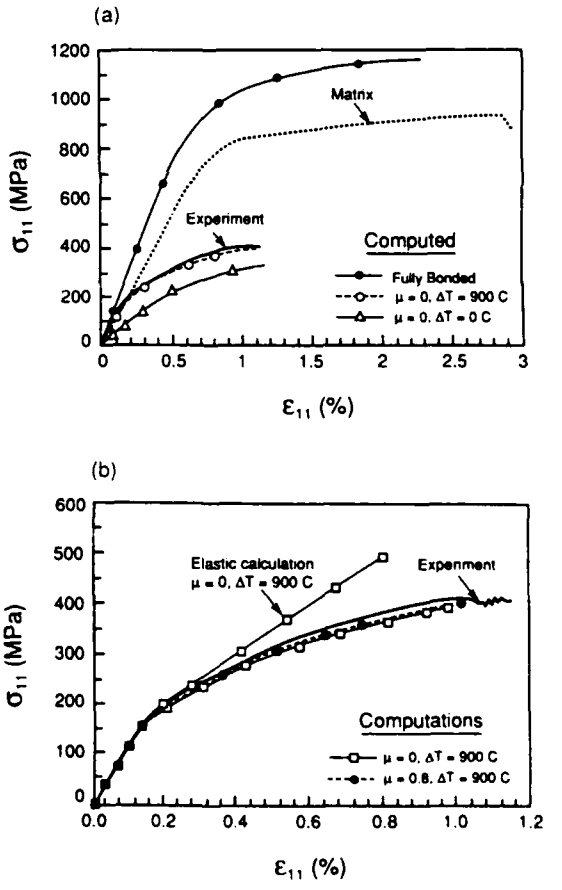

Fig. 7. Transverse tensile stress–strain behavior for different interface characteristics. (a) Effect of interface bond condition. (b) Effect of friction at the interface.

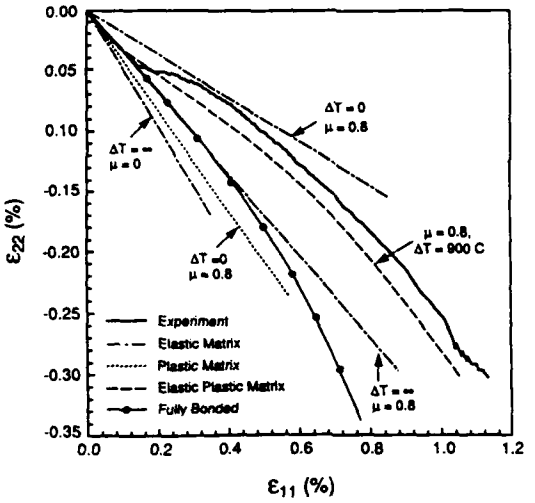

Fig. 8. Contraction in unloaded transverse direction for transverse loading. $\Delta T = 0$ indicates an initially open interface and $\Delta T = \infty$ indicates an interface that remains closed.

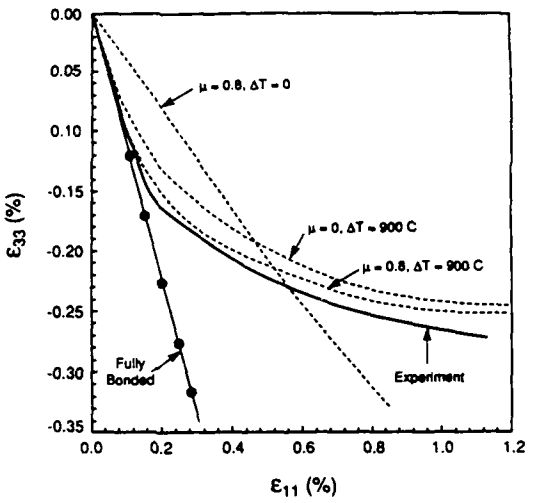

Fig. 9. Contraction in longitudinal direction for transverse loading.

stress–strain behavior is not noticeable until after debond. This is illustrated in Fig. 7(b) where the stress–strain curve for a linear elastic matrix shows the same response up to debond and the non-linearity caused by plasticity is only evident after the initiation of debond.

The presence of the weak interface reduces the transverse strength of the composite to approximately 40% of the matrix strength. A limit load calculation, based on a constant tensile stress in the ligament, gives the limit strength [1] as

$$\sigma_{TL} = \frac{2}{\sqrt{3}} A_{fm} \sigma_{um} \tag{4}$$

where A_{fm} is the matrix area fraction and σ_{um} is the matrix strength. The limit load calculated using equation (4) is 420 MPa which agrees well with experimental and computational values.

The measured contraction in the unloaded transverse direction for transverse loading is shown in Fig. 8. The initial linear response is closely given by a linear elastic calculation based on a value of $\mu = 0.8$ at the interface and a residual stress state sufficiently high to maintain continuity at the interface. Following the initial linear response, when debond occurs there is substantial strain increment in the loaded direction. The total strain just after debond is closely given by a calculation for a fully debonded interface with a linear elastic matrix. For higher stress the contraction increases as the region of plastic deformation increases in the matrix. The slope then follows the calculation for a fully plastic matrix and a debonded interface. The full simulation following consolidation temperature of 900°C has all the features of the observed deformation but slightly overestimates the contraction.

The longitudinal contraction resulting from the transverse loading is shown in Fig. 9. The initial linear response and the limit behavior are closely modelled using a consolidation temperature of 900°C and a sliding interface. While a coefficient of friction $\mu = 0.8$ fits the experiments most closely the sliding resistance has modest influence on the response.

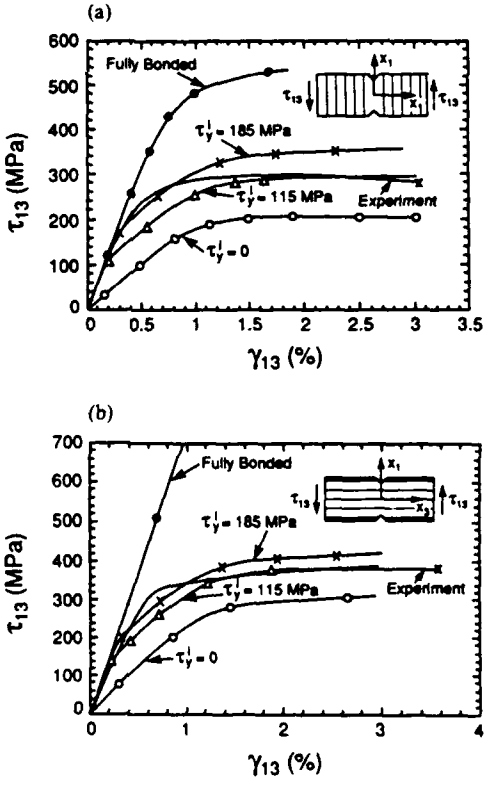

Fig. 10. In-plane shear stress–strain curves for different sliding conditions at the interface. (a) Longitudinal loading (b) Transverse loading.

3.4. *In plane shear*

Experimental results are available for the Iosipescu specimen for two fiber orientations [7]. In one set of experiments the fibers are oriented in the direction of the notches, Fig. 10(a), and is referred to as longitudinal loading. The other case when the fibers are oriented perpendicular to the notches, Fig. 10(b) is referred to as transverse loading. It was observed experimentally that the initial elastic moduli are close for the two orientations but the limit strength for transverse loading at 400 MPa was approximately 40% higher than the value of 280 MPa observed for longitudinal loading. In longitudinal loading the fibers are oriented such that the global stress field is constant over a long segment of the matrix orientated in the fibers direction. This condition permits highly concentrated bands of shear to develop in the matrix along the fibers at the weakest plane. In the case of transverse loading only a short segment of the matrix along the fiber directions is subjected to the higher stress in the gauge section. This effect suppresses the development of bands of concentrated shear since the stresses decrease with increasing distance from the gauge section. Consequently the limit strength is higher for transverse loading compared to longitudinal loading. No such dependence on fiber orientation was observed [1] for a system that has a strong interface and a smaller fiber diameter.

The computed and experimental shear stress–strain curves for longitudinal loading are shown in Fig. 10(a). The computations for a fully bonded interface predict an initial elastic response which agrees with experiment, but the final limit strength is substantially higher than the experimental value. A calculation based on an interface yield strength of 185 MPa exhibits an initial non-linear response that agrees with experiment but the predicted limit strength is higher than the experimental value. The correct limit strength is given by a computation for which the interface yield strength is 115 MPa. Hence, it might be inferred that the interface is initially in full contact. Sliding first develops when the shear stress at the interface is 185 MPa and the sliding stress is subsequently reduced during the slip to a saturation value of 115 MPa.

The initial linear elastic response for transverse loading, Fig. 10(b), is identical to the response for longitudinal loading. This suggests that the calculations based on the assumption that the local displacement field consists of linear and periodic components, equation (1), also predict the correct linear elastic response for transverse loading. However the limit strength is higher for transverse loading, Fig. 10(b), than the longitudinal loading, Fig. 10(a). This implies that the calculations based on equation (1) underestimate the limit strength for transverse loading. As mentioned earlier, the plastic deformation in the matrix is very constrained for this loading and the assumption of a displacement field with linear and periodic, equation (1), components fails to pick up this feature.

To simulate this constraint the deformation field in the elastic fiber was still assumed to have linear and periodical components. However the deformation field in the matrix was assumed to have only linear components, to be given by

$$u_3 = u_3^0 + \langle \gamma_{13} \rangle x_1. \tag{5}$$

This formulation suppresses the development of regions with high concentrations of shear. The calculated responses assuming the same interface characteristics as those assumed for longitudinal loading are shown in Fig. 10(b). It can be observed that use of the same interfacial shear strength as that for longitudinal loading predicts the correct limit behavior for transverse loading. The initial shear modulus before debond and limit strengths for calculations based on an interface shear stress of 115 MPa are listed in Table 2 for the two loading cases.

A simple estimate of the limit strength for longitudinal loading is given by considering a deformation that is given by a slip in the matrix on the surface $x_1 = 0$ and at the fiber matrix interfaces. This gives

$$\tau_L = \tau_y^i \frac{\pi}{2}(1 - A_{fm}) + \frac{1}{\sqrt{3}} \sigma_{Lm} A_{fm} \tag{6}$$

where τ_L is the limiting strength of τ_{13}, τ_y^i is the shear strength of the interface, σ_{Lm} is the limit stress of the matrix under uniaxial tension and A_{fm} is the matrix area fraction of the weakest plane. For the system under consideration $A_{fm} = 0.4$ and use of equation (6) with experimental limit strength $\tau_L = 300$ MPa gives an interface shear strength $\tau_y^i = 95$ MPa, which is close to the computed value of 115 MPa.

The limit strength for the transverse loading can be estimated by assuming that the deformation in the matrix is linear and as given equation (5). This deformation causes a plastic deformation throughout the matrix with slip at the interface. A work balance gives

$$\tau_L = \frac{1}{\sqrt{3}} \sigma_{Lm}(1 - f) + \frac{4}{\pi} \tau_y^i f \tag{7}$$

where f is the fiber volume fraction. This expression is a modified version of the upper bound given by Majumdar and McLaughlin [8] for a strong interface. Using the experimental strength $\tau_L = 400$ MPa in this relation gives an interfacial shear strength of $\tau_y^i = 100$ MPa, which is consistent with the value of 115 MPa determined from the computations.

3.5. *Transverse shear*

While no experimental results are available for this form of loading, the calculations were performed to provide a more complete understanding of the anisotropic behavior of the material. Shear loading τ in the transverse plane is represented by the principal stress state shown in Fig. 11. Two loading conditions

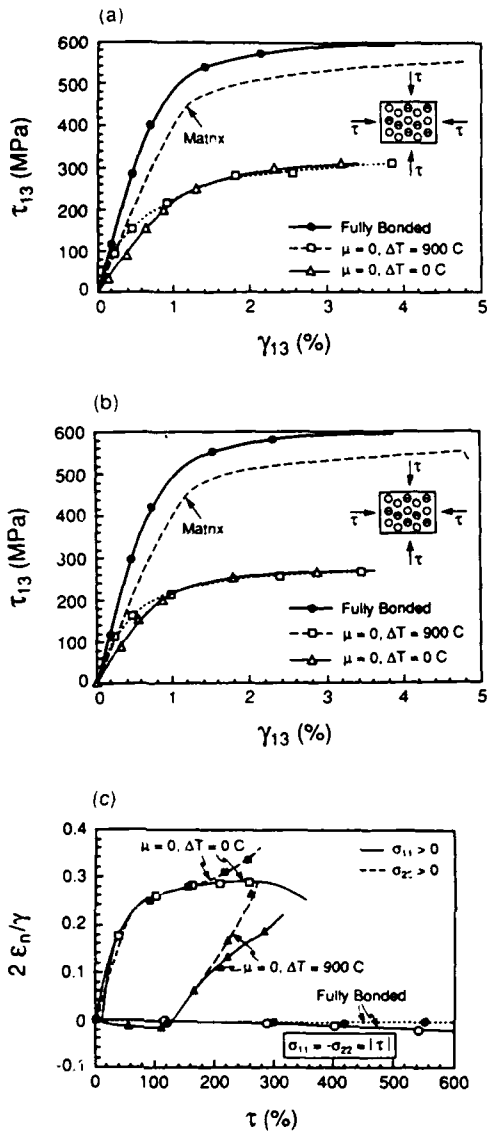

Fig. 11. Calculated transverse shear stress–strain curves for different consolidation temperatures and interface bound conditions. (a) Stress–strain curve for $\sigma_{11} = -\sigma_{22} = \tau$. (b) Stress–strain curve for $\sigma_{22} = -\sigma_{22} = \tau$. (c) Normal strain components for the two loadings.

have been investigated: one loading defined by $\sigma_{11} = -\sigma_{22} = \tau$ and the other by $-\sigma_{11} = \sigma_{22} = \tau$, where $\tau > 0$. Computed shear stress–strain curves for a fully bonded and a frictionless interface following a consolidation temperature of 900°C are shown in the Fig. 11(a) and (b). For the fully bonded interface the two loading cases, $\sigma_{11} > 0$ and $\sigma_{22} > 0$ exhibit very similar behavior with a limit strength of 600 MPa. However in the case of a weak interface, the strength for $\sigma_{11} > 0$ is 310 MPa while the strength for $\sigma_{22} > 0$ is 270 MPa. This difference indicates that a system with a debonded interface does not exhibit the transverse isotropy commonly assumed for fiber reinforced composites. It was observed in the calculations that the debond always initiated close to the point of the interface whose normal coincides with the direction global maximum principal stress.

Pure transverse shear loading results in global strains that have both shear and normal components. For a fully bonded interface the normal strain component exists only when one of the constituents has a non-linear response. However for this case, as shown in Fig. 11(c), the normal component is very small compared to the shear strain. For a weak interface the normal strain is small before debond and grows to 30% of the shear strain after debond, Fig. 11(c). For an initially stress free state the debond occurs earlier and the normal strain component is greater.

4. FAILURE MECHANISMS

The computational procedures described previously provide the local stress and strain distributions in the composite which can be used to determine local failure conditions of the constitutents. Macroscopic failure condition for the composite can then be predicted for different loadings.

4.1. Longitudinal tension

The fracture in the longitudinal tension is dominated by fiber failure. The observed failure strain of the composite is of the same magnitude as the fiber failure strain ϵ_f. The stress at failure can be written as

$$\sigma_{UTS} = f\sigma_F + (1 - f)\sigma_{ym}\left(\epsilon_f + \frac{\sigma_{rm}}{E_m}\right) \tag{8}$$

where σ_{ym} is yield stress of the matrix at fiber failure and σ_F is the stress in the fibers at failure. For the present residual stress state $\sigma_{rm} = 900$ MPa at failure.

The exact nature of the fiber failure is still an open question. Failure occurs when a defect of critical size has formed in the composite. One extreme estimate of the strength is to assume that fracture occurring in two adjacent fibers within a stress transfer length causes a critical defect. The average stress in the fibers when this occurs is given by

$$\sigma_f = \frac{\overline{\sigma_f}}{\Gamma(1 + 1/m)}\left[\frac{\pi d l_0^2}{12 v f}\frac{\Gamma(1 + 1/m)\tau_c}{\overline{\sigma_f}} \times \frac{(m + 1)(k - 1)}{k^{m+1} + m - k(m + 1)}\right]^{1/m} \tag{9}$$

where v is the loaded volume, k the stress concentration in a fiber next to a broken fiber, d is the fiber diameter, δ_c is the stress transfer length and Γ is the gamma function. This is the model by Zweben and Rosen [9] modified to account for a linearly varying fiber stress within the transfer length of the fiber. Based on data for the SCS6 fiber given by Bain *et al.* [10] it was deduced that the average fiber strength is $\sigma_f = 4.3$ GPa for a gauge length $l = 6.25$ mm and the

Weibull modulus is $m = 9.4$. For the present specimen the loaded volume $v = 125\ \text{mm}^3$ and the transfer length is estimated to be $\delta_t = \sigma_F \tau_i^s d\ 4$, where the sliding resistance of the interface $\tau_i^s = 115$ MPa. An upper bound on k for fibers arranged in an hexagonal array is $k = 1.17$. Use of these values in equation (9) gives a failure strength $\sigma_{UTS} = 1880$ MPa.

The other extreme is to assume that fiber fractures do not introduce local stress concentrations in adjacent fibers and that global load sharing occurs. The fiber contribution at the load maximum for the global load sharing model has been estimated in an approximate way by Curtin [11] and Neumeister [12] as

$$\sigma_F = \frac{\overline{\sigma_F}}{\Gamma(1+1/m)}\frac{m+1}{m+2}\left[\frac{4}{m+2}\frac{l_0\tau_i^s\Gamma(1+1/m)}{d\overline{\sigma_F}}\right]^{\frac{1}{m+1}}. \tag{10}$$

This model predicts a strength $\sigma_{UTS} = 2060$ MPa. Both models predict the strength within 10% and are in good agreement with the experimental result. Tests of specimens of different volumes and with stress gradients are required to reveal the exact nature of the failure process and to discriminate between the models.

4.2. *Transverse tension and shear*

The observed failure strain in transverse tension is 1.2% which is approximately 40% of the uniaxial matrix failure strain (Fig. 1). The computations for transverse tension and shear indicate that the stiff fibers cause multiaxial stress fields to develop in the matrix. When a ductile material is subjected to stress states with a high hydrostatic tension component the failure ductility is reduced. Hancock and Mackenzie [13] suggested that failure is the result of void nucleation and growth. They estimated that the effective plastic strain at failure, ϵ_f^s, for multiaxial stress states is related to the uniaxial failure strain by

$$\epsilon_f^s = 1.65\epsilon_0 \exp\left[-\frac{1}{2}\frac{\sigma_{kk}}{\sigma^e}\right] \tag{11}$$

where ϵ_0 is the plastic component of the uniaxial failure strain of the matrix, σ_{kk} is the hydrostatic stress and σ^e is the von Mises equivalent stress. From the uniaxial stress-strain curve for the Ti alloy in Fig. 1, it can be deduced that $\epsilon_0 = 3\%$. This value for the matrix foil is substantially lower than what is normally observed for β-Ti alloys. The low matrix ductility implies that large strain effects can be neglected in the analysis. For a time dependent stress state, the void growth rate has to be integrated over the history and the used portion of the matrix ductility is given by

$$D = \frac{\int \exp\left[\frac{\sigma_{kk}}{2\sigma^e}\right] d\bar{\epsilon}}{1.65\epsilon_0} \tag{12}$$

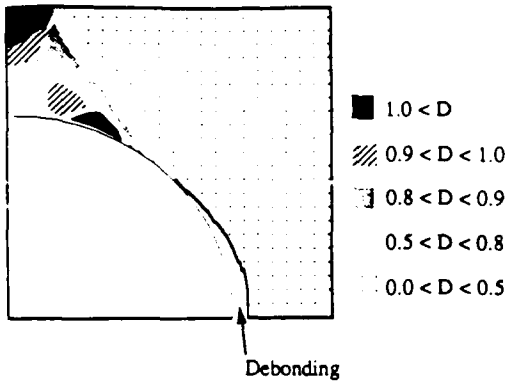

Fig. 12. Distribution of damage parameter D for transverse tension, at $\epsilon_{11} = 1\%$.

where the variable D is used as a damage variable with $D = 0$ for a virgin material and $D = 1$ when the material has lost its load carrying capacity and $\epsilon^e = \epsilon_f^s$. The evolution of the damage D has been calculated by integrating equation (12) numerically using the stresses and strain increments from the computations.

The distribution of the damage parameter D in transverse tension is shown in Fig. 12 for a global strain of 1%, which is close to the observed failure strain of 1.2%. The computations indicate that most of the load carrying capacity is lost. A region of high damage is localized in the matrix ligament between the fibers and stimulates fracture on a plane approximately at 45° to the loading direction. Microscopic observations [1] showed the failure surface consists of plastically deformed matrix ligaments and debonded matrix fiber interfaces.

The damage distribution for transverse shear with $\tau > 0$ is shown in Fig. 13 for a global shear strain of 1.6%. The trend is similar to transverse tension with a region of high damage in the matrix ligament between the fibers, orientated in the direction of the global tensile principal direction. The damage starts to exceed unity in some regions of the matrix when the global stress is 272 MPa, which is 13% lower than the predicted limit strength of 310 MPa. This suggests

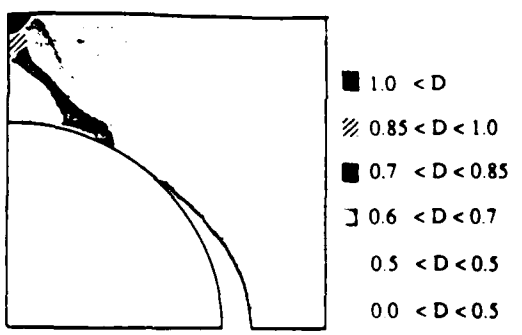

Fig. 13. Distribution of damage parameter D for transverse shear at $\gamma = 1.6\%$.

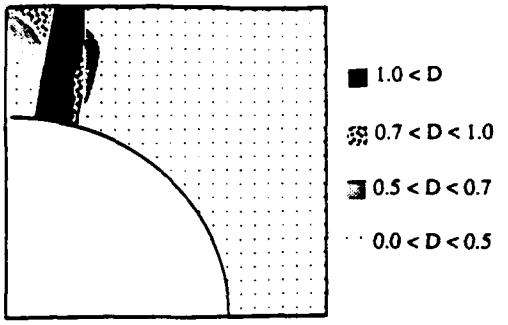

Fig. 14. Distribution of damage parameter D for in-plane shear, at $\gamma_{13} = 3\%$.

that the available matrix ductility may be exceeded in portions of the matrix before the limit condition is reached.

4.3. In-plane shear

The only non-vanishing stress components in-plane shear, except for the residual thermal stresses, are the shear stresses τ_{13} and τ_{23}. This implies that this type of loading does not cause high hydrostatic stresses to build up in the matrix. The effect of the initial residual stress is small and the failure criterion described previously then simplifies to

$$D = \frac{1}{1.65}\left[\frac{\epsilon^e}{\epsilon_0}\right]. \tag{13}$$

The computed damage distribution for longitudinal loading corresponding to the observed failure strain $\gamma_{13} = 3\%$ is shown in Fig. 14. The damage exceeds unity across the whole matrix ligament between the fibers indicating that the model predicts a failure strain slightly lower than the experimental value.

5. CONCLUSIONS

The longitudinal and transverse tensile properties can be predicted by a computational model which makes use of fiber and matrix properties, fiber distribution and an interface which debonds when the interface is subjected to normal tension. In addition to predicting the elastic properties and limit strength the calculations also predict the failure strains. The residual stresses following the fabrication strongly affect the mechanical behavior. The compressive normal residual stress at the interface dictates that the initial elastic properties are consistent with normal continuity at the interface. In transverse tension the applied stress can overcome the residual stress and interface debonding occurs which gives arise to a loss of stiffness. The presence of the debond also decreases greatly the transverse limit strength, with the composite strength being dictated by a matrix perforated by un-reinforced holes.

The in-plane shear properties cannot be predicted by a frictionless interface. It is necessary to assume an initial sliding stress of 185 MPa that subsequently reduces to 115 MPa when the sliding is fully developed. However the interface characteristics determined from the shear test with longitudinal loading predict the substantially different strength for the shear test with transverse loading. The different limit behavior for transverse and longitudinal shear loading indicates that the in-plane shear response is strongly dependent on the extent of the plastic zone along the fiber direction. This feature has to be addressed in the formulation of macroscopic constitutive equations.

The analysis of the transverse tension test indicates that the sliding resistance at the interface can be modeled by Columb friction with a coefficient of friction $\mu \approx 0.8$. Use of this value and the residual stress state following a consolidation temperature of 900°C predicts an initial sliding resistance of 160 MPa for in-plane shear. This is close to the value determined from the in-plane shear test of 185 MPa. However, during the in-plane shear loading after matrix yielding the normal pressure at the interface relaxes and the steady state sliding resistance vanishes for a Columbs friction model. Microscopic observations of the fibers showed that the fibers have a surface texture with ridges oriented in the hoop direction. For in-plane shear loading the sliding direction is normal to the ridges while it is parallel to the ridges for transverse tension and this could cause the observed steady state sliding resistance for in-plane shear.

Using the mechanism of interface debonding and a void growth model for matrix failure it was possible to predict with accuracy the macroscopic failure strains for matrix dominated failure modes. The exact nature of the longitudinal failure is still an open question. However, models of two extreme failure conditions give approximately the same predictions of the failure stress.

It has been demonstrated that the composite properties can be predicted from the matrix, fiber and interface properties by using established computational procedures. In this case the interfacial properties have not been measured but have been inferred from the longitudinal shear test of the composite. Independent push-through tests [14] show sliding resistances that are close to the saturation value used here. The push-through test may therefore be used as a means of providing some information on the sliding characteristics for the analysis.

Acknowledgements—Funding for this work has been provided by NASA-Lewis Research Center (NAG3-834), Pratt and Whitney (F432052) and the DARPA URI at UCSB (ONR N442-2494-23100).

REFERENCES

1. S. Jansson, *J. Mech. Mater.* **12**, 47 (1991).
2. R. P. Nimmer, R. J. Bankert, E. S. Russell, G. S. Smith and P. K. Wright, *J. Comp. Technol. Res.* **13**, 3 (1991).

3. R. P. Nimmer, *J. Comp. Technol. Res.* **12,** 65 (1990).
4. ABAQUS Finite Element Program, (Version 4.7). Hibbitt, Karlson and Sorensen (1988).
5. E. E. Underwood, *Quantitative Stereology*, pp. 25–27. Addison-Wesley, Reading Mass. (1970).
6. S. Jansson, *Int. J. Solids Struct.* **29,** 2181 (1992).
7. S. Jansson, H. E. Deve and A. G. Evans, *Metall. Trans. A* **22A,** 2975 (1991).
8. S. Majumdar and P. V. Jr. McLaughlin, *J. appl. Mech.* **95,** 824 (1973).
9. C. Zweben and B. W. Rosen, *J. Mech. Phys. Solids* **18,** 189 (1970).
10. K. R. Bain, M. L. Byrnes and S. K. Jain, Allison Gas Turbine, Indianapolis, Indiana, EDR 13084 (1985).
11. Curtin, *J. Am. Ceram. Soc.* **75,** 2837 (1991).
12. J. Neumesitrer, Dept of Solid Mechanics, Chalmers University, Sweden (1992).
13. J. W. Hancock and A. C. Mackenzie, *J. Mech. Phys. Solids* **24,** 141 (1976).
14. P. D. Warren, A. G. Mackin and A. G. Evans, *Acta metall. mater.* **40,** 1243 (1992).

MATERIALS

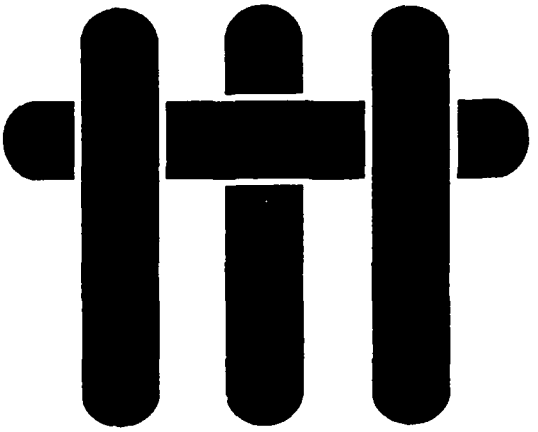

ON THE TENSILE PROPERTIES OF A FIBER REINFORCED TITANIUM MATRIX COMPOSITE I. UNNOTCHED BEHAVIOR

C.H. Weber, X. Chen, S.J. Connell and F.W. Zok

Materials Department
University of California
Santa Barbara, California 93106

Submitted to Acta Metallurgica et Materialia

January, 1994

71:MS35(December 22, 1993)1:57 PM/mef

ABSTRACT

An investigation of the ultimate tensile strength and fracture strain of a fiber-reinforced Ti-matrix composite has been conducted. Comparisons have been made between experimental measurements and predictions of two micromechanical models: one assumes that the fibers behave independently of the matrix, i.e. as in a dry fiber bundle, and the other assumes frictional coupling between the fibers and the matrix, characterized by a constant interfacial sliding stress. To conduct such comparisons, a number of constituent properties have been measured, including the fiber strength distribution, the thermal residual stress and the interfacial sliding stress. In addition, the effects of gauge length on the tensile properties of the composite have been studied. The comparisons indicate that the model prediction based on frictional coupling provide a good representation of the experimental results. In contrast, predictions based on the dry fiber bundle approach strongly underestimate both the ultimate strength and the fracture strain and predict a gauge length dependence that is inconsistent with the experiments.

1. INTRODUCTION

There has been considerable interest in fiber-reinforced Ti matrix composites for use in advanced aerospace propulsion systems, motivated by the attractive stiffness, strength and creep resistance characteristics of this class of composite at low and intermediate temperatures (to ~ 600°C)[1]. The present article focuses on the room temperature tensile properties of a unidirectionally reinforced composite. A study of the notched strength characteristics of this material is presented in a companion paper[2].

In unidirectional materials, the tensile response is characterized by two, approximately linear regimes[2-4]. In the first, the material is elastic, with a modulus given by the rule-of-mixtures. In the second, the matrix is yielded whereas the fibers remain essentially elastic. In the latter regime, fiber fracture also occurs, resulting in a slight deviation from linearity and ultimately causing composite fracture. The main objective of this work is to assess the utility of micromechanical models in predicting both the ultimate tensile strength (UTS) and the fracture strain of this class of composite.

The paper is organized in the following way. Section 2 reviews the existing models pertaining to the tensile properties of unidirectional MMCs. The models identify the relevant constituent properties that need to be measured in order to rationalize the properties of the composite and assess the utility of the models. Section 3 describes the various experimental measurements made in this study, with the results being presented in Section 4. Analysis of the results and comparisons with model predictions are presented in Section 5.

2. THEORETICAL BACKGROUND

The axial tensile stress-strain response, $\sigma_c(\varepsilon)$, of a unidirectional MMC can be written as

$$\sigma_c(\varepsilon) = f\,\sigma_f(\varepsilon) + (1\text{-}f)\,\sigma_m(\varepsilon) \tag{1}$$

where f is the fiber volume fraction, and $\sigma_f(\varepsilon)$ and $\sigma_m(\varepsilon)$ represents the volume-average axial stresses in the fiber and the matrix, respectively. If both phases respond elastically, then

$$\sigma_f(\varepsilon) = E_f\,\varepsilon \tag{2a}$$

and

$$\sigma_m(\varepsilon) = E_m\,\varepsilon \tag{2b}$$

whereupon the composite response becomes linear, with a modulus,

$$E = f\,E_f + (1\text{-}f)\,E_m \tag{3}$$

with E_f and E_m being the Young's moduli of the fibers and the matrix, respectively.

In the absence of residual stress, non-linearity in the stress-strain curve occurs at a strain equal to the matrix yield strain, ε_m^y. Assuming the matrix to be elastic-perfectly plastic, the subsequent tensile response ($\varepsilon > \varepsilon_m^y$) is given by

$$\sigma_c(\varepsilon) = f\,\sigma_f(\varepsilon) + (1\text{-}f)\,\sigma_m^y \tag{4}$$

where σ_m^y is the matrix yield stress ($= E_m\,\varepsilon_m^y$).

The fiber contribution, $\sigma_f(\varepsilon)$, is governed by the statistical distribution in strengths generally characterized by the Weibull function[5],

$$P_f = 1 - \exp \frac{-L}{L_o}\left(\frac{\sigma}{\sigma_o}\right)^m \tag{5}$$

where P_f is the cumulative failure probability, σ is the tensile stress acting on the fiber, L is the fiber length, σ_o and L_o are reference values of stress and length, and m is the Weibull modulus. In some cases, the *in-situ* strength characteristics of the fibers differ from those of the pristine fibers and therefore require independent measurement following composite consolidation. This can be achieved by extracting fibers from the composite and measuring their tensile strengths[4,6,7]. Moreover, it has been recognized that the fiber bundle within a composite behaves differently from that of a dry fiber bundle, a result of the sliding resistance of the fiber/matrix interface[8-11]. The coupling between the fibers and matrix in combination with the fiber strength characteristics represent dominant features in the fiber response.

Traditionally, the approach to evaluating $\sigma_f(\varepsilon)$ has been based on the behavior of a *dry* fiber bundle, assuming that no coupling exists between the fibers and the matrix (the so-called "rule-of-mixtures" approach)[12]. In this case, the fiber response is simply

$$\sigma_f(\varepsilon) = (1-P_f)\,\varepsilon\,E_f \tag{6}$$

Combining this result with Eqn. 5 and recognizing that $\sigma = \varepsilon E_f$ yields the result

$$\frac{\sigma_f(\varepsilon)}{\sigma_o} = \left(\frac{\varepsilon E_f}{\sigma_o}\right) \exp \frac{-L}{L_o}\left(\frac{\varepsilon E_f}{\sigma_o}\right)^m \tag{7}$$

The composite tensile strength σ_u and the corresponding fracture strain ε_u are evaluated by setting

$$\frac{d\sigma_c(\varepsilon)}{d\varepsilon} = f\frac{d\sigma_f(\varepsilon)}{d\varepsilon} = 0 \tag{8}$$

whereupon

$$\sigma_u = f\sigma_o\left(\frac{me\,L}{L_o}\right)^{-1/m} + (1-f)\sigma_m^y \tag{9a}$$

and

$$\varepsilon_u = \frac{\sigma_o}{E_f}\left(\frac{mL}{L_o}\right)^{-1/m} \tag{9b}$$

Trends in the normalized strength, $\sigma_u/f\,\sigma_o$, with gauge length, L/L_o, and Weibull modulus, m, are plotted in Fig. 1. A key feature predicted by this model is the reduction in strength with increased gauge length.

Recently, models have been developed to account for the frictional coupling between the fibers and the matrix and its effect on the statistics associated with fiber fracture[9-11]. At the simplest level, the coupling can be characterized by a constant interfacial shear stress, τ, acting along the debonded interface. Such debonding occurs in regions adjacent to the fiber failure sites and leads to the development of shear tractions at the fiber ends, allowing stress to be transferred from the matrix to the fibers. The length over which this transfer occurs is the slip length, d, given by

$$d = \frac{\sigma R}{2\tau} \tag{10}$$

where σ is the tensile stress acting on the fiber when it failed and R is the fiber radius. Outside of this region, the fiber stress remains unchanged. Upon further loading, the fiber may fail at numerous other points along its length, with each failure event occurring essentially independently of all others.* Consequently, the stress-strain response of a fiber bundle embedded within a ductile matrix is essentially identical to that of a single fiber embedded in the same matrix[9,10].

The tensile response of a fragmenting, embedded fiber can be expressed as

$$\sigma_f(\varepsilon) = \varepsilon E_f(1-\alpha) + \frac{\varepsilon E_f}{2}\alpha \tag{11}$$

where α is the fractional length of the fiber contained within the slip zones adjacent to fiber breaks. The factor of 2 in Eqn. 11 arises because the *average* fiber stress within the slipped region is one-half of that in the unslipped regions (provided that none of the fragments are shorter than 2d). The parameter α can be interpreted as the cumulative fiber failure probability within a gauge length, $\ell = 2d$, at a stress, σ. Consequently,

$$\alpha = P_f = 1 - \exp\frac{-2d}{L_o}\left(\frac{\sigma}{\sigma_o}\right)^m \tag{12}$$

which, combined with Eqn. 10, gives

$$\alpha = 1 - \exp\left(\frac{\sigma R}{\tau L_o}\right)\left(\frac{\sigma}{\sigma_o}\right)^m \tag{13}$$

* Provided the fragment length remains large in comparison to the slip length.

This result can be re-written as

$$\alpha = 1 - \exp - \left(\frac{\sigma}{\sigma_*}\right)^{m+1} \tag{14}$$

where σ_* is a characteristic stress defined by

$$\sigma_* = \left(\frac{\sigma_o^m \tau L_o}{R}\right)^{1/m+1} \tag{15}$$

Provided the argument within the exponential term in Eqn. 14 is sufficiently small compared with unity, the term can be approximated by the first two terms in the Taylor series expansion,

$$\exp - \left(\frac{\sigma}{\sigma_*}\right)^{m+1} \approx 1 - \left(\frac{\sigma}{\sigma_*}\right)^{m+1} \tag{16}$$

Combining this result with Eqns. 11 and 14 yields the stress-strain response[9,10],

$$\frac{\sigma_f(\varepsilon)}{\sigma_*} = \lambda\left[1 - \frac{1}{2}\lambda^{m+1}\right] \tag{17}$$

where λ is the normalized strain,

$$\lambda = \varepsilon E_f/\sigma_* \tag{18}$$

The *maximum* average stress σ_B that the fragmenting fiber can support is evaluated by setting $d\sigma_f/d\varepsilon = 0$, whereupon

$$\frac{\sigma_B}{\sigma_*} = \left(\frac{2}{2+m}\right)^{\frac{1}{m+1}} \left(\frac{m+1}{m+2}\right) \tag{19}$$

with a corresponding strain of

$$\varepsilon_B = \frac{\sigma_*}{E_f}\left(\frac{2}{m+2}\right)^{\gamma_{(m+1)}} \tag{20}$$

Trends in both the ultimate strength and the failure strain with Weibull modulus predicted by this model are presented in Fig. 2*.

It should be recognized that Eqns. 19 and 20 represent *upper* bound estimates of the UTS and fracture strain. This is a consequence of the implicit assumption that all volume elements within the composite are equivalent. However, for statistical reasons, the process of fiber fragmentation may occur more rapidly in some regions than in others, leading to strain localization prior to the stress maximum predicted by Eqn. 19. A set of *lower* bound conditions for fracture can be obtained by assuming all the fiber failure sites within a section of length 2d to be aligned in a plane perpendicular to the loading direction. Along this plane, the response of the fibers is given by

$$\sigma_f(\varepsilon) = \varepsilon E_f (1-\alpha) \tag{21}$$

* A more rigorous solution to the fiber fragmentation problem has recently been developed, accounting for the potential overlap of slip lengths of adjacent fiber breaks and the "shadowing" of defects that occurs within the slipped regions[11]. The predictions of ultimate strength resulting from this solution are essentially the same as those of the approximate solution, differing by $< 5\%$ for $m \geq 4$.

differing from Eqn. 11 by the contribution associated with the slipped region ($\varepsilon E_f \alpha/2$). The local stress maximum is again evaluated by setting $d\sigma_f/d\varepsilon = 0$, whereupon the fracture stress becomes:

$$\frac{\sigma'_B}{\sigma_*} = \left(\frac{1}{2+m}\right)^{\frac{1}{m+1}} \left(\frac{m+1}{m+2}\right), \tag{22}$$

This estimate differs from the upper bound (Eqn. 19) by a factor of $2^{1/(m+1)}$. The fracture strain is then evaluated by substituting Eqn. 22 into the constitutive law, Eqn. 17. Comparisons of the upper and lower bound estimates of the tensile strength and fracture strain are shown in Fig. 2.

Following similar arguments, the average fiber fragment length, $\bar{\ell}_f$, during tensile loading can be expressed as

$$\bar{\ell}_f = \frac{2d}{P_f} \tag{23a}$$

which, combined with Eqns. (10), (12) and (15), gives

$$\frac{\bar{\ell}_f}{\ell_o} = \left(\frac{\varepsilon E_f}{\sigma_o}\right)^{-1/m} \tag{23b}$$

Another factor influencing the composite response is the residual stress, arising from thermal expansion mismatch and phase transformations. In most metal matrix systems, the matrix thermal expansion coefficient, α_m, exceeds that of the fibers, α_f. Consequently, after cooling from the processing temperature, the matrix experiences an axial tensile stress, σ^r_m, whereas the fiber experiences an axial

compression, $-\sigma_f^r$. Neglecting relaxation effects due to matrix creep or plasticity, the residual stresses due to a misfit strain, Ω, are[13]

$$\sigma_m^r/E_m = \beta\,\Omega \tag{24a}$$

and

$$\sigma_f^r/E_f = -\,\omega\,\beta\,\Omega \tag{24b}$$

where

$$\beta = \frac{f(1+E_f/E)}{1+(1-2\nu)E/E_f} \tag{24c}$$

and

$$\omega = \frac{(1-f)E_m}{f\,E_f} \tag{24d}$$

with ν being the Poisson's ratio (assumed to be the same for the fibers and the matrix). The misfit strain is

$$\Omega = (\alpha_f - \alpha_m)\,\Delta T + \Omega_p \tag{24e}$$

where ΔT is the temperature change and Ω_p is the (unconstrained) linear strain associated with phase transformations.

In general, Ti matrix composites are consolidated at temperatures at which the matrix can readily creep, and thus the relevant temperature governing the residual stresses is ill-defined. Furthermore, Ti alloys undergo a phase transformation from the high temperature BCC (β) phase to the low temperature

HCP (α) phase. For the Ti alloy of interest in this study, the transformation temperature lies in the range 950-1000°C[14]: lower than the processing temperature (~ 1100-1200°C). The volume expansion associated with the $\beta \rightarrow \alpha$ transformation is ~ 2.2%, resulting in a linear strain, $\Omega_p \sim 0.7\%$[14]. Because of the difficulties in accurately ascertaining both the relevant misfit strain and the flow and creep characteristics of the matrix over the entire processing cycle, experimental methods for evaluating residual stresses are preferred.

The effects of residual stress on the composite response can be understood with the aid of the schematic in Fig. 3. Provided $\sigma_m^r < \sigma_m^y$, the material initially behaves elastically with a modulus, E, given by Eqn. 3. Yielding of the matrix occurs at a strain, ε_c^y, at which the total matrix strain (thermal plus mechanical) reaches the (unconstrained) matrix yield strain, ε_m^y. This result can be expressed as

$$\varepsilon_c^y = \varepsilon_m^y - \varepsilon_m^r \tag{25}$$

Upon further loading ($\varepsilon > \varepsilon_c^y$), the slope (or tangent modulus) of the curve is dictated by the fiber properties. Provided the extent of fiber failure is small and the matrix is elastic-perfectly plastic, the slope in this regime is $\approx f E_f$. Fiber bundle failure then occurs when the average fiber stress reaches σ_B. This occurs at a strain, ε_c^*, of

$$\varepsilon_c^* = \varepsilon_B - \sigma_f^r/E_f \tag{26}$$

The corresponding stress, σ_c^*, is

$$\sigma_c^* = f\,\sigma_B + (1\text{-}f)\,\sigma_m^y \tag{27}$$

where σ_B is given by either Eqn. 20 or 22, and the matrix yield stress, σ_m^y, is related to the composite yield strain through

$$\sigma_m^y = (\varepsilon_c^y + \varepsilon_m^r) E_m \tag{28}$$

The axial residual stress in the fibers also influences the average fiber fragment length. This effect can be incorporated into Eqn. (23b) by adding the thermal component of stress to the mechanical one, yielding the result

$$\frac{\bar{\ell}_f}{\ell_o} = \left(\frac{\varepsilon E_f + \sigma_i^r}{\sigma_o} \right)^{-\gamma_m} \tag{29}$$

The preceding background identifies a number of key measurements that are required in order to assess the models. The measurements include: (i) the tensile *stress-strain response of the composite,* (ii) the *in-situ* fiber strength distribution, (iii) the interfacial sliding resistance, τ, and (iv) the axial residual stresses. In addition, tensile tests conducted on specimens of various gauge lengths should provide additional evidence, supporting either the dry fiber bundle model (which predicts gauge length *dependent* behavior) or the fiber fragmentation model (which predicts gauge length *independent* behavior). The experimental portion of this study is based on this insight.

3. EXPERIMENTS

The material used in this study was a Ti-6Al-4V matrix reinforced with unidirectional, continuous SiC fibers*, 100 μm in diameter. The composite panel

* Sigma fiber, produced by British Petroleum.

was comprised of six plies, with a total thickness of 1.0 mm. The fiber volume fraction was 32%. Prior to consolidation, the fibers had been coated with ~ 1 μm of C, followed by ~ 1 μm of TiB_2. The TiB_2 coating serves as a diffusion barrier between the fiber and the matrix. During consolidation, the TiB_2 reacts with the matrix to form a layer of TiB needles, ~ 0.7 μm thick. Micrographs of a transverse section through the composite showing the distribution of fibers and the fiber coatings are shown in Fig. 4.

Uniaxial tensile tests were conducted at ambient temperature. The specimens were ~ 6 mm wide and cut parallel to the fiber axis. Aluminum or steel tabs with a 10° bevel were bonded to the specimen ends. Tests were conducted in a servohydraulic testing machine, using hydraulic wedge grips to load the specimen. The specimen gauge length was varied between 12 mm and 220 mm. Axial strains were monitored using a 12.7 mm contacting extensometer. Tests were conducted at fixed displacement rates, corresponding to a nominal strain rate of 0.5%/min..

The average fiber fragment length of one of the long specimens was measured following fracture, using a two step process. First, the tabbed end of the broken specimen and a small portion of the gauge length were masked with an epoxy adhesive, and the matrix material within the remaining portion of the composite dissolved using HF acid. The length of the dissolved section was ~ 140 mm. During this process, the broken fibers within the gauge section were extracted and discarded. The remaining "brush" of fibers protruding from the masked section was then impregnated with epoxy and the epoxy allowed to cure. The brush was subsequently cut along the edge of the mask and the fiber fragments extracted from the epoxy by dissolving the epoxy in a solvent. The lengths of the individual fragments were measured using vernier calipers. Provided that none of the remaining fragments spans the entire length of the dissolved section, the average fiber length measured in this fashion corresponds to exactly one-half of the

average fragment length within the composite. In the present case, only ~ 5% of the fibers spanned this length.

The axial residual stresses were measured using a matrix dissolution technique[15,16]. A long, thin strip was cut from the composite panel parallel to the fiber axis. Both the composite strip and a reference steel strip of known length were mounted adjacent to one another on a glass plate. Scratches were then scribed on the sample near both ends of the steel strip. The distances between the scratches and the ends of the steel strip were measured in an optical microscope. The ends of the composite strip (including the scratches) were masked with epoxy and the matrix in the central region dissolved using HF acid. The length of the dissolved section, ℓ, was 32 mm. The masks were subsequently removed and the specimen again mounted on the glass plate adjacent to the reference strip. The distances between the scratches and the ends of the reference strip were re-measured. These measurements were combined with those taken prior to dissolution to obtain the *length change* δ *in the fibers due to the relaxation of residual stress.* The residual axial stresses in the matrix σ_m^r and in the fiber σ_f^r prior to dissolution are related to δ by[15,16]

$$\sigma_f^r = -\delta E_f/L \tag{30a}$$

and

$$\sigma_m^r = -f\sigma_f^r/(1-f) = \delta E_f f/L(1-f) \tag{30b}$$

An independent measure of the matrix yield stress was obtained using micro-hardness measurements. Vickers indentations were made in the matrix rich regions between fibers on a composite section cut perpendicular to the fibers. Following several preliminary tests, it was found that the indentation size could be kept to within $\lesssim 1/3$ of the edge-to-edge fiber spacing for an indentation load of 200 g

(Fig. 5). This load was used for all subsequent measurements. The matrix yield stress was estimated using the relation[17]

$$\sigma_m^y = H/C \tag{31}$$

where H is the Vickers hardness (expressed in units of MPa) and C is a plastic constraint factor, taken to be ~ 2.5.

The *in-situ* strength characteristics of the fibers were measured on individual filaments that had been extracted from the composite. The tests were conducted in a dedicated fiber tensile tester*. Four gauge lengths were used: 5, 12.7, 25 and 265 mm. For each length, a minimum of 50 fibers were tested. The strength distribution was characterized using the Weibull function (Eqn. 5). For comparing the strength characteristics of fibers of different gauge lengths, it is convenient to re-write Eqn. 5 as

$$\ell n\,(-\ell n\,(1-P_f)) - \ell n\,L/L_o = m\,\ell n\,\sigma - m\,\ell n\,\sigma_o \tag{32}$$

such that a plot of $\ell n\,(-\ell n\,(1-P_f)) - \ell n\,L/L_o$ vs. $\ell n\,\sigma$ can be used to evaluate m and σ_o. The results were compared with those obtained on pristine fibers with a length of 25 mm, provided by the fiber manufacturer.

The sliding resistance of the fiber-matrix interface was measured using fiber pushout tests[18]. Specimens for pushout testing were prepared by cutting sections ~ 500 μm thick transverse to the fibers, followed by grinding and polishing to a final thickness of ~ 400 μm. The matrix on one side of the specimen was then carefully etched to a depth of ~ 30 μm, leaving the fibers protruding above the matrix surface.

---

* Micropull Science

A 300 μm tall cylindrical indentor was placed on top of a selected fiber. (The indentors had been machined from the Sigma-SiC fibers themselves.) The fibers were subsequently pushed out of the section and the load-displacement characteristics measured. Additional details of the testing apparatus can be found elsewhere[18]. In calculating the interfacial sliding resistance, τ, the shear stress was assumed to be uniform along the interface and given by

$$\tau = \frac{P}{2\pi R(t-u)} \tag{33}$$

where P is the applied load, t is the section thickness and u is the amount of sliding displacement.

4. MEASUREMENTS AND OBSERVATIONS

The tensile stress-strain curves exhibited the features shown in Fig. 6. Upon initial loading, the response was elastic with a modulus, E = 201 ± 11 GPa. This value is consistent with one calculated from the rule of mixtures, E = 203 GPa, using a matrix modulus, E_m = 110 GPa[19], and a fiber modulus, E_f = 400 GPa*. The onset of yielding occurred at a tensile strain of ~ 0.45%. This strain corresponds to a nominal matrix stress (*neglecting* the residual stress) of ~ 500 MPa. Fracture occurred at an average tensile stress of 1590 ± 100 MPa and a tensile strain of 0.94 ± 0.05%. There was no apparent effect of the specimen gauge length on the shape of the stress-strain curve, the ultimate tensile strength or the fracture strain (Fig. 7).

The apparent fiber length distribution following dissolution of a broken specimen is shown in Fig. 8. The average length in this distribution is $\bar{\ell}$ = 39mm,

* Provided by fiber manufacturer.

corresponding to an *in-situ* fiber fragment length, $\bar{\ell}_f = 2\,\bar{\ell} = 78$ mm. No correction was made for the fibers that had remained intact over the entire length of the dissolved section, though the number of these was small (~ 5%) and is not expected to substantially alter the result.

The dissolution experiment to measure residual stress yielded a length change of 85 μm in a gauge length of 32 mm. Combining this result with Eqn. 30 yields axial residual stresses of $\sigma_m^r = 490$ MPa and $\sigma_f^r = -1040$ MPa. These results have been combined with the measured composite yield strain along with Eqn. 28 to obtain the (unconstrained) matrix yield stress, $\sigma_m^y = 1000$ MPa. This value is in reasonable agreement with the range of values inferred from the microhardness measurement: $\sigma_m^y = 940$ MPa. In addition, both of these values are consistent with the yield strengths of similar Ti-6Aℓ-4V alloys, which range from ~ 900 to ~ 1050 MPa[19].

The results of the fiber tensile tests, presented in the form suggested by Eqn. 32, are shown in Fig. 9. In this form, the data collapse onto essentially a single band. This result confirms the scaling of failure probability with gauge length via Eqn. 32. Though the curve exhibits some non-linearity at low values of strength, the majority of the data can be reasonably well approximated by the two parameter Weibull function, using values $\sigma_0 = 1.47 \pm 0.2$ GPa and $m = 5.3^*$. It should also be noted that the strengths of the extracted fibers are substantially lower than those of the pristine fibers, indicating that additional flaws are introduced into the fibers during composite consolidation.

The results of the pushout tests are presented in Fig. 10. In all cases, sliding initiated at a stress, $\tau \approx 90$-120 MPa. Upon further loading, the sliding resistance increased and reached a saturation level of $\tau \approx 130$ MPa following ~ 0.5 μm of fiber

* Based on linear regression analysis, neglecting the 5 lowest strength values. These 5 constitute ~ 2% of the total number of tests. A more detailed discussion of the effects of gauge length on the strength distribution can be found in Ref. 7.

displacement. The same sliding resistance was measured for fiber displacements up to ~ 20 μm.

5. COMPARISON OF EXPERIMENT AND THEORY

Comparisons of the experimental results with the model predictions are shown in Figs. 6 and 11. The relevant constituent properties used in the models are summarized in Table 1.

In Fig. 7, the predicted upper and lower bounds to the fracture stress and fracture strain from the fiber fragmentation model are plotted as solid horizontal lines. The error bars represent the range of predicted values, resulting from the uncertainty in the fiber reference strength ($\sigma_0 = 1.47 \pm 0.2$ GPa). The dashed lines correspond to the predictions of the dry fiber bundle model. It is evident that the dry fiber bundle model strongly underestimates both the fracture stress and fracture strain, a consequence of the assumption that no coupling exists between the fibers and the matrix. In addition, the model predicts a gauge length dependence that is inconsistent with the experimental measurements. Conversely, the fiber fragmentation model predicts a fracture stresses and a fracture strain that are broadly consistent with the experimental measurements, with the better correlation being established with the lower bound estimates. Furthermore, the fragmentation model predicts gauge length *independent* behavior, consistent with the experiments.

The predicted average fragment lengths for the relevant range of values of σ_0 are also in good agreement with the experimentally measured values (Fig. 11), providing yet additional support for the fragmentation model.

6. CONCLUDING REMARKS

The present work demonstrates that the axial tensile properties of unidirectional Ti/SiC composites can be described using models based on fiber fragmentation, taking into account the effects of the thermal residual stress, the *in-situ* fiber strength distribution, the matrix yield stress and the sliding resistance of the fiber-matrix interface. Clearly, models based on the behavior of a *dry* fiber bundle model are inadequate. Moreover, the conclusion that the strength of the composite is *independent* of gauge length has important implications regarding the design of large structures, particularly since material characterization is generally conducted on relatively small coupons.

An important additional feature incorporated into the fragmentation model is the lower bound condition for fiber bundle failure. The present results indicate that this bound is consistent with the measurements of both fracture stress and fracture strain in the Ti/SiC composite. Moreover, since this bound is conservative, it would be appropriate for use in the design of composite structures.

TABLE 1 Summary of Constituent Properties

Fibers	
Young's modulus, E_f	400 GPa
Axial Residual Stress, σ_f^r	-1040 MPa
Weibull Modulus, m	5.3
Reference Strength, σ_o	1.47 ± 0.2 GPa
Volume fraction, f	0.32
Diameter, 2R	100 μm
Matrix	
Young's Modulus, E_m	110 GPa
Axial Residual Stress, σ_m^r	490 MPa
Yield Stress, σ_m^y	1000 MPa
Volume fraction, 1-f	0.68
Interface	
Sliding stress, τ	130 MPa

ACKNOWLEDGMENTS

Funding of this work was supplied by the DARPA University Research Initiative Program at UCSB under ONR contract N-0014-92-J-1808.

REFERENCES

1. J. Doychak, *J. Metals*, **44** (1992), No. 6, 46-51.

2. S.J. Connell, F.W. Zok, Z.Z. Du and Z. Suo, submitted to *Acta Metall. Mater.*, (1993).

3. S. Jansson, H. Déve and A.G. Evans, *Metall. Trans.*, **22A** (1991), 2975-84.

4. S.L. Draper, P.K. Brindley and M.V. Nathal, *Metall. Trans.*, **23A** (1992), 2541-48.

5. G.J. DeSalvo, "Theory and Structural Design Applications of Weibull Statistics," General Westinghouse, Pittsburgh, PA (1970).

6. J.R. Porter, *Mat. Res. Soc. Symp. Proc.*, **273** (1992), 315-24.

7. F.W. Zok, X. Chen and C.H. Weber, submitted to *J. Am. Ceram. Soc.*, (1993).

8. B.W. Roxen, "Mechanics of Composite Materials: Recent Advances," Pergamon Press, Oxford, (1983), p. 105.

9. W.A. Curtin, *J. Mater. Sci.*, **26** (1991), 5239-53.

10. W.A. Curtin, *J. Am. Ceram. Soc.*, **74** (1991), 2837-45.

11. J. Neumeister, *J. Mech. Phys. Solids*, **41** (1991),1383-1404.

12. K.K. Chawla, "Composite Materials, Science and Engineering," Springer-Verlag, New York (1987), Chap. 12.

13. B. Budiansky, J.W. Hutchinson and A.G. Evans, *J. Mech. Phys. Solids*, **34** (1986), 164-89.

14. C. Barrett and T.B. Massalski, "Structure of Metals," 3rd ed., Pergamon Press (1980), p. 631.

15. B.N. Cox, M.R. James, D.B. Marshall and R.C. Addison, Jr., *Metall. Trans.*, **21A** (1990), 2701-7.

16. D. Beyerle, S.M. Spearing, F.W. Zok and A.G. Evans, *J. Am. Ceram. Soc.*, **75** (1992), 2719-25.

17. T.H. Courtney, "Mechanical Behavior of Materials," McGraw Hill Pub. Co., New York (1990), Chap. 1.

18. P.D. Warren, T.J. Mackin and A.G. Evans, *Acta Metall. Mater.*, **40** (1992), 1243.

19. Metals Handbook, Ninth Ed. (1990), Vol. 3, "Properties and Selection: Stainless Steels, Tool Materials and Special Purpose Metals, ASM, Metals Park, OH, pp. 388-91.

FIGURES

Fig. 1 Trends in normalized tensile strength, $\sigma_u/f\,\sigma_o$, with gauge length, ℓ/ℓ_o, and Weibull modulus, m, for $\sigma_m^y = 0$ based on dry fiber bundle behavior.

Fig. 2 Predictions of the upper and lower bounds to (a) the fracture stress and (b) the fracture strain, resulting from the fiber fragmentation model.

Fig. 3 Schematic diagram showing the effects of thermal residual stress on the composite response.

Fig. 4 Transverse section through composite, showing (a) the spatial distribution of fibers and (b) the fiber/matrix interfacial region.

Fig. 5 Optical micrograph of the indentation produced using a 200 g load.

Fig. 6 Typical tensile stress-strain response of the Ti/SiC composite. Also shown is the prediction from the fragmentation model, with the two thin arrows corresponding to the lower and upper bond estimates of the fracture point.

Fig. 7 Influence of gauge length on (a) the ultimate tensile strength and (b) the fracture strain. Also shown are the upper and lower bounds predicted by the fiber fragmentation model, and the prediction of the dry fiber model.

Fig. 8 Distribution of fiber fragment lengths following tensile fracture.

Fig. 9 Results of the fiber tensile tests, presented in the form suggested by Eqn. 32. Also shown are the results for the pristine fibers, derived from > 1000 fiber tests conducted by the fiber manufacturer.

Fig. 10 Results of fiber pushout tests.

Fig. 11 Comparison of predicted average fiber fragment length with the measured values.

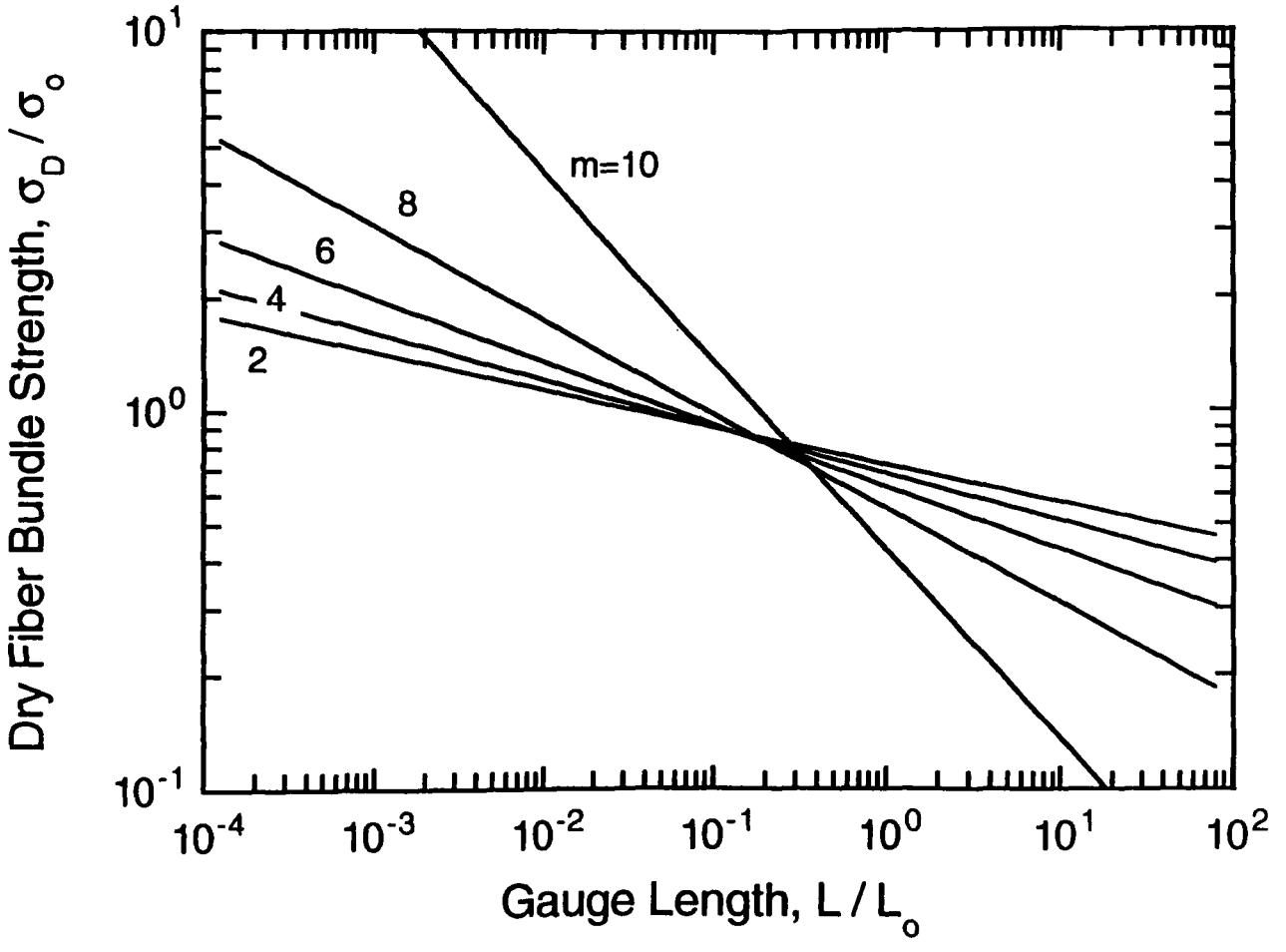
Dry Fiber Bundle Strength, σ_D / σ_o
10^1
10^0
10^{-1}
m=10
8
6
4
2
10^{-4}
10^{-3}
10^{-2}
10^{-1}
10^0
10^1
10^2
Gauge Length, L / L_o

Figure 1

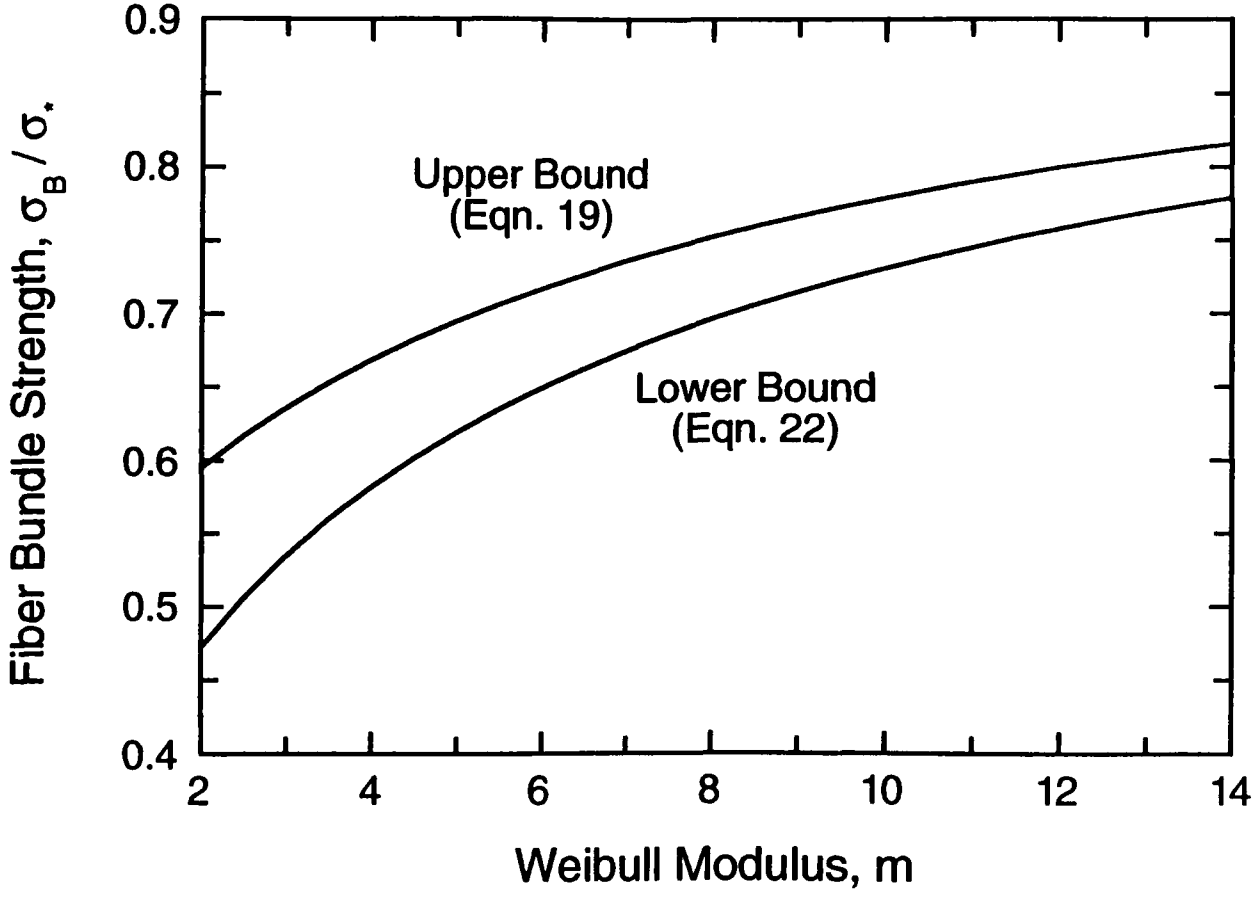
0.9
0.8
0.7
0.6
0.5
0.4
Fiber Bundle Strength, σ_B / σ_*
Upper Bound
(Eqn. 19)
Lower Bound
(Eqn. 22)
2
4
6
8
10
12
14
Weibull Modulus, m

Figure 2(a)

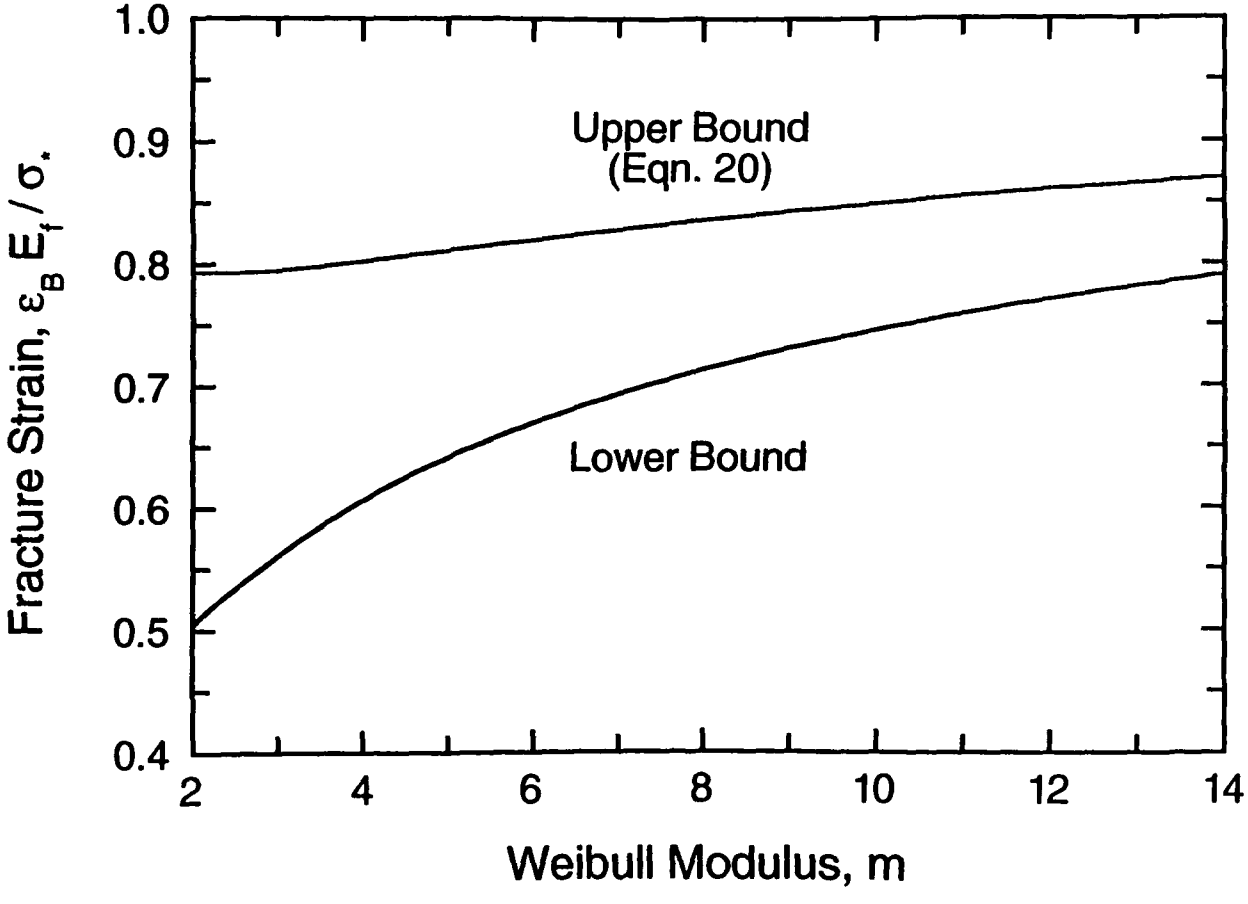
1.0
0.9
0.8
0.7
0.6
0.5
0.4
Fracture Strain, $\varepsilon_B E_f / \sigma_*$
Upper Bound
(Eqn. 20)
Lower Bound
2
4
6
8
10
12
14
Weibull Modulus, m

Figure 2(b)

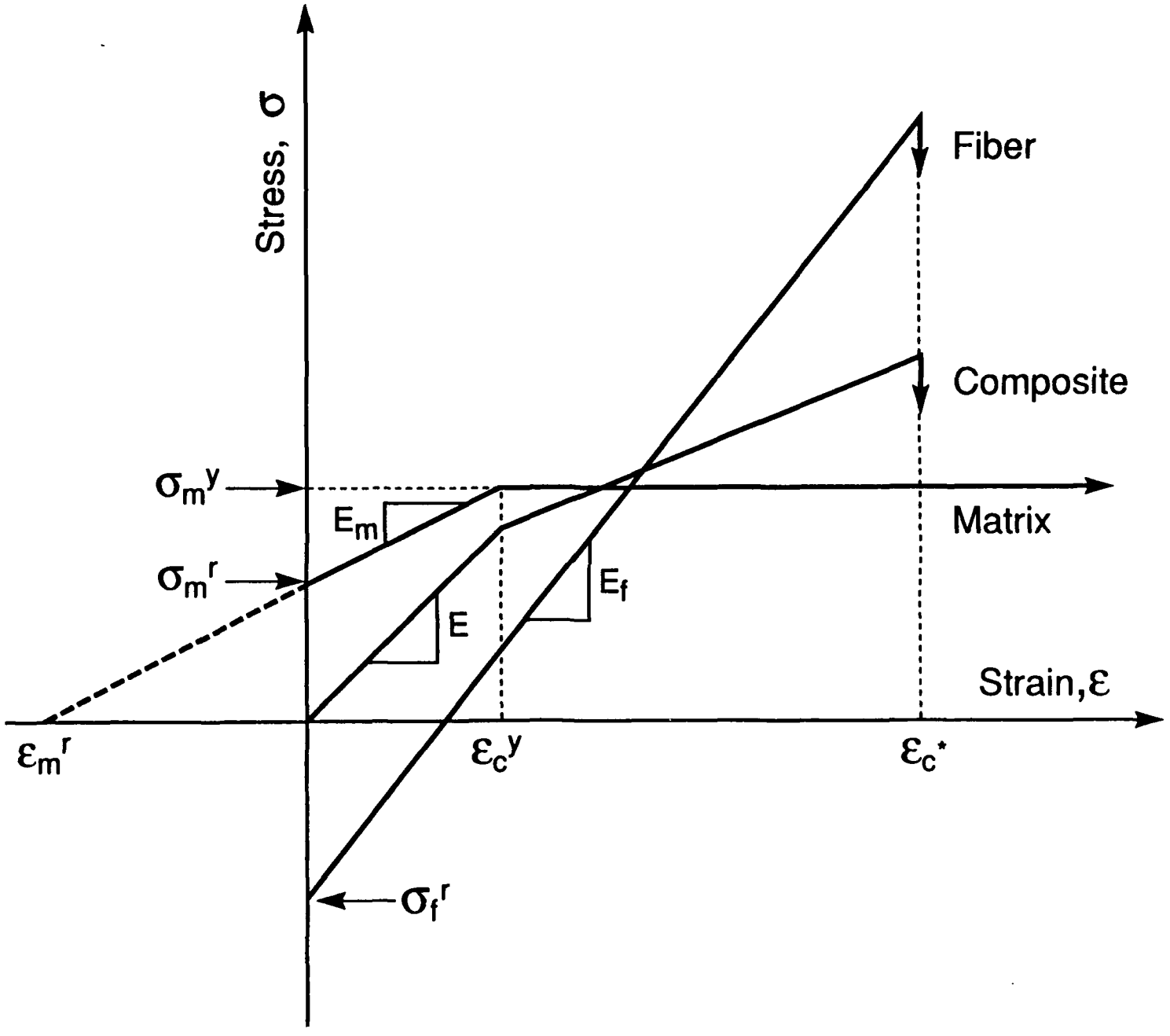

ZokONR-9/93-amk-D14#1204-3

Figure 3

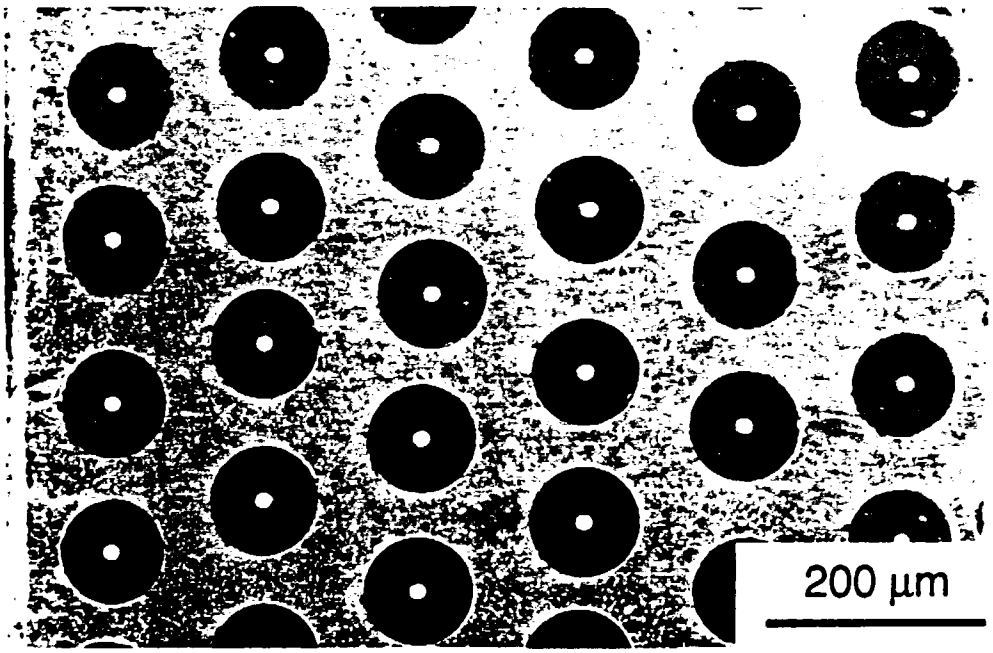

Figure 4(a)

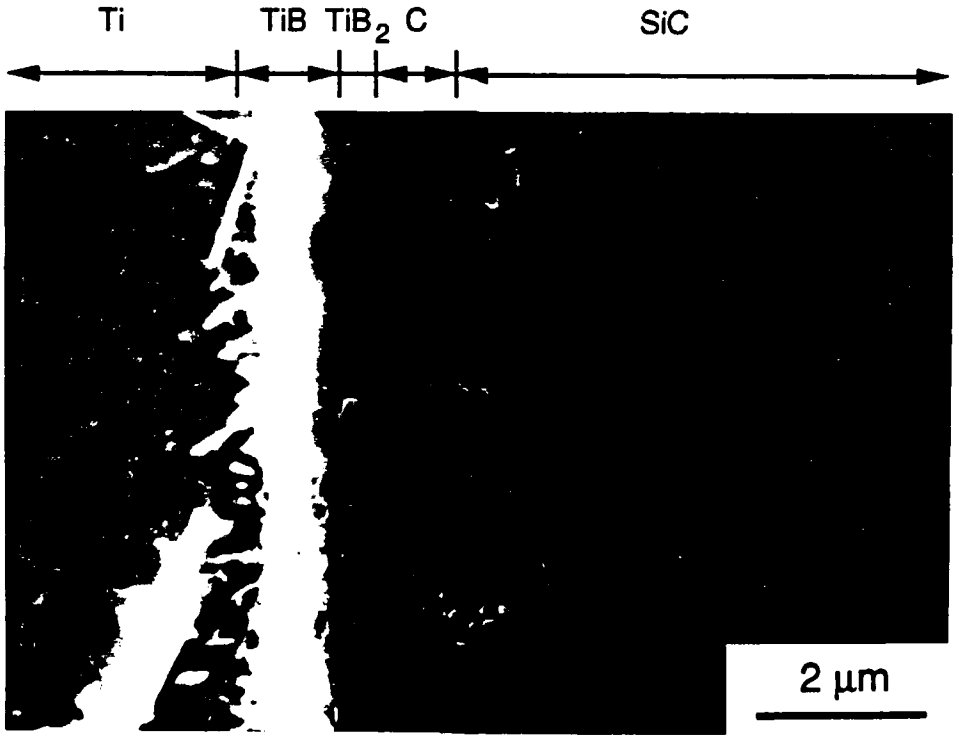

Figure 4(b)

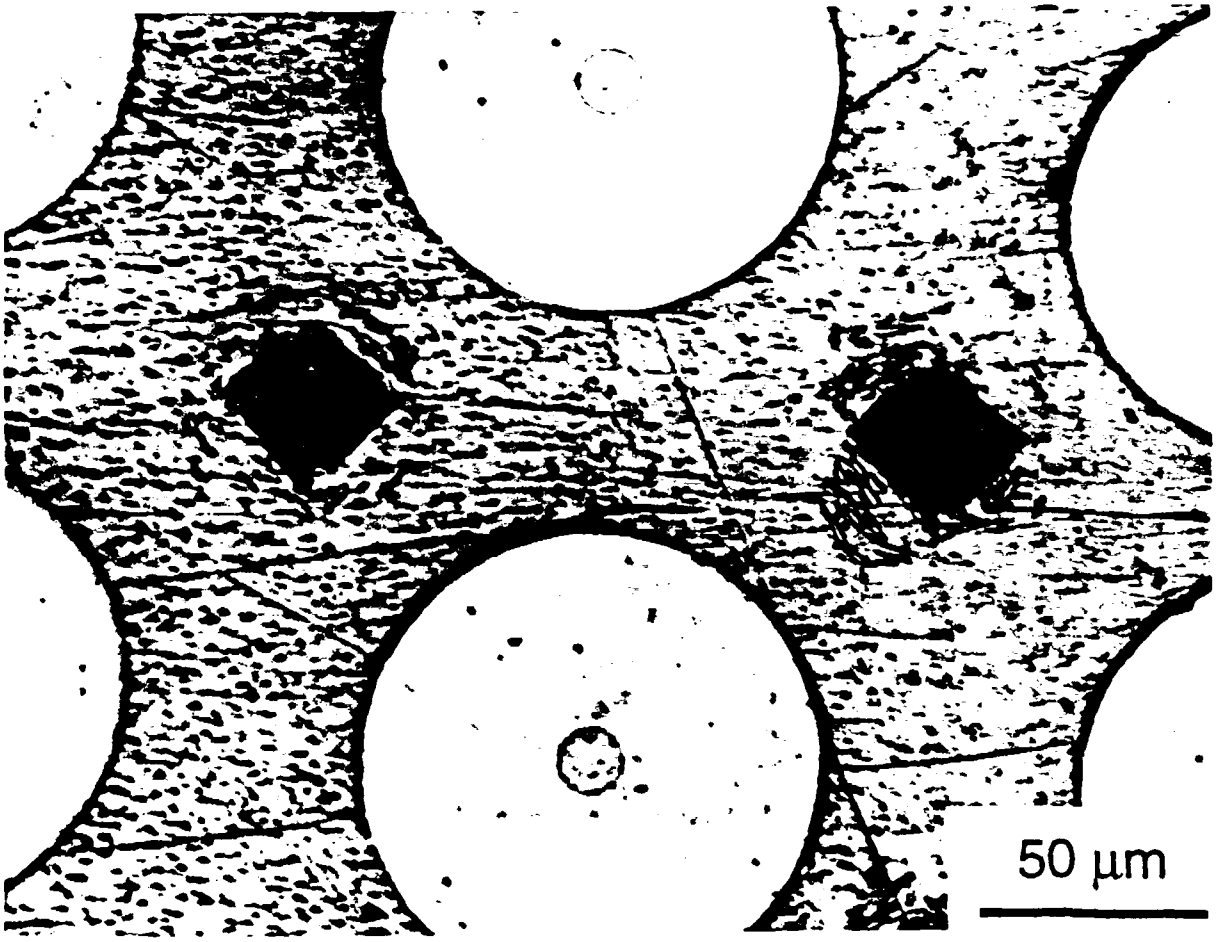

Figure 5

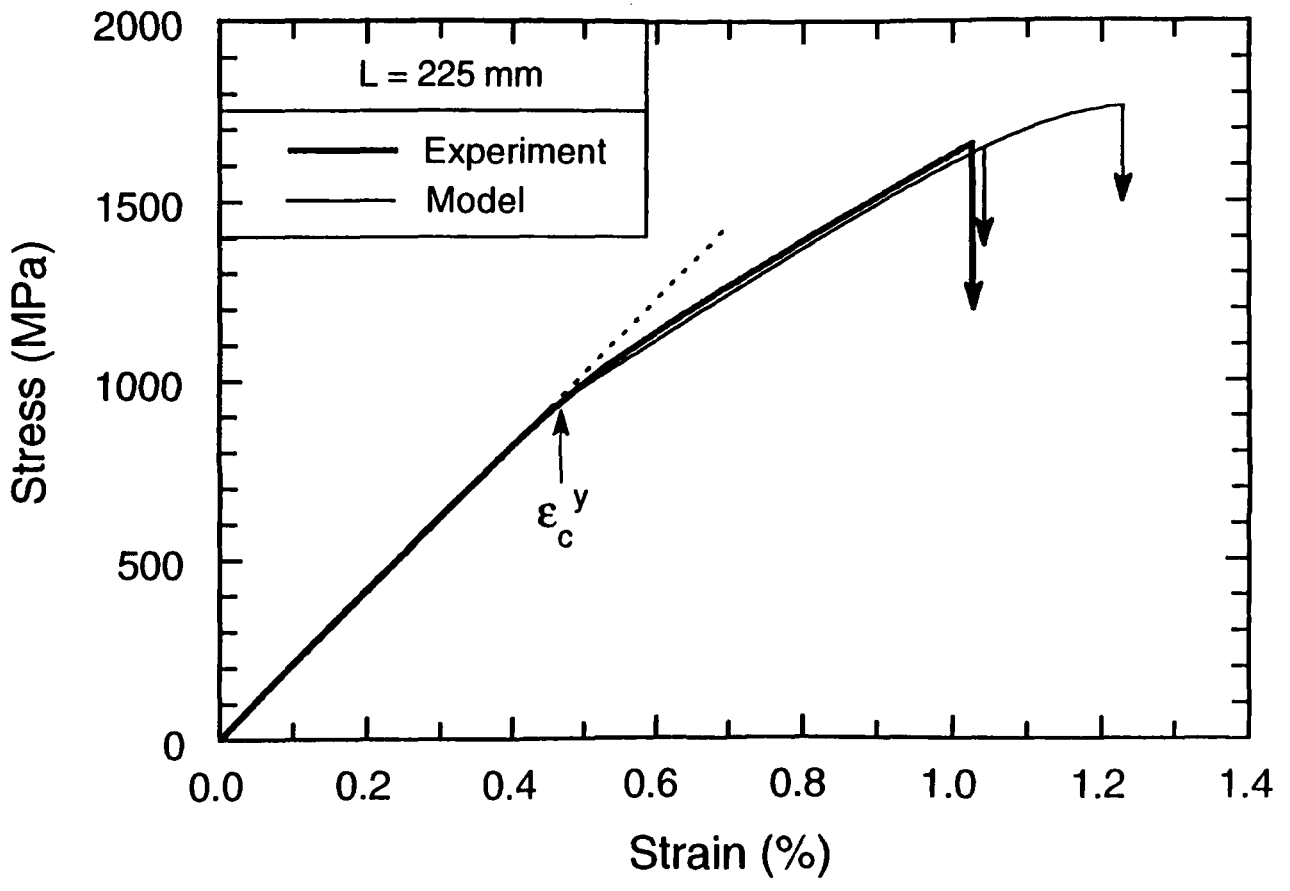
2000
1500
1000
500
0
Stress (MPa)
L = 225 mm
Experiment
Model
ε_c^y
0.0
0.2
0.4
0.6
0.8
1.0
1.2
1.4
Strain (%)

Figure 6

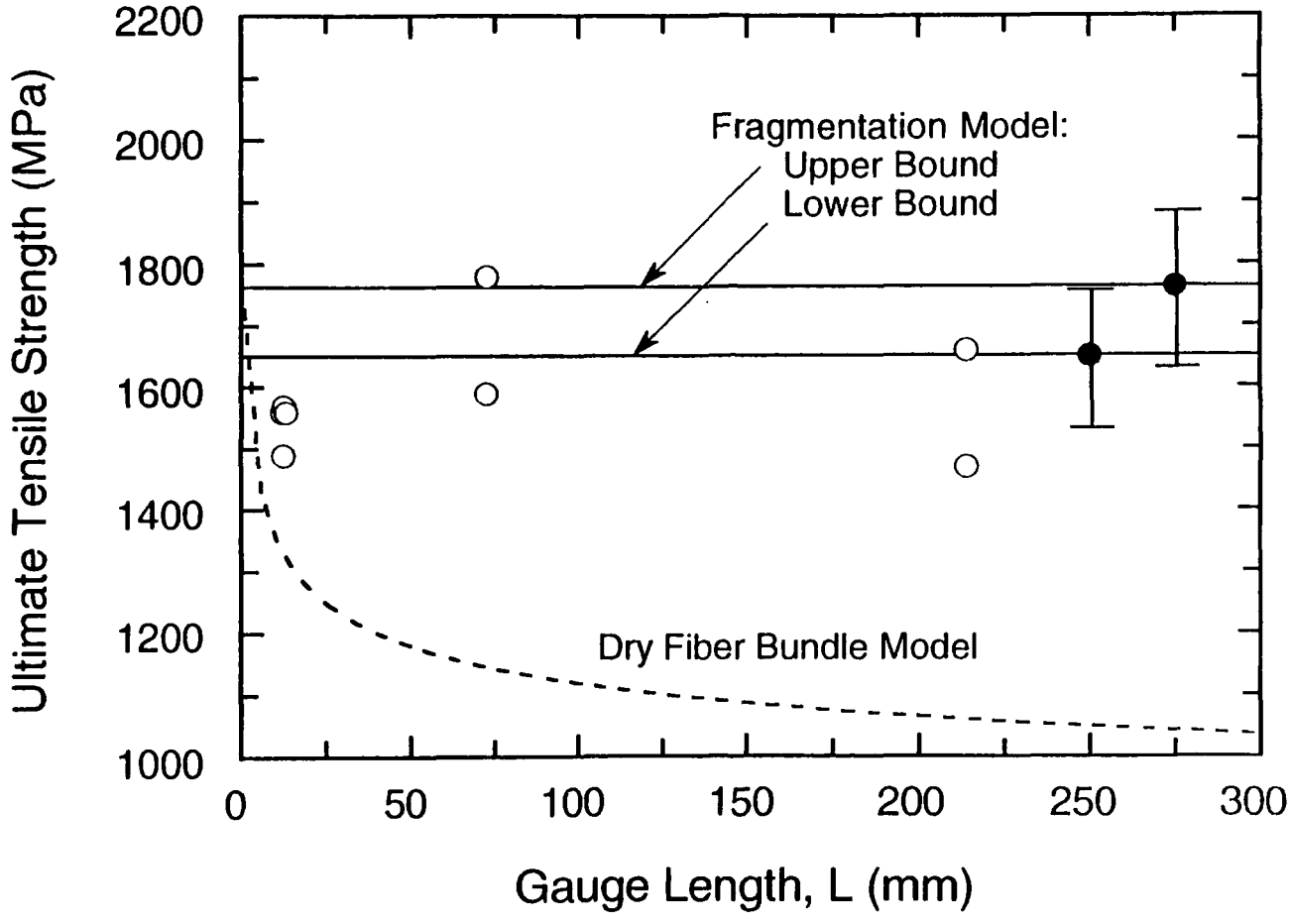
Ultimate Tensile Strength (MPa)
2200
2000
1800
1600
1400
1200
1000
0
50
100
150
200
250
300
Gauge Length, L (mm)
Fragmentation Model:
Upper Bound
Lower Bound
Dry Fiber Bundle Model

Figure 7(a)

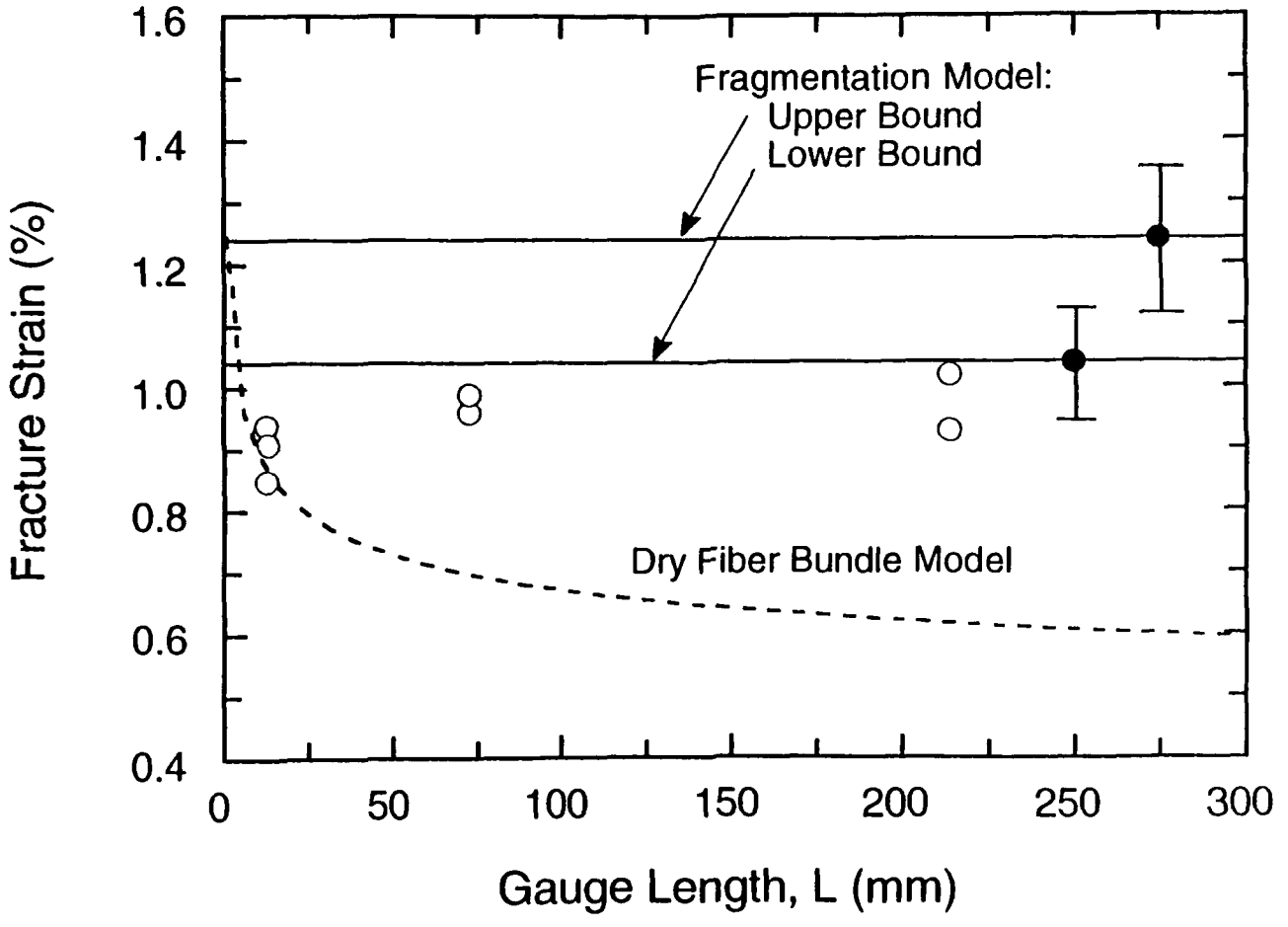
Fragmentation Model:
Upper Bound
Lower Bound
Dry Fiber Bundle Model
Fracture Strain (%)
1.6
1.4
1.2
1.0
0.8
0.6
0.4
0
50
100
150
200
250
300
Gauge Length, L (mm)

Figure 7(b)

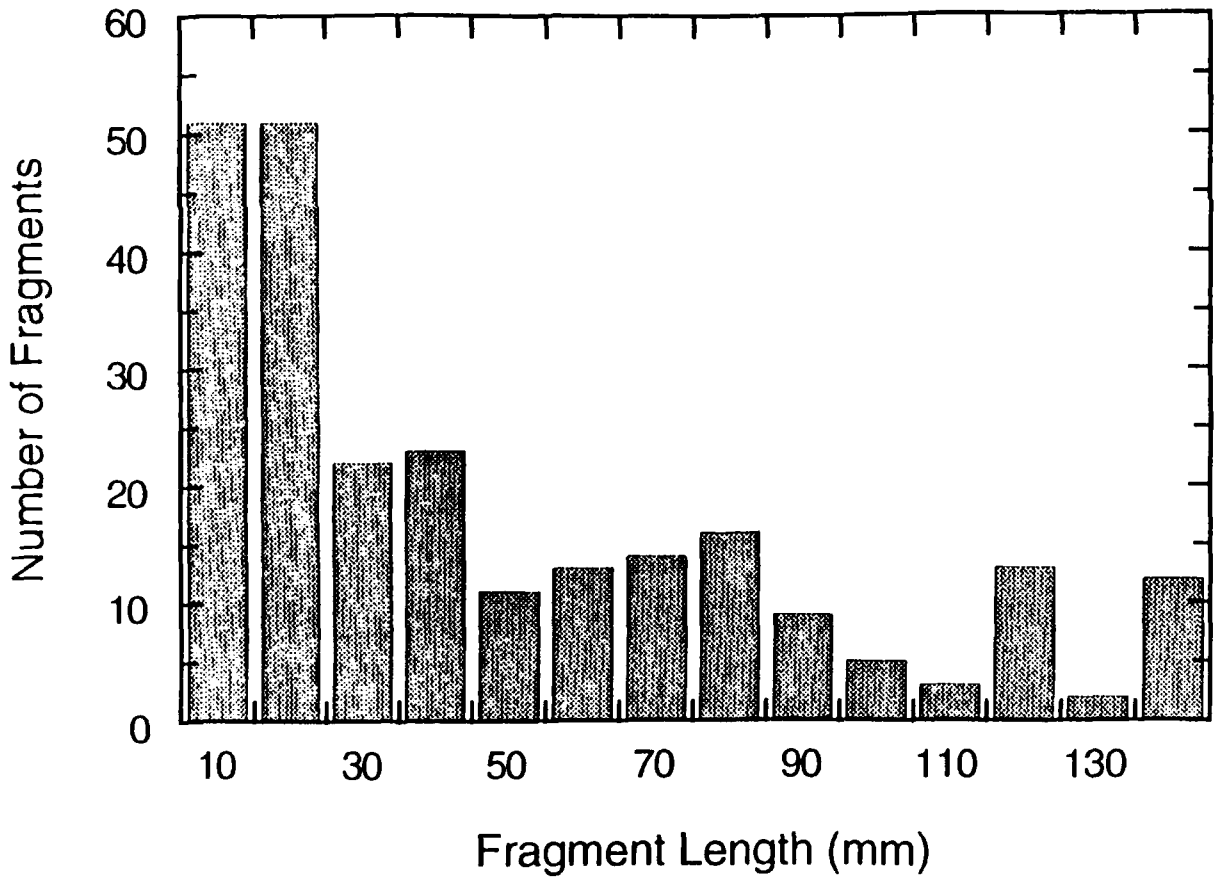
60
50
40
30
20
10
0
Number of Fragments
10
30
50
70
90
110
130
Fragment Length (mm)

Figure 8

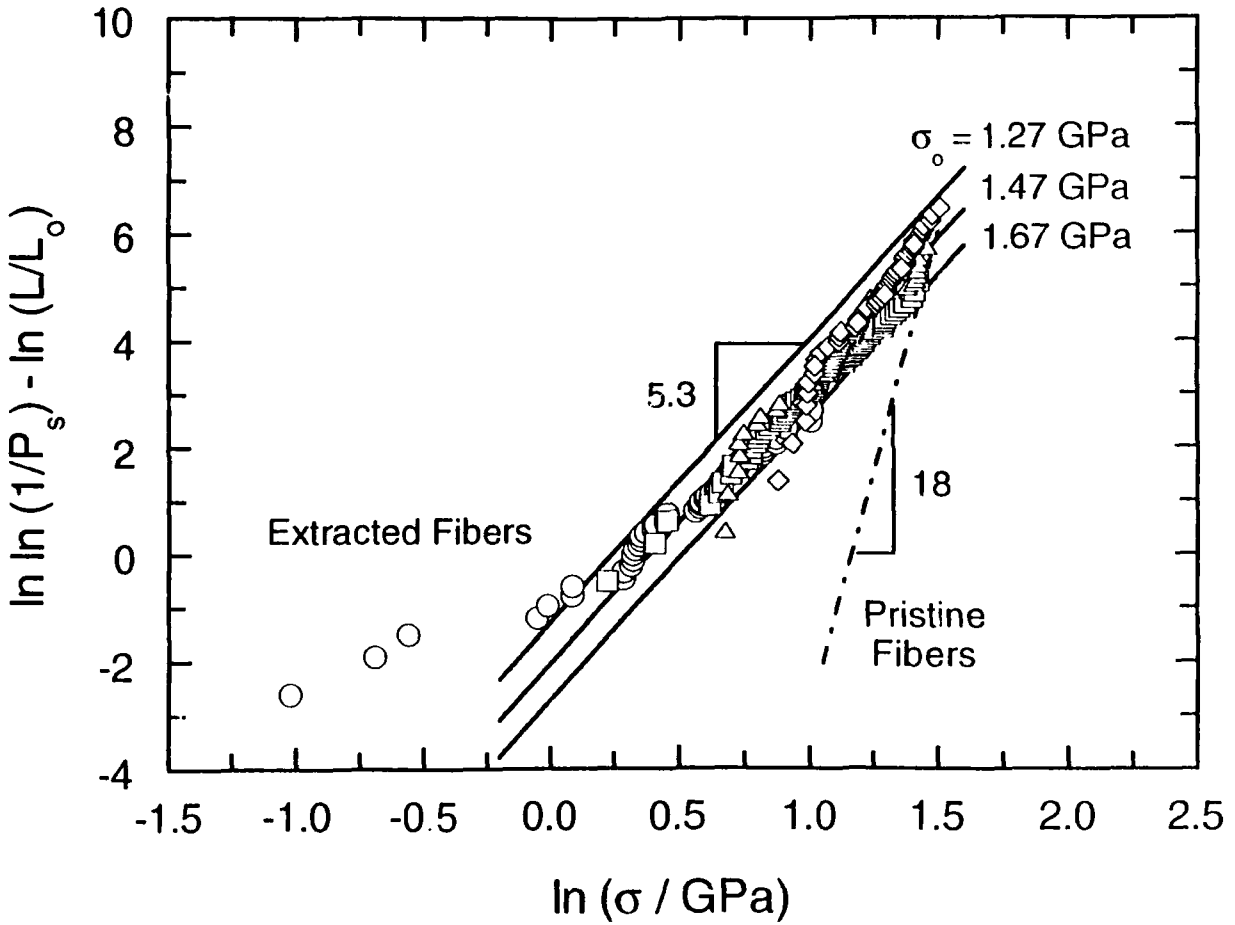
10
8
6
4
2
0
-2
-4
-1.5
-1.0
-0.5
0.0
0.5
1.0
1.5
2.0
2.5
ln ln (1/P_s) - ln (L/L_o)
ln (σ / GPa)
σ_o = 1.27 GPa
1.47 GPa
1.67 GPa
5.3
18
Extracted Fibers
Pristine
Fibers

Figure 9

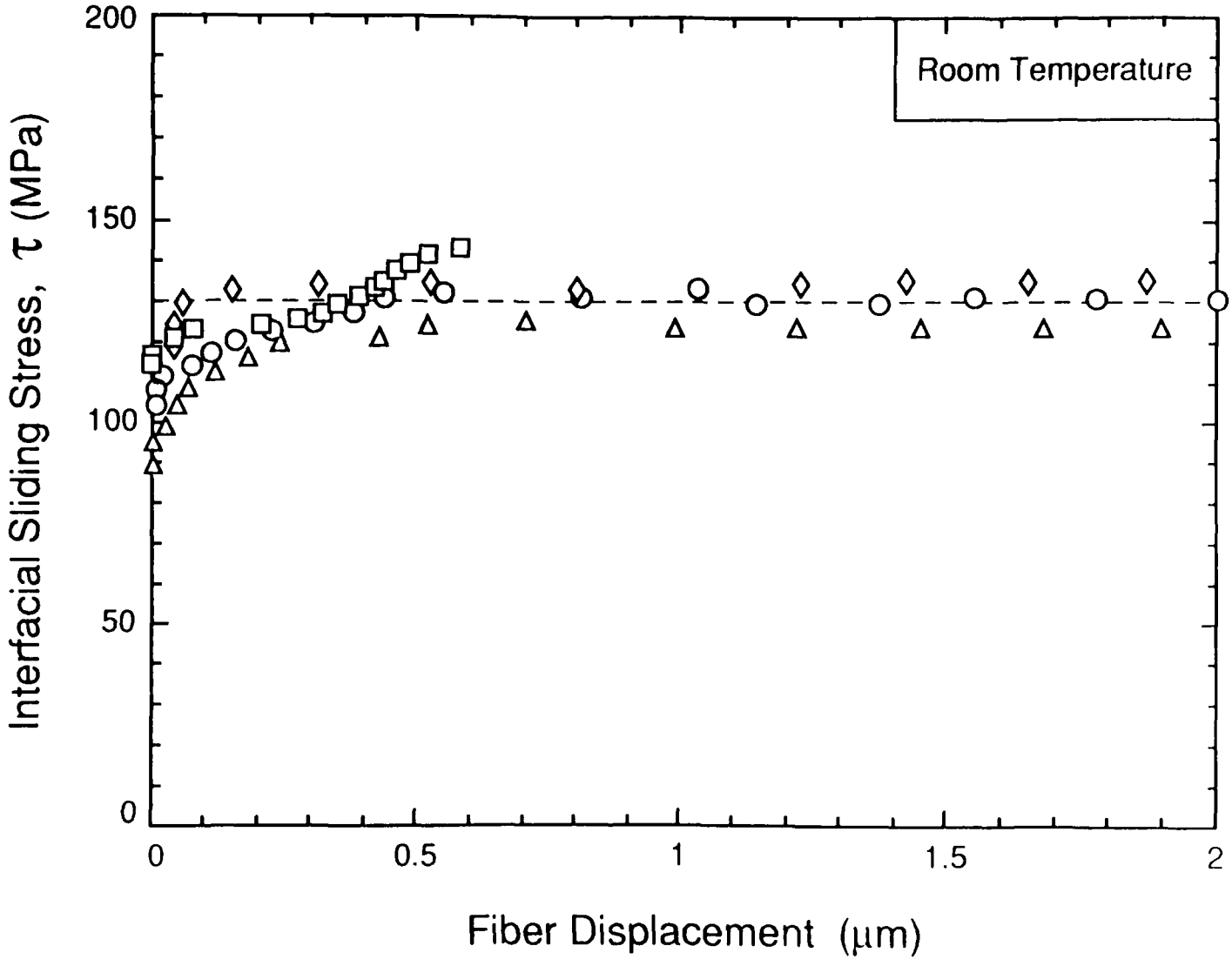
Room Temperature
Interfacial Sliding Stress, τ (MPa)
200
150
100
50
0
0
0.5
1
1.5
2
Fiber Displacement (μm)

Figure 10

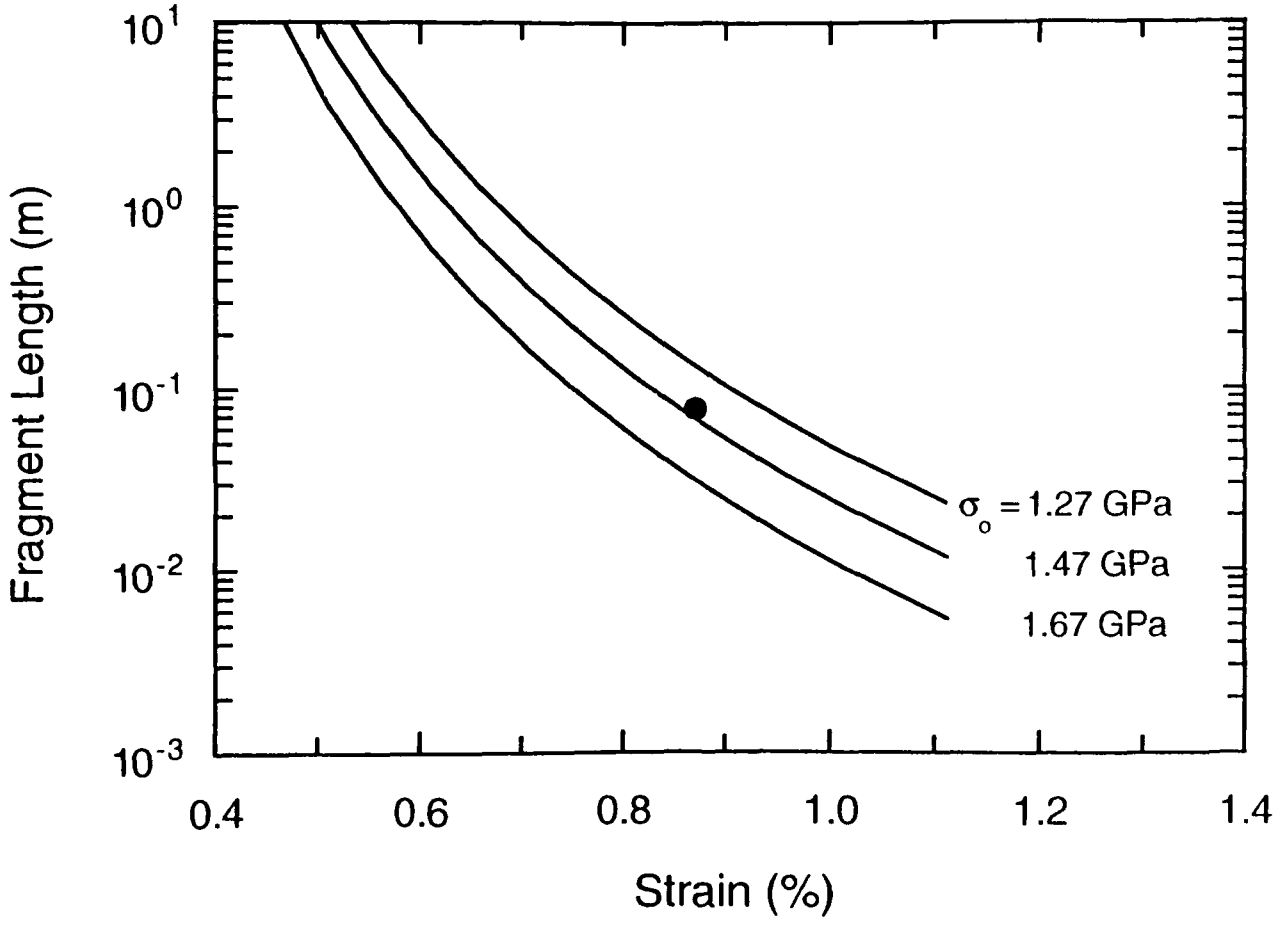
Fragment Length (m)
10^{1}
10^{0}
10^{-1}
10^{-2}
10^{-3}
0.4
0.6
0.8
1.0
1.2
1.4
Strain (%)
σ_o = 1.27 GPa
1.47 GPa
1.67 GPa

Figure 11

Control of Strength Anisotropy of Metal Matrix Fiber Composites

Z.-Z. Du and R.M. McMeeking*

Materials Department and Mechanical Engineering Department*

University of California

Santa Barbara, California 93106

March. 1994

Abstract

This paper examines theoretically the stress distribution around fiber breaks in a unidirectional reinforced metal matrix composite subjected to axial loading when plastic yielding of the matrix is allowed to occur. The composites considered have a ductile interphase bonding the matrix to the fiber. The likelihood of failure of a fiber adjacent to the existing broken fiber is considered. Detailed and systematic results are given for composites with a wide range of fiber volume fractions, Young's modulus of the fibers and the matrix, interphase properties and Weibull modulus for the strength of the fibers. The objective is the optimization of these material and geometric variables to ensure global load sharing among the fibers in the longitudinal direction which will give the composite good longitudinal strength. Calculations are also carried out for transverse loading of the composite to determine the effect of the ductile interphase on the yield strength. Characteristics of the ductile interphase are determined that will provide good longitudinal strength through global load sharing and a relatively high yield strength in the direction transverse to the

fibers. This, in turn, will allow control of the strength anisotropy of uniaxially reinforced metal matrix composites.

1 Introduction.

Metal matrix composites ($SiC/Ti, Al_2O_3/Al$) as engineering materials are now in the process of development. The metal matrix can be reinforced by fibers, particulates or whiskers. Continuous fiber reinforced metal matrix composites are particularly attractive as they offer outstanding unidirectional mechanical properties, such as high stiffness, strength and creep resistance in comparison with composites reinforced by particulates or whiskers.

Engineering components made of continuous fiber reinforced metal matrix composites are usually formed by one of a range of processes, which involve dry pressing, hydrostatic molding, extrusion or injection molding, followed by final machining. The processing can cause damage of the fibers in the finished component. Final machining of the component further increases the probability of failures in the fibers. When mechanical load is applied to the finished component, further damage initiates in the form of isolated fiber breaks. The failure of one fiber in a homogeneous stress state may then cause a neighboring fiber to fail because of stress concentration. This behavior is associated with localized load sharing among fibers around a broken fiber. Thus a single fiber failure may tend to cause a spreading of damage in the form of fiber breaks near a single plane across the section. This will lead to localized high plastic and elastic strains in the matrix near the breaks perhaps giving rise to ma-

trix failure and, eventually, leading to a complete failure of the composite. To avoid this situation, it is necessary to ensure global load sharing, whereby the load shed from a broken fiber is shared nearly equally among all intact fibers. This can be achieved with a weak interface between the fiber and the matrix. All successful fiber reinforced metal matrix composites have a weak interface giving rise to global load sharing among the fibers and thus have significant longitudinal strength(1-3). However, the weak interface leads to debonding under transverse load and the strength in this orientation is usually less than the un-reinforced matrix material. This represents a significant deficiency of fiber reinforced metal matrix composites.

An alternative approach, which has not received significant attention, is to provide a low strength interface between the fiber and the matrix in the form of a well bonded shearable interphase. This will diminish stress concentrations around fiber breaks and limit the spread of fiber failure just as when a weak, debonding interface is present. However, a well bonded shearable interphase between the fiber and the matrix should be capable of providing adequate transverse strength. Such an approach is explored in this paper.

Theoretical studies on fiber failure stochastics have already been carried out by several investigators leading to statistical strength prediction procedures for composites (1,4,5). He et. al.(1) developed a criterion to predict the transition from global load sharing to local load sharing by evaluating around a broken fiber the relative survival probabilities ϕ_s of the nearest neighbor fibers (ϕ_s^N) and the next nearest neighbor fibers (ϕ_s^{NN}). They noted that the survival probability of a ring of N fibers that fracture in accordance with a two parameter Weibull distribution and subjected

to a uniform stress σ_{ZZ} over a length δ_c is given by

$$-ln\phi_s = N[\sigma_{ZZ}/S_o]^m(\delta_c/L_o) \tag{1}$$

where S_o and L_o are strength and length parameters of the Weibull distribution and m is the Weibull modulus. When $\phi_s^{NN} \leq \phi_s^N$, the survival probability of the nearest neighbor exceeds that of the next nearest neighbor. He et al.(1) argued that this condition would ensure that the development of a well-defined crack from an initial fiber failure cannot occur and thus a global load sharing mechanism would apply. Fiber failure would be more likely to occur far from an existing break rather than in the nearest neighbors. Consequently, the condition for global load sharing depends on the number of fibers around a broken fiber and on the stress ratio

$$\lambda = \frac{\sigma_{ZZ}^N}{\sigma_{ZZ}^{NN}} \tag{2}$$

where σ_{ZZ}^N is the stress in the nearest neighbor fibers around a break and σ_{ZZ}^{NN} is the stress in the next nearest neighbors. Furthermore, the condition $\phi_s^{NN} \leq \phi_s^N$ from (1) ensuring global load sharing occurs when

$$\lambda \leq (N^{NN}/N^N)^{\frac{1}{m}} \tag{3}$$

where N^N is the number of nearest neighbors around a break and N^{NN} is the number of next nearest neighbors. For a typical close packed arrangement of fibers, where $N^N = 6$ and $N^{NN} = 9$, He et al.(1) found for fibers with m=10 that a stress concentration ratio, λ, less than 1.04 appeared to be required for global load sharing.

Based on this criterion, detailed axisymmetric finite element calculations were conducted by He et al.(1) to examine the influence of fiber volume fraction, interface

sliding stress and the Young's modulus of the fibers and the matrix on the levels of stress concentration relevant to global and local load sharing when there is fiber breakage. It was found that for a homogeneous material ($E_f = E_m$), only at very large fiber volume fraction did the stress ratio λ exceed the levels required for global load sharing. A lower matrix stiffness increased the stress concentration in neighboring fibers and made it more likely that the composite would experience local load sharing. However, the presence of a weak interface with a low sliding stress reduced the stress concentration and made global load sharing more likely. This was consistent with experimental observations(2) for ceramic matrix composites. However, the numerical results(1) were limited to the situation where both the fibers and the matrix were elastic and the influence of matrix plastic yielding was not examined. In the present work, we consider the situation where the fibers are elastic but the matrix can yield. This influences the stress concentration around fiber breaks.

Recently, the anisotropic mechanical behavior of metal matrix fiber composites has been examined by Jansson et al.(2) and Gunnawardena et al.(3). However, their results are for a specific set of properties (Ti/SiC) for a material with a weakly bonded fiber-matrix interface. In the present work, systematic studies are conducted for a material with a well bonded interphase between the fiber and matrix to examine the influence of the fiber volume fraction, the elastic stiffness of the fibers and the matrix and the interphase properties on the degree of global load sharing and on the transverse yield strength of the composite. The objective is to ensure global load sharing among the fibers for longitudinal strength and a relatively high load carrying capacity in the direction transverse to the fiber.

Axisymmetric models similar to those used by He et al.(1) are used to analyze the longitudinal behavior of a metal matrix fiber composite which exhibits matrix plastic deformation. Cell models, widely used for both continuous and discontinuous reinforcements(6,7), are used to conduct the analyses for the transverse yielding of the composite. Both perfectly bonded interfaces and cases with a shearable interphase bonding the matrix to the fiber are considered. The shearable interphase is modeled by a very thin elastic perfectly plastic layer between the matrix and the fibers. The thin layer has a perfect bond with both the fibers and the matrix and was considered to have a tensile yield strength which is lower than that of the matrix. The low strength interphase permits fiber-matrix sliding at a reduced shear stress compared to the yield strength in shear of the matrix. The results for the longitudinal behavior of the composite presented below are therefore identical to those for the material with a weak debonding interface permitting sliding by friction with a uniform shear stress. However, the calculations for transverse behavior given below are not relevant to the material with a debonding interface where it is known that the transverse strength is severely reduced by debonding of the interface between fiber and matrix(2,3).

2 Numerical Model

The close-packed arrangement of fibers shown in Fig.1 is analyzed. For the longitudinal problem, an axisymmetric volume containing one broken fiber is modeled as shown. This model is similar to that used by He et al.(1) for analyzing weakly bonded composites with fibers and matrix deforming elastically. An axisymmetric view of the

finite element model is given in Fig.1. A thin ring of ductile material surrounds the broken fiber. The nearest (N) and the next nearest neighbor (NN) fibers are represented by annuli having the fiber elastic modulus. All components of the composite material (fiber, matrix and interphase) are isotropic. The matrix is considered to be an elastic perfectly plastic material. The interphase is omitted between the matrix and the annuli representing the intact fibers. Beyond the annulus representing the next nearest neighbors, the material is considered to be homogeneous and to have the composite properties, which are defined in accordance with the rule of mixtures. That is, the Young's modulus of the composite, E_L equals $fE_f + (1-f)E_m$ and the post yield stress-strain relationship is given by $\varepsilon = [\sigma - (1-f)\sigma_o]/fE_f$, where E_f and E_m are the Young's moduli of the fibers and the matrix respectively, σ is the applied stress and σ_o is the yield stress of the matrix. First yield occurs at $\sigma = \sigma_o E_L/E_m$, after which the material hardens according to the above stress-strain relationship. Although in reality it is anisotropic, the material properties of the region representing composite behavior are assumed to be isotropic such that the properties defined above are used in all directions. This approximation can be made because the emphasis in this analysis is on the longitudinal behavior. The transverse behavior is dealt with in a separate cell model.

It is assumed that the number of nearest neighbor fibers, N^N is 6 and the number of next nearest neighbor fibers, N^{NN} is 12 in the finite element calculations. A range of geometries with fiber volume fractions varying from 0.15 to 0.65 are analyzed. As shown in Fig.1, the annulus representing the nearest neighbor fibers has its inner radius at the closest location of the nearest neighbor fibers to the broken fiber. The

cross-sectional area of the annulus equals the sum of the cross-sectional area of the nearest neighbor fibers. The annulus representing the next nearest fibers is located so that the spacing represents the volume fraction.

Cell models are used also for the transverse strength problems. Two fiber arrangements have been considered: hexagonal and square with the fiber volume fraction ranging from 0.1 to 0.7. Finite element grids for cells with a fiber volume fraction of 0.35 are shown in Fig.2 (a) and (b) for the square and hexagonal arrangement respectively. In the transverse analysis, the fibers are treated as rigid and the analysis is plane strain since the emphasis is on the fully plastic behavior. Modeling the fiber as rigid significantly influences the results of the elastic and elastic-plastic stages of the analysis, but not the fully plastic behavior.

For both the longitudinal and transverse problems, the surfaces of the unit cell (except those bonded to the fibers) remain planar during loading with zero shear traction. Kinematic boundary conditions are used to impose distortions on the unit cell to simulate straining. The distortions are chosen to impose uniaxial stress in the longitudinal problem and a tensile stress in the transverse problem.

A commercial finite element code ABAQUS(8) on an IBM/Risc workstation is used for the calculations. Isoparametric second order hybrid and non-hybrid elements with reduced integration are used to model the transverse and longitudinal problems respectively in order to avoid the problem of mesh locking associated with incompressible deformation. The matrix deforms by small strain J_2 flow theory with a non-hardening tensile yield stress σ_o in all calculations such that the yield strain $\varepsilon_o = \sigma_o/E_m = 1.5 \times 10^{-3}$. The matrix Poisson's ratio is 0.33. For the longitudinal

problem, the fiber is elastic and has the same Poisson's ratio as the matrix.

Both perfectly bonded interfaces and shearable interphases between the fibers and the matrix are considered, where the shearable interphase is modeled by a very thin elastic perfectly plastic layer around the broken fiber in the longitudinal problem and between the matrix and all fibers in the transverse problem. The yield strength in shear of the thin interphase, τ_0 is varied from 0.01 to $1/\sqrt{3}$ times the tensile yield strength of the matrix, σ_o. When $\tau_o = \sigma_o/\sqrt{3}$, the interphase yield strength in shear is the same as that of the matrix and the interphase disappears as a distinct material. In most of the calculations, the thickness of the thin interphase equals 0.025 times the fiber diameter. However, in one case with a fiber volume fraction of 0.35, the ratio of the thickness of the interphase, t, to the fiber diameter, D, is varied to assess its influence on the transverse strength and the stress concentration in the neighboring fibers.

3 Results

3.1 Longitudinal Behavior

Since the failure of fibers is governed by statistics, the values of the average stress at the cross sections of the fibers should be used in eqn(2) to determine the degree of global load sharing. Therefore, only the results associated with the average stress on the cross sections of the nearest and the next nearest fibers are presented in this section.

3.1.1 Strong Interface

Before examining the influence of the interphase properties on the longitudinal strength. it is instructive to examine other factors such as the fiber volume fraction and the Young's modulus of the fibers and the matrix when the interface is perfectly bonded. This allows us to identify the major features of the longitudinal behavior when plastic yielding of the matrix is allowed to occur. When the interface is perfectly bonded. the stress on average at a cross section in the nearest and the next nearest neighboring fibers is presented as a function of a normalized distance, Z/D in Fig.3 (marked no interphase), where Z is measured from the plane of the fiber break along the fiber direction and the strain is at such a level that the ratio of the average stress concentration in the nearest to the next nearest fibers reaches its peak value. It is found that the average stress in the neighboring fibers has its maximum value at a position which is some distance from the plane of the break. The difference of the fiber stress at Z/D=5 in the nearest neighbors and the next nearest neighbors, i.e. the difference of the remote fiber stress, is due to the constraint effect of the imposed boundary condition. It is notable that the stress concentration even in the nearest neighbor is mild even when the interface is strong.

The ratio of stress concentration in the nearest to the next nearest fibers is presented in Fig.4 as a function of the remote fiber stress σ_f normalized by the yield strength of the matrix for a range of fiber volume fractions when $E_f/E_m = 3$. The remote fiber stress can be related to the axial strain by $\sigma_f = E_f\varepsilon$. The stress concentration ratio λ is defined as the largest longitudinal stress in the nearest neighbor divided by the largest longitudinal stress in the next nearest neighbor. In all cases.

the stresses used in the calculation are the averages over the cross section of the fiber. Fig.5 illustrates the influence of the elastic mismatch E_f/E_m on the ratio of the stress concentration when the fiber volume fraction is 0.35. Examination of the results (Figs.4 and 5) reveals that the stress concentration ratio initially increases with the applied stress due to the plastic deformation in the matrix adjacent to the fiber break. The plastic zone around the fiber break tends to concentrate stress in the nearest neighbor fiber(N) but only increases the stress in the next nearest neighbor (NN) slightly. The stress concentration ratio reaches a peak value, then drops off with increasing applied stress. Eventually, when the matrix is completely yielded, the stress concentration ratio approaches an asymptotic value and remains constant with further increase of the applied stress. For a fixed value of the fiber volume fraction (i.e. as in Fig.5), an increase of E_f/E_m tends to reduce the peak value of the stress concentration ratio. For a fixed modulus ratio (i.e. as in Fig.4), increasing the volume fraction of fibers enhances the average stress concentration ratio.

The peak value of the stress concentration ratio for each vc ne fraction is plotted in Fig.6 (marked yielded matrix) as a function of the modulus ratio. For comparison, the value obtained when the matrix deforms elastically (equivalent to the results of He et al.(1)) is shown also (marked elastic matrix). It is evident from the results in Fig.6 that the plastic yielding of the matrix increases the maximum stress concentration ratio with the value rising with an increase of fiber volume fraction. When plastic deformation of the matrix occurs, the stress ratio decreases with an increase of E_f/E_m in contrast to the situation where both the matrix and the fiber deform only elastically.

Examination of Fig.6 also reveals that when both the fiber and the matrix deform

only elastically, most of the composites satisfy the condition for global load sharing except for those materials with very large values of f and E_f/E_m. That is, the stress concentration ratio for almost all cases is less than 1.04 which is the critical value for fibers with m=10 when $N^{NN}/N^{N} = 1.5$ as found by He et al.(1). Note that $N^{NN}/N^{N} = 1.5$ is a conservative choice. Its value will often be larger than 1.5 in practical materials which makes global load sharing more likely. However, when plastic deformation occurs in the matrix, the average stress concentration ratio for a composite with typical values of fiber volume fraction and stiffness ratio is larger than 1.04, placing the composite in the global load sharing regime.

3.1.2 Shearable Interphase

The results for the average stress in the nearest and the next nearest neighbor fibers when a shearable interphase is present between the fiber and the matrix with $\tau_o/\sigma_o = 0.25$ and $\tau_o/\sigma_o = 0.1$ are illustrated in Fig.3 alongside that obtained with a perfectly bonded interface. Note that the strain for each case is different and it is at such a level that the ratio of stress concentration in the nearest to the next nearest fibers has reached its peak value in each case. It is found that similar to the case with a perfectly bonded interface, the average stress in the neighboring fibers has its peak value at a position which is some distance from the plane of the break. The position of the maximum stress moves toward the plane of the fiber break with decrease of τ_o/σ_o.

Fig.7(a) shows the stress concentration ratio as a function of remote fiber stress for various values of τ_o/σ_o for a composite with a fiber volume fraction of 0.35 and

E_f/E_m equal to 3. It can be seen that a low strength interphase reduces the peak stress concentration ratio. Examination of the figure also reveals that two peaks of stress concentration ratio occur when the interphase has a low yield strength compared to the matrix. The first peak is associated with the yielding of the thin interphase while the second one is associated with the yielding of the matrix. The smaller the ratio τ_o/σ_o, the smaller is the applied stress required for the stress concentration ratio to achieve its peak value. Similar to the results obtained for the perfectly bonded interface, the stress concentration ratio decays and approaches an asymptotic value as the load is increased after the second peak. The results obtained with different values of fiber volume fraction and modulus ratio E_f/E_m show similar trends. These results are summarized in Fig.7 (b) through (c).

The peak value of the stress concentration ratio for each case is plotted as a function of τ_o/σ_o for various fiber volume fractions and Young's moduli in Fig.8 (a) through (c). The results show broadly that the stress concentration ratio increases with increasing fiber volume fraction and decreases with increasing modulus ratio E_f/E_m. However, the latter trend is reversed when τ_o/σ_o is very low. It is evident from these results that in general the peak stress concentration ratio decreases with decrease of τ_o/σ_o. Close examination of these results, however, reveals that the peak stress concentration ratio is sensitive to the variation of τ_o/σ_o only in a small range values of τ_o/σ_o. Outside this range, change of τ_o/σ_o has negligible effect on the stress concentration ratio. The higher the ratio of E_f/E_m and the higher the fiber volume fraction, the higher is the value of the ratio of τ_o/σ_o at which the stress concentration ratio rises from low to high. For example, for f=0.215 and $E_f/E_m = 3$,

the stress concentration ratio is sensitive to the variation of τ_o/σ_o within the range $0 < \tau_o/\sigma_o < 0.2$ while for $E_f/E_m = 10$, the corresponding range of sensitivity is $0.4 < \tau_o/\sigma_o < 0.577$. These values should be compared with the ranges $0.1 < \tau_o/\sigma_o < 0.35$ for f=0.5 and $E_f/E_m = 3$ and $0.45 < \tau_o/\sigma_o < 0.577$ for f=0.5 and $E_f/E_m = 10$. These results clearly suggest that in a composite with a large fiber volume fraction and fiber to matrix stiffness ratio, a ductile interphase with a very small yield strength is no more effective at diminishing the stress concentration ratio than an interphase with a larger yield strength as long as the interphase yield strength is below the transition level. Thus a strategy is suggested in which an interphase is introduced with a yield strength just below the range of high sensitivity. It is not effective to use a yield strength much below this level since the transverse strength may be adversely affected.

By examining the values of the stress concentration ratio in Figs.7-8, the maximum value of τ_o/σ_o which permits global load sharing according to the criterion of He et al.(1), i.e. from eqn(3), can be determined. These values of τ_o/σ_o are presented in Figs.9-11 as functions of fiber volume fraction for some representative values of E_f/E_m, Weibull modulus, m and the ratio of "fiber strength" to yield strength of the matrix, S_f/σ_o. The number of nearest neighbor fibers N is 6 and the number of the next nearest neighbor fibers NN is assumed to be 9. As noted previously, this assumption is conservative. For values of τ_o/σ_o below the relevant curve, the composite is in the global load sharing regime up to stresses in the fiber equal to S_f. This parameter S_f can be considered to be the strength of the fibers, although an interpretation is required since the fibers have a statistical distribution of strengths.

For a metal matrix composite experiencing global load sharing, the ultimate tensile strength is given by Curtin (4) as

$$\sigma_u = f\sigma_c(\frac{2}{m+2})^{1/(m+1)}\frac{m+1}{m+2} + (1-f)\sigma_o \tag{4}$$

where σ_c is given by

$$\sigma_c = (\frac{2S_o^m\tau_o L_o}{D})^{1/(m+1)} \tag{5}$$

where D is the diameter of the fiber. At the ultimate stress, the strain is $(\frac{2}{m+2})^{\frac{1}{m+1}}\frac{\sigma_c}{E_f}$ so that the stress in a fiber far from any break is $[2/(m+2)]^{1/(m+1)}\sigma_c$. At strains greater than that causing the ultimate strength of the composite, global load sharing is no longer important since the stress on the composite is falling. Therefore, the effective strength of the fiber is considered to be

$$S_f = [2/(m+2)]^{1/(m+1)}\sigma_c \tag{6}$$

and the global load sharing criterion is required to be met for fiber stresses up to this level. That will ensure that the predicted ultimate strength in eqn(4) can be achieved. The maps in Figs.9-11 therefore ensure that global load sharing is retained up to the ultimate strength of the composite if τ_o/σ_o lies below the relevant curve. For a given fiber and interface/interphase, σ_c is fixed and the value of S_f/σ_o will reflect the strength level of the matrix which can be modified by heat treatment.

When the fibers are effectively strong and the matrix weak (e.g. $S_f/\sigma_o = 10$ as in Fig.9(c)) the requirements for global load sharing are stringent and τ_o/σ_o may have to be very low to ensure it. This occurs because the relatively high strains at maximum load of the composite induce the high peak values of $\sigma_{ZZ}^N/\sigma_{ZZ}^{NN}$ which occur at large

values of σ_f/σ_o in Figs.7 and 8. However, when the fiber strength is effectively weak or the matrix is strong (e.g. $S_f/\sigma_o = 2$ as in Fig.9(a)), the ultimate strength is reached at low values of σ_f/σ_o. As a result, the composite fails before the peak values of $\sigma_{ZZ}^N/\sigma_{ZZ}^{NN}$ in Figs.7 and 8 are reached and global load sharing is therefore easier to preserve even with large values of τ_o/σ_o. This feature is clear in Fig.9(a) where global load sharing can be achieved without a weak interface or interphase up to fairly significant fiber volume fractions. This is in contrast to Fig.9(c), where global load sharing without a weak interface or interphase can only be achieved when the Weibull modulus is low. When S_f/σ_o is higher than 10, the resulting maps of the type shown in Figs.9(c), 10(c) and 11(c) are almost exactly the same as those for $S_f/\sigma_o = 10$. Therefore, Figs.9(c), 10(c) and 11(c) actually serve as maps for $S_f/\sigma_o = 10$ and greater. This indicates that when $S_f/\sigma_o = 10$ for $E_f/E_m = 3, 5$ and 10, the peak values of $\sigma_{ZZ}^N/\sigma_{ZZ}^{NN}$ are reached before ultimate failure and that global load sharing can only be ensured by keeping those peak values down to acceptable levels.

Another parameter which plays a role in determining global and local load sharing is the ratio E_f/E_m. When S_f/σ_o is small, e.g. 2, the matrix has a yield strength approaching the effective strength of the fiber and it is found that the composite with a large value of E_f/E_m is more likely to be in the local load sharing regime. This is consistent with the elastic calculations performed by He et al.(1). However, when the ratio S_f/σ_o increases to 5 or 10 so that the yield strength of the matrix is relatively low and therefore plasticity is more likely to occur, the situation is more complicated. On the one hand, with a strongly bonded interface, a composite with a fiber volume fraction of 0.35 and a small ratio E_f/E_m could be in the local load sharing regime,

whereas the same composite with a higher ratio of E_f/E_m may be in the global load sharing regime. For example, with $S_f/\sigma_o = 5$, m=7, f=0.35 and $E_f/E_m = 3$, Fig.9(b) indicates that a composite with a strongly bonded interface is in local load sharing, while the same composite with E_f/E_m equal to 10 as illustrated in Fig.11(b) is in the global load sharing regime. On the other hand, if a shearable interphase is present, a low value of τ_o/σ_o is much more effective in placing the composites with smaller values of E_f/E_m in global load sharing than composites with higher values of E_f/E_m. As an example, when f=0.5, $S_f/\sigma_o = 5$ and m=5, examination of Fig.9(b) reveals that global load sharing could be achieved for the composite with a value of τ_o/σ_o of 0.2 when $E_f/E_m = 3$. Global load sharing can never be achieved for the composite with the same material properties and interphase when $E_f/E_m = 10$ as illustrated in Fig.11(b).

3.2 Transverse Behavior

In previous studies, the transverse yielding of metal matrix fiber composites with strong interfaces were analyzed by the authors(6,9). It was found for perfectly plastic matrices that with increasing transverse strain, the transverse average stress approaches an asymptotic value, which is the transverse limit load. When a shearable interphase is present in the composite, the transverse behavior is similar. Typical transverse stress strain curves are given in Fig.12 for various ratios of the yield strength in shear of the thin interphase to the yield strength of the matrix for both square and hexagonal arrangements of fibers at a volume fraction of 0.35. It can be seen that the transverse limit strength of the composite is reduced when a shearable

interphase with a low yield strength is present. (These calculations were carried out with rigid fibers so that the elastic and elastic-plastic response represents the behavior for extremely stiff fibers only. However, the limit strength is correctly calculated for any fiber stiffness since it is independent of fiber and matrix elasticity)

The transverse limit strength $\overline{\sigma}$ calculated for hexagonal and square arrangements of fibers is presented in Fig.13 for a range of fiber volume fractions and for various ratios of the yield strength in shear of the thin interphase to the yield strength of the matrix. The transverse limit strength is the asymptotic value of the transverse stress at large strain for each case. It is evident from these results that the ratio of the yield strength in shear of the thin interphase to the yield strength of the matrix strongly influences the transverse limit strength. For all the problems analyzed, the transverse limit strength decreases monotonically with decreasing τ_o/σ_o. An interesting feature of the results is that when τ_o/σ_o is very small, the values of the limit strength decrease dramatically with the decrease of τ_o/σ_o. When τ_o/σ_o is greater than about 0.1, the transverse limit strength increases almost linearly with τ_o/σ_o. When the fiber volume fraction is small, there is little sensitivity of the transverse limit strength to τ_o/σ_o. However, for larger values of f the effect of τ_o/σ_o on the limit strength is significant. This is attributed to the fact that for the large fiber volume fraction, the volume of the thin interphase is a larger fraction of the volume of the composite than in the low fiber volume case. Therefore, the reduction of the yield strength of the thin interphase in the high fiber volume fraction case will have a more significant effect on the reduction of the transverse limit strength.

When the fiber volume fraction is small, the results obtained for the transverse

limit strength for the hexagonal arrangement of fibers are very close to those obtained for square arrangement of the fibers. However, when the fiber volume fraction is large, the transverse strength for the square arrangement is much more sensitive to the variation of τ_o/σ_o than for the hexagonal arrangement.

For a composite with a fiber volume fraction of 0.35, the ratio of the thickness t of the thin interphase to the fiber diameter D was varied to allow assessment of the effect on the transverse limit strength. Fig.14 illustrates the transverse limit strength as a function of τ_o/σ_o for a range interphase thicknesses for the square arrangement of fibers. It is evident from these results that for any given yield strength of the thin interphase, the thicker the interphase, the lower the transverse limit strength with the strength decreasing almost linearly with the yield strength of the interphase except at low values of τ_o/σ_o when the interphase is very thin. It is worth noting that the longitudinal results discussed in the previous section have been found to be independent of the interphase thickness.

4 Discussion

An important result of this study is that around a broken fiber, plastic yielding of the matrix tends to increase the ratio of stress concentration in the nearest fiber to that in the next nearest fiber. The introduction of plasticity has the same effect as reducing the matrix modulus in the purely elastic case. Both matrix plasticity and a low matrix elastic modulus have the effect of making the matrix more compliant. In the range of parameters studied, the impact of a more compliant matrix is a higher stress

concentration in the nearest neighbor fiber. The higher stress concentration and the higher stress concentration ratio λ will tend to promote spreading of damage in the form of fiber breaks near a single plane across a section of the composite. Indeed for a metal matrix composite with technologically typical values of fiber volume fraction (e.g. f=0.35) and with a ratio of E_f/E_m typical of technological systems (e.g. SiC Ti alloy with $E_f/E_m = 3$), numerical results indicate that plastic yielding places the composite with a strongly bonded interface near the transition from global load sharing to local load sharing. Local load sharing will mean that one broken fiber will tend to cause its neighbor to break, leading to composite failure. This is in contrast to the situation if both fibers and the matrix are assumed to deform only elastically (1). For f=0.35 and $E_f/E_m = 3$, He et al.(1) found the composite to be in the global load sharing regime even when the interface is strongly bonded. Therefore, when the matrix is capable of yielding, it is important to determine when global load sharing occurs so that a high longitudinal strength can be achieved.

In the present work, a ductile interphase with lower yield strength than the matrix is introduced in the composite to achieve global load sharing among fibers in the longitudinal direction. This ductile interphase can represent just as well as a debonded interface with sliding resisted by friction, which is known to ensure satisfactory longitudinal strength(1-3). From the set of problems analyzed, the circumstances in which global load sharing will occur have been identified. This has been done based on a criterion introduced by He et al.(1).

Maps have been provided delineating in terms of material parameters the region in which global load sharing will occur (i.e. Figs.9, 10 and 11). The maps indicate that

a low interface/interphase shear strength, a high matrix yield strength, a low fiber strength and a low Weibull modulus all make global load sharing easier to achieve. Although just about all material parameters influence the tendency for global load sharing to occur or not, most interest centers on the shear strength of the interface or interphase and the yield strength of the matrix since those quantities can be tailored for a given composite in which the fiber and other matrix properties and the fiber volume fraction are set. Not surprisingly, a low value of the interface or interphase shear strength compared to the matrix yield strength is desirable to induce global load sharing. As noted above, this is commonly achieved by use of a weak interface which debonds easily and slides frictionally with low friction thereafter. The disadvantage of this approach is that when transverse stress is applied, the interface can debond. This limits the transverse strength, which is often below the unreinforced matrix strength(2), leading to relatively poor transverse properties and significant anisotropy in terms of longitudinal and transverse strength.

An alternative approach is to introduce a well bonded ductile interphase between the fiber and the matrix with the interphase having a relatively low yield strength. With the appropriate choice of yield strength for the interphase, global load sharing can be assured. Moreover, the interphase will affect the transverse strength by yielding or by fracture. The results presented in this paper show that by keeping the interphase relatively thin and not too weak in yielding, a reasonable transverse limit strength can be retained. A reasonable transverse strength would be equal to or above the unreinforced matrix yield strength. This assertion can be made because results have shown that only limited transverse strengthening above the matrix

strength can be achieved with well bonded fibers (no interphase) unless the fiber volume fraction is so high that the fibers are almost touching(6). Therefore, there is little point in expecting transverse strengths much in excess of the unreinforced matrix strength. Given that the transverse stresses in the composite will be, at the most, comparable to the matrix strength, it should be relatively easy to select an interphase which will resist fracture at those stresses and, therefore, ensure that the projected transverse strength can be achieved. The results in Fig.13 indicate that the limit transverse strength is only weakly dependent on the interphase yield strength as the latter parameter is reduced except when τ_o is very low. Thus there exists a window of reasonable values of τ_o which will retain reasonable transverse strength but permit longitudinal global load sharing.

For example, consider a Ti matrix/SiC fiber composite with a fiber volume fraction of 0.35. The Young's moduli are such that $E_f/E_m = 3$ and it has been established(2) that SCS6 fibers with a diameter of $140\mu m$ have m=9 with $S_o = 4500MPa$ and $L_o = 1m$. A matrix yield strength $\sigma_o = 950MPa$ is appropriate for Ti alloy. From eqns(5) and (6), we can determine that

$$\frac{S_f}{\sigma_o} = (\frac{2}{m+2})^{1/m+1} (\frac{2S_o^m L_o}{D\sigma_o^m})^{1/m+1} (\frac{\tau_o}{\sigma_o})^{1/m+1} \tag{7}$$

An estimate for S_f/σ_o can be obtained by taking $\tau_o/\sigma_o = 0.5$ which is reasonable since even if τ_o/σ_o is significantly less than 0.5, $(\tau_o/\sigma_o)^{1/1+m}$ will be similar to $0.5^{1/1+m}$ because m=9. Thus we take S_f/σ_o=8.5. Since the stress concentration ratio as indicated in Fig.7(a) for the case with f=0.35 and $E_f/E_m = 3$ peaks well before $S_f/\sigma_o = 8.5$ for any value of τ_o/σ_o, it is relevant to choose the map with $S_f/\sigma_o = 10$

(i.e. Fig.9(c)) for this particular material system. Fig.9(c) shows that global load sharing can be achieved for this case if τ_o/σ_o is 0.18 or less. With an interphase of thickness $3.5\mu m$ so that t/D=0.025, Fig.13(b) shows that the transverse strength will be greater than the unreinforced matrix strength as long as τ_o/σ_o is greater than 0.1. Therefore, we conclude that an interphase with a yield strength in shear anywhere from 95MPa ($\tau_o/\sigma_o = 0.1$) to 170MPa ($\tau_o/\sigma_o = 0.18$) would ensure global load sharing and therefore good longitudinal strength without degrading the transverse strength. An ultimate strength of 2.75GPa for $\tau_o = 95MPa$ and 2.88GPa for $\tau_o = 170MPa$ is predicted from eqn(4). The transverse strength would be in excess of 950MPa. For comparison, it has been established that a Ti alloy composite with 35% by volume of SCS6 SiC fibers which has a weak, debonding interface has a ultimate strength of 1.8GPa and a transverse strength of 420MPa, which is $0.4\sigma_o$(2). It is worth noting that the difference between the experimental data and the predictions for the ultimate strength using eqn(4) is probably due to the effect of the short specimen gauge length used in experiments of Jansson et al.(2) and discussed by them.

5 Closure

It is evident from the above discussion that the key to designing a metal matrix fiber composite with good longitudinal and transverse strength lies in the development of maps such as those in Figs.9-14, from which one can optimize the material parameters. The present study of global versus local load sharing based on axisymmetric finite element models and the criterion of He et al.(1) provides a preliminary set of maps

for technologically significant combinations of material parameters relevant to Ti/SiC and Al/Al_2O_3 composites among others. These maps can be extended by further calculation to cover other material systems and can be refined by more elaborate computations.

6 Acknowledgments

The work was sponsored by the Advanced Research Projects Agency through the University Research Initiative at University of California, Santa Barbara (ONR Contract N-0014-92-J-1808). Helpful discussions with H. Deve and A.G. Evans are gratefully acknowledged. The ABAQUS finite element code was made available by Hibbitt, Karlsson and Sorenson Inc., Pawtucket, R.I. through an academic licence.

7 References

1. M.Y. He, A.G. Evans and W. A. Curtin, (1993) The ultimate tensile strength of metal and ceramic-matrix composites, Acta. Metall. **41**. 871

2. S. Jansson, H.E. Deve and A.G. Evans, (1991) The anisotropic mechanical properties of a Ti matrix composite reinforced with SiC fibers, Metal Tran. **22a**, 2975

3. S. R. Gunawardena, S. Jansson and F.A. Leckie, (1993), Modeling of anisotropic behavior of weakly bonded fiber reinforced MMC's, Acta Metall **41**, 3147

4. W.A. Curtin, (1991), Theory of mechanical properties of ceramic matrix composites, J. Am. Ceramic Sol. **74**, 2837

5. F. Hild, J. Domergue, F.A. Leckie and A.G. Evans, (1994), Tensile and flexural ultimate strength of fiber-reinforced ceramic matrix composite, Int. J. Solids and Structures (In Press)

6. D. B. Zahl, S. Schmauder and R.M. McMeeking, (1993), Transverse strength of metal matrix composites reinforced with strongly bonded continuous fibers, to appear

7. G. Bao, J.W. Hutchinson and R.M. McMeeking, (1991), Particle reinforcement of ductile matrices against plastic flow and creep, Acta Metall. **39**. 1871

8. ABAQUS User Manual (1993). Hibbitt, Karlsson and Sorensen, Inc., 1080 Main street, Pawtucket, R.I.

9. Z.-Z Du, R. M. McMeeking and S. Schmauder, (1994). Transverse yielding and matrix flow past the fibers in metal matrix composites. (to be published)

List of Figures

Fig.7 The ratio of the stress concentration in the nearest and the next nearest neighbor fibers adjacent to a broken fiber as a function of the interphase yield strength in shear normalized by the yield strength of the matrix for a material with (a) f=0.35 and $E_f/E_m = 3$ (b) f=0.35 and $E_f/E_m = 5$ (c) f=0.35 and $E_f/E_m = 10$ (d) f=0.5 and $E_f/E_m = 3$ and (e) f=0.215 and $E_f/E_m = 3$

Fig.8 The peak value of the average stress concentration ratio in the nearest and the next nearest neighbor fibers as a function of the ratio of the shear yield strength of the interphase to the yield strength of the matrix for a range of ratios of fiber to matrix Young's moduli for (a) f=0.215 (b) f=0.35 (c) f=0.5

Fig.9 Maps of the global load sharing domain for a material with fibers having a Young's modulus three times that of the matrix with various ratios of effective fiber strength to matrix tensile yield strength and fiber Weibull modulus m. The global load sharing domain lies below the curves which are shown for (a) $S_f/\sigma_o = 2$ (b) $S_f/\sigma_o = 5$ and (c) $S_f/\sigma_o = 10$

Fig.10 Maps of the global load sharing domain for a material with fibers having a Young's modulus five times that of the matrix with various ratios of effective fiber strength to matrix tensile yield strength and fiber Weibull modulus m. The global load sharing domain lies below the curves which are shown for (a) $S_f/\sigma_o = 2$ (b) $S_f/\sigma_o = 5$ and (c) $S_f/\sigma_o = 10$

Fig.11 Maps of the global load sharing domain for a material with fibers having a Young's modulus ten times that of the matrix with various ratios of effective fiber strength to matrix tensile yield strength and fiber Weibull modulus m.

The global load sharing domain lies below the curves which are shown for (a) $S_f/\sigma_o = 2$ (b) $S_f/\sigma_o = 5$ and (c) $S_f/\sigma_o = 10$

Fig.12 Transverse stress-strain curves for various ratios of interphase shear yield strength τ_o to matrix tensile yield strength σ_o for (a) a square and (b) a hexagonal fiber arrangement when the fiber volume fraction is 35%. The fibers are rigid and the interphase thickness is 2.5% of the fiber diameter.

Fig.13 The transverse limit strength of the composite as a function of the ratio of the interphase shear yield strength τ_o to the matrix tensile yield strength σ_o for a range of fiber volume fractions in (a) a square and (b) a hexagonal fiber arrangement when the interphase thickness is 2.5% of the fiber diameter.

Fig.14 The transverse limit strength of the composite as a function of the ratio of interphase shear yield strength τ_o to matrix tensile yield strength σ_o for various ratios of the interphase thickness t to the fiber diameter D for a square fiber arrangement when the fiber volume fraction is 0.35.

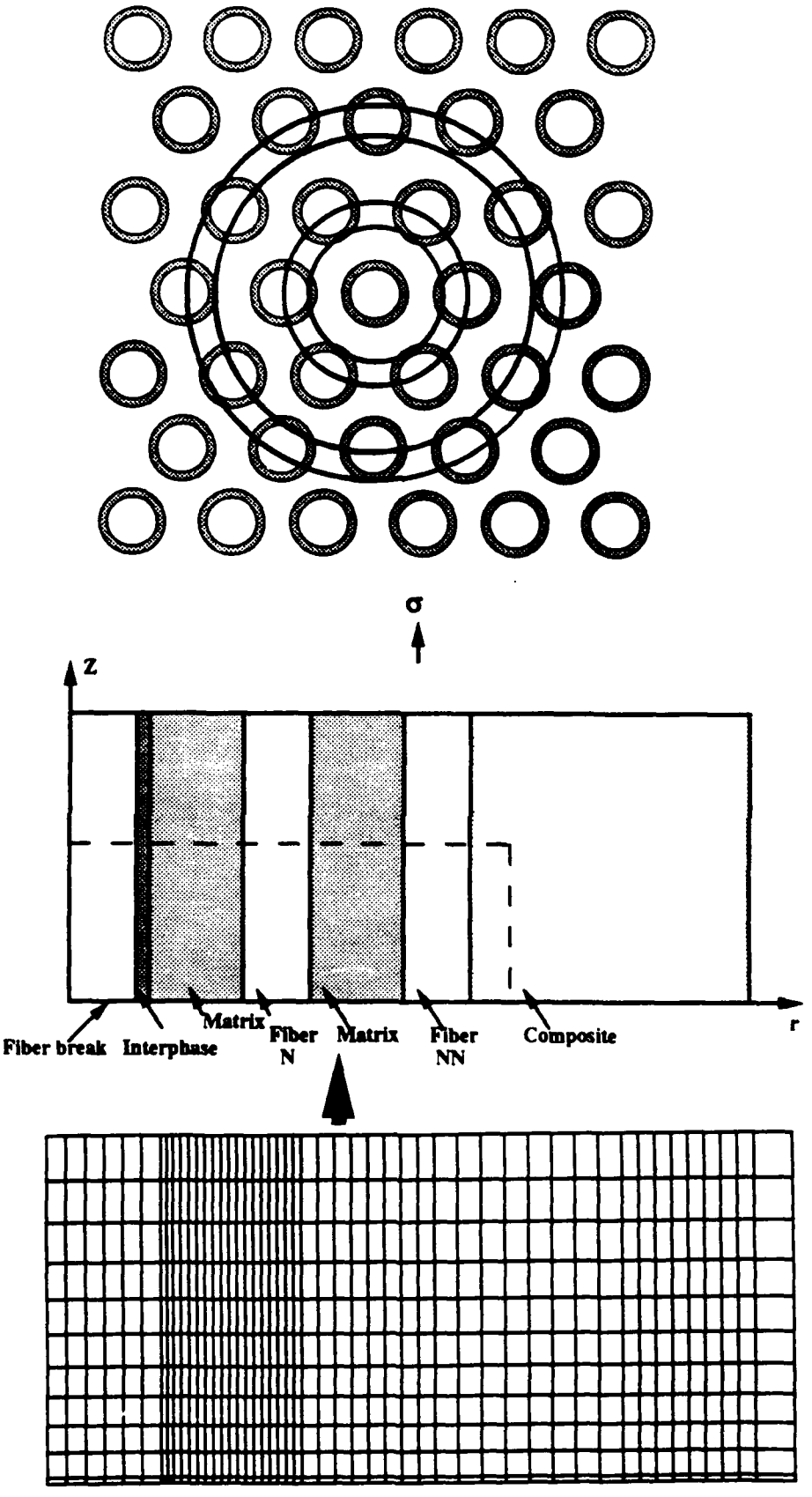
σ
z
r
Fiber break
Interphase
Matrix
Fiber
N
Matrix
Fiber
NN
Composite

Fig.1

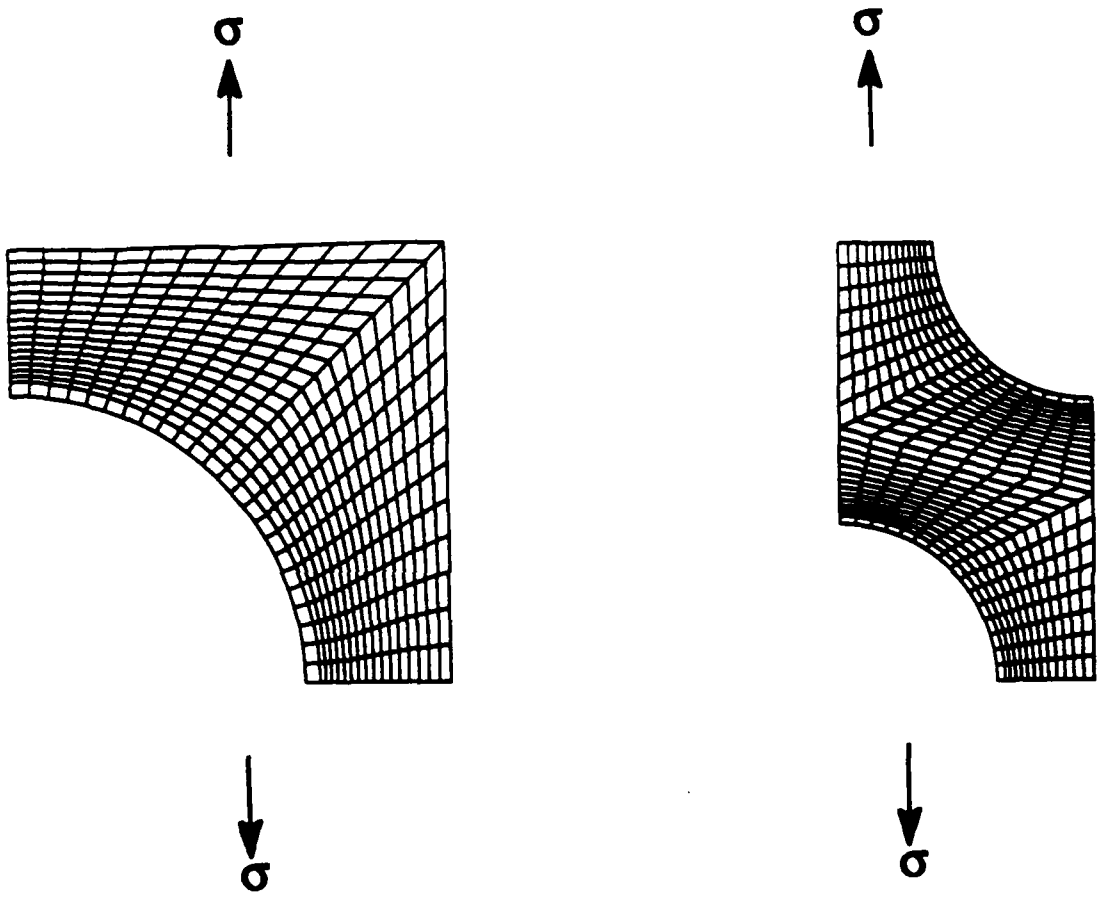

(a) (b)

Fig.2

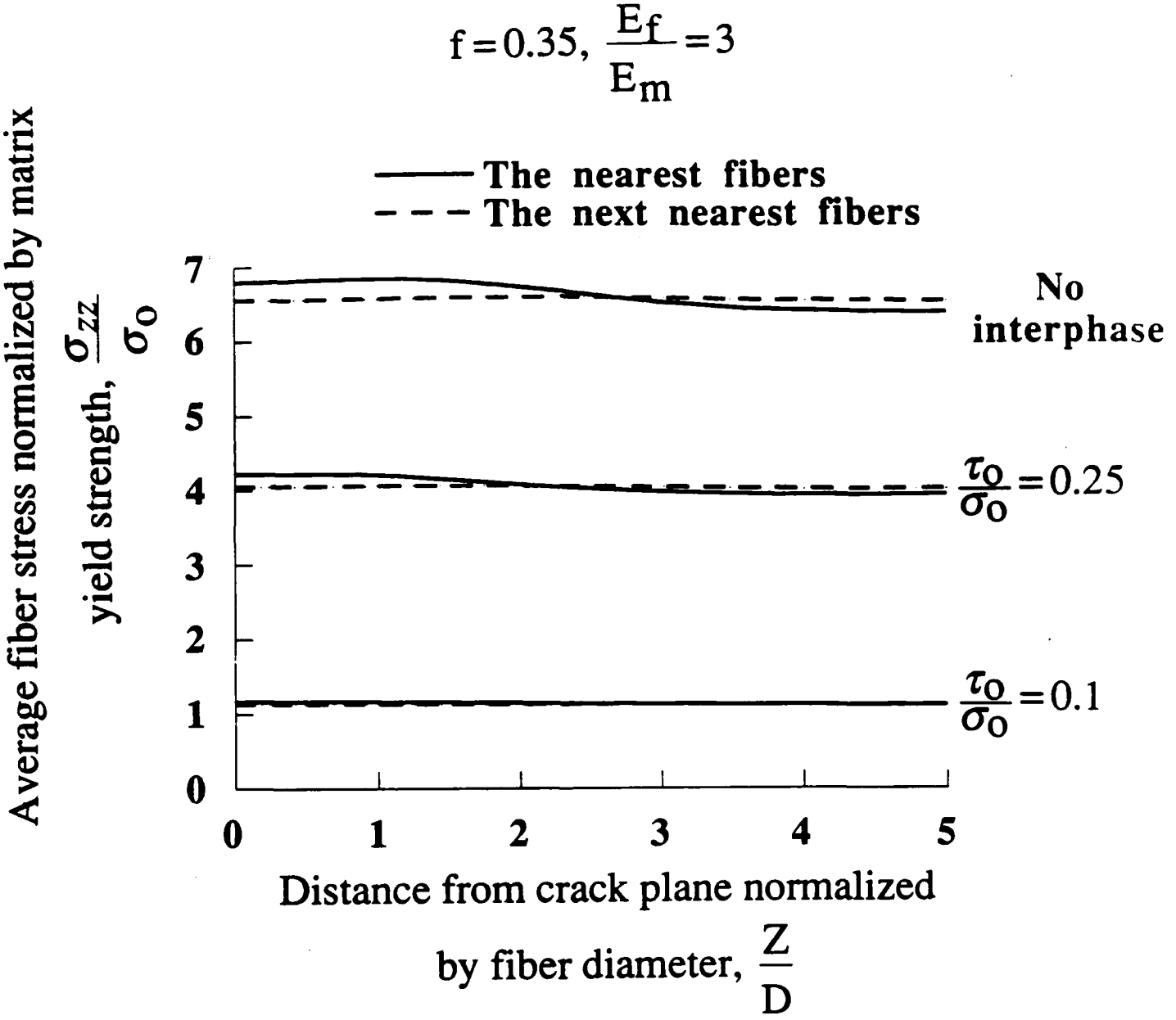
$f = 0.35, \frac{E_f}{E_m} = 3$
The nearest fibers
The next nearest fibers
Average fiber stress normalized by matrix yield strength, $\frac{\sigma_{zz}}{\sigma_o}$
No interphase
$\frac{\tau_o}{\sigma_o} = 0.25$
$\frac{\tau_o}{\sigma_o} = 0.1$
0
1
2
3
4
5
6
7
Distance from crack plane normalized by fiber diameter, $\frac{Z}{D}$

Fig.3

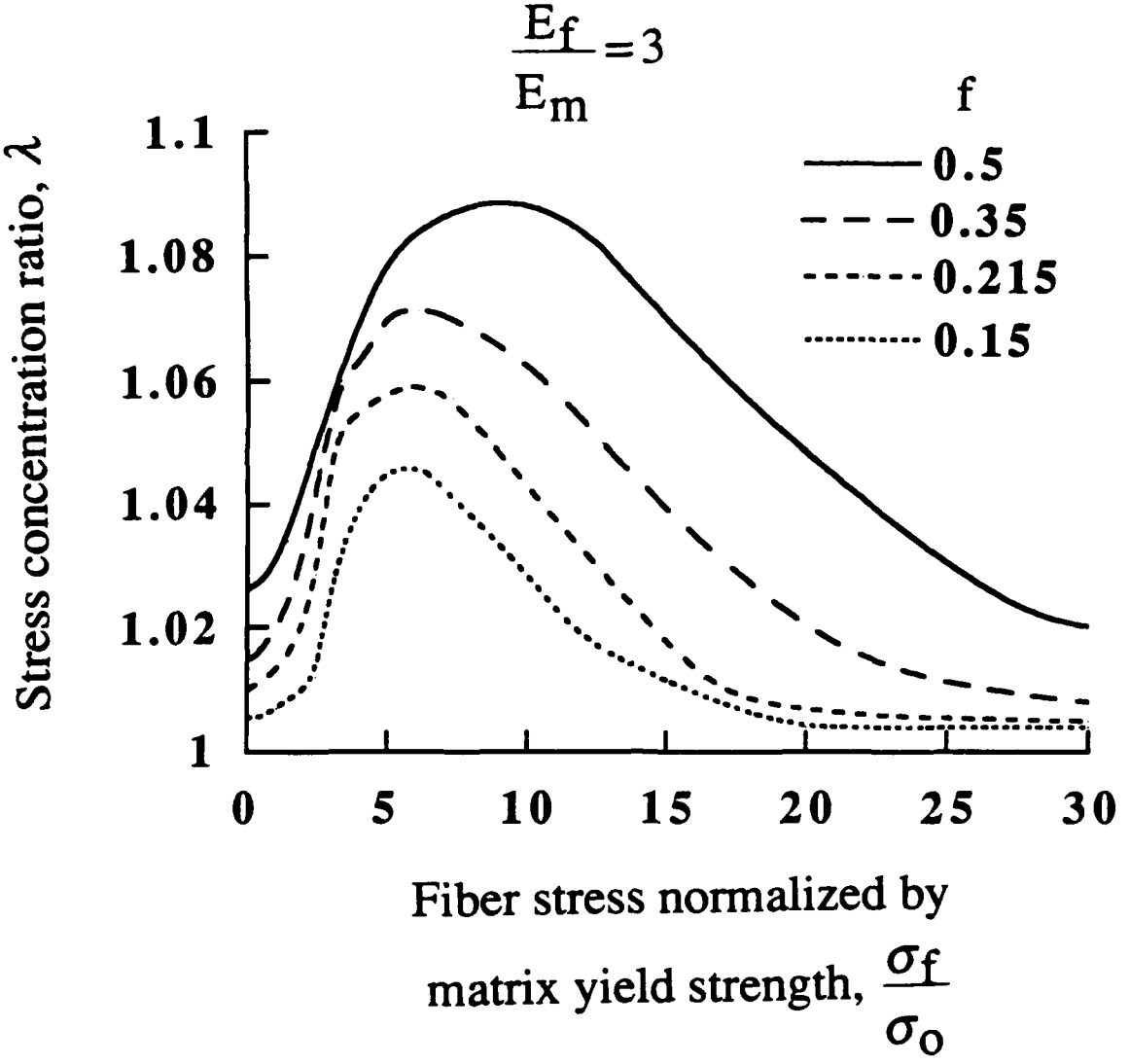
$\frac{E_f}{E_m} = 3$
f
0.5
0.35
0.215
0.15
Stress concentration ratio, λ
1.1
1.08
1.06
1.04
1.02
1
0
5
10
15
20
25
30
Fiber stress normalized by
matrix yield strength, $\frac{\sigma_f}{\sigma_o}$

Fig.4

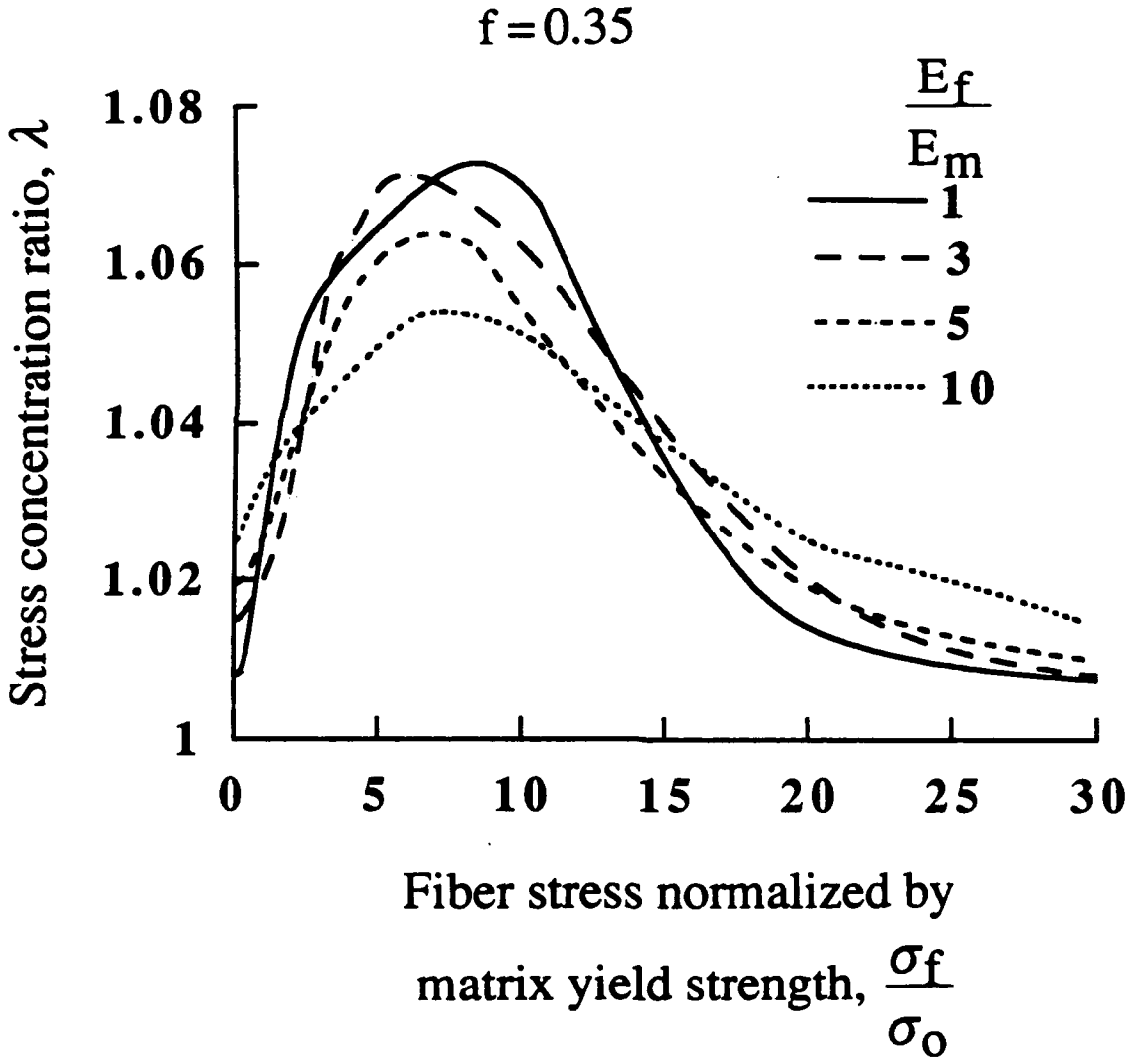
f = 0.35
Ef / Em
1
3
5
10
Stress concentration ratio, λ
1.08
1.06
1.04
1.02
1
0
5
10
15
20
25
30
Fiber stress normalized by
matrix yield strength, σf / σo

Fig.5

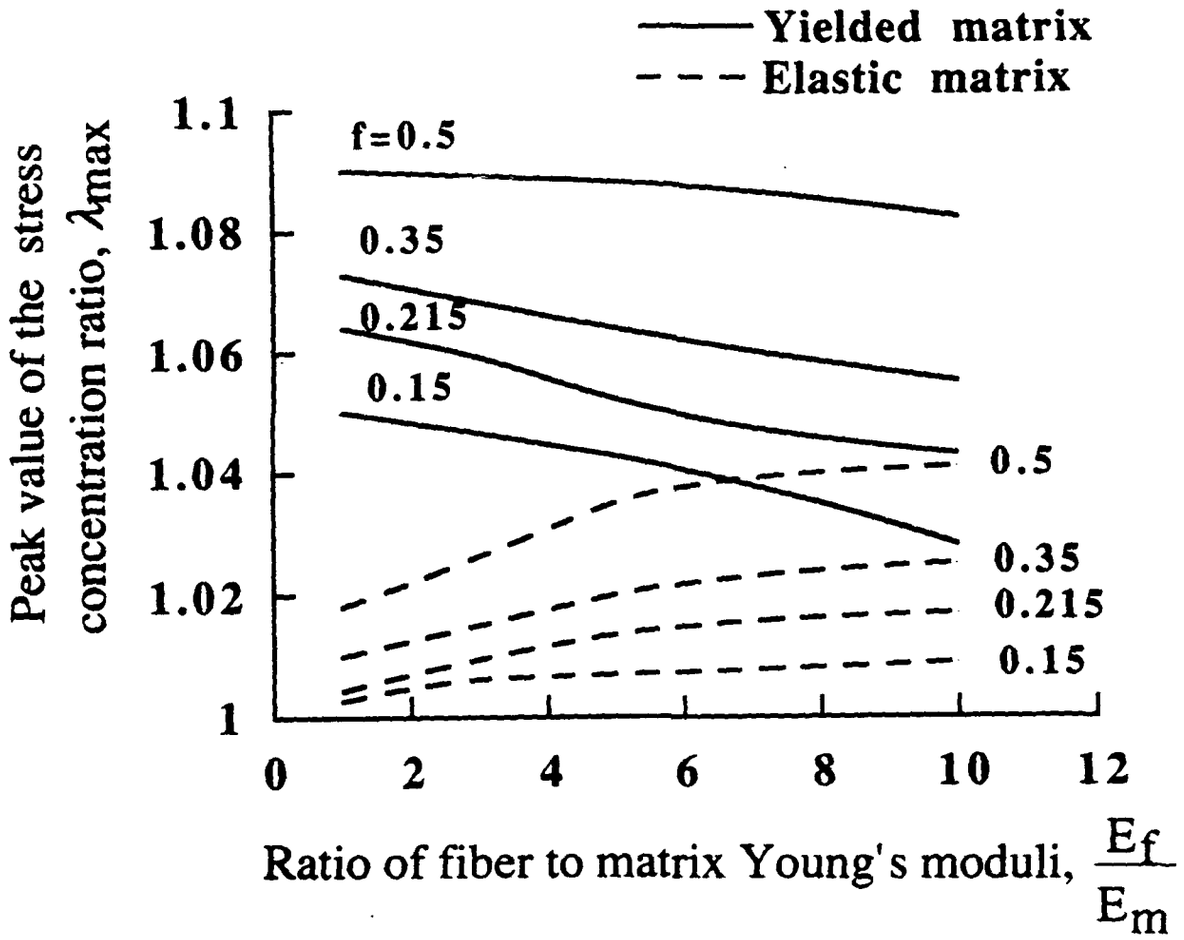
Yielded matrix
Elastic matrix
Peak value of the stress concentration ratio, λ_{max}
1.1
1.08
1.06
1.04
1.02
1
f=0.5
0.35
0.215
0.15
0.5
0.35
0.215
0.15
0
2
4
6
8
10
12
Ratio of fiber to matrix Young's moduli, $\frac{E_f}{E_m}$

Fig.6

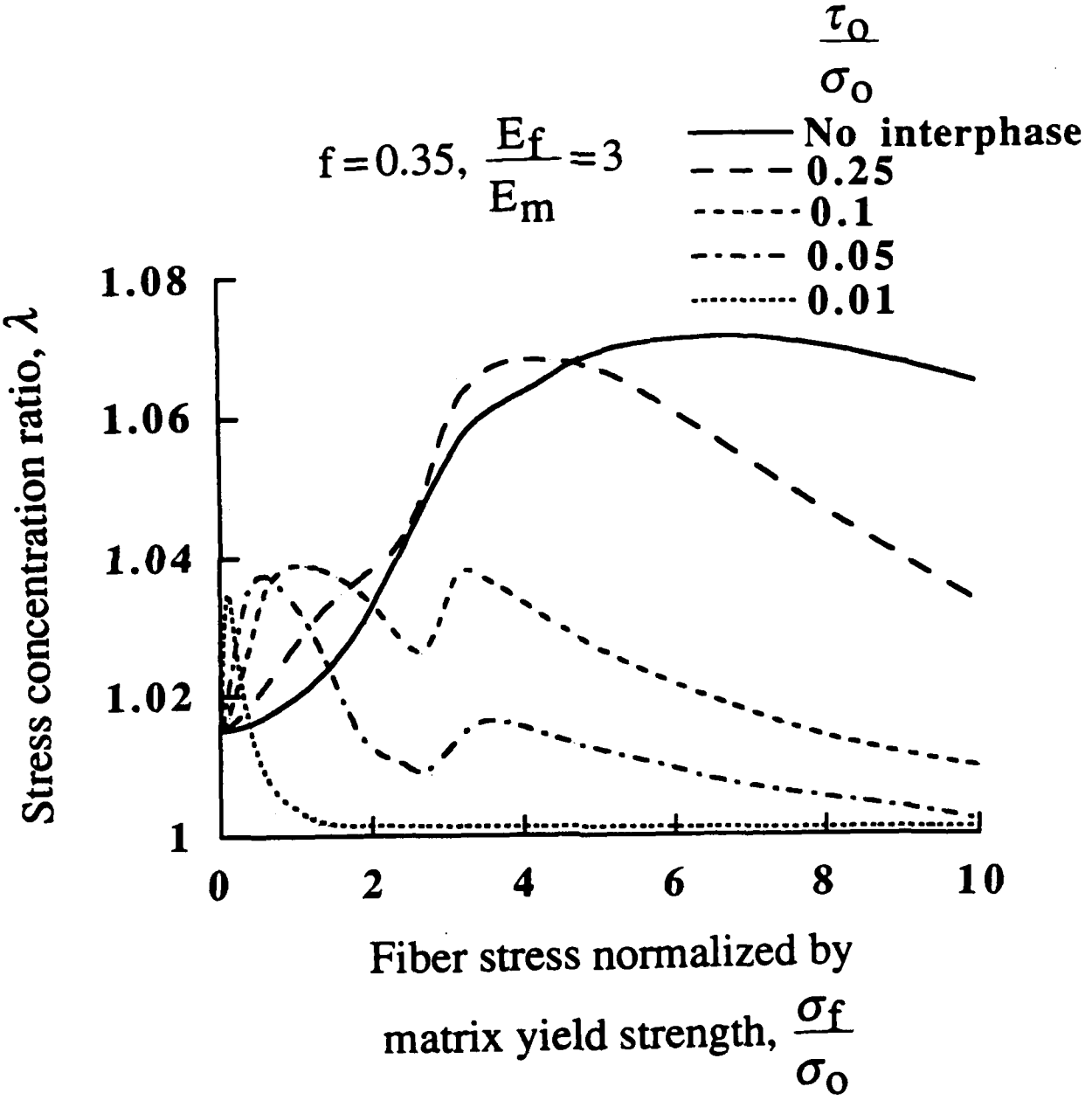
$\frac{\tau_o}{\sigma_o}$
No interphase
0.25
0.1
0.05
0.01
f=0.35, $\frac{E_f}{E_m}$=3
Stress concentration ratio, λ
1.08
1.06
1.04
1.02
1
0
2
4
6
8
10
Fiber stress normalized by
matrix yield strength, $\frac{\sigma_f}{\sigma_o}$

Fig.7(a)

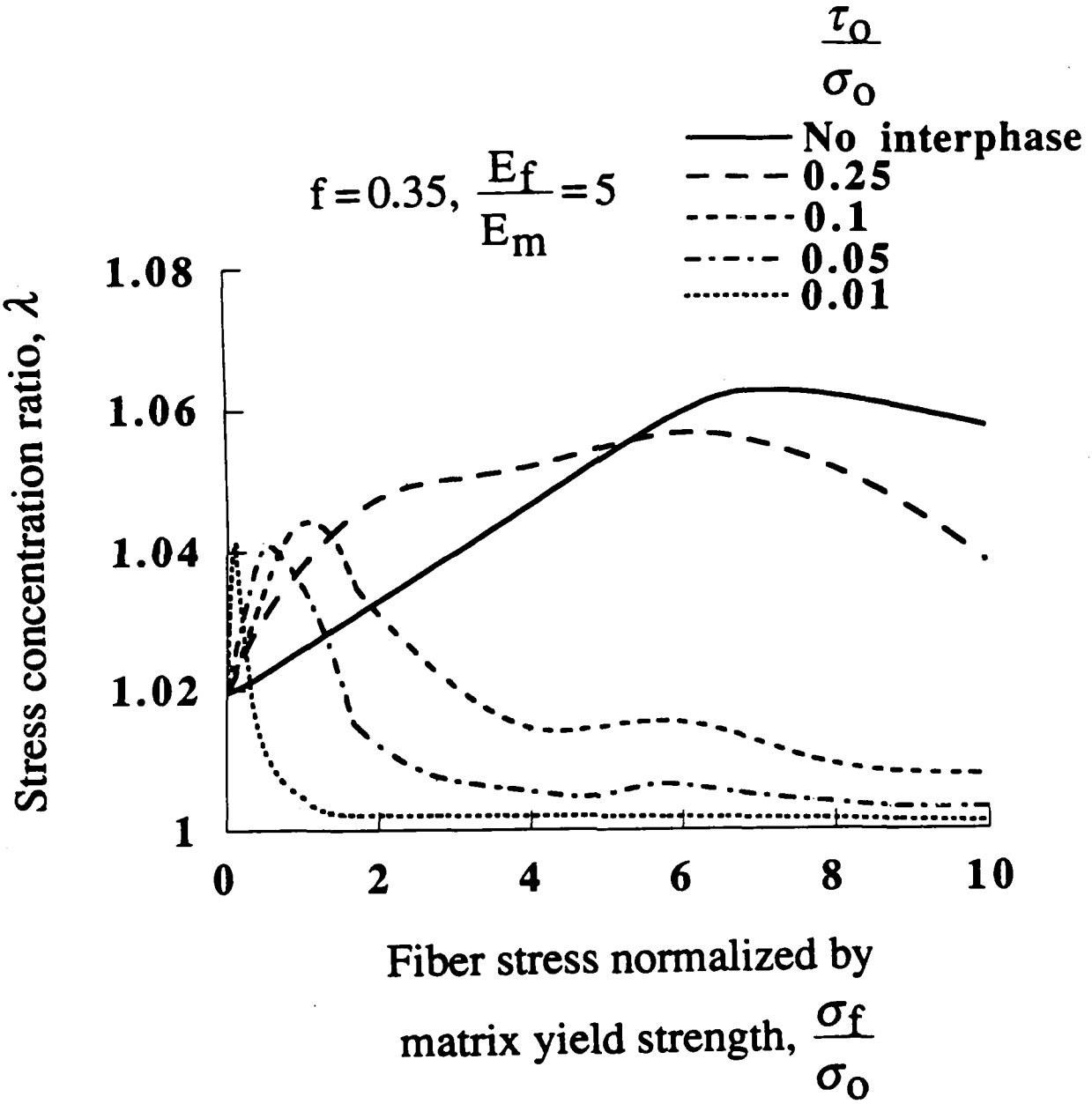
$\frac{\tau_o}{\sigma_o}$
No interphase
0.25
0.1
0.05
0.01
f=0.35, $\frac{E_f}{E_m}$=5
Stress concentration ratio, λ
1.08
1.06
1.04
1.02
1
0
2
4
6
8
10
Fiber stress normalized by
matrix yield strength, $\frac{\sigma_f}{\sigma_o}$

Fig.7(b)

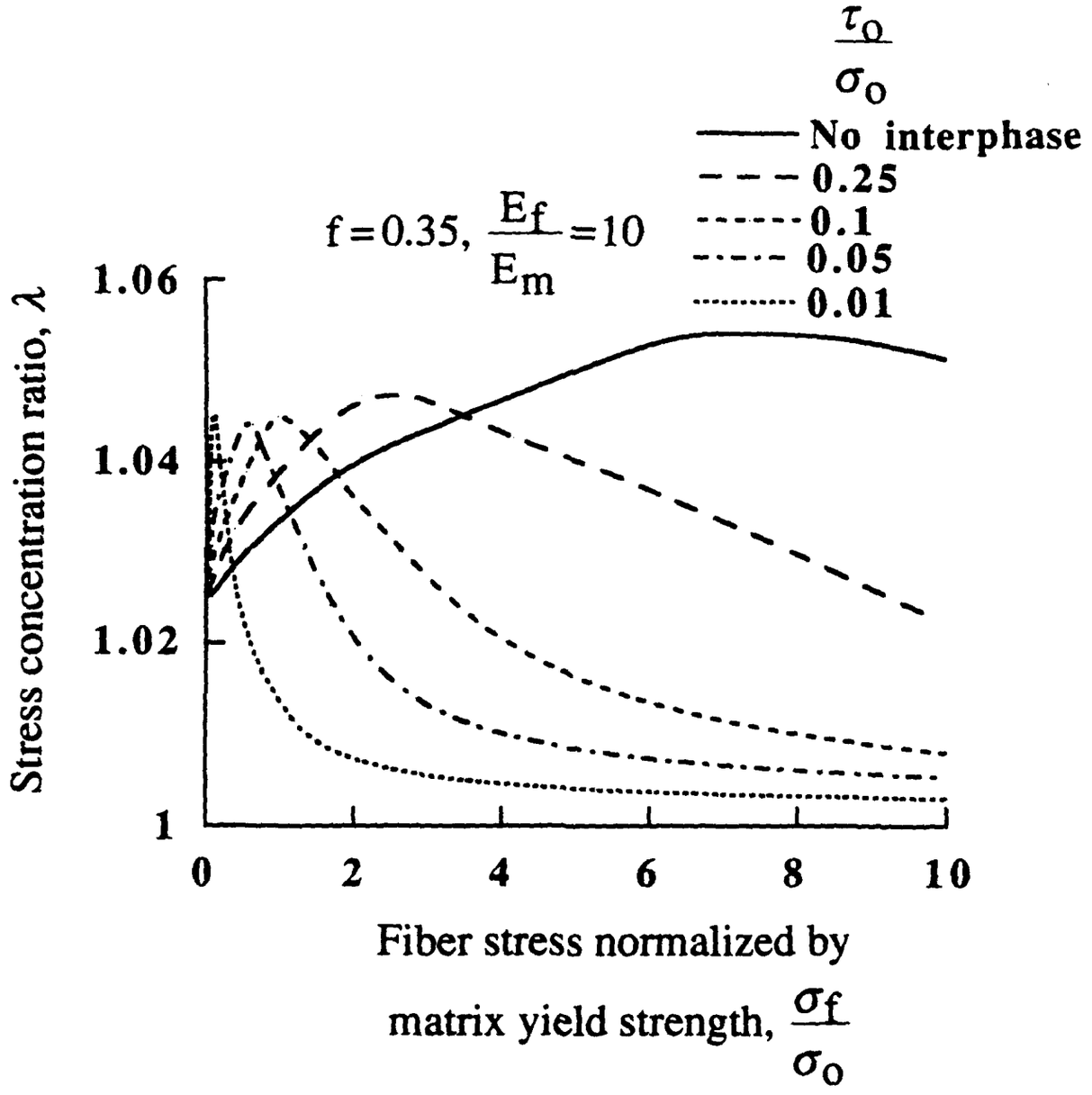
$\frac{\tau_o}{\sigma_o}$
No interphase
0.25
0.1
0.05
0.01
f=0.35, $\frac{E_f}{E_m}$=10
Stress concentration ratio, λ
1.06
1.04
1.02
1
0
2
4
6
8
10
Fiber stress normalized by
matrix yield strength, $\frac{\sigma_f}{\sigma_o}$

Fig.7(c)

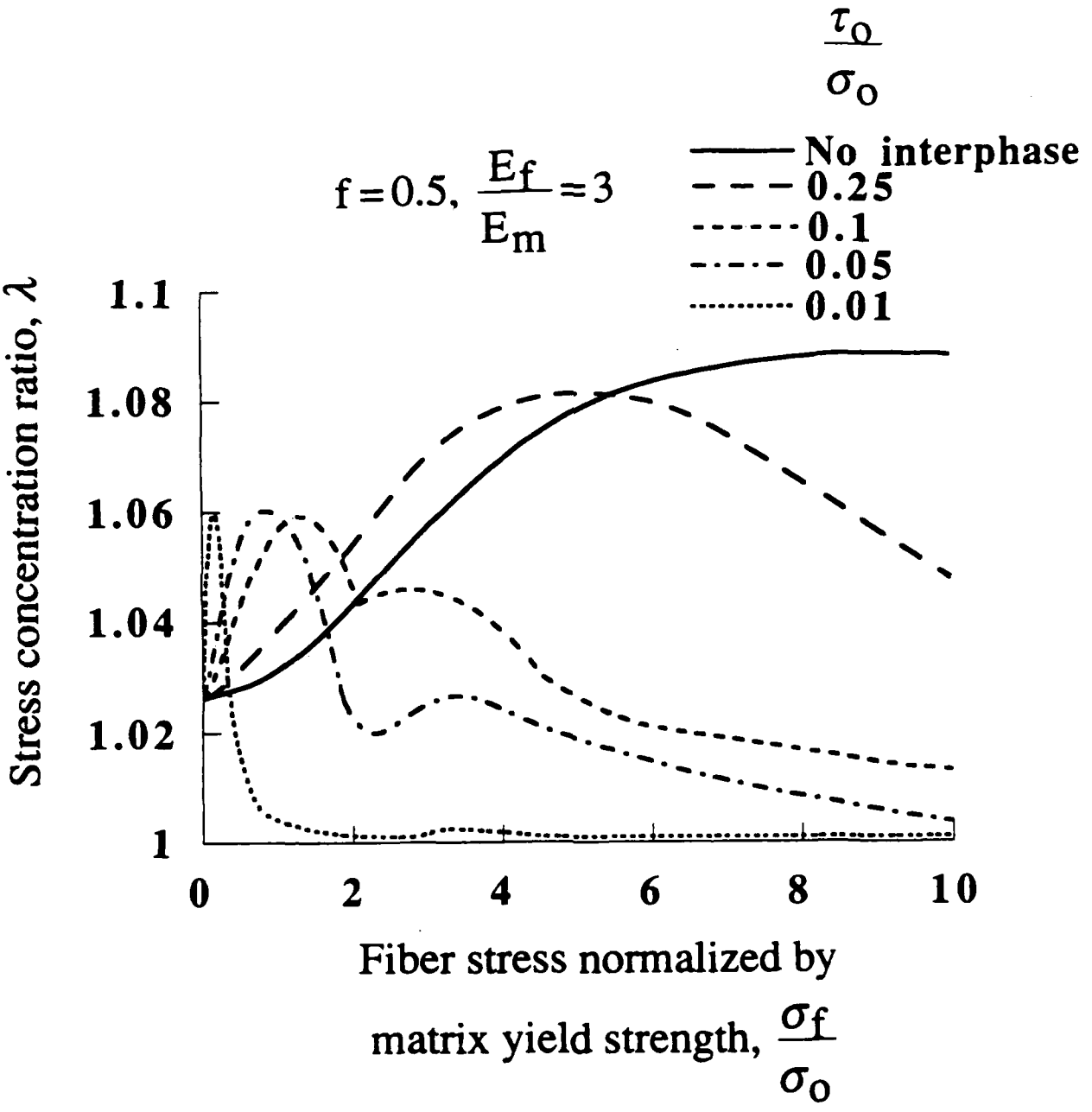
$\frac{\tau_o}{\sigma_o}$
No interphase
0.25
0.1
0.05
0.01
f=0.5, $\frac{E_f}{E_m}$=3
Stress concentration ratio, λ
1.1
1.08
1.06
1.04
1.02
1
0
2
4
6
8
10
Fiber stress normalized by
matrix yield strength, $\frac{\sigma_f}{\sigma_o}$

Fig.7(d)

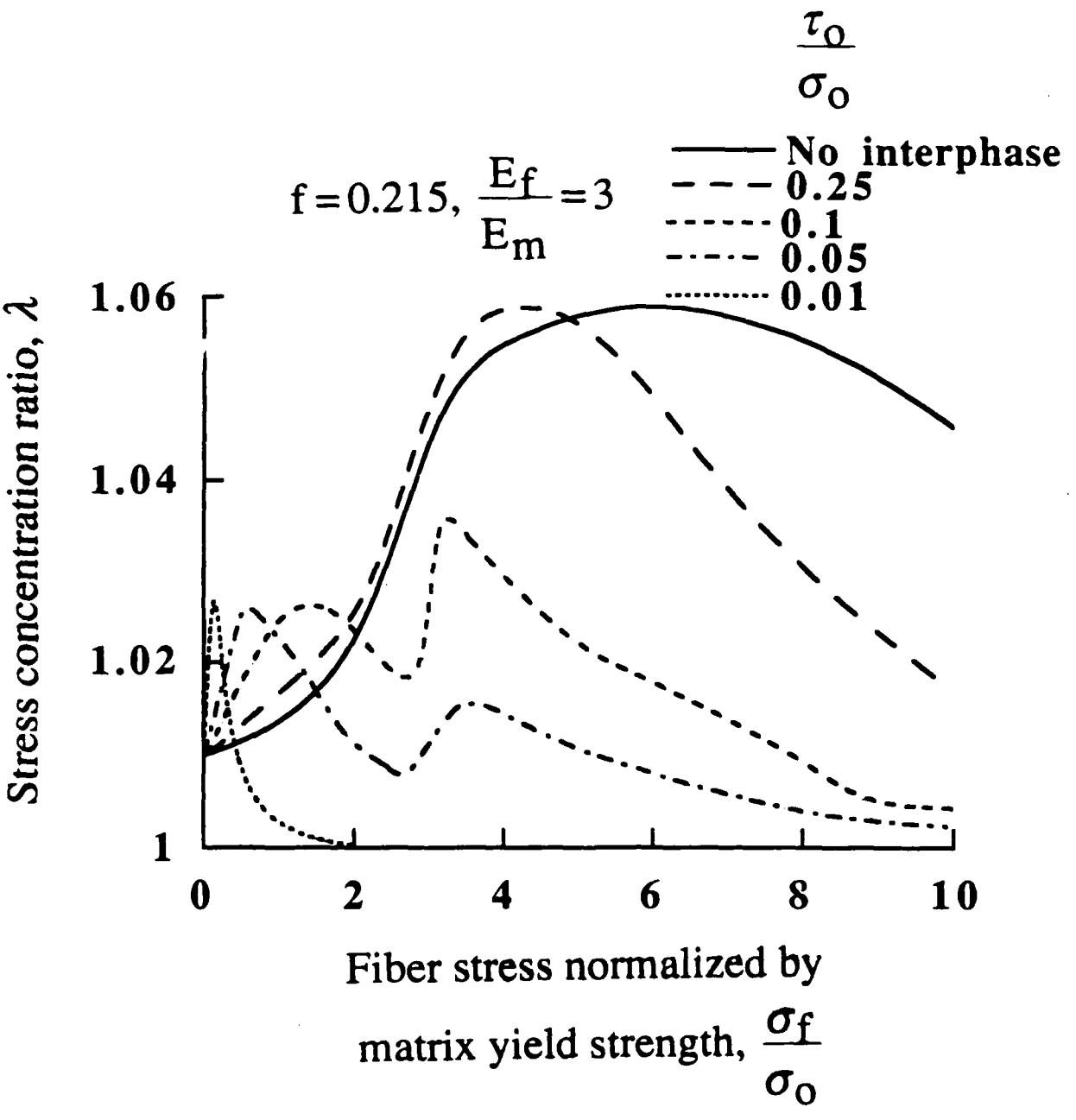
$\frac{\tau_o}{\sigma_o}$
No interphase
0.25
0.1
0.05
0.01
f = 0.215, $\frac{E_f}{E_m}$ = 3
Stress concentration ratio, λ
1.06
1.04
1.02
1
0
2
4
6
8
10
Fiber stress normalized by
matrix yield strength, $\frac{\sigma_f}{\sigma_o}$

Fig.7(e)

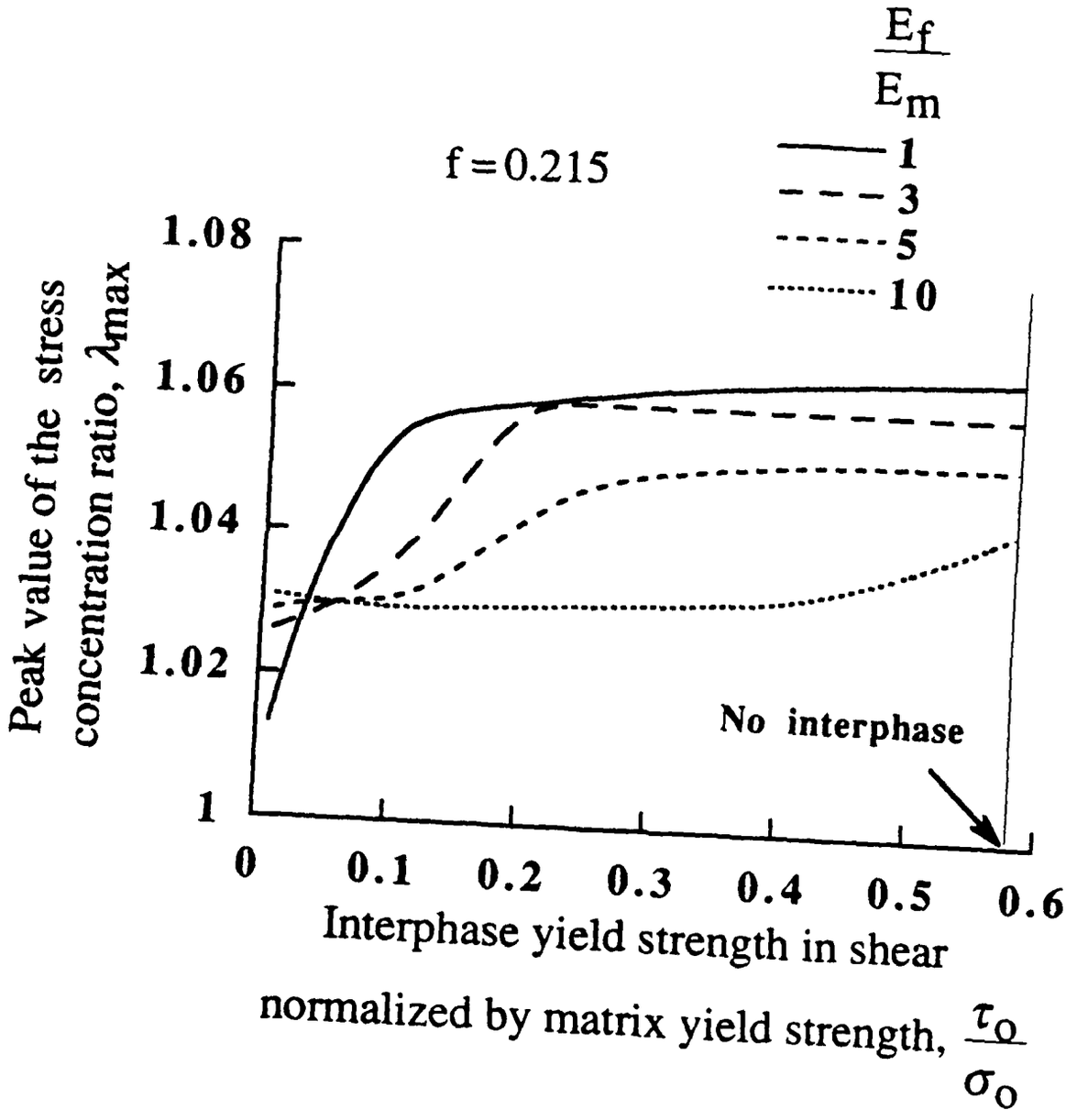
$\frac{E_f}{E_m}$
1
3
5
10
f = 0.215
Peak value of the stress concentration ratio, λ_{max}
1.08
1.06
1.04
1.02
1
No interphase
0
0.1
0.2
0.3
0.4
0.5
0.6
Interphase yield strength in shear normalized by matrix yield strength, $\frac{\tau_o}{\sigma_o}$

Fig.8(a)

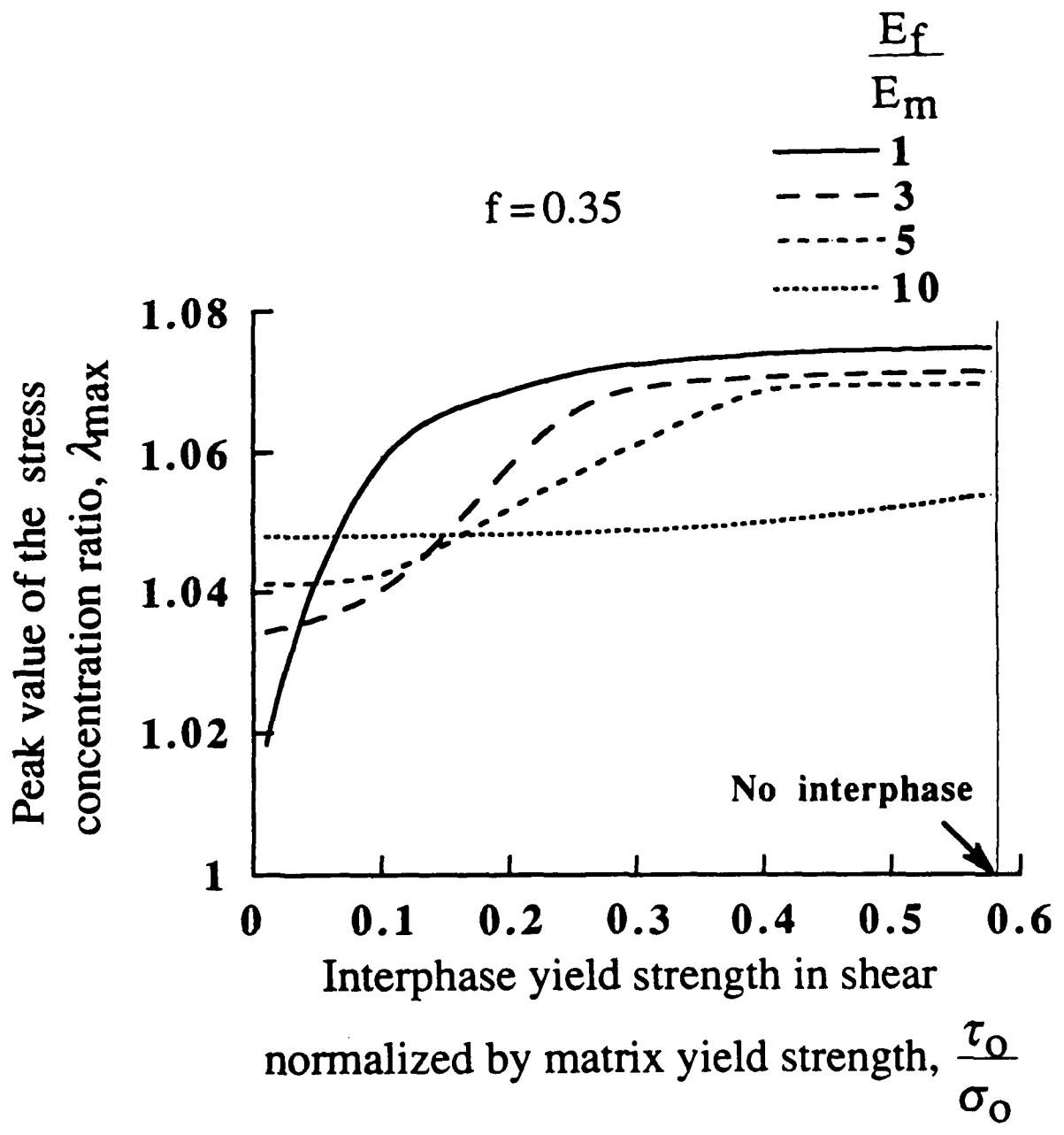
$\frac{E_f}{E_m}$
1
3
5
10
f = 0.35
1.08
1.06
1.04
1.02
1
Peak value of the stress concentration ratio, λ_{max}
No interphase
0
0.1
0.2
0.3
0.4
0.5
0.6
Interphase yield strength in shear
normalized by matrix yield strength, $\frac{\tau_o}{\sigma_o}$

Fig.8(b)

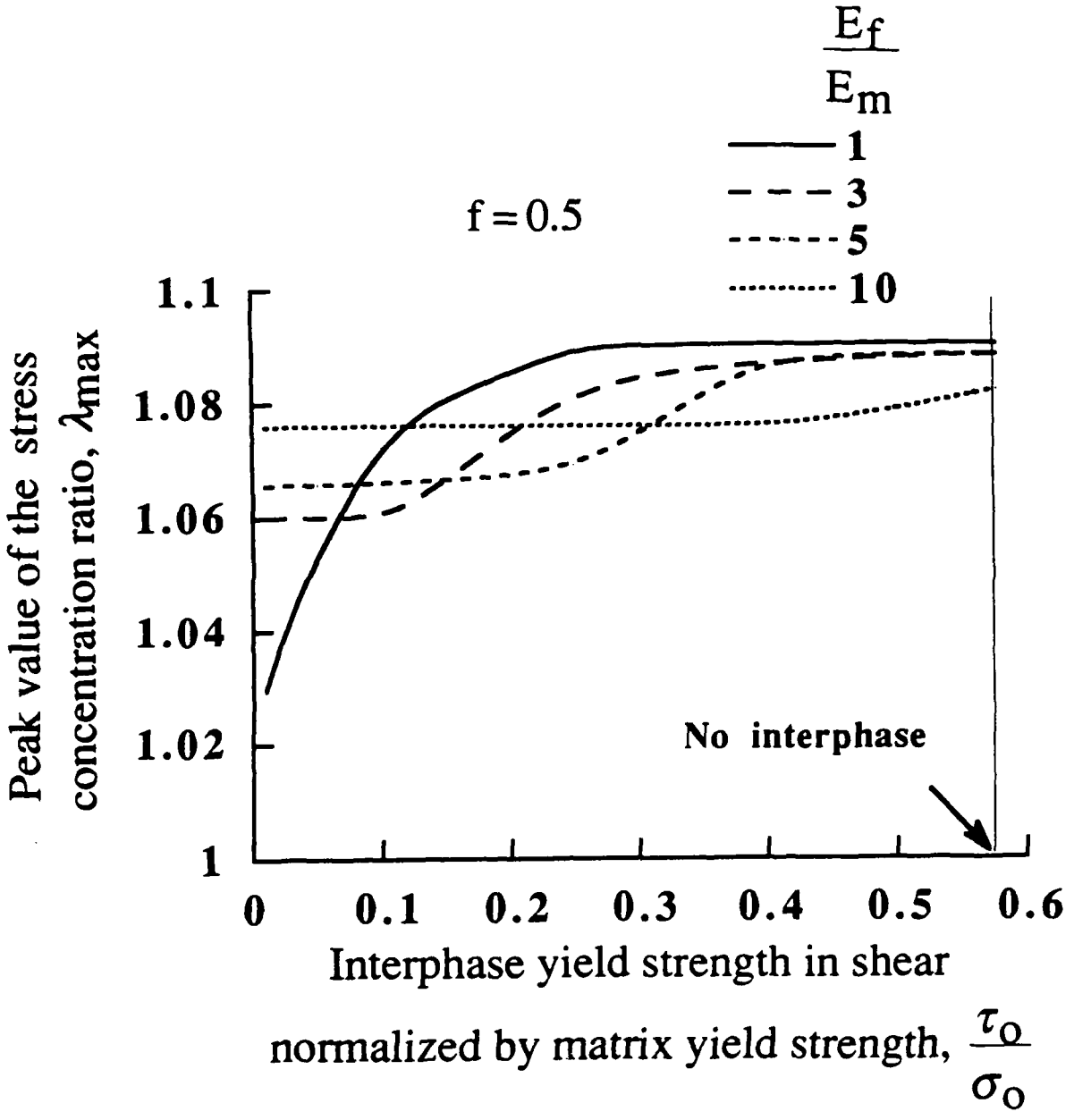
$\frac{E_f}{E_m}$
1
3
5
10
f = 0.5
1.1
1.08
1.06
1.04
1.02
1
Peak value of the stress concentration ratio, λ_{max}
No interphase
0
0.1
0.2
0.3
0.4
0.5
0.6
Interphase yield strength in shear
normalized by matrix yield strength, $\frac{\tau_o}{\sigma_o}$

Fig.8(c)

$$\frac{E_f}{E_m} = 3, \frac{S_f}{\sigma_o} = 2$$

m	λ
10	(1.04)
9	(1.05)
7	(1.06)
6	(1.07)
5	(1.08)

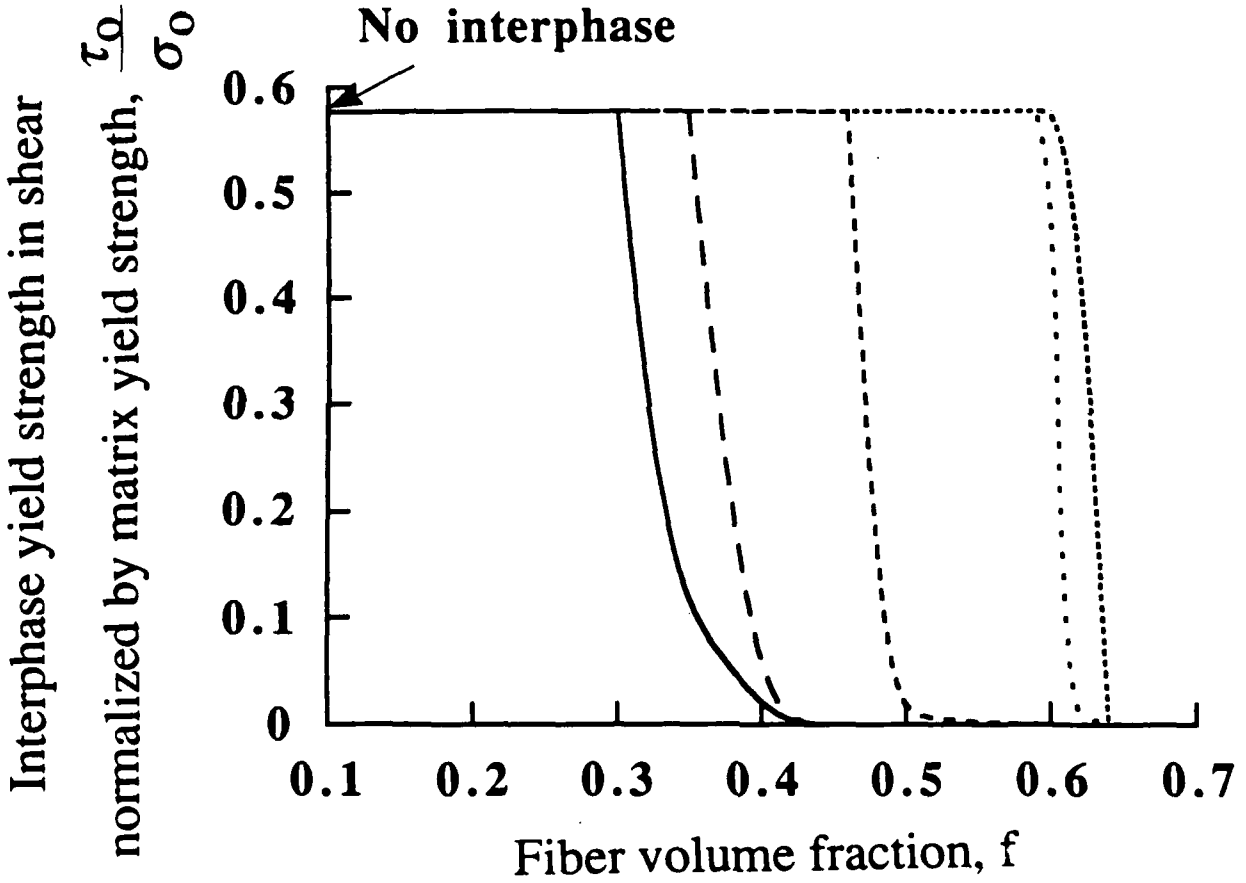

Fig.9(a)

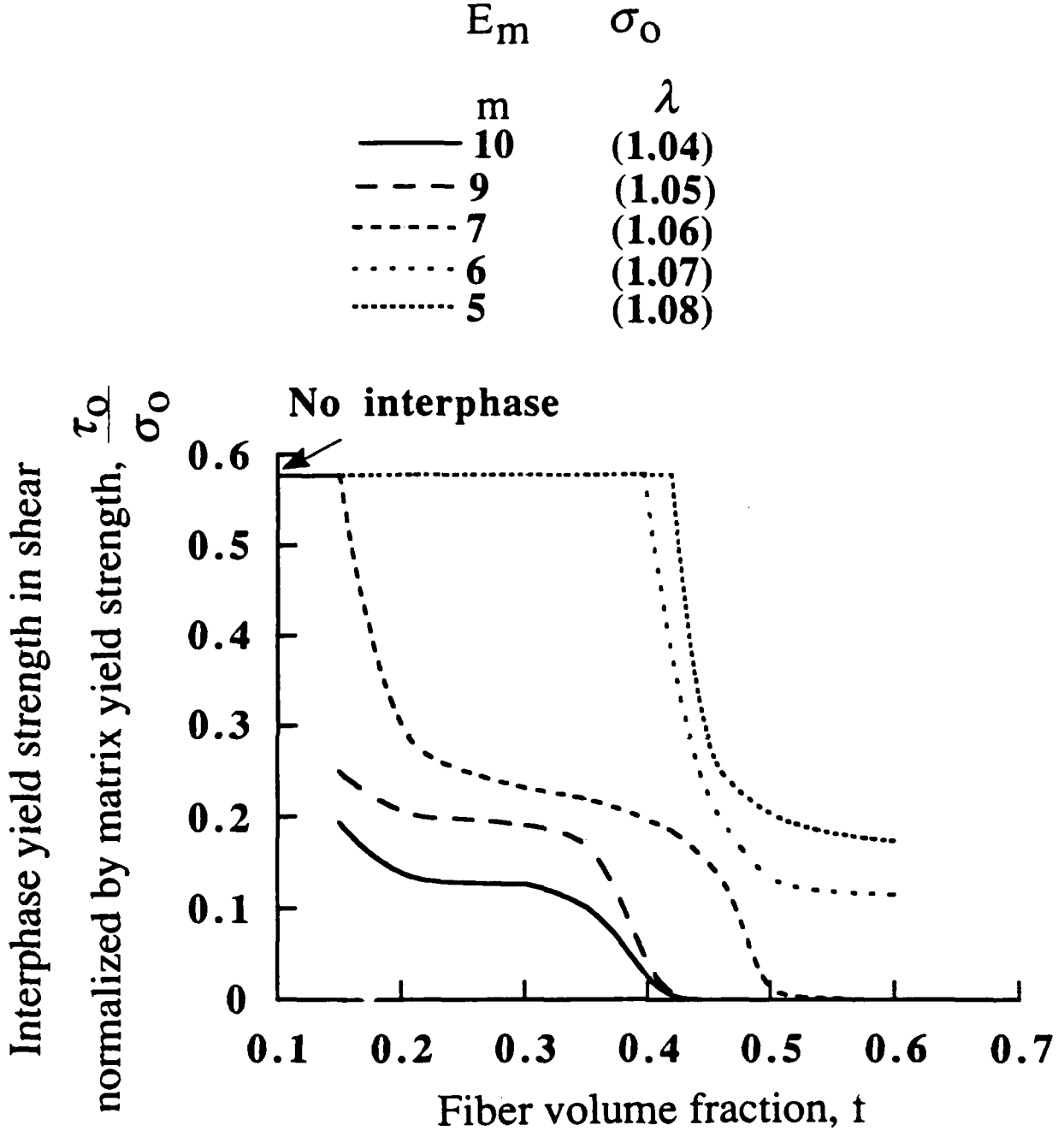
$\frac{E_f}{E_m} = 3, \frac{S_f}{\sigma_o} = 5$
m
λ
10 (1.04)
9 (1.05)
7 (1.06)
6 (1.07)
5 (1.08)
No interphase
Interphase yield strength in shear normalized by matrix yield strength, $\frac{\tau_o}{\sigma_o}$
0.6
0.5
0.4
0.3
0.2
0.1
0
0.1 0.2 0.3 0.4 0.5 0.6 0.7
Fiber volume fraction, t

Fig.9(b)

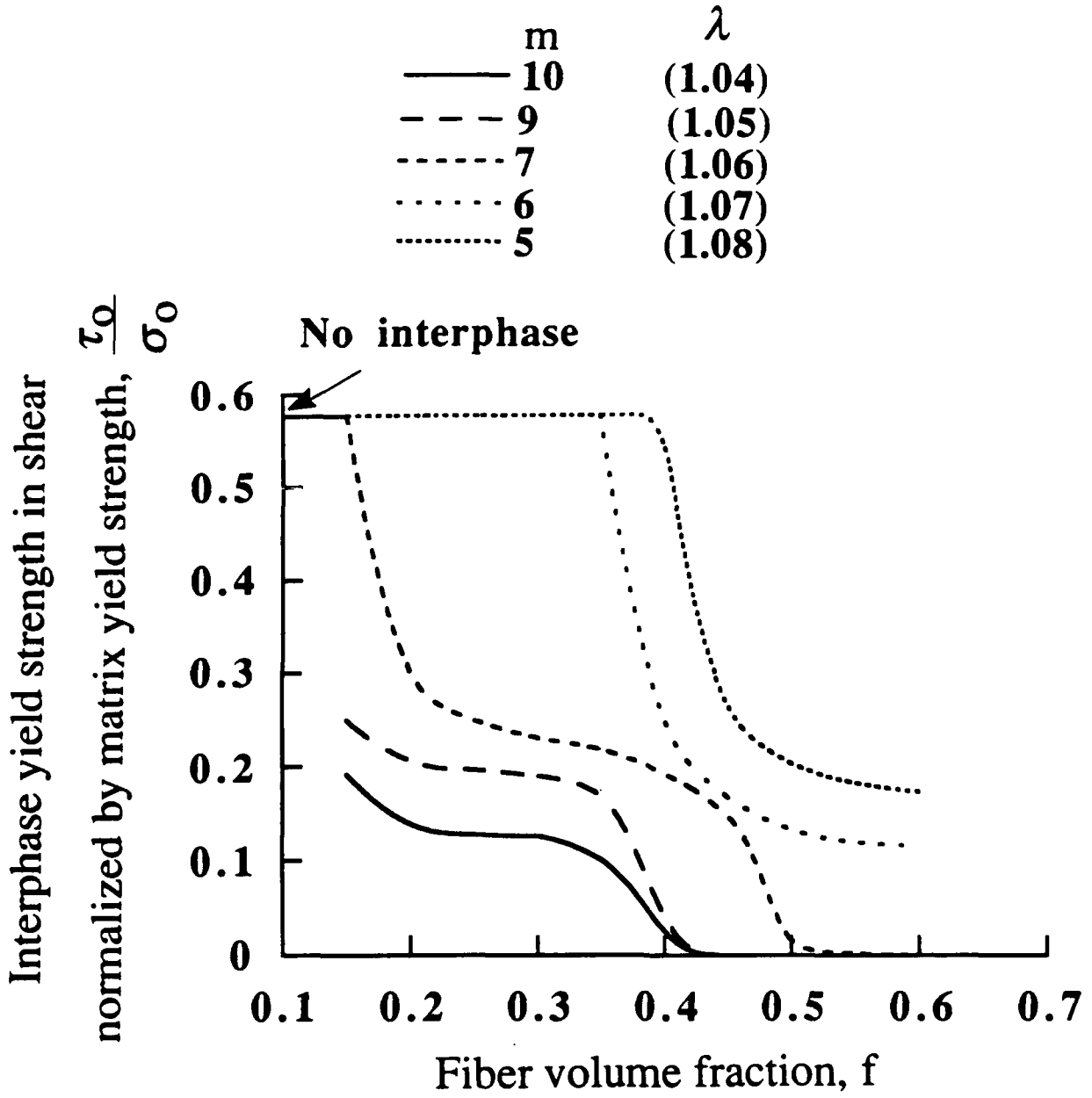
$\frac{E_f}{E_m} = 3, \frac{S_f}{\sigma_o} = 10$
m
λ
10 (1.04)
9 (1.05)
7 (1.06)
6 (1.07)
5 (1.08)
No interphase
Interphase yield strength in shear
normalized by matrix yield strength, $\frac{\tau_o}{\sigma_o}$
0.6
0.5
0.4
0.3
0.2
0.1
0
0.1 0.2 0.3 0.4 0.5 0.6 0.7
Fiber volume fraction, f

Fig.9(c)

$$\frac{E_f}{E_m} = 5, \frac{S_f}{\sigma_o} = 2$$

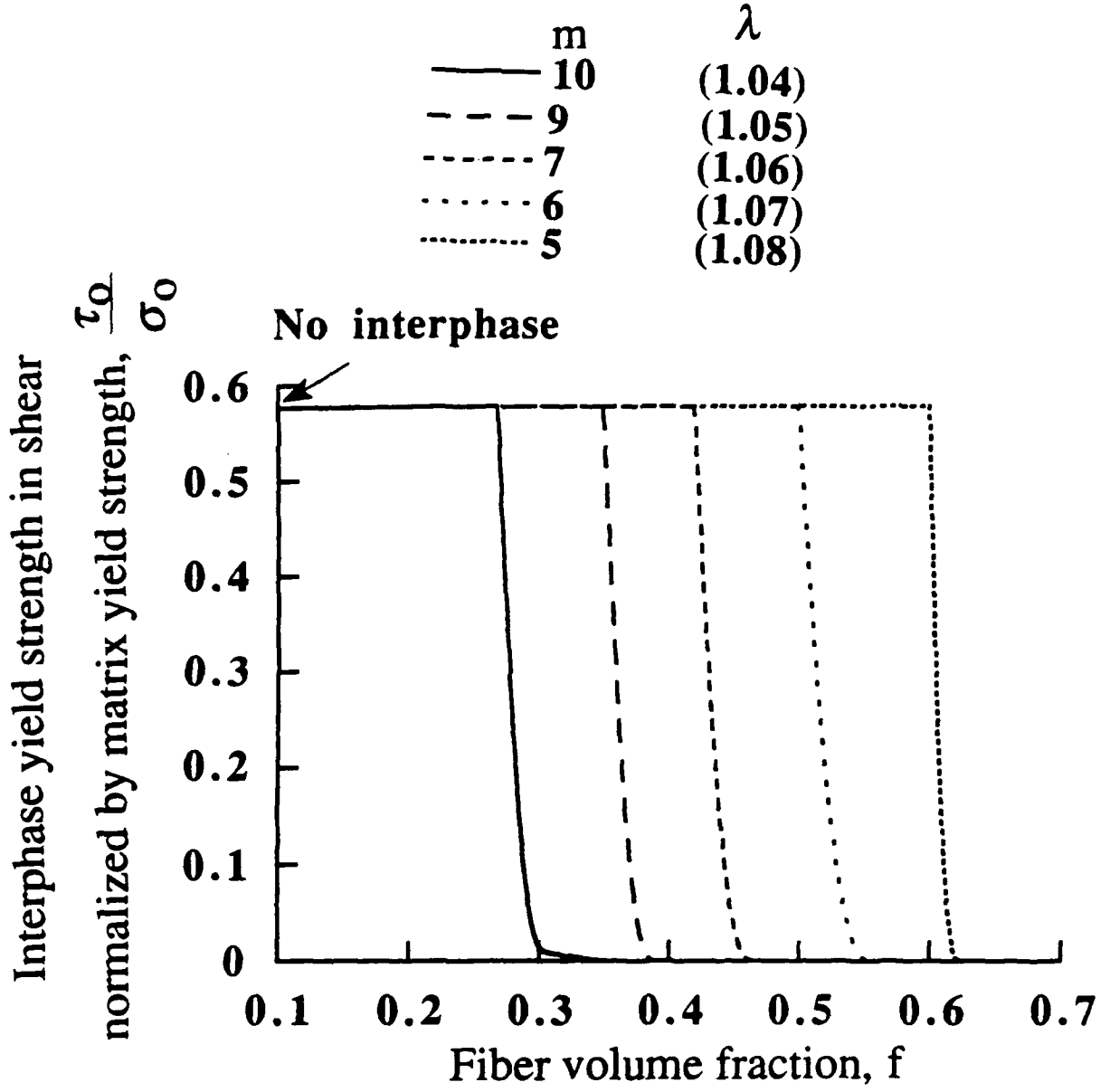

Fig.10(a)

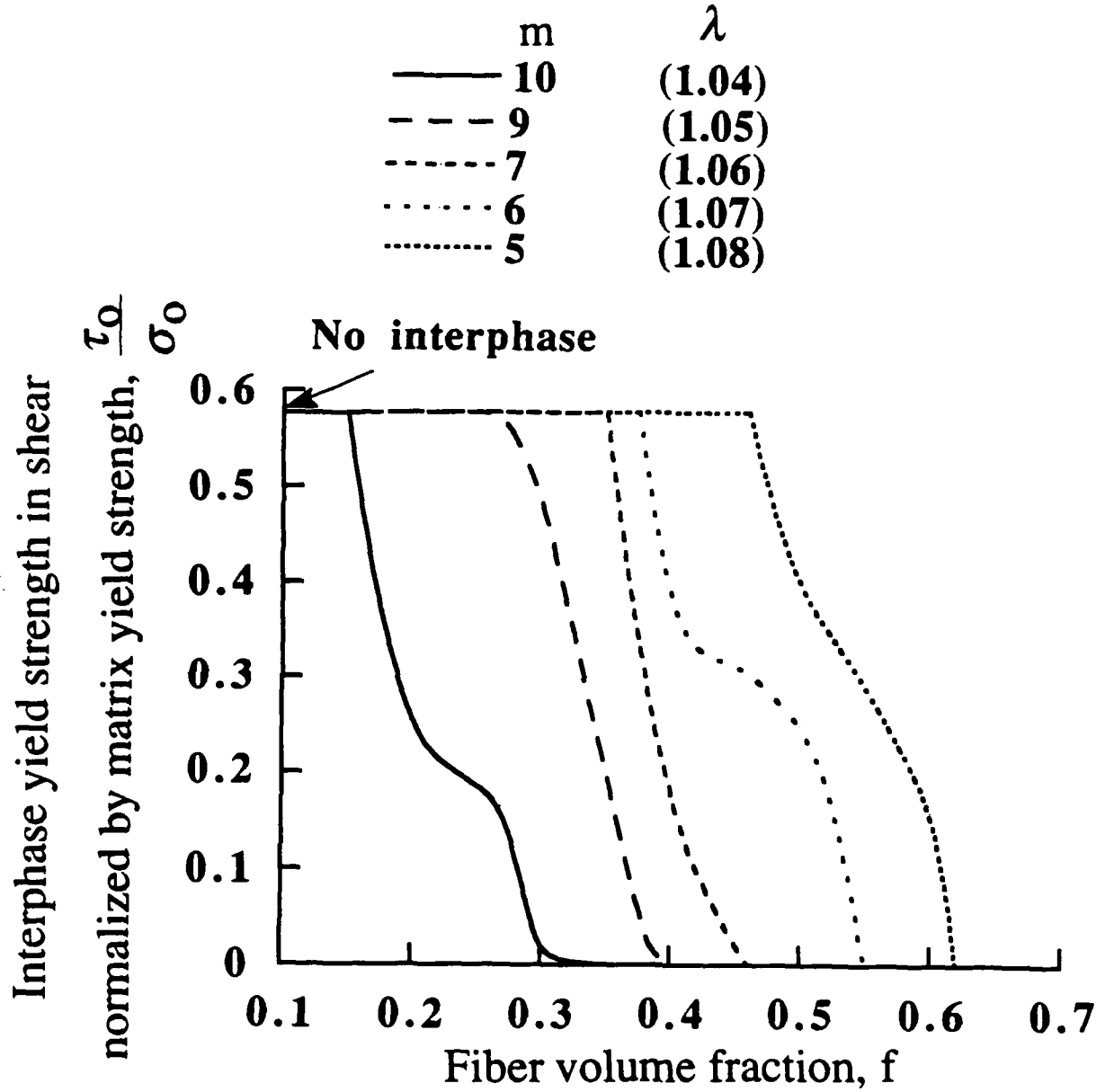
$\frac{E_f}{E_m} = 5, \frac{S_f}{\sigma_o} = 5$
m
λ
10 (1.04)
9 (1.05)
7 (1.06)
6 (1.07)
5 (1.08)
No interphase
Interphase yield strength in shear normalized by matrix yield strength, $\frac{\tau_o}{\sigma_o}$
0.6
0.5
0.4
0.3
0.2
0.1
0
0.1 0.2 0.3 0.4 0.5 0.6 0.7
Fiber volume fraction, f

Fig.10(b)

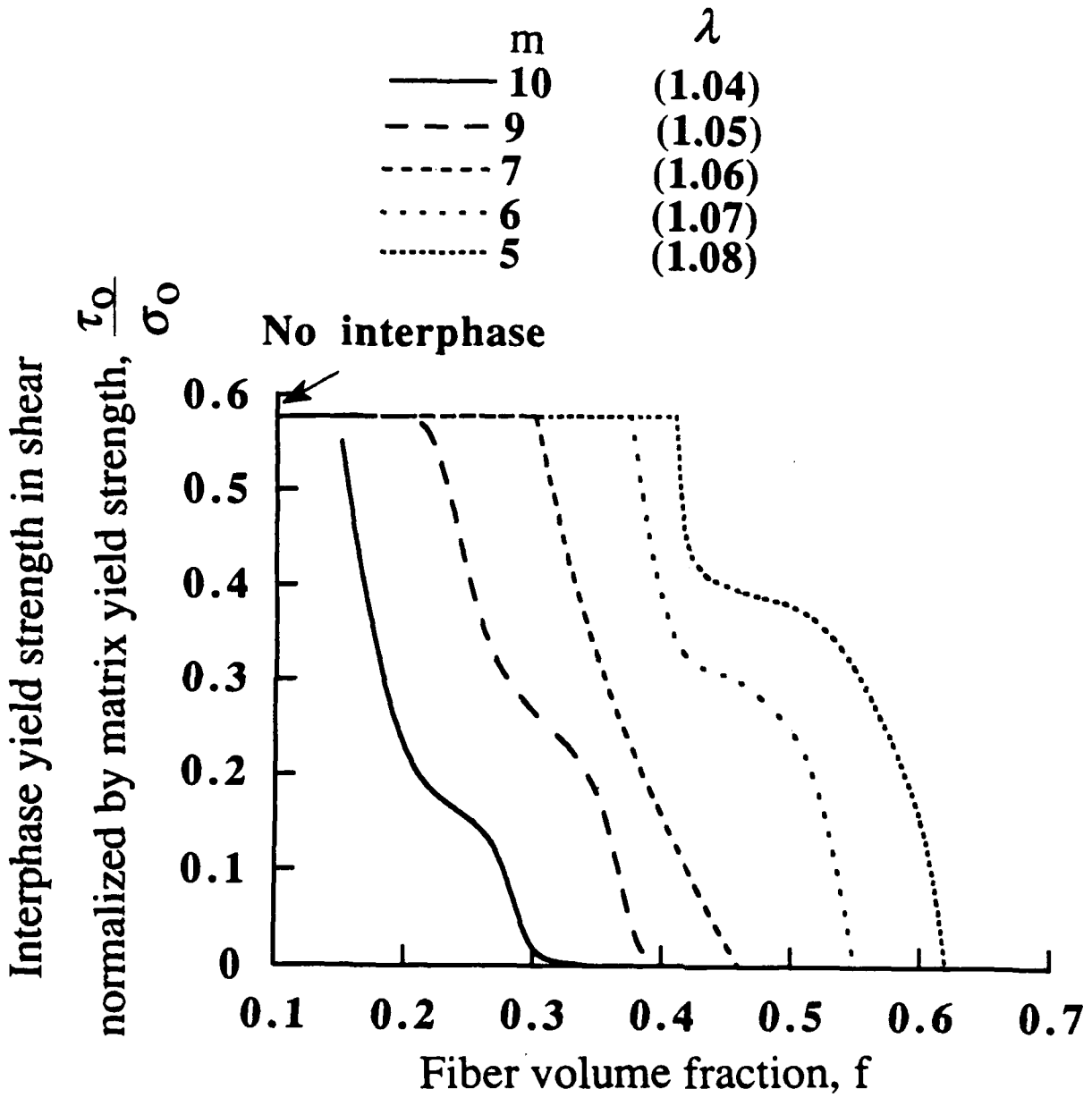
$\frac{E_f}{E_m} = 5, \frac{S_f}{\sigma_o} = 10$
m
λ
10 (1.04)
9 (1.05)
7 (1.06)
6 (1.07)
5 (1.08)
No interphase
Interphase yield strength in shear normalized by matrix yield strength, $\frac{\tau_o}{\sigma_o}$
0.6
0.5
0.4
0.3
0.2
0.1
0
0.1 0.2 0.3 0.4 0.5 0.6 0.7
Fiber volume fraction, f

Fig.10(c)

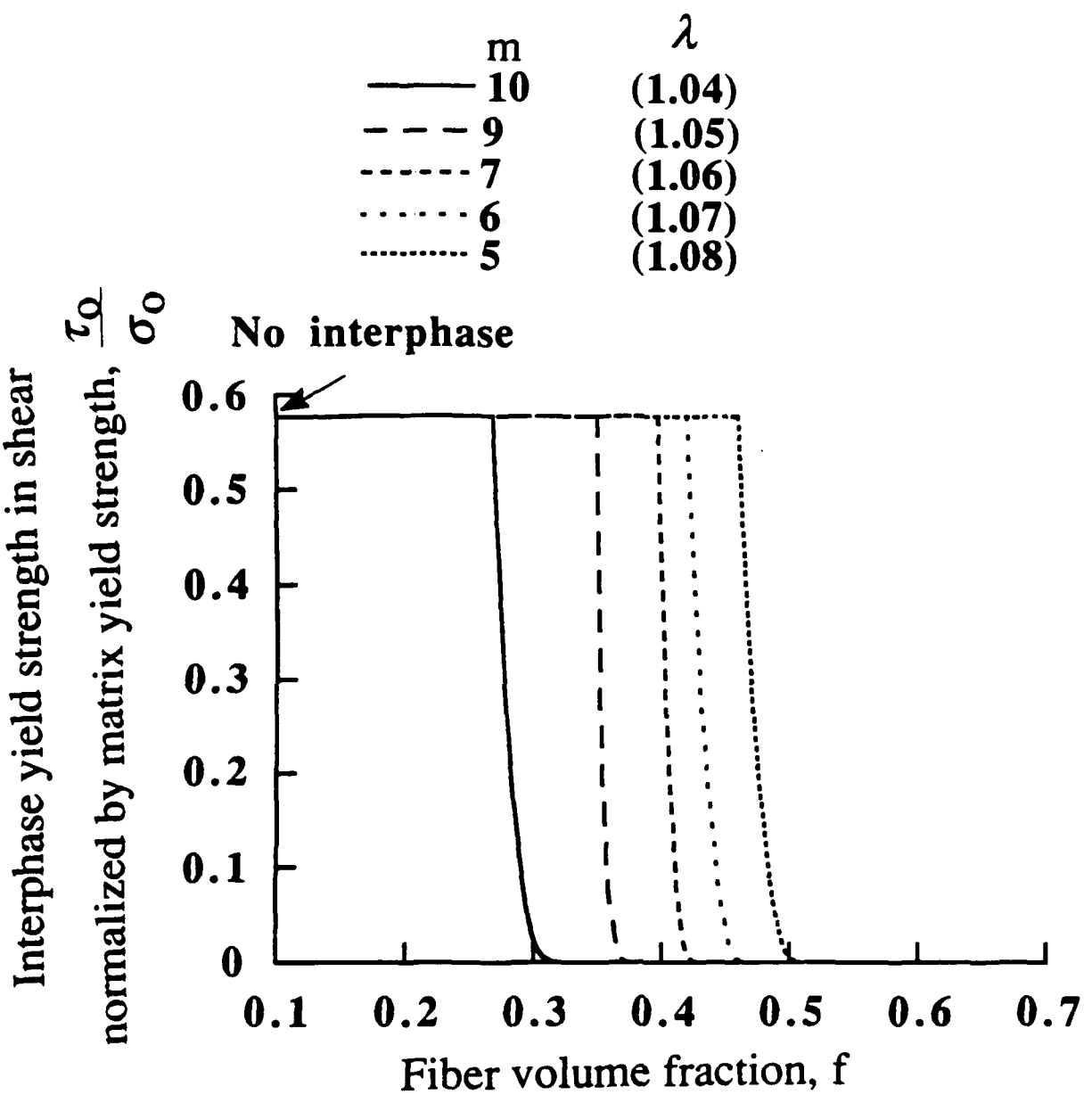
$\frac{E_f}{E_m} = 10, \frac{S_f}{\sigma_o} = 2$
m
λ
10 (1.04)
9 (1.05)
7 (1.06)
6 (1.07)
5 (1.08)
No interphase
Interphase yield strength in shear normalized by matrix yield strength, $\frac{\tau_o}{\sigma_o}$
0.6
0.5
0.4
0.3
0.2
0.1
0
0.1 0.2 0.3 0.4 0.5 0.6 0.7
Fiber volume fraction, f

Fig.11(a)

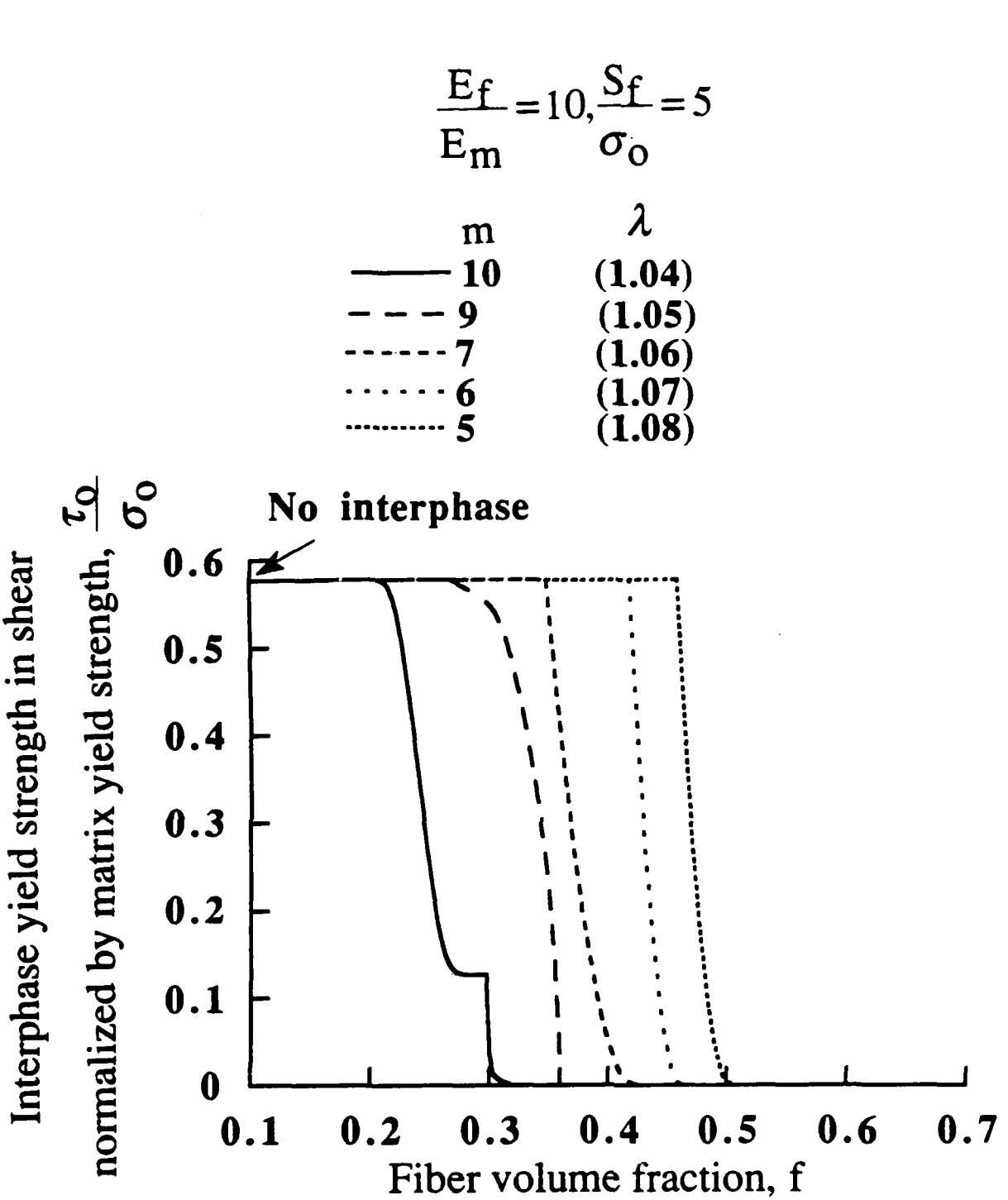
$\frac{E_f}{E_m} = 10, \frac{S_f}{\sigma_o} = 5$
m
λ
10 (1.04)
9 (1.05)
7 (1.06)
6 (1.07)
5 (1.08)
No interphase
Interphase yield strength in shear normalized by matrix yield strength, $\frac{\tau_o}{\sigma_o}$
0.6
0.5
0.4
0.3
0.2
0.1
0
0.1 0.2 0.3 0.4 0.5 0.6 0.7
Fiber volume fraction, f

Fig.11(b)

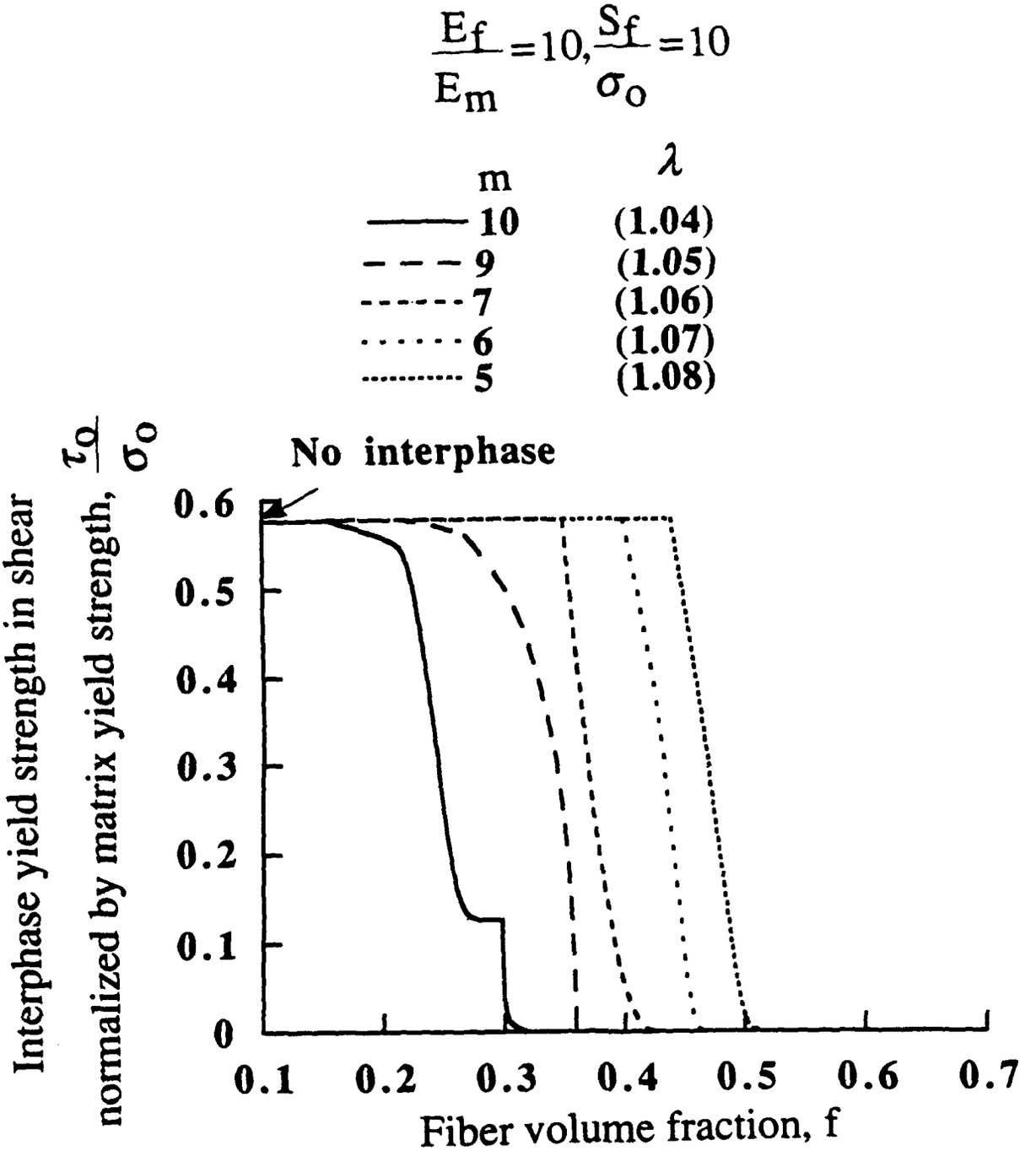
$\frac{E_f}{E_m}=10, \frac{S_f}{\sigma_o}=10$
m
λ
10 (1.04)
9 (1.05)
7 (1.06)
6 (1.07)
5 (1.08)
No interphase
Interphase yield strength in shear
normalized by matrix yield strength, $\frac{\tau_o}{\sigma_o}$
0.6
0.5
0.4
0.3
0.2
0.1
0
0.1 0.2 0.3 0.4 0.5 0.6 0.7
Fiber volume fraction, f

Fig.11(c)

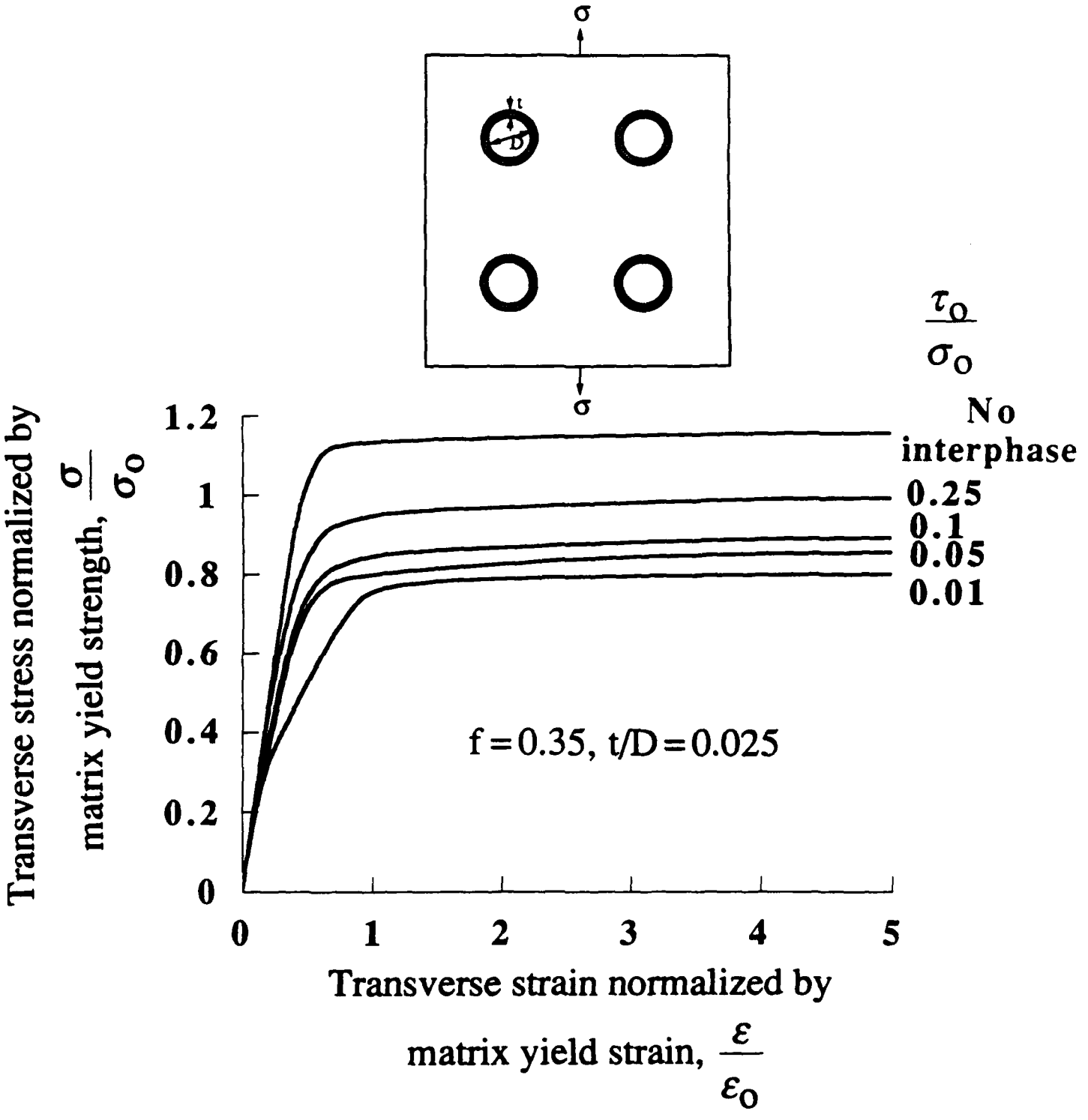
σ
t
D
σ
$\frac{\tau_o}{\sigma_o}$
No interphase
0.25
0.1
0.05
0.01
f = 0.35, t/D = 0.025
Transverse stress normalized by matrix yield strength, $\frac{\sigma}{\sigma_o}$
Transverse strain normalized by matrix yield strain, $\frac{\varepsilon}{\varepsilon_o}$
0
0.2
0.4
0.6
0.8
1
1.2
0
1
2
3
4
5

Fig.12(a)

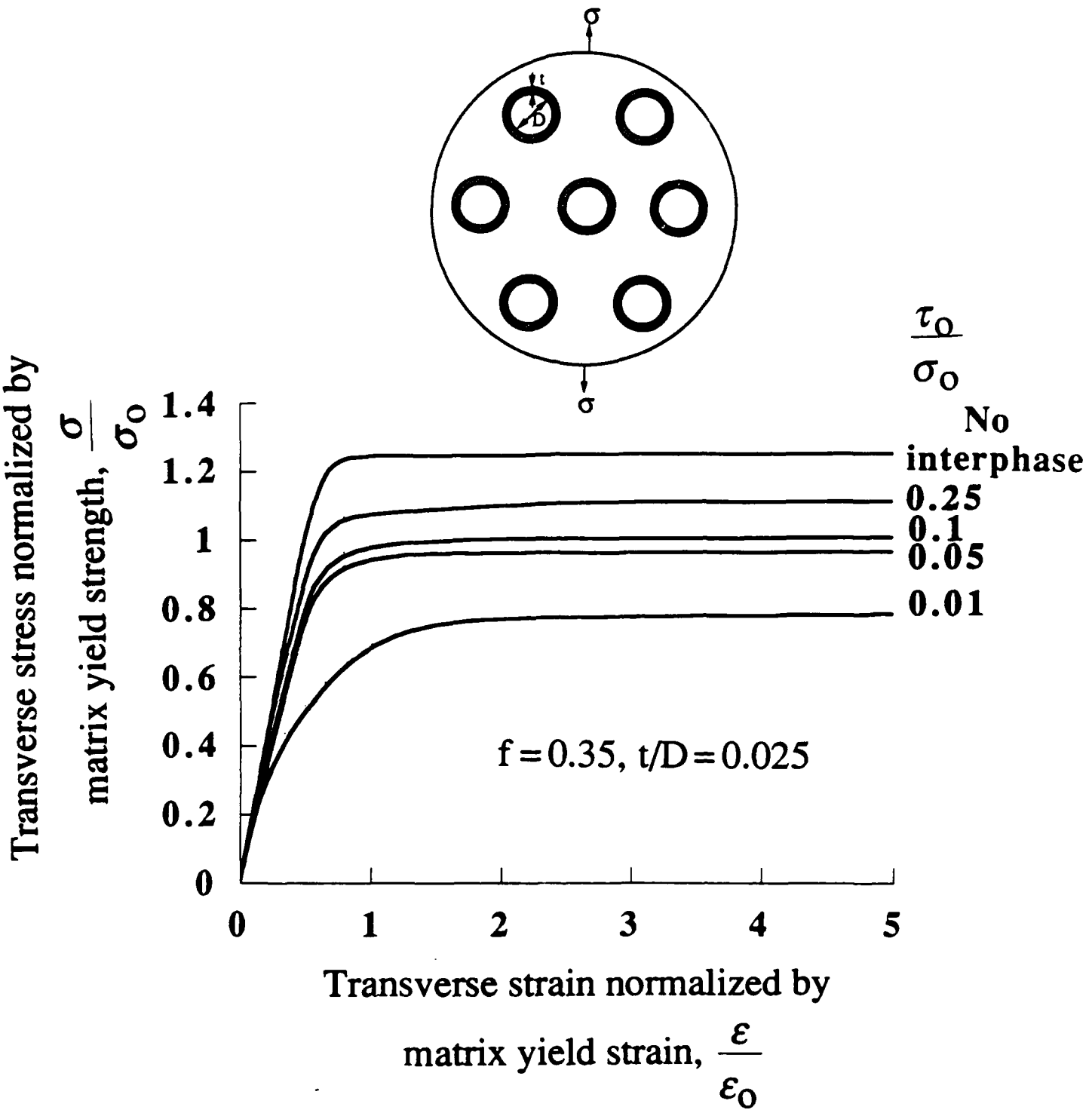
σ
t
D
σ
$\frac{\tau_o}{\sigma_o}$
No interphase
0.25
0.1
0.05
0.01
f = 0.35, t/D = 0.025
Transverse stress normalized by matrix yield strength, $\frac{\sigma}{\sigma_o}$
1.4
1.2
1
0.8
0.6
0.4
0.2
0
0
1
2
3
4
5
Transverse strain normalized by matrix yield strain, $\frac{\varepsilon}{\varepsilon_o}$

Fig.12(b)

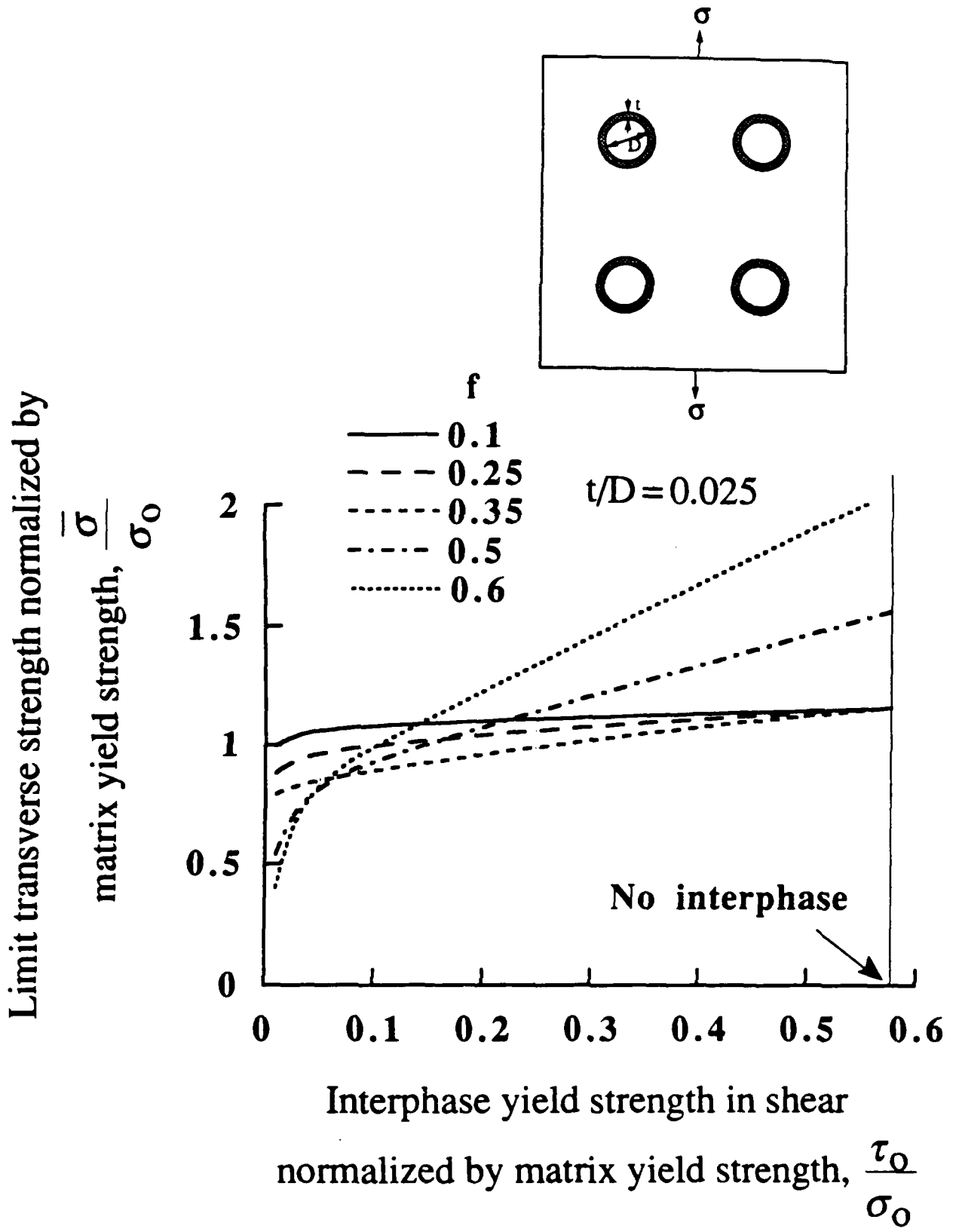
σ
t
D
σ
f
0.1
0.25
0.35
0.5
0.6
t/D=0.025
2
1.5
1
0.5
0
No interphase
0
0.1
0.2
0.3
0.4
0.5
0.6
Limit transverse strength normalized by matrix yield strength, $\frac{\bar{\sigma}}{\sigma_o}$
Interphase yield strength in shear normalized by matrix yield strength, $\frac{\tau_o}{\sigma_o}$

Fig.13(a)

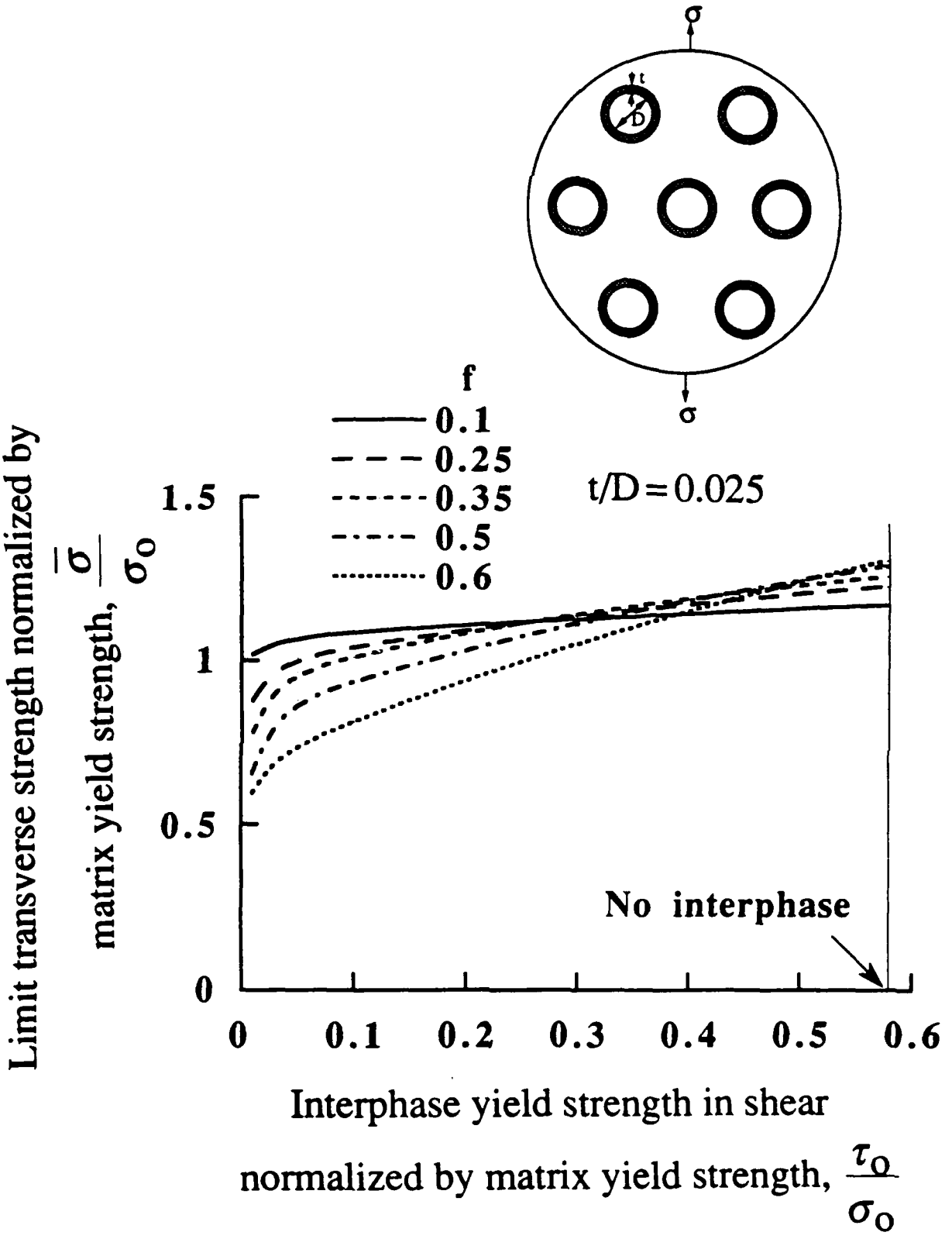
σ
t
D
σ
f
0.1
0.25
0.35
0.5
0.6
t/D=0.025
1.5
1
0.5
0
No interphase
0
0.1
0.2
0.3
0.4
0.5
0.6
Limit transverse strength normalized by matrix yield strength, $\frac{\bar{\sigma}}{\sigma_o}$
Interphase yield strength in shear normalized by matrix yield strength, $\frac{\tau_o}{\sigma_o}$

Fig.13(b)

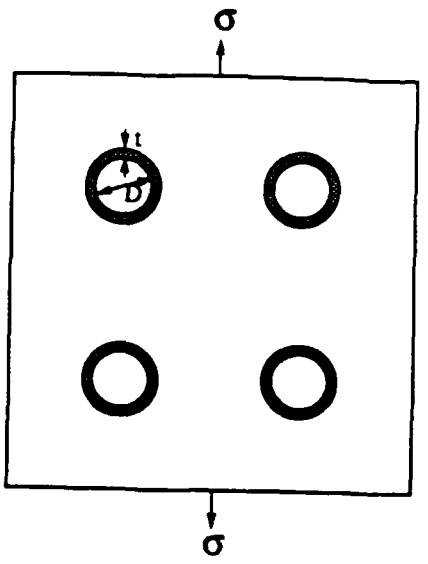
σ
t
D
σ

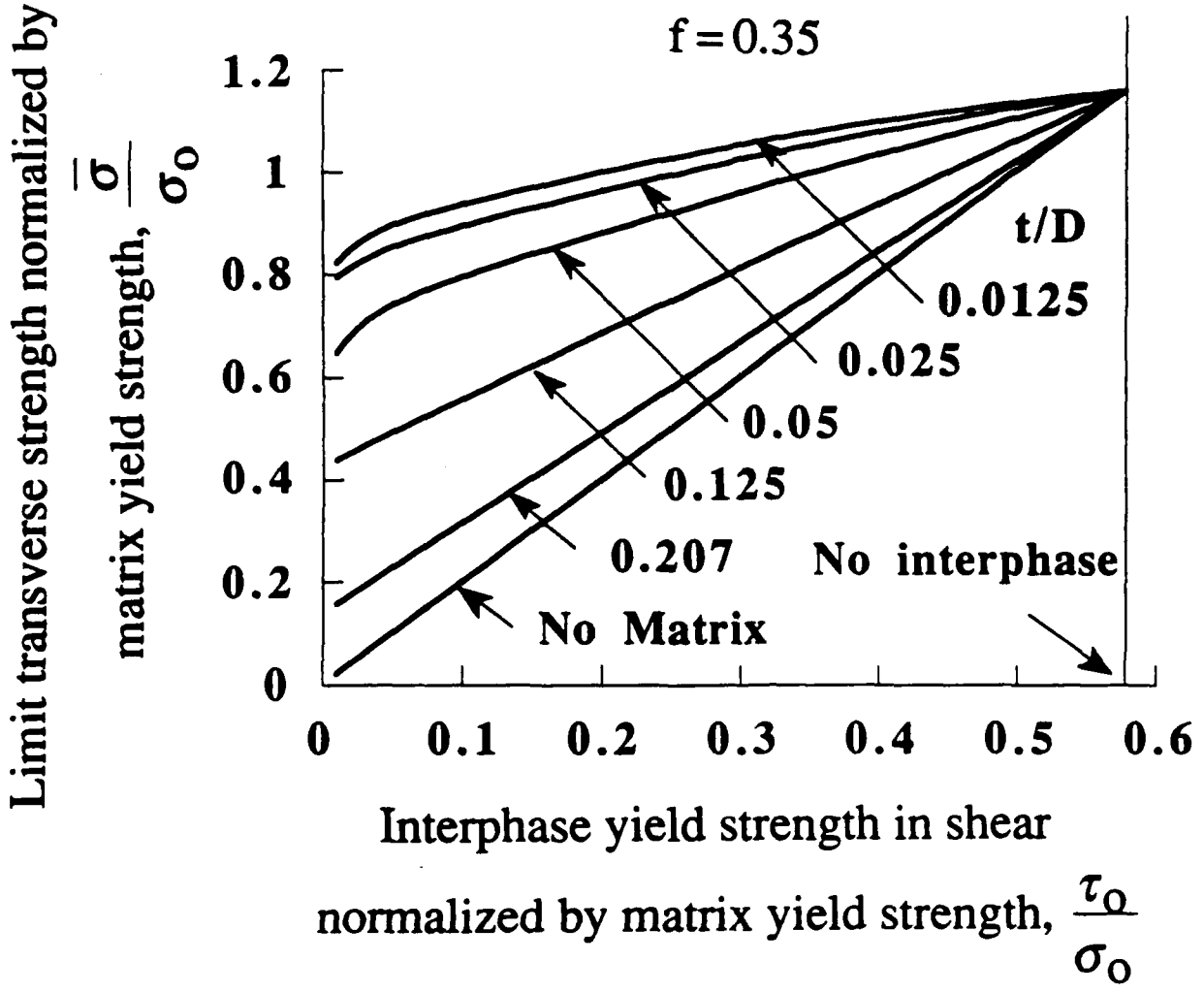
f = 0.35
Limit transverse strength normalized by matrix yield strength, $\frac{|\sigma|}{\sigma_0}$
1.2
1
0.8
0.6
0.4
0.2
0
t/D
0.0125
0.025
0.05
0.125
0.207
No interphase
No Matrix
0
0.1
0.2
0.3
0.4
0.5
0.6
Interphase yield strength in shear normalized by matrix yield strength, $\frac{\tau_0}{\sigma_0}$

Fig.14

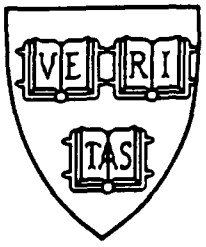

INELASTIC STRAINS DUE TO MATRIX CRACKING IN UNIDIRECTIONAL FIBER-REINFORCED COMPOSITES

M. Y. He, B.-X. Wu, A. G. Evans
Materials Department, College of Engineering
University of California
Santa Barbara, CA 93106-5050

and

J. W. Hutchinson
Division of Applied Sciences
Harvard University
Cambridge, MA 02138

Division of Applied Sciences
HARVARD UNIVERSITY
Cambridge, Massachusetts 02138

October 1993

INELASTIC STRAINS DUE TO MATRIX CRACKING IN UNIDIRECTIONAL FIBER-REINFORCED COMPOSITES

M. Y. He, B.-X. Wu, A. G. Evans
Materials Department, College of Engineering
University of California
Santa Barbara, CA 93106-5050
and
J. W. Hutchinson
Division of Applied Sciences
Harvard University
Cambridge, MA 02138

ABSTRACT

Simulations of the inelastic strains caused by matrix cracking in unidirectional CMCs are performed. They are based on a cell model, which has previously been analyzed by a shear lag approximation. Here, finite element solutions are used to arrive at more accurate formulae, differing from the shear lag results mainly in the range of small debonds. The model relates the inelastic strain to the constitutive properties, particularly the interface sliding and debonding resistances. Comparisons with experimental results indicate good correspondence for a SiC/SiC composite but divergences for a SiC/CAS composite. The divergences are attributed to the contribution to the inelastic strain from fiber failure.

1. INTRODUCTION

In composites with either a ceramic (CMCs) or intermetallic (IMCs) matrix, cracks can form in the matrix while the fibers remain essentially intact (Aveston, Cooper and Kelly, 1971; Kim and Pagano,1991; Marshall and Evans, 1985; Beyerle, Spearing, Zok and Evans, 1992; Evans, 1991). This capability is imparted to the material by using a fiber coating that allows debonding and frictional sliding as the cracks interact with the fibers (Evans, Zok and Davis, 1991). Furthermore, in metal (MMCs) and polymer (PMCs) matrix materials, similar matrix cracks form upon cyclic loading. The matrix cracks may develop upon either tensile or shear loading (Bronsted, Heredia and Evans, 1993). Both beneficial and detrimental effects arise when matrix cracks form. The *beneficial* effect occurs because the cracks introduce inelastic strains (Aveston, et al, 1971; Nardonne and Prewo, 1988; Beyerle, et al, 1992; Evans, Domergue and Vagaggini, 1993). Such strains provide stress redistribution mechanisms, which impart *notch*

insensitivity when the composite constituents are *optimized* (Evans, et al, 1993; Cady, Mackin and Evans, 1993). For optimization purposes, it is important to understand the factors that govern the formation of matrix cracks, as well as their effect on the inelastic, or 'plastic', strains. The detrimental consequence concerns the *stress concentrations* induced in the fibers by matrix cracks, especially at ply interfaces and in the vicinity of manufacturing flaws (Budiansky and Cui, 1993). These stress concentrations, when they exist, may weaken the composite.

Most composites with practical utility include fibers having at least two orientations. The simplest such configuration is a $0^o/90^o$ laminated material such as that shown in Fig. 1. Analyses concerned with such materials are basic. Upon tensile loading, cracks in the 90^o layers first form by a three dimensional tunneling process, spreading from initial flaws (Xia, Carr and Hutchinson, 1993). At higher stresses, the cracks in the 90^o plies begin to spread into neighboring 0^o plies as plane strain matrix cracks, bridged by fibers. The associated uniaxial stress/strain behavior is depicted schematically in Fig. 2 (Beyerle, et al, 1992; Evans, et al, 1993). The behavior addressed in the present article concerns the tensile stress-strain behavior of 0^o plies, following earlier work on the same problem (Pryce and Smith, 1992; Weitsman and Zhu, 1993; Evans, et. al. 1993; Vagaggini and Evans 1993). The largest contributions to the inelastic strains arise due to matrix cracking and fiber debonding and sliding in the 0^o plies. Knowledge of the behavior of these plies is an essential part of gaining an understanding of the performance of a laminated composite.

The inelastic strains caused by matrix cracks are most directly assessed on unidirectional materials. For such materials, the stress/strain behavior is sketched in Fig.3. At stresses above $\bar{\sigma}_{mc}$, matrix cracks develop. The average spacing d between the matrix cracks diminishes as the stress increases. At $\bar{\sigma}_s$, the cracks saturate, with a spacing d_s. The slope of the stress/strain curve usually increases as the stress approaches and exceeds $\bar{\sigma}_s$. A methodology, described in references cited above, has been developed for predicting the uniaxial stress-strain behavior in terms of the constitutive properties of the fiber/matrix system such as fiber volume fraction, interface debond energy, frictional sliding stress, and residual stresses. For the most part, solutions available for carrying out this methodology are obtained from approximate shear lag analyses. The primary purpose of this paper will be to present a fairly comprehensive set of more accurate results which will allow assessment of the shear lag predictions and, more importantly, to enable workers in the field to carry out accurate implementation of the general methodology.

2. PRELIMINARIES AND RESULTS FROM SHEAR LAG ANALYSIS

The focus will be on the stress-strain behavior of a unidirectional fiber reinforced composite under uniaxial stressing parallel to the fibers such that the overall strain is monotonically

increasing. Fig. 3 depicts the stress-strain behavior of such a composite. As already remarked, matrix cracks begin forming when the overall stress $\bar{\sigma}$ reaches the matrix cracking stress $\bar{\sigma}_{mc}$ with debonding and sliding occurring along the fiber/matrix interfaces. Let E be the modulus of the uncracked composite. There are several contributions to the overall strain $\bar{\varepsilon}$ in addition to the strain expected for the uncracked composite, $\bar{\sigma}/E$. Even without debonding and sliding, the matrix cracks increase the compliance of the composite. Debonding and sliding further increase the compliance and thereby add to the overall strain. The modulus of the cracked and debonded composite at a *fixed average spacing* of matrix cracks d and at *fixed* debond length ℓ (see Fig. 4) will be denoted as E_C such that in the absence of interface friction and of any residual stress

$$\bar{\varepsilon} = \bar{\sigma} / E_C \tag{1}$$

Friction along the fiber/matrix interface reduces the overall strain relative to (1). Conversely, a residual tensile stress in the matrix is relieved by matrix cracking and gives rise to additional overall straining relative to (1).

In this paper, attention is restricted to systems with a residual compressive stress acting across the fiber/matrix interface such that the debonding process involves mode II cracking and such that the debonded interfaces remain closed. A constant friction stress τ is assumed to act within the debond region as depicted in Fig. 4. The misfit strain giving rise to residual stress in the uncracked composite is denoted by Ω. Following the scheme in Hutchinson and Jensen, 1990 (hereafter designated by HJ), Ω is identified with the axial strain mismatch between the fiber and the matrix such that a positive Ω corresponds to residual tension in the matrix. A difference in radial and axial strain mismatches between the fiber and matrix is taken into account; $\lambda\Omega$ denotes the radial strain mismatch. The results for the quantities of interest will be calculated using the axisymmetric cell displayed in Fig. 4. Details of the specification of this cell will be given in the next section, as will the method for calculating the quantities which follow. In the remainder of this section, we present the form of the mechanics solution for this cell model, introducing the essential nondimensional coefficients. We also present the approximate results from shear lag analysis for these coefficients. In the next section, the more accurate results for the coefficients based on full numerical calculations will given along with some further motivation for the particular form of the mechanics solutions, as well as assessments of the shear lag approximations.

2.1 Form of the mechanics solution

At *fixed* average matrix crack spacing d and at *fixed* debond length ℓ, the overall strain depends *linearly* on $\bar{\sigma}$, τ and Ω. Specifically, for the cell model of Fig. 4 the solution for the overall strain can be written as

$$\bar{\varepsilon} = \frac{\bar{\sigma}}{E_c} + D_1 \frac{\Omega E_m f a_2 R}{E(1 - a_1 f)d} - D_3 \frac{\tau \ell^2}{ERd} \tag{2}$$

where the incremental modulus of the cracked and debonded composite is written as

$$\frac{1}{E_c} = \frac{1}{E}\left[1 + \frac{D_1 R}{d}\right] \tag{3}$$

In these equations R is the radius of the fiber, $f=(R/B)^2$ is the volume fraction of fibers where B is the outer radius of the cell, and E_m is the matrix modulus. The coefficients a_i, (and b_i and c_i introduced in subsequent equations) are coefficients introduced in HJ. Recipes for these coefficients are given in HJ for arbitrary fiber and matrix moduli, including the most general cases where the fiber has transversely isotropic moduli, the matrix is isotropic, and the ratio of the radial to axial mismatch strains is λ. Except when indicated to the contrary, the appropriate coefficients for the present work are those in HJ associated with Type II boundary conditions (see discussion in next section). The coefficients D_i in (2) and (3), and in (4) given below, are nondimensional functions of f, ℓ/R, d/R and nondimensional moduli parameters, such as E_f/E_m, ν_f and ν_m. These are the coefficients for which extensive numerical results will be presented in the next section. We note in advance that their dependence on d/R is relatively weak over most of the parameter range of interest and for many purposes this dependence can be neglected. For *fixed* d and ℓ the mode II stress intensity factor K_{II} is also a linear function of $\bar{\sigma}$, τ and Ω. The form of the solution for K_{II} for the cylindrical cell of Fig.4 is

$$K_{II} = D_2 \bar{\sigma}\sqrt{R} + D_2 \frac{\Omega E_m f\, a_2 \sqrt{R}}{(1 - a_1 f)} - D_4 \frac{\tau \ell}{\sqrt{R}} \tag{4}$$

The fact that D_1 appears in the contributions in (2) from both $\bar{\sigma}$ and Ω, and D_2 in the corresponding contributions in (4), is a rigorous feature of the solution which is shown in the next section.

The energy release rate G of the mode II debond crack is related to K_{II} by

$$G = K_{II}^2 / \hat{E} \tag{5}$$

where $\hat{E}$ is a modulus quantity dependent on the moduli of the fiber and the matrix. When the fiber and matrix are each isotropic,

$$\frac{1}{\hat{E}} = \frac{1}{2}\left(1 - \beta^2\right)\left[\frac{1 - \nu_f^2}{E_f} + \frac{1 - \nu_m^2}{E_m}\right] \tag{6}$$

where β is the second plane strain Dundurs parameter. For most systems the numerical influence of β^2 in (6) is quite small and can be neglected.

2.2 Shear lag results for the D_i

Shear lag modeling of fiber debonding and frictional sliding for systems where the fiber/matrix interface remains closed have been carried out by a number of authors (Gao, Mai and Cotterell, 1988; Marshall, 1992; HJ). Here the results of HJ will be used and these can be expressed in the form given in (2) and (4). (Indeed, it was the form of the shear lag results which, in part, guided the choice of these forms.) The expressions for the D_i listed below are obtained by identification from the HJ expressions. Specifically,

$$D_1 = 8\, f \frac{E}{E_m} \frac{\ell}{R} c_1^2 \tag{7a}$$

$$D_2 = \sqrt{\hat{E}/E_m}\; c_1 \tag{7b}$$

$$D_3 = 2\frac{E}{E_m}\, b_2 \tag{7c}$$

$$D_4 = \sqrt{(b_2 + b_3)\left(\hat{E}/E_m\right)} \tag{7d}$$

The relevant recipes for the coefficients above are those for the Type II boundary conditions in HJ, which are appropriate to the present study because they model a cell in an array as discussed below. It should be remarked that the above result for D_2 is not from a shear lag calculation. Instead, it is the exact result for the cylindrical model of Fig. 4 for the case $d/R=\infty$ in the steady-state limit when ℓ/R becomes sufficiently large. Nevertheless, for brevity, the above set of formulas will be referred to collectively as the shear lag approximation.

3. NUMERICAL RESULTS FOR THE D_i

3.1 The Cell Model

The scheme behind the model envisages a hexagonal array of fibers in a matrix with uniformly spaced matrix cracks aligned normal to the fiber direction. As is now common practice, for computational reasons, a cylindrical cell is used to approximate the hexagonal cell (cf. Fig.5 and Fig. 4). The cell is subject to an overall stress, $\bar{\sigma}$, parallel to the fiber axis, and the height of the cell is taken to be equal to the crack spacing, d. The cell has a matrix crack at its mid-plane. The lateral faces are required to remain a circular cylinder with zero shear traction and zero average

normal traction. The faces of the cell perpendicular to the stressing direction are constrained to remain planar with zero shear traction and with *average* normal traction equal to $\bar{\sigma}$. As already introduced, the volume fraction of the fiber is $f=(R/B)^2$, where B is the cell radius; ℓ is the length of the debond zone. Residual compressive stress is assumed to act across the fiber matrix interface keeping the debonded interface closed.

The appearance of D_1 in the two contributions in (2) and D_2 in the two terms in (4) is a rigorous consequence of the close connection of the effects of applied stress and residual stress on the overall strain and the stress intensity factor due to cracking and debonding. The connections are now established with the aid of the solution schematics in Fig. 6. Prior to any cracking or debonding, the two contributions to the axial stress in the fiber and the matrix are given by results from the appropriate Lame problem in HJ:

$$\sigma_f = a_1\bar{\sigma} \qquad \text{and} \qquad \sigma_f^R = -a_2E_m\Omega \tag{8a}$$

$$\sigma_m = (1-a_1f)\bar{\sigma}/(1-f) \qquad \text{and} \qquad \sigma_m^R = fa_2E_m\Omega/(1-f) \tag{8b}$$

The additional overall strain due to cracking and debonding (with zero friction) in the presence of $\bar{\sigma}$ is given by problem C in Fig. 6; denote it by $\Delta\bar{\varepsilon} = (\sigma_m/E_m)h$, where h is a dimensionless function of the geometric and moduli variables. By (2) and (3), h and D_1 are connected by

$$h = D_1\frac{(1-f)E_mR}{(1-a_1f)Ed} \tag{9}$$

Now consider the additional overall strain due to release of the residual stress. From problem C' in Fig. 6, this is $\Delta\bar{\varepsilon} = (\sigma_m^R/E_m)h$, where h is the same as in problem C. The expression in (2) for the contribution due to Ω immediately follows using (11b) and (12). The argument for the dual roles of D_2 in (4) is similar.

3.2 Numerical Results and More Accurate Formulas for the D_i's

Plots of D_1 as a function of ℓ/R are shown in Fig. 7a for three levels of fiber volume fraction and three values of E_f/E_m; d/R=16 has been chosen for this cell. The results in this plot, and others to follow for the cell model, have been computed with $\nu_f=\nu_m=0.3$. The value of D_1 for $\ell=0$, D_1^0, reflects the compliance increase due to matrix cracks without debonding. Plots of D_1^0 computed, again with d/R=16, are given in Fig. 7b. When used in (3), the results for D_1^0 in Fig. 7b provide an estimate of compliance which is valid for sufficiently dilute crack spacings, typically d greater than about one fiber diameter. Estimates of D_1^0 which account for crack interaction could be presented but are generally not needed for the present purposes since the crack spacing only

drops to values as small as several fiber diameters when appreciable debonding occurs as well. Under these circumstances the predominant contribution arises from the fiber/matrix sliding, as can be seen in Fig. 7a. The linear dependence of D_1 on ℓ evident in Fig. 7a persists until the debond is within about one radius of the cell end. As the debond reaches the end of the cell (i.e. ℓ=d/2) the value of D_1 then drops to the HJ result (7a). An approximation which captures the various features mentioned above is

$$D_1 = D_1^0\left(1-\frac{2\ell}{d}\right)+8f\frac{E}{E_m}\frac{\ell}{R}c_1^2 \tag{10}$$

Numerical results for D_2 for the same sets of parameters are shown as a function of ℓ/R in Fig.8. The results from (7b) from the steady-state limit are included. The slow, slight increase of the numerical results above the steady-state limit as ℓ/R increases above about 3 or 4 is due to the interaction between ℓ and d, i.e. an influence of d/R. But this influence is quite small until the debond approaches the end of the cell. The results presented here were computed for a cell with d/R=16. The steady-state estimate of D_2 is also in error as ℓ/R becomes less than about 1/2, but that too can probably be overlooked in most applications of the present results since the details of the emerging debond precipitated by the matrix crack are likely to be fairly complicated and three dimensional in nature. In conclusion, the steady-state estimate (7b) of D_2 should be sufficiently accurate for use in (4).

The reduction in the overall strain caused by the friction between the fiber and the matrix is given by the third term in (2). Numerical results for D_3 are plotted in Figs. 9 a,b. Since the dependence of D_3 on ℓ/R is very strong as ℓ/R becomes small, the abscissa in Fig. 9a is taken to be the inverse normalized debond length. As ℓ/R becomes large, the numerical results for D_3 do approach the shear-lag prediction (7c), but clearly there are significant discrepancies at smaller ℓ/R. An approximation for D_3 is developed in the Appendix. It has the features that it approaches the shear-lag result (7c) as ℓ/R becomes large and approaches an approximation to the asymptotic solution when ℓ/R is small; it is

$$D_3 = \left\{\left[\left(\frac{32}{3}\sqrt{\frac{2}{\pi}}\right)\frac{fc_1E}{\sqrt{\hat{E}E_m}}\sqrt{\frac{R}{\ell}}\right]^2+\left[2\frac{E}{E_m}b_2\right]^2\right\}^{1/2} \tag{11}$$

Comparisons of the prediction from (11) with some of the numerical results for f=0.3 are shown in Fig. 9b where it is seen that the approximate formula (11) gives a reasonably accurate interpolation over the entire range of ℓ/R.

The frictional reduction in the mode II stress intensity factor depends on D_4, as plotted in Figs. 10a,b. This coefficient has a very strong dependence on ℓ/R but almost no dependence on f. The approach to the shear-lag result as ℓ/R increases is very slow. The strong dependence on ℓ/R is again addressed by an interpolation approximation obtained in the Appendix, which approaches the shear-lag result (7d) for large ℓ/R and approaches an approximation to the asymptotic solution for the limit of small ℓ/R. This interpolation formula is

$$D_4 = \left\{ \left(\frac{\pi R}{\ell}\right)^2 + \left[(b_2 + b_3)\left(\frac{\hat{E}}{E_m}\right)\right]^2 \right\}^{1/4} \tag{12}$$

A comparison between (12) and the more accurate numerical results in Fig. 10b shows that (12) provides an adequate approximation to D_4 over the entire range of ℓ/R, although not quite as accurate as the approximation for D_3.

4. PREDICTION OF TENSILE STRESS-STRAIN BEHAVIOR

4.1 Behavior Prior to Matrix Crack Saturation

Debonding is controlled by the mode II debonding toughness Γ_i. The matrix crack spacing $d(\bar{\sigma})$ is a function of the applied stress. This functional dependence is assumed to be known from experimental observation or from other theoretical modeling(Curtin, 1993; Spearing and Zok, 1993); no attempt is made to predict $d(\bar{\sigma})$ here. The relationship between the debond length ℓ and the applied stress $\bar{\sigma}$ is obtained from (4) by imposing the debond condition $K_{II} = \sqrt{\hat{E}\Gamma_i}$. Let $\bar{\sigma}_i$ be the debond initiation stress, defined as the overall stress at which the debond can begin to spread up the fiber from the matrix crack surface. This stress can be larger or smaller than the matrix cracking stress, depending on the properties of the composite. If it is larger, debonding is postponed beyond the onset of matrix cracking until the overall stress reaches $\bar{\sigma}_i$; if it is smaller, the debond jumps to a finite length as soon as a matrix crack forms. From (4) and (7b), the debond initiation stress is

$$\begin{aligned} \bar{\sigma}_i &= (1/D_2)\sqrt{\hat{E}\Gamma_i/R} - f a_2 E_m \Omega/(1-f a_1) \\ &= (1/c_1)\sqrt{E_m\Gamma_i/R} - (c_2/c_1)E_m\Omega \\ &\equiv \bar{\sigma}_D - \bar{\sigma}_R \end{aligned} \tag{13}$$

Since D_2 is given by (7b) for the more accurate results as well as for the shear lag model, this result holds for both levels of approximation. Equation (7b) has been used to arrive at the second expression, along with the identity $c_2/c_1=fa_2/(1-fa_1)$ from HJ. The third line in (13) is used to define the two contributions to $\bar{\sigma}_i$, one due to the mode II debond toughness and the other due to the residual stress in the uncracked composite. For applied stresses greater than $\bar{\sigma}_i$, (4) gives

$$\frac{\ell}{R} = \frac{D_2}{D_4(\ell)} \frac{(\bar{\sigma} - \bar{\sigma}_i)}{\tau} \tag{14}$$

One of the main differences between predictions from the more accurate cell model and the shear lag model is the debond length when it is not large. By (14) with (7d) and (12), the ratio of the predicted debond lengths at a given value of applied stress depends on ℓ/R from the more accurate model according to

$$\frac{\ell_{\text{shear lag model}}}{\ell_{\text{accurate model}}} = \left\{ 1 + \left(\frac{\pi R}{\ell} \right)^2 \left[(b_2 + b_3) \left(\frac{\hat{E}}{E_m} \right) \right]^{-2} \right\}^{1/4} \tag{15}$$

Plots of this ratio are presented in Fig. 11. It can be seen that there is little dependence on the moduli choices, but the shear lag model significantly overestimates the extent of debonding for debonds less than about one fiber diameter.

The relation (14) giving ℓ/R, together with $d(\bar{\sigma})$, can now used in conjunction with (2) to predict $\bar{\varepsilon}$ as a function of $\bar{\sigma}$. The ℓ-dependence of D_1 and D_3 in (2) and of D_4 in (14) must be taken into account. The most straight-forward procedure to generate stress-strain curves with these relations is to use ℓ as a free parameter which is increased monotonically (until it reaches d/2), using (14) to obtain $\bar{\sigma}$ and then (2) to obtain $\bar{\varepsilon}$. Specific examples will be given in § 5 where they will be compared with closed form representations for the stress-strain behavior valid for a shear lag approximation given in § 4.3

4.2 Consistency Condition for the Cell Height d_s at Matrix Crack Saturation

With reference to Fig. 3, let $\bar{\sigma}_s$ be the overall stress at which the matrix cracking saturates at spacing d_s. In modeling the response of the composite by a representative cell of height d, we do not attempt to capture the statistics of the matrix cracking process wherein new cracks form at randomly located flaw sites in portions of the composite which have not yet experienced fiber debonding and sliding. Here we will assume that the matrix cracks are uniformly spaced with the spacing d identified as the cell height. For this model, d decreases and ℓ increases as $\bar{\sigma}$ is increased. Additional matrix cracks cannot be nucleated once complete fiber debonding has

occurred. Conversely, further matrix cracks will nucleated under increasing stress if the fibers have not fully debonded. It follows, then, that within the framework of this model, $\bar{\sigma}$ must attain $\bar{\sigma}_s$ as the fibers become fully debonded (i.e. as ℓ approaches d/2). By (14), this requirement provides the consistency relation between d_s and $\bar{\sigma}_s$ as

$$\frac{d_s}{R} = \frac{2D_2}{D_4(d_s/2)} \frac{(\bar{\sigma}_s - \bar{\sigma}_i)}{\tau} \tag{16}$$

Well known statistical arguments (e.g.. Curtin, 1993) suggest that the mean matrix crack spacing at saturation should fall between d_S as predicted by (16) and $d_S/2$. A limitation of any model based on a single representative cell is that it cannot realistically reproduce the effects of variations in the matrix crack spacing. Here, (16) will be used to specify the limit when matrix crack saturation occurs, denoting also the point where the fibers have fully debonded.

4.3 Specialization to the Shear Lag Approximation

The above prescriptions simplify for the shear lag approximations of the D_i's in §2.2. Now, D_4 is independent of ℓ in (14). In evaluating $\bar{\varepsilon}$ using (2) for $\bar{\sigma} < \bar{\sigma}_s$, D_3 is independent of ℓ and D_1 varies linearly with ℓ. By eliminating ℓ in (2) using (14), one can readily obtain an equation of the form

$$\bar{\varepsilon} = \frac{\bar{\sigma}}{E} + \frac{1}{d(\bar{\sigma})}\left\{A_1(\bar{\sigma} - \bar{\sigma}_i)^2 + A_2(\bar{\sigma} - \bar{\sigma}_i)\right\} \tag{17}$$

where the coefficients A_1 and A_2 involve the HJ coefficients and parameters such as τ and Γ_i.

A further simplification is achieved if one assumes that $\nu_f = \nu_m = \nu$ and if one uses the formulas in HJ for Type I boundary conditions rather than Type II conditions. Type I conditions are appropriate for a cell with completely unconstrained lateral sides; these are the conditions assumed by most authors in carrying out shear lag analyses. Some discussion is given in the Appendix concerning the error involved in making this replacement, which is generally small for the present purposes. Under these conditions, (14) and (17) reduce exactly to, respectively,

$$\frac{\ell}{R} = \frac{(1-f)}{2f} \frac{E_m}{E} \frac{(\bar{\sigma} - \bar{\sigma}_i)}{\tau} \tag{18a}$$

$$\bar{\varepsilon} = \frac{\bar{\sigma}}{E} + \frac{1}{d(\bar{\sigma})}\left[\frac{(1-f)^2 E_m{}^2 R}{2f^2 E^2 E_f \tau \chi^2}\right]\left\{(\bar{\sigma} - \bar{\sigma}_i)^2 + 2\bar{\sigma}_D(\bar{\sigma} - \bar{\sigma}_i)\right\} \tag{18b}$$

$$\bar{\sigma}_i = \bar{\sigma}_D - \bar{\sigma}_R \quad , \qquad \bar{\sigma}_D = \chi\sqrt{\frac{4f^2 E_f E \Gamma_i}{(1-f)E_m R}} \quad , \qquad \bar{\sigma}_R = \frac{E}{E_m}\sigma_m^R \tag{18c}$$

where χ is a factor close to unity given by

$$\chi = \sqrt{\frac{(1+\nu)E_f + (1-\nu)E}{(1+\nu)[E_f + (1-2\nu)E]}} \tag{18d}$$

The consistency condition (16) becomes

$$\frac{d_s}{R} = \frac{(1-f)}{f}\frac{E_m}{E}\frac{(\bar{\sigma}_s - \bar{\sigma}_i)}{\tau} \tag{19}$$

4.4 Stress-Strain Behavior Subsequent to Matrix Crack Saturation

Formula (2) for the strain continues to hold when saturation has been attained in the range $\bar{\sigma} > \bar{\sigma}_s$ with ℓ fixed at the value $d_s/2$. In this state, the fibers are fully debonded and are carrying all the axial load. There is a minor variation of the axial stress along the fibers due to the frictional 'clamping' of the matrix segments. In the fully debonded state, Type I boundary conditions of HJ become applicable because there are no longer segments of undebonded material to impose the transverse constraint associated with Type II conditions. The shear lag approximation to E_C, given by (3) and (7a), is essentially exact in this state, assuming that the matrix is still in contact with the fiber. Thus, for stress levels above $\bar{\sigma}_s$, overall stress and strain increments are related by $\Delta\bar{\varepsilon} = \Delta\bar{\sigma}/E_c$. Type I conditions with $\nu_f = \nu_m$ give the following expression for the modulus E_C of the composite with saturated matrix cracks,

$$\frac{1}{E_c} = \frac{1}{E}\left[1 + \frac{(1-f)E_m}{fE_f\chi^2}\right] \tag{20}$$

If χ is taken to be unity (it is nearly always within a few percent of unity), the above reduces to the result $E_C = f\,E_f$, which would be expected were it not for the interaction of the fiber and the cracked matrix through Poisson contraction effects when the fiber remains in contact with the matrix.

Assuming fiber/matrix contact is maintained with the friction stress τ still operating, the composite strain in the fully debonded state is given by

$$\bar{\varepsilon} = \frac{\bar{\sigma}}{E_c} - \frac{\sigma_f^R}{E_f} - \frac{\tau\, d_s}{2E_f R} \tag{21}$$

The second term is the residual strain in the fiber, which is largely released in the saturated state. The third term is the strain resulting from the friction 'clamping' stress on each segment between matrix cracks. This later term has been determined using a simple shear lag calculation which neglects any Poisson interaction between the fiber and the matrix (which *is* accounted for in the third term in (2) as it stands). This result also applies when fibers have broken, assuming this occurs beyond matrix crack saturation. Then f should be identified with the effective volume fraction of fibers, or portions of fibers, carrying their full share of the applied stress. Finally, if the fibers and the matrix have lost contact and the friction stress is lost, then (21) holds with E_C=f E_f and the third term omitted.

4.5 TRANSVERSE STRAIN

The cell model can also be used to predict the overall transverse strain $\bar{\varepsilon}_T$ of the composite in the various regimes of matrix cracking. There is a substantial literature on elastic properties of uncracked composites, and no attempt here will be made to summarize results in that regime. A limited set of results obtained by the finite element analysis of the cell of Fig. 4 is displayed in Fig. 12, showing the effect of matrix crack spacing on the effective Poisson's ratio in the absence of any debonding ($\ell = 0$) or residual stress. In this figure, $\nu_{eff} \equiv -\bar{\varepsilon}_T / \bar{\varepsilon}$ and the values of the Poisson's ratios used in the calculation are $\nu_f = \nu_m = 0.3$.

With minor extension, the results of HJ can be used to give general formulas for the transverse strain in the regime in which matrix crack saturation has been achieved and the fibers are fully debonded. Neglecting the very small effect due to frictional clamping on the transverse strain, one can extend the HJ analysis to compute the change in radius ΔB of the outer boundary of the cell. This is computed with B as the value in the unloaded, uncracked state, subject to residual stresses associated with the mismatch Ω. With $\bar{\varepsilon}_T$ defined as $\Delta B/B$, this analysis gives

$$\bar{\varepsilon}_T = -\nu_{eff}\bar{\varepsilon} + C_\Omega \Omega \tag{22a}$$

where

$$\nu_{eff} = \frac{2f}{(1-f)} \frac{\left[b_1(1-fa_1)+fa_3\right]}{\left[b_2(1-fa_1)+fa_5\right]} \tag{22b}$$

$$C_\Omega = \left[\nu_{eff} b_2 + \frac{f}{(1-f)}(-2b_1 + \nu_m)\right] a_2 \tag{22c}$$

The coefficients in these equations are those of HJ for Type I conditions. For $\nu_f = \nu_m = \nu$,

$$\nu_{eff} = \frac{2\nu f E_f}{[1+\nu+f(1-\nu)]E_f + (1-f)(1+\nu)(1-2\nu)E_m} \tag{23a}$$

and, in addition, if $E_f = E_m$, then

$$\nu_{eff} = \frac{\nu f}{\left[f+(1-f)(1-\nu^2)\right]} \quad \text{and} \quad C_\Omega = \nu_{eff}(1-f)(1+\lambda\nu) \tag{23b}$$

where λ is the ratio of the radial to axial mismatch strains defined in HJ.

The above results only apply in the range in which $\bar{\varepsilon}$ exceeds $\bar{\varepsilon}_s$, the strain at which the matrix cracks saturate, and is less than $\bar{\varepsilon}_o$, the strain at which the fibers lose contact with the matrix. The HJ model (Type I conditions apply) gives for the axial strain at which the radial compression across the fiber/matrix interface drops to zero,

$$\begin{aligned} \bar{\varepsilon}_o &= \left[\lambda/\nu_f + (a_2 - 2\nu_f a_4)E_m/E_f\right]\Omega \\ &= \left[\lambda/\nu + (1-f)E_m/E\right]\Omega \end{aligned} \tag{24}$$

where the second expression applies when $\nu_f = \nu_m = \nu$. This estimate of the strain at which contact is lost across the fiber/matrix interface takes no account of any possible increase in effective radial mismatch due to sliding in combination with fiber surface roughness. An example showing the variation of the transverse strain as a function of the axial strain will be given at the end of the next section.

5. STRESS-STRAIN CURVES

To illustrate application of the results presented above we will present theoretical stress-strain curves for two unidirectional composites (Beyerle. et al, 1992; Evans, et al, 1993; Guillaumat, 1993), one with relatively low frictional sliding stress and interface debonding toughness (SiC/CAS) and the other with relatively large values of these properties (SiC/SiC). In each case, the fiber is Nicalon SiC. The constituent properties are summarized in Table I. In each case, $\bar{\sigma}_{mc}$ and $\bar{\sigma}_s$ have been experimentally determined as, respectively, the stress at which matrix cracks first begin to spread and the stress at which matrix cracks saturate. The experimental data on the matrix crack density development indicates that the density varies approximately linearly with applied stress in the range, $\bar{\sigma}_{mc} < \bar{\sigma} < \bar{\sigma}_s$, according to (Evans, Domergue and Vagaggini,1993)

$$\frac{1}{d} = \frac{1}{d_s}\left(\frac{\bar{\sigma}_s - \bar{\sigma}}{\bar{\sigma}_s - \bar{\sigma}_{mc}}\right) \tag{25}$$

In carrying out the calculations of the tensile stress-strain curves, we will use the saturation matrix crack spacing, d_S, from the consistency condition (16) rather than the experimentally observed average crack spacing at saturation, for reasons discussed in §4.2. The results for d_S, obtained from (16) for both the more accurate model and the shear lag model, are:

$$\begin{aligned} &\text{SiC/CAS:} \quad (d_s/R)_{\text{accurate model}} = 16.9 \quad \text{and} \quad (d_s/R)_{\text{shear lag}} = 17.1 \\ &\text{SiC/SiC:} \quad (d_s/R)_{\text{accurate model}} = 3.6 \quad \text{and} \quad (d_s/R)_{\text{shear lag}} = 4.3 \end{aligned} \tag{26}$$

These are larger than the experimentally observed average values (Table I). There is little difference between the two theoretical values of d_S. The experimental values for the average matrix crack spacing at saturation fall in the range between d_S and $d_S/2$, consistent with statistical arguments (Curtin, 1993).

Tensile stress-strain curves calculated for the two levels of approximation are shown in Fig. 13 for the SiC/CAS material and in Fig. 14 for the SiC/SiC material. These results were generated under the assumption that contact is maintained between the fibers and the matrix over the whole range of stress shown. It is noteworthy that, in spite of the significant differences between the two approximations in some of the coefficients and in the difference in the predicted debond lengths, there is very little difference in the predicted stress-strain curves from the two approximations. (It should be borne in mind that the value of d_S in the calculations depended on the approximation; the value in (26) appropriate for the particular approximation was used.) Moreover, while the results in these figures were computed using the appropriate coefficients from HJ for the Type II cell boundary conditions, the predictions obtained from the simpler shear lag formulas in (18) through (21) are essentially indistinguishable from the more elaborate shear lag results. It follows, then, that the simpler formulas for the shear lag model can be used to predict the overall tensile stress-strain curve with essentially the same accuracy as the more accurate model, as long as d_S is derived from (19), and provided that it is understood that the predicted debond length will exceed the more accurate prediction when the debond length is small.

Comparison between the simulation and the experimental results require some discussion. For the SiC/SiC composite, there appears to be a good correspondence. However, the composite fails before matrix crack saturation occurs. This is a consequence of the large matrix cracking stress caused by the large τ and Γ_i, as well as some fiber degradation during composite processing. For the SiC/CAS composite, there is substantial discrepancy at large strains. In this

composite, the tangent modulus after matrix crack saturation is much smaller than (21) would predict (Spearing and Zok, 1993). Such a discrepancy does not arise in other composites that attain saturation prior to composite failure (Guillaumat, 1993). One implication is that the discrepancy is a consequence of fiber failure. Should this hypothesis be correct, the experimental results can be used to infer the contribution to the inelastic strain from fiber failure. The difference, $\Delta\bar{\varepsilon}$, between the experimentally measured strain and the theoretical strain from Fig. 13 is plotted in Fig. 15. The shape of this curve is atypical of the inelastic strains caused by fiber failure, exemplified by simulations for a monomodal flaw distribution in the fibers (Hild, et al, 1993) given by the dashed curves in Fig. 15. For fiber failure to be responsible for the present discrepancy, it would be necessary that the fiber have a *bimodal* flaw distribution. Should this be the case, the implications for the ultimate tensile strength (UTS) need to be addressed. Preliminary analysis (W.A.Curtin, work in progress) has indicated that the measured UTS is consistent with a bimodal distribution that indeed gives a fiber contribution to the strain compatible with Fig. 15.

There is an additional discrepancy between simulation and experiment regarding the incremental elastic modulus, E_c, measured from initial unloading data for SiC/CAS (Evans, et al, 1993), as shown in Fig. 16. Under the assumption that the initial unloading response involves no reversed slipping, E_c should be given by (3) with ℓ=0, where D_1 is plotted in Fig. 7b. Specifically, for the SiC/CAS composite, the value of D_1 from Fig. 7b is ≈ 1, whereas a value ≈ 4 gives a much better fit to the experimental data. Such discrepancies are commonly found in CMCs. The phenomenon is attributed to fiber straightening effects that occur as the matrix crack density increases.

Finally, it is instructive to address the transverse strain $\bar{\varepsilon}_T$ with reference to experimental data for unidirectional SiC/CAS (Harris, Habib, and Cooke, 1992) shown in Fig. 17. The model results of §4.5 for $\bar{\varepsilon}_T$ may be cursorily compared with these data by assuming that the Poisson's ratios of the fibers and the matrix are the same, as given by the experimentally determined value for the composite, ν=0.24; the specific values of ν_f and ν_m are not known. The model results displayed in Fig. 17 show: (i) the initial segment governed by the composite modulus ν, (ii) the segment with slope ν_{eff} from (23a) governing behavior in the regime of fully saturated matrix cracking, together with the offset $C_\Omega\,\Omega$ from (22c), (iii) a segment (arbitrarily taken to be straight) connecting (i) and (ii) between $\bar{\varepsilon}_{mc}$ and $\bar{\varepsilon}_s$, and (iv) the value estimated for $\bar{\varepsilon}_o$ from (24), beyond which contact between fiber and matrix is lost. The model results agree quite well with the data for axial strains $\bar{\varepsilon}$ less than about 0.5%, even with the simplifying assumption about the Poisson's ratios. The discrepancy with the data at larger axial strains coincides with a similar discrepancy found above for the axial inelastic strain, attributed to an influence of fiber failure. Analysis of the effects of fiber failure on $\bar{\varepsilon}_T$ has yet to be performed.

6. CONCLUDING REMARKS

The inelastic strain caused by matrix cracking in unidirectional CMCs has been analyzed using an accurate cell model. The formulae provided allow the straightforward prediction of these strains from the constituent properties, such as the interface sliding and debonding resistances. In some cases, the results do not fully account for the measured inelastic deformation. There are additional contributions from the fibers. For fibers having a monomodal flaw distribution, the additional inelastic strains caused by stochastic fiber failure are well known. These can be simply added to the matrix cracking strain. However, it remains to establish fiber failure contributions when more complex distributions exist. Such effects are believed to be responsible for the discrepancy between the measured stress-strain curve for SiC/CAS and the curve simulated using only the matrix cracking contribution. The strain caused by the fibers may also have a contribution from the straightening of initially curved fibers, as the matrix crack density increases upon loading. This effect is a possible cause of the smaller elastic unloading modulus measured on SiC/CAS than that predicted by the cell model.

The next important step is to extend the modeling to cross ply laminates, based on cracks extending into the 0^o plies from tunnel cracks that have previously formed in the 90^o plies (Fig. 1). Such analyses are in progress.

ACKNOWLEDGMENT

This work was sponsored by the Advanced Project Research Agency under the University Research Initiative Grant No. N00014-92-1808 with the University of California, Santa Barbara. The work of JWH was sponsored in part by this same grant (Subagreement P.O.#KK3007) and by the Division of Applied Sciences, Harvard University.

REFERENCES

Aveston, J., G. Cooper and A. Kelley (1971), Single and multiple fracture, in Properties of Fiber Composites, *Proceedings of the National Physical Laboratories*, IPC Science and Technology Press Ltd., Surrey, U. K., 1971, 15-26.

Beyerle, D., S. M. Spearing, F. W. Zok and A. G. Evans (1992), Damage and failure in unidirectional ceramic-matrix composites, *J. Am. Ceram. Soc. 75*, 2719-2725.

Brønsted, P. A., F. E. Heredia and A. G. Evans (1993), The in-plane shear properties of 2D ceramic matrix composites, *J. Am. Ceram. Soc.*, in press.

Budiansky, B. and L. Cui (1993), On the tensile strength of a fiber-reinforced ceramic composite containing a crack-like flaw, 1993, to be published in *J. Mech. Phys.Solids.*

Cady, C., T. J. Mackin and A. G. Evans (1993), Stress redistribution and notch insensitivity in a ceramic matrix composite, to be published.

Curtin, W. A. (1993), Multiple matrix cracking in brittle matrix composites, *Acta Metall. Mater. 41*, 1369-1377.

Evans, A. G. (1991), The mechanical properties of reinforced ceramic, metal and intermetallic matrix composites, *Materials Science and Engineering, A143*, 63-76.

Evans, A. G., F. W. Zok and J. B. Davis (1991), The role of interfaces in fiber-reinforced brittle matrix composites, *Composites Science and Technology 42*, 3-24.

Evans, A. G., J. M. Domergue and E. Vagaggini (1993), A methodology for relating the tensile constitutive behavior of ceramic matrix composites to constituent properties, in High Temperature Ceramic Matrix Composites (Ed. R. Naslain, et al) Woodhead, 5-35.

Gao, Y-C., Y-W. Mai and B. Cotterell (1988), Fracture of fiber reinforced materials, *J. Appl. Math. and Phys. (ZAMP) 39*, 550-572.

Guillaumat, L. (1993), Ph.D. Thesis, Laboratoire des Composites Thermostructuraux, Domaine Universitaire, Bordeaux, France.

Harris, B., F. A. Habib and R. G. Cooke (1992), Matrix cracking and the mechanical behavior of SiC-CAS composites, *Proc. Roy. Soc. Lond.* A437, 109-131.

Hild, F, J. M. Domergue, F. A. Leckie and A. G. Evans (1993), Tensile and flexural ultimate strength of fiber-reinforced ceramic-matrix composites, *Int. J. of Solids and Structures*, in press.

Hutchinson, J. W. and H. M. Jensen (1990), Models of fiber debonding and pullout in brittle composites with friction, *Mech. of Matls.*, *9*, 139-163.

Kim, R. Y. and N. J. Pagano (1991), Crack initiation in unidirectional brittle-matrix composites, *J. Am. Ceram. Soc.*, *74*, 1082-1090.

Marshall , D.B., B.N. Cox and A. G. Evans (1985), The mechanics of matrix cracking in brittle-matrix fiber composites", *Acta. Met* 33, 2013-2021.

Marshall, D. B. and A. G. Evans (1985), Failure mechanisms in ceramic fiber/ceramic matrix composites, *J. Am. Ceram. Soc. 68*, 225-231.

Marshall, D. B. (1992), Analysis of fiber debonding and sliding experiments in brittle matrix composites, *Acta Metall. mater. 40*, 427-441.

Nardonne, V. C. and K. M. Prewo (1988), Tensile performance of carbon-fiber-reinforced glass, *J. Mater. Sci. 23*, 168-180.

Pryce, A. W. and P. Smith (1992), Modelling the stress/strain behavior of unidirectional ceramic matrix composite laminates, *J. Mater. Sci., 27*, 2695-2704.

Spearing, S. M. and F. W. Zok (1993), Stochastic aspects of matrix cracking in brittle matrix composites, *J. Eng. Materials Tech. 115*, 314-318.

Vagaggini, E. and A. G. Evans (1993), Relationships between the macroscopic performance of ceramic matrix composites and constituent properties, I: Theory and methodology, *J. Am. Ceramic Soc.*, in press.

Weitsman, Y. and H. Zhu (1993), Multi-fracture of ceramic composites, *J. Mech. Phys. Solids, 41*, 351-388.

Xia, Z. C., R. R. Carr and J. W. Hutchinson (1993), Transverse cracking in fiber-reinforced brittle matrix cross-ply laminates, *Acta Metall. Mater. 41*, 2365-2376.

APPENDIX

Approximation to D_3

The shear lag approximation to D_3 given by (7c) becomes increasingly accurate at large ℓ. An approximation is first developed for small ℓ, and then the two limits are combined as (11) to interpolate over the entire range of ℓ. To obtain an approximation for small ℓ, use is made of the following consequence of the reciprocal theorem for two independent loadings, τ and Σ, on the cell of Fig.4

$$-2\pi R\int_0^{\ell}\tau V(z)dz = \pi B^2(d/2)\Sigma\bar{\varepsilon} \tag{A1}$$

Here, $\bar{\varepsilon}$ is the overall strain due to τ, while $V(z)$ is the distribution of the relative tangential displacement of the crack faces due to a average normal traction Σ acting on the ends of the cell. The numerical results indicate that (7b) gives a reasonably accurate representation of K_{II} for the end load problem at short debond lengths, i.e. $K_{II} = c_1\Sigma\left(R\hat{E}/E_m\right)^{1/2}$. The relative tangential displacements of the faces of an interface crack near its tip are given by the plane strain relation $V(z) = (8K_{II}/\hat{E})\sqrt{(\ell - z)/2\pi}$, neglecting any effect of the second Dundurs parameter. Using these approximations in (A1) and noting the definition of D_3 in (2), gives

$$D_3 = \frac{32}{3}\sqrt{\frac{2}{\pi}}\frac{fc_1E}{\sqrt{\hat{E}E_m}}\sqrt{\frac{R}{\ell}} \tag{A2}$$

The form given by (11) was found to give the most accurate interpolation formula among several considered.

Approximation to D_4

The approximation for K_{II} due to τ for small ℓ simply makes use of the solution to the problem of a crack of length 2ℓ along an interface between two semi-infinite plane strain blocks loaded by the shear traction τ. If, again, the second Dundurs parameter is taken to be zero, then $K_{II} = -\tau\sqrt{\pi\ell}$. This approximation is combined with the shear lag result (7d) as the interpolation formula (12).

Simplification of the shear lag results using Type I boundary conditions

Certain of the predictions of the shear lag model of HJ are fairly sensitive to the type of boundary conditions for the cell, I or II. Discussion of some of the issues surrounding the influence of boundary conditions is given by Marshall (1992). Here we show that the important

coefficient A_1 in (17) is not strongly dependent on the choice of boundary condition for many composites of interest. This same coefficient also appears in the widely used traction-displacement law for bridging fibers whose interface with the matrix has zero debond toughness and a frictional sliding stress τ (Marshall, Cox and Evans, 1985). In the present notation, this bridging law is $\delta = A_1\overline{\sigma}^2$, where δ is the total opening displacement due to fiber sliding. From (18b) it is seen that Type I conditions, with $v_f=v_m$, give

$$A_1 = \frac{(1-f)^2 E_m{}^2 R}{2f^2 E^2 E_f \tau \chi^2} \tag{A3}$$

where χ is defined in (18d). (In passing, we note that the factor χ is not normally included in the bridging law. It is associated with a Poisson's ratio interaction between the fiber and matrix which is not taken into account in the simpler shear lag analyses which have been used to arrive at the bridging law coefficient.) Table II presents the ratio of A_1 for Type I boundary conditions from (A3) to that for Type II conditions computed using results from HJ for various combinations of fiber to matrix moduli and two values of Poisson's ratio. Except for large fiber to matrix moduli mismatches, the difference between the predictions for these two conditions is small.

TABLE I

Constituent Properties for Composite Systems

	SiC/CAS	SiC/SiC
E_f (GPa)	200	200
E_m (GPa)	100	300
R (μm)	7	7
ν	0.25	0.25
f	0.4	0.4
τ (MPa)	20	150
Γ_i (Jm^{-2})	0.1	6
σ_m^R (MPa)	80	100
$\bar{\sigma}_{mc}$ (MPa)	125	350
$\bar{\sigma}_s$ (MPa)	275	700
$\bar{d}_s/R$	11	2

TABLE II

Values of $(A_1)_I/(A_1)_{II}$

E_f/E_m	ν = .2	ν = .3
0.5	.99	.98
1	1	1
2	1.03	1.01
3	1.06	1.21
10	1.19	1 77

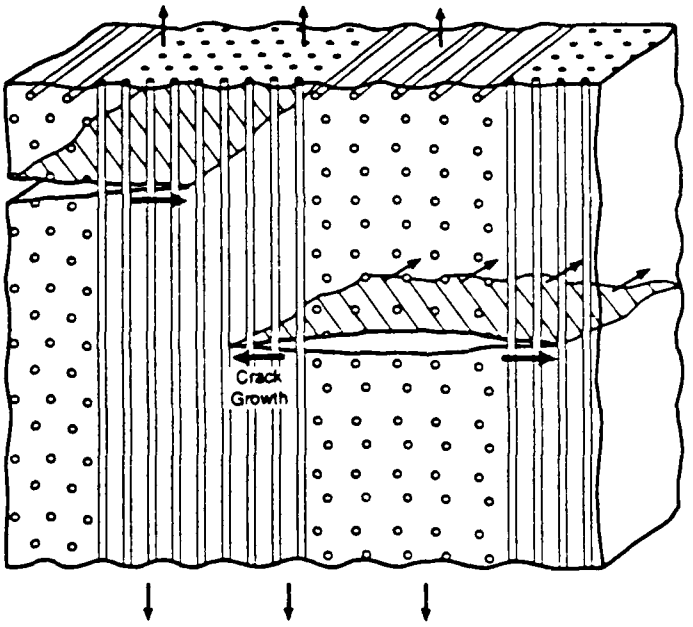

Fig. 1 A cross-ply composite with tunnel cracks, which have first formed in the 90° plies, spreading as plane strain cracks into the 0° plies.

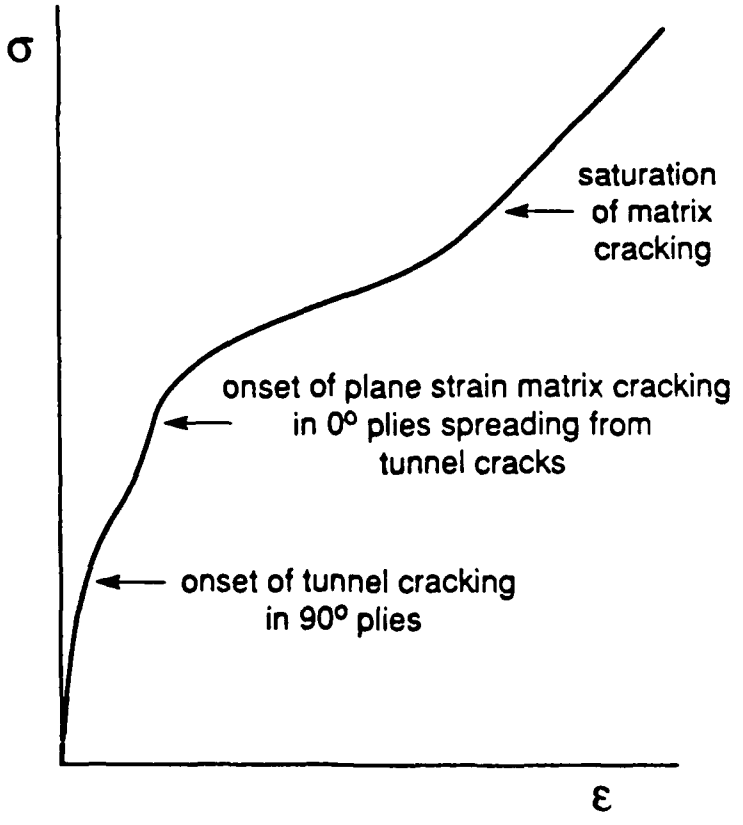

Fig. 2 Schematic tensile stress-strain curve of a cross-ply composite.

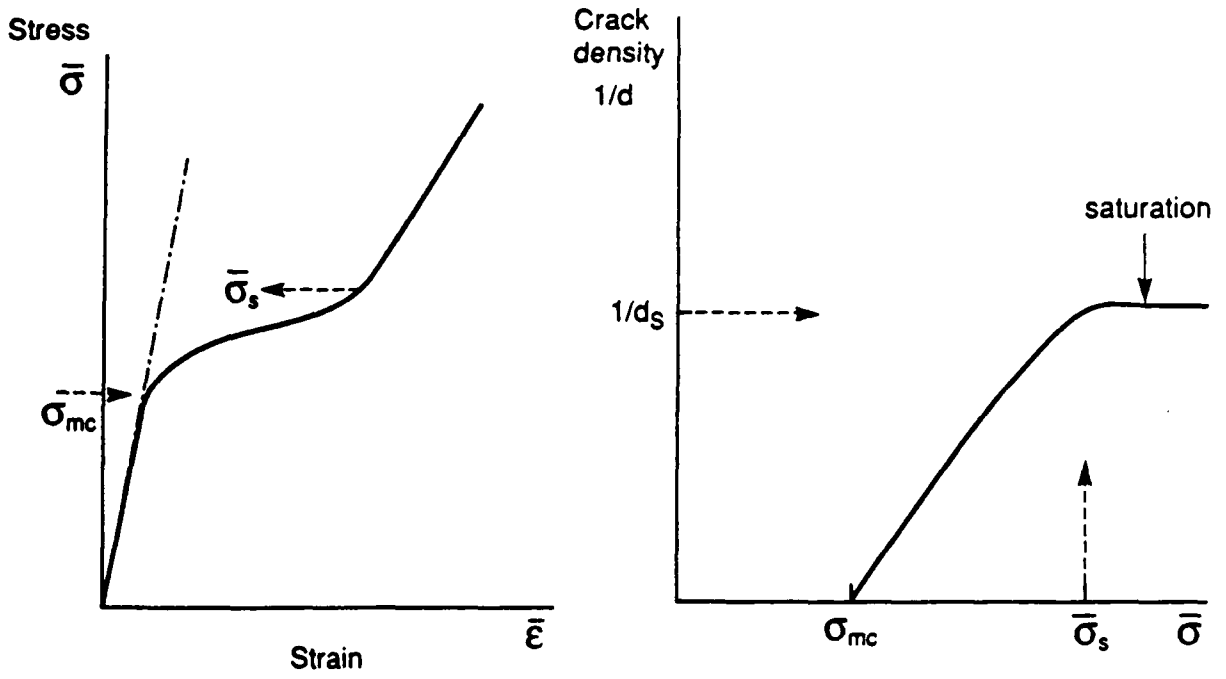

Fig. 3 Tensile stress-strain behavior of a uni-directional fiber reinforced composite stressed parallel to the fibers, and evolution of matrix crack density.

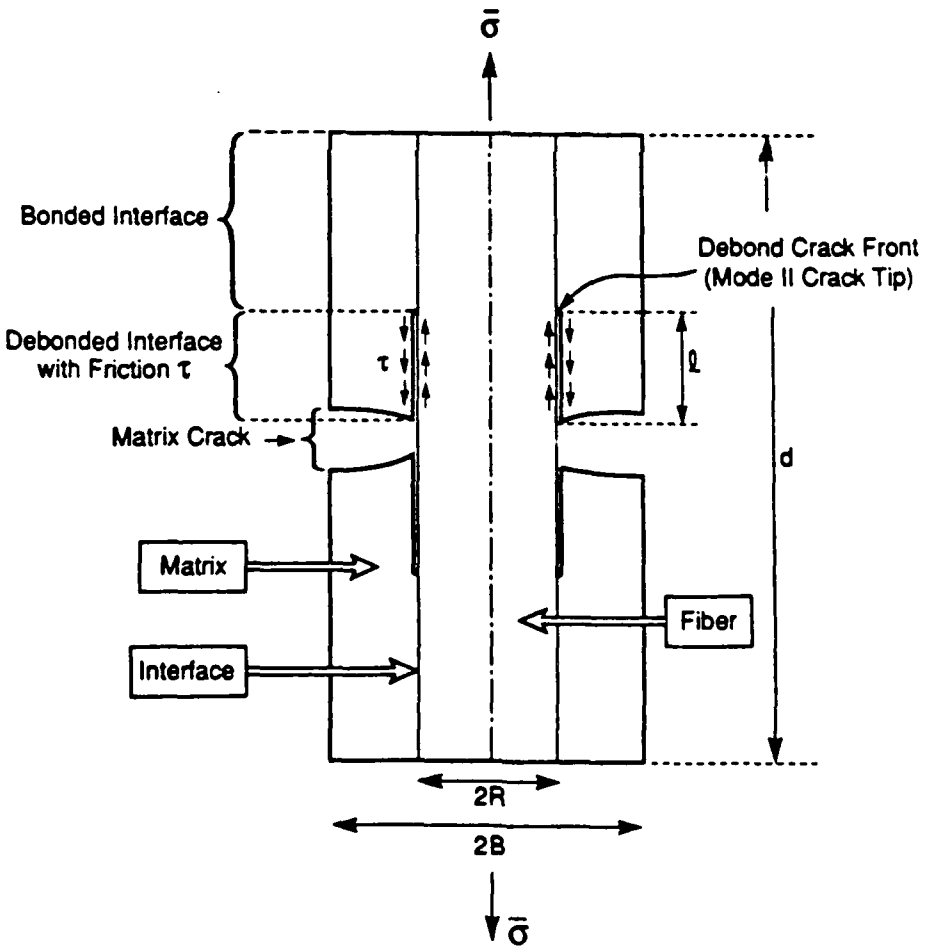

Fig. 4 Conventions for axisymmetric cell model.

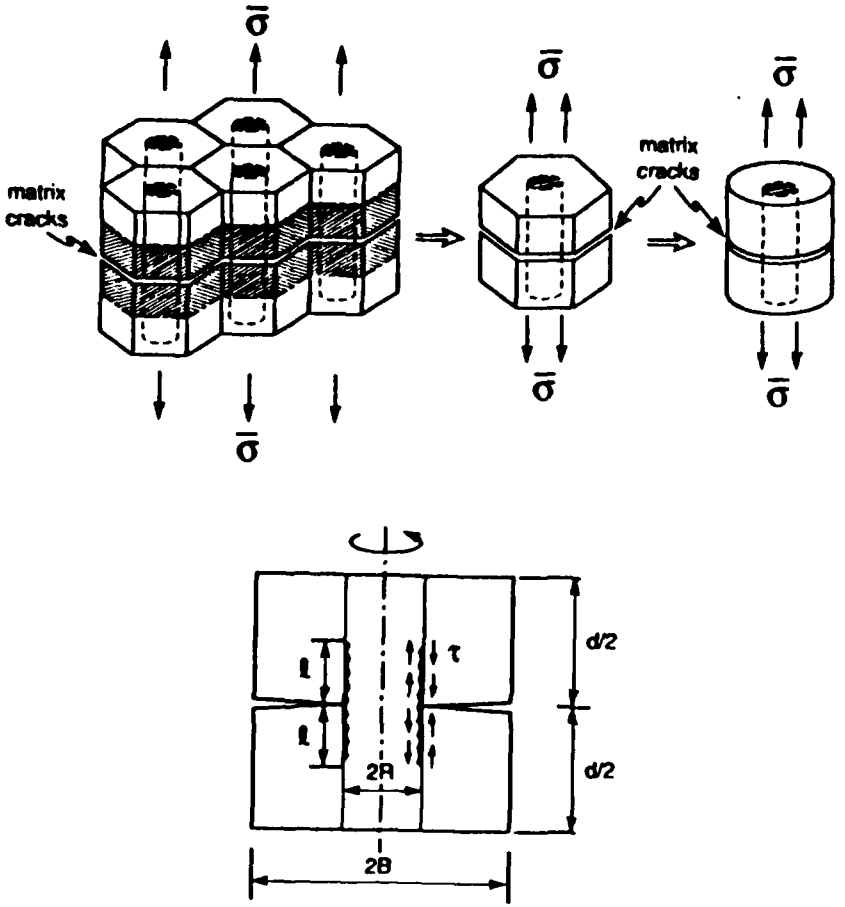

Fig. 5 Motivation for axisymmetric cell model.

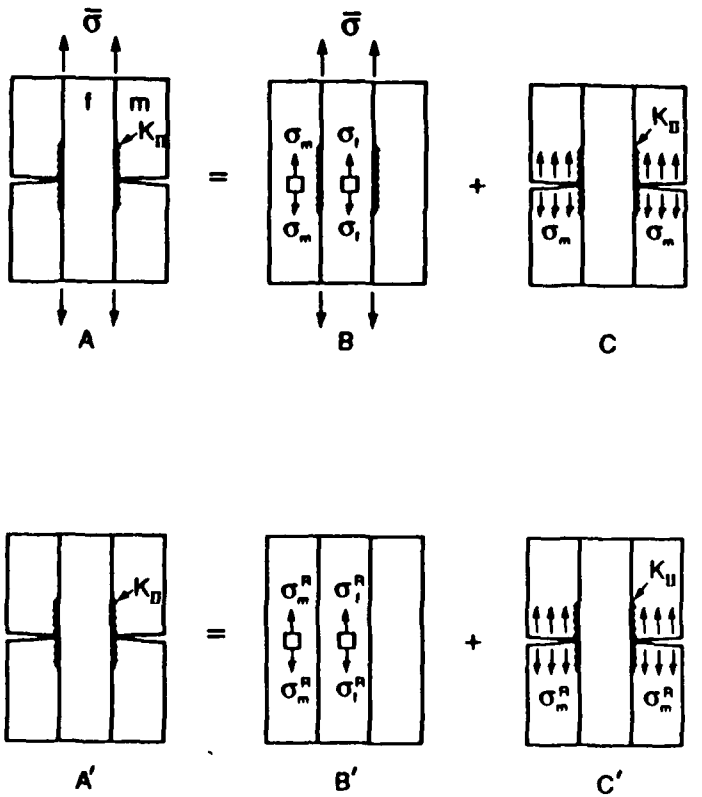

Fig. 6 Solution schematics for establishing the connection between solutions for two loadings.

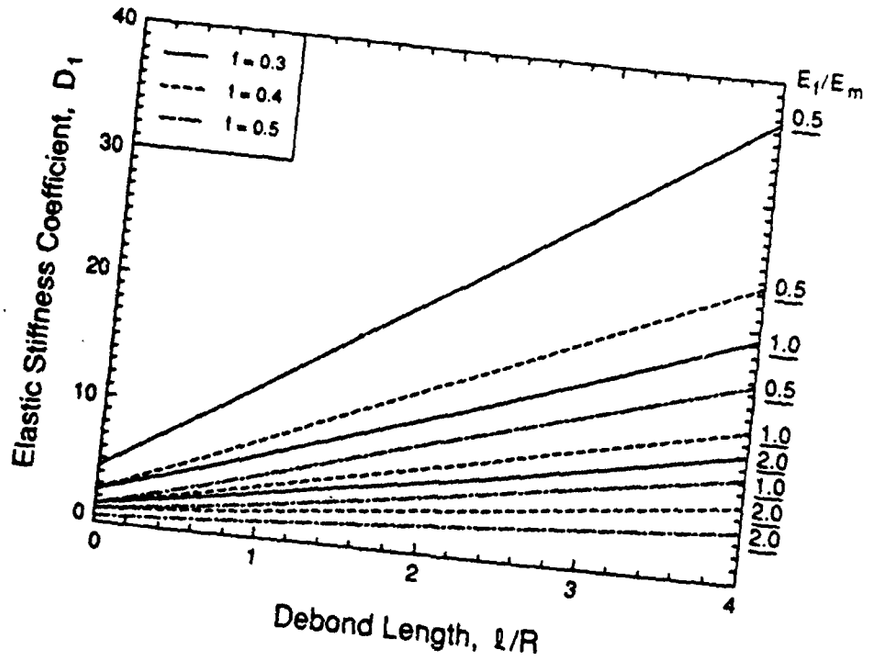

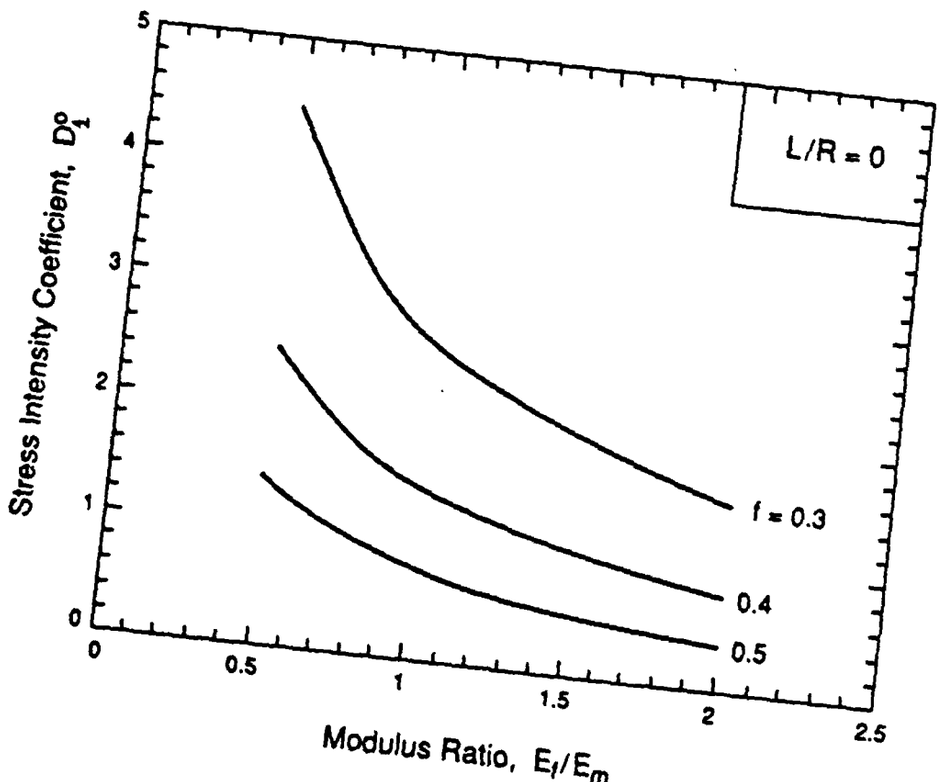

Fig. 7 a) Numerical results from cell model for D_1. b) Numerical results from cell model for value of D_1 in absence of any debonding, D_1^0.

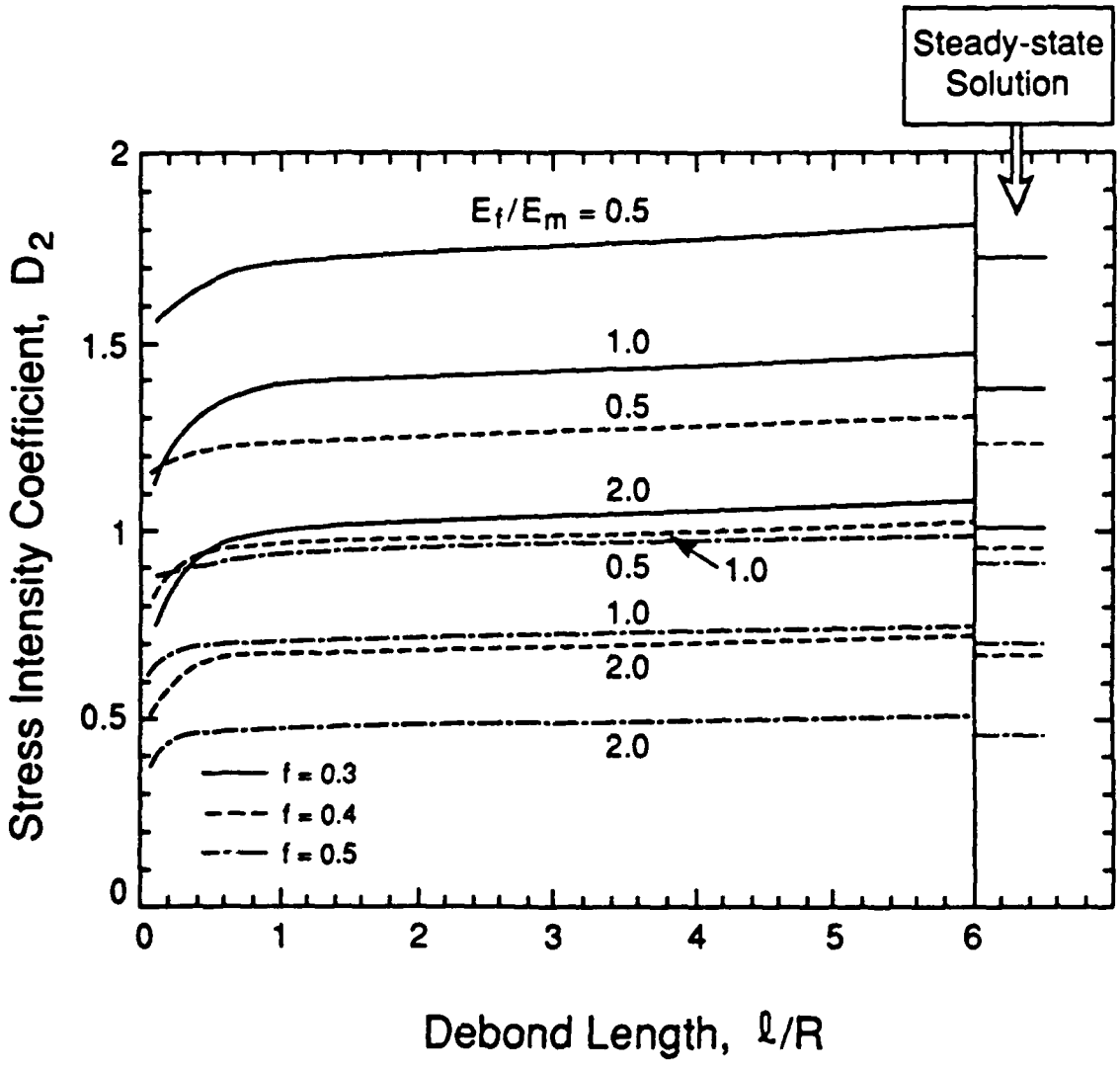

Fig. 8 Numerical values for D_2 from cell model.

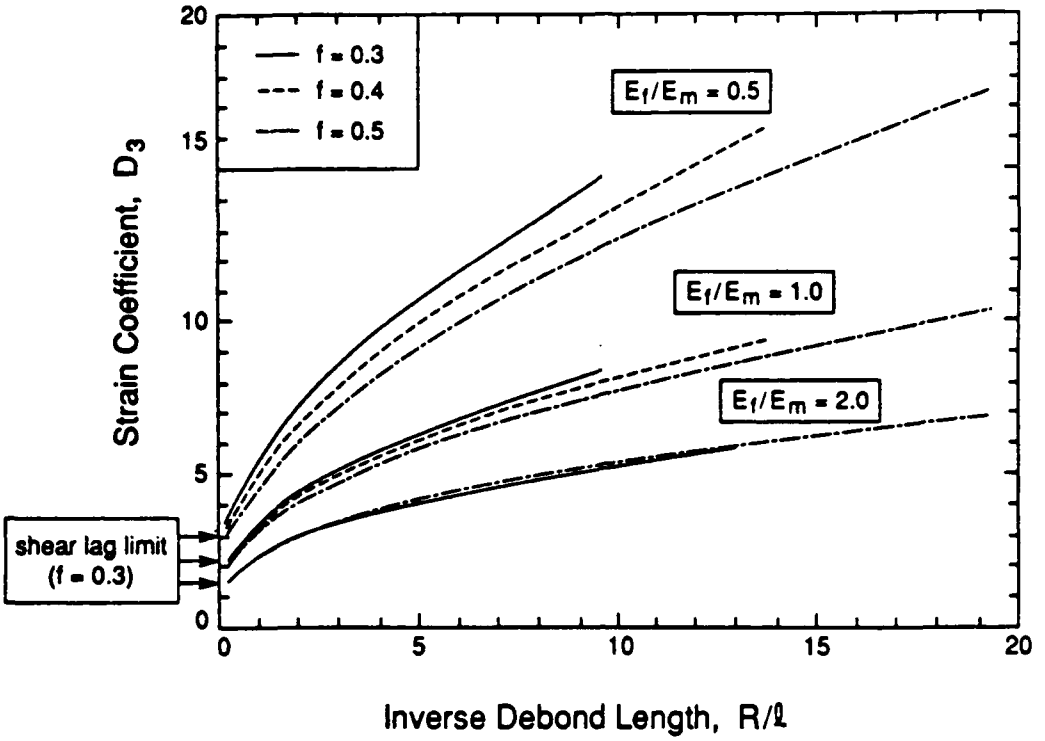

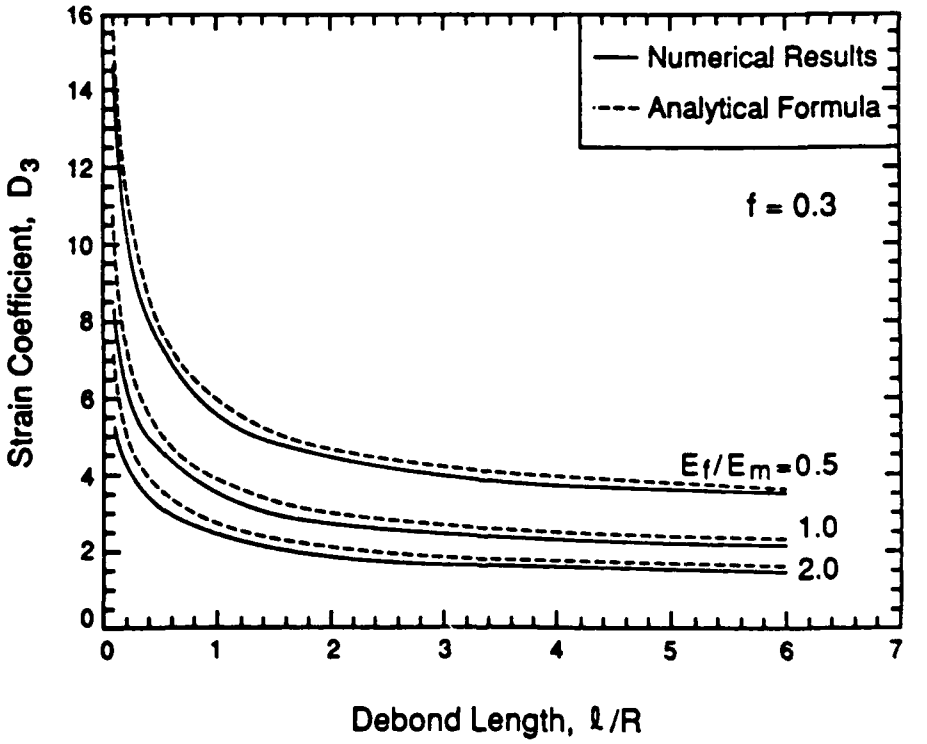

Fig. 9 a) Numerical values of D_3 from cell model as a function of inverse debond length. b) Comparison of numerical results from cell model with formula (11).

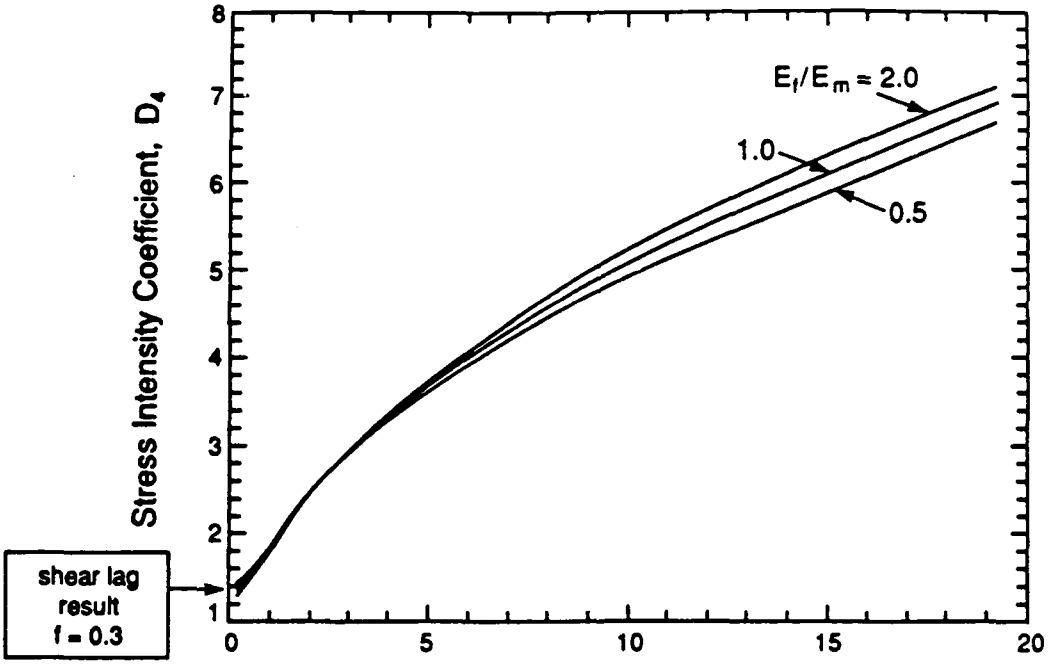

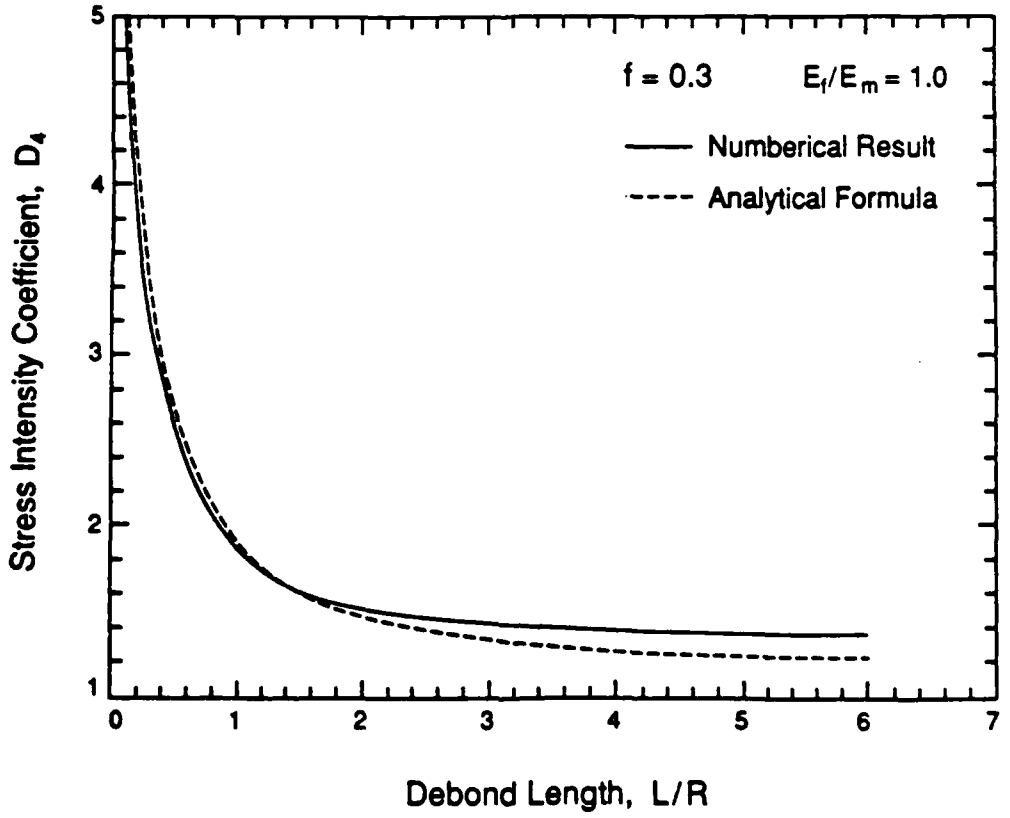

Fig. 10 a) Numerical results for D_4 from cell model as a function of inverse debond length. b) Comparison of numerical results from cell model with formula (12).

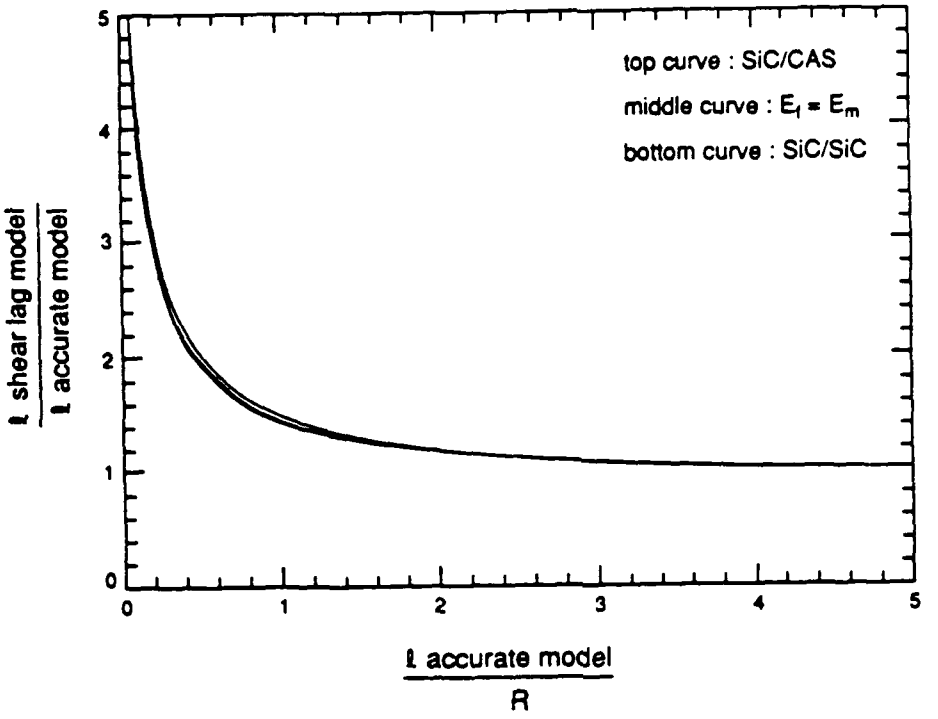

Fig. 11 Ratio of debond length predicted by shear lag model to that predicted by cell model as a function of normalized debond length from cell model.

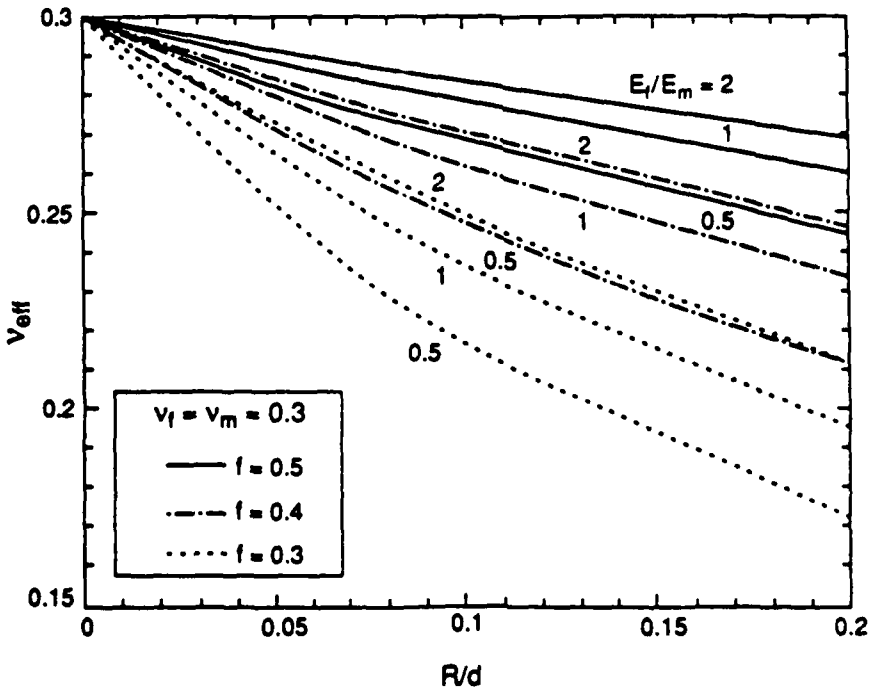

Fig. 12 Effective Poisson's ratio governing transverse strain under axial load for a composite which has undergone matrix cracking with spacing d but no debonding. The effect of initial residual stress is not included.

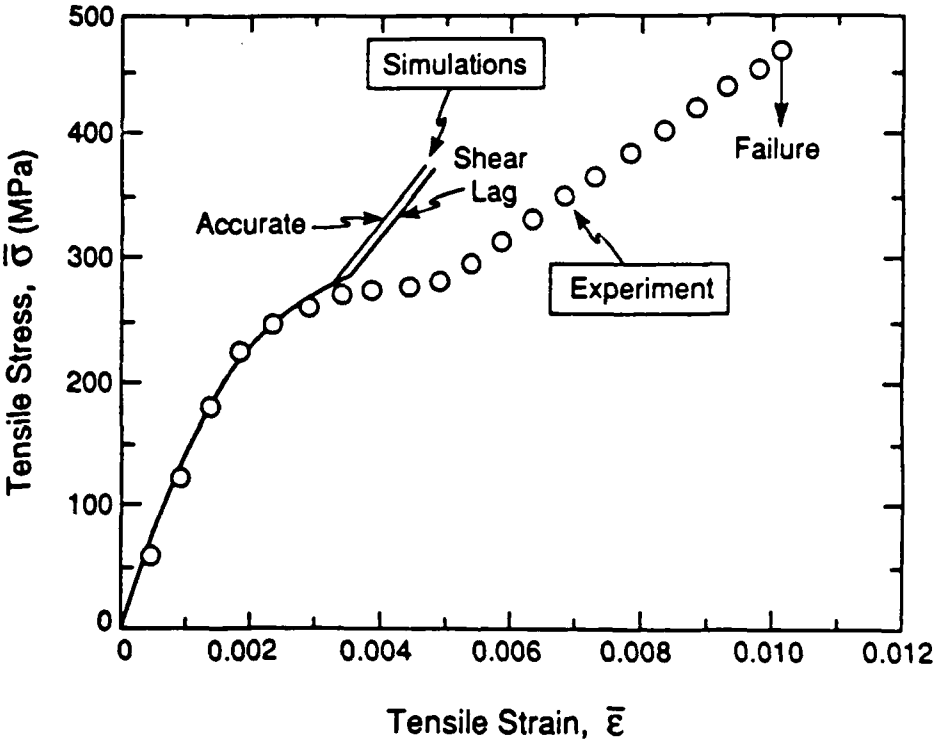

Fig. 13 Theoretical stress-strain curves for the SiC/CAS composite and comparison with experimental data.

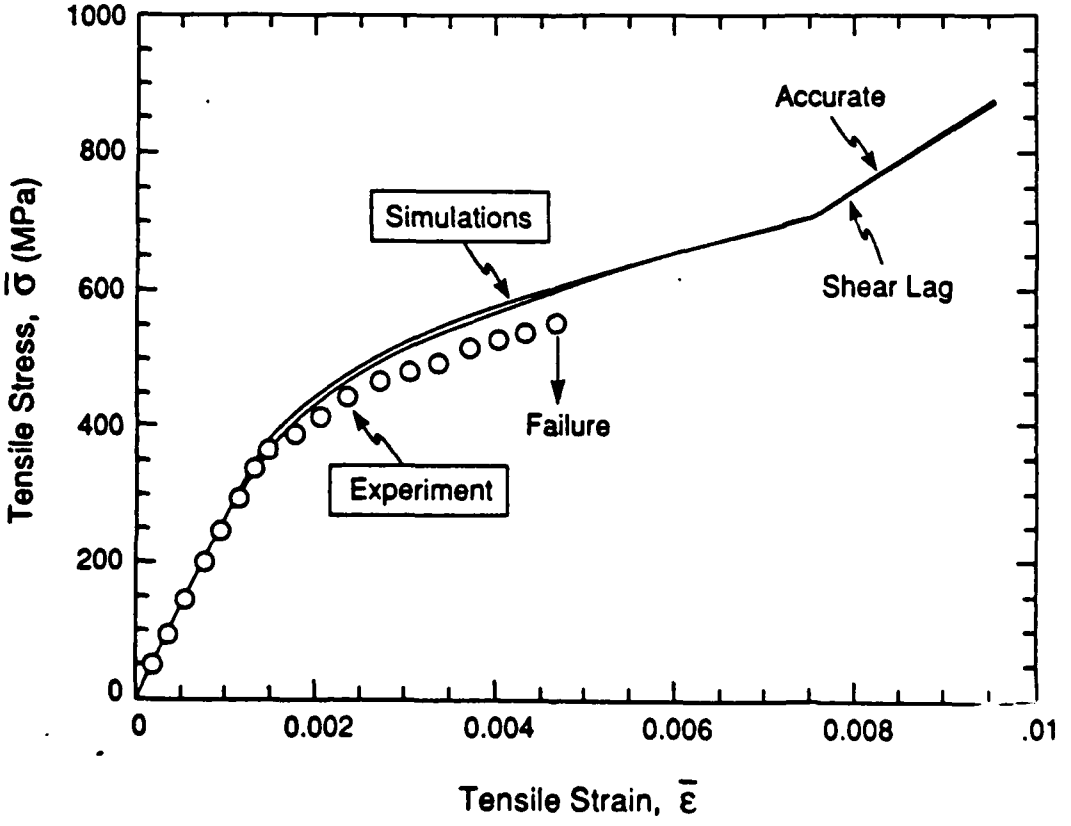

Fig. 14 Theoretical stress-strain curves for the SiC/SiC composite and comparison with experimental data.

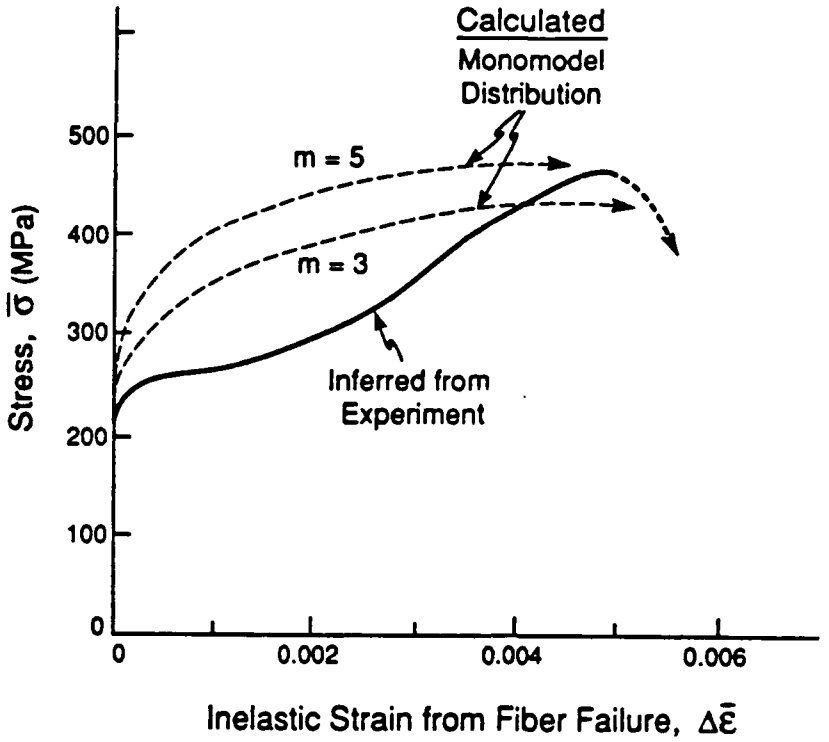

Fig. 15 Inferred inelastic strain contribution due to fiber failure for the SiC/CAS composite and comparison with the inelastic strain contribution expected from fiber failure given a monomodal distribution of fiber flaws from (Hild, et al, 1993). Here, m is the modulus associated with the Weibull statistics of the flaw distribution.

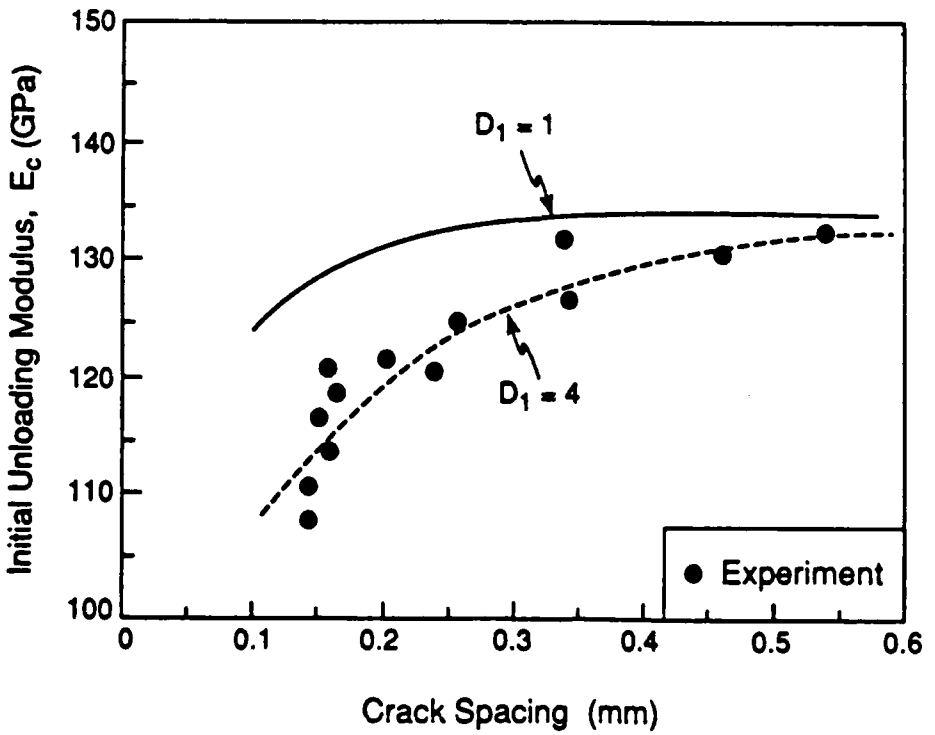

Fig. 16 Experimentally measured initial unloading modulus as a function of matrix crack spacing for the SiC/CAS uni-directional composite. Also shown are theoretical predictions from equation (3) for two values of D_1: the value D_1=1 predicted by the cell model and the value D_1=4 which gives a better fit to the data.

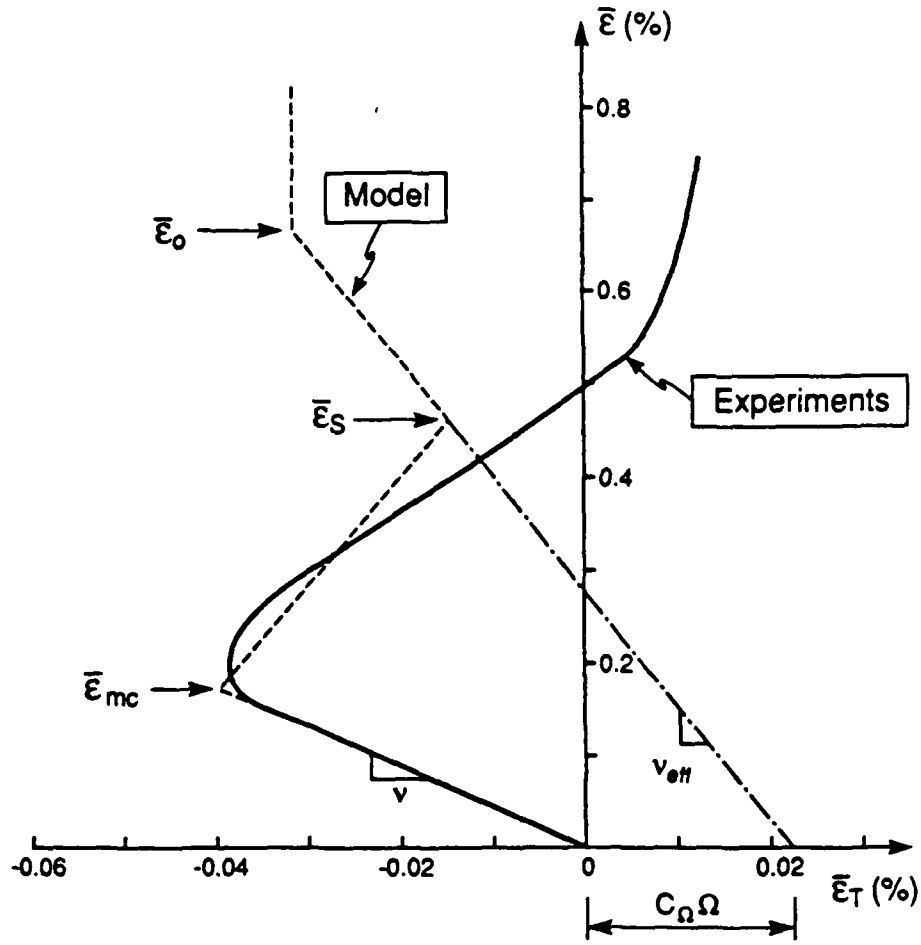

Fig. 17 Experimental data for transverse strain for SiC/CAS from Harris, et al (1992) and comparison with trends predicted by the model (Eqs. (22) and (24)).

LOCALIZATION AND ULTIMATE TENSILE STRENGTH OF FIBER-REINFORCED CERAMIC-MATRIX COMPOSITES

François Hild and Alain Burr

Laboratoire de Mécanique et Technologie,
E.N.S. de Cachan / C.N.R.S. URA 860 / Université Paris 6
61 avenue du Président Wilson, F-94235 Cachan Cedex, France.

Introduction

The stress-strain behavior of ceramic-matrix composites (CMCs) is often non-linear. The loading of such composites results in two *independent* damage mechanisms: fiber failure and matrix cracking. Furthermore, the fibers are supposed to be subject to global load sharing, whereby the load transmitted from each failed fiber is shared equally among the intact fibers. Some aspects of the associated fiber failure stochastics have already been addressed [1-2]. One key parameter, a *characteristic strength* [3] is associated with ultimate strengths

$$S_c = \left(\frac{L_0 S_0^m \tau}{R} \right)^{1/(m+1)} \tag{1}$$

where τ is the interface shear resistance, m the shape parameter, S_0 the stress scale parameter, L_0 a reference length, and R the fiber radius. When the gauge length, L, is sufficiently large, the fibers

are capable of *multiple failures* within the gauge section. Consequently, the ultimate tensile strength, $\bar{\sigma}_{UTS}$, is predicted to be gauge length independent, and given by [2]

$$\bar{\sigma}_{UTS} = fS_c \left(\frac{2}{m+2}\right)^{1/(m+1)} \frac{m+1}{m+2} \tag{2}$$

where f is the fiber volume fraction along the loading direction. In this paper, the problem is analyzed in the light of results related to localization of small strains [4].

Expression of the Ultimate Tensile Strength

A composite with a saturation density of matrix cracks is considered, spacing L_m, within a unit cell of length L_R. The length L_R is the *recovery length* and refers to the longest fiber that can be pulled out and cause a reduction in the load carrying capacity. The recovery length is thus related to the reference stress T in unbroken fibers by

$$L_R = \frac{RT}{\tau} \tag{3}$$

If the fibers exhibit a statistical variation of strength that obeys a two-parameter law [5], then the probability that a fiber would break anywhere within the recovery length L_R at or below a reference stress T can be written as

$$P_F(T) = 1 - \exp\left\{ - \left(\frac{T}{S_c}\right)^{m+1} \right\} \tag{4}$$

The average stress $\bar{\sigma}$ applied to the composite is related to the reference stress T by

$$\bar{\sigma} = f\,T \left\{ 1 - P_F(T) \right\} + \bar{\sigma}_{FP}(T) \tag{5}$$

where $\bar{\sigma}_{FP}(T)$ denotes that component of the stress provided by *failed fibers* as they pull out from the matrix. For global load sharing, the pull-out stress is given by

$$\bar{\sigma}_{FP}(T) = f\,P_F(T)\,\bar{\sigma}_b(T) \tag{6}$$

where $\bar{\sigma}_b(T)$ denotes the average stress at $x = 0$ when a fiber breaks at location $x = t$, and at the reference stress level T. Provided that the composite length $L > L_R$, the average pull-out stress, at reference stress level T, is

$$\bar{\sigma}_b(T) = T / 2 \tag{7}$$

Then, the average applied stress takes the form

$$\bar{\sigma} = f\,T \left\{ 1 - P_F(T) \right\} + f \frac{T}{2} P_F(T) = \bar{\sigma}_{FB}(T) + \bar{\sigma}_{FP}(T) \tag{8}$$

The expression of the external stress is composed of the contribution of unbroken fibers, $\bar{\sigma}_{FB}(T)$, and the fiber pull-out stress, $\bar{\sigma}_{FP}(T)$. In Fig. 1, the contributions of the two mechanisms are plotted when $m = 4$. It is worth noting that the fiber pull-out stress is a strictly increasing function, whereas the fiber stress reaches a maximum value. The latter induces overall softening. Because of the decrease of the fiber stress, an ultimate stress may exist. This decrease leads to a loss of uniqueness of the stress-strain relationship. Since the fiber stress level decreases, there are two alternatives. The first one, referred to as *homogeneous solution*, corresponds to the case where fiber breakage continues to evolve uniformly in the whole specimen. The second one, referred to as *localized solution*, consists in elastic unloading of the unbroken fibers in one part of the specimen, and further fiber breakage in the other part. Consequently Eqn. (8) after the localization point corresponds to the homogeneous solution, which usually cannot be reached. The applied stress level corresponding to the onset of localization will be referred to as localization tensile strength, and will be denoted by $\bar{\sigma}_{LTS}$. In most cases, this stress level corresponds to the ultimate tensile strength of a CMC. The aim of the remainder of this Section is to derive this stress level and to compare it with the ultimate tensile strength given by the homogeneous solution.

The localization tensile strength of the composite is thus defined by the condition

$$d\bar{\sigma}_{FB} / d\bar{\varepsilon} = 0 \quad \text{or} \quad d\bar{\sigma}_{FB} / dT = 0 \tag{9}$$

because the reference stress T is proportional to the average strain on the composite

$$\bar{\varepsilon} = T / E_F \tag{10}$$

where E_F denotes the Young's modulus of the *unbroken* fibers. The localization tensile strength arises when

$$\frac{T}{S_c} = \left(\frac{1}{m+1} \right)^{1/(m+1)} \tag{11}$$

Consequently, the localization tensile strength becomes

$$\bar{\sigma}_{LTS} = \frac{fS_c}{2}\left(\frac{1}{m+1}\right)^{1/(m+1)}\left\{1+\exp\left(-\frac{1}{m+1}\right)\right\} \tag{12}$$

The ultimate tensile strength corresponding to the homogeneous solution is given by

$$d\bar{\sigma} / d\bar{\varepsilon} = 0 \tag{13}$$

This equation cannot be solved analytically. A first order solution of the ultimate tensile strength is given by Eqn. (2). The ultimate tensile strength then arises when

$$\frac{T}{S_c} = \left(\frac{2}{m+2}\right)^{1/(m+1)} \tag{14}$$

In Fig. 2, the exact tensile strength is compared with the localization tensile strength for different values of m. It is worth noting that in terms of stress levels, the two strengths are very close. However, in terms of failure strains, and softening, the two differ more significantly (Fig. 1). In the following, the tensile strength derived from Eqn. (13) is compared with the localization tensile strength given by Eqn. (12).

Comparison with Experiment

Comparison of the above stochastics will be made with two different experimental results for CMCs. Experiments on LAS matrix composites reinforced by SiC (Nicalon) fibers provide the general information summarized on Table 1 [6]: τ = 2–3 MPa, R = 8 μm, L_0 = 25 mm. The corresponding predictions are given in Table 1. It is apparent that the agreement between experiment and prediction is quite good, especially for τ = 3 MPa.

EXPERIMENTAL RESULTS

Sample No.	f	m	S_0 (MPa)	$\bar{\sigma}_{UTS}$ (MPa)
2369 (p)	0.46	3.8	1740	758
2369 (c)	0.46	2.7	1740	664
2376 (p)	0.44	3.9	1615	670
2376 (c)	0.44	3.1	1632	680

PREDICTIONS

Sample No.	$\bar{\sigma}_{LTS}$ (MPa) (τ = 2 MPa)	$\bar{\sigma}_{LTS}$ (MPa) (τ = 3 MPa)	$\bar{\sigma}_{UTS}$ (MPa) (τ = 2 MPa)	$\bar{\sigma}_{UTS}$ (MPa) (τ = 3 MPa)
2369 (p)	680	745	720	790
2369 (c)	700	780	775	860
2376 (p)	615	670	655	710
2376 (c)	625	690	680	750

Table 1: Experimental results and predictions for LAS matrix composite.

Experiments performed on two carbon matrix composites (material A and C) reinforced by SiC (Nicalon) fibers [7] are summarized in Table 2: L_0 = 25 mm, R = 6.5 μm. Again, the predictions agree well with experiments.

EXPERIMENTAL RESULTS

Material	f	S_0 (MPa)	m	τ	$\bar{\sigma}_{UTS}$ (MPa)
A	0.2	1165	4.5	10	290
C	0.2	1140	4.5	14	345

PREDICTIONS

Material	$\bar{\sigma}_{LTS}$ (MPa)	$\bar{\sigma}_{UTS}$ (MPa)
A	295	310
C	310	325

Table 2: Experimental results and predictions for carbon–matrix composites.

Acknowlegments

The authors are indebted to Prof. Frederick A. Leckie for valuable discussions. This work has been supported by DARPA through the URI, University of California at Santa Barbara.

References

1. W.A. Curtin, J. Mat. Sci., **26**, 5239 (1991).
2. W.A. Curtin, J. Am. Ceram. Soc., **74** [11], 2837 (1991).
3. R.B. Henstenburg and S.L. Phoenix, Polym. Comp., **10** [5], 389 (1989).
4. F. Hild, P.-L. Larsson and F.A. Leckie, Int. J. Solids Struct., **29** [24], 3221 (1992).
5. W. Weibull, Ing. Vetenskap Akad., Handlingar No. 153 (1939).
6. K.M. Prewo, J. Mat. Sci., **21**, 3590 (1986).
7. F.E. Heredia, S.M. Spearing, A.G. Evans, P. Mosher and W.A. Curtin, J. Am. Ceram. Soc., **75** [11], 3017-3025 (1992).

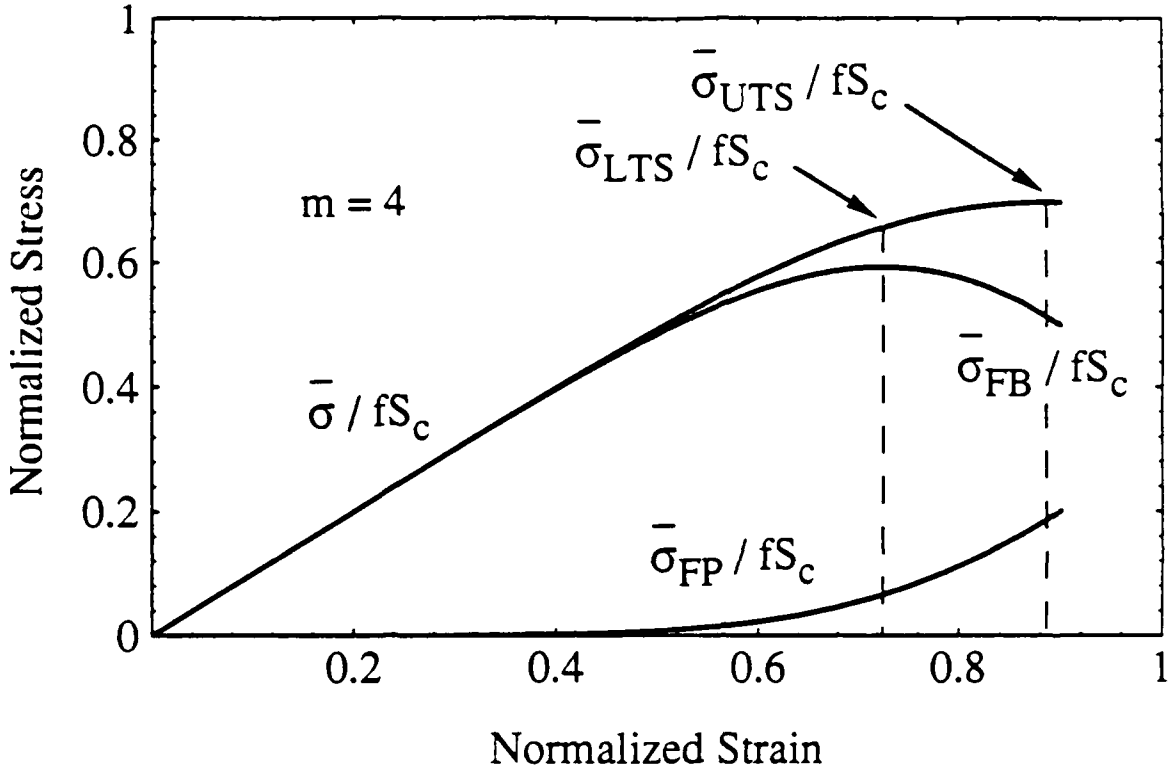

Figure 1: Normalized stresses, $\bar{\sigma} / fS_c$, $\bar{\sigma}_{FB} / fS_c$, $\bar{\sigma}_{FP} / fS_c$ vs. strain, $\bar{\varepsilon}E_F / S_c$.

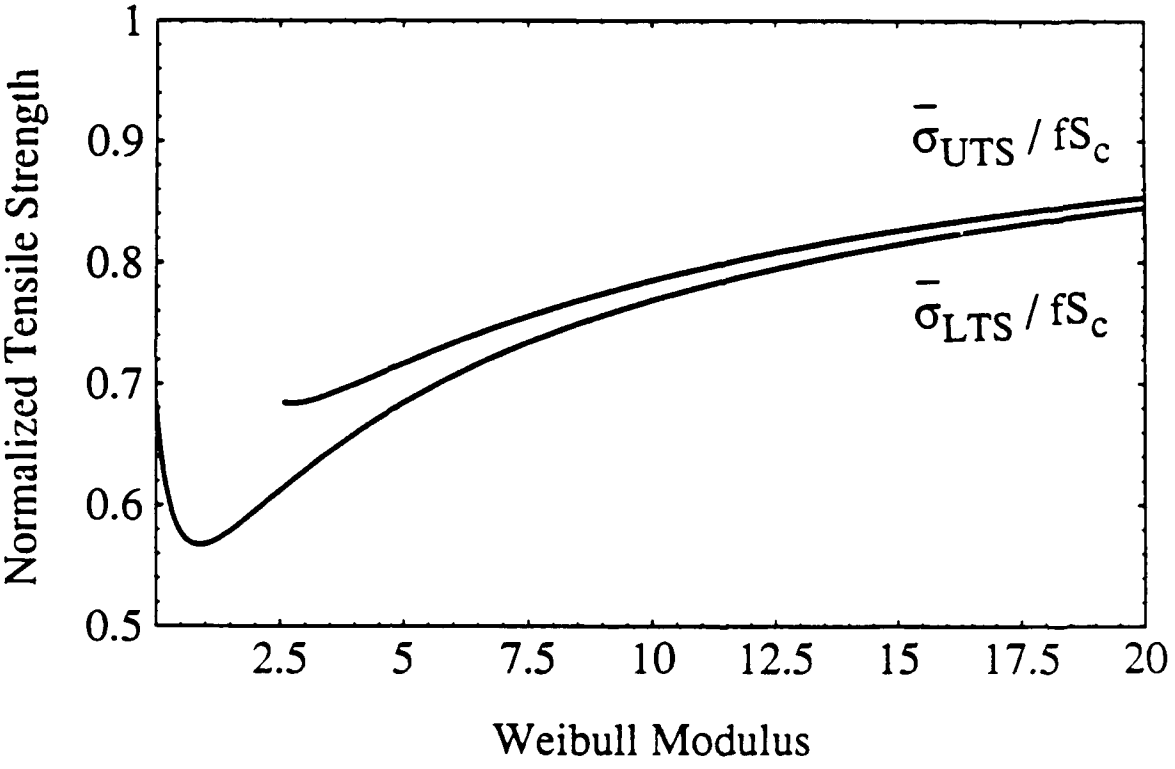

Figure 2: Normalized tensile strengths, $\bar{\sigma}_{LTS} / fS_c$, $\bar{\sigma}_{UTS} / fS_c$ vs. Weibull parameter, m.

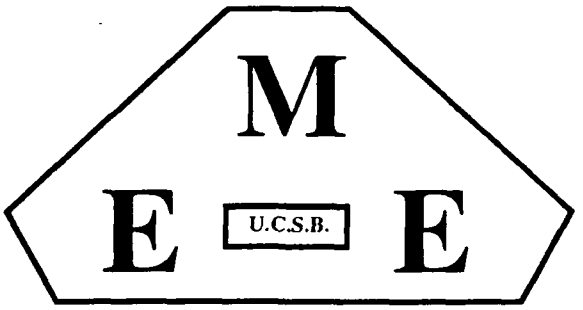

MECHANICAL AND ENVIRONMENTAL
ENGINEERING DEPARTMENT

Department of Mechanical and Environmental Engineering
University of California, Santa Barbara CA 93106-5070, U.S.A.

MATRIX CRACKING AND DEBONDING OF CERAMIC–MATRIX COMPOSITES

By

François Hild,[1] Alain Burr,[1] and Frederick A. Leckie

[1]Also at Laboratoire de Mécanique et Technologie,
E.N.S. de Cachan/C.N.R.S. URA 860/Université Paris 6
61 avenue du Président Wilson, F–94235 Cachan Cedex, France.

MATRIX CRACKING AND DEBONDING OF CERAMIC–MATRIX COMPOSITES

By

François Hild, Alain Burr, and Frederick A. Leckie

Abstract

A micromechanical model is introduced to study the effects of matrix cracking and debonding occurring in Ceramic–Matrix Composites. These two mechanisms induce loss of stiffness, anelastic strains, hysteresis loops, and crack closure. These features are analyzed in the framework of Continuum Mechanics through the introduction of internal variables. Based upon experimental data and micromechanical modeling, the evolution of the internal variables can be obtained. The influence of residual stress fields due to processing are included. Comparisons between theory and experiments performed on layered materials are carried out.

1. Introduction

The stress–strain behavior of continuous fiber Ceramic–Matrix Composites (CMCs) is non–linear, when the interfaces can slide with low shear resistance, τ. The loading of such composites causes matrix cracking and debonding which reduce the secant modulus $\bar{E}$, introduce anelastic strains upon complete unloading, $\bar{\varepsilon}_{an}$, and hysteresis loops, $\delta\bar{\varepsilon}$ [Beyerley et al., 1992; Pryce and Smith, 1992].

In this paper, the effects of matrix cracking and debonding are addressed within the framework of Continuum Damage Mechanics. Constitutive laws are derived by introducing internal variables which are identified in a micromechanical description of matrix cracking and debonding. The effects of residual stresses due to thermal mismatch are also included. The features exhibited in this paper for unidirectional loading will be used in a later study to derive a constitutive model for multiaxial loading conditions, making use of the evolution laws of the internal variables in terms of their associated forces. The results are used to analyze the tensile behavior of a layered laminate made of alternating layers of alumina and unidirectional carbon/epoxy prepreg tapes. This composite has a weak interface as all the composites considered in the present analysis.

2. Study of a Cracked System

Upon loading, a brittle matrix reinforced by fibers or stronger layers exhibits multiple cracking. The matrix cracking mechanism is mainly driven by principal strains or stresses. Two commonly used criteria are the Rankine criterion based on the maximum principal stresses, and the Saint–Venant criterion which uses principal strains. In fiber–reinforced systems and layered architectures, matrix cracking is usually accompanied by debonding. Fiber breakage is accompanied by fiber pull–out

and is mainly driven by the normal stresses or strains in the fiber directions. These two mechanisms need different treatments.

Let us suppose that the matrix cracking process occurs at load levels significantly lower than the fiber breakage mechanism, and that we can assume that both mechanisms are uncoupled. Post–mortem analysis of broken specimens indicate the presence of arrays of microcracks in the matrix. These microcraks are usually aligned with the principal stress or strain directions. By studying a cracked panel with crack of length $2a$ in a cell of area 4LW (Fig. 1), the reduction in stiffness may be calculated. The length 2L corresponds to the crack spacing. If the initial behavior of the elementary cell is isotropic, and the Young's modulus is E, it can be shown that the stiffness loss depends on the crack density defined as $\pi a^2 / 4LW$. By assuming plane stress conditions, and assuming that the crack density is small, a first approximation for the Young's modulus reduction $\tilde{E} / E$ can be written as

$$\frac{\tilde{E}}{E} = \frac{1}{1 + \frac{\pi a^2}{4LW}} \qquad (1)$$

where $\tilde{E}$ is the new value of the Young's modulus. This relationship can be rewritten in the framework of Continuum Damage Mechanics as [Lemaitre and Chaboche, 1978; Lemaitre and Dufailly, 1987]

$$\frac{\tilde{E}}{E} = 1 - D \qquad (2.1)$$

with

$$D = \frac{\frac{\pi a^2}{4LW}}{1 + \frac{\pi a^2}{4LW}} \tag{2.2}$$

and where D denotes the damage variable associated with the presence of cracks. The damage variable D is therefore related directly to the crack density. When D is small, a first order solution to Eqn. (2.2) is given by

$$D \approx \frac{\pi a^2}{4LW} \tag{2.3}$$

where the damage variable is proportional to the crack density. For a cracked system, the macroscopic secant modulus $\bar{E}$ is equal to $\tilde{E}$, since no friction is involved. The effect of this change of Young's modulus can also be interpreted in terms of effective stress [Rabotnov, 1963; Lemaitre and Chaboche, 1978]. The microscopic stress $\sigma = \bar{\sigma} / (1-D)$ is higher than the macroscopic stress $\bar{\sigma}$ because of the presence of a crack. Therefore the stress/strain relationship becomes

$$\sigma = \frac{\bar{\sigma}}{(1-D)} = E\,\bar{\varepsilon} \tag{3}$$

Matrix cracking is usually accompanied with debonding or friction at the fiber/matrix interface [HSueh, 1993; Vagaggini et al., 1994], and the next Section is devoted to the study of the features related to the friction on planes perpendicular to a crack face.

3. The Micromechanics of Debonding

In this Section a simple micromechanical model is developed which describes the process of sliding at the fiber/matrix interfaces, or in the case of laminate interfaces between different layers, during the loading–unloading–reloading sequences. The relevant experimental quantities are identified which provide a simple description of the composite behavior.

3.1. The Initial Loading

Consider the elementary cell shown in Fig. 1. For the sake of simplicity, the quantities used in this section are *unidirectional*. The cell is of length 2L, width 2W, and contains a crack of length $2a$. The normalized crack length, a/W, is denoted by f. It is assumed that at the end of the crack a friction area of length $2l_F$ develops perpendicular to the crack face (Fig. 2). The frictional shear stress, τ, is assumed to be constant.

Initially, for the sake of simplicity we assume that the Young's modulus of each material in the elementary cell is E. Because of the presence of a crack, the macroscopic Young's modulus is $\tilde{E}$ in the 1–direction as shown in the previous Section. The evolution of $\tilde{E}$ depends upon the evolution the cell length L, which is the average crack spacing, and upon the crack size a.

Upon loading, the equilibrium of region (1) in the elementary cell gives the relation of the friction length, l_F, to the microscopic stress, σ, by (Fig. 3a)

$$l_F = \frac{a\,\sigma}{\tau} \tag{4}$$

The total applied strain, corresponding to the average strain of region (2), is given by

$$\bar{\varepsilon} = \frac{\sigma}{E}\left(\frac{f}{1-f}\frac{l_F}{2L} + 1\right) \tag{5}$$

and the crack opening displacement, defined as the difference in displacement of a cracked region (2) and an unbroken region (2), is given by (Fig. 4)

$$\delta(\sigma_M) = \frac{l_{FM}}{E}\frac{\sigma_M}{2} \tag{6}$$

The crack opening displacement is also related to the total strain by

$$\bar{\varepsilon}(\sigma) - \frac{f}{1-f}\frac{\delta(\sigma)}{L} = \frac{\sigma}{E} \tag{7}$$

3.2. The Unloading–Reloading Sequence

An unloading–reloading sequence following the first loading is accompanied by regions of reverse slip. Reversed motion of fibers relative to the matrix has been studied by numerous authors [Marshall and Oliver, 1987; McMeeking and Evans, 1990; Pryce and Smith, 1992; HSueh, 1993; Vagaggini et al., 1994].

After reaching a maximum stress value σ_M, when the maximum friction length is l_{FM}, the load is reversed (Fig. 3b). The maximum friction length is related to the maximum stress σ_M by

$$l_{FM}(\sigma_M) = \frac{a\,\sigma_M}{\tau} \tag{8}$$

Upon unloading by $\Delta\sigma_U$, in the range $0 \le |z| \le l_{FU}$, where l_{FU} is the unloading friction length, both the relative sliding direction and the frictional shear stress reverse (Fig. 3b). Between $l_{FU} \le |z| \le l_{FM}$, the shear stress remains unchanged from that prevailing during the loading process. When the stress level is $\sigma = \sigma_M - \Delta\sigma_U$, the unloading friction length l_{FU} is related to $\Delta\sigma_U$ by

$$l_{FU} = \frac{a\,\Delta\sigma_U}{2\tau} = l_{FM}\left(\frac{\Delta\sigma_U}{2}\right) \tag{9}$$

Then, the expression for the total strain is

$$E\,\bar{\varepsilon} = \left(\sigma_M - \Delta\sigma_U\right) + \frac{f}{1-f}\frac{l_{FM}}{L}\frac{2\sigma_M^2 - \Delta\sigma_U^2}{4\,\sigma_M} \tag{10}$$

and the expression of the crack opening displacement

$$\delta(\sigma_M, \Delta\sigma_U) = \frac{l_{FM}}{E}\frac{2\sigma_M^2 - \Delta\sigma_U^2}{4\sigma_M} \tag{11}$$

It is worth noting that Eqn. (7) is still valid for the applied strain during the unloading sequence, with $\bar{\varepsilon}(\sigma_M, \Delta\sigma_U)$ being related to $\delta(\sigma_M, \Delta\sigma_U)$, the opening displacement during unloading.

Because of friction, anelastic strains remain upon complete unloading ($\sigma = 0$, or $\Delta\sigma_U = \sigma_M$) and are given by

$$\bar{\varepsilon}_{an}(\sigma = 0) = \frac{f}{1-f}\frac{\sigma_M}{4E}\frac{l_{FM}}{L} \tag{12}$$

The anelastic strains depend upon the maximum load level, as well as the friction length, $2l_{FM}$, within the cell of length 2L.

If unloading continues below $\Delta\sigma_U = \sigma_M$, closure of matrix cracks occurs when δ is equal to zero, which leads to the result

$$\Delta\sigma_U = \sigma_c = \sqrt{2}\,\sigma_M \tag{13}$$

Eqn. (13) shows that a closure condition happens only in compression, although it is shown later that this criterion alters when residual stresses are present. This matter shall be addressed later.

After reaching a minimum value of stress when $\Delta\sigma_U = \sigma_m$, the load is reversed again (Fig. 3c) causing reloading. Upon reloading, characterized by $\sigma = \Delta\sigma_R$, sliding is confined to $0 \le |z| \le l_{FR}$ and,

$$l_{FR} = \frac{a\,\Delta\sigma_R}{2\tau} \tag{14}$$

The expression for total strain is then,

$$E\,\bar{\varepsilon} = \left(\sigma_M - \sigma_m + \Delta\sigma_R\right) + \frac{f}{1-f}\frac{l_{FM}}{L}\frac{2\sigma_M^2 - \sigma_m^2 + \Delta\sigma_R^2}{4\,\sigma_M} \tag{15}$$

Finally the evolution of the crack opening displacement during the reloading sequence is given by

$$\delta(\sigma_M,\sigma_m,\Delta\sigma_R) = \frac{l_{FM}}{E}\frac{2\sigma_M^2-\sigma_m^2+\Delta\sigma_R^2}{4\,\sigma_M} \qquad (16)$$

Eqn. (7) is still valid for the applied strain during the reloading sequence with $\bar{\varepsilon}(\sigma_M,\sigma_m,\Delta\sigma_R)$ being related to the opening displacement during unloading, $\delta(\sigma_M,\sigma_m,\Delta\sigma_R)$.

The resulting hysteresis loops can also be characterized by the crack opening displacement δ or by the maximum hysteresis loop width. Because the relationship between anelastic strains and load level is parabolic, the results concerning the hysteresis loop width are simple. The maximum hysteresis loop width, $\delta\bar{\varepsilon}_{U-R}$, is reached when the unloading amplitude is equal to half of the maximum unloading amplitude (σ_m) and is given by

$$\delta\bar{\varepsilon}_{U-R} = \frac{f}{1-f}\frac{l_{FM}}{2L}\frac{\sigma_m^2}{4E\,\sigma_M} \qquad (17)$$

It is worth noting that the crack opening displacement characterizes completely the different steps of a complicated history of unloading–reloading sequences. One of the main results of this section is that Eqn. (7) is valid in any loading–unloading–reloading sequence. As mentioned in the previous Section, the actual microscopic stress or effective stress is $\sigma = \bar{\sigma}/(1-D)$, therefore Eqn. (7) can be rewritten as

$$\bar{\varepsilon} - \frac{f}{1-f}\frac{\delta}{L} = \frac{\bar{\sigma}}{E(1-D)} \qquad (18)$$

In the next Section, the previous results will be modeled in the framework of Continuum Mechanics based upon the thermodynamics of irreversible processes.

4. Continuum Mechanics Modeling

In the following Section, the results of the micromechanical study are used to develop a Continuum Mechanics formulation [Germain, 1973; Lemaitre and Chaboche, 1985].

In the framework of the thermodynamics of irreversible processes [Bataille and Kestin, 1979; Germain et al., 1983], the first step to establish the model is to select the relevant state variables which define the condition of the material. The second step is to write the expression of the state potential in terms of the state variables and the third step to define the evolution laws of the internal variables. In the following development, the state potential is derived using results of the micromechanics discussed previously. In practice, it is not always necessary to model all the details revealed by micromechanics and in what follows two models are developed which are progressively more faithful to the earlier analysis.

4.1. First Model – No Hysteresis

The most important features to model are the reduction in stiffness due to matrix cracking and the anelastic strains. The hysteresis loops are generally of lesser importance and are not accounted for by this model. The macroscopic model is based upon the measurement of the unloading secant modulus $\bar{E} = E(1-\bar{D})$ and the anelastic strains $\bar{\varepsilon}_{an}$ upon complete unloading (Fig. 5). It is assumed that the unloading process is linear, and is characterized by a damage variable $\bar{D}$ and that the expression of the state potential ψ is written as [Lemaitre and Chaboche, 1985]

$$\psi = \frac{1}{2} E (1-\bar{D}) \left(\bar{\varepsilon}-\bar{\varepsilon}_{an}\right)^2 \qquad (19)$$

The stress is obtained by partial differentiation of ψ with respect to the total strain $\bar{\varepsilon}$

$$\bar{\sigma} = \frac{\partial \psi}{\partial \bar{\varepsilon}} = E\,(1-\bar{D})\left(\bar{\varepsilon}-\bar{\varepsilon}_{an}\right) \tag{20.1}$$

and the associated forces to the anelastic strains, $\bar{\varepsilon}_{an} = \bar{\varepsilon}_{an}(\bar{\sigma} = 0)$, and to the damage variable, $\bar{D}$, are respectively given by

$$\bar{\sigma} = -\frac{\partial \psi}{\partial \bar{\varepsilon}_{an}} \tag{20.2}$$

$$\bar{Y} = -\frac{\partial \psi}{\partial \bar{D}} = \frac{1}{2} E \left(\bar{\varepsilon}-\bar{\varepsilon}_{an}\right)^2 \tag{20.3}$$

Within the framework of Continuum Damage Mechanics, $\bar{Y}$ is the strain energy release rate density [Chaboche, 1978]. In this study, the evolutions of the internal variables are obtained from experiments by plotting their evolution against the respective associated force. The measurement of the anelastic strains is easy to carry out since it involves complete unloading. The measurement of the damage variable can be performed through the measurement of the unloading modulus $\bar{E}$ (Fig. 5) and is related to the anelastic strains and the maximum stress level by

$$\bar{D} = 1 - \frac{\bar{E}}{\bar{E}} = 1 - \frac{\bar{\sigma}_M}{E\,(\bar{\varepsilon}_M - \bar{\varepsilon}_{an})} \tag{21}$$

Eqn. (21) corresponds to a macroscopic description of the degradation which is taking place in the material [Lemaitre and Dufailly, 1987].

The evolution laws have to satisfy the second principle of thermodynamics. The positiveness of the intrinsic dissipation Φ ensures the latter principle. The dissipation Φ is written as

$$\Phi = \bar{\sigma} \dot{\bar{\varepsilon}}_{an} + \bar{Y} \dot{\bar{D}} > 0 \qquad (22)$$

and is a positive function.

In this approach the internal variables are obtained from macroscopic measurements. In the next section, it will be shown how these quantities can be related to microscopic quantities.

4.2. Second Model – With Hysteresis Loops

This second model accounts for the three aspects induced by matrix cracking and debonding, viz. the reduction in stiffness due to matrix cracking, the anelastic strains due to friction and the hysteresis loops. The development of the model closely follows the treatment using the micromechanics described earlier (Fig. 6). The details of the unloading and reloading process are complex and by introducing the crack opening displacement δ it is possible to avoid complex calculations. The model can also account for the closure phenomenon when the loading is compressive. Four different state variables are required, and are related to the overall strain $\bar{\varepsilon}$, the friction length l_F, the cell length L, and the crack opening displacement, δ.

To derive the free energy density associated with a loading sequence, we consider two different elastic steps to reach a given state. The first step consists in moving the unbroken part (2) with respect to the broken part (1) with no external load by an amount Δ (with $\Delta = \delta / (1-f)$) over a length l_{FM} (Fig. 7)). This displacement Δ gives rise to a self balanced linear stress field along a length l_{FM} in parts (1) and (2) as

shown in Fig. 7. By integration over l_{FM}, and then averaging over the total length L, the elastic energy density associated with this process is given by

$$\psi^s = \frac{2}{3} E \left\{ \frac{\Delta(1-f)}{l_{FM}} \right\}^2 \frac{f}{1-f} \frac{l_{FM}}{L} \tag{23}$$

The crack opening displacement δ induces an overall opening strain α expressed as

$$\alpha = f \frac{\Delta}{L} = \frac{f}{1-f} \frac{\delta}{L} \tag{24}$$

The second step consists of an elastic loading so that the elastic energy density is given by

$$\psi^e = \frac{1}{2} E (1-D) \left(\bar{\varepsilon} - \alpha \right)^2 \tag{25}$$

The total free energy density is the sum of the two previous energies

$$\psi = \frac{1}{2} E (1-D) \left(\bar{\varepsilon} - \alpha \right)^2 + \frac{2}{3} E \left\{ \frac{\Delta(1-f)}{l_{FM}} \right\}^2 \frac{f}{1-f} \frac{l_{FM}}{L} \tag{26}$$

For convenience the free energy can be expressed in a more compact form by using state variables which are the total strain $\bar{\varepsilon}$, the damage variable D modeling the loss of stiffness due to the cracking mechanism, the damage variable $d = f / (1-f) \, l_{FM} / L$ which defines the size of the slip zone related to the crack spacing, and the crack opening strain α. The free energy density in terms of the new internal variables is

$$\psi = \frac{1}{2} E (1-D) \left(\bar{\varepsilon} - \alpha \right)^2 + \frac{2}{3} E \left(\frac{\alpha^2}{d} \right) \tag{27}$$

The crack opening strain α is similar to a kinematic hardening variable, and the associated force corresponds to the back-stress induced by the slipping mechanism. The force associated with the previous variables are respectively given by

$$\bar{\sigma} = \frac{\partial \psi}{\partial \bar{\varepsilon}} = E\,(1-D)\left(\bar{\varepsilon} - \alpha\right) \tag{28.1}$$

$$Y = -\frac{\partial \psi}{\partial D} = \frac{E}{2}\left(\bar{\varepsilon} - \alpha\right)^2 \tag{28.2}$$

$$y = -\frac{\partial \psi}{\partial d} = \frac{2E}{3}\left(\frac{\alpha}{d}\right)^2 \tag{28.3}$$

$$X = \frac{\partial \psi}{\partial \alpha} = -\bar{\sigma} + \frac{4E}{3}\frac{\alpha}{d} \tag{28.4}$$

By using Eqn. (28.1) and the definitions of the internal variables, it is possible to determine their evolution by a macroscopic measurement. A micromechanical model is also able to model its evolution but involves tedious derivations based upon results obtained on a single filament model [Curtin, 1991]. Another way to find the evolution of D is to use experimental data.

To get some additional information, a complete loading-unloading-reloading sequence is needed (Fig. 8). The useful information is the maximum applied stress, $\bar{\sigma}_M$, the anelastic strains corresponding to a complete unloading, $\bar{\varepsilon}_{an}$, and the secant Young's modulus, $\bar{E}$. It is worth remembering that the secant Young's modulus, $\bar{E}$, is used to define the damage variable, $\bar{D}$, for model No. 1 (Eqn. (21)). From Eqn. (12), and using the effective stress concept developed to derive Eqn. (18), the measure of the anelastic strains gives information on the values of the damage variables d and D

$$\frac{d}{4} = \frac{E(1-D)\,\bar{\varepsilon}_{an}}{\bar{\sigma}_M} \tag{29}$$

From Eqns. (10) (20.1), (28.1), (29), and the concept of effective stress, the value of the damage variable $\bar{D}$ can be related to the damage variable D and d by

$$\bar{D} = \frac{D + \frac{d}{4}}{1 + \frac{d}{4}} \tag{30}$$

Eqn. (30) shows that the macroscopic damage variable depends upon the *two* microscopic damage variables d and D. This definition of damage can be seen by inspection to be consistent with the usual bounds 0 and 1.

A means of determining the variable D is to measure the initial unloading modulus, which is equal to $\tilde{E} = E(1-D)$. Similarly, the initial reloading modulus is equal to $\tilde{E} = E(1-D)$ as shown in Fig. 8. Another means of determining the damage variables is to measure the maximum hysteresis loop width, $\delta\bar{\varepsilon}$. Again, the effective stress concept applied in Eqn. (17) when $\sigma_m = \sigma_M$ is used to relate the maximum hysteresis loop width to the damage variables

$$2\delta\bar{\varepsilon} = \frac{d}{4}\frac{\bar{\sigma}_M}{E(1-D)} \tag{31.1}$$

By inspection of Eqn. (29), the maximum hysteresis loop width is then related to the anelastic strain by a very simple relationship

$$2\delta\bar{\varepsilon} = \bar{\varepsilon}_{an} \tag{31.2}$$

This last result is important, since it allows a quick check of the model with respect to experimental data.

If the identification is performed using Eqns. (28.1), (29) and (30), the damage variables d and D are related to the anelastic strains $\bar{\varepsilon}_{an}$, the macroscopic damage variable $\bar{D}$, and to the maximum strain $\bar{\varepsilon}_M$ by

$$\frac{d}{4} = \frac{\bar{\varepsilon}_{an}}{\bar{\varepsilon}_M - 2\bar{\varepsilon}_{an}} \tag{32.1}$$

$$D = \frac{\bar{\varepsilon}_M \bar{D} - \bar{\varepsilon}_{an}(1+\bar{D})}{\bar{\varepsilon}_M - 2\bar{\varepsilon}_{an}} \tag{32.2}$$

Eqn. (32.1) shows that when no anelastic strains appear, the damage variable d is equal to zero. Eqn. (32.2) indicates that when the anelastic strains are small compared with the corresponding total strains, the damage variable D is very close to the macroscopic damage variable $\bar{D}$. Moreover, when the anelastic strains vanish, the damage variable D is equal to the macroscopic damage variable $\bar{D}$.

The evolution law of the internal variable α uses the results derived during the loading–unloading–reloading sequence described in Section 3. The only difference again comes from the concept of effective stress. Upon loading, the evolution of α is given by

$$\alpha = \frac{d}{2} \frac{\bar{\sigma}_M}{E(1-D)} \tag{33.1}$$

The variation of α, $\Delta\alpha = \alpha - \alpha_0$, with respect to minimum or maximum value, α_0 (corresponding to a maximum unloading or reloading level characterized by $\bar{\sigma}_0$) is related to the strain variation, $\Delta\bar{\sigma} = \bar{\sigma} - \bar{\sigma}_0$, by

$$\Delta\alpha = \frac{d}{4}\frac{\left(\Delta\bar{\sigma}\right)^2}{E(1-D)\bar{\sigma}_M}\,\mathrm{Sgn}\left(\Delta\bar{\sigma}\right) \tag{33.2}$$

The crack closure condition can be obtained by computing the condition when the anelastic strain α vanishes (α cannot be negative). This calculation gives $\Delta\sigma = \sqrt{2}\,\sigma_M$. Moreover, the free energy density catches this crack closure phenomenon, and does not correspond to a partition in positive/negative strains or positive/negative stresses as is usually assumed [Lemaitre, 1992].

The dissipation Φ is

$$\Phi = -X\,\dot{\alpha} + Y\,\dot{D} + y\,\dot{d} > 0 \tag{34}$$

and has to be positive. Since the model satisfies the principles of thermodynamics on a micro level, and since this model is directly derived from the micromechanics, the dissipation is positive.

If the elementary cell is made of parts with different Young's moduli E_1 and E_2, respectively, the previous results are easily extended. The only difference is in the definition of the state variables D, d, and α. First, the description of the relationship between D and the crack density is altered, and is not as simple as that given in Eqn. (2.2). The value of d is then given by $d = fE_1 / (1-f)E_2\, l_{FM} / L$, and the value of α is equal to $fE_1 / (1-f)E_2\, \delta / L$. All the other relationships derived in this Section remain valid.

5. The Effect of Residual Stresses

Mismatches between parts (1) and (2) occur during processing (e.g. due to cooling, plasticity, creep, or phase transformation). A self–balanced residual stress field develops and is characterized by the stresses $-\rho_1$, and ρ_2 in parts (1) and (2) respectively.

If, for example, the mismatch is due only to thermal strains, the stresses ρ_1, and ρ_2 in parts (1) and (2) are given by

$$\rho_1 = (1-f)E\,\Delta\alpha_{12}\,\Delta T \tag{35}$$

$$\rho_2 = fE\,\Delta\alpha_{12}\,\Delta T \tag{36}$$

where α_1 is the thermal expansion coefficient of part (1), α_2 is the thermal expansion coefficient of part (2), $\Delta\alpha_{12} = \alpha_1 - \alpha_2$ is the thermal coefficient mismatch and $\Delta T = T_0 - T_p$ the negative temperature drop between the room temperature T_0 and the processing temperature T_p. When a crack appears, part of these residual stresses are relieved within the slipping region. However, not all the residual stresses are relieved.

The free energy density is derived using similar steps as in the previous Section. The first step consists in moving the unbroken part (2) with respect to the broken part (1) with no external load by an amount δ over a length l_{FM} (Fig. 9). The expression of the free energy density is identical to that given in Eqn. (27). Therefore the forces associated with the previous variables are respectively given by Eqns. (28). From a macroscopic point of view, the results obtained by taking account of the residual stresses are unaltered. However, the results obtained from a microscopic analysis (Eqns. (12) and (13)) depend upon the residual stress field.

By using Eqn. (28.1) and the definitions of the internal variables, it is possible to measure the internal variables macroscopically. To get the necessary additional information, a complete loading–unloading–reloading sequence is again needed. The useful information are the maximum applied stress, $\bar{\sigma}_M$, the anelastic strains corresponding to a complete unloading, $\bar{\varepsilon}_{an}$, the maximum hysteresis loop width, $\delta\bar{\varepsilon}$, and the Young's modulus, $\bar{E}$. Since the residual stresses are unknown, additional information is needed. When $\Delta\sigma_U = \sigma_M$ the anelastic strains are now given by

$$\bar{\varepsilon}_{an} = \frac{d}{4}\frac{2[\bar{\sigma}_M - \rho_1(1-D)]^2 - \bar{\sigma}_M^2}{E(1-D)[\bar{\sigma}_M - \rho_1(1-D)]} \tag{37}$$

and the closure condition ($\Delta\sigma_U = \sigma_c$) is given by

$$\bar{\sigma}_c = \sqrt{2}\,[\bar{\sigma}_M - \rho_1(1-D)] \tag{38}$$

Eqns. (37) and (38) when compared with Eqns. (29) and (13) are changed because of the residual stress field. However, as D increases, the effect of the initial residual stress field becomes less important.

The evolution law of the internal variable α uses the results derived during the loading–unloading–reloading sequence. Upon loading, the evolution of α is given by

$$\alpha = \frac{d}{2}\frac{\bar{\sigma}_M - \rho_1(1-D)}{E(1-D)} \tag{39.1}$$

The variation of α, $\Delta\alpha = \alpha - \alpha_0$, with respect to minimum or maximum value, α_0 (corresponding to a maximum unloading or reloading level characterized by $\bar{\sigma}_0$) is related to the strain variation, $\Delta\bar{\sigma} = \bar{\sigma} - \bar{\sigma}_0$, by

$$\Delta\alpha = \frac{d}{4}\,\frac{\left(\Delta\bar{\sigma}\right)^2}{E(1-D)\left[\bar{\sigma}_M - \rho_1(1-D)\right]}\,\mathrm{Sgn}\left(\Delta\bar{\sigma}\right) \tag{39.2}$$

Instead of the complicated pattern of friction and reverse friction, a unique variable is introduced, i.e. the opening strain, and Eqns. (39) are similar to Eqns. (33). The only difference is that the maximum effective stress $\bar{\sigma}_M / (1-D)$ is replaced by the corrected maximum effective stress $\bar{\sigma}_M / (1-D) - \rho_1$. This effect is due to the thermal residual stress field. The expression of the hysteresis loop width, $\delta\bar{\varepsilon}$, becomes

$$\delta\bar{\varepsilon} = \frac{d}{4}\,\frac{\bar{\sigma}_M^2}{2E(1-D)[\bar{\sigma}_M - \rho_1(1-D)]} \tag{40}$$

It is worth noting that the simple result given in Eqn. (31.2) is not valid anymore. Eqn. (40) shows the role of residual stresses on the relationship between anelastic strains and maximum hysteresis loop width.

From the knowledge of the three previous quantities, the expressions for the damage variables are given by

$$D = \frac{\bar{\varepsilon}_M \bar{D} - \bar{\varepsilon}_{an} \bar{D} - 2\delta\bar{\varepsilon}}{\bar{\varepsilon}_M - \bar{\varepsilon}_{an} - 2\delta\bar{\varepsilon}} \tag{41}$$

$$\frac{d}{4} = \frac{\sqrt{(\bar{\varepsilon}_{an} + 2\delta\bar{\varepsilon})\delta\bar{\varepsilon}}}{\bar{\varepsilon}_M - \bar{\varepsilon}_{an} - 2\delta\bar{\varepsilon}} \tag{42}$$

and the residual stress in part (1)

$$-\rho_1 = \left(\sqrt{\frac{\bar{\varepsilon}_{an} + 2\delta\bar{\varepsilon}}{4\delta\bar{\varepsilon}}} - 1 \right) E\,(\bar{\varepsilon}_M - \bar{\varepsilon}_{an} - 2\delta\bar{\varepsilon}) \qquad (43)$$

It is worth noting that when ρ_1 vanishes, the results given in Eqns. (41–43) are identical to those of Eqns. (32).

In the following the previous results are applied to a layered material. It is however worth noting that these results can also be applied to fiber–reinforced systems. The definition of the damage variables and the opening strain may change slightly, but the essential features obtained in this paper are *identical*. In particular, the method of deriving the free energy density through two elastic steps can be conserved.

6. Analysis of Experiment Results of a Layered Material

The previous models will be used to predict the behavior of a layered material subject to tension. The material is constructed by alternating three alumina plates and two unidirectional carbon/epoxy prepreg tapes. At room temperature, the laminate is put in a Kapton vacuum bag, then hot pressed to a moderate pressure of 350 kPa, at a temperature of 135°C for 90 minutes [Lange et al., 1990; Sherman, 1992]. The tensile stress/strain response is shown in Fig. 10. Because of the discrete process of matrix cracking, there are stress drops at each new break.

6.1. Identification of the First Model

This first model is completely macroscopic. Therefore, by curve fitting the evolution of the macroscopic damage variable $\bar{D}$, and the anelastic strains $\bar{\varepsilon}_{an}$, against maximum applied strain $\bar{\varepsilon}_M$, this model is completely identified. Fig. 11 shows the

evolution of the macroscopic damage variable as a function of the maximum strains, $\bar{\varepsilon}_M$. This variable saturates together with the crack spacing. A convenient way of describing this saturation is the exponential form

$$\bar{D} = \bar{D}_\infty \left\{ 1 - \exp\left(- \frac{\bar{\varepsilon}_M - \bar{\varepsilon}_0}{\bar{\varepsilon}_1} \right) \right\} \qquad \text{if } \bar{\varepsilon}_M - \bar{\varepsilon}_0 > 0 \tag{44}$$

The parameter $\bar{D}_\infty$ corresponds to the saturation value of the damage variable $\bar{D}$, the parameter $\bar{\varepsilon}_0$ corresponds to the threshold strain below which no cracking takes place, and $\bar{\varepsilon}_1$ is a normalizing strain. For this particular system the following values are obtained

$$\begin{aligned} \bar{D}_\infty &= 0.80 \\ \bar{\varepsilon}_0 &= 0.00069 \\ \bar{\varepsilon}_1 &= 0.00086 \end{aligned} \tag{45}$$

Fig. 12 shows the evolution of the anelastic strains as a function of the maximum strains, $\bar{\varepsilon}_M$. A three order polynomial describes well the experimental measurements

$$\bar{\varepsilon}_{an} = a_0 + a_1 \bar{\varepsilon}_M + a_2 \bar{\varepsilon}_M^2 + a_3 \bar{\varepsilon}_M^3 \tag{46}$$

with

$$a_0 = -0.00014$$
$$a_1 = 0.42$$
$$a_2 = -64. \qquad (47)$$
$$a_3 = 3700$$

The agreement between experiments and identification are quite good in terms of stress/strain response (Fig. 13) as well. The identifications performed in this sub–Section constitute the basis of the identification of the second model. It is worth remembering that this model does not account for the hysteresis loops, and that in this Section, the evolution laws were not known a priori. The identification consisted in choosing the type of function describing the experiments, and in fitting the parameters of each function.

6.2. Identification of the Second Model

This model introduces quantities related to microscopic data, viz. the damage measures of d and D, the anelastic strain α and the residual stress ρ_1. The residual stress is important since it defines the onset of the first matrix crack in a composite system [Budiansky et al., 1986]. The first step is to compute the residual stress ρ_1. By using Eqn. (43), and the experimental data concerning $\bar{\varepsilon}_M$, $\bar{\varepsilon}_{an}$, and the maximum hysteresis loop width, $\delta\bar{\varepsilon}$, the residual stress ρ_1 can be calculated at each experimental data point. It is found that the value of $-\rho_1$ varies only slightly, and since the residual stress is constant, the average for $-\rho_1$ was taken to be +57. MPa (tensile stress). Since $\bar{D}$ and $\bar{\varepsilon}_{an}$ are easy to measure (Section 6.1), these measurements will be used to establish their evolution laws as a fit of those experimental data. By using Eqn. (43), the evolution law of the maximum hysteresis loop width, $\delta\bar{\varepsilon}$, is then completely known and given by

$$2\delta\bar{\varepsilon} = \bar{\varepsilon}_{an} \frac{1}{2\left[1 + \dfrac{-\rho_1}{E\,(\bar{\varepsilon}_M - \bar{\varepsilon}_{an} - 2\delta\bar{\varepsilon})}\right]^2 - 1} \tag{48}$$

Fig. 14 shows the comparison between the experiments and the predictions. The agreement is good. These results are compared with those obtained when residual stresses are assumed to be negligible. In that case, Eqn. (31.2) applies and leads to an overestimate of the maximum hysteresis loop width. The knowledge of the parameter ρ_1 is therefore crucial to the evolution of the maximum hysteresis loop width, and the anelastic strains.

The values of the damage variables can be determined by using Eqns. (41) and (42). Measuring the initial unloading Young's modulus gives directly the value of D which can be compared with the prediction. Fig. 15 shows the comparison between the experiments and the predictions. The agreement is very good. These results are again compared to those obtained when the residual stresses can be neglected. In this case there is a slight change in the initial unloading Young's modulus, measured by the damage variable D, this changes disappears as D increases. The residual stresses have a weak effect on the damage variable D, modeling the change of stiffness due to matrix cracks. Unfortunately, there is no way of comparing the damage variable d obtained experimentally and numerically.

In Fig. 16, the crack closure stresses are computed as a function of the applied strains, when $-\rho_1 = 0.$ MPa, and $-\rho_1 = 57.$ MPa. Because of the presence of residual stresses, the crack closure stresses are lower when $-\rho_1 = 57.$ MPa then those when $-\rho_1 = 0.$ MPa. However, as damage evolves the difference in crack closure stresses decreases since the residual stresses are gradually relieved. There are no experimental evidences of crack closure to support this prediction. To get some information, the

unloading should have been conducted in compression, provided buckling was prevented.

The final step is to derive the evolution laws of the internal variables as a function of their associated forces. This will be convenient in the future to derive constitutive laws under multiaxial loading conditions.

7. Conclusions

A micromechanical model is derived to describe loading and unloading sequences. These sequences induce slip and reverse slip. Because of friction, permanent strains appear upon complete unloading. Moreover, hysteresis loops are observed upon unloading and reloading. These hysteresis loops characterize the amount of energy that is dissipated during one unloading–reloading cycle. A way of characterizing the sequences is to introduce the opening displacement between broken and unbroken parts.

In the framework of Continuum Mechanics, two models have been studied. The first model considered damage measured as a macroscopic loss of stiffness and anelastic strains and was close to a macroscopic model. It was able to model the loading portion, anelastic strains, but not hysteresis loops. Because of the friction zone, the difference is the onset of anelastic strains. The second model considered three internal variables, viz. two damage variables on a microscopic level, and opening strains defined as the opening displacement divided by the average crack spacing. The identification procedure involves the value of the macroscopic damage $\bar{D}$, the anelastic strain $\bar{\varepsilon}_{an}$ and the maximum hysteresis loop width, $\delta\bar{\varepsilon}$, which are easy to measure experimentally. These quantities can be used to calculate the residual stresses $-\rho_1$. Only the evolution laws of the macroscopic damage and the anelastic strain need to be fitted to the experimental data. From Eqns. (41–42), the damage variables D and d are

computed. The evolution law of $\delta\bar{\varepsilon}$ is given by a micromechanical analysis in Eqn. (43).

The procedures were applied to experiments performed on an alumina–carbon/epoxy prepreg layered material. The predictions in terms of hysteresis loop width and initial unloading Young's modulus agree well with the experiments. It is shown that the residual stress field has a strong influence on the evolution of the anelastic strains and the maximum hysteresis loop width. On the other hand, the evolution of the initial unloading Young's modulus is weakly affected by the residual stress field. This model was able to capture all the details of the microscopic study with only three internal variables. This general framework can also be used in the case of more detailed analyses taking into account friction and debonding [HSueh, 1993; Vagaggini et al., 1994]. The expression of the free energy would be identical. The only difference would come from the evolution laws.

This model will constitute the basis of a constitutive law applied to Ceramic–Matrix Composites subject to complex loading conditions. In particular the knowledge of the free energy density, the internal variables and their associated forces are crucial. These laws have to be generalized under more complex loading conditions.

Acknowledgments

This work was supported by the Defense Advanced Research Project Agency through the University Research Initiative under Office of Naval Research Contract No. N–00014–92–J–1808.

References

Bataille, J., Kestin, J., 1979, Irreversible Processes and Physical Interpretations of Rational Thermodynamics, *J. Non Equil. Thermodynamics*, **4**, 229-258.

Beyerley, D., Spearing, S. M., Zok, F. W., Evans, A. G., 1992, Damage, Degradation and Failure in a Unidirectional Ceramic-Matrix Composite, *J. Am. Ceram. Soc.*, **75** [10], 2719-2725.

Budiansky, B., Hutchinson, J. W., Evans, A. G., 1986, Matrix Fracture in Fiber-Reinforced Ceramics, *J. Mech. Phys. Solids*, **34**, 167-189.

Chaboche, J.-L., 1978, Description thermodynamique et phénoménologique de la viscoplasticité cyclique avec endommagement, Thèse de doctorat d'Etat, Université Paris 6.

Curtin, W. A., 1991, Exact Theory of Fiber Fragmentation in Single-Filament Composite, *J. Mat. Sci.*, **26**, 5239-5253.

Germain, P., 1973, Cours de mécanique des milieux continus, Masson, Paris.

Germain, P., Nguyen, Q. S., Suquet, P., 1983, Continuum Thermodynamics, *J. Appl. Mech.*, **50**, 1010-1020.

HSueh, C.-H., 1993, Evaluation of Interfacial Properties of Fiber-Reinforced Ceramic Composites Using a Mechanical Properties Microprobe, *J. Am. Ceram. Soc.*, **76** [12], 3041-3050.

Lange, F. F., Marshall, D. B., Folsom, C. F., 1990, UCSB Patent Application, University of California, Santa Barbara.

Lemaitre, J., 1992, A Course on Damage Mechanics, Springer-Verlag, Berlin.

Lemaitre, J., Chaboche, J.-L., 1978, Aspect phénoménologique de la rupture par endommagement, *J. Méc. Appl.*, **2** [3], 317-365.

Lemaitre, J., Chaboche, J.-L., 1985, Mécanique des matériaux solides, Dunod (Paris).

Lemaitre, J., Dufailly, J., 1987, Damage measurements, *Eng. Fract. Mech.*, **28** [5-6], 643-661.

Marshall, D. B., Oliver, W. C., 1987, Measurement of Interfacial Mechanical Properties in Fiber-Reinforced Ceramic Composites, *J. Am. Ceram. Soc.*, **70**, 542.

McMeeking, R. M., Evans, A. G., 1990, Matrix Fatigue Cracking in Fiber Composites, *Mech. of Mat.*, **9**, 217-227.

Pryce, A. W., Smith, P. A., 1992, Modelling of the Stress/Strain Behavior of Unidirectional Ceramic Matrix Composite Laminates, *J. Mat. Sci.*, **27**, 2695-2704.

Rabotnov, Y. N., 1963, On the Equation of State for Creep, in *Prager Anniversary Vol.*, McMillan, New-York.

Sherman, D., 1992, The Mechanical Behavior of Brittle Ductile Laminated System, PhD dissertation, University of California, Santa Barbara.

Vagaggini, E., Domergue, J.-M., Evans, A. G., 1994, Relationships Between The Macroscopic Performance of Ceramic matrix Composites and Constituent Properties, I: Theory and Methodology, *in preparation*.

Figure Captions

Figure 1: Elementary cell of size 2L x 2W containing a crack of size $2a$.

Figure 2: Elementary cell of size 2L x 2W containing a crack of size $2a$. A debond zone is characterized by the debond length l_F.

Figure 3a: Depiction of the friction length, l_F, upon loading, and the corresponding axial stress in the longitudinal direction.

Figure 3b: Depiction of the unloading friction length, l_{FU}.

Figure 3c: Depiction of the reloading friction length, l_{FR}.

Figure 4: Depiction of the opening displacement δ.

Figure 5: Stresses, $\bar{\sigma}$, versus strain, $\bar{\varepsilon}$, during a loading–unloading–reloading sequence for model No. 1.

Figure 6: Stresses, $\bar{\sigma}$, versus strain, $\bar{\varepsilon}$, during a loading–unloading–reloading sequence for model No. 2.

Figure 7: Motion of the unbroken part (2) with respect to the broken part (1) with no external load by an amount Δ over a length l_F.

Figure 8: Stresses, $\bar{\sigma}$, versus strain, $\bar{\varepsilon}$, during a loading–unloading–reloading sequence for model No. 2.

Figure 9: Motion of the unbroken part (2) with respect to the broken part (1) with no external load by an amount Δ over a length l_F. The residual stresses are denoted by ρ_1 and ρ_2.

Figure 10: Experimental stress/strain curve of a layered material subject to tension (after [Sherman, 1992]).

Figure 11: Experimental and fitted evolution of the macroscopic damage variable as a function of the maximum applied strains

Figure 12: Experimental and fitted evolution of the anelastic strains as a function of the maximum applied strains

Figure 13: Experimental and predicted stress/strain curve of a layered material subject to tension.

Figure 14: Experimental and predicted evolution of the maximum hysteresis loop width as a function of the maximum applied strain, when $-\rho_1 = 0.$ MPa, and $-\rho_1 = 57.$ MPa.

Figure 15: Experimental and predicted evolution of the damage variable D as a function of the maximum applied strain, when $-\rho_1 = 0.$ MPa, and $-\rho_1 = 57.$ MPa.

Figure 16: Predicted evolution of the crack closure stress as a function of the maximum applied strain, when $-\rho_1 = 0.$ MPa, and $-\rho_1 = 57.$ MPa.

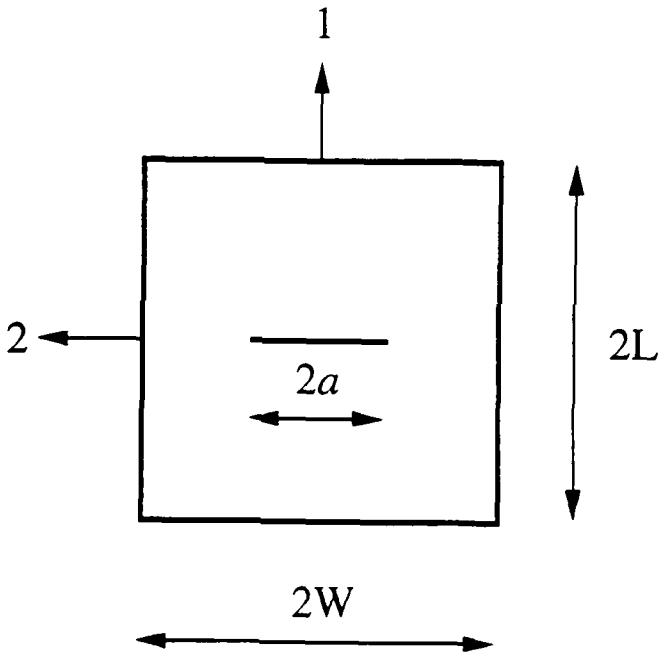

Figure 1

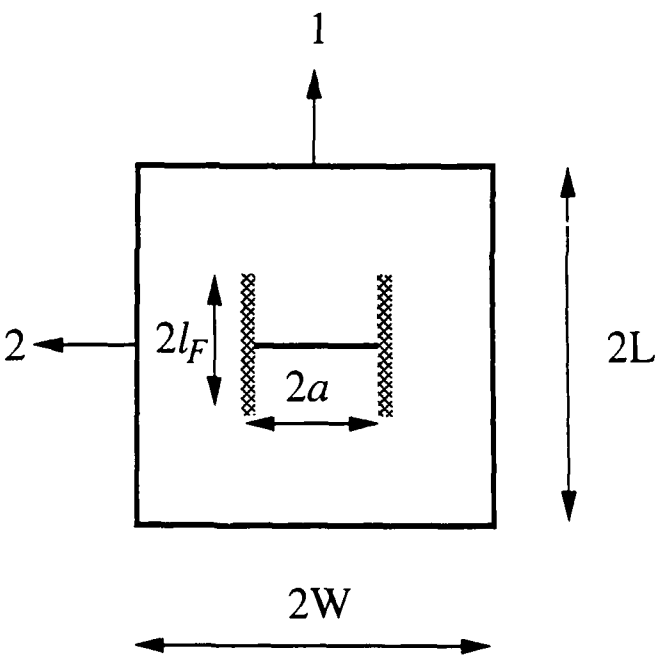

Figure 2

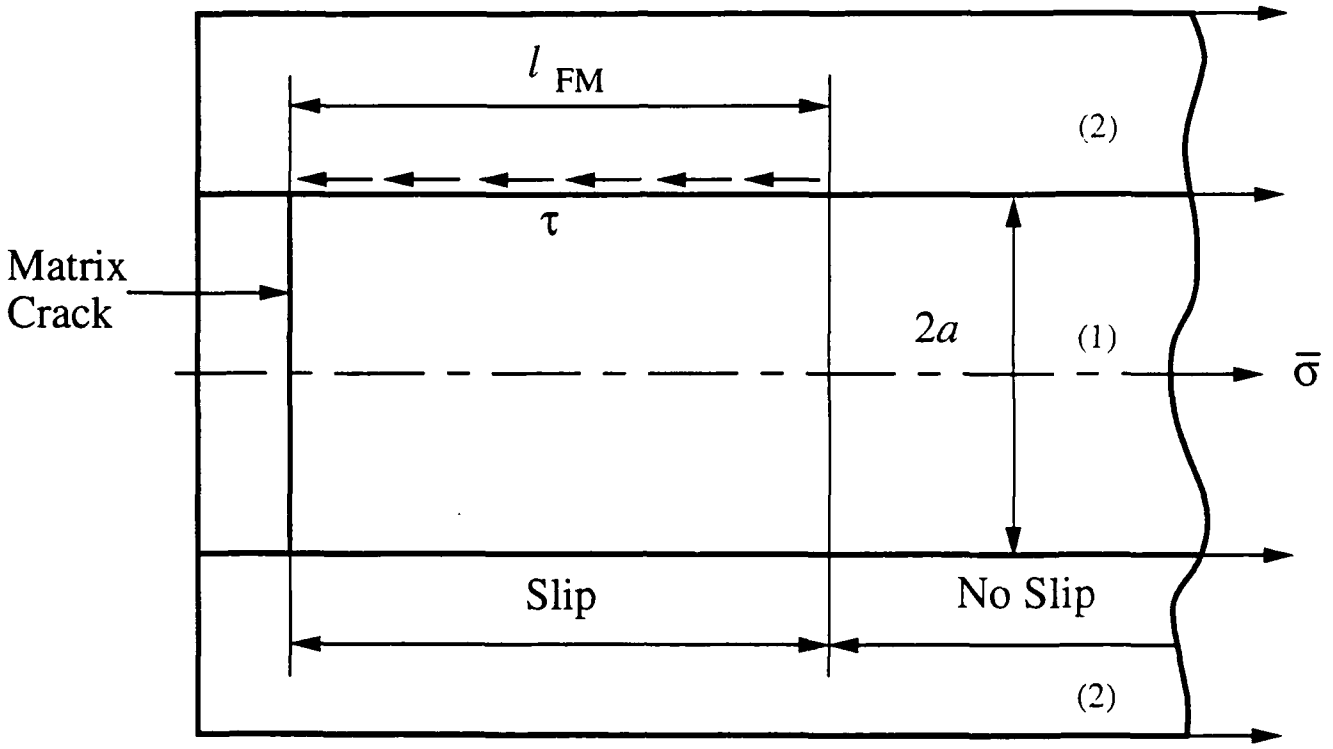
l_{FM}
(2)
τ
Matrix
Crack
2a
(1)
σ̄
Slip
No Slip
(2)

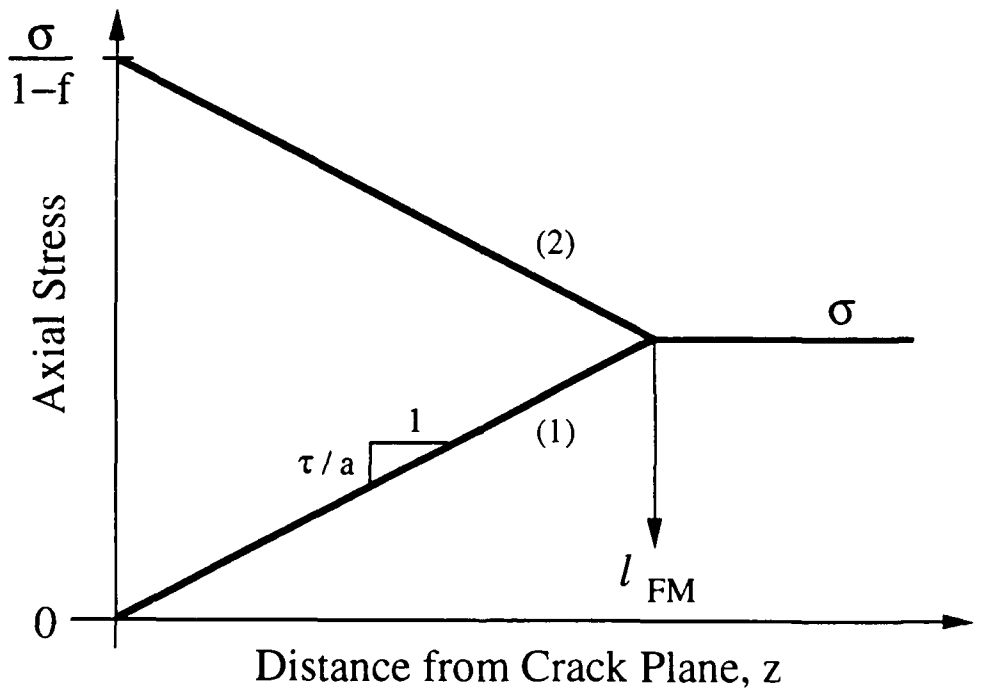
σ / 1−f
Axial Stress
(2)
σ
1
τ / a
(1)
l_{FM}
0
Distance from Crack Plane, z

Figure 3a

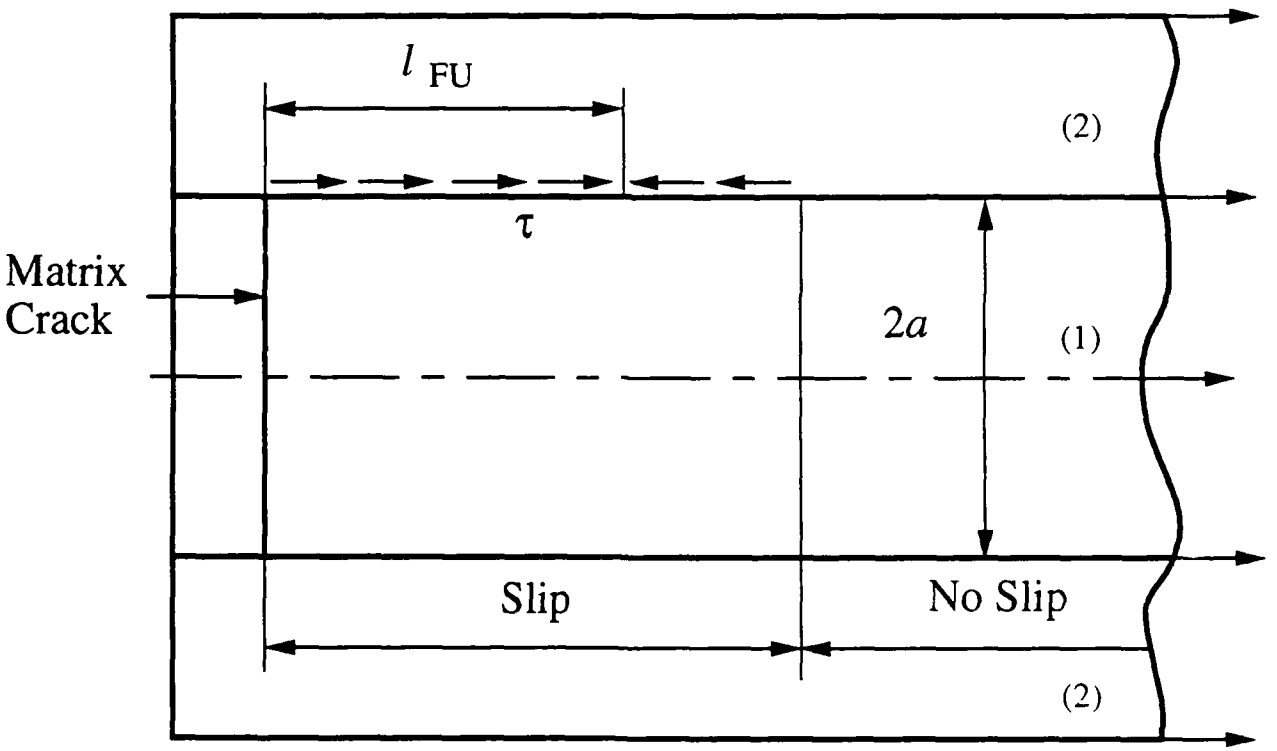

Figure 3b

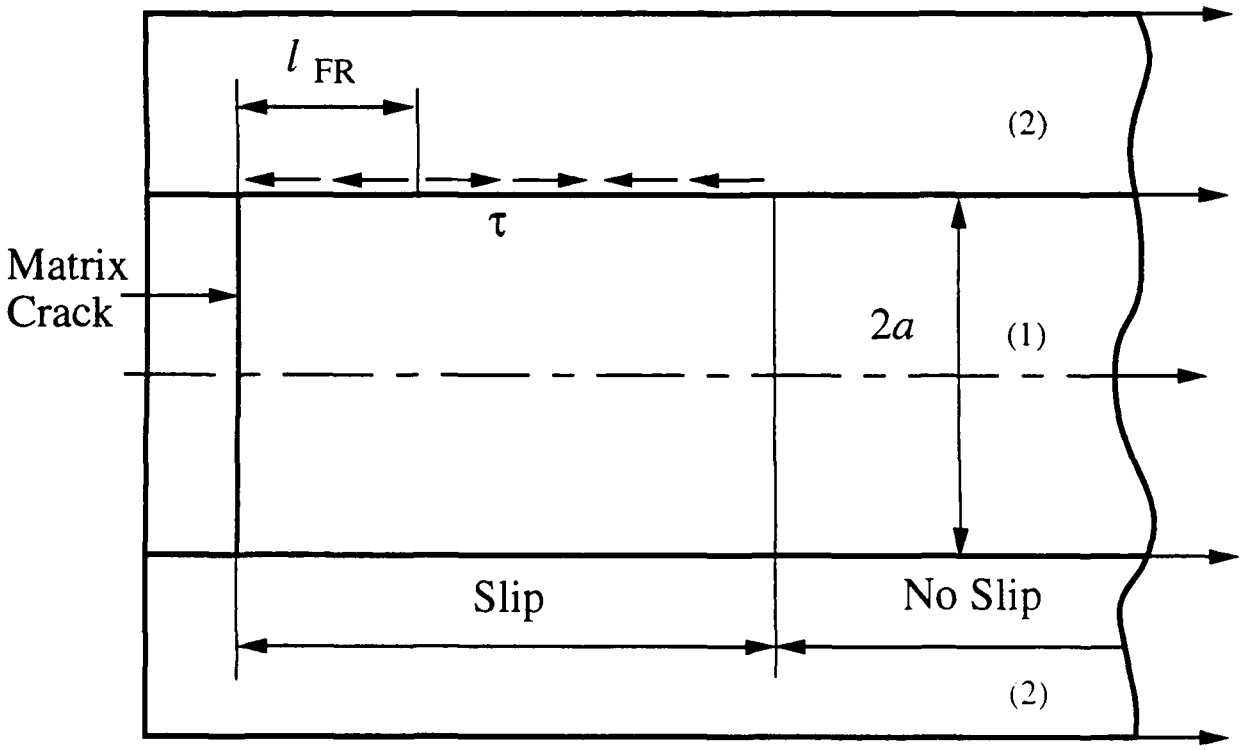

Figure 3c

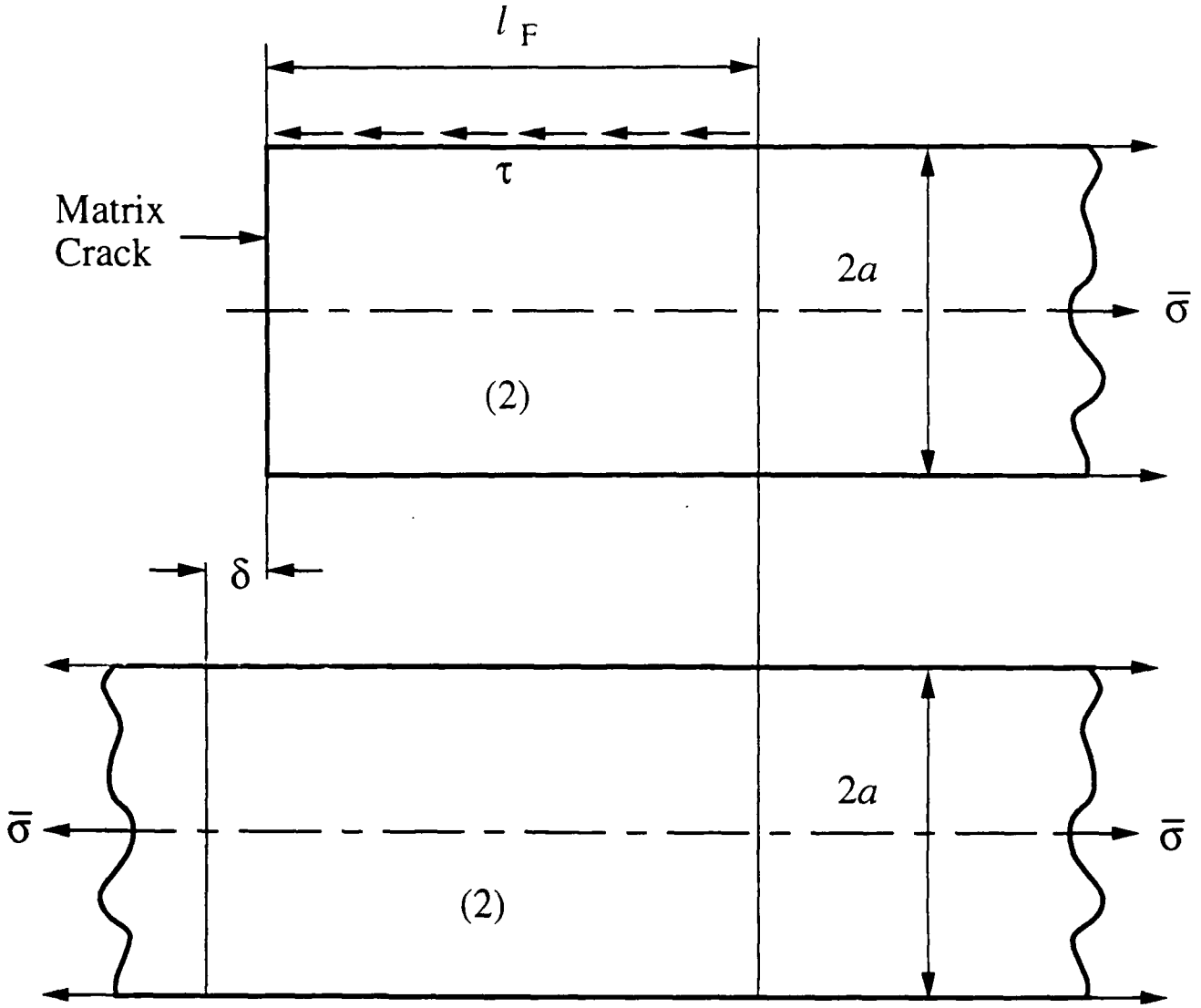

Figure 4

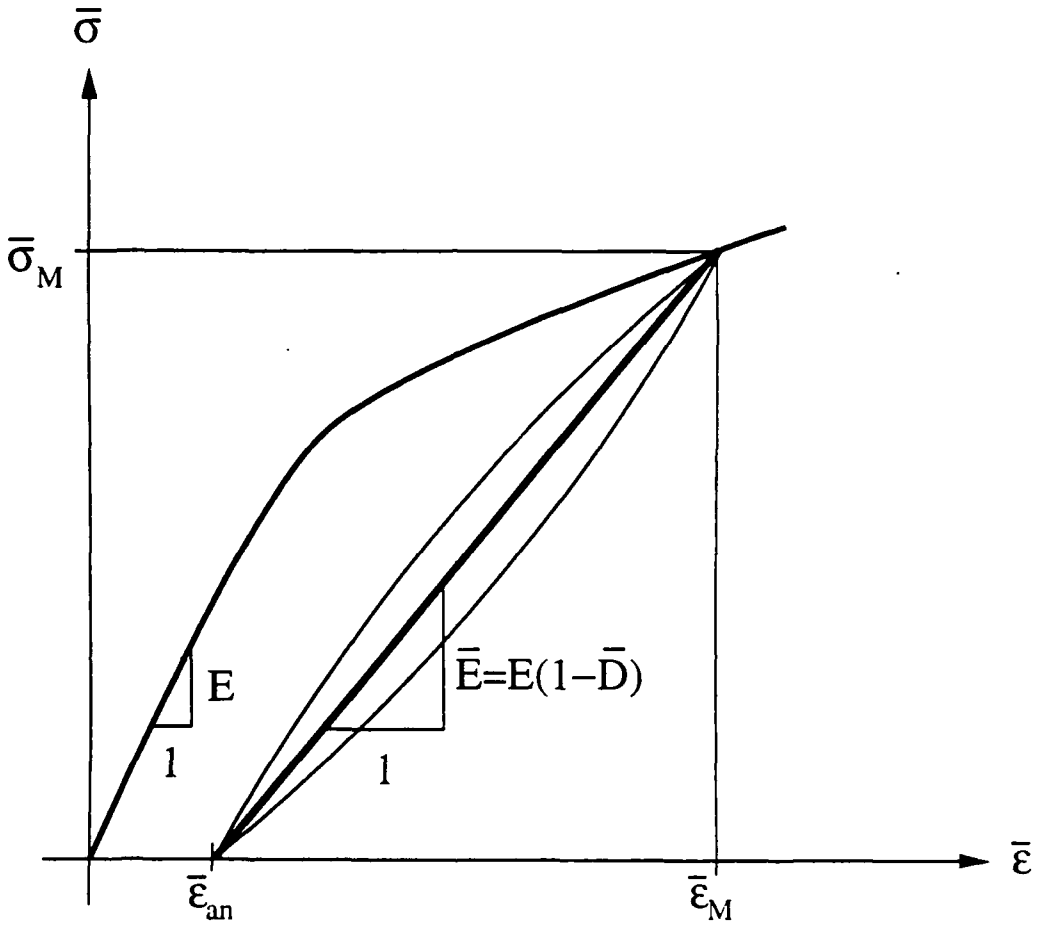
$\bar{\sigma}$
$\bar{\sigma}_M$
E
1
$\bar{E}=E(1-\bar{D})$
1
$\bar{\varepsilon}$
$\bar{\varepsilon}_{an}$
$\bar{\varepsilon}_M$

Figure 5

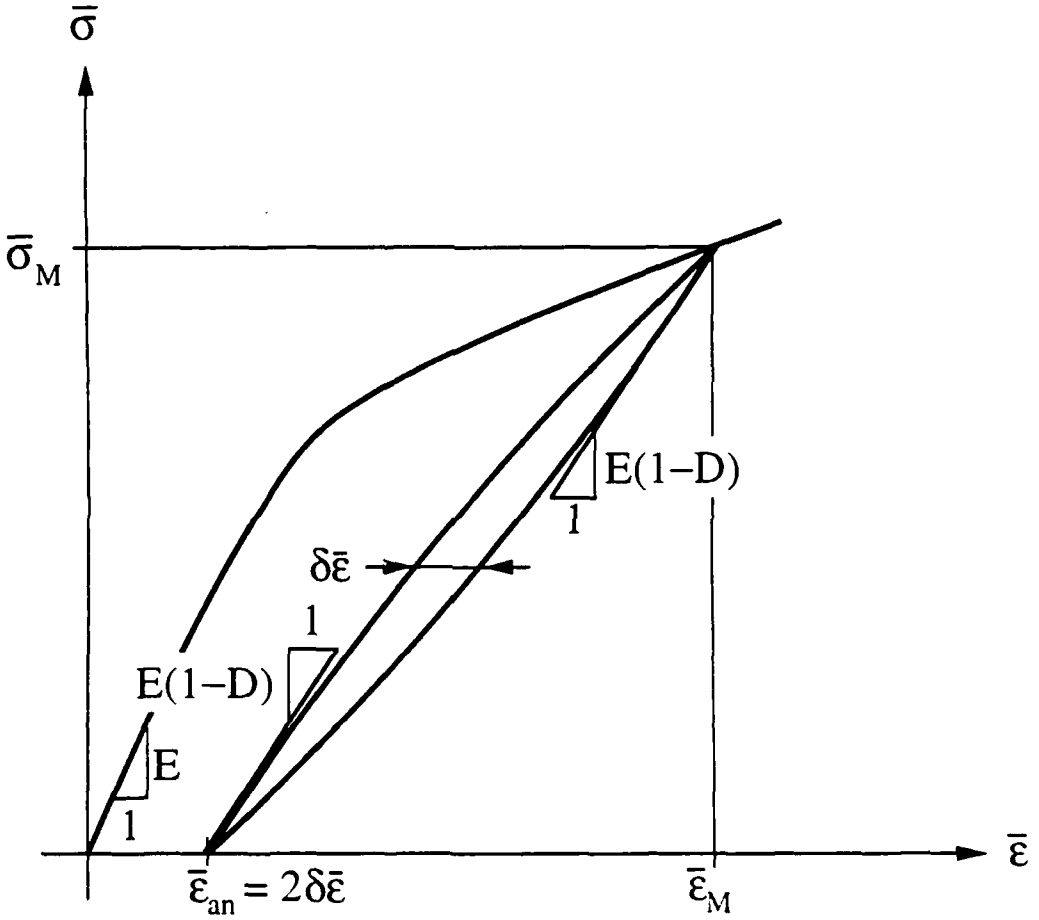
$\bar{\sigma}$
$\bar{\sigma}_M$
E(1−D)
1
$\delta\bar{\varepsilon}$
1
E(1−D)
E
1
$\bar{\varepsilon}_{an} = 2\delta\bar{\varepsilon}$
$\bar{\varepsilon}_M$
$\bar{\varepsilon}$

Figure 6

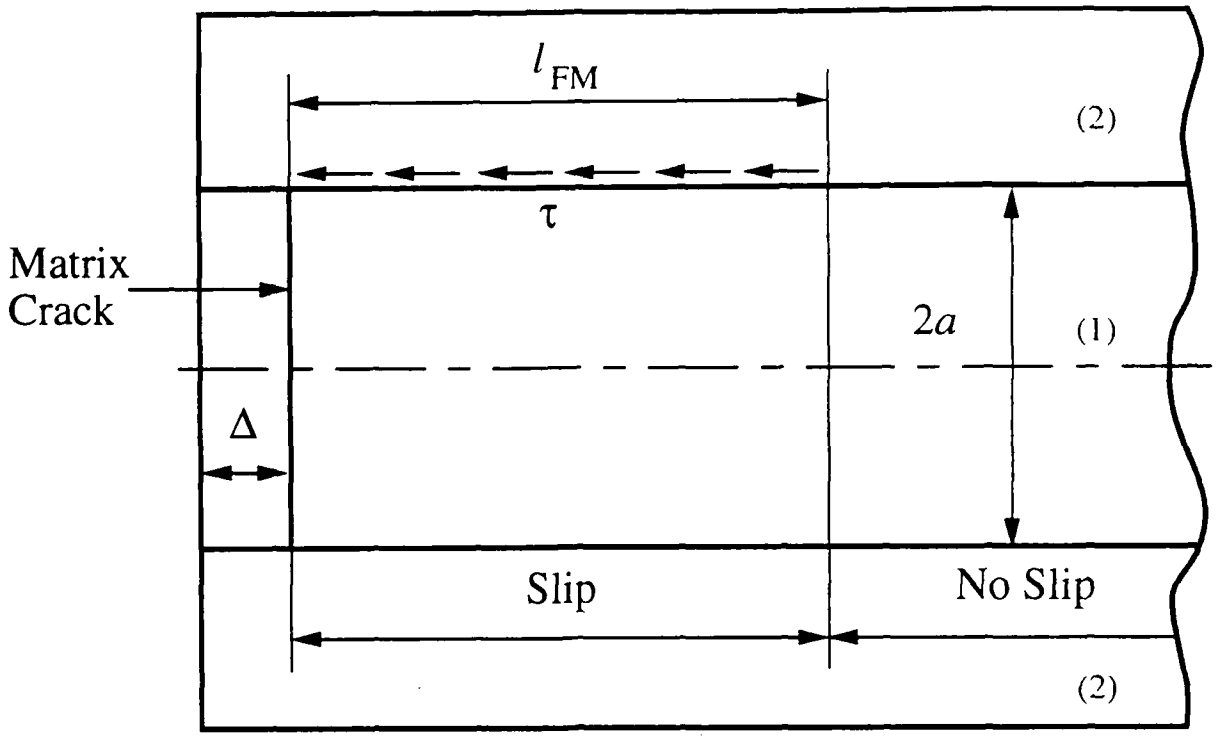
l_{FM}
(2)
τ
Matrix
Crack
2a
(1)
Δ
Slip
No Slip
(2)

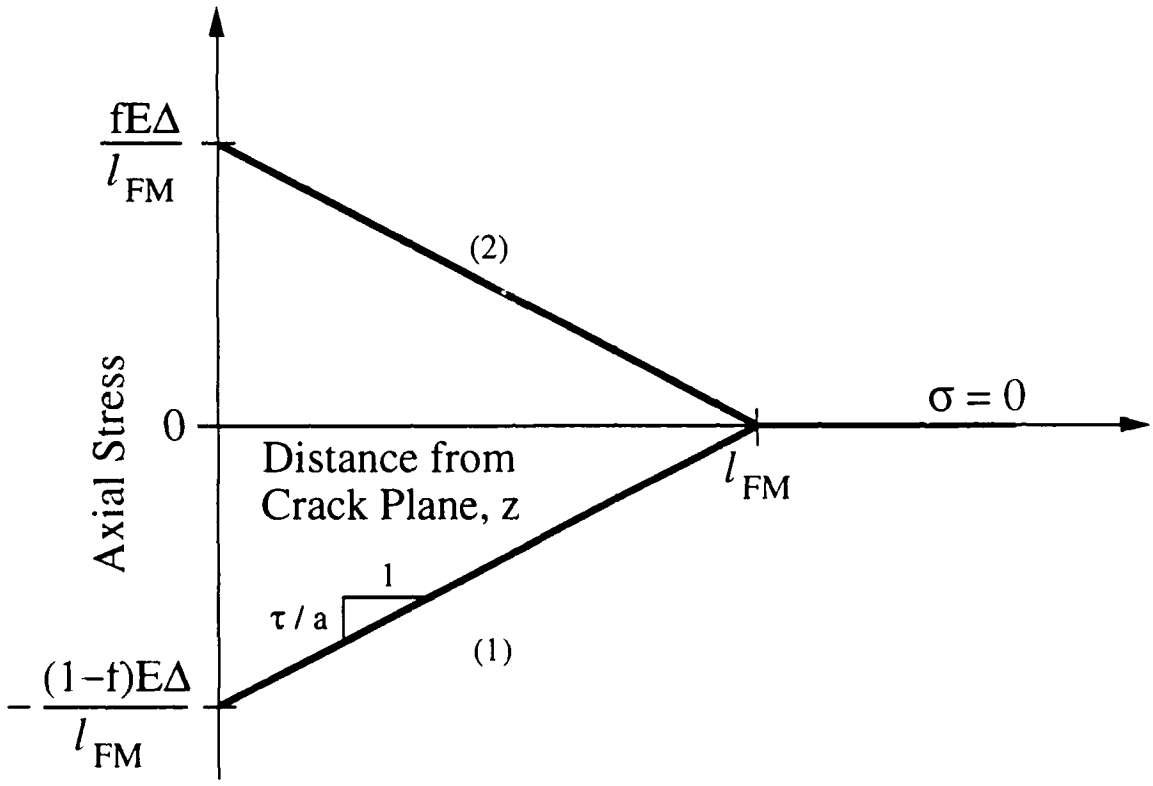
fEΔ / l_{FM}
(2)
Axial Stress
0
σ = 0
Distance from
Crack Plane, z
l_{FM}
1
τ / a
(1)
−(1−f)EΔ / l_{FM}

Figure 7

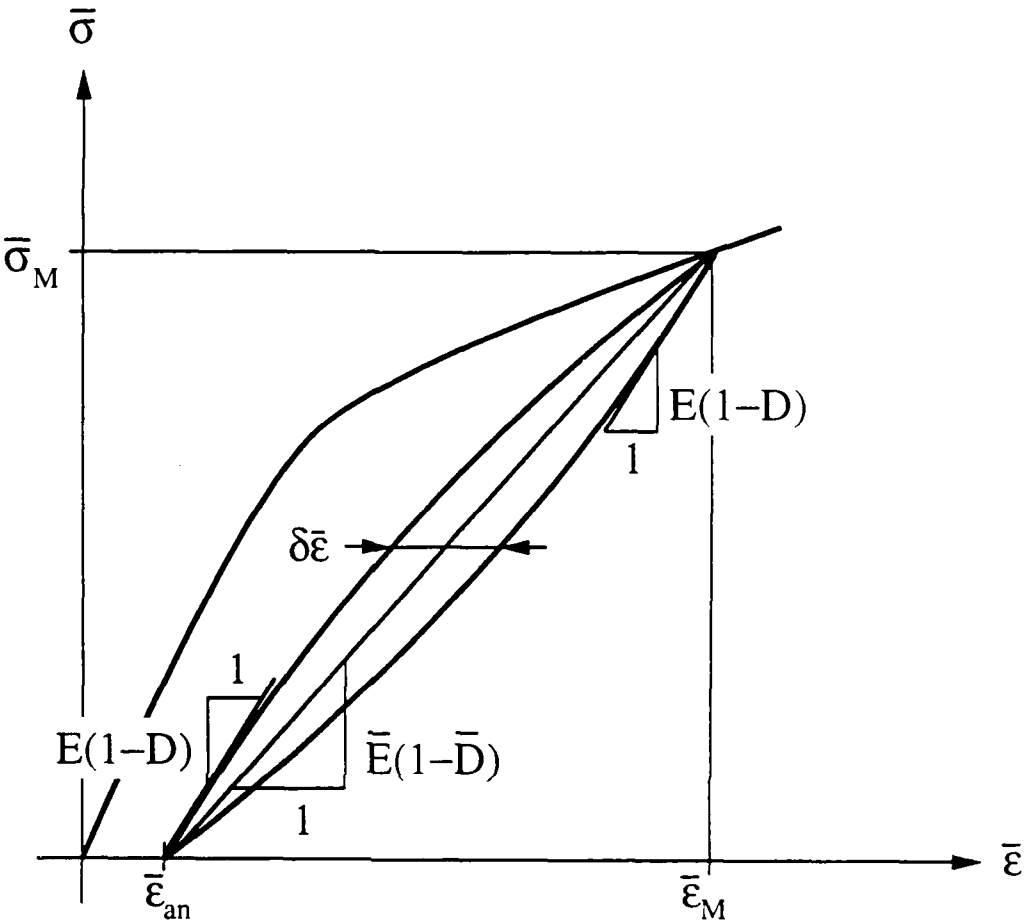
$\bar{\sigma}$
$\bar{\sigma}_M$
E(1−D)
1
$\delta\bar{\varepsilon}$
1
E(1−D)
$\bar{E}(1-\bar{D})$
1
$\bar{\varepsilon}$
$\bar{\varepsilon}_{an}$
$\bar{\varepsilon}_M$

Figure 8

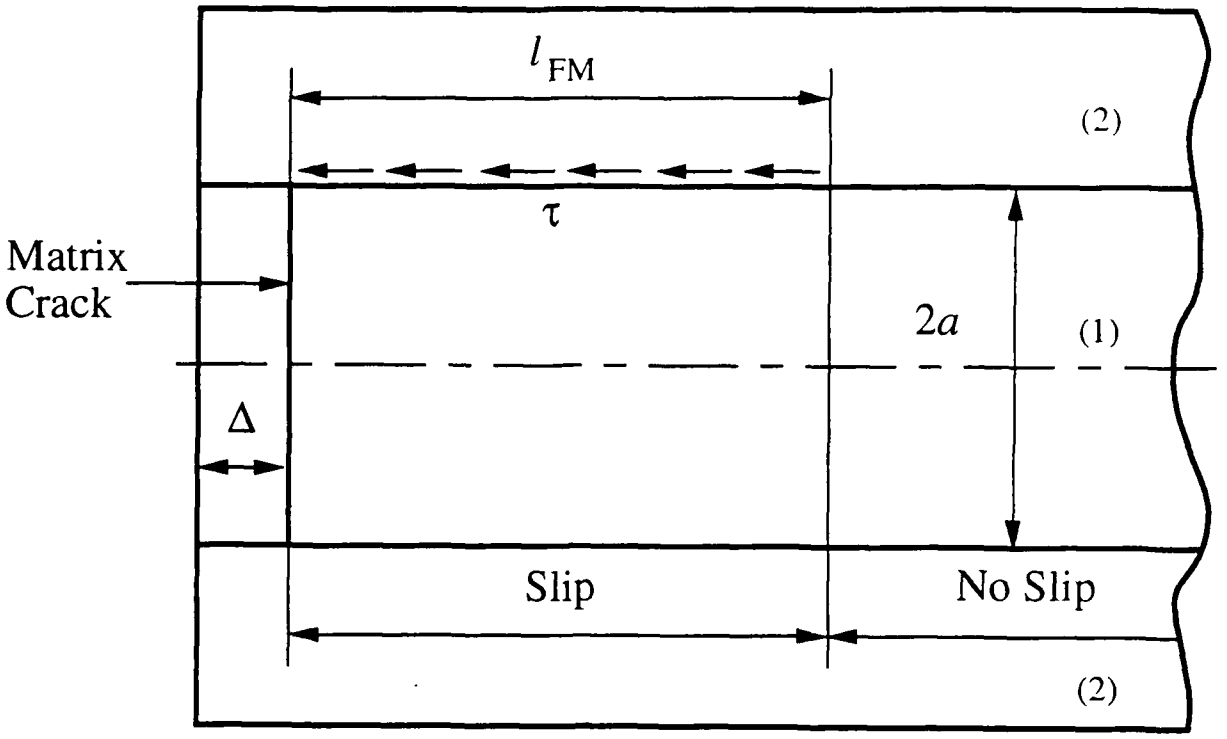
l_{FM}
(2)
τ
Matrix
Crack
2a
(1)
Δ
Slip
No Slip
(2)

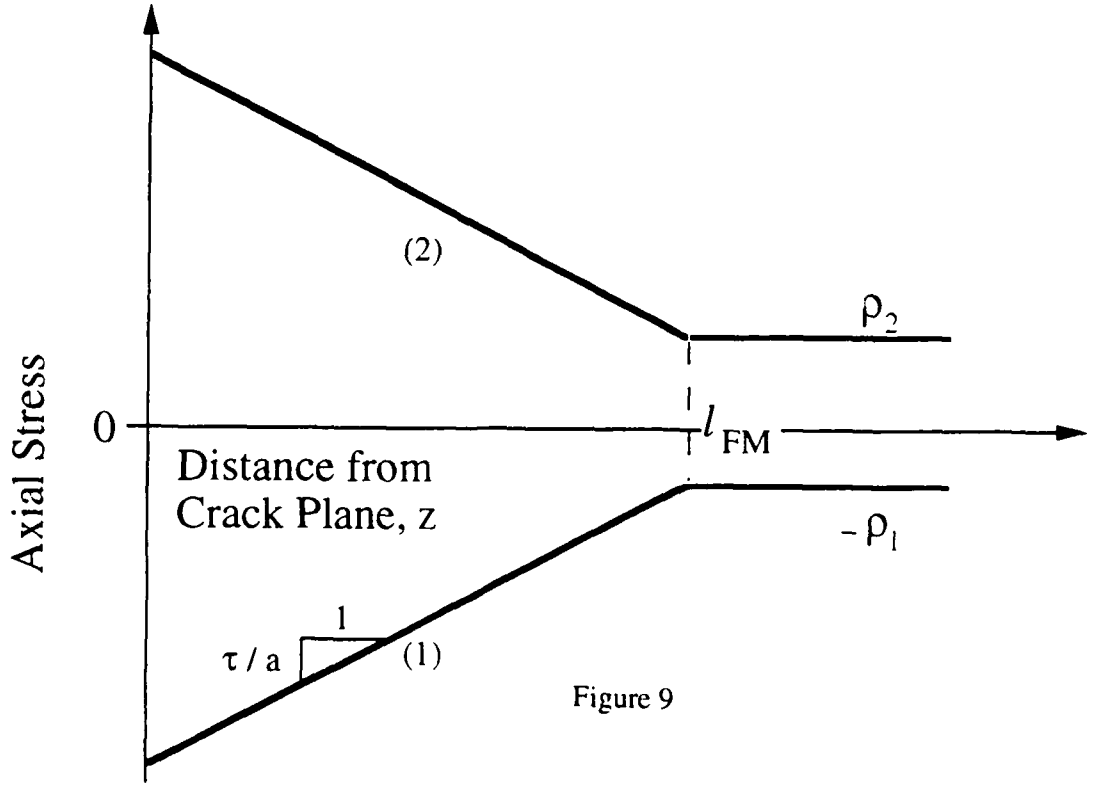
(2)
ρ_2
Axial Stress
0
l_{FM}
Distance from
Crack Plane, z
$-\rho_1$
1
τ / a
(1)

Figure 9

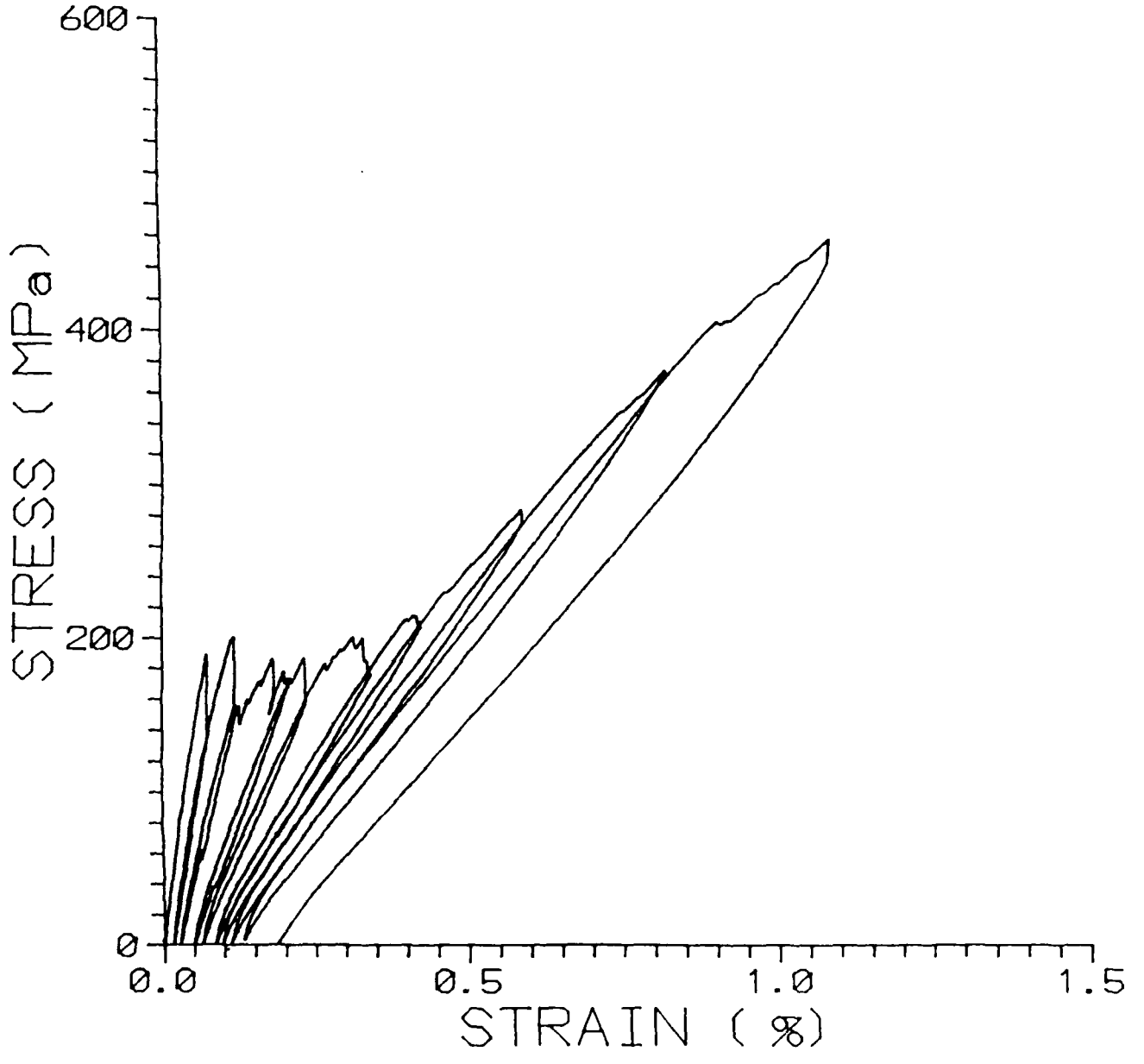

Figure 10

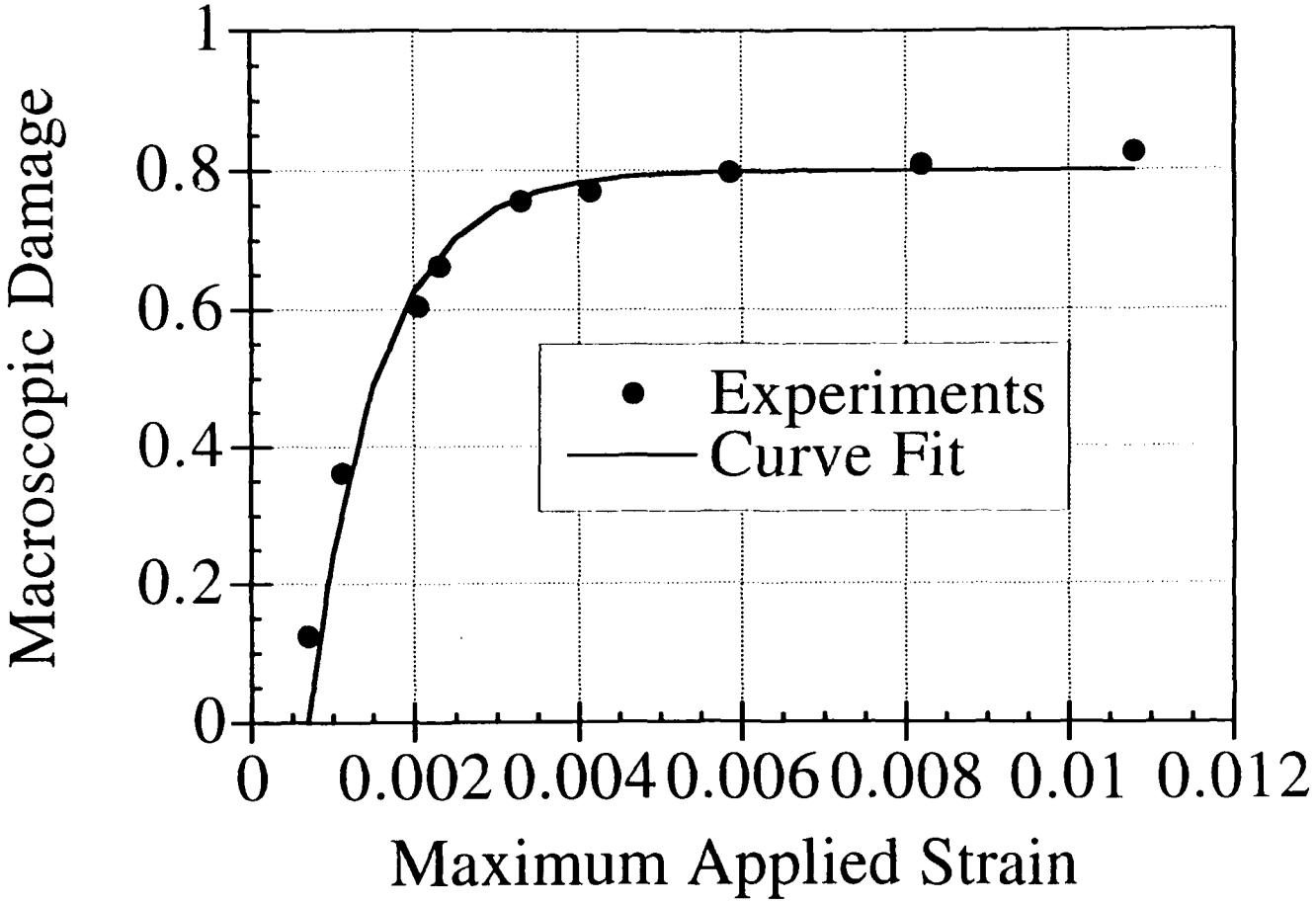
Macroscopic Damage
1
0.8
0.6
0.4
0.2
0
0
0.002
0.004
0.006
0.008
0.01
0.012
Maximum Applied Strain
Experiments
Curve Fit

Figure 11

Anelastic Strain
0.002
0.001
0.001
0.0008
0.0006
0.0004
0.0002
0
0
0.002
0.004
0.006
0.008
0.01
0.012
Maximum Applied Strain
Experiments
Curve Fit

Figure 12

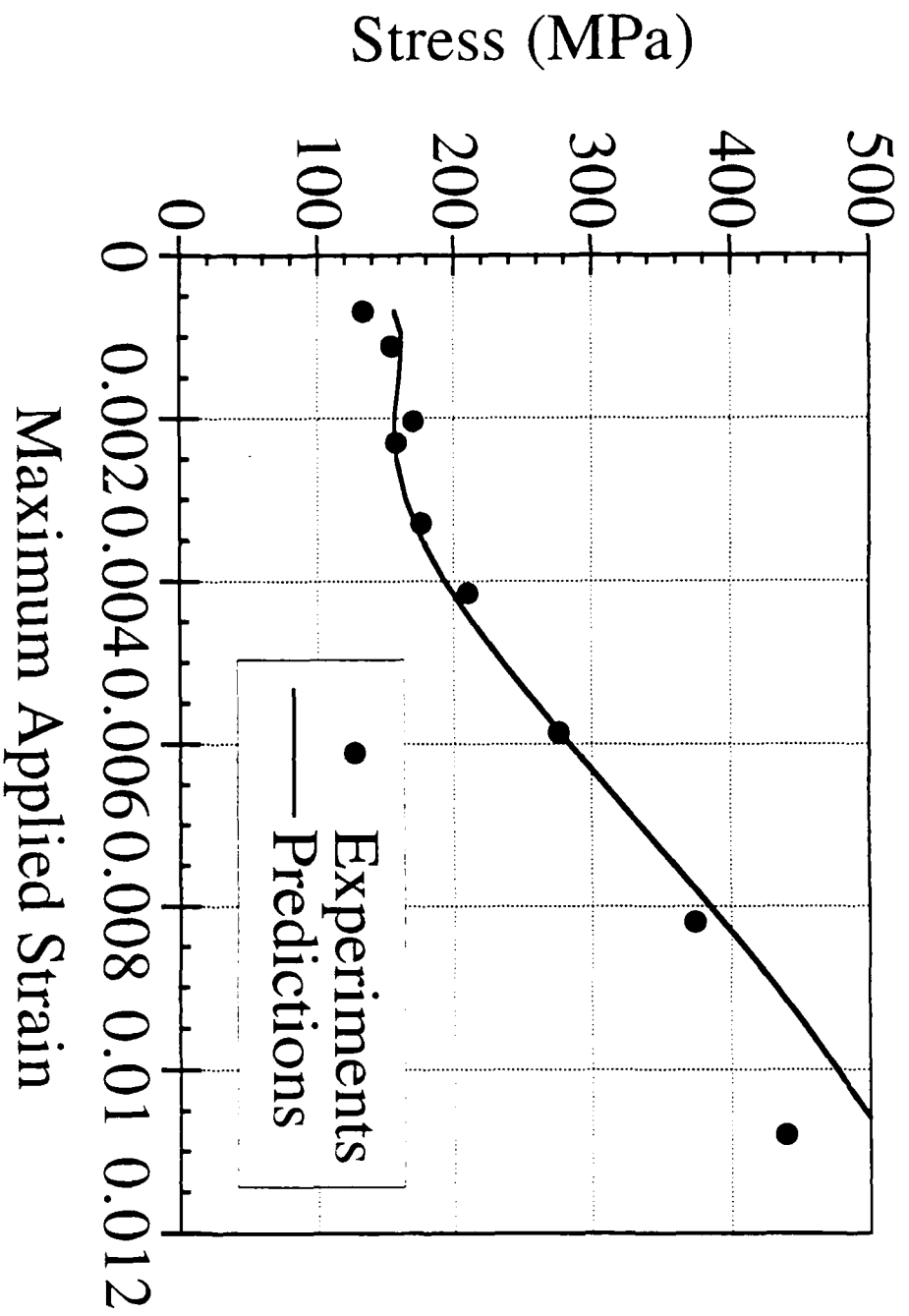
Stress (MPa)
500
400
300
200
100
0
0
0.002
0.004
0.006
0.008
0.01
0.012
Maximum Applied Strain
Experiments
Predictions

Figure 13

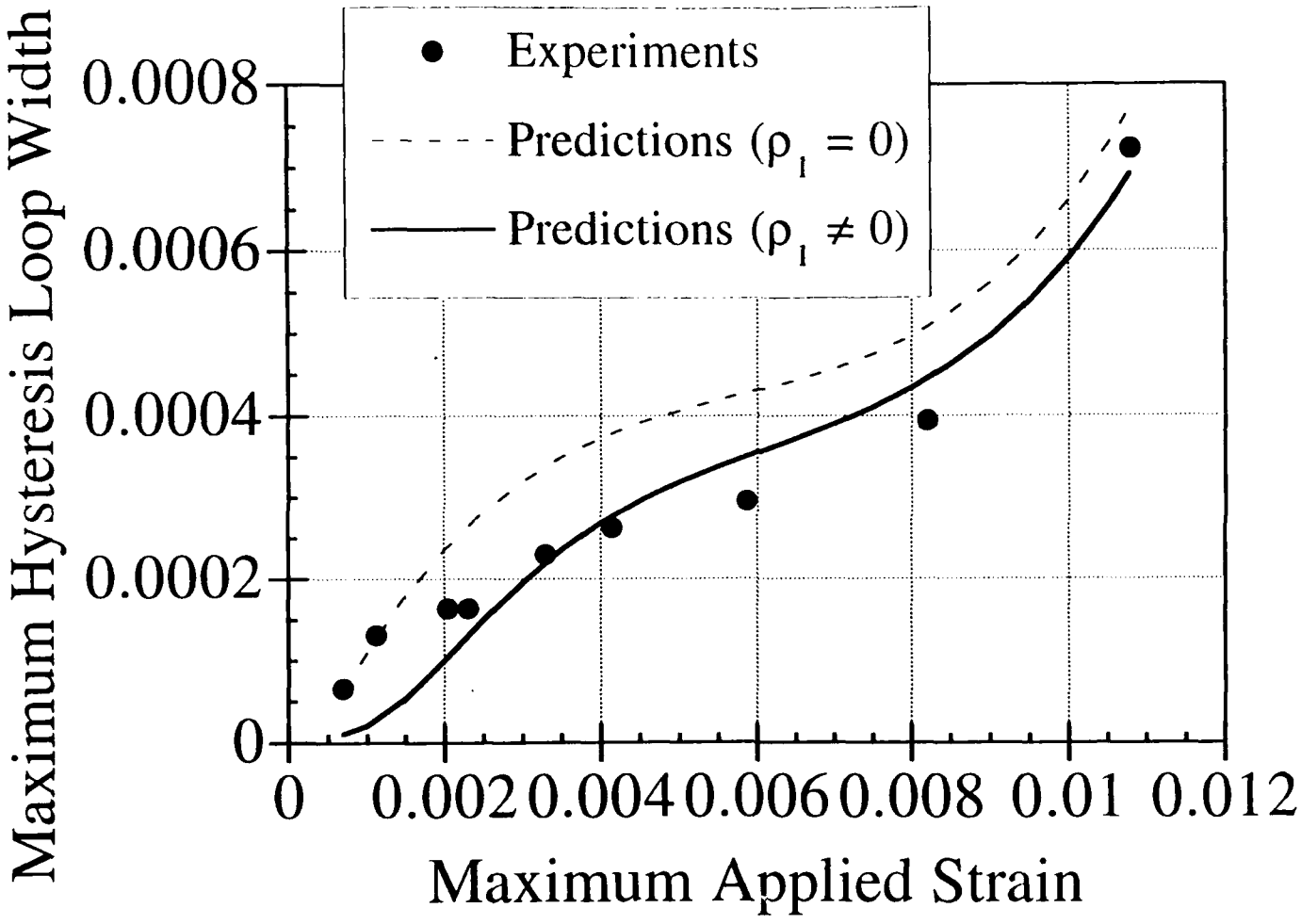
Experiments
Predictions ($\rho_1 = 0$)
Predictions ($\rho_1 \neq 0$)
Maximum Hysteresis Loop Width
0.0008
0.0006
0.0004
0.0002
0
0
0.002
0.004
0.006
0.008
0.01
0.012
Maximum Applied Strain

Figure 14

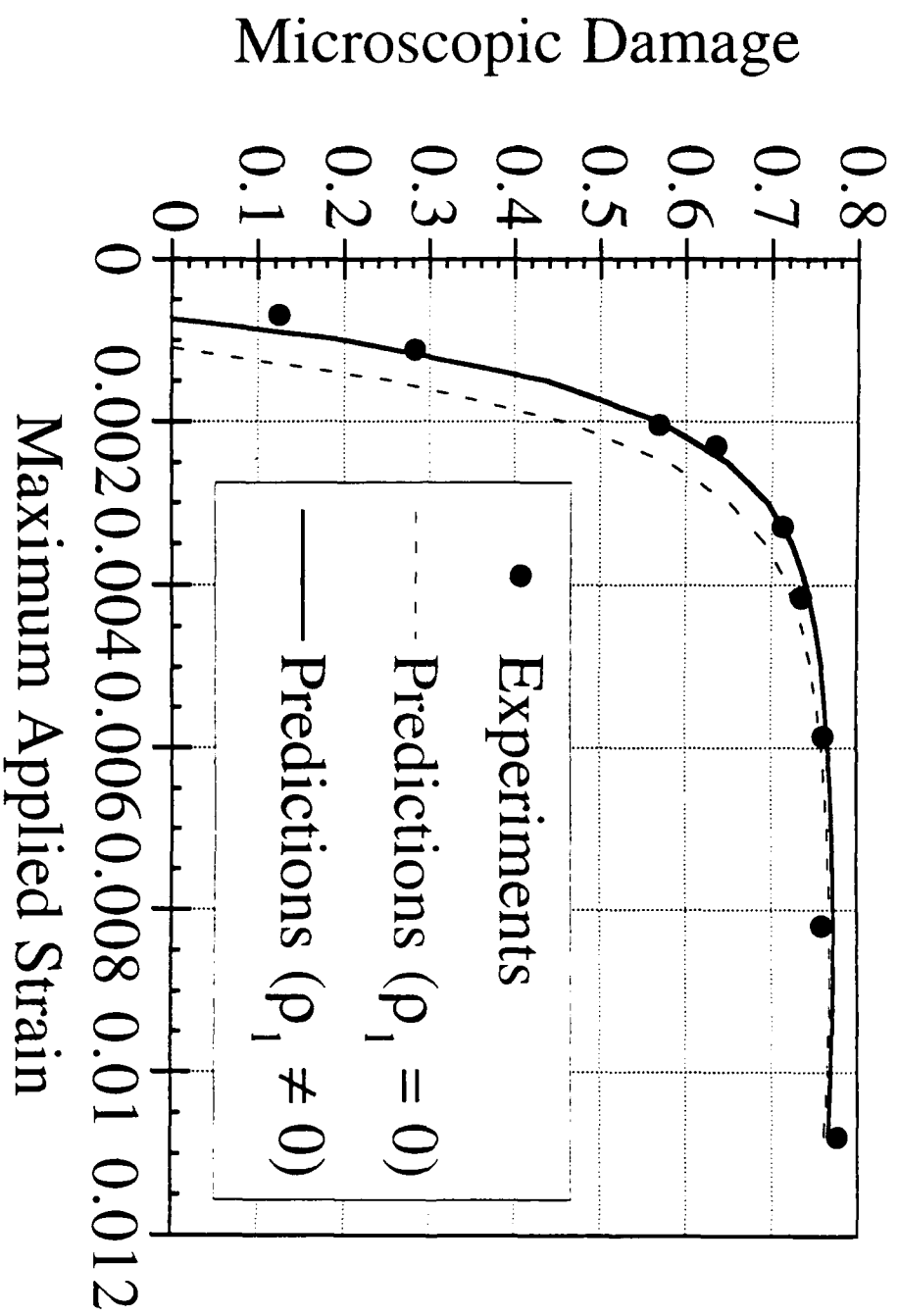
Microscopic Damage
0
0.1
0.2
0.3
0.4
0.5
0.6
0.7
0.8
0
0.002
0.004
0.006
0.008
0.01
0.012
Maximum Applied Strain
Experiments
Predictions ($\rho_1 = 0$)
Predictions ($\rho_1 \neq 0$)

Figure 15

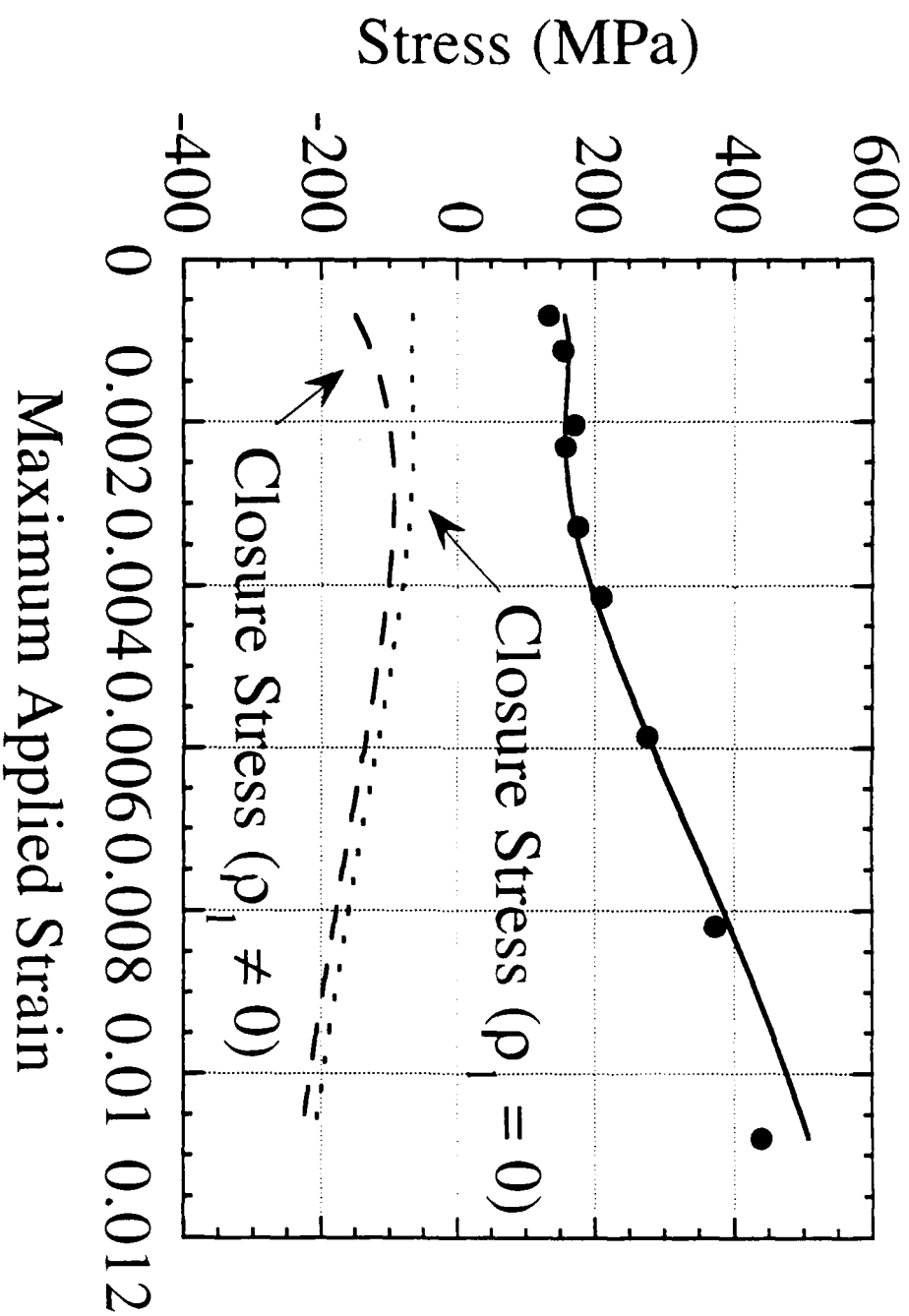
Stress (MPa)
600
400
200
0
-200
-400
0
0.002
0.004
0.006
0.008
0.01
0.012
Maximum Applied Strain
Closure Stress ($\rho_1 = 0$)
Closure Stress ($\rho_1 \neq 0$)

Figure 16

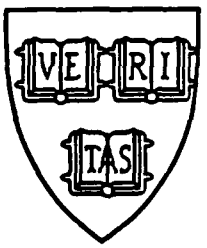

MECH-218

MATRIX CRACKING OF CROSS-PLY CERAMIC COMPOSITES

Z. Cedric Xia and John W. Hutchinson

Division of Applied Sciences
HARVARD UNIVERSITY
Cambridge, Massachusetts 02138

September 1993

MATRIX CRACKING OF CROSS-PLY CERAMIC COMPOSITES

Z. Cedric Xia and John W. Hutchinson
Division of Applied Sciences
Harvard University
Cambridge, MA. U.S.A.

ABSTRACT

A micromechanics study is presented of the matrix cracking behavior of laminated, fiber-reinforced ceramic cross-ply composites when subject to tensile stressing parallel to fibers in the 0^o plies. Cracks extending across the 90^o plies are assumed to exist, having developed at relatively low tensile stresses by the tunnel cracking mechanism. The problem addressed in this study is the subsequent extension of these initial cracks into and across the 0^o plies. Of special interest is the relation between the stress level at which the matrix cracks are able to extend all the way through the 0^o plies and the well known matrix cracking stress for steady-state crack extension through a uni-directional fiber-reinforced composite. Depending on the initial crack distribution in the 90^o plies, this stress level can be as large as the uni-directional matrix cracking stress or it can be as low as about one half that value. The cracking process involves a competition between crack bridging by the fibers in the 0^o plies and interaction among multiple cracks. Crack bridging is modeled by a line-spring formulation where the nonlinear springs characterize the sliding resistance between fibers and matrix. Crack interaction is modeled by two representative doubly periodic crack patterns, one with collinear arrays and the other with staggered arrays. Material heterogeneity and anisotropy are addressed, and it is shown that a homogeneous, isotropic average approximation can be employed. In addition to conditions for matrix cracking, the study provides results which enable the tensile stress-strain behavior of the cross-ply to be predicted, and it provides estimates of the maximum stress concentration in the bridging fibers. Residual stress effects are included.

Notation (Partial listing)

a	half crack length
c_f, c_m	fiber and matrix volume concentration ($c_f+c_m=1$)

t	half ply thickness
A	orthotropy factor
E_f, E_m	Young's moduli of fibers and matrix
$\bar{E}$, $\bar{E}_{sec}$	average Young's modulus of plane strain, secant modulus of the cracked composite
L	half crack spacing
R	fiber radius
β	a material parameter (defined in Eq. (7))
ε	total tensile strain
$\Delta\varepsilon$	extra tensile strain (inelastic strain due to cracking)
σ_f	tensile stress in bridging fibers
σ_p	largest stress a composite can sustain before the matrix crack is fully extended
σ_R	residual stress
τ	fiber/matrix sliding shear resistance
Γ_m	critical energy release rate of the matrix
E_L, ν_L, μ_L	longitudinal Young's modulus, Poisson's ratio and shear modulus of a single ply
E_T, ν_T, μ_T	transverse Young's modulus, Poisson's ratio and shear modulus of a single ply

1. Introduction

The process by which a fiber-reinforced cross-ply ceramic composite is damaged and eventually fails under tension is very complex. When the tensile stress is applied along one of the fiber directions, one often observes an overall stress-strain response as schematically illustrated in Fig. 1. After an initial elastic response, the damage starts with matrix cracking in the 90^o plies. These cracks spread as 3D tunneling cracks from small flaws located in the matrix of the 90^o plies, and generally arrest at the interfaces between $0^o/90^o$ plies before spreading into the adjacent 0^o plies [1]. With further increase of the applied stress, more tunneling cracks develop in the 90^o plies until they saturate. At about this stage, the fully tunneled cracks begin to extend into the adjacent 0^o plies without fiber failure and extend until they overlap. The matrix cracks eventually coalesce at even higher stress with the matrix of the laminate being fully cracked. The intact fibers in the 0^o plies, which are now carrying all the load, fail at the fiber bundle fracture stress $c_fS/2$.

The matrix cracking in the 90^o plies has been a subject of research efforts for the past two decades. While most of the work in this area deals with the effect of matrix cracking on the degradation of the stiffness of the laminate (for example, as reviewed in [2]), relatively less has been done to relate the full details of the overall stress-strain response to the constituent properties of the laminate. An attempt along this direction was recently made in [3] where the concept of steady-state tunneling cracks was employed to model matrix cracking as a three-dimensional process. The minimum tensile stress required for the onset of tunneling cracks (the start of nonlinearity in Fig. 1) was predicted. The evolution of the crack density in the 90^o plies was related to the applied stress, and the overall stress-strain behavior (from onset to saturation of the tunneling cracks in the 90^o plies) was obtained as a function of the basic geometry of the composite, the toughness of the matrix, and the residual stress between plies.

The next logical step is to investigate subsequent damage where matrix cracks spread into the neighboring 0^o plies. This is an unavoidable step if progress is to be made in the effort to understand the complete tensile behavior of a laminated cross-ply composite. Several new considerations come into play. Firstly, the matrix cracks are partially bridged by intact fibers in the 0^o plies. The fiber-bridged length of the crack is comparable to the unbridged length (the 90^o ply thickness), and small scale bridging (SSB) does not apply. To fully solve this problem, a rigorous large scale bridging (LSB) analysis is required. Recent research efforts on this general topic can be found in [4, 5], where the main concern centered on the tensile strength of unidirectional fiber-reinforced ceramic composites containing a single crack-like flaw. Secondly, interaction among multiple cracks plays an important, and sometimes even critical, role in the crack growth process. The modeling of this process under large scale bridging conditions has not been addressed. Lastly, the laminated composites are anisotropic and heterogeneous in nature. The importance of material anisotropy and heterogeneity on the fracture performance of such laminates must also be addressed.

To provide some quantitative feel for the damage sequence of a cross-ply laminate under tensile loading, we take as an example the CAS/SiC laminate system used in the experiments in [1]. It consists of Nicalon fibers in a calcium-alumino-silicate matrix in a cross-ply configuration.

The constituent properties are

$$E_m=97GPa,\ E_f=200GPa,\ c_f=0.37,\ R=7.5\mu m,\ \Gamma_m=25J/m^2,\ \tau=20MPa$$

and the half ply thickness t is 90μm. Two types of residual stresses exist in the laminate, introduced during manufacturing process because of mismatch of the thermal properties of fibers and matrix. One is the overall residual stress between different plies which was measured to be approximately 30MPa in tension perpendicular to the fibers in the 90° plies, and about same amount of compression in the 0° plies acting parallel to the fibers. At a smaller scale within each layer, is the residual stress between fibers and matrix which has both an axial and radial component. The measured residual stress in matrix in the axial direction is $\sigma_R^m=100 \sim 120MPa$. Based on the above information, we can evaluate several important stress quantities, which are also indicated on the ordinate of Fig.1:

(1). σ_{onset}, the stress for onset of tunneling cracking (the formula is given in [3]). This stress sets the condition under which matrix cracking first can occur in the 90° plies. Accurate prediction of σ_{onset} requires knowledge of the toughness of the 90° plies in the tunneling mode. An estimated value of σ_{onset} for the above CAS/SiC system is around 80MPa. Since there exists a residual tension of 30MPa in the 90° plies, the net applied stress σ needed for the onset of tunneling cracking will be around 50MPa [3].

(2). σ_0, a stress quantity measuring the condition at which plane strain cracks in the 90° plies begin to spread into the neighboring 0° plies. It is one of the basic parameters in this study, and it will be introduced in more detail later in the development. The calculated σ_0 from Eq. (6) (see below) is 88MPa. The residual tension in the 90° plies will lower the net applied stress to about 58MPa.

(3). σ_{mc}, the steady-state matrix cracking stress for a *uni-directional composite* [6, 7]. It is the other basic stress parameter used in this study. It depends on the matrix toughness and the bridging capabilities of the fibers. It is given by Eq. (5) in next section and is calculated to be 323MPa. Since there exists a residual tension in matrix in the amount of $\sigma_R^m=100 \sim 120MPa$, the critical applied stress needed to advance the steady-state matrix crack will be in the range 156 ~ 184MPa. This range of the value is consistent with the experimentally measured range of 140 ~

160MPa in [1]. One of the main objectives of this paper is to determine the relation between σ_{mc} for the uni-directional composite and the stress at which matrix cracks first cross the 0^o plies in the cross ply composite.

The above three stress values support the illustration in Fig. 1 of the damage process in a cross-ply laminate. Similar behavior was reported in [1] based on their experimental observations.

Thus, the aim of the present work is a micromechanics investigation of the tensile behavior of a laminated fiber-reinforced cross-ply ceramic composite with matrix cracks in the 90^o plies penetrating into the adjacent 0^o plies. As emphasized, it should be regarded as a continuation of the work of [3] on tunnel cracking in the 90^o plies. Here, the main focus will be on the constraining effect of bridging fibers and the interaction among multiple cracks during the crack growth process. The overall tensile behavior of such laminates will be determined. We first examine the problem of material anisotropy and heterogeneity, and demonstrate that anisotropy can be accounted for in a simple manner such that accurate approximate solutions can be then be generated from results for a homogeneous, isotropic material. The effect of bridging fibers is modeled as distribution of nonlinear springs obeying a traction-separation law characterizing fibers slipping relative to the matrix under a constant friction stress τ. Two doubly periodic crack patterns are analyzed in order to understand interactions among cracks, one, a collinear pattern (Fig. 2a), and the other, a staggered pattern (Fig. 2b). The collinear pattern models the extreme situation where stress intensity enhancement due to interactions is maximal. The staggered pattern represents perhaps a more realistic situation in which overlapping of matrix cracks in the 0^o plies will occur. This type of pattern, opposed to the collinear pattern, models the more or less random development expected for the tunnel cracks in the 90^o plies. Also investigated in this work is the stress concentration in the bridging fibers. This is an important issue because failure of bridging fibers constitutes the ultimate failure mechanism for these composites.

The paper is organized as follows. We begin with a general description of the problem including the fiber bridging model, and go on to demonstrate the validity of the scheme for accounting for the laminate anisotropy using results from plane strain isotropy. The body of paper is devoted to the presentation and discussion of the crack growth process and overall tensile

behavior for each of the two crack patterns. The applied tensile stress and extra strain due to the crack growth process are presented for various crack densities, together with the stress concentration in bridging fibers. The role of residual stresses introduced during the manufacturing process is also illustrated and discussed. The mathematical formulation and numerical solution procedure are detailed in the Appendices. A numerical example for the above mentioned CAS/SiC laminate is given in the last section as an illustration. The predicted secant modulus as a function of the applied stress is compared with experiment data reported in [1].

2. Characterization of the Problem

2.1. An Approximation accounting for the Anisotropy of the Laminate

Previous studies usually take a uni-directional fiber-reinforced composite to be transversely isotropic about the fiber directions. With fibers aligned with the 1-axis, the constitutive relation for an undamaged ply is

$$\begin{aligned}
\varepsilon_{11} &= \frac{1}{E_L}\sigma_{11} - \frac{\nu_L}{E_L}(\sigma_{22}+\sigma_{33}) \\
\varepsilon_{22} &= -\frac{\nu_L}{E_L}\sigma_{11} + \frac{1}{E_T}\sigma_{22} - \frac{\nu_T}{E_T}\sigma_{33} \\
\varepsilon_{33} &= -\frac{\nu_L}{E_L}\sigma_{11} - \frac{\nu_T}{E_T}\sigma_{22} + \frac{1}{E_T}\sigma_{33} \\
\varepsilon_{23} &= \frac{1}{2\mu_L}\sigma_{23} \quad \varepsilon_{13} = \frac{1}{2\mu_T}\sigma_{13} \quad \varepsilon_{12} = \frac{1}{2\mu_T}\sigma_{12}
\end{aligned} \tag{1}$$

where the subscript L stands for longitudinal properties and the subscript T stands for transverse properties. All the elastic properties can be calculated either on the basis of the Hill [6] self-consistent model or from other models.

The anisotropic effect for a unidirectional fiber-reinforced composite can be characterized by an orthotropy factor [5]. However, it is less clear how one should account for the heterogeneous nature of a cross-ply associated with the two orientations of layers. For most ceramic composites, the ratio E_f/E_m of the fiber modulus to the ceramic matrix modulus ranges generally from 1 to 5. To obtain some insight into the role of material anisotropy and heterogeneity, finite element analyses of single and multiple cracking have been performed for several typical values of E_f/E_m

and fiber volume fractions c_f of a laminated composite. Two plane strain crack configurations have been analyzed as shown in the inserts of Fig. 3a and 3b, with crack tips located in the 0^o plies. No bridging tractions are applied. For each geometrical configuration and loading, two sets of material properties are adopted for the calculations. For the first set, the stress-strain behavior of each of the plies is taken to be elastically orthotropic obeying (1), with due regard for the two orientations. For the second set, the composite is approximated to be homogeneous and isotropic, with an overall Young's modulus E and Poisson's ratio ν given by

$$E = \frac{\frac{1}{4}(1+\frac{E_L}{E_T})^2 - \nu_L^2}{\frac{1}{2}(1+\frac{E_L}{E_T})(\frac{1}{E_T} - \frac{\nu_L^2}{E_L})}$$

$$\nu = \frac{2\nu_L}{1+\frac{E_L}{E_T}} \qquad (2)$$

$$\bar{E} = \frac{E}{1-\nu^2}$$

As introduced in [3], E is the uniaxial modulus of the composite in a direction parallel to either set of fibers, while ν is the Poisson's ratio associated with the out-of-plane strain component. Thus, $\bar{E}$, defined above, is the modulus governing plane strain tension parallel to the fibers in the 0^o plies (with the out-of-plane strain imposed to be zero). Since the results of interest here are quite insensitive to the value chosen for the in-plane Poisson's ratio, we have also used the value ν given above as the in-plane ratio.

The calculated ratios of mode I stress intensity factors from the two calculations, K_I^{iso}/K_I, for the single crack problem are plotted in Fig. 3a, where the geometrical configuration is shown. The Poisson's ratios of both fibers and matrix are taken to be 0.2 and the fiber volume concentration is 0.5. The deviation from unity reflects the error of the isotropic average approximation for K to that obtained from the anisotropic, heterogeneous model. Similar results for a doubly periodic crack pattern are shown in Fig. 3b, where ratios of both stress intensity factors and compliances are shown. As indicated in Fig. 3a and 3b, the errors introduced by the isotropic average approximation to the stress intensity factor and compliance for all practical ranges of E_f/E_m are within 8%. As cracks become longer in the 0^o plies, it is seen that the errors are further reduced.

This indicates that the isotropic average approximation with elastic properties defined in (2) involves little error for the study of fracture performance with cracks spanning both the 90^o and the 0^o plies. The major advantage of the isotropic average approximation is that it permits one to use analytical techniques and results to set up the computational problems. In this work we have used integral equation methods which employ kernels derived using complex variable methods of elasticity.

The generally adopted criterion for the growth of matrix cracks in the 0^o plies is that the average energy release rate along the crack front remain equal to the critical value $c_m\Gamma_m$, where Γ_m is the matrix toughness (for example, [5, 7-8]). The mode I intensity toughness, K_{Ic}, for the crack tip located in the 0^o plies is [5]

$$K_{Ic} = \sqrt{\frac{A E_L}{1-\nu_L^2}\, c_m \Gamma_m} \tag{3}$$

where A is the orthotropy factor characterizing the effect of orthotropy of the 0^o plies. This result follows from the formula given in [9] for the energy release rate of an orthotropic material in terms of stress intensity factor. The value of A for a wide range of E_f/E_m and c_f of fiber reinforced ceramic composite has been calculated and presented in [5] based on Hill's self consistent model. For all practical ceramic composites, it falls between 0.84 and 1.0.

2.2. Characterization of Bridging Fibers

As in most previous studies, the debonding energy between the fibers and the matrix is ignored and sliding between the fibers and the matrix takes place when the interfacial shear stress exceeds the friction stress τ. When slip lengths are relatively large, as is often the case for many ceramic fibrous composites, the bridging fiber stress p(x) is related to the crack opening displacement $\delta(x)$ by [10]

$$p(x) = \left\{ \frac{2E_f E_L^{\,2} c_f^{\,2} \tau}{R E_m^{\,2} c_m^{\,2}}\, \delta(x) \right\}^{\frac{1}{2}} \tag{4a}$$

If residual stresses between fibers and matrix are present, the above fiber bridging law can be easily modified by an extra term [11] such that

$$p(x) = \left\{ \frac{2E_f E_L^{\,2} c_f^{\,2} \tau}{R E_m^{\,2} c_m^{\,2}}\, \delta(x) \right\}^{\frac{1}{2}} - \frac{E_L}{E_m} \sigma_R^{\,m} \tag{4b}$$

where σ_R^m is the average residual stress parallel to the fibers in the uncracked matrix.

The matrix cracking stress σ_{mc}, defined as the tensile stress required for the steady-state propagation of a single, long matrix crack in unidirectional fibrous composites is given by [7-8]

$$\sigma_{mc} = \left\{ \frac{6E_f E_L^2 c_f^2 \tau}{R E_m^2 c_m} \Gamma_m \right\}^{\frac{1}{3}} \tag{5}$$

In the presence of residual stress, the critical applied stress needed to advance the steady-state matrix crack is given by a modification similar to that in (4b) as σ_{mc}-$(E_L/E_m)\sigma_R^m$ [8].

The remaining important stress quantity to be introduced is

$$\sigma_0 = \frac{K_{Ic}}{\sqrt{\pi t}} \tag{6}$$

where t is the half thickness of each ply. Under the isotropic average approximation for the composite, σ_0 is the remote tensile stress required for the initiation of propagation into the adjacent 0^o plies of an isolated pre-existing matrix crack in a 90^o ply. For multiple cracks such as those in Fig. 2, the stress at which the cracks will begin advancing into the 0^o plies will usually be lower than σ_0 due to crack interaction. It is worth noting that this initiation stress depends only on σ_0 and the crack configuration for the reason that the cracks are not yet bridged at this stage.

2.3. Description of the crack growth process

Now suppose the matrix cracks in the 90^o plies are fully tunneled and saturated as has been analyzed in [3]. Under further increase of applied tensile stress σ, these cracks will spread into the neighboring 0^o plies under plane strain conditions. The $0^o/90^o$ interfaces are assumed to be perfectly bonded. Neither delamination nor splitting along interfaces of the plies or the fiber/matrix occurs. The bridging fibers in the 0^o plies are assumed to remain intact throughout the crack growth process.

Consider a cross-ply laminate subject to in-plane tensile loading only. We shall analyze the two representative crack patterns, where plane strain matrix cracks have already formed in the 90^o plies, which are shown in Fig.2 and which were introduced earlier. Suppose all cracks are growing quasi-statically in the same manner, with current crack length 2a. The average tensile stress σ applied remotely is determined by imposing the condition that the mode I stress intensity factor K_I maintain the critical value K_{Ic} as defined in (3). This large scale bridging problem is

intrinsically nonlinear. It has been solved rigorously by formulation of a nonlinear singular integral equation which is solved by iteration. The logarithmic singularity of the crack opening displacement gradient at the bridging/unbridging point (*i.e.*, at the $90^o/0^o$ interface) is explicitly accounted for in the formulation. Mathematical details can be found in the Appendices.

The solution to this problem, in the absence of pre-existing residual stresses, is found to be completely determined by the crack geometry and a non-dimensional quantity $\sigma_0/(\beta\sigma_{mc})$, which encompasses information about both materials and the fiber bridging constraint. The material parameter β is given by (see Appendix A)

$$\beta = \left\{ \frac{A E_L}{\bar{E}(1-\nu_L^2)} \right\}^{\frac{1}{3}} \tag{7}$$

which arises in the isotropic average approximation. For all practical fibrous composites, β is very close to 1, and reduces to 1 if the fibers and matrix have identical elastic properties. For the CAS/SiC system discussed before, β=0.998. For a given laminated ceramic composite, $\sigma_0/(\beta\sigma_{mc})$ measures the relative compliance of the fiber bridging law. A larger value of $\sigma_0/(\beta\sigma_{mc})$ represents softer bridging, while smaller values give stronger bridging. The CAS/SiC system that Beyerle *et al* [1] used in their experiments has $\sigma_0/(\beta\sigma_{mc})$=0.27. Results will be presented for $\sigma_0/(\beta\sigma_{mc})$ in the range from 0.1 to 1.0 to cover all practical cases.

In non-dimensional form, the average tensile stress σ applied remotely during the crack growth process can be expressed as

$$\frac{\sigma}{\beta\sigma_{mc}} = F_1\left(\frac{a}{t}, \frac{\sigma_0}{\beta\sigma_{mc}}, \frac{t}{L}\right) \tag{8}$$

where a/t is the non-dimensional current crack length, and t/L is the crack density as defined in either Fig. 2a or Fig. 2b. The extra overall tensile strain $\Delta\varepsilon$ (*i.e.*, the inelastic strain), caused by the presence of the matrix cracks, takes the non-dimensional form

$$\frac{\bar{E}\,\Delta\varepsilon}{\beta\sigma_{mc}} = F_2\left(\frac{a}{t}, \frac{\sigma_0}{\beta\sigma_{mc}}, \frac{t}{L}\right) \tag{9}$$

Because of the nonlinearity of the fiber bridging law, the extra strain is no longer proportional to the applied stress σ. The total tensile strain ε at any time during the crack growth process is given by the sum

$$\varepsilon = \frac{\sigma}{\bar{\bar{E}}} + \Delta\varepsilon \tag{10}$$

If there exists residual stress in the composite, additional strain will be introduced due to release of such residual stress by the growth of matrix cracks, as will be included later.

For the convenience of presenting results it is useful to define the plane strain secant modulus $\bar{\bar{E}}_{sec}$, which is also a function of a/t, $\sigma_0/(\beta\sigma_{mc})$ and t/L, as the ratio

$$\bar{\bar{E}}_{sec} = \frac{\sigma}{\varepsilon} \tag{11}$$

Due to stress concentration arising from presence of the crack, the tensile stress in the bridging fibers is not simply σ/c_f, as it is well behind the crack tip in steady-state matrix cracking of uni-directional fiber-reinforced ceramics. In all cases studied, it is found that the maximum stress in the fibers always occurs in the bridging fibers located at the $90^o/0^o$ interfaces (the bridging/unbridging point). Denote this stress by σ_f; it is given by

$$\frac{c_f \sigma_f}{\beta\sigma_{mc}} = F_3\left(\frac{a}{t}, \frac{\sigma_0}{\beta\sigma_{mc}}, \frac{t}{L}\right) \tag{12}$$

Extensive results will be presented in next section for the non-dimensional functions defined in (8), (9), (11) and (12) for each of the two doubly periodic crack patterns. In addition, numerical examples will be presented to illustrate the influence of some of the parameters on the tensile behavior of laminated fibrous ceramic composites.

3. Crack Growth Process and Overall Tensile Response

A complete analysis of the crack growth problem with bridging fibers in the 0^o plies is performed, as described in the previous Section. The crack growth process initiated from a single through-the-fibers crack in a uni-directional fiber-reinforced ceramic composite was discussed in [5], where emphasis was placed on the tensile strength of the composite. It was found in their analysis that a typical curve of applied stress σ vs. matrix crack growth a/t always has following features, assuming no fibers break. Following initiation of the matrix crack growth at σ_0, the applied stress σ increases due to the constraining effects of crack-bridging fibers, until a peak value σ_p is reached. The applied stress σ then decreases as further growth continues with σ approaching the steady-state matrix cracking stress σ_{mc} asymptotically for $a \to \infty$. Thus σ_p is the

largest stress the composite can sustain before the matrix crack is fully extended.

For the cross-ply laminate studied in the present work, matrix cracks in the 0^o plies are bridged by intact fibers, but not those in the 90^o plies. The largest stress a laminate can sustain before the matrix crack is fully extended, σ_p, is thus not necessarily same as that for a uni-directional fibrous composite. There are two possibilities. One is that the applied stress reaches the peak value before the matrix crack grows into the next 90^o ply, and this peak value is the desired σ_p. Another possibility is that the applied stress σ is still increasing when the matrix crack reaches the next $90^o/0^o$ interface. Since no fiber-bridging constraint can occur in the 90^o plies, the matrix crack will run dynamically across the next 90^o under constant stress loading. Therefore in this situation the stress when crack reaches the $90^o/0^o$ interfaces is the peak stress, σ_p, the largest stress the laminate can sustain before the matrix is fully cracked. The peak value σ_p for one single crack in a 90^o ply is plotted in Fig. 4 as solid line. It turns out that for most range of $\sigma_0/(\beta\sigma_{mc})$ studied, σ_p is associated with the second case mentioned above. Also plotted in Fig. 4 are peak values for other crack configurations. They will be explained later.

For the crack patterns shown in Fig. 2a and 2b, a somewhat different crack growth process is found resulting from crack interaction. Results will be first presented for the collinear crack pattern (Fig. 2a), followed by those for the staggered crack pattern (Fig. 2b). The influences of fiber bridging constraint and crack density on the tensile behavior of the laminates are also demonstrated. The last subsection will be devoted to the effect of the residual stress on the crack growth process and the overall tensile response.

3.1. Collinear Crack Pattern

The numerical results for the collinear crack arrays are given in Fig. 5, for the case that the crack density t/L is equal to 1. For other values of t/L, including the case of a single line of cracks with $t/L=0$, the trends are similar. Fig. 5a shows curves of the applied stress σ vs. the matrix crack half length a for a wide range of $\sigma_0/(\beta\sigma_{mc})$. These results are obtained by imposing the condition $K_I=K_{Ic}$ on the solution, as discussed. Crack growth into the adjacent 0^o plies starts when the applied stress σ reaches a critical value which is somewhat below σ_0 due to crack interaction. This initiation stress is independent of $\sigma_0/(\beta\sigma_{mc})$. The actual initiation process of

crack growth through an interface is very complicated. It depends on the elastic mismatches of the two materials as well as other features such as flaw size in a way which is not yet established. No attempt is made to address this issue since it is not critical in the present study. In this study, the interface is ignored as a potential barrier to the advancing matrix cracks.

As matrix cracks grow, the constraint of the crack-bridging fibers requires an increasing applied stress σ. However, interaction among cracks also becomes stronger, especially the stress intensity enhancement from the neighboring collinear cracks. The competition between fiber bridging constraint and crack interaction yields a peak value of σ occurring after an initial increase. This peak value, σ_p, is plotted in Fig. 4. Also plotted for comparison is the peak value for the case t/L=0 (*i.e.*, a simple array of collinear cracks). It is clear that the main effect of interaction arises from the collinear neighbors. After σ_p is reached, the matrix cracks grow under decreasing applied stress σ until the collinear cracks coalesce at middle of the 0^o plies and the matrix becomes fully cracked.

The competition between fiber bridging constraint and crack interaction is evident in Fig. 5a. The crack length at which σ_p is reached is longer for tougher bridging (smaller $\sigma_0/(\beta\sigma_{mc})$). The corresponding extra tensile strains during the crack growth process are shown in Fig. 5b. Unlike the applied stress σ, extra strains are monotonically increasing except near the coalescence of the cracks, where the applied stress σ drops sharply. To gain some feel of what a tensile stress-strain curve will look like during this crack growth process, we have also presented the results for the secant modulus $\bar{E}_{sec}$ as defined by (11), which is shown in Fig. 5c. It is seen that the nonlinearity of tensile stress-strain behavior will be greater for softer bridging fibers (*i.e.*, larger $\sigma_0/(\beta\sigma_{mc})$).

The tensile stresses σ_f in the fibers at the interface between the $0^o/90^o$ plies (where the fiber stress is maximum) is plotted in Fig. 5d as a function of a/t. For $\sigma_0/(\beta\sigma_{mc})<0.4$, the bridging stress $c_f\sigma_f$ is above matrix cracking stress σ_{mc}. Comparison of values in Fig. 5d with the fiber bundle strength will determine the likelihood of fiber fracture during the crack growth process for this type of crack pattern. Work currently in progress by the authors indicates that the stress concentration in the fibers at the $0^o/90^o$ interface is generally exaggerated by the line-spring model of bridging. Improved estimates of the stress concentration in the bridging fibers will be reported

in a subsequent paper.

3.2. Staggered crack pattern

For the staggered crack pattern (shown in Fig. 2b), the collinear cracks are spaced every two plies as opposed to every other ply for the other doubly periodic cracks. Consequently matrix cracks will grow all the way through the adjacent 0^o plies, and possibly extend into the next 90^o plies. If they do extend into the next 90^o plies, cracks will coalesce dynamically because of lack of fiber bridging constraint as well as stress intensity enhancement from neighboring collinear cracks. It is therefore only necessary to consider crack growth in the 0^o plies.

For small crack density t/L, the crack growth behavior is determined by the competition between fiber bridging constraint and stress intensity enhancement from the neighboring collinear cracks. Fig. 6 shows such a crack growth process for t/L=0.5. The arrangement of the plots in Fig. 6 is same as Fig. 5, except that the range of all the abscissae a/t are now from 1 to 3, reflecting crack extension through the entire 0^o plies. This process is qualitatively similar to what was discussed in connection with the collinear crack arrays, except that no crack coalescence occurs in this range.

A more interesting behavior is found if the crack density t/L becomes larger, as represented in Fig. 7 with t/L=1. As matrix cracks pass the center of the 0^o plies, the shielding effect from neighboring parallel cracks becomes strong, and the crack growth process is now governed by the competition among fiber bridging constraint, stress intensity enhancement from neighboring collinear cracks, *and* the shielding effect from parallel cracks. For a large crack density, the parallel cracks are sufficiently close that shielding becomes dominant. This is reflected in Fig. 7a by curves of applied stress σ vs. crack length a. Beyerle *et al* [1] reported from their experimental observations that some of the longer matrix cracks in the 0^o plies seem to arrest under increasing load. The shielding effect on matrix crack growth displayed by the staggered crack pattern may explain this observation. The change of secant modulus $\bar{E}_{sec}$ for this crack pattern is much bigger than that for the regular crack pattern (compare Fig. 7c and Fig. 5c, both for t/L=1). This is due to the fact that staggered cracks advance all the way through the 0^o plies, producing more inelastic strain.

The peak value stress σ_p for two typical staggered crack patterns are shown in Fig. 4, namely, the cases for t/L=0.0 and t/L=1.0. The difference between them is seen to be relatively small. It is clear from Fig. 4 that the most deleterious pattern is the collinear arrays. Even with t/L=0, this pattern can result in a reduction of the peak stress for matrix cracks to spread across the plies of almost 50% of σ_{mc}. This is not surprising since the collinear patterns shed all the load carried by the 90^o plies into the 0^o plies in the collinear plane, increasing the ligament loads by a factor of two. Collinear arrays are unlikely from a statistical point; and, as mentioned earlier, the staggered arrays are probably more realistic. The conclusion to be drawn from the peak stress plots in Fig. 4 is that the single layer, uni-directional matrix cracking stress σ_{mc} provides a reasonable estimate of the matrix cracking stress of the 0^o plies in the cross ply composite, assuming the initiating cracks in the 90^o plies do not line up in a collinear fashion. Considering the significantly lower peak stress associated with the collinear arrays, it may be worthwhile to investigate other related crack configurations which have a high likelihood of occurrence, e.g., two collinear cracks in the neighboring 90^o plies.

This model has been used to generate overall tensile stress-strain behavior as dependent on several of the key parameters. In Fig. 8a plots are displayed of the normalized applied stress against the normalized strain for cases t/L=1. The solid lines represent the behavior subsequent to initiation of crack growth into the 0^o plies, which is the range considered in this paper. The initial elastic response, which is also shown as solid line, is terminated at the onset of tunnel cracks in the 90^o plies. The transition response connecting the onset of tunnel cracking and the 0^o ply cracking has not been computed here, but a typical response is shown as a dashed line curve. The effect of crack density on the overall stress-strain relation is illustrated in Fig. 8b, where $\sigma_0/(\beta\sigma_{mc})=0.3$. The nonlinear behavior shown in these two figures is in general agreement with experimental data reported in the literature.

3.3. Residual Stress Effect

Residual stresses and strains are generally introduced during manufacturing process of a fiber-reinforced cross-ply laminate. As we discussed earlier, two types of residual stresses exist within different scales. When fibers and matrix are bonded together to form a uni-directional fibrous ply,

residual stresses in axial and radial directions are introduced between fibers and matrix due to mismatch of their thermal properties. Another type of residual stresses exists at the ply level. When the plies are bonded together to form the cross-ply laminates, misfit strain results in residual stresses between plies. Both types of residual stresses can be rigorously modeled in the present analysis by a simple stress superposition and possible modification of fiber bridging law according to (4b), as discussed in Appendix A. For the sake of simplicity, only the results for residual stress between plies will be presented in this paper. Consistent with our material approximation, we may assume that an initial, uniform residual tension σ_R exists in the 90^o plies acting parallel to the applied stress, with same level of compression in the 0^o plies.

Fig. 9 shows the effect of a residual stress σ_R in the laminate, where σ_R is scaled with the reference stress σ_0. Since a residual tension is assumed in the 90^o plies, the initiation value of σ is smaller than that if no residual stress were present. As matrix cracks grow, larger applied stress σ is required to overcome the residual compression in the 0^o plies. The process is clearly indicated in Fig. 9a. In any case, the secant modulus $\bar{E}_{sec}$ (shown in Fig. 9b) is smaller than that if no residual stresses are present. As matrix cracks become long, the differences in $\bar{E}_{sec}$ for various σ_R become small. The overall stress-strain response for different residual stresses are plotted in Fig. 9c.

4. A numerical example

To obtain some real feel of our approach, A numerical calculation is performed for the CAS/SiC laminate discussed earlier. Based on its constituent properties, the values of relevant parameters are obtained to be

$$A=0.97,\ \bar{E}=140GPa,\ \sigma_0=88MPa,\ \beta=0.998,\ \sigma_{mc}=323MPa$$

The measured residual stress in the matrix σ_R^m is in the range 100~120MPa. We shall use σ_R^m=110MPa in our calculation. The residual stress between plies σ_R=30MPa is also accounted for in the calculation.

Based on the above information, we are able to perform our calculation using the staggered crack pattern. The crack density is taken to be t/L=0.88, which is the average saturation crack density measured in the experiment. The results for secant modulus $\bar{E}_{sec}$ vs. applied stress σ are

presented in Fig. 10 as solid lines. The experimental data from [1] are also plotted as solid dots. Also presented in Fig. 10 is the predicted secant modulus $\bar{E}_{sec}$ for crack density t/L=0.5. The comparison with the experimental data suggests that in the stress range from 70 to 100MPa the density of matrix cracks in the 90^o plies may be still increasing at the same time the matrix cracks are growing into the 0^o plies.

Acknowledgment

This work was supported in part by the DARPA URI (Subagreement P.O.#KK3007 with the University of California, Santa Barbara, ONR Prime Contract N00014-92-J-1808), by the Materials Research Lab under Grant NSF-DMR-89-20490, and by the Division of Applied Sciences, Harvard University.

REFERENCES

1. D. S. Beyerle, S. M. Spearing and A. G. Evans, *J. Am. Ceram. Soc.*, **75**, 3321 (1992).
2. N. Laws and G. J. Dvorak, *J. Composite Materials* **22**, 900 (1988).
3. Z. C. Xia, R. R. Carr and J. W. Hutchinson, *Acta. Metall. Mater.* **41**, 2365 (1993).
4. D. B. Marshall and B. N. Cox, *Acta. Met.* **35**, 2607 (1987).
5. B. Budiansky and Y. L. Cui, *J. Mech. Phys. Solids*, in press.
6. R. Hill, *J. Mech. Phys. Solids* **13**, 189 (1965).
7. J. Aveston, G.A. Cooper and A. Kelly, in *Conference proceedings, National Physical Laboratory, Guildford*, p15, IPC Science and Technology Press Ltd (1971).
8. B. Budiansky, J. W. Hutchinson and A. G. Evans, *J. Mech. Phys. Solids* **34**, 167 (1986).
9. H. Tada, P. Paris and G. Irwin, *The Stress Analysis of Cracks Handbook*. Del Research, St. Louis (1985).
10. D. B. Marshall, B. N. Cox and A. G. Evans, *Acta. Met.* **33**, 2013 (1985).
11. D. B.Marshall and A. G. Evans, *Materials Forum*, **11**, 304 (1988).
12. J. R. Rice, in *Fracture* (edit by H. Liebowitz), Vol. II, Academic Press (1968).
13. B. Budiansky and J. W. Hutchinson, *J. Appl. Mech.* **45**, 267 (1978).
14. J. R. Rice, in *Fatigue Crack Propagation*, ASTM STP **415**, p. 247 (1967).

15. Z. C. Xia and J. W. Hutchinson, *Int. J. Solids. Structures*, in press.

Appendix A

Integral Equation Formulation for the Partially Bridged Matrix Cracking Problem

An integral equation for the partially bridged matrix cracking problem is formulated based on the dislocation distribution method (cf. [12]). In this method, cracks are represented as a superposition of continuously distributed dislocations. For the two doubly periodic crack patterns studied in this work, we only need to model half of a representative crack by distribution of edge dislocation $b(\eta)=b_y(\eta)$ (Fig. A1). The stress $\sigma_y(x)$ along crack face induced by edge dislocations $b(\eta)$ at $x=\eta$ and $-b(\eta)$ at $x=-\eta$ is given by

$$\sigma_y(x) = \frac{\bar{E}}{4\pi}\left[\frac{1}{x-\eta} + A(x,\eta)\right]b(\eta) \qquad \text{(A-1)}$$

The kernel function $A(x,\eta)$ for the two crack patterns is given in Appendix B.

An integral equation is obtained by choosing the dislocation distribution to meet the traction conditions along the line of the crack and within crack bridging zone

$$\frac{\bar{E}}{4\pi}\int_0^a \left\{\frac{1}{x-\eta} + A(x,\eta)\right\} b(\eta)\, d\eta = -\sigma^0(x) + p(x) \ , \qquad \text{for } 0 < x < a \qquad \text{(A-2)}$$

where $\sigma^o(x)$ is the stress normal to the crack surface prior to cracking, including remotely applied stress σ and the residual stress among plies, and $p(x)$ is the fiber bridging stress. Thus the right hand side of (A-2) should be $-(\sigma+\sigma_R)$ for $0<x<t$ (in the 90^o plies), and $-(\sigma-\sigma_R)+p(x)$ for $t<x<a$ (in the 0^o plies).

The crack opening displacement $\delta(x)$ is given by

$$\delta(x) = \int_x^a b(\eta)\, d\eta \qquad \text{(A-3)}$$

Since only crack surfaces in the 0^o plies (*i.e.*, $t<x<a$, where t is half ply thickness) are bridged by fibers, the solution $b(\eta)$ to the integral equation exhibits a logarithm singularity at $\eta=t$ (cf. [13-14]; [9] for crack opening displacement solutions of Dugdale-Barenblatt model). Accordingly we can approximate $b(\eta)$ with the correct singularities built-in as

$$b(\eta) = \frac{4\pi\sigma_0}{\bar{E}}\left\{ c_0 \ln\frac{t-\eta}{t} + \sum_{j=1}^{N_1-1} c_j T_{j-1}\left(\frac{2\eta}{t}-1\right)\right\} \qquad \text{for } 0 \le \eta < t$$

$$b(\eta) = \frac{4\pi\sigma_0}{\bar{E}}\left\{ d_0 \ln\frac{\eta-t}{a-t} + \sqrt{\frac{a-t}{2(a-\eta)}}\sum_{j=1}^{N_2-1} d_j T_{j-1}\left(\frac{2(\eta-t)}{a-t}-1\right)\right\} \qquad \text{for } t < \eta < a \tag{A-4}$$

where $T_j(\zeta)$ is the Chebyshev polynomial of first kind of degree j. c_j's and d_j's are (N_1+N_2) unknown coefficients which are to be determined.

The asymptotic behavior of $b(\eta)$ near crack tip $\eta=a$ gives the mode I stress intensity factor K_I in terms of the unknown coefficients as

$$K_I = \pi\sigma_0\sqrt{\pi(a-t)}\sum_{j=1}^{N_2-1} d_j \tag{A-5}$$

The crack opening displacement $\delta(x)$ for $t<x<a$ can be expressed as, by substituting (A-4) into (A-3),

$$\delta(x) = \frac{2\pi(a-t)\sigma_0}{\bar{E}}\sum_{j=0}^{N_2-1} d_j\, f_j(x) \tag{A-6}$$

where

$$f_0(x) = \int_s^1 \ln\frac{1+\zeta}{2}\,d\zeta\ , \quad f_j(x) = \int_s^1 \frac{T_{j-1}(\zeta)}{\sqrt{1-\zeta}}\,d\zeta\ \ , \text{ and } s = \frac{2(x-t)}{a-t} - 1 \tag{A-7}$$

The fiber bridging stress p(x) is given by, from (3)-(6) in the main text and (A-6) above,

$$\frac{p(x)}{\sigma_0} = \sqrt{\frac{2(a-t)}{3t}\left(\frac{\beta\sigma_{mc}}{\sigma_0}\right)^3 \sum_{j=0}^{N_2-1} d_j\, f_j(x)} - \frac{\frac{E_L}{E_m}\sigma_R{}^m}{\sigma_0}, \text{ where } \beta = \left\{\frac{A E_L}{\bar{E}(1-\nu_L{}^2)}\right\}^{\frac{1}{3}} \tag{A-8}$$

Substitution of (A-4), (A-8) into (A-2) yields

$$\sum_{j=0}^{N_1-1} I_{1j}(x)\, c_j + \sum_{j=0}^{N_2-1} I_{2j}(x)\, d_j = -\frac{\sigma+\sigma_R}{\sigma_0}\ , \qquad \text{for } 0 \le x < t$$

$$\sum_{j=0}^{N_1-1} I_{3j}(x)\, c_j + \sum_{j=0}^{N_2-1} I_{4j}(x)\, d_j = -\frac{\sigma-\sigma_R}{\sigma_0} + \sqrt{\frac{2(a-t)}{3t}\left(\frac{\beta\sigma_{mc}}{\sigma_0}\right)^3 \sum_{j=0}^{N_2-1} d_j\, f_j(x)} - \frac{\frac{E_L}{E_m}\sigma_R{}^m}{\sigma_0}, \quad \text{for } t < x < a \tag{A-9}$$

The I(x)'s in the above equation are given by following integrals, after scaling the integration limits into (-1, 1),

$$I_{10}(x),\quad I_{30}(x)=\frac{t}{2}\int_{-1}^{1}\left[\frac{1}{x-\eta}+A(x,\eta)\right]\ln\frac{1-\zeta}{2}\,d\zeta$$
$$I_{1j}(x),\quad I_{3j}(x)=\frac{t}{2}\int_{-1}^{1}\left[\frac{1}{x-\eta}+A(x,\eta)\right]T_{j-1}(\zeta)\,d\zeta \qquad \text{(A-10)}$$

where $\eta=t(1+\zeta)/2$, and

$$I_{20}(x),\quad I_{40}(x)=\frac{a-t}{2}\int_{-1}^{1}\left[\frac{1}{x-\eta}+A(x,\eta)\right]\ln\frac{1+\zeta}{2}\,d\zeta$$
$$I_{2j}(x),\quad I_{4j}(x)=\frac{a-t}{2}\int_{-1}^{1}\left[\frac{1}{x-\eta}+A(x,\eta)\right]\frac{T_{j-1}(\zeta)}{\sqrt{1-\zeta}}\,d\zeta \qquad \text{(A-11)}$$

where $\eta=t+(a-t)(1+\zeta)/2$. In the designated ranges of x, Cauchy Principle values are understood for $I_1(x)$'s and $I_4(x)$'s in (A-10) and (A-11).

The choice of allocation points for solving (A-9) is somewhat arbitrary. Chebyshev points are used in our calculation

$$x_i=\frac{t}{2}\left\{1+\cos\left[\frac{(2i-1)\pi}{2N_1}\right]\right\},\qquad i=1,\,2,\,...,\,N_1\quad \text{for}\quad 0\le x<t$$
$$x_i=t+\frac{a-t}{2}\left\{1+\cos\left[\frac{(2i-1)\pi}{2N_2}\right]\right\},\quad i=1,\,2,\,...,\,N_2\quad \text{for}\quad t<x<a \qquad \text{(A-12)}$$

An additional equation is obtained by imposing the crack growth condition $K_I=K_{Ic}$. The combination of (6) in the main text with (A-5) gives

$$\sum_{j=1}^{N_2-1}d_j=\frac{1}{\pi}\sqrt{\frac{t}{a-t}} \qquad \text{(A-13)}$$

Introduction of (N_1+N_2) allocation points in (A-12) to (A-9), together with (A-13), provides (N_1+N_2+1) equations for solving (N_1+N_2+1) unknowns $c_0, c_1, ..., c_{N_1-1}$; $d_0, d_1, ..., d_{N_2-1}$, and remotely applied stress σ. This set of nonlinear equations are solved numerically by Newton's method.

It is not difficult to show that the inelastic strain $\Delta\varepsilon$ introduced by matrix cracking can be obtained from

$$\Delta\varepsilon=\frac{1}{4Lt}\int_0^a\delta(x)\,dx \qquad \text{(A-14)}$$

where $\delta(x)$ can be calculated from (A-3).

Appendix B. Kernel Function A(x,η)

The kernel function A(x,η) used in Appendix A to formulate the integral equation is obtained by superposition of the stress $\sigma_y(x)$ induced by arrays of periodic edge dislocations. The complete stress field for an array of periodic edge dislocations can be found in [15].

For collinear arrays,

$$A(x,\eta)=\left[\frac{\frac{\pi}{4t}}{\tan\frac{\pi}{4t}(x-\eta)}-\frac{1}{x-\eta}\right]-\frac{\frac{\pi}{4t}}{\tan\frac{\pi}{4t}(x+\eta)}+\frac{\pi}{t}\sum_{y=2L,4L,\ldots}^{\infty}\left\{\frac{\sin\frac{\pi}{2t}(x-\eta)}{2\left[\cosh 2y-\cos\frac{\pi}{2t}(x-\eta)\right]}\right.$$

$$\left.+\frac{y\sin\frac{\pi}{2t}(x-\eta)\sinh 2y}{\left[\cosh 2y-\cos\frac{\pi}{2t}(x-\eta)\right]^2}-\frac{\sin\frac{\pi}{2t}(x+\eta)}{2\left[\cosh 2y-\cos\frac{\pi}{2t}(x+\eta)\right]}-\frac{y\sin\frac{\pi}{2t}(x+\eta)\sinh 2y}{\left[\cosh 2y-\cos\frac{\pi}{2t}(x+\eta)\right]^2}\right\}$$

(B-1)

For staggered arrays,

$$A(x,\eta)=\left[\frac{\frac{\pi}{8t}}{\tan\frac{\pi}{8t}(x-\eta)}-\frac{1}{x-\eta}\right]-\frac{\frac{\pi}{8t}}{\tan\frac{\pi}{8t}(x+\eta)}+\frac{\pi}{2t}\sum_{y=2L,4L,\ldots}^{\infty}\left\{\frac{\sin\frac{\pi}{4t}(x-\eta)}{2\left[\cosh 2y-\cos\frac{\pi}{4t}(x-\eta)\right]}\right.$$

$$\left.+\frac{y\sin\frac{\pi}{4t}(x-\eta)\sinh 2y}{\left[\cosh 2y-\cos\frac{\pi}{4t}(x-\eta)\right]^2}-\frac{\sin\frac{\pi}{4t}(x+\eta)}{2\left[\cosh 2y-\cos\frac{\pi}{4t}(x+\eta)\right]}-\frac{y\sin\frac{\pi}{4t}(x+\eta)\sinh 2y}{\left[\cosh 2y-\cos\frac{\pi}{4t}(x+\eta)\right]^2}\right\}$$

$$-\frac{\pi}{2t}\sum_{y=L,3L,\ldots}^{\infty}\left\{\frac{\sin\frac{\pi}{4t}(x-\eta)}{2\left[\cosh 2y+\cos\frac{\pi}{4t}(x-\eta)\right]}+\frac{y\sin\frac{\pi}{4t}(x-\eta)\sinh 2y}{\left[\cosh 2y+\cos\frac{\pi}{4t}(x-\eta)\right]^2}\right.$$

$$\left.-\frac{\sin\frac{\pi}{4t}(x+\eta)}{2\left[\cosh 2y+\cos\frac{\pi}{4t}(x+\eta)\right]}-\frac{y\sin\frac{\pi}{4t}(x+\eta)\sinh 2y}{\left[\cosh 2y+\cos\frac{\pi}{4t}(x+\eta)\right]^2}\right\}$$

(B-2)

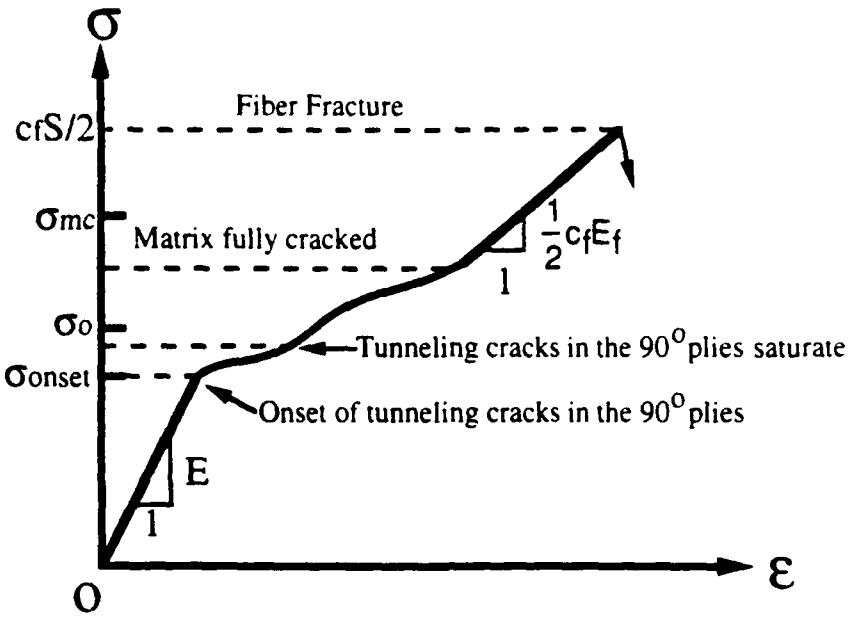

Fig. 1. A schematic illustration of stress-strain curve for a cross-ply laminate under tensile loading.

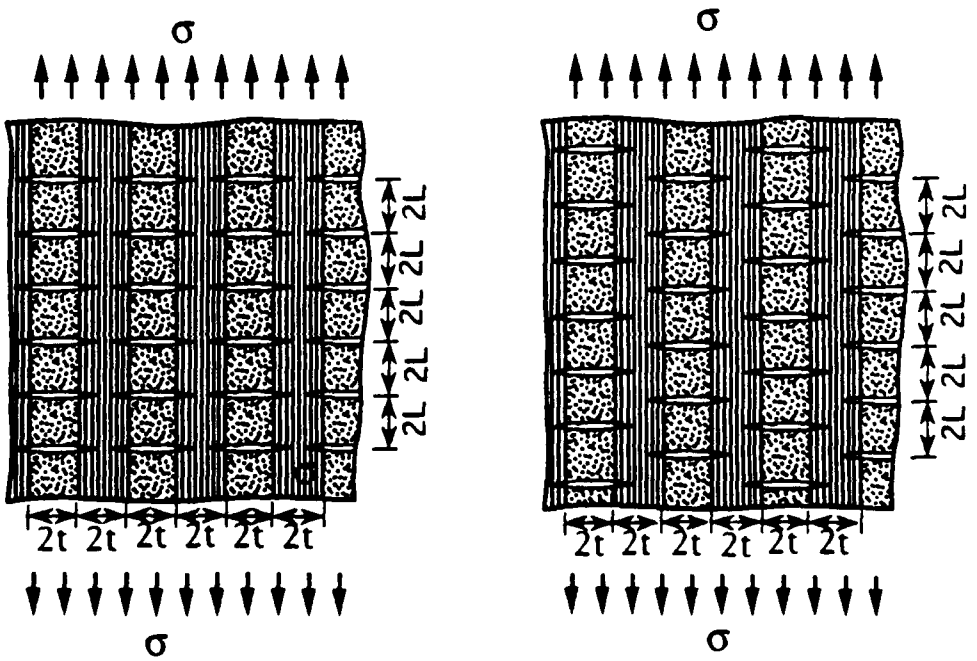

Fig. 2. Two representative doubly periodic crack patterns (a) collinear arrays (b) Staggered arrays.

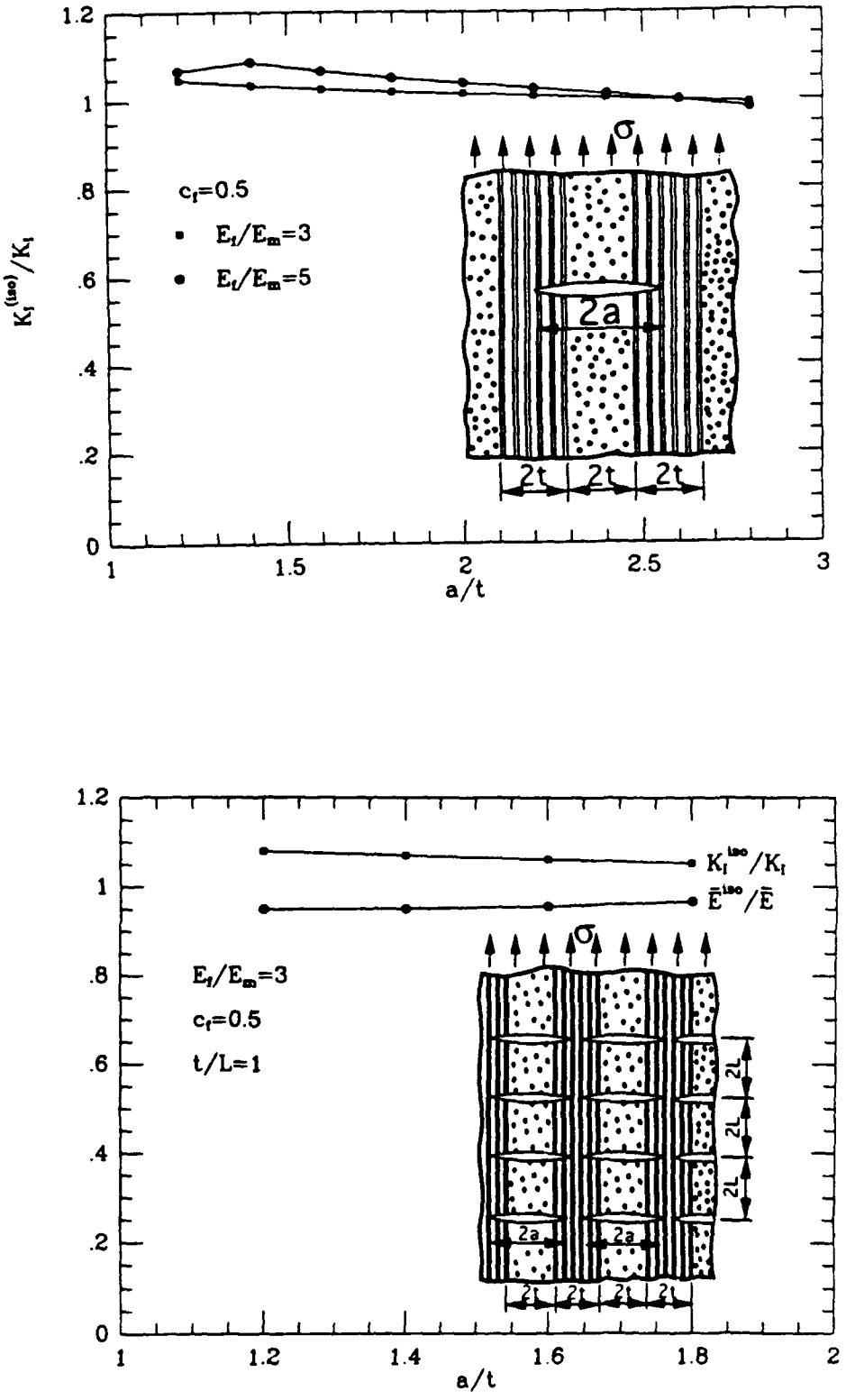

Fig. 3. Demonstrations of the validity of isotropic average approximation (a). an isolated crack (b) doubly periodic cracks

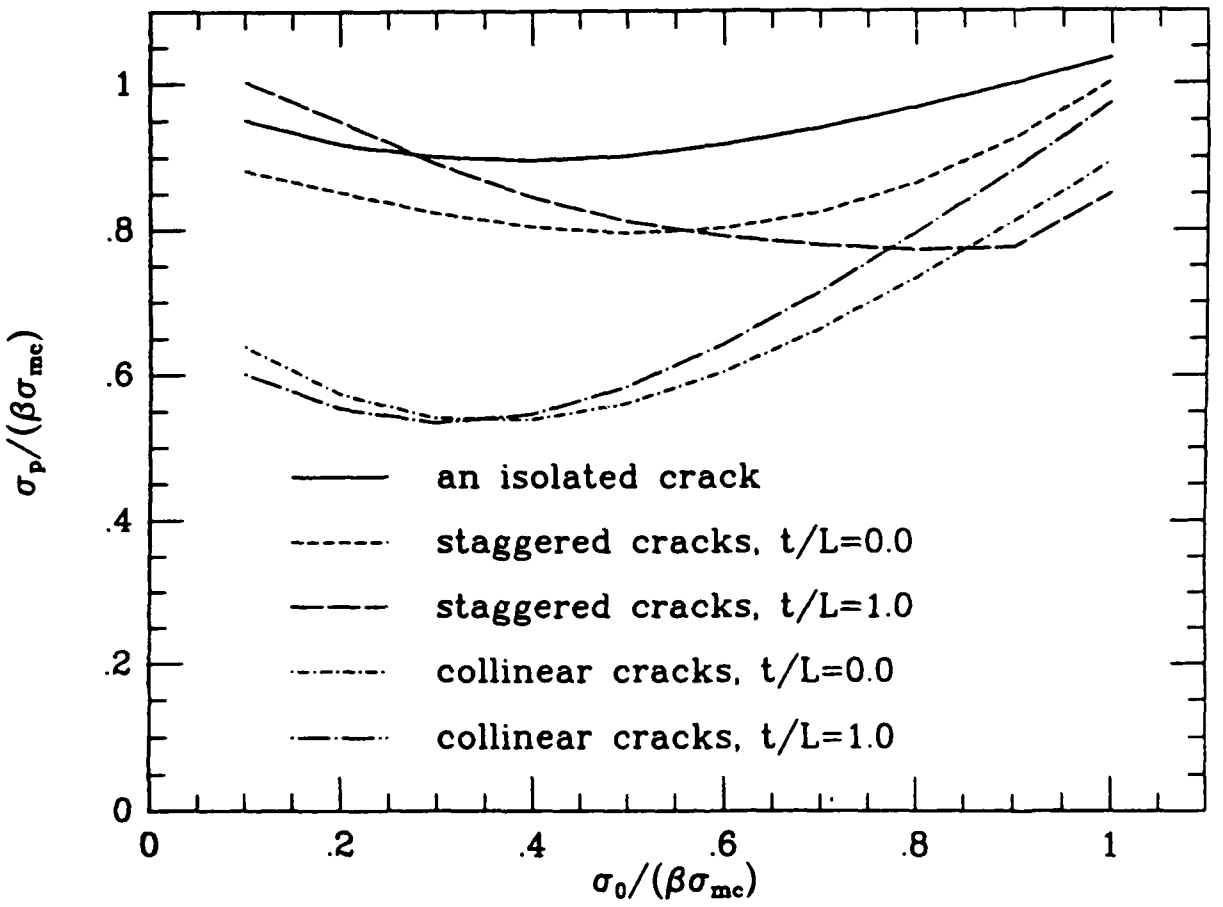

Fig. 4. Peak stress σ_p for several crack configurations.

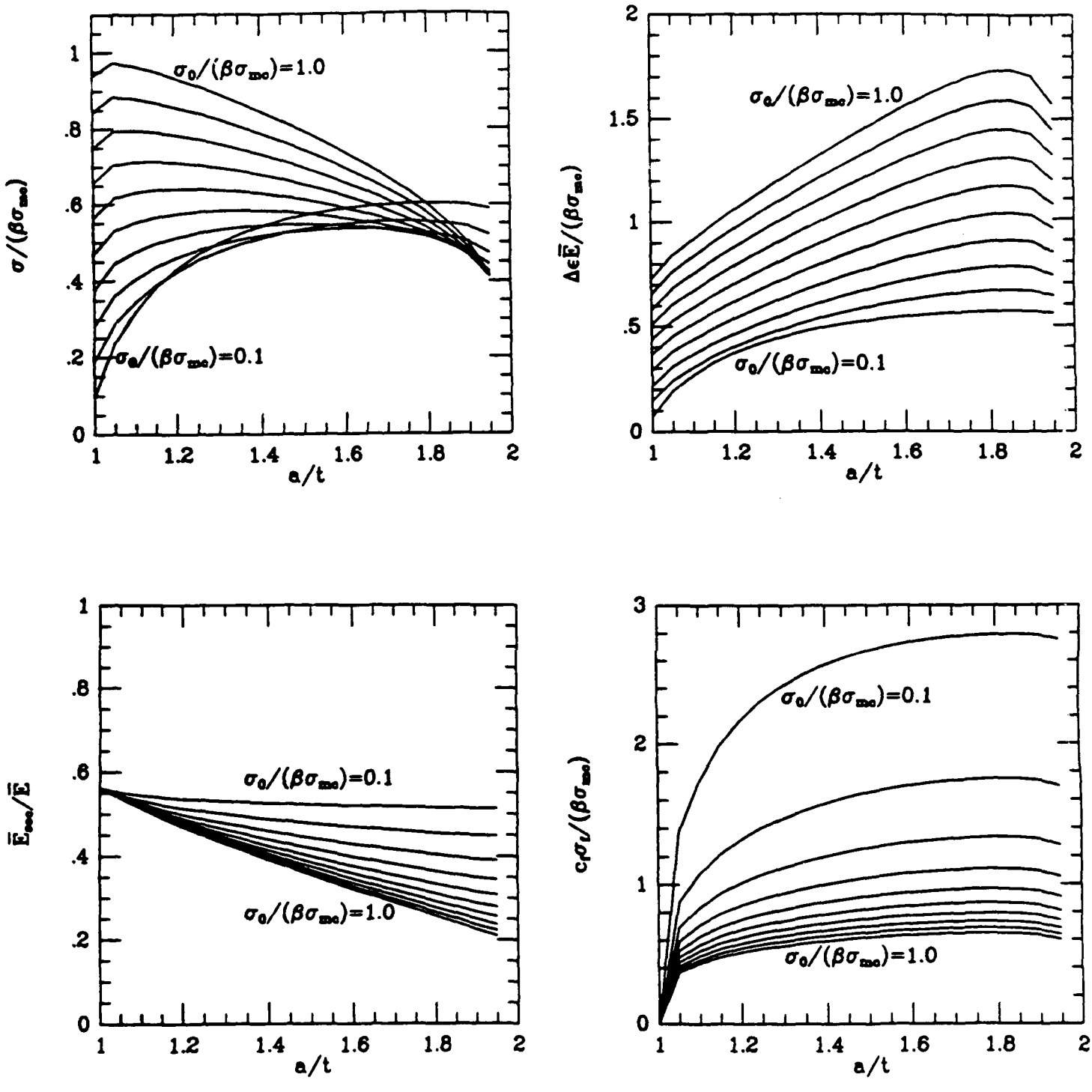

Fig. 5. Matrix crack process for collinear arrays, with crack density $t/L=1.0$
(a) Applied stress vs. matrix crack growth length.
From bottom to top: $\sigma_0/(\beta\sigma_{mc})=0.1, 0.2, 0.3, 0.4, 0.5, 0.6, 0.7, 0.8, 0.9, 1.0$
(b) Inelastic strain vs. matrix crack growth length
From bottom to top: $\sigma_0/(\beta\sigma_{mc})=0.1, 0.2, 0.3, 0.4, 0.5, 0.6, 0.7, 0.8, 0.9, 1.0$
(c) Secant modulus vs. matrix crack growth length
From top to bottom: $\sigma_0/(\beta\sigma_{mc})=0.1, 0.2, 0.3, 0.4, 0.5, 0.6, 0.7, 0.8, 0.9, 1.0$
(d) Maximum fiber bridging stress vs. matrix crack growth length
From top to bottom: $\sigma_0/(\beta\sigma_{mc})=0.1, 0.2, 0.3, 0.4, 0.5, 0.6, 0.7, 0.8, 0.9, 1.0$

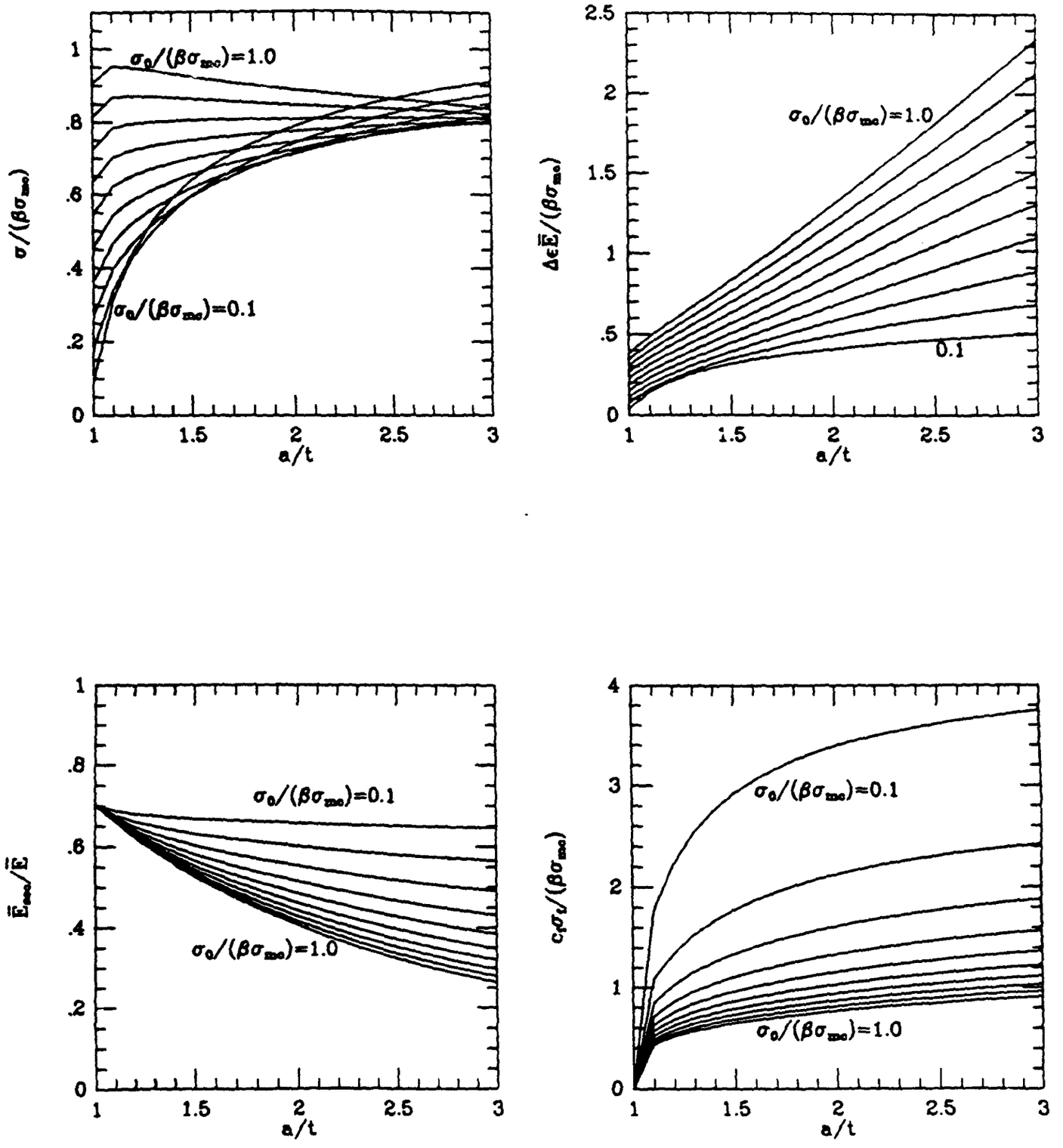

Fig. 6. Matrix crack process for staggered arrays, with crack density t/L=0.5
(a)-(d): same arrangement as Fig. 5.

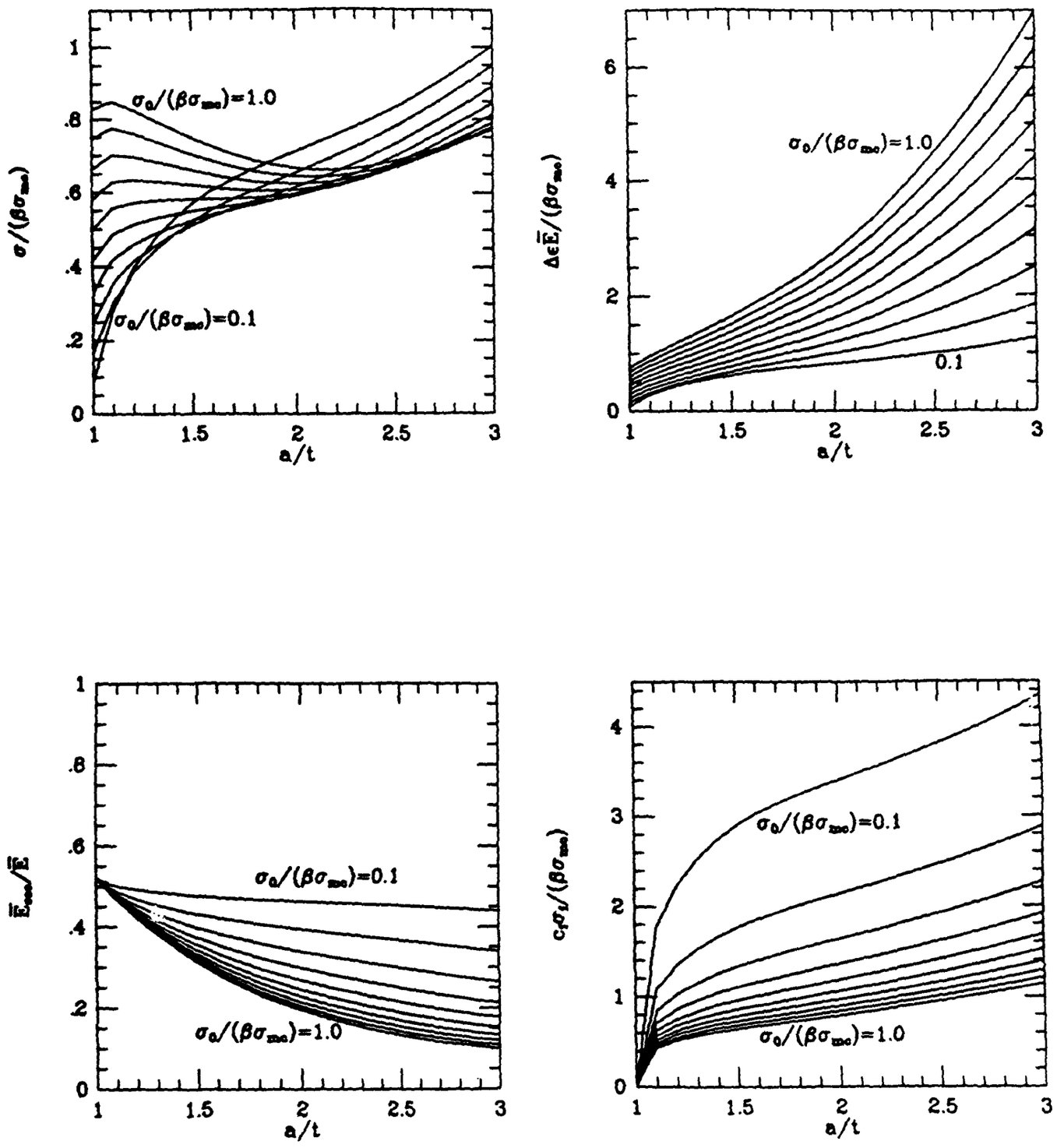

Fig. 7. Matrix crack process for staggered arrays, with crack density t/L=1.0
(a)-(d): same arrangement as Fig. 5.

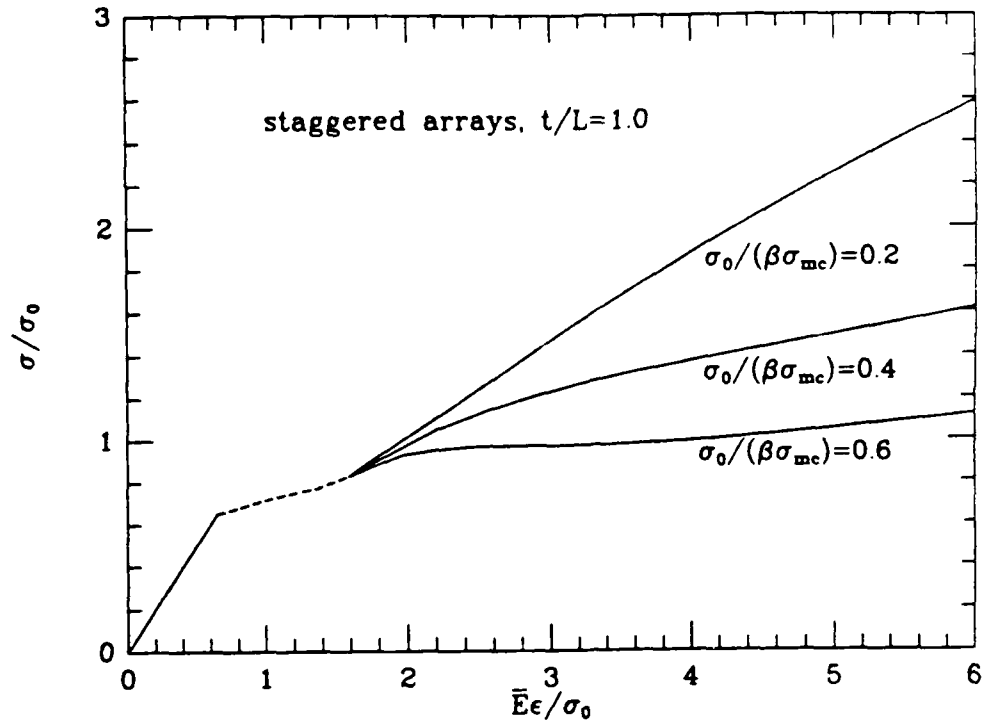

Fig. 8a. Stress-strain curves for different $\sigma_0/(\beta\sigma_{mc})$, staggered arrays, t/L=1.0

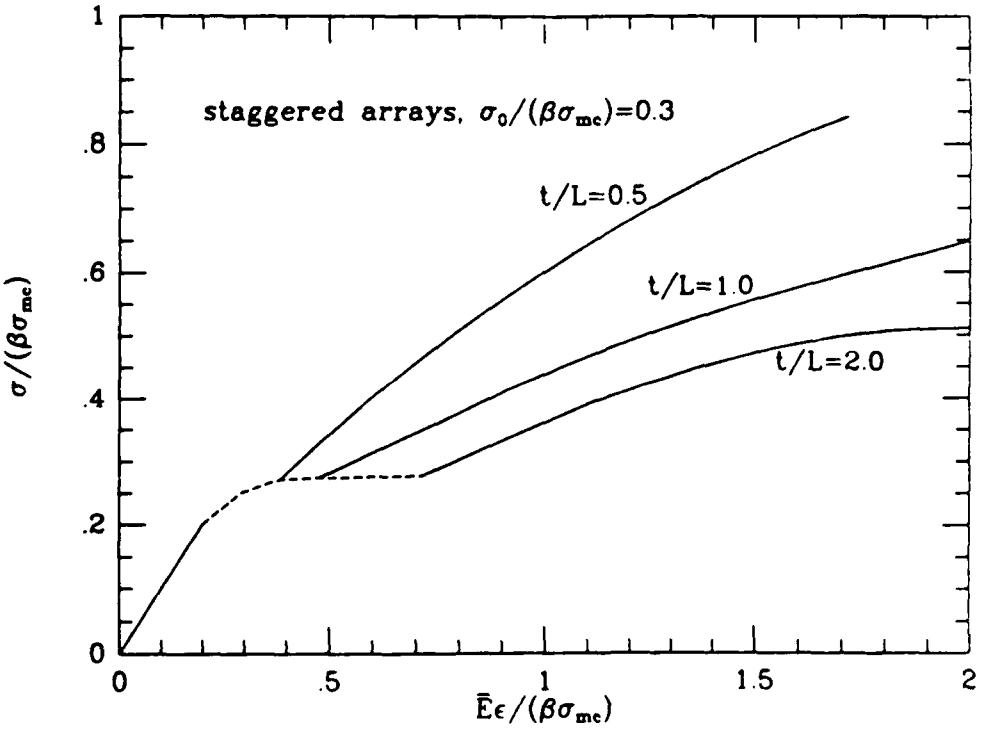

Fig. 8b. Stress-strain curves for different t/L, staggered arrays, $\sigma_0/(\beta\sigma_{mc})$=0.3

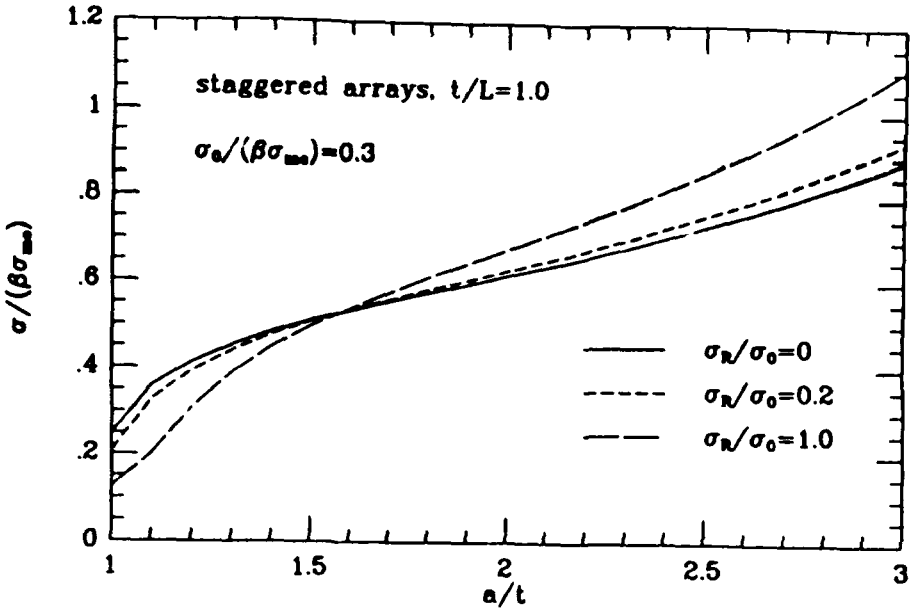

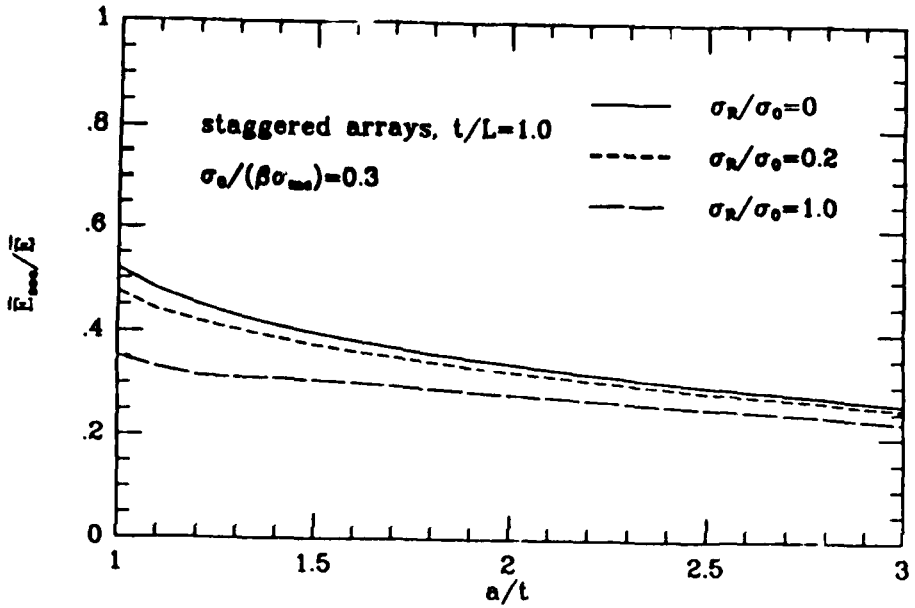

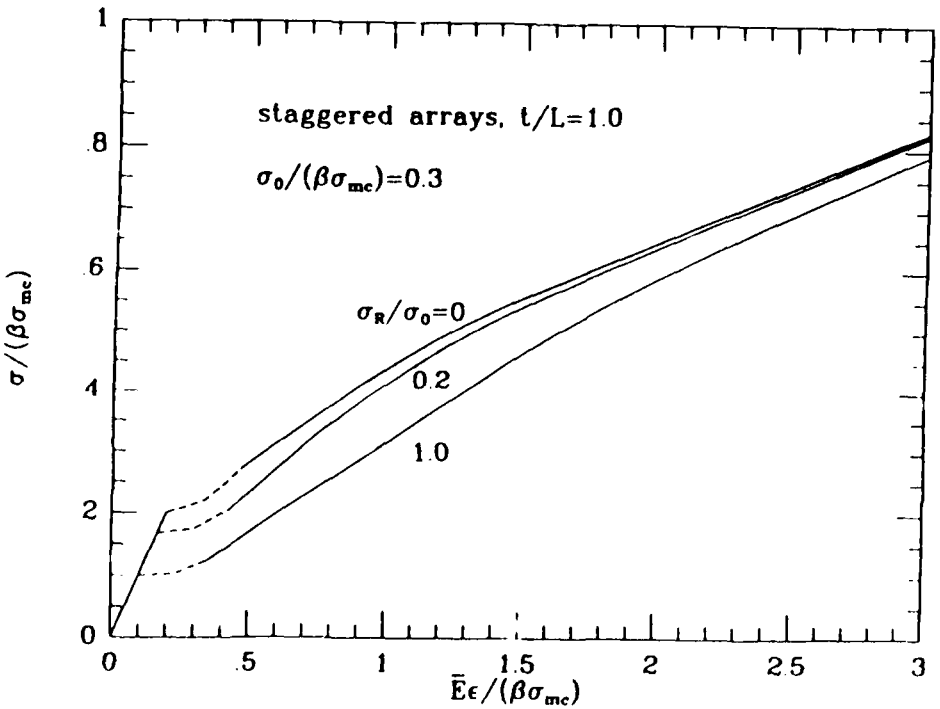

Fig. 9. Demonstration of effect of residual stress on matrix crack growth.
(a). Applied stress vs. matrix crack growth length
(b). Secant modulus vs. matrix crack growth length
(c). Overall stress-strain response

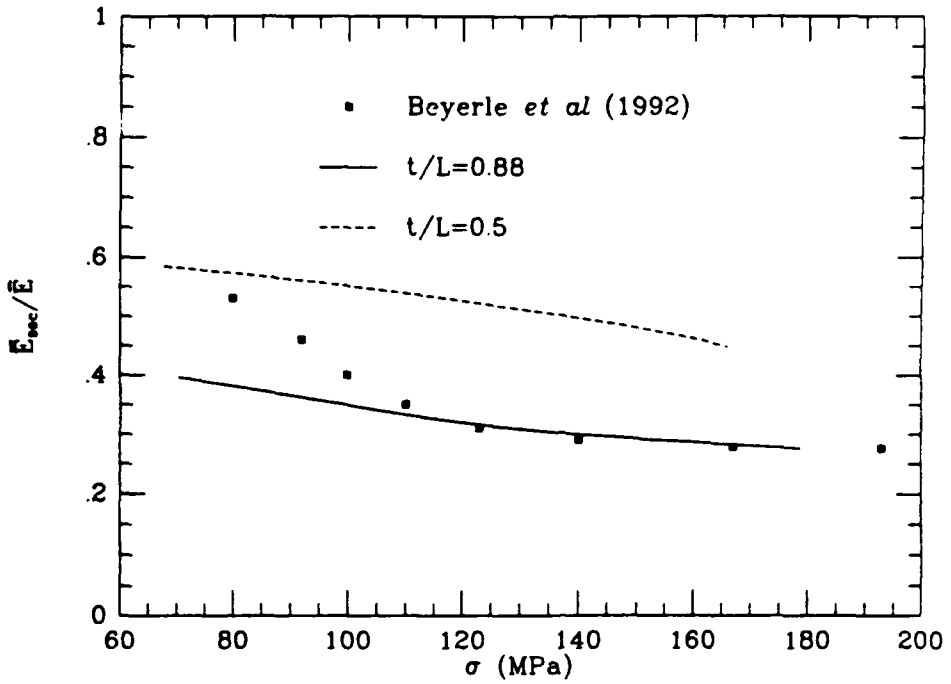

Fig. 10. Predicted secant modulus for a CAS/SiC laminate, compared with experimental data reported in Beyerle *et al* (1992)

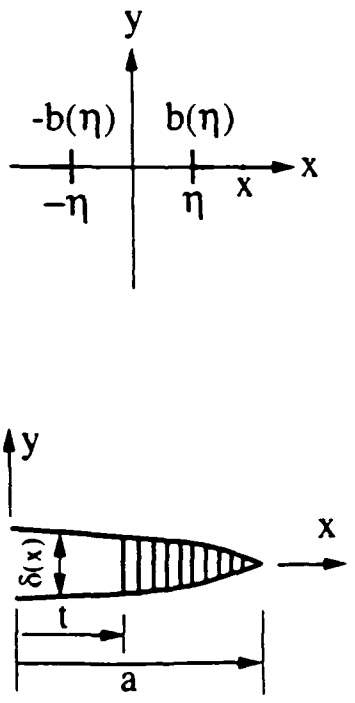

Fig. A1. (a). Dislocations used for each crack to obtain the kernel function in the integral equation
(b). A representative half crack modeled to formulate the integral equation

Acta metall. mater. Vol. 41, No. 8, pp. 2365–2376, 1993
Printed in Great Britain.

0956-7151/93 $6.00 + 0.00

TRANSVERSE CRACKING IN FIBER-REINFORCED BRITTLE MATRIX, CROSS-PLY LAMINATES

Z. C. XIA, R. R. CARR and J. W. HUTCHINSON
Division of Applied Sciences, Harvard University, Cambridge, MA 02138, U.S.A.

(Received 5 February 1993)

Abstract—The topic addressed in this paper is transverse cracking in the matrix of the 90° layers of a cross-ply laminate loaded in tension. Several aspects of the problem are considered, including conditions for the onset of matrix cracking, the evolution of crack spacing, the compliance of the cracked laminate, and the overall strain contributed by release of residual stress when matrix cracking occurs. The heart of the analysis is the plane strain problem for a doubly periodic array of cracks in the 90° layers. A fairly complete solution to this problem is presented based on finite element calculations. In addition, a useful, accurate closed form representation is also included. This solution permits the estimation of compliance change and strain due to release of residual stress. It can also be used to predict the energy release rate of cracks tunneling through the matrix. In turn, this energy release rate can be used to predict both the onset of matrix cracking and the evolution of crack spacing in the 90° layers as a function of applied stress. All these results are used to construct overall stress–strain behavior of a laminate undergoing matrix cracking in the presence of initial residual stress.

1. INTRODUCTION

The macroscopic tensile properties of uni-directional fiber-reinforced brittle composites have been studied extensively since the 70's, where matrix cracking with intact fibers plays an important role in longitudinal strength. The transverse and shear strengths of such composites are invariably lower than the longitudinal strength. Consequently, in applications where multi-axial stress states are encountered, cross-ply laminates are commonly used. While there has been considerable attention to the elastic properties of cross-ply laminates, relatively less has been done to establish their fracture performance in terms of the properties of the constituent phases. This is the topic of the present paper where emphasis is on brittle matrix composites and explicit results for the effect of matrix cracking on overall stress–strain behavior are developed and presented. Studies of the topic have been carried out within a framework of damage mechanics where the effects of cracks are not explicitly predicted as represented by [1, 2]. More closely related to the present work are studies in [3, 4] where explicit results for the effect of cracks are given for general laminates. These four papers provide additional references to the general problem area.

Recently, a comprehensive experimental study was conducted on a laminated 0°/90° ceramic/matrix composite [5]. When the tensile stress was applied along one of the fiber directions, cracks were first observed in the 90° layer and always spanned the entire ply, but arrested at the interfaces between layers, as sketched in Fig. 1. With further increase of the applied stress, additional matrix cracks developed in the 90° layers in the same way as previous cracks. These cracks spread as 3D tunneling cracks from small flaws located on the matrix of the 90° layers in the direction transverse to the applied stress, as depicted in Fig. 1. At even higher applied stress, it was observed that the pre-existing cracks began to extend into the adjacent 0° layers stably and without any fiber failure, until these transverse cracks began overlapping in the 0° layers.

The work in this paper deals with conditions for the onset and subsequent multiplication of tunnel cracks in the 90° layers of cross-ply laminates. In addition, the effect of the tunnel cracks on the overall stress–strain relation of the composite will be determined, including the contribution from the release of residual stress. Such constitutive relations are required if progress is to be made in the effort to understand the role of micro-cracking in altering stress concentration at holes and notches in these materials. The paper is organized as follows. We begin by posing the problem for the energy release rate of steady-state tunnel cracks. This problem can be solved using information from a 2D plane strain problem, which also provides the results needed for the desired constitutive changes. Extensive finite element calculations are then reported, providing conditions for the onset of tunnel cracking and for subsequent multiple crack formation. The results permit one to predict the spacing expected between the 90° layer matrix cracks as a function of the applied stress. Given crack spacing in terms of applied stress, one can then predict the overall stress–strain behavior. This point is illustrated by giving examples of stress–strain behavior as a function of the basic geometry of the composite, the toughness of the matrix, and the residual stress in the

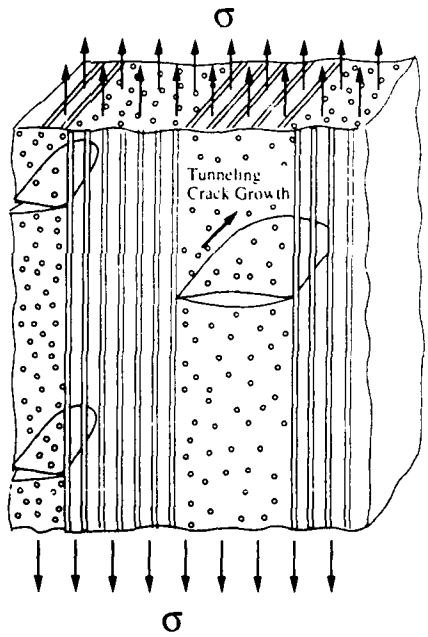

Fig. 1. A schematic of the 3D tunneling cracks in the 90 layers.

next section. An approximate analysis is carried out in the final section leading to closed form expressions for the overall compliance change and the tunneling energy release rate as a function of crack density. These results, which are quite accurate, will be very useful for practical applications.

2. BASIC MECHANICS

2.1. Basic equations for laminates

The elastic properties of an undamaged unidirectional fiber reinforced ply are accurately taken to be transversely isotropic about the fiber direction. With the fibers aligned with the 1-axis, the constitutive relation for the undamaged ply is

$$\epsilon_{11} = \frac{1}{E_L}\sigma_{11} - \frac{\nu_L}{E_L}(\sigma_{22}+\sigma_{33})$$

$$\epsilon_{22} = -\frac{\nu_L}{E_L}\sigma_{11} + \frac{1}{E_T}\sigma_{22} - \frac{\nu_T}{E_T}\sigma_{33}$$

$$\epsilon_{33} = -\frac{\nu_L}{E_L}\sigma_{11} - \frac{\nu_T}{E_T}\sigma_{22} + \frac{1}{E_T}\sigma_{33}$$

$$\epsilon_{23} = \frac{1}{2\mu_L}\sigma_{23} \quad \epsilon_{13} = \frac{1}{2\mu_T}\sigma_{13} \quad \epsilon_{12} = \frac{1}{2\mu_T}\sigma_{12} \tag{1}$$

where the subscript L stands for longitudinal properties and the subscript T stands for transverse properties. Notice that $\mu_T = E_T/[2(1+\nu_T)]$ but generally $\mu_L \neq E_L/[2(1+\nu_L)]$.

To limit the number of material parameters in the subsequent development, the difference between the fiber and matrix Poisson's ratios will be neglected (i.e. $\nu_m = \nu_f = \nu$). This approximation is known to involve little error. The moduli of the ply are related to the constituent properties by

$$E_L = cE_f + (1-c)E_m \tag{2}$$

$$\mu_L = \frac{\mu_f(1-c)+\mu_m(1+c)}{\mu_f(1-c)+\mu_m(1+c)}\mu_m \tag{3}$$

and

$$\nu_L = \nu_T = \nu \tag{4}$$

where c is the fiber volume fraction. Formula (2) is the rule of mixtures for the longitudinal stiffness, and (3) was given in [6] using the composite cylinders model. The remaining modulus, E_T, has a somewhat greater dependence on the spatial arrangement of the fibers. The approximation used here is taken from [6]

$$E_T = \frac{1+2\eta c}{1-\eta c}E_m \tag{5}$$

where

$$\eta = \frac{\dfrac{E_f}{E_m}-1}{\dfrac{E_f}{E_m}+2}. \tag{6}$$

The above formulas apply under the condition that no debonding occurs between the fiber and matrix in the plies. To obtain some insight into the role of fiber/matrix debonding, results will be computed in addition for the limiting case where it is assumed that the complete debonding has occurred. To model this, we have followed the suggestion in [5] and have taken $E_f = 0$ in (6), thereby reducing the transverse modulus. The effect of debonding on the longitudinal shear modulus is ignored since this effect is relatively unimportant.

Now consider a cross-ply laminate with equal thicknesses of 0 and 90° plies subject to in-plane

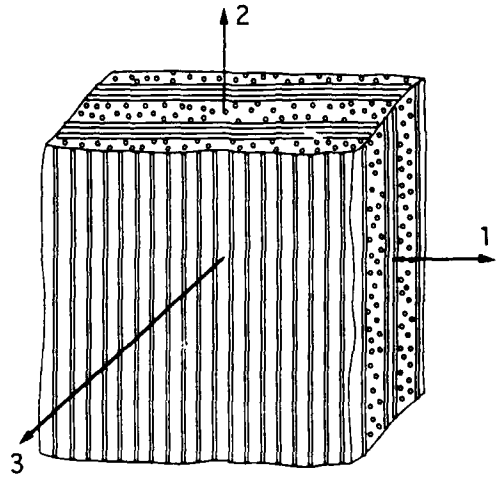

Fig. 2. Conventions for the 3D cross-ply laminate.

loading only, as illustrated in Fig. 2. A standard derivation based on the assumption that the in-plane strains are identical in every ply and that there are an equal number of 0 and 90 plies, gives the overall relation for the laminate to be

$$\epsilon_{11} = \frac{1}{E_0}\sigma_{11} - \frac{\nu_0}{E_0}\sigma_{22}$$

$$\epsilon_{22} = -\frac{\nu_0}{E_0}\sigma_{11} + \frac{1}{E_0}\sigma_{22}$$

$$\epsilon_{12} = \frac{1}{2\mu_0}\sigma_{12} \tag{7}$$

where

$$E_0 = \frac{\frac{1}{4}\left(1+\frac{E_L}{E_T}\right)^2 - \nu_L^2}{\frac{1}{2}\left(1+\frac{E_L}{E_T}\right)\left(\frac{1}{E_T}-\frac{\nu_L^2}{E_L}\right)}$$

$$\nu_0 = \frac{2\nu_L}{1+\frac{E_L}{E_T}}$$

$$\mu_0 = \mu_L \tag{8}$$

are Young's modulus, Poisson's ratio and shear modulus of the laminate, respectively, in the defined coordinates.

The plane strain Young's modulus defined as

$$\bar{E}_0 = \frac{E_0}{1-\nu_0^2} = \frac{\frac{1}{2}E_L\left(1+\frac{E_L}{E_T}\right)}{\frac{E_L}{E_T}-\nu_L^2} \tag{9}$$

will appear frequently in the sequel. Since the transverse modulus E_T depends on whether the fiber/matrix interfaces are bonded or not, $\bar{E}_0$ also differs for these two cases.

2.2. Concept of steady-state tunneling cracks

Cracking in layered materials often occurs in the tunneling mode within individual layers, as illustrated in Fig. 1. The energy release rate at the tunnel front can be computed in principle by a three dimensional analysis. However, as the length of the tunnel becomes long compared with layer thickness, a steady-state is reached in which the same mode I energy release rate G_{SS} is attained at every point on the front and is independent of tunnel length [7]. From an energy argument, the steady-state energy release rate G_{SS} can be computed using quantities from the two-dimensional plane strain solution to the crack problem depicted in Fig. 3. The result is

$$G_{SS} = \frac{1}{2}\left\{\frac{1}{2t}\int_{-t}^{t}\sigma_0(x)\,\delta(x)\,dx\right\} \tag{10}$$

where $2t$ is the layer thickness, σ_0 is the stress normal to the crack surface prior to cracking, and δ is the crack opening displacement. This is applicable to linear elastic anisotropic materials and can be used when residual stress is present.

3. FINITE ELEMENT ANALYSIS

3.1. Isolated cracks and the onset of tunnel cracking

A complete analysis of the isolated crack problem depicted in Fig. 3, is performed by finite element analysis for all practical ranges of fiber volume fraction c and the ratio of Young's modulus of fiber to matrix, for both bonded and separated fiber/matrix interfaces. The results for propagation of an isolated tunneling crack will be used to generate the conditions under which extensive matrix cracking first occurs.

Figure 3 shows the cross section of a laminate with a single transverse crack spanning the entire central 90° layer. The stress–strain behavior of each of the plies is taken to be elastically orthotropic obeying (1), with due regard for the two orientations. The interfaces between the layers are assumed to be perfectly bonded. Plane strain conditions are assumed in the z-direction and $\nu_m = \nu_f = 0.2$. The average tensile stress applied at infinity is σ, and the tensile stress in the 90° layer, prior to cracking, is

$$\frac{2E_T}{E_L+E_T}\sigma.$$

One can readily show that the normalized steady-state, tunneling energy release rate,

$$\frac{G_{SS}\bar{E}_0}{\sigma^2 t}$$

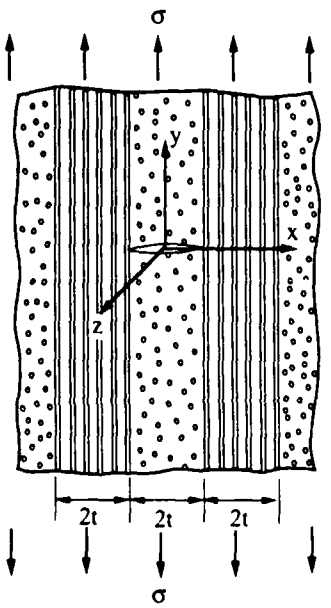

Fig. 3. An isolated crack in a 90° layer.

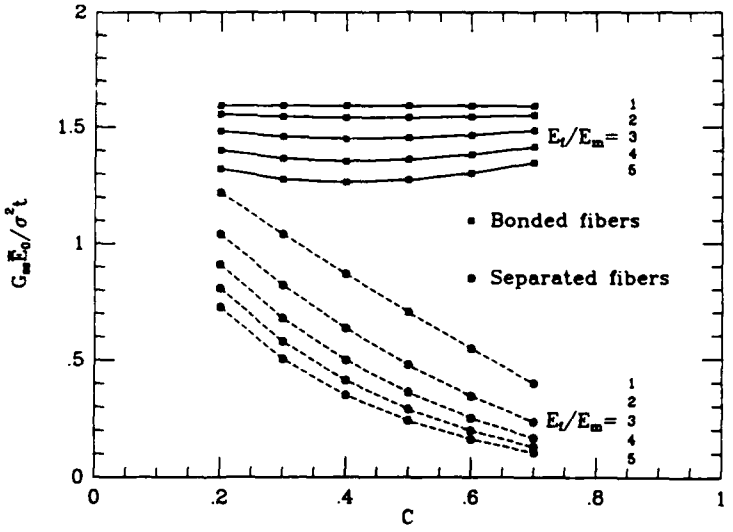

Fig. 4. The function, $f(E_f/E_m, c)$, providing the tunneling energy release rate in (11) for an isolated crack.

defined from (10) is a function only of fiber volume fraction c and the modulus ratio E_f/E_m, assuming the Poisson's ratios have been assigned, i.e.

$$\frac{G_{SS}\bar{E}_0}{\sigma^2 t} = f\left(\frac{E_f}{E_m}, c\right) \tag{11}$$

where $\bar{E}_0$ is defined in (9) for the two cases, bonded and unbonded fibers mentioned in connection with (6). Results displaying the dependence are shown in Fig. 4 for the two cases. These results were computed using a 7-layer laminate model with the crack in the central layer, but they should apply for an arbitrary large number of layers with high accuracy. In fact, results computed using a 3-layer model and normalized in exactly the same way differ only very slightly from those shown in Fig. 4.

Denote the toughness of the layers in the tunneling cracking mode by Γ, measured in units of energy per unit area. For a crack propagating entirely in the matrix, this would be the mode I toughness of the matrix, Γ_m. For a tunnel crack front encompassing the unbonded interfaces between the fiber and matrix, Γ would be some fraction of Γ_m. The minimum stress σ_{onset} required for propagation of tunneling cracks in the 90° layers is obtained from (11) as

$$\sigma_{onset} = \sqrt{\frac{\Gamma\bar{E}_0}{tf\left(\frac{E_f}{E_m}, c\right)}}. \tag{12}$$

This sets the condition for the *onset* of extensive cracking in 90° layers. Note that this first cracking stress is inversely proportional to the square root of the ply thickness. If an initial residual tensile stress, σ_R, exists in the 90° layers acting parallel to the applied stress, then the sum of $\sigma_R(E_L + E_T)/(2E_T)$ and σ_{onset} should appear on the left hand side of (12). In other words, residual tension in the layer, modified by the factor $(E_L + E_T)/(2E_T)$, is equivalent to an overall

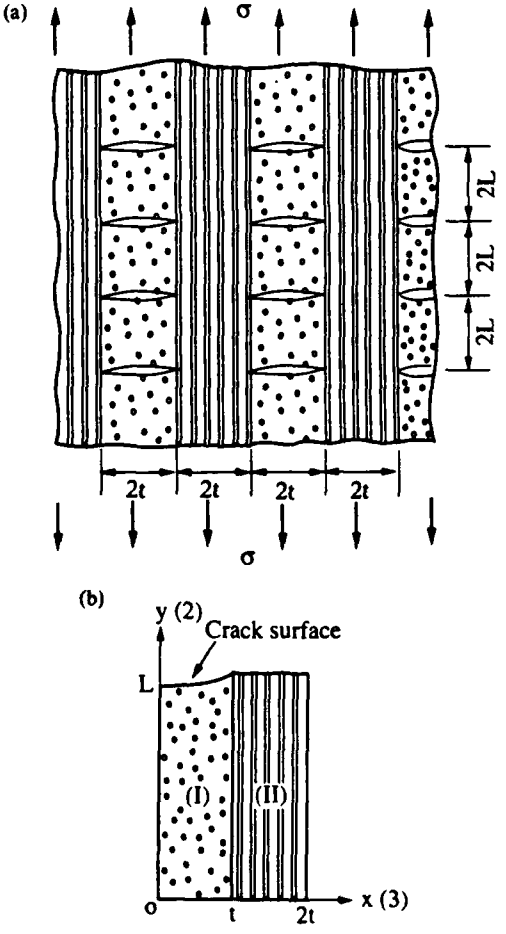

Fig. 5 (a). The doubly periodic crack pattern analysed in this paper. (b) A quarter of a periodic cell used for the finite element model.

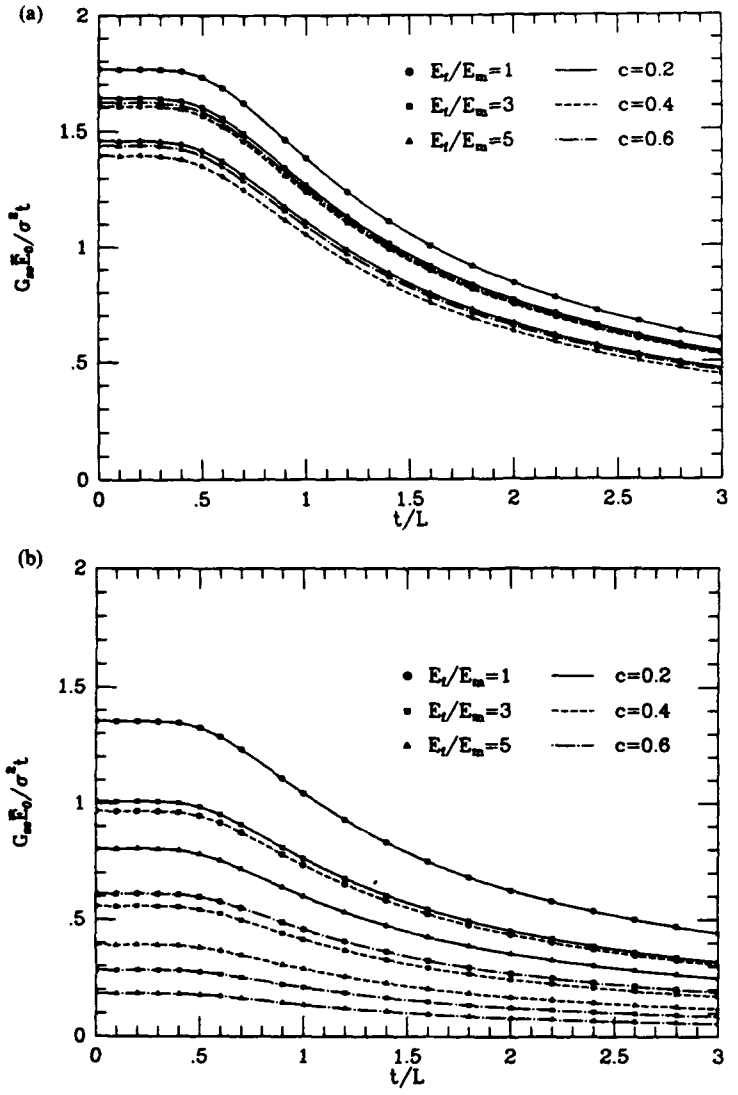

Fig. 6. The function, $g(E_f/E_m, c, t/L)$, providing the energy release rate for a doubly periodic array of tunneling cracks in (13). (a) Bonded fiber/matrix interfaces. (b) Separated fiber/matrix interfaces.

applied stress contribution as far as tunnel cracking is concerned.

3.2. *Multiple cracking*

Multiple cracking in 90° layers occurs when the applied stress exceeds the critical level given by (12). Results will be presented in this subsection for the doubly periodic, plane strain crack problem depicted in Fig. 5(a). Specifically, results will be presented which allow one to predict: (1) the evolution of crack density in the 90° layers, (2) the increase in overall compliance as a function of crack density, and (3) the extra overall strain released by the cracks in the presence of residual stress. The cracks are taken to be equally spaced within all 90° layers, with spacing $2L$ and with the doubly periodic pattern shown in Fig. 5(a). Plane strain conditions are again invoked and no traction is applied in the x-direction. Because of symmetry, only one quarter of a periodic cell needs to be considered in setting up the finite element model, which is shown in Fig. 5(b). Standard symmetry boundary conditions are applied on all edges of the quarter cell in Fig. 5(b) except along the crack face where traction-free conditions are imposed. The average traction on the vertical faces is required to vanish, consistent with the assumption that no stress is applied in the x-direction.

The finite element results for G_{SS}, expressed in non-dimensional form as

$$\frac{G_{SS}\bar{E}_0}{\sigma^2 t} = g\left(\frac{E_f}{E_m}, c, \frac{t}{L}\right) \tag{13}$$

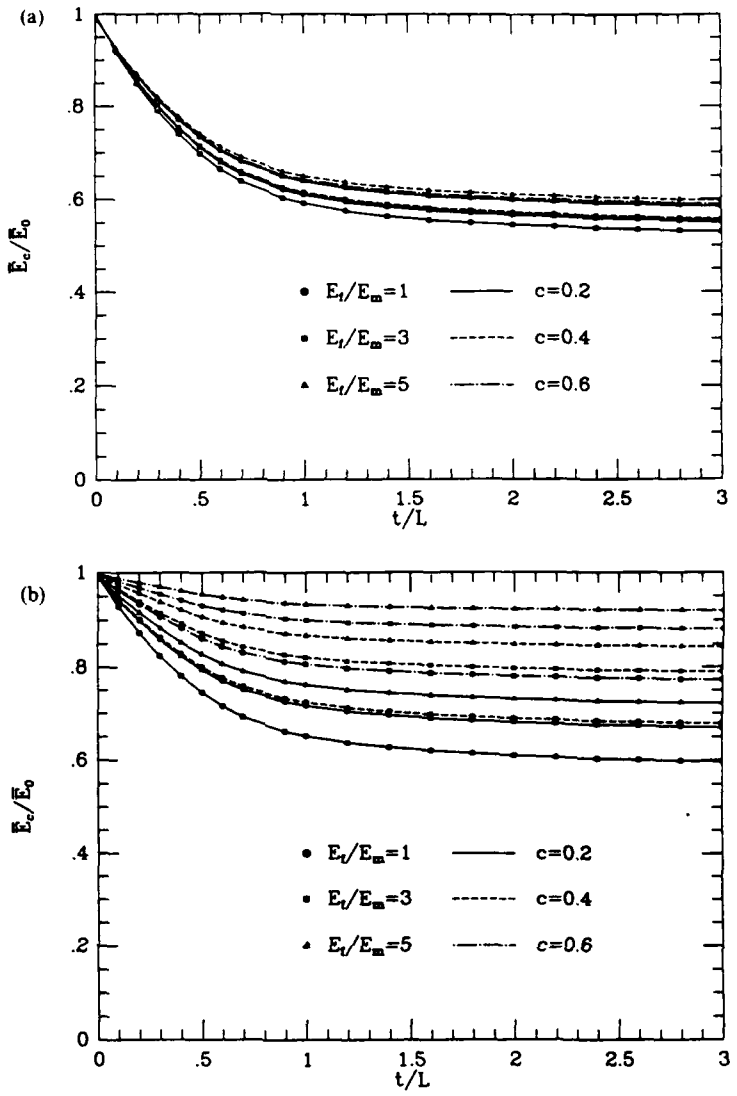

Fig. 7. The function, $h(E_f/E_m, c, t/L)$, providing the effective Young's modulus for the cracked laminate in (14). (a) Bonded fiber/matrix interfaces. (b) Separated fiber/matrix interfaces.

are shown in Figs 6(a,b), respectively, for bonded and separated fiber/matrix interfaces. In Section 4, it will be shown how to use this result for steady-state cracking to predict crack spacing as a function of applied stress. The corresponding results for the effective plane strain Young's modulus for the periodically cracked composite, defined as $\bar{E}_c = \sigma/\epsilon$ where ϵ is the average strain in the y direction, are shown in Figs 7(a,b) as

$$\frac{\bar{E}_c}{\bar{E}_0} = h\left(\frac{E_f}{E_m}, c, \frac{t}{L}\right). \tag{14}$$

As the crack density t/L becomes larger than about 2, the results have asymptoted to the limit in which only the 0° layers carry the load, which are simply

$$\frac{\bar{E}_c}{\bar{E}_0} = \frac{E_L}{E_L + E_T}. \tag{15}$$

It can be shown, by the reciprocal theorem of elasticity, that (13) and (14) are related by

$$\frac{1}{h\left(\frac{E_f}{E_m}, c, \frac{t}{L}\right)} = 1 + \frac{t}{2L} g\left(\frac{E_f}{E_m}, c, \frac{t}{L}\right). \tag{16}$$

Residual stresses and strains are generally introduced during the process when the plies are bonded together to form the layered composite. As discussed

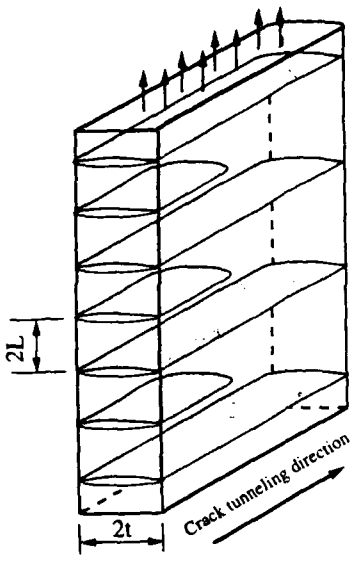

Fig. 8. A new set of tunneling cracks bisecting an existing set of cracks in a given layer.

earlier, if an initial, uniform residual stress σ_R exists in the 90° layers acting parallel to the applied stress σ, the effect on the tunneling energy release rate is taken into account by replacing σ on the left side of (13) by the sum of $\sigma_R(E_L + E_T)/(2E_T)$ and σ. An additional overall strain, ϵ_A, occurs due to the release of residual stress by the formation of the cracks in the 90° layers. By a simple process of superposition (see Appendix), one can show that

$$\epsilon_A = \left(\frac{1}{\bar{E}_c} - \frac{1}{\bar{E}_0}\right)\frac{E_L + E_T}{2E_T}\sigma_R = (h^{-1} - 1)\frac{E_L + E_T}{2E_T}\frac{\sigma_R}{\bar{E}_0}. \tag{17}$$

In the limit where the crack spacing becomes small (i.e. t/L becomes larger than about 2), the stress in the 0° layers due to the residual stress is reduced to zero. Consequently, in this limit, ϵ_A is just the negative of the initial strain in the 0° layers in the uncracked composite, i.e.

$$\epsilon_A = \frac{E_L + E_T}{2E_L}\frac{\sigma_R}{\bar{E}_0} = \left(1 - \frac{E_T}{E_L}\nu_L^2\right)\frac{\sigma_R}{E_L}. \tag{18}$$

4. APPLICATION TO PREDICT CRACK SPACING AND OVERALL STRESS–STRAIN BEHAVIOR

4.1. Prediction of crack spacing

Results obtained in the last section will be used here to predict the tunneling crack spacing in 90° layers as a function of applied stress. The method employed here is identical to that of Hutchinson and Suo [7] used to predict the crack spacing in thin films under residual tension. It considers the effect of a sequential cracking process where a new set of cracks tunnels between an existing set of cracks as the stress is increased, rather than a process where all the cracks tunnel together.

The calculation of the energy release rate for the cracks tunneling in the sequential process makes use of the basic solution (13) for simultaneous steady-state cracking. That solution is for simultaneous tunneling of all the cracks, periodically spaced a distance $2L$ apart, in the 90° layers, as in Fig. 5. For any such laminate, the steady-state tunneling energy release rate for each crack is given by (13)

$$\frac{G_{SS}\bar{E}_0}{\sigma^2 t} = g\left(\frac{t}{L}\right) \tag{19}$$

where here the dependence of g on E_f/E_m and c is left implicit. As noted before, when a residual stress σ_R

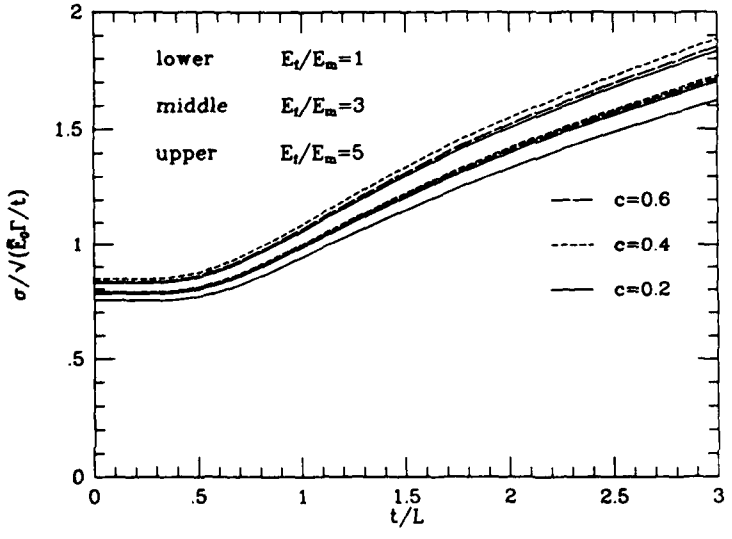

Fig. 9. Relationship between applied stress and crack spacing.

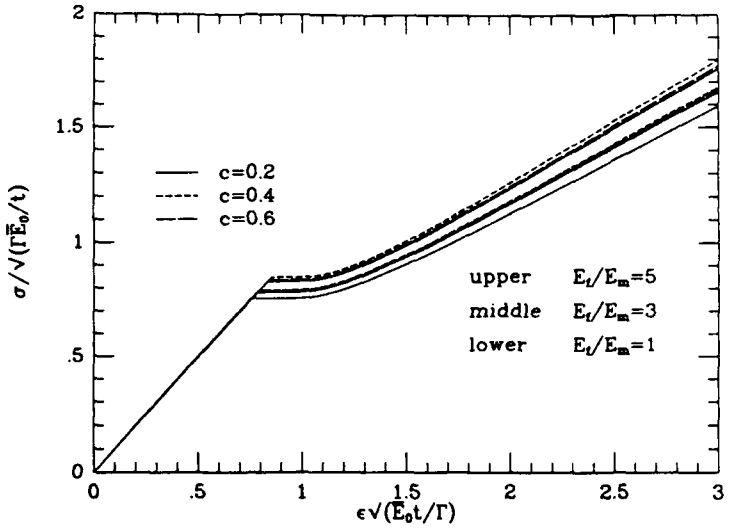

Fig. 10. Overall stress–strain behavior in the absence of residual stress.

exists in the 90° layers acting parallel to the overall applied stress σ, then σ in the above formula should be replaced by $\sigma + (E_L + E_T)\sigma_R/(2E_T)$.

Now consider the sequential cracking situation depicted in Fig. 8, where one set of cracks spaced a distance $4L$ apart has already tunneled across all 90° layers, and where a second set bisecting the first set is in the process of tunneling across the layers. We depicted in Fig. 8 only an isolated 90° layer for better viewing. The steady-state energy release rate for the cracks in the process of tunneling can be obtained exactly from the strain energy difference far behind and far ahead of the tunneling fronts as

$$\frac{G_{SS}\bar{E}_0}{\sigma^2 t} = 2g\left(\frac{t}{L}\right) - g\left(\frac{t}{2L}\right). \tag{20}$$

Under the assumption that new cracks will always be nucleated half-way between cracks that have already formed and tunneled, and with G_{SS} identified with the mode I toughness Γ along fiber direction of 90° layers, (20) predicts the relationship between σ and the crack spacing t/L. This relation is plotted in Fig. 9 for bonded fiber/matrix interfaces. There are two features worth noting. For spacing larger than L/t of about 2, there is essentially no interaction between the cracks and the spacing is indeterminate by the present analysis. For smaller spacings the ratio t/L increases approximately linearly with stress σ, and the dependence on the parameters c and E_f/E_m is largely captured in the non-dimensional stress variable $\sigma/\sqrt{(\bar{E}_0\Gamma/t)}$. Implicit in the spacing relationship in Fig. 9 is the assumption that initial flaws exist in the 90°

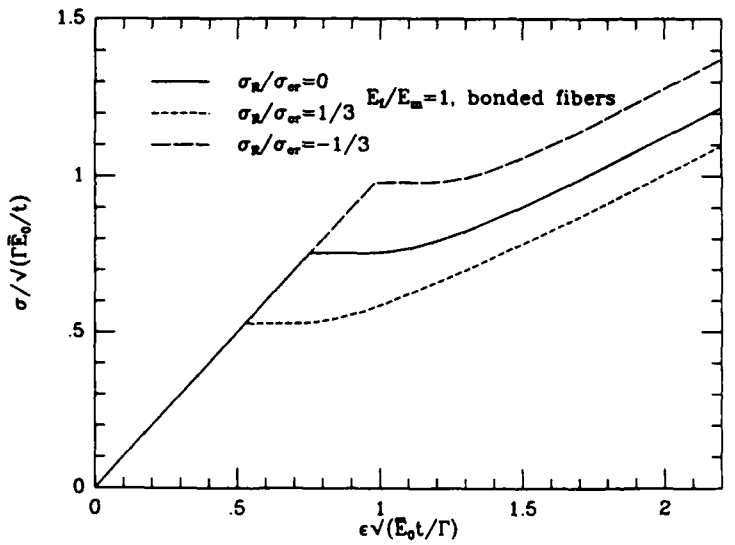

Fig. 11. An illustration of the effect of residual stress on overall stress–strain behavior.

layers of sufficient size and density such that the tunnel cracks *will* initiate when the steady-state condition is met. In this sense, the relation between spacing and stress may predict somewhat smaller spacings at a given stress than actually occurs.

4.2. *Prediction of overall stress–strain relation accounting for progressive cracking*

Let σ be the overall stress applied to the composite and suppose that a residual stress σ_R exists in the uncracked 90° layers acting parallel to the applied stress. With σ replaced by $\sigma + (E_L + E_T)\sigma_R/(2E_T)$ in the non-dimensional stress variable on the ordinate in Fig. 9, the appropriate curve in this figure can be used to predict t/L as a function of σ. Next, combine (14) and (17) to give the overall strain ϵ as

$$\epsilon = \frac{1}{\bar{E}_c}\sigma + \epsilon_A = \frac{1}{h}\frac{\sigma}{\bar{E}_0} + \left(\frac{1}{h} - 1\right)\frac{E_L + E_T}{2E_T}\frac{\sigma_R}{\bar{E}_0}. \quad (21)$$

Here $h(E_f/E_m, c, t/L)$ can be obtained from Fig. 7 once one has obtained the relation between t/L and σ as just described.

The calculations described above are now illustrated. In Fig. 10 plots are displayed of the normalized overall applied stress against the normalized overall strain for cases in which there is no residual stress. As noted earlier, the stress remains essentially unchanged until the crack spacing reaches an L/t of about 2. This corresponds to the flat portion of the stress–strain curves in Fig. 10. As L/t diminishes to small values (below about 1/2) the 0° layers carry most of the load, leading to the linear response evident in the figure, with (15) providing the asymptotic slope of these curves. A remarkable feature of these curves is the fact that the

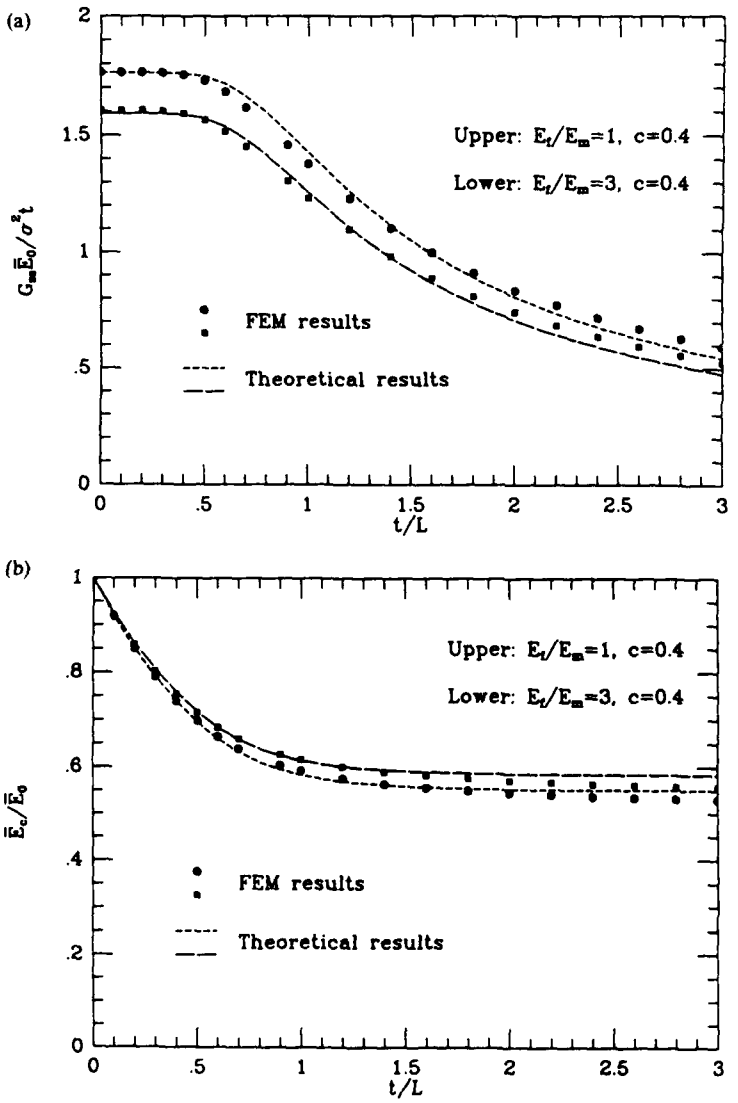

Fig. 12. (a) Demonstration of the accuracy of explicit formula (39). (b) Demonstration of the accuracy of explicit formula (41).

non-dimensional overall stress and strain variables used in Fig. 10 nearly collapse all the curves for a wide range of E_f/E_m and c.

Figure 11 shows the effect of a residual stress σ_R in the 90° layers, a positive value representing a residual tension and a negative value representing a residual compression. The critical stress σ_{cr} used to normalize the residual stress in Fig. 11 is the stress at which cracks begin to tunnel in all the layers in the absence of any residual stress. From (13), this stress is

$$\sigma_{cr} = \sqrt{\frac{\bar{E}_0 \Gamma}{tg(E_f/E_m, c, 0)}}. \tag{22}$$

This critical stress is between 5 and 10% higher than the onset stress for tunneling of an isolated crack given by (12). In Fig. 11, σ is the applied stress. Depending on its sign, the residual stress increases or decreases the applied stress at which matrix cracking occurs and makes a contribution to the overall strain due to its partial release.

5. AN APPROXIMATE THEORETICAL SOLUTION

5.1. The theoretical development

In this section we shall develop an approximate analytical solution to the doubly periodic plane strain crack problem posed in Fig. 5(b). Except for a modification suggested at the end of this section, the approximation follows fairly closely a similar solution in [8], where it was developed to predict the stress transfer between 0 and 90° plies of a cracked laminate. The solution in [8] applies to periodic cracks in a single layer sandwiched between 0° layers on both sides. The following equilibrium equations must be satisfied in both 90° (denoted as material I) and 0° (denoted as material II) plies

$$\frac{\partial \sigma_x}{\partial x} + \frac{\partial \tau_{xy}}{\partial y} = 0 \tag{23}$$

$$\frac{\partial \tau_{xy}}{\partial x} + \frac{\partial \sigma_y}{\partial y} = 0. \tag{24}$$

The stress–strain relations for plane strain conditions can be easily derived from (1). They are, for 90° plies

$$\epsilon_x \equiv \frac{\partial u}{\partial x} = \left(\frac{1}{E_T} - \frac{\nu_L^2}{E_L}\right)\sigma_x - \left(\frac{\nu_T}{E_T} + \frac{\nu_L^2}{E_L}\right)\sigma_y \tag{25}$$

$$\epsilon_y \equiv \frac{\partial v}{\partial y} = -\left(\frac{\nu_T}{E_T} + \frac{\nu_L^2}{E_L}\right)\sigma_x + \left(\frac{1}{E_T} - \frac{\nu_L^2}{E_L}\right)\sigma_y \tag{26}$$

$$\epsilon_{xy} \equiv \frac{1}{2}\left(\frac{\partial u}{\partial y} + \frac{\partial v}{\partial x}\right) = \frac{1}{2\mu_T}\tau_{xy} \tag{27}$$

and for 0° plies

$$\epsilon_x \equiv \frac{\partial u}{\partial x} = \left(\frac{1-\nu_T^2}{E_T}\right)\sigma_x - \frac{\nu_L(1+\nu_T)}{E_L}\sigma_y \tag{28}$$

$$\epsilon_y \equiv \frac{\partial v}{\partial y} = -\frac{\nu_L(1+\nu_T)}{E_L}\sigma_x + \frac{1-\frac{E_T}{E_L}\nu_L^2}{E_L}\sigma_y \tag{29}$$

$$\epsilon_{xy} \equiv \frac{1}{2}\left(\frac{\partial u}{\partial y} + \frac{\partial v}{\partial x}\right) = \frac{1}{2\mu_L}\tau_{xy}. \tag{30}$$

The boundary conditions for a typical cell of the doubly periodic problem are the standard ones reflecting symmetry and the relations between the overall quantities and the averages of local quantities over the cell boundaries.

To proceed, we assume that the stress component σ_y in both plies is independent of x. In other words, we look for an approximate solution of the form

$$\sigma_y^{I} = -F(y) + \sigma^{I} \tag{31}$$

$$\sigma_y^{II} = F(y) + \sigma^{II} \tag{32}$$

where σ^I and σ^{II} are the stresses in the 90 and 0° plies, respectively, that would result in a damage-free laminate subject to average remote tensile stress σ. They are given by

$$\sigma^{I} = \frac{2E_T}{E_T + E_L}\sigma \tag{33}$$

$$\sigma^{II} = \frac{2E_L}{E_T + E_L}\sigma. \tag{34}$$

We shall omit a detailed derivation for briefness; most of the details are similar to those given in [8]. After satisfying equations (23–25), (27), (28), (30) exactly, equations (26) and (29) in an average sense with respect to the x-direction, and satisfying all the boundary conditions except those listed below in (36) and (37), we obtain the following linear integral-differential equation for $F(y)$

$$t^4 F''''(y) - 2a_2 t^2 F''(y) + a_1^2 F(y) + a_0 \frac{1}{L}\int_0^L F(y)\,dy = 0 \tag{35}$$

where

$$a_2 = \frac{15}{2\Lambda}\left\{\left(\frac{1}{E_T} - \frac{\nu_L^2}{E_L} + \frac{1-\nu_T^2}{E_T}\right)\left(\frac{1}{\mu_T} + \frac{1}{\mu_L}\right) - 4\left[\left(\frac{1}{E_T} - \frac{\nu_L^2}{E_L}\right)\left(\frac{\nu_L(1+\nu_T)}{E_L}\right) + \left(\frac{\nu_T}{E_T} + \frac{\nu_L^2}{E_L}\right)\left(\frac{1-\nu_T^2}{E_T}\right)\right]\right\}$$

$$a_1^2 = \frac{45}{\Lambda}\left\{\left(\frac{1}{E_T} - \frac{\nu_L^2}{E_L} + \frac{1-\nu_T^2}{E_T}\right)\left(\frac{1}{E_T} - \frac{\nu_L^2}{E_L} + \frac{1-\frac{E_T}{E_L}\nu_L^2}{E_L}\right)\right.$$

$$-\left[\left(\frac{\nu_T}{E_T}+\frac{\nu_L^2}{E_L}\right)-\left(\frac{\nu_L(1+\nu_T)}{E_L}\right)\right]^2\Bigg\}$$

$$a_0=\frac{45}{\Lambda}\left[\left(\frac{\nu_T}{E_T}+\frac{\nu_L^2}{E_L}\right)-\left(\frac{\nu_L(1+\nu_T)}{E_L}\right)\right]^2$$

$$\Lambda=\left(\frac{1}{E_T}-\frac{\nu_L^2}{E_L}+\frac{1-\nu_T^2}{E_T}\right)^2+20\left(\frac{1}{E_T}-\frac{\nu_L^2}{E_L}\right)\left(\frac{1-\nu_T^2}{E_T}\right).$$

The remaining boundary conditions to be satisfied are given by

$$F(0)=0,\quad F(L)=\sigma^1,\quad \text{and}\quad F(L)=0. \tag{36}$$

In addition, it is required that $F(y)$ be an even function in y

$$F(y)=F(-y). \tag{37}$$

The solution to (35) can be used to express the integral of $F(y)$ as

$$\int_0^L F(y)\,dy=t\Phi\left(\frac{t}{L}\right)\sigma^1 \tag{38}$$

where Φ (which is also a function of a_0, a_1 and a_2) will be given below. The Young's modulus of the cracked composite, $\bar{E}_c$, is then approximately

$$\bar{E}_c\approx\frac{\sigma}{\bar{v}^{II}(L)/L}=\frac{\bar{E}_0}{1+\dfrac{t}{L}\dfrac{E_T}{E_L}\Phi} \tag{39}$$

and the tunneling energy release rate G_{SS}, calculated from

$$G_{SS}=\sigma^1[\bar{v}^{II}(L)-\bar{v}^1(L)] \tag{40}$$

is given by the approximation

$$\frac{G_{SS}\bar{E}_0}{\sigma^2 t}=\frac{2E_T}{E_L}\Phi \tag{41}$$

In equations (39) and (40), terms such as $\bar{v}(L)$ stand for the average y-displacement along $y=L$.

For the case a_2/a_1 is less than 1, Φ is given by

where

$$m=\sqrt{(a_1+a_2)/2}$$
$$n=\sqrt{|a_1-a_2|/2}$$
$$h=\frac{a_0}{a_0+a_1^2}.$$

For cases where a_2/a_1 is equal to or greater than 1, similar solutions can be obtained. However, for most practical fiber-reinforced composites, a_2/a_1 is either less than 1 or sufficiently close to 1 such that (42) is a good approximation.

5.2. *Modification using the FEM results*

The analytical approximation given by equations (39), (41) and (42) can be further enhanced by a slight modification of Φ in (42), which was suggested by the comparison of the approximate predictions with the more accurate FEM results obtained in Section 3. We found that the accuracy of the above approximation was improved when we replaced m and n is (42) by $1.1m$ and $1.1n$, respectively, and then multiplied Φ by the numerical factor of 0.82. Thus the modified Φ is given by

$$\Phi\left(\frac{t}{L}\right)=\frac{0.82\dfrac{2(1-h)mn}{m^2+n^2}\left(\cosh\dfrac{2.2mL}{t}-\cos\dfrac{2.2nL}{t}\right)}{1.1m\sin\dfrac{2.2nL}{t}+1.1n\sinh\dfrac{2.2mL}{t}-\dfrac{2hmn}{m^2+n^2}\dfrac{t}{L}\left(\cosh\dfrac{2.2mL}{t}-\cos\dfrac{2.2nL}{t}\right)}. \tag{43}$$

Several comparisons of the results given by FEM analysis and the explicit formulas of equations (39) and (41) are demonstrated in Figs 12(a,b). The differences for all practical ranges of E_f/E_m and c are within 5%, and thus we believe the formulas given above are well suited for practical applications.

Acknowledgements—This work was supported in part by the DARPA URI (Subagreement P.O. # KK3007 with the University of California, Santa Barbara, ONR Prime Contract N00014-92-J-1808) and by the Division of Applied Sciences, Harvard University. Finite element analyses are carried using ABAQUS (Hibbitt, Karlsson & Sorensen Inc., Providence, Rhode Island, U.S.A.).

REFERENCES

1. D. H. Allen, C. E. Harris and S. E. Groves, *Int. J. Solids Struct.* **23**, 1301 (1987).
2. D. H. Allen, C. E. Harris and S. E. Groves, *Int. J. Solids Struct.* **23**, 1319 (1987).
3. P. Gudmundson and S. Ostlund, *J. Comp. Mater.* **26**, 1009 (1992).

$$\Phi\left(\frac{t}{L}\right)=\frac{\dfrac{2(1-h)mn}{m^2+n^2}\left(\cosh\dfrac{2mL}{t}-\cos\dfrac{2nL}{t}\right)}{m\sin\dfrac{2nL}{t}+n\sinh\dfrac{2mL}{t}-\dfrac{2hmn}{m^2+n^2}\dfrac{t}{L}\left(\cosh\dfrac{2mL}{t}-\cos\dfrac{2nL}{t}\right)} \tag{42}$$

4. P. Gudmundson and W. Zang, SICOMP Tech. Report 92-007 (1992).
5. D. S. Beyerle, S. M. Spearing and A. G. Evans. *J. Am. Ceram. Soc.* **75**, 3321 (1992).
6. R. M. Christensen, *Mechanics of Composite Materials*. Wiley, New York (1979).
7. J. W. Hutchinson and Z. Suo, in *Advances in Applied Mechanics* (edited by J. W. Hutchinson and T. Y. Wu), Vol. 29, p. 64. Academic Press, New York (1991).
8. L. N. McCartney, *J. Mech. Phys. Solids* **40**, 27 (1992).

APPENDIX

When an initial residual stress σ_R exists in the 90° layers acting parallel to the applied stress, an additional overall strain ϵ_A occurs due to the release of residual stress by the formation of the cracks in the 90° layers. This additional strain can be calculated by applying a normal stress of $(-\sigma_R)$ to the crack surface. Figure A1(a) depicts a quarter of such a periodic cell, with standard symmetry boundary conditions applied. By a linear superposition argument, one can easily verify that the displacement and stress fields of Fig. A1(a) can be obtained by subtracting that in Fig. A1(c) from Fig. A1(b), where (b) has the same crack configuration as (a), and (c) depicts the crack-free laminate. The elements in (b) and (c) are both subject to an average stress $(E_L + E_T)\sigma_R/(2E_T)$. The overall strain ϵ_b associated with (b) is given by (14)

$$\epsilon_b = \frac{1}{E_c}\frac{E_L + E_T}{2E_T}\sigma_R = h^{-1}\frac{E_L + E_T}{2E_T}\frac{\sigma_R}{E_0} \tag{A1}$$

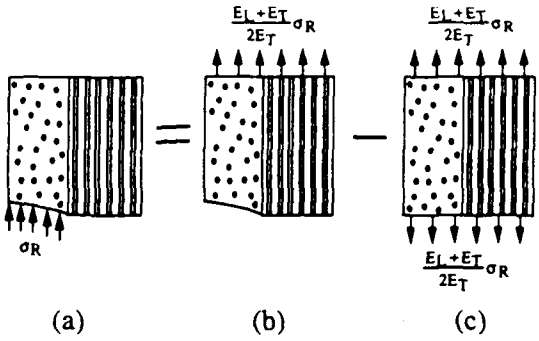

Fig. A1. Superposition for obtaining ϵ_A due to the release of residual stress.

and the overall strain ϵ_c in (c) is given by a uniform plane strain tension

$$\epsilon_c = \frac{1}{E_0}\frac{E_L + E_T}{2E_T}\sigma_R. \tag{A2}$$

The overall strain ϵ_A in (a) is then

$$\epsilon_A = \epsilon_b - \epsilon_c = (h^{-1} - 1)\frac{E_L + E_T}{2E_T}\frac{\sigma_R}{E_0} \tag{A3}$$

which is (16) given in Section 3.

MATERIALS

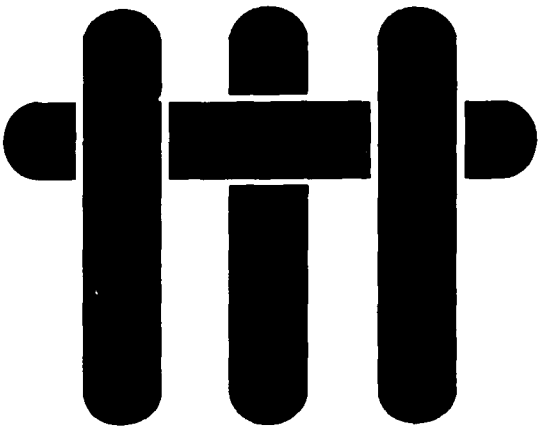

THE MECHANISMS OF DEFORMATION AND FAILURE IN CARBON MATRIX COMPOSITES SUBJECT TO TENSILE AND SHEAR LOADING

by

K.R. Turner, J.S. Speck and A.G. Evans
Materials Department
College of Engineering
University of California, Santa Barbara
Santa Barbara, California 93106–5050

ABSTRACT

The operative damage mechanisms in a series of C matrix composites loaded in tension and shear have been investigated. The composites contained either C-fibers or Nicalon fibers, both with and without a carbon coating. The matrix consisted primarily of ex-phenolic carbon with a final carbon layer introduced by chemical vapor infiltration (CVI). Some composites have a high fiber/matrix sliding stress, τ. In these composites, failure is characterized by localized fiber pull-out. Other composites have a low τ. Failure of these materials is characterized by stochastic fiber failure with a diffuse fracture surface. The operative damage mechanisms have been identified and used in conjunction with available models to rationalize composite performance in terms of constituent properties(fiber, matrix, interface). The properties emphasized include the inelastic strain, as well as the ultimate tensile and shear strengths.

1. INTRODUCTION

Carbon matrix composites represent an important class of high-temperature structural material.[1-5] Such composites, reinforced with either C or SiC fibers, have mechanical characteristics that exhibit both similarities and differences to ceramic matrix composites (CMCs), such as SiC/CAS and SiC/SiC.[6-10] In tension, the C matrix materials have minimal non-linearity, whereas CMCs exhibit considerable inelastic strain associated with matrix cracking and interface sliding[9-11] (Fig. 1a). This strain initiates at a stress,[12-14] σ_{mc}, appreciably below the ultimate tensile strength[15] (UTS). In *shear*, the C matrix materials experience substantial inelastic deformation at relatively small strength levels and are relatively ductile[10] (Fig. 1b). The shear strengths of CMCs are larger but the ductilities smaller.

Related responses occur upon tensile loading in the presence of notches. In C matrix materials bands of localized shear damage form and extend parallel to the principal loading direction[5] (Fig. 2). These "shear bands" redistribute stress and diminish the notch sensitivity of the material.[5] In CMCs, tensile matrix cracking is the preferred damage mode which dominates stress redistribution at notches. The differences in behavior found between the CMCs and the C matrix materials have been attributed to differences in matrix modulus, E_m, relative to that of the fibers, E_f.[5,9] For most CMCs, E_m/E_f is in the range, $0.3 \rightarrow 2$; whereas for C matrix material, $E_m/E_f < 0.1$[9] (Table I).

While the damage mechanisms and their role in stress redistribution have been extensively studied and modelled in CMCs,[9,16] the corresponding mechanisms operating in C matrix composites are not appreciated. The limited knowledge about stress-induced damage reflects, in part, the experimental challenge in detecting damage and separating such damage from processing flaws. The current article addresses this

issue by devising and applying experimental procedures for detecting and characterizing processing flaws and distinguishing them from mechanically-induced damage.

2. MATERIALS

The materials to be used in this study, consisting of both C/C and SiC/C, have been described in previous studies[4,5] (Table I). Briefly, the composites contained either C-fibers or Nicalon fibers, both with and without a carbon coating. The composites are 2-D materials with an 8-harness satin-weave fiber architecture surrounded by an ex-phenolic carbon and a final carbon layer introduced by chemical vapor infiltration (CVI). The fabric layers are positioned back-to-back and front-to-front, yielding a composite cross-section that resembles a laminate of 0° fiber plies and 90° fiber plies, with an occasional interply weave bundle (Fig. 3a). For simplicity, the following nomenclature will be used throughout:

(1) *0° fiber layer or ply*—a ply that consists primarily of 0° fibers. In tension, 0° fibers lie parallel to the tensile loading axis, and

(2) *90° fiber layer or ply*—a ply or layer of fibers that lies perpendicular to 0° plies.

However, it must be appreciated that this is not a 0° - 90° laminate: there are occasional intrusions into all 'plies' by the weave bundles.

3. MECHANICAL MEASUREMENTS

A range of mechanical tests (described elsewhere[4,6,8,16]) have been performed in order to activate all of the potential damage mechanisms that operate in C matrix materials. The tests performed include tension (un-notched, notched, center-hole and

center-crack) and Iosipescu shear. Additionally, flexural tests have been performed and observed *in-situ* in an optical microscope to monitor damage evolution on the tensile surface.

The stress/strain characteristics obtained with each of these tests re-affirm that C matrix materials are readily susceptible to inelastic deformation in shear, but are essentially linear in tension (Fig. 1). Moreover, there is a substantial property difference between the two SiC/C materials. These are designated HT and LT. This notation refers to the interfaces, which have high shear resistance (HT) and low shear resistance (LT), respectively (Table I). The difference is governed by the fiber coating. The HT material has the lower tensile strength and seemingly fails from notches by the growth of a dominant mode I crack.[5] The LT material has a high tensile strength and develops "shear bands" from notches that redistribute stress and cause large notch opening displacements prior to failure.[5]

4. DAMAGE CHARACTERIZATION

4.1 Procedures

The experimental methods devised for damage characterization in C matrix composites have been elaborated separately.[17] They are briefly reviewed here. The methods are based on both optical and scanning electron (SEM) microscopy, using either ion etching or penetrants to highlight and distinguish the damage. Diamond polishing followed by ion etching has been shown to generate surfaces that are representative of the state of the material, without further damage being created by the surface preparation procedure. The penetrant approach relies on the use of ZnI, which infuses the damaged regions and highlights them upon backscatter imaging in the SEM.[4,5,18]

A vital feature that distinguishes processing flaws from stress-induced damage arises because of the final chemical vapor infiltration (CVI) step used in the composite processing sequence. This step deposits a 3 - 10 μm thick C layer onto the surfaces of all accessible porosity and processing flaws.[17] This layer is comprised of oriented columnar grains with the carbon basal sheets running parallel to the local deposition surface. This layer can be distinguished by polarized light microscopy (Fig. 3b).

It has been found that damage observations are more readily performed on SiC/C than C/C because of the contrast between the fibers, the matrix and the interfacial zone. The contrast enhancement of the former, in optical microscopy, is attributed to the optical isotropy of Nicalon fibers as opposed to the high optical anisotropy of graphitized C fibers and CVI carbon. Most of the observations and analyses are performed on the SiC/C composites, but the general implications are considered relevant to C/C composites.

4.2 As-Processed Flaws

The as-processed composites display two major types of processing flaw (hereafter referred to as "processing damage"): transply shrinkage cracks and interfiber axial porosity. (i) Transply shrinkage cracks with opening displacements of ~10-30 μm are located periodically within the plies (Fig. 3b). These usually extend fully across the ply, but do not penetrate adjacent plies.[17] There is no obvious spatial correlation between shrinkage cracks in alternating plies. Such cracks are delineated by the CVI surface layer, as noted above. (ii) Interfiber axial porosity is prevalent in regions between individual fibers within a ply (Fig. 3c). These pores are often circumvented by the CVI layer. Both types of processing damage are attributed to matrix constraint, caused by the fiber preform, during pyrolysis of the phenolic precursor used for the matrix.

4.3 Stress-Induced Damage

4.3.1 Tensile Loading

Studies performed on SiC/C composite specimens subject to *tensile loading* indicated minimal stress-induced matrix damage within the 0° plies prior to fiber failure. Such behavior is markedly different from CMCs,[6-9] which exhibit multiple matrix cracking at stresses well below the UTS. The role of the modulus ratio, E_m/E_f, on this difference in behavior is discussed below.

The following observations were made after testing the composite to failure in tension. (i) The fracture surface of the HT material displayed nearly co-planar fiber and matrix fracture with some fiber pull-out (Fig. 4a). Conversely, the fracture surface of the LT material had an irregular appearance, with a wide variation in matrix failure location (Fig. 4b). (ii) The coating on many of the fibers in the LT material exhibited sawtooth 'cracks' extending away from the fiber fracture surface, along the length of the exposed fiber (Fig. 5). Similar features were not apparent in the HT material. (iii) In both composites, the fibers had multiple fracture sites along the length of the specimen, with residual opening displacements (ROD). In the LT material (Fig. 6a), the ROD was relatively large, implying that fiber/matrix interface sliding had taken place. Conversely, in the HT material, the ROD was small, indicating minimal sliding (Fig. 6b). There were also matrix cracks associated with some of the fiber fractures in the HT material.

In-situ observations of the tensile surface of a sample loaded in flexure revealed additional differences between the LT and HT materials. The LT material appeared to be free of matrix cracking in either the 0° or 90° plies, but there was considerable 0° fiber failure at stresses below the UTS, at essentially random locations (Fig. 7a). Conversely, the HT material exhibited periodic stress-induced matrix cracks in the 90° plies at loads

exceeding ~ 0.7 σ_{max}. These cracks formed normal to the tensile loading axis and partially penetrated the 0° plies, causing subsequent fiber fractures (Fig. 7b).

Observations of the transply processing flaws upon loading also resolved important distinctions between the two materials. In the LT material, these flaws open uniformly as the load is applied. The opening increases with load such that, just prior to failure, the increase in opening displacement approaches ~3μm. Conversely, in the HT material the openings are much smaller (~0.1 μm) and essentially elastic in nature. The openings that occur in the LT material imply relative sliding displacements between the 0° and 90° plies, with a characteristic shear resistance, designated τ_p (Appendix). It has not been possible to identify the mechanisms that allow these displacements to occur. However, the matrix between the fibers at the ply interface must experience microcracking. It is presumed that the behavior is similar to sawtooth cracking (Fig. 5) which is typical of Mode II crack growth in brittle materials[25].

4.3.2 In-Plane Shear Loading

Observations made on SiC/C specimens after *in-plane shear* loading indicate modes of damage that differ from those found in tension. In the LT material, multiple small cracks formed in the coating and the CVI layer between the fibers and the matrix (Fig. 8a). These cracks were oriented at ~ 15° - 45° to the fiber axis and connect to the axial porosity (see Fig. 3b). The range of crack angles is attributed to the variation in the preferred alignment of the carbon next to the fiber.[17] At locations having the lower cracking angles, the carbon layers are well-aligned along the fiber axis. When the resolved *tensile* stress exceeds the carbon interlayer strength, cracks initially extend on these layers parallel to the fiber axis. During fiber sliding, these cracks 'rotate' and increase their inclination with respect to the fiber axis. Alternatively, where the cracks form at angles of ~ 45°, the carbon is found to be more isotropic.[17]

In matrix dominated regions, relatively large, periodic matrix cracks occur in both the LT and HT materials (Fig. 8b), oriented ~ 45° to the loading axis.[10]

4.3.3 Notched Tension

Observations of SiC/C specimens after notched tensile loading revealed combined damage modes, similar to those found in the unnotched specimens. Namely, sawtooth coating damage and variable fiber failure planes in the LT material. Shear damage was also evident, especially in the LT material, similar to that found on the shear specimens. The damage consists primarily of multiple microcracks in the coating and CVI layer around the fibers, as well as 45° matrix cracks in the matrix-dominated region (Fig. 8).

5. ANALYSIS

5.1 Tension

The *inelastic strain* and the damage obtained upon *tensile loading* are addressed by analysis of the two contributions: fiber failure and matrix cracking. Multiple *fiber failure* subject to interface sliding produces inelastic strains. When these failures occur in accordance with global load sharing[15] (GLS), subject to interface sliding at stress τ, the *uniaxial stress-strain* $\bar{\sigma}(\bar{\varepsilon})$ *relationship* is;[23]

$$\bar{\sigma}/fS_c = \left(E_f \bar{\varepsilon}/S_c\right)\left[1 + \sum_{n\geq 1} \frac{(-1)^n}{2n!} \frac{2 + n(m+1)}{1 + n(m+1)} \left(E_f \bar{\varepsilon}/S_c\right)^{n(m+1)}\right] \quad (1)$$

where S_c is the characteristic fiber strength and m is the shape parameter.[15] Upon using the values of S_c and m obtained independently, from fracture mirror measurements[4,5] (Table I), the stress-strain curves predicted by Eqn. (1) have been calculated and superposed onto the experimental curves (Fig. 9). For this purpose, the initial modulus

has been matched to the experimental value and it has been assumed that *all of the load is carried by the 0° plies*. It is evident that the inelastic strains are well-represented by predictions based on stochastic fiber failure, with interface sliding. It is also apparent from Fig. 9 that the ultimate tensile strength (UTS) of the LT material is predicted with good accuracy by Eqn. (1), consistent with the operation of GLS in this material.[4] However, the UTS for the HT material is substantially less than the predicted value. This material violates GLS, as noted previously,[4] and as elaborated below.

Matrix cracking is subject to lower bound values of stress. For the 0° plies, this bound, designated σ_{mc}, is given by:[12-14]

$$\sigma_{mc} = \left[\frac{6\tau\Gamma_m f^2 E_f E_L^2}{(1-f)E_m^2 R}\right]^{1/3} - \sigma^T \qquad (2)$$

where Γ_m is the matrix fracture energy, f the fiber volume fraction within the plies, τ the interface sliding stress, R the fiber radius, σ^T the misfit stress, E_f the fiber modulus, E_m the matrix modulus and E_L the longitudinal ply modulus. In practice, matrix cracks develop at stresses in the range $(1 \rightarrow 2)\ \sigma_{mc}$.[20] The corresponding result for the 90° plies is[22]

$$\sigma_t \approx \left[E\Gamma_m/hg\right]^{1/2} - \sigma^R(E_L + E_T)/2E_T \qquad (3)$$

where E_T is the transverse Young's modulus, E is the composite modulus, h is the ply thickness, σ^R is the residual stress in the plies and g is a function that depends on f, E_f/E_m as well as the interface bonding (Fig. 10). When the interface is weak and debonds readily as transverse loads are applied, g is relatively small and the matrix

cracking stress σ_τ is large. Conversely, when the interface has high transverse strength and remains intact upon transverse loading σ_τ is considerably smaller.

Inspection of Eqns. (2) and (3) indicates that the matrix cracking stresses must be relatively large for C matrix composites because E_m is small (~ 20 GPa). Moreover, for polycrystalline graphite, Γ_m is usually quite large ($\Gamma_m > 10^2$ Jm^{-2}).[21] These constituent properties signify large values of σ_{mc} (Eqn. 2) of order $1 \rightarrow 2$ GPa, consistent with the absence of stress-induced matrix damage in the 0° plies.

A major difference in the incidence of 90° ply cracking between the HT and LT material is rationalized by eqn. (3). The interface in the LT material is 'weak' and prone to debond upon transverse loading, consistent with the small sliding stress, τ (Table I). Conversely, the interfaces remain attached in the HT material, having the larger τ. This difference is manifest in the magnitudes of σ_τ predicted by eqn. (3), upon assuming that $\sigma^R \approx 0$. For the HT material with attached interfaces, $\sigma_\tau \approx 150$ MPa. For the LT material with separated interfaces, $\sigma_\tau \approx 300$ MPa. These values are in accordance with the observations of cracking which occurs in the HT material below the UTS, whereas cracking is absent in the LT material.

Another phenomenon supresses 90° ply cracking in the LT material. Sliding displacements along the ply interface that emanate from the transply procesing flaws reduce the stress in the 90° plies over zones ~ 250 μm in length (Appendix). Within these slip zones, the stress in the 90° plies is substantially lower than that generated by the external load.

Two factors remain to be addressed: the mechanism that governs interface sliding and the differences in UTS between the LT and HT materials. Sliding in the LT materialappears to occur between the coating and matrix . It is speculated that the carbon coating on the fibers is oriented such that debonding and sliding are facilitated. In consequence, τ is relatively small. By contrast, the coating layer is absent in the HT material, resulting in a larger τ because the matrix and/or particulates interact with the

fibers and inhibit sliding. However, it has not yet been possible to predict τ from the constituent properties. A new sliding model would be needed for this purpose.

For the LT material, the UTS has already been shown to conform with GLS predictions.[4] Such behavior is consistent with the absence of matrix damage and the low sliding stress. The lower strength found in the HT material was previously attributed to a violation of GLS, because of the large τ. The present observations provide a possible mechanism: matrix cracking at fiber failure sites (Fig. 7b). It is supposed that these cracks extend across the 0° plies and cause simultaneous fiber failure, resulting in a pull-out dominated UTS which is lower than that expected when GLS applies.[9]

The consistent interpretation of the tensile properties, based on fiber failure with sliding interfaces, provides an opportunity to predict changes in the UTS. This capability is provided by Eqn. (1). However, real progress is still impeded by two factors. (i) The absence of a fundamental model that relates sliding to the constituent properties. (ii) The incidence of a fiber failure mechanism change from GLS to pull-out as τ increases.

5.2 Shear

Inelastic shear deformation in brittle materials proceeds by the formation and evolution of en echelon microcracks[24,25] (Fig. 12). Models of the growth of this microcrack array predict a maximum shear resistance, τ_s (Fig. 12), given by;[25]

$$\tau_c = \beta\sqrt{\Gamma_R G_m / h} \qquad (4)$$

where Γ_R is the fracture energy for the layer, G_m is its shear modulus, h is the layer thickness and β is a coefficient between 1 and 1.5. The in-plane shear strength measured for SiC/C ($\tau_s \approx 100$ MPa) refers to a layer thickness, $h \approx 2$ μm (Fig. 8a) and a matrix

shear modulus, $G_m \approx 8$ GPa (Table I). Hence, the measured shear strength would be compatible with eqn.(4) for a fracture energy, $\Gamma_R \approx 10$ Jm^{-2}. This fracture energy is much smaller than the macroscopic fracture resistance of graphite.[21] However, it may be reasonable for small microcracks in a thin C layer. Indeed, it is of the same order as the mode II debond energy measured for C fiber coatings in SiC/SiC composites.[9] It remains to be explained why the mode II crack is confined to the thin CVI C layer.

5.3 Notch Properties

Tensile loading in the presence of a notch results in "shear bands" normal to the notch, as elaborated elsewhere.[5] These bands arise because of the relatively low ratio of the shear-to-tensile strength (Fig. 1). The shear deformation mechanism, based on en-echelon microcracks described above, operates within these bands. An important function of the shear bands is their role in stress redistribution, whereby a shear induced reduction in tensile stress concentration at the notch tip results in a relatively high nominal fracture toughness.[5]

The present observations indicate that the failure from the notch in the presence of a reduced stress concentration (due to "shear bands") is also preceded by stochastic fiber failure in the 0° plies. This mode of damage is accompanied by inelastic strains (Fig. 9) which must further redistribute the stress. A complete failure model would need to account for these additional effects and ascertain the critical event that causes eventual rupture.

6. CONCLUDING REMARKS

The microstructural and damage observations conducted in the present study have provided a basis for rationalizing the inelastic deformation behavior of a class of ex-phenolic C matrix composites in both tension and shear. In tension, the stochastic

failure of fibers with sliding interfaces dominates, with virtually no contribution from the matrix. By contrast, the in-plane shear properties appear to be dominated by the coating and CVI layers between the fiber and the matrix, with the fibers having a secondary influence. In consequence, the tensile and shear behaviors have no direct interdependence through the constituent properties. Such behavior is in contrast to that found in typical CMCs, wherein the matrix, the fibers and the interface have important interrelated influences on both the tensile and shear behaviors.[6-10]

Various models for the inelastic strain, the UTS and shear cracking are consistent with the measured behavior. Such consistency assists in the rationalization and interpretation of the observed behavior. However, a predictive capability has yet to be conceived, because there is no fundamental basis for several of the parameters used in the model, such as the sliding stress τ and the shear crack width, b (Fig. 11).

The notch properties are generally explicable in terms of the tensile and shear behavior, as elaborated elsewhere.[5] The basic effect concerns the influence of shear bands on stress redistribution ahead of the notch (Fig. 2). However, a detailed understanding would require an additional level of sophistication that includes the influence of fiber failure and pull-out at the notch root on the redistribution of stress and the failure criterion.

Appendix

Influence of Interply Sliding on Stress Redistribution

In the LT material, interply sliding has been inferred from the opening displacements exhibited by the transply processing flaws. If these displacements occur subject to a uniform shear resistance, τ_p acting along the ply interfaces, a simple shear lag analysis gives the stress redistribution. The stress σ_z in the 90° ply near the flaw is (Fig A1),

$$\sigma_z = \frac{\tau_p z}{h} \tag{A1}$$

where z is the distance from the flaw. The increase in opening displacement, u*, of the flaw is then

$$u^* = \int_0^{\ell} \frac{\sigma_z}{E_T} dz$$

$$= \frac{\tau_p \ell^2}{E_T h} \tag{A2}$$

where ℓ is the sliding length. Furthermore, equilibrium relates ℓ to the remote stress in the 90° plies, designated σ_T, by

$$\ell = \frac{\sigma_T h}{\tau_p} \tag{A3}$$

Combining eqns (A2) and (A3) gives

$$\tau_p = \frac{\sigma_T^2 h}{E_T u^*} \tag{A4}$$

and

$$\ell = \frac{u^*}{\varepsilon_T} \tag{A5}$$

where ε is the applied strain. Inserting measured values of u^* at failure gives $\tau_p \approx 60$ MPa and $\ell \approx 250$ μm. This value of τ_p is similar to that found for the in-plane shear strength, τ_s, in the LT material (Table I). The value of ℓ corresponds to the approximate spacing between transply shrinkage cracks in a given ply.

TABLE I

Constituent Properties of Carbon Matrix Composites

Fibers	Matrix	Elastic Moduli (GPa)		Sliding Stress, τ (MPa)	In-Plane Shear Strength, τ_s(MPa)
		E_f†	G_f		
Nicalon	LT	200	84	10 ± 5	80
	HT			90 ± 20	120
Carbon	X			—	35
	Y	230	5		40

E_m = 20 GPa‡

S_C = 2.3 GPa(LT), 2.5 GPa(HT)[4]

m = 4.5[4]

† Manufacturers information.

‡ A value of 20 GPa is consistent with values reported for ex-phenolic carbon.[26]

REFERENCES

[1] E. Fitzer, "The Future of Carbon-Carbon Composites," *Carbon*, **25** [2] 163–190 (1987).

[2] J.D. Buckley, "Carbon-Carbon, an Overview," *Ceramic Bulletin* **67** [2] 364–368 (1988).

[3] A.J. Klein, "Carbon/Carbon Composites," *Adv. Mat. and Proc.* **137** [5] 64-68 (1986).

[4] F.E. Heredia, S.M. Spearing, A.G. Evans, P. Mosher and W.A. Curtin, "Mechanical Properties of Continuous-Fiber-Reinforced Carbon Matrix Composites and Relationships to Constituent Properties," *J. Am. Ceram. Soc.*. **75** [11] 3017–25 (1992).

[5] F.E. Heredia, M.Y. He, T.J. Mackin, S.M. Spearing, A.G. Evans and P. Mosher, "Notch Effects in Carbon Matrix Composites," *J. Am. Ceram. Soc.*, in press.

[6] D. Beyerle, S.M. Spearing and A.G. Evans, "Damage Mechanisms and the Mechanical Properties of a Laminated 0/90 Ceramic Matrix Composite," *J. Am. Ceram. Soc.*, **75** [12] 3321–30 (1992).

[7] A. Pryce and P. Smith, "Behaviour of unidirectional and crossply ceramic matrix composites under quasi-static tensile loading," *J. Mater. Sci.*, **27** 2695–2704 (1992).

[8] X. Aubart, Thèse de Doctorat de L'Université de Paris (Nov. 1991), "Modélisation et Identification du Comportement de Composites à Matrice Céramique."

[9] A.G. Evans, F.W. Zok and T.J. Mackin, "The Mechanical Behavior of Brittle Matrix Composites," *J. Mater. Sci.*, in press.

[10] P.A. Brøndsted, F.E. Heredia and A.G. Evans, "The In-Plane Shear Properties of 2-D Ceramic Matrix Composites," *J. Am. Ceram. Soc.*, in press.

[11] J.W. Hutchinson and H.M. Jensen, "Models of Fiber Debonding and Pullout in Brittle Composites with Friction,"*Mech. of Mtls.*, **9** 139–163 (1990).

[12] J. Aveston, G.A. Cooper and A. Kelly, "Single and Multiple Fracture: The Properties of Fiber Composites," pp. 15-24 in *The Properties of Fibre Composites*, Conference Proceedings, National Physical Laboratory (Guildford, U.K.). IPC Science and Technology Press, Ltd., Teddington, U.K., 1971.

[13] B. Budiansky, J.W. Hutchinson and A.G. Evans, "Matrix Fracture in Fiber-Reinforced Ceramics," *J. Mech. Phys. Solids*, **34** [2] 167–189 (1986).

[14] D.B. Marshall, B.N. Cox and A.G. Evans, "The Mechanics of Matrix Cracking in Brittle Matrix Composites," *Acta Metall.*, **33** [11] 2013–21 (1985).

[15] W.A. Curtin, "Theory of Mechanical Properties of Ceramic Matrix Composites," *J. Am. Ceram. Soc.*, **74** [11] 2837–2845 (1991).

[16] C. Cady, T.J. Mackin and A.G. Evans, "A Notch Insensitive Ceramic Matrix Composite," submitted to *J. Am. Ceram. Soc.*,

[17] K.R. Turner and J.S. Speck, "Microstructure etc.

[18] S.M. Spearing, P.W.R. Beaumont, M.F. Ashby, "Fatigue Damage Mechanics of Notched Graphite-Epoxy Laminates," pp. 596–616 in *Composite Materials: Fatigue and Fracture*, ASTM STP 1110. Edited by T.K. O'Brien. American Society for Testing and Materials, Philadelphia, PA, 1991.

[19] C.H. Weber, K.T. Kim, F.E. Heredia and A.G. Evans, "High Temperature Deformation and Rupture in a Brittle Matrix Composite with Creeping Fibers," to be published.

[20] S.M. Spearing and F.W. Zok, "Matrix Crack Spacing in Brittle Matrix Composites," *Acta Metall. Mater.*, **40** [8] 2033–2043 (1992).

[21] M. Sakai and R.C. Bradt, "Graphical Methods for Determining the Nonlinear Fracture Parameters of Silica and Graphite Refractory Composites." pp. 127–142 in *Fracture Mechanics of Ceramics*, Vol. 7, edited by R.C. Bradt, A.G. Evans, D.P.H. Hesselman and F.F. Lange. Plenum, New York, 1986.

[22] C. Xia, R.R. Carr and J.W. Hutchinson, "Transverse Cracking in Fiber-Reinforced Brittle Matrix, Cross-Ply Laminates," Acta Metall. Mater., in press.

[23] F. Hild, J.M. Domergue, F.A. Leckie and A.G. Evans, "Tensile and Flexural Ultimate Strength of Fiber-Reinforced Ceramic Matrix Composites," *Int. J. Solids Struct.*, in press.

[24] N. Fleck, "Brittle Fracture Due to an Array of Microcracks," *Proc. Roy. Soc., London* A **432** 55–76 (1991).

[25] Z.C. Xia and J.W. Hutchinson, "Mode II Fracture Toughness of a Brittle Adhesive Layer," Int. Jnl. Sol. and Struct., in press.

[26] J.X. Zhao, R.C. Bradt, P.L. Walker, "The Fracture Toughness of Glassy Carbons at Elevated Temperatures," *Carbon*, **23** 15-18 (1985).

FIGURE CAPTIONS

Fig. 1 a) Tensile stress-strain curves for several CMCs, compared with those for C matrix composites.

b) In-plane shear stress-strain curves.

Fig. 2. A schematic of shear band formation from a notch in C matrix composites showing calculated effects of the shear band, on the stress distribution ahead of the notch. A radiograph of damage induced upon tensile loading of notched sample is also shown.

Fig. 3. a) Optical micrograph of a SiC/C composite cross-section showing the ply designation.

b) A polarized light optical micrograph showing the CVI layer on a transply shrinkage crack.

c) Interfiber axial porosity present after processing.

Fig. 4. Fracture profiles of SiC/C materials HT and LT after tensile test to failure.

Fig. 5. Sawtooth damage found in the LT SiC/C composite within the CVI carbon layer, after tensile testing to failure.

Fig. 6. Fiber fracture at regions away from primary composite failure plane. Residual opening displacement in HT(a) and LT(b) after testing to failure in tension.

Fig. 7. a) Optical micrograph of LT SiC/C material at $\sigma > 0.7\sigma_{max}$ showing random fiber fractures with no matrix cracking.

b) 90° matrix crack in the HT SiC/C material extending into 0° plies causing subsequent 0° fiber fracture at $\sigma > 0.7\sigma_{max}$.

Fig. 8. a) In-plane shear loading multiple microcracks found within the coating and CVI layer in the LT SiC/C composite.

b) 45° matrix cracks formed in the matrix-rich regions of in-plane shear sample (Photo courtesy of F.E. Heredia).

Fig. 9. A comparison of the tensile properties measured for the SiC/C composite (Fig. 1) with curves predicted for a stochastic fiber failure model, with interface sliding (Eqn. 1): a) LT material b) HT material.

Fig. 10. Effects of elastic properties and fiber volume fraction on the lower band shear for tunnel cracking across the 90° plies.

Fig. 11. A schematic of en-echelon microcracks associated with the inelastic deformation in brittle materials.

Fig. A1. A schematic of slip occuring at the ply intefaces which causes transply shrinkage crack (TSC) opening when tensile loads are applied.

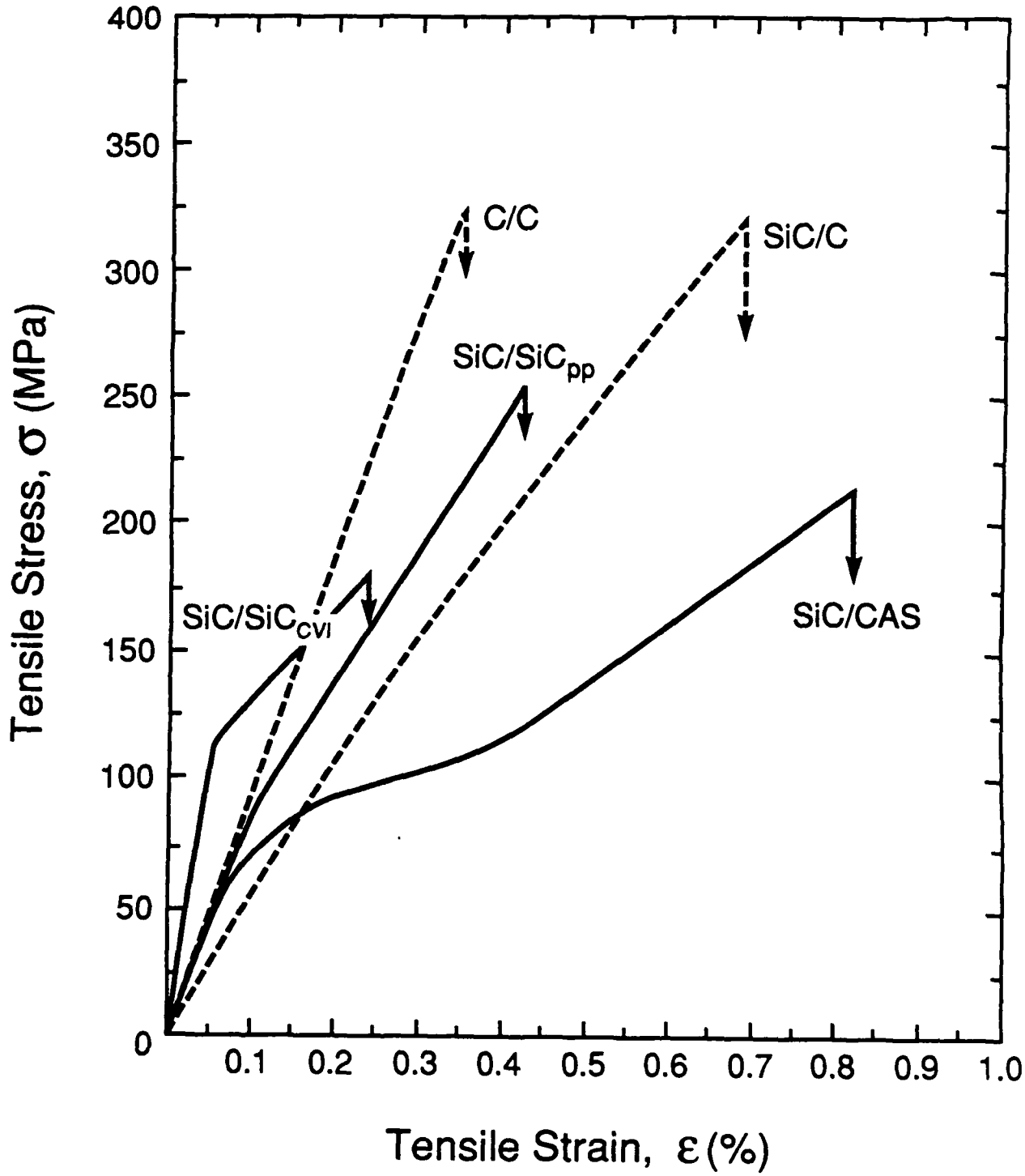
400
350
300
250
200
150
100
50
0
0.1
0.2
0.3
0.4
0.5
0.6
0.7
0.8
0.9
1.0
Tensile Stress, σ (MPa)
Tensile Strain, ε (%)
C/C
SiC/C
SiC/SiC$_{pp}$
SiC/SiC$_{CVI}$
SiC/CAS

Figure 1a

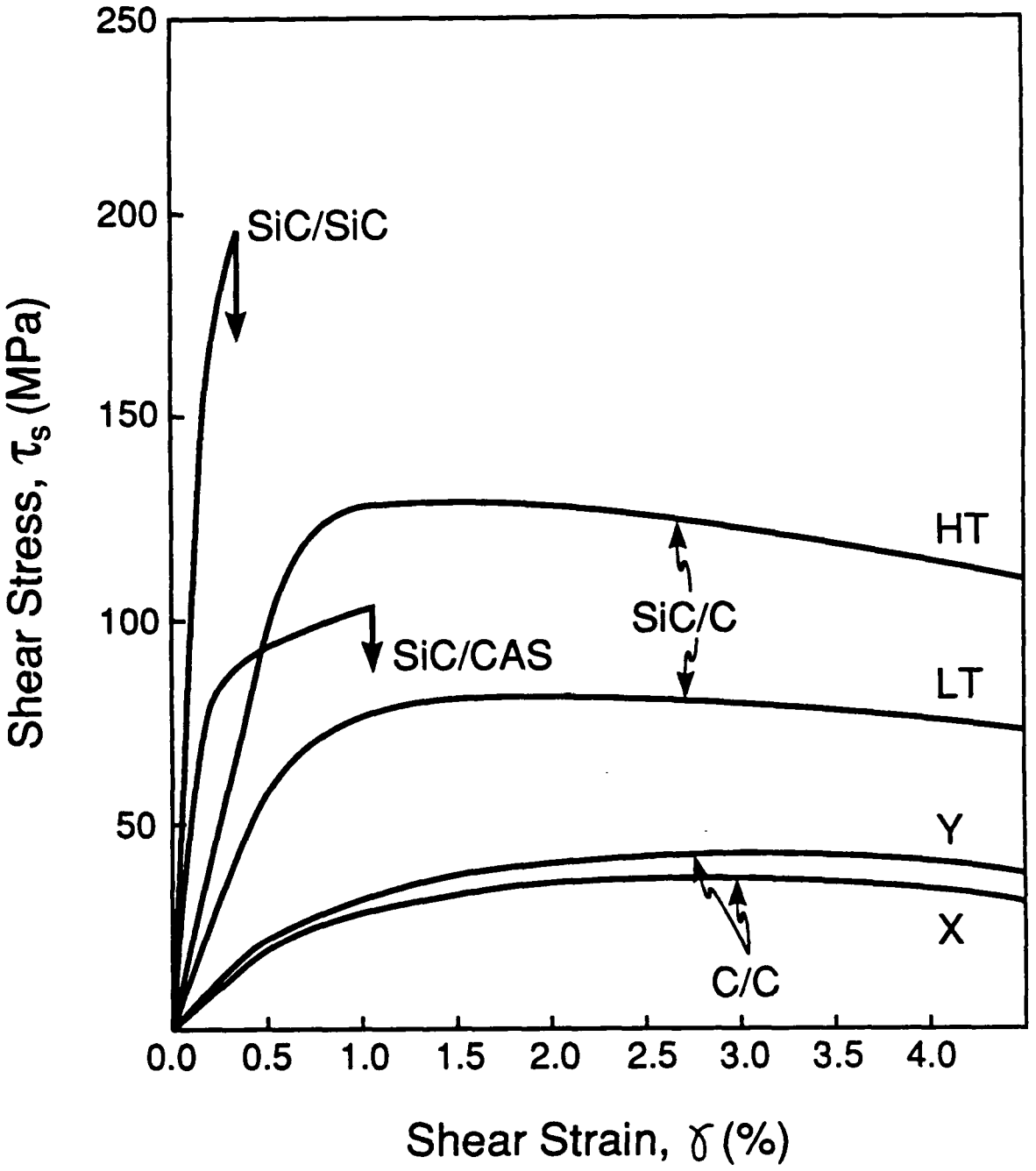
250
200
150
100
50
Shear Stress, τ_s (MPa)
SiC/SiC
SiC/CAS
SiC/C
HT
LT
Y
X
C/C
0.0
0.5
1.0
1.5
2.0
2.5
3.0
3.5
4.0
Shear Strain, γ (%)

Figure 1b

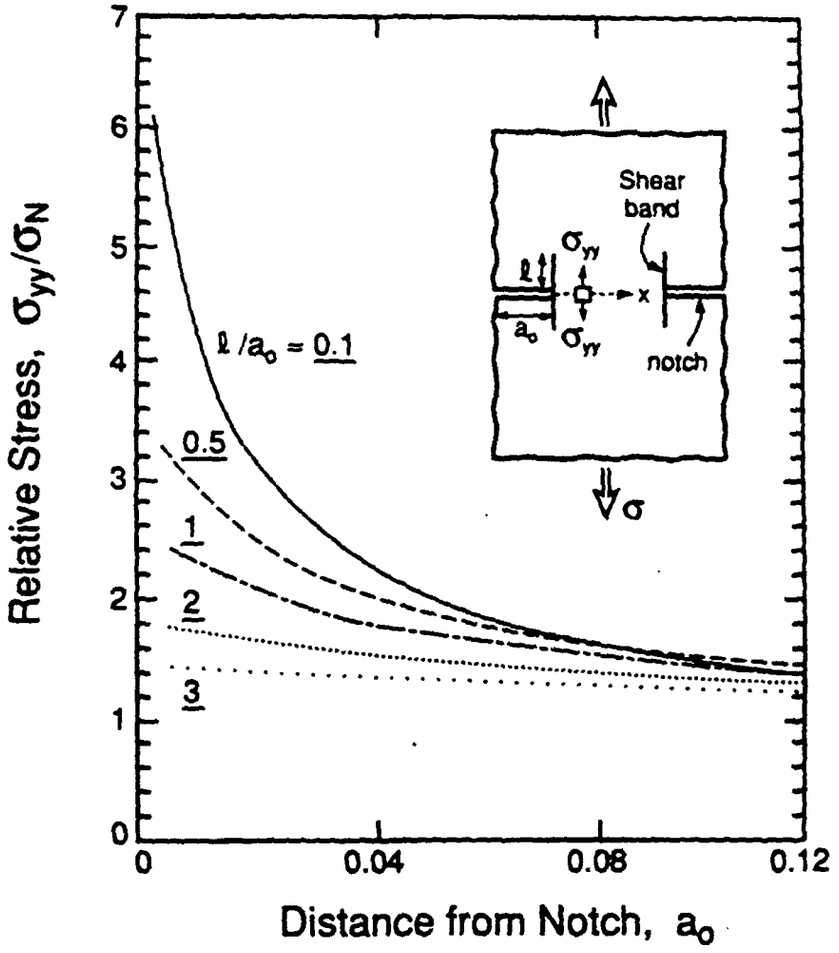
Relative Stress, σ_{yy}/σ_N
Distance from Notch, a_o
ℓ/a_o = 0.1
0.5
1
2
3
Shear band
notch
σ_{yy}
σ
0
0.04
0.08
0.12
1 mm

Figure 2

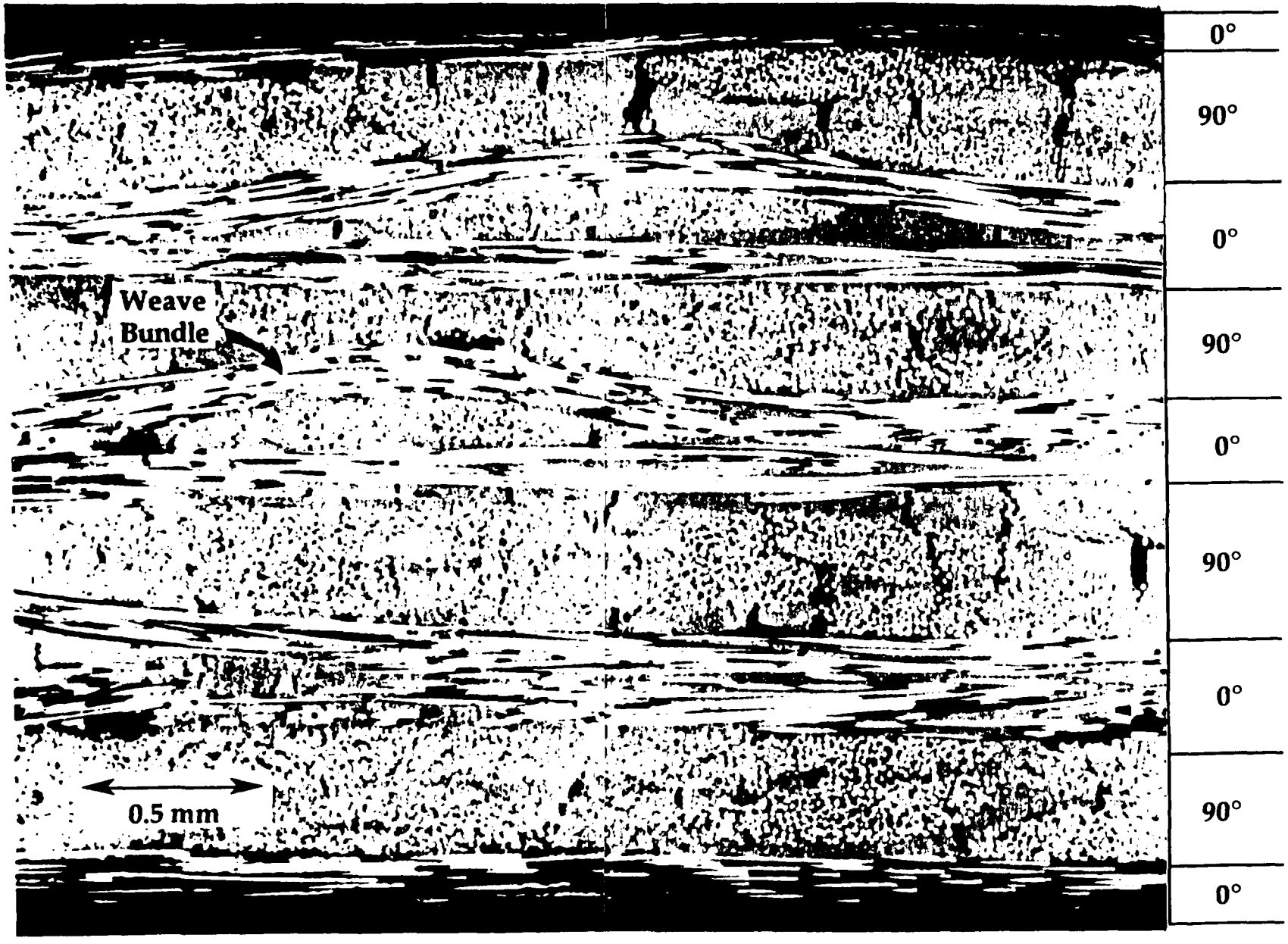

Figure 3a

Figure 3b

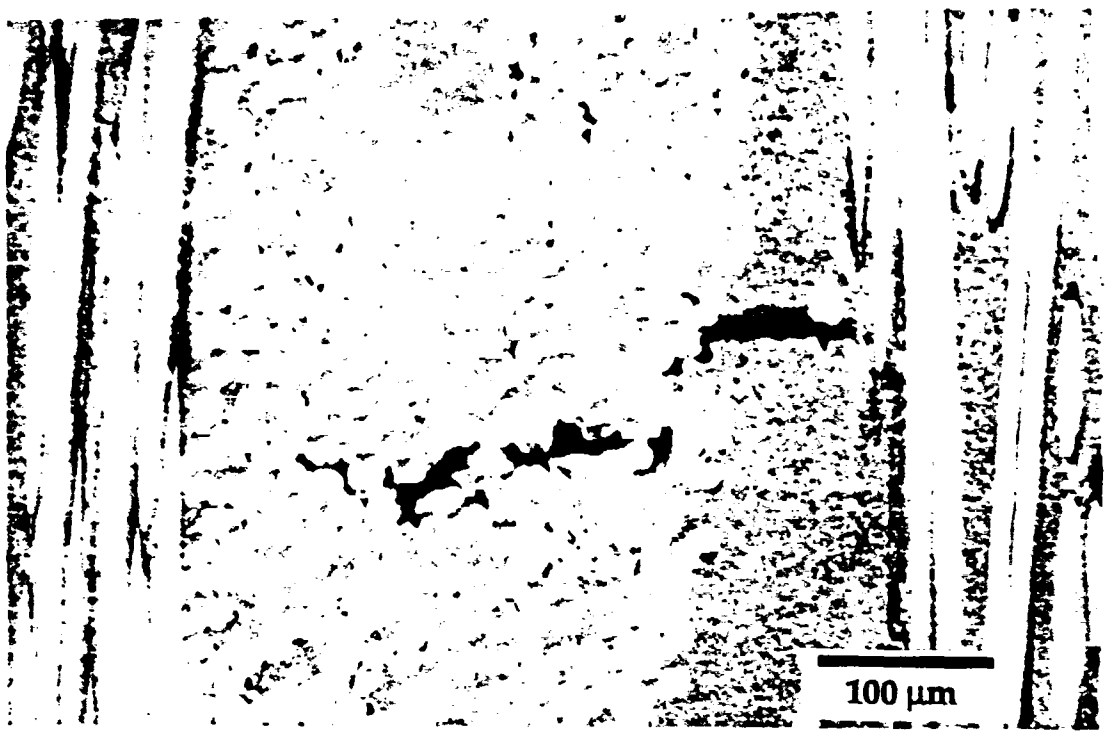

Figure 3c

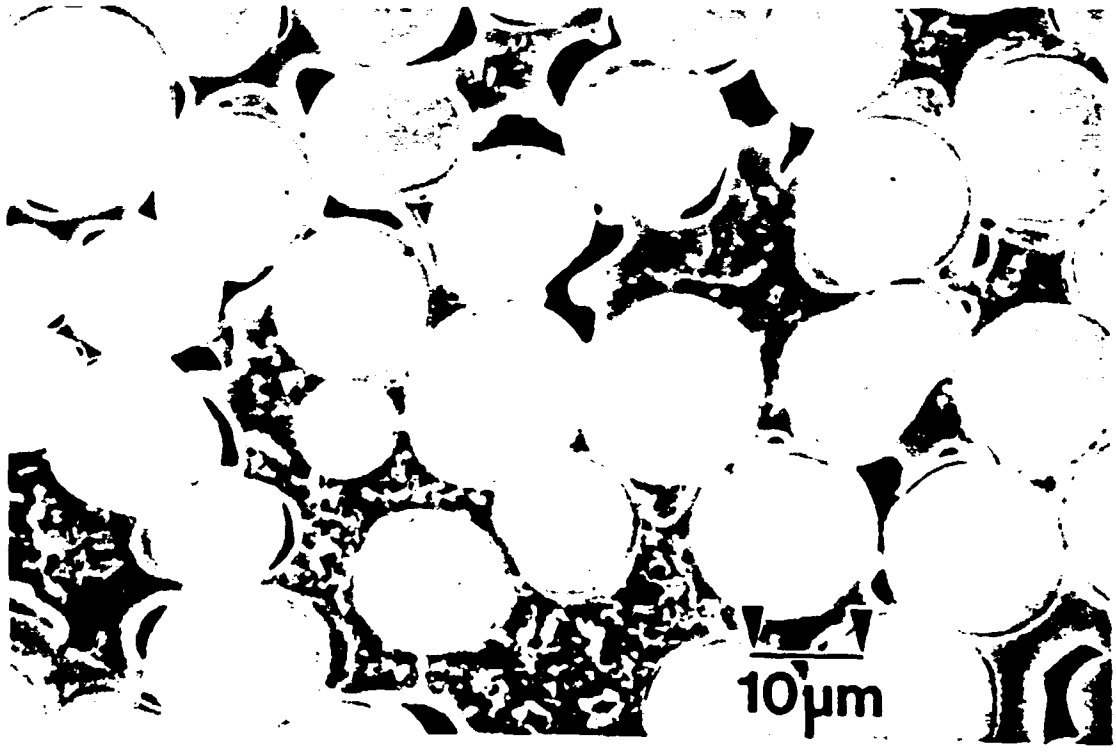

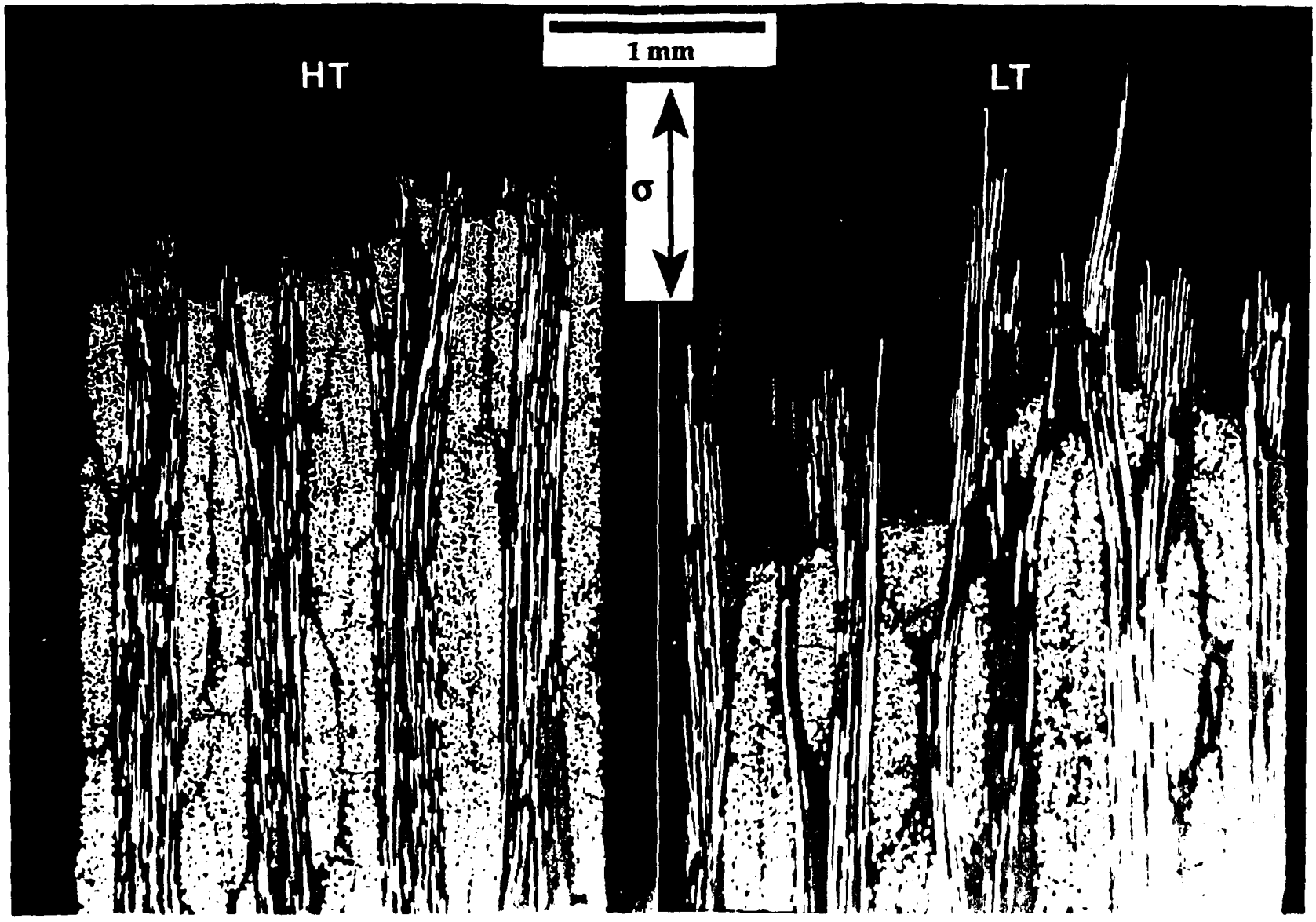

Figure 4

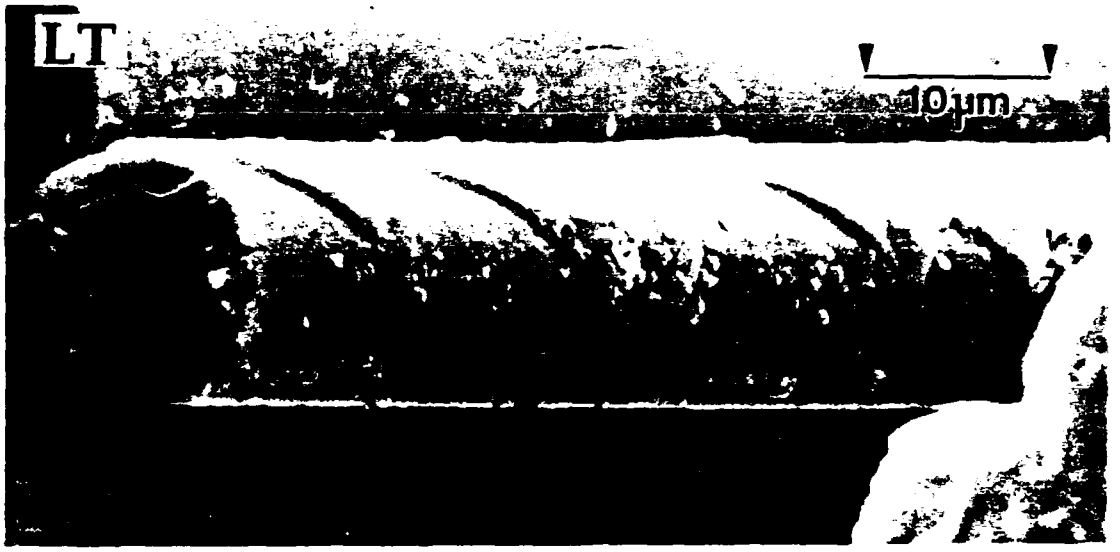

Figure 5

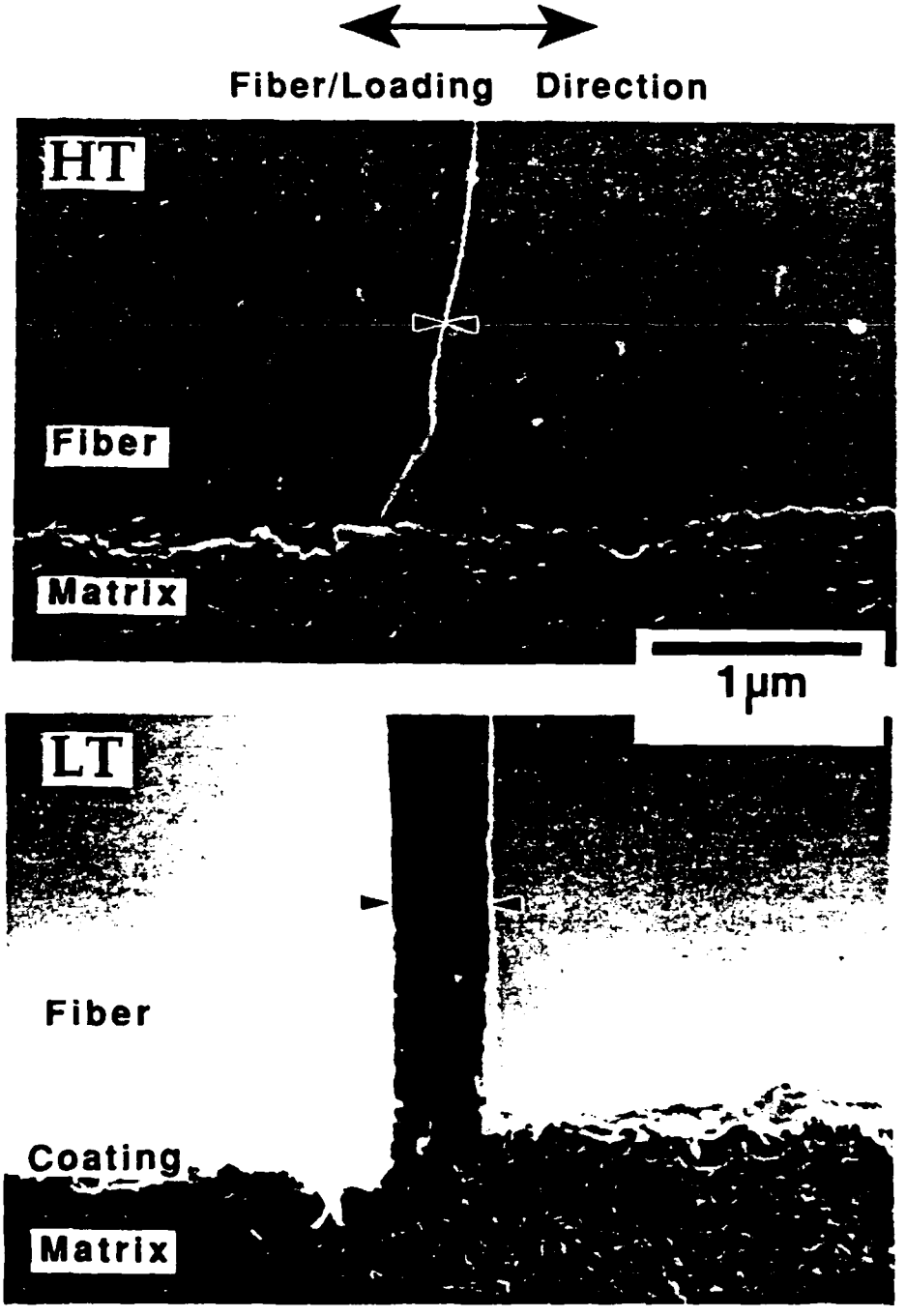
Fiber/Loading Direction
HT
Fiber
Matrix
1 μm
LT
Fiber
Coating
Matrix

Figure 6

Figure 7a

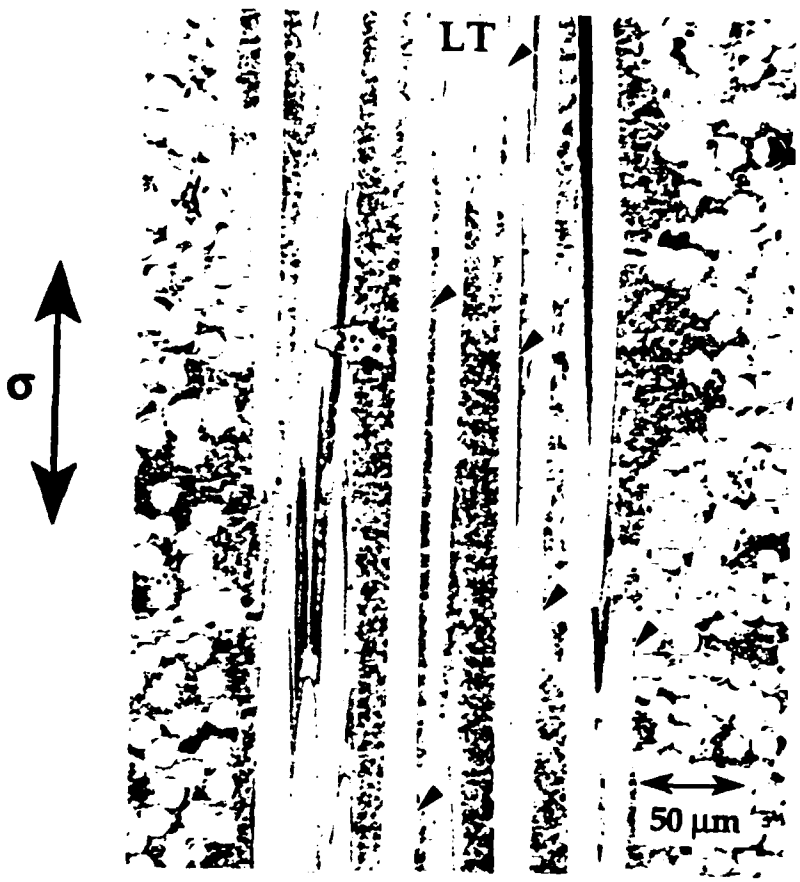

Figure 7b

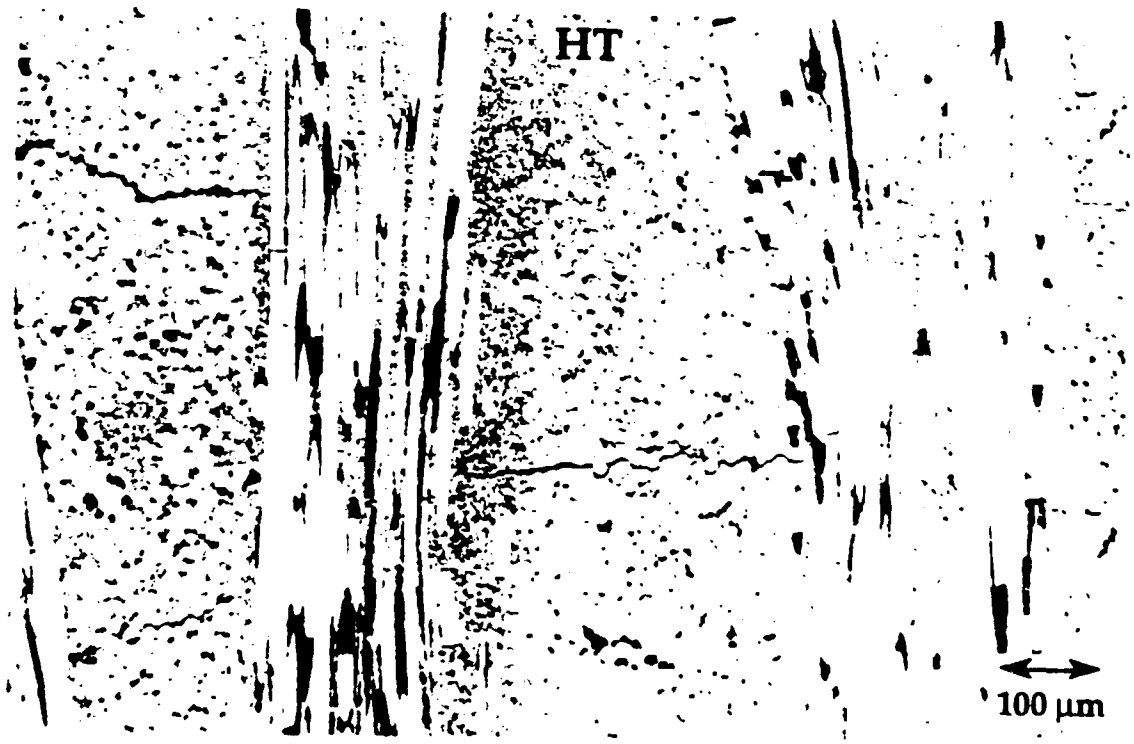

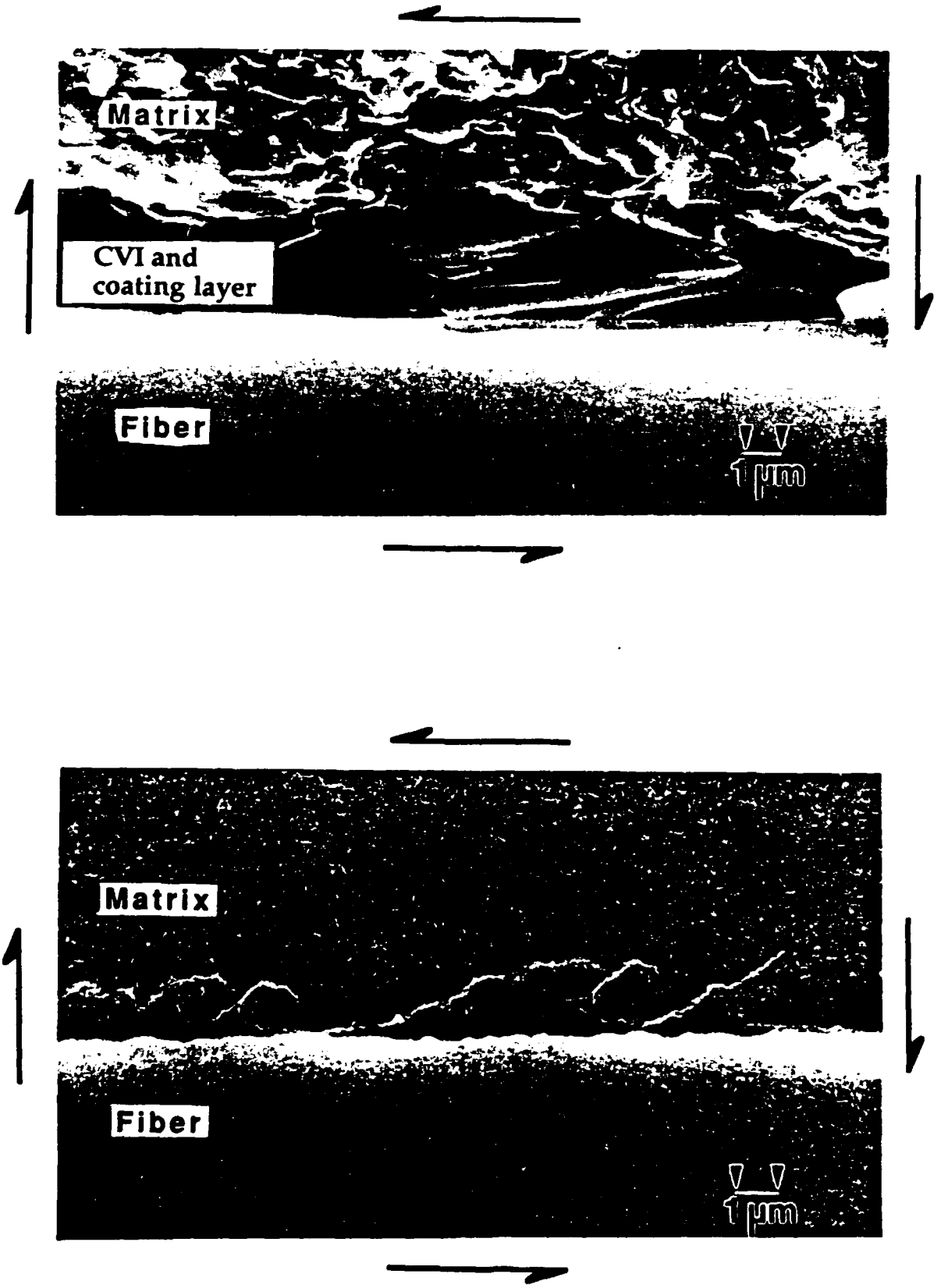

Figure 8a

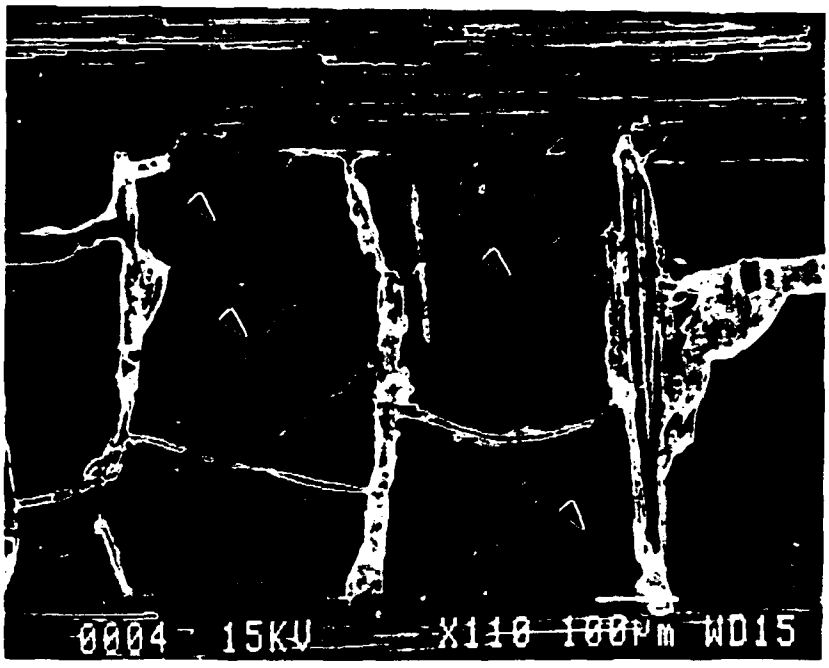

Figure 8b

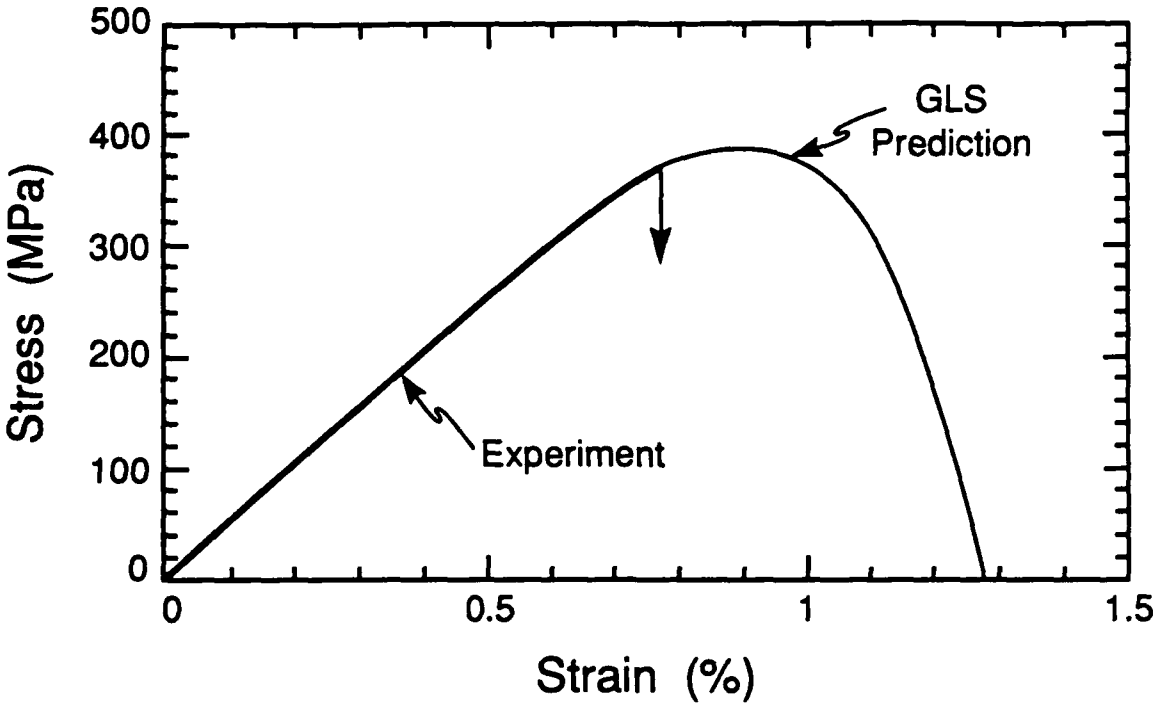

a) LT Material

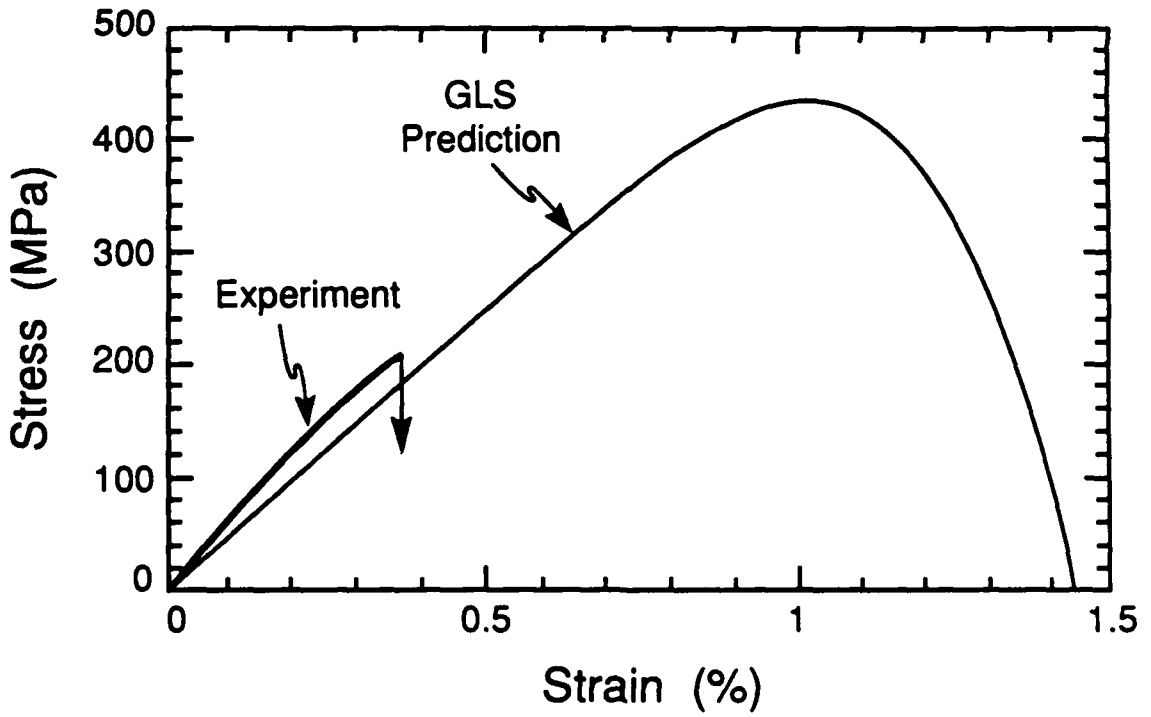

b) HT Material

Figure 9

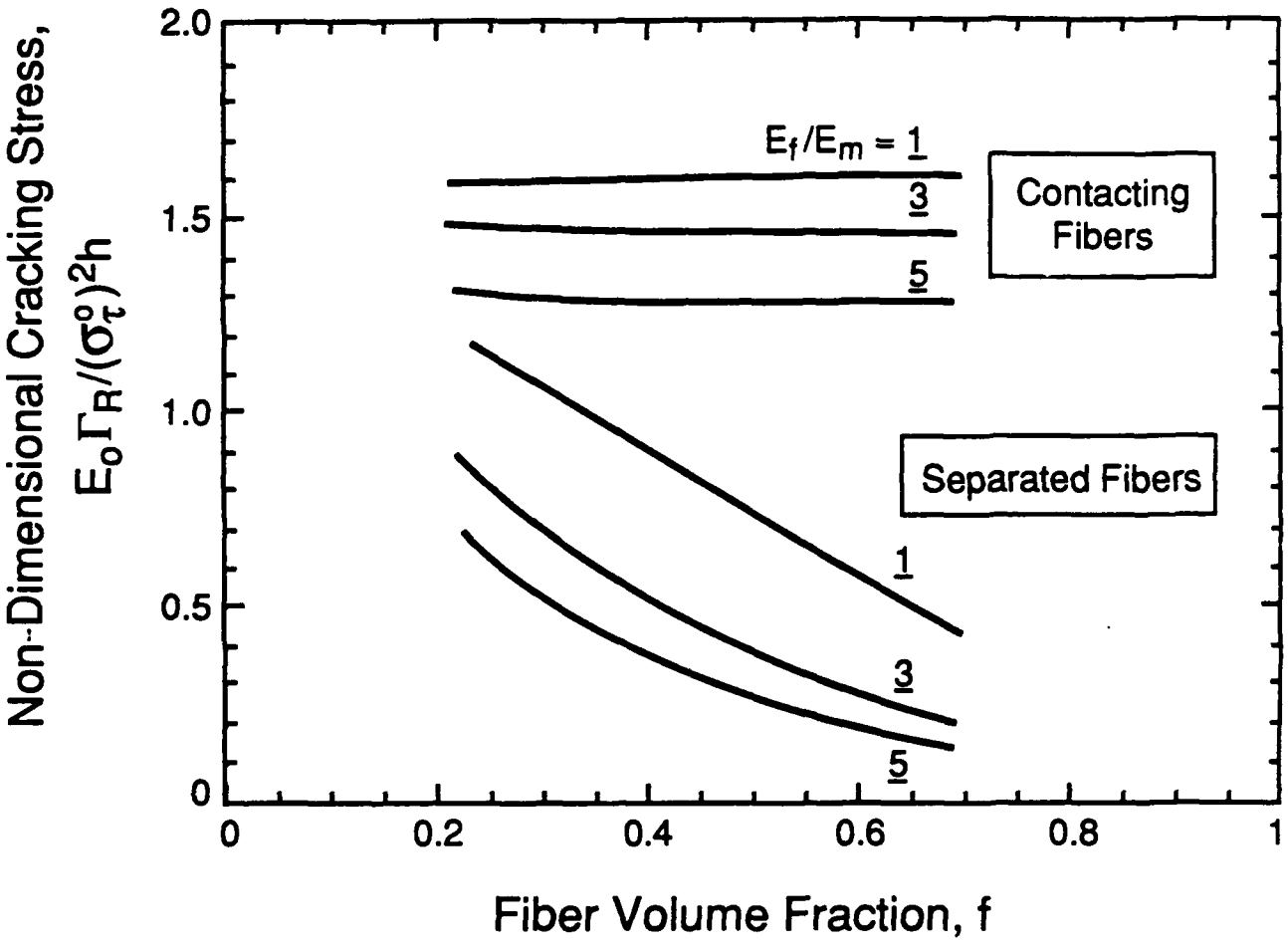
Non-Dimensional Cracking Stress,
$E_o\Gamma_R/(\sigma_\tau^o)^2h$
2.0
1.5
1.0
0.5
0
0
0.2
0.4
0.6
0.8
1
Fiber Volume Fraction, f
E_f/E_m = 1
3
5
Contacting Fibers
Separated Fibers
1
3
5

Figure 10

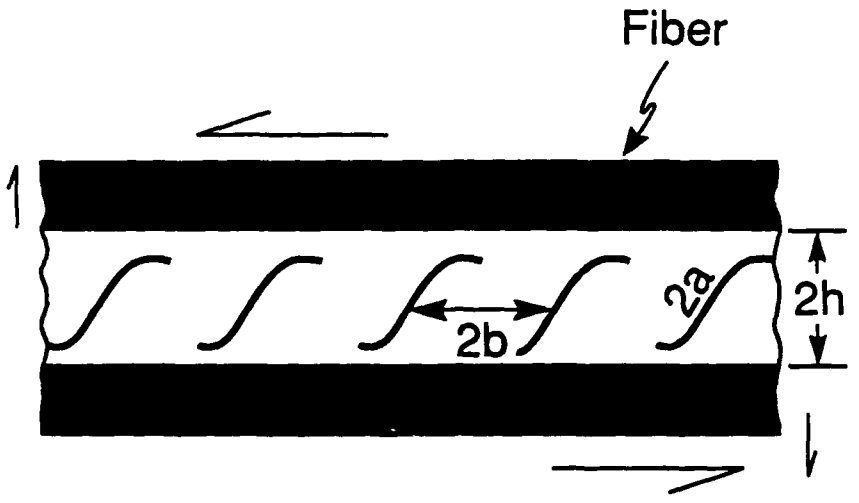

Figure 11

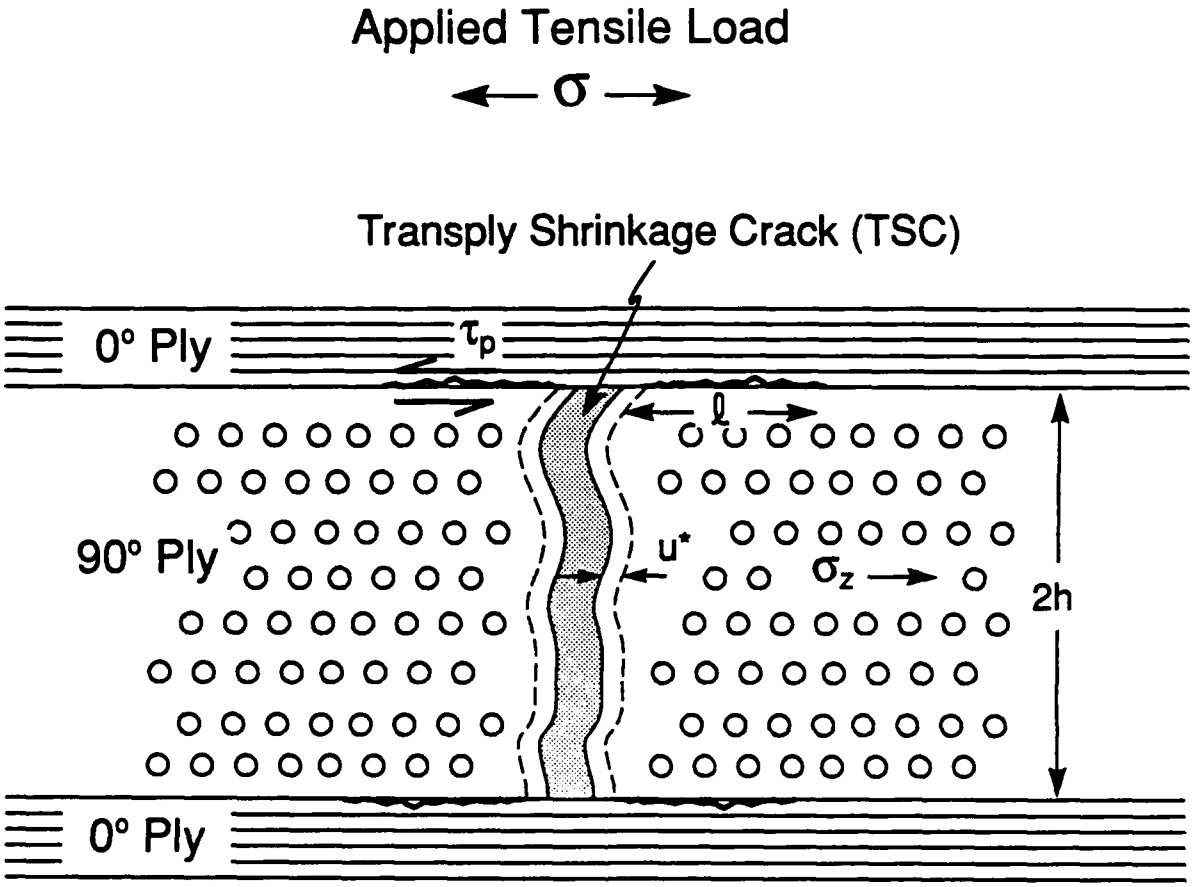
Applied Tensile Load
σ
Transply Shrinkage Crack (TSC)
0° Ply
τp
ℓ
90° Ply
u*
σz
2h
0° Ply

Figure A1

UNCOUPLED AND COUPLED APPROACHES TO PREDICT MACROCRACK-INITIATION IN FIBER REINFORCED CERAMIC-MATRIX COMPOSITES

François HILD,[1] Per-Lennart LARSSON,[2] and Frederick A. LECKIE

MECHANICAL AND ENVIRONMENTAL ENGINEERING DEPARTMENT

Department of Mechanical and Environmental Engineering
University of California, Santa Barbara, CA 93106, U.S.A.

[1]Laboratoire de Mécanique et Technologie,
E.N.S. de Cachan / C.N.R.S. / Université Paris 6
61 avenue du Président Wilson, F-94235 Cachan Cedex, France

[2]Department of Solid Mechanics, Royal Institute of Technology,
S-100 44 Stockholm, Sweden

UNCOUPLED AND COUPLED APPROACHES TO PREDICT MACROCRACK-INITIATION IN FIBER REINFORCED CERAMIC-MATRIX COMPOSITES

by

François HILD, Per-Lennart LARSSON, and Frederick A. LECKIE

Abstract: Localized fiber pull-out is one of the fracture features of fiber reinforced ceramic matrix composites. The onset of this mechanism is predicted by using Continuum Damage Mechanics, and corresponds to a localization of the deformations. After deriving two damage models from a uniaxial bundle approach, and criteria at localization, different axisymmetric configurations are analyzed through two different approaches to predict macrocrack-initiation.

1. Introduction

To achieve the new goals of high performance structures, Ceramic Matrix Composites (CMC's) become a suitable candidate, especially when the elements are subjected to high mechanical and thermal load histories[1]. Indeed, their low density combined with high strength and good performances at high temperature are appealing features. For example, in the design of the new generation of jet engines, CMC's will be used in the combuster, the turbine disks and the nozzle section[1].

In this paper we will focus our attention on rotating parts, i.e. an element in the turbine stages where angular rotation induces mechanical loading. To simplify the analysis, we will consider axisymmetric structures. The structures are assumed to be reinforced by fibers in the circumferential direction. The main goal of this paper is to predict the initiation of a macrocrack in the structure, which often constitutes the early stages of the final failure by fracture of the structure. Starting from a material which is assumed free from any initial macro defect, the initiation can be predicted using Continuum Damage Mechanics (CDM). In this paper we will neglect the matrix cracking process. This degradation takes place at an early stage of loading and often does not lead to final failure of a structure. Matrix cracks gradually develop as the load level increases. They usually saturate because of the shear effects induced by the interface between fibers and matrix[2]. The results presented herein are valid when the steady matrix stress[3] is less than the ultimate strength of a fiber reinforced composite[4]. When that hypothesis is satisfied, the key mechanism leading to final failure is fiber breakage. The fiber breakage mechanism is accompanied with a distributed fiber pull–out; a broken fiber pulls out of the matrix and involves shear stresses along the interface to recover its original load level. This mechanism distinguishes the behavior of fiber reinforced CMC's from a classical fiber bundle behavior[5]. From a design point of view, it is interesting to evaluate their differences especially in terms of load levels.

The degradation mechanism will be described by an internal variable called *damage*. In

the framework of CDM, the initiation of a macrocrack corresponds to a localization of the deformations, which corresponds to the onset of a surface across which the velocity gradient is discontinuous. Physically, it corresponds to localized pull-out, whereby one macrocrack develops and pull-out continues to evolve in the vicinity of that macrocrack only. This phenomenon leads to a different behavior as compared to the homogeneous solution for which damage is still evolving in a diffusive manner. Under small deformations assumption, localization is mainly driven by the damage mechanism that causes strain softening[6].

In Section 2, the main results concerning loss of uniqueness and localization will be recalled. In particular a property giving a necessary and sufficient condition of loss of uniqueness and localization will be proven and will be applied in Section 3. Section 3 deals with two constitutive laws modeling fiber breakage. The condition of localization and loss of uniqueness will be studied and general criteria may be derived using the property given in Section 2. Section 4 presents two strategies to predict the initiation of a macrocrack. The first one, which is referred to as *fully coupled* approach consists in calculating the stresses and strains evolution in elasticity coupled with damage; therefore the damage evolution is fully coupled with the evolution of the stresses and the strains. On the other hand, the second approach, which is referred to as *decoupled* approach and which is an easier calculation more amenable to design consists of an elastic computation and the use of the failure criterion derived from the localization analysis in Section 3. The difference between the two approaches are analyzed. The results in terms of loads at localization are also compared to the corresponding cumulative failure probability when the structure is assumed to be made of a brittle material.

2. Localization and Loss of Uniqueness

2.1. General Theory

The failure at a meso-level, which corresponds to the initiation of a macrocrack, is defined

as the bifurcation of the rate problem in certain modes, viz. the appearance of a surface across which the velocity gradient is discontinuous[7]. This phenomenon is referred to as *localization*, and corresponds to the failure of the ellipticity condition[8]. The condition of localization can also be compared to the loss of uniqueness of the rate problem.

Stationary waves were studied by Hadamard[9] in elasticity, by Hill[10] and Mandel[11] in elasto–Plasticity. Rice[12] related the localization of plastic shear bands to jumps of the velocity gradient. Borré and Maier[13], who extended the results given by Rice[12] and Rice and Rudnicki[14-15], have given necessary and sufficient conditions for the onset of modes inside the body.

Under small strain assumption and in elasticity coupled with damage, the behavior of a material is assumed to be described by the following piece-wise linear rate constitutive law

$$\dot{\boldsymbol{\sigma}} = \begin{cases} \mathbb{E} : \dot{\boldsymbol{\varepsilon}} & \text{if } \dot{D} = 0 \\ \mathbb{H} : \dot{\boldsymbol{\varepsilon}} & \text{if } \dot{D} \neq 0 \end{cases} \tag{1}$$

where $\dot{\boldsymbol{\sigma}}$ and $\dot{\boldsymbol{\varepsilon}}$ respectively denote the stress and strain rates, $\mathbb{E}$ and $\mathbb{H}$ are fourth rank tensors, $\mathbb{E}$ is assumed to be positive definite, and D is either a single damage variable or a set of damage variables. Localization occurs *inside* the body, *if and only if*[13-14]

$$\text{Det } (\mathbf{n}.\mathbb{H}.\mathbf{n}) = 0 \qquad \text{for any vector } \mathbf{n}\neq 0 \text{ and at any point inside a structure } \Omega \tag{2}$$

This criterion corresponds to the failure of the ellipticity condition of the rate equilibrium equation; it also can be used as an indicator of the local failure of the material, at a meso-scale[7].

Furthermore, any loss of uniqueness, considered as bifurcation of the rate boundary value problem, is excluded provided the operator

$$\mathbb{H}_s = \frac{1}{2}(\mathbb{H}+\mathbb{H}^T) \tag{3}$$

is strictly positive definite everywhere within the structure. This condition is equivalent to the condition of hardening

$$\dot{\boldsymbol{\sigma}} : \dot{\boldsymbol{\varepsilon}} > 0 \tag{4}$$

Eqns. (2) and (3) show that the quantity that defines loss of uniqueness and localization is the linear tangent modulus $\mathbb{H}$. In the following, we analyze loss of uniqueness and loss of ellipticity (i.e. localization) for states when

$$\begin{cases} \varepsilon_{11} = \alpha\, \varepsilon_{22} \text{ with } \alpha \in \mathbb{R} \\ \varepsilon_{12} = 0 \end{cases} \tag{5}$$

The parameter α is referred to as strain ratio. These particular states only are considered since the computations will deal with shear free states. These states lead to a tangent modulus that takes the following form

$$\mathbb{H} = \begin{Bmatrix} H_{1111} & H_{1122} & 0 \\ H_{2211} & H_{2222} & 0 \\ 0 & 0 & H_{1212} \end{Bmatrix} \tag{6}$$

For problems under hypothesis (5), the non-vanishing components of vector $\mathbf{n}$ are n_1 and n_2, and the matrix $\mathbf{A} = \mathbf{n}.\mathbf{H}.\mathbf{n}$ reduces to[16]

$$\mathbf{A} = \begin{Bmatrix} n_1^2 H_{1111} + n_2^2 H_{1212} & n_1 n_2 (H_{1212} + H_{1122}) \\ n_1 n_2 (H_{1212} + H_{2211}) & n_1^2 H_{1212} + n_2^2 H_{2222} \end{Bmatrix} \tag{7}$$

We rewrite $(n_1,n_2) = (\cos\theta,\sin\theta)$, let X be equal to $\tan^2\theta$, and let Y be equal to 1/X. The localization condition (Eqn> (2)) can be written in terms of X or Y

$$a X^2 + b X + c = 0 \quad , \quad a \neq 0 \tag{8.1}$$

$$c Y^2 + b Y + a = 0 \quad , \quad c \neq 0 \tag{8.2}$$

with

$$a = H_{1212}H_{2222} \tag{9.1}$$

$$b = H_{1111}H_{2222} - H_{1122}H_{2211} - H_{1122}H_{1212} - H_{2211}H_{1212} \tag{9.2}$$

$$c = H_{1212}H_{1111} \tag{9.3}$$

If real positive roots are found, then the localization direction is perpendicular to the vector $(n_1,n_2,0) = (\cos\theta,\sin\theta,0)$, characterized by the angle θ (Fig. 1). The values of H_{1111}, H_{2222}, H_{1122}, H_{2211} and H_{1212} are model dependent.

2.2. Necessary and sufficient Condition at localization

A necessary and sufficient condition at localization *and* loss of uniqueness will be derived under the following conditions. Let us assume that $H_{1122} = H_{2211} = \nu H_{2222}$ ($\nu < \sqrt{2}$), that H_{1111} and H_{1212} are positive numbers and that H_{2222} can become negative. This condition will be satisfied in the models used later. It can be seen from Eqns. (3) and (6) that there is no loss of uniqueness provided

$$\lambda > 0 \tag{10.1}$$

where

$$2\lambda = H_{1111} - H_{2222} + \sqrt{(H_{1111} - H_{2222})^2 + 2\nu^2 (H_{2222})^2} \qquad (10.2)$$

Furthermore, it can be noticed that when H_{2222} is equal to zero then λ is equal to zero (loss of uniqueness) and that the coefficients a, b, and c of Eqns. (8) reduce to

$$a = 0,\ b = 0,\ c = H_{1111}\, H_{1212} > 0 \qquad (11)$$

Localization occurs since it is possible to find Y satisfying Eqn. (8.2): $Y = 0$, and the localization direction is given by $\theta = \pi/2$. Therefore a *sufficient* condition of loss of uniqueness *and* localization is that H_{2222} be equal to zero.

Since localization corresponds to a particular mode of all the solutions after loss of uniqueness, it suffices to show that H_{2222} equal to zero is a sufficient conditic for loss of uniqueness. Using the triangular inequality, we have

$$\frac{2 - \nu\sqrt{2}}{2} H_{2222} \le \lambda \qquad (12)$$

Loss of uniqueness corresponds to λ equal to zero, and therefore $H_{2222} \le 0$. Since it has been shown that H_{2222} equal to zero is sufficient to define localization and loss of uniqueness, we have the following property:

a necessary and sufficient condition to have localization and loss of uniqueness is H_{2222} equal to zero. The angle at localization is equal to $\pi/2$.

Conversely, under the conditions $H_{1122} = H_{2211} = \nu H_{1111}$ ($\nu < \sqrt{2}$), H_{2222} and H_{1212} are positive numbers and H_{1111} can become negative, *a necessary and sufficient condition to have localization and loss of uniqueness is H_{1111} equal to zero. The angle at localization is equal to 0.*
The proof is the same as previously when studying Eqn. (8.1).

3. Constitutive Laws

This Section is concerned with the development of two constitutive laws in the case of CMC's reinforced in one direction. Since these models will be used to study spinning structures, we choose a cylindrical coordinate system (r,φ) as shown in Fig. 2a. We assume a plane stress hypothesis. The fibers are assumed to be in the hoop direction, and the two analyzed geometries are a disk of outer radius a, and a ring of outer radius a and inner radius b (a = 2b) shown in Figs. 2b and 2c. We let ω denote the angular rotation speed. Since the structure, the boundary conditions and the loading are axisymmetric, the problem is axisymmetric, and the only non zero stresses are related to the corresponding strains by[17]

$$\sigma_{rr} = \frac{E_\varphi}{k\{1-\nu_{r\varphi}^2(1-D_\varphi)k\}}\{\varepsilon_{rr}+\nu_{r\varphi}(1-D_\varphi)k\varepsilon_{\varphi\varphi}\} \tag{13}$$

$$\sigma_{\varphi\varphi} = \frac{E_\varphi(1-D_\varphi)}{1-\nu_{r\varphi}^2(1-D_\varphi)k}(\varepsilon_{\varphi\varphi}+\nu_{r\varphi}\varepsilon_{rr}) \tag{14}$$

where E_φ denotes the Young's modulus in the hoop direction, $\nu_{r\varphi}$ denotes the Poisson's ratio, k denotes the ratio of the Young's modulus in the fiber direction (E_φ) to the Young's modulus in the radial direction (E_r), and D_φ denotes the damage variable modeling the fiber degradation. The damage variable can be defined as percentage of broken fibers[17-19]. The percentage of broken fibers is given by the corresponding cumulative failure probability which will be modeled by a Weibull expression[20]. A first expression of the damage variable can be obtained[17] by extending a study of a fiber bundle to 2D configurations, and will be referred to as model No. 0

$$D_\varphi^{(0)} = 1-\exp\left\{-\frac{r}{r_0}\left\{\frac{\sigma_{\varphi\varphi}}{(1-D_\varphi^{(0)})f\sigma_0}\right\}^m\right\} \quad \text{if } \varepsilon_{\varphi\varphi} > 0 \text{ and } \dot{\varepsilon}_{\varphi\varphi} > 0 \tag{15}$$

where m and σ_0 are the shape and scale parameters of a Weibull law, r_0 is the corresponding gauge length, r is the fiber radius (since the fiber length is $2\pi r$), and f is the volume fraction of fibers in the hoop direction. This first expression corresponds to a generalization the behavior of a fiber bundle in the hoop direction embedded in a matrix. This means that if a fiber breaks, then it will not be able to carry any load (i.e. no distributed pull–out takes place), and therefore this model constitutes a *lower* bound of the expected behavior of the composite.

On the other hand, it has been proven[21] that due to distributed pull–out, the evolution of fiber breakage is *not* dictated by the total length of the fiber (here $2\pi r$), *but* by the length over which the tensile stress field recovers its original level. Using a shear lag approach[22-23] with constant interfacial shear stress τ, this length, also called *recovery length*, L_{rec}, is given by (Fig. 3)

$$L_{rec} = \frac{RT}{\tau} \tag{16}$$

where R is the fiber radius, T is the tensile stress in the unbroken fibers. In this case, the relevant length to consider is the recovery length L_{rec}. By equilibrium considerations, the tensile stress T is related to the external applied stress $\sigma_{\varphi\varphi}$ by

$$fT = \frac{\sigma_{\varphi\varphi}}{(1-D_{\varphi})} \tag{17}$$

Therefore, instead of r in Eqn. (15), we will consider L_{rec}. We then end up with a second type of damage evolution, which will be referred to as model No. 1

$$D_{\varphi}^{(1)} = 1 - \exp\left\{ - \left\{ \frac{\sigma_{\varphi\varphi}}{(1-D_{\varphi}^{(1)}) f \sigma_1} \right\}^{m+1} \right\} \quad \text{if } \varepsilon_{\varphi\varphi} > 0 \text{ and } \dot{\varepsilon}_{\varphi\varphi} > 0 \tag{18.1}$$

where the expression of the scaling σ_1 stress is given by

$$\sigma_1 = \left(\frac{\sigma_0^m r_0 \tau}{R}\right)^{1/m+1} \tag{18.2}$$

This stress has been previously used by Henstenburg and Phoenix[24], and by Curtin[25] and is referred to as characteristic strength. It can also be noted that this expression is valid under a global load sharing hypothesis, i.e. when a fiber breaks then the load it was carrying is distributed to *all* the unbroken fibers.

With these two models the ultimate tensile strength in the fiber direction is given by

$$\sigma_{\varphi\varphi} = \sigma_u = \begin{cases} f\,\sigma_0 \left(\frac{r_0}{e\ m\ r}\right)^{1/m} & \text{for model No. 0} \\ f\,\sigma_1 \left(\frac{1}{e\ (m+1)}\right)^{1/m+1} & \text{for model No. 1} \end{cases} \tag{19}$$

It is worth noting that the ultimate tensile strength in the fiber direction *does* depend on the fiber length for model No. 0, whereas it is *independent of* the fiber length for model No. 1. Eqn. (19) shows that the characteristic strength σ_1 corresponds to the scaling stress of the ultimate tensile strength in the fiber direction. In particular, this result shows that the ultimate strength is independent of the total length of the fiber. Instead it depends on the recovery length at the ultimate, which is proportional to the characteristic length[25] $L_1 = R\,\sigma_1 / \tau$. Furthermore, in this paper *only* the fiber breakage mechanism is taken into account since it is the most important mechanism compared to the pull–out mechanism in terms of the contribution to the stress levels[21-26-27]. The damage level at the ultimate tensile point is given by

$$D_\varphi = D_c = \begin{cases} 1 - \exp\left(\frac{-1}{m}\right) & \text{for model No. 0} \\ 1 - \exp\left(\frac{-1}{m+1}\right) & \text{for model No. 1} \end{cases} \tag{20}$$

In both models it can be noticed that the percentage of broken fibers at the ultimate tensile point (D_c) is independent of all material parameters but the Weibull modulus[17].

For both models the tangent operator $\mathbb{H}$ takes the form

$$H_{rrrr} = F_1 - \frac{F_2 F_4 F_3^{(i)}}{1+F_5 F_3^{(i)}} \tag{21.1}$$

$$H_{\varphi\varphi\varphi\varphi} = \frac{F_6}{1+F_5 F_3^{(i)}} \tag{21.2}$$

$$H_{rr\varphi\varphi} = H_{\varphi\varphi rr} = \nu_{r\varphi} H_{\varphi\varphi\varphi\varphi} \tag{21.3}$$

$$H_{r\varphi r\varphi} = 2G_{r\varphi} > 0 \tag{21.4}$$

where $G_{r\varphi}$ corresponds to the shear modulus of the composite (assumed to be constant), the explicit expressions for F_j are given in Appendix 1; the superscript (i) refers to either model No. 0 (0) or to model No. 1 (1). It is worth noting that all conditions presupposed in the property derived in Section 2 are satisfied. Furthermore, it is easily seen that when D_φ is equal to D_c then $F_3^{(i)}$ tends to infinity, and thus $H_{\varphi\varphi\varphi\varphi}$ vanishes. On the other hand, H_{rrrr} and $H_{r\varphi r\varphi}$ remain positive. Consequently, localization *and* loss of uniqueness occur if and only if

$$D_\varphi = D_c \tag{22.1}$$

$$\sigma_{\varphi\varphi} = \sigma_u \tag{22.2}$$

These two criteria are easier to compute than the general criteria of localization and loss of uniqueness. Moreover, the criterion refers to a maximum critical stress which does not need a computation when elasticity is coupled with damage. Indeed, an elastic computation can use criterion (22.2), whereas a computation where elasticity is coupled with damage can use both criteria. Therefore a post-processing approach described by Lemaitre[28] is not necessary, in this particular case, since criterion (22.2) does not refer to damage variables. On the other hand, as it

will be shown in the next Section, the damaged zone is not small compared to dimensions of the structures. Therefore a *locally coupled* approach[28] is not very interesting in this particular case.

It is also worth noting that criteria (22) are independent of the strain ratio α (5) and therefore the knowledge of the ultimate tensile strength is particularly crucial. The angle at localization is equal to $\pi/2$, i.e. perpendicular to the fiber direction (Fig. 4a).

If the fibers are in the radial direction, then using the corollary of the property derived in Section 2, we find that localization and loss of uniqueness can be characterized by

$$D_r = D_c \tag{23.1}$$

$$\sigma_{rr} = \sigma_u \tag{23.2}$$

where D_r denotes the damage variable modeling the degradation of the fibers in the radial direction. The angle at localization is equal to 0, i.e. again perpendicular to the fiber direction (Fig. 4b).

4. Initiation of Macrocracks in Spinning Structures

As mentioned earlier, we will apply these results to two spinning geometries (Figs. 2b and 2c). In each case, the external boundaries are supposed to be traction free. The first part of this Section is devoted to the direct application with the two models presented in Section 3. The second part deals with a simplified approach using elastic computations. Finally, the third part is concerned with the comparisons between the previous computations and the assessment of the reliability of those structures using a Weibull–type of approach.

4.1. Fully Coupled Computations

When the constitutive equations presented in Section 3 are considered, it proved impossible to derive a closed–form solution for the stress state and the damage state. Instead the problem is

solved using the Finite Element Method. Constitutive laws (13), (14), (15), and (18) are implemented into a standard finite element code ABAQUS[29], and a solution is sought for by discretizing the problem using 2–node axisymmetric shell elements. Since the linear tangent modulus $\mathbb{H}$ had to be implemented into the finite element code, the load (i.e. the angular rotation speed) required for loss of uniqueness and localization could be conveniently calculated using ABAQUS through a UMAT routine. In summary, the complete constitutive equations given by damage coupled with elasticity were implemented. Therefore these computations will be referred to as *fully coupled.*

It should be noted that due to the non-explicit expression for the damage parameter given in (15) and (18) an iterative procedure had to be outlined to determine the damage state characterized by D_φ at every time the calculated strain field did change at a certain Gauss point. This was done by using a standard bisection method. A test of mesh dependence of the numerical results is also performed. The number of elements proves to have a very weak influence on the solution and satisfactory results for the stress and state variable can be obtained by modeling the disk with only 20 elements.

The material analyzed herein is a CMC defined in Appendix 2. The numerical values are close to those found by Jansson and Leckie[30] for a Lithium Alumino–Silicate (LAS) matrix reinforced with Silicon Carbide fibers (commercial name Nicalon).

In Fig. 5, the stress field in the hoop direction obtained with a fully coupled computation is compared to the elastic stress field at the same load level. It can be noted that the load level corresponds to the localization speed for the ring with model No. 1. Due to the damage coupling, a redistribution takes place. In particular it is worth noting that the stress levels in the most loaded part ($r \geq .23$ m) is larger in the elastic computation. This trend is the same for both models and both structures.

In Fig. 6, the outer displacement of the ring obtained by an elastic computation and a fully coupled computation (model No. 1) are compared. Due to the gradual distribution of the damage all over the structure, the 'global' stiffness of the damaged structure softens as the applied load

increases. The higher the load, the higher the softening.

In terms of load levels at localization, Table 1a summarizes the results. It can be noticed that model No. 1 gives much higher load levels than model No. 0. This is mainly due to the radius dependence of the ultimate tensile strength (19) of model No. 0 compared to the radius independence of model No. 1. In Figs. 7 and 8 where the stresses in the hoop direction are plotted against the radius, the stress levels at localization (i.e. when the curve $\sigma_{\varphi\varphi}(r)$ intersects the curve σ_u: criterion (22.2)) are in the same ratio as the load levels. It is worth noting that as mentioned earlier the ultimate tensile strength is r–dependent for model No. 0 (Fig. 7) and r–independent for model No. 1 (Fig. 8). Criterion (22.1) is shown in Figs. 9 and 10 for model No. 0 and No. 1 respectively; note the different values of the critical damage value. In this case the localization point is very easy to spot compared to Figs. 7 and 8.

Although the load levels in terms of $\rho\omega^2$ at localization are very different for model No. 0 and No. 1, it can be noticed that when the dimensionless parameter $\rho\omega^2a^2/\sigma_u(r_{loc})$ is studied (where $\sigma_u(r_{loc})$ denotes the ultimate tensile strength at the localization radius) the results between model No. 0 and No. 1 come close together and the main change is given by the ratio b/a (Table 1b). In first approximation, a good estimate for the dimensionless parameter $\rho\omega^2a^2/\sigma_u(r_{loc})$ is 2.1 (b/a = .0) for the disk and 2.6 for the ring (b/a = .5).

Finally, the accuracy of the numerical investigations is addressed. Fig. 11 shows that the radius at localization is well characterized all over the range of loads exceeding the localization load level. On the other hand, in terms of damage at localization (Fig. 12) and hoop stress at localization (Fig. 13), localization needs to be spotted more precisely. This phenomenon is more important in terms of angle at localization (Fig. 14). In this latter case, the number of decimal positions to get an angle at localization of 89° (instead of 90°) is equal to 8! In summary, from a numerical perspective localization needs to be spotted very accurately especially in terms of angle at localization.

4.2. Decoupled Computations

In this sub-Section, we will take advantage of the criterion (22.2) which does not require a fully coupled computation. Therefore a purely elastic set of computations has been carried out. The aim of this Section is to compare the load levels predicted by the two types of approaches. The results are summarized in Table 2a. It can be noticed that all the load levels at localization are lower for the decoupled analysis. This is due to redistribution noticed earlier in Figs. 7 and 8. Moreover, the error measured as the ratio of the difference between the decoupled angular speed and the fully coupled angular speed to the fully coupled angular speed is lower in the case of model No. 1. This is due to a lower stress redistribution at localization for model No. 1 since the value of critical damage is equal to .181 (=1−exp(−1/5)) compared to model No. 0 for which the critical damage is equal to .221 (=1−exp(−1/4)).

Again the load levels in terms of $\rho\omega^2$ at localization are very different for model No. 0 and No. 1, but in terms of the dimensionless parameter $\rho\omega^2a^2/\sigma_u(\eta_{loc})$, the results are very close and the main change is given by the ratio b/a (Table 2b). In first approximation, a good estimate for the dimensionless parameter $\rho\omega^2a^2/\sigma_u(\eta_{loc})$ is 2.0 (b/a = .0) for the disk and 2.5 for the ring (b/a = .5). These results constitute a lower bound when compared to the fully coupled results.

The maximum difference between the two models approaches is −6.1%, which is not significant. Therefore a decoupled computation gives good information of the loads these kind of structures can support. Furthermore, due to the stress field redistribution, the decoupled approach gives conservative results in all the analyzed cases. Therefore it constitutes a 'good' lower bound approximation of the models No. 0 and No. 1.

4.3. Comparison with a Weibull–Type of Analysis

In this sub-Section we compare the load levels at localization obtained by both approaches to the cumulative failure probability obtained by modeling the material as an elastic brittle material.

This kind of analysis may be used to assess the reliability of these spinning structures supposed to be made of brittle material. In the framework of the weakest link assumption, the expression of the cumulative failure probability P_F is given by a Weibull expression[20]

$$P_F = 1 - \exp\left\{ - \frac{1}{A_0} \int_S \left\{ \frac{\sigma_{\varphi\varphi}}{\sigma_0} \right\}^m dA \right\} \tag{24}$$

where A_0 is the gauge section ($A_0 = \pi r_0^2$). Using the same normalization as in the previous Sections, the elastic stress filed can be scaled by writing the hoop stress as follows

$$\sigma_{\varphi\varphi}(r) = (\rho\omega^2 a^2)\, f(r) \tag{25}$$

where the function f is a dimensionless function. Since the function f depends only on the shape of the stress field but not on its level, it can characterize the stress field heterogeneity, and the cumulative failure probability can be rewritten as

$$P_F = 1 - \exp\left\{ - \frac{A}{A_0} H_m \left(\frac{\rho\omega^2 a^2}{\sigma_0} \right)^m \right\} \tag{26a}$$

where H_m is a generalized definition of the stress heterogeneity factor[31] associated with a Weibull law, and is defined as

$$H_m = \frac{1}{a^2 - b^2} \int_b^a 2r \, \{f(r)\}^m \, dr \tag{26b}$$

It can be noticed that if the hoop stress is homogeneous then H_m is equal to 1; otherwise as the stress field gets more heterogeneous, H_m gets closer to zero. In the case of the disk H_m = .04 and

in the case of the ring H_m = .02. These stress heterogeneity factors fully characterize the elastic stress field for the spinning disk and the spinning ring in terms of cumulative failure probability, i.e. in terms of reliability of these structures.

The results of cumulative failure probability for the same load levels as those predicted by the fully coupled approach are summarized in Table 3. It can be noticed that the cumulative failure probabilities are very high. Therefore a design strategy using this kind of reliability assessment can expect quite high value in terms of the cumulative failure probability corresponding to the load levels at localization.

5. Conclusions

In the framework of Continuum Damage Mechanics a localization criterion corresponds to the initiation of a macrocrack. Under certain hypotheses, the localization criterion can be rewritten in terms of a necessary and sufficient condition in terms of one component of the tangent operator. This result is applied to derive criteria at localization in terms of a critical damage value and a maximum normal stress for constitutive laws modeling the fiber breakage for unidirectionally reinforced ceramic matrix composites.

The constitutive laws are used to study axisymmetric spinning structures made of CMC's. Two approaches are analyzed. The fully coupled approach where the complete constitutive law is implemented in a FE code is compared to the decoupled approach that consists in using a elastic computation. Indeed, one of the previous criteria can be used in an elastic computation. The result predicting localization are on the same order of magnitude. Furthermore, the decoupled approach gives conservative results in terms of load at localization, and the results in the analyzed structures are very close to those predicted by a fully coupled method. The fact that the decoupled approach gives conservative results is due to a stress redistribution when the fully coupled approach is used.

This kind of approach will also be carried out in the case of structures reinforced by fibers in two perpendicular directions. This enables us to look for an optimum volume fraction of fibers

in terms of load at localization.

6. Acknowledgements

The authors gratefully acknowledge the financial support of the U.S. Air Force through contract AFOSR-90-0132 with the Department of Mechanical and Environmental Engineering, University of California at Santa Barbara, and the support by the Defense Advanced Research Project Agency through the University Research Initiative under Office of Naval Research Contract No. N–00014–92–J–1808.

References

1. U.R.I., University Research Initiative, Winter Study Group, University of California, Santa Barbara, (U.S.A.), (1992).
2. Aveston, J., Cooper, G. A. & Kelly, A., Single and Multiple Fracture. Conference Proceedings of the National Physical Laboratory: Properties of Fiber Composites, (1971).
3. Budiansky, B., Hutchinson, J. W. & Evans, A. G., Matrix Fracture in Fiber-Reinforced Ceramics. *J. Mech. Phys. Solids*, **34** (1986) 167-189.
4. Budiansky, B., Tensile Strength of Aligned-Fiber Composites. University Research Initiative, Winter Study Group, University of California, Santa Barbara, (U.S.A.), (1993).
5. Coleman, B. D., On the Strength of Classical Fibers and Fiber Bundles. *J. Mech. Phys. Solids*, **7** (1958) 60-70.
6. Lemaitre, J., *A Course on Damage Mechanics*, Springer-Verlag, Berlin, (1992) .
7. Billardon, R. & Doghri, I., Prévision de l'amorçage d'une macro-fissure par la localisation de l'endommagement. *C. R. Acad. Sci. Paris*, **308** (II) (1989) 347-352.
8. Benallal, A., Billardon, R. & Geymonat, G., Localization Phenomena at the Boundaries and Interfaces of Solids. Proceedings 3rd Conference on Constitutive Laws for Engineering Materials: Theory and Applications, Tucson, AZ (U.S.A.), (1991).
9. Hadamard, J., *Leçon sur la propagation des ondes et les équations de l'hydrodynamique*, Paris, (1903) .
10. Hill, R., Acceleration Waves in Solids. *J. Mech. Phys. Solids*, **10** (1962) 1-16.
11. Mandel, J., Ondes plastiques dans un milieu indéfini à trois dimensions. *J. de Mécanique*, **1** (1) (1962) 3-30.
12. Rice, J. R., The Localization of Plastic Deformations. Proceedings Theoretical and Applied Mechanics, Koiter, W. T., (1976).
13. Borré, G. & Maier, G., On Linear versus Nonlinear Flaw Rules in Strain Localization Analysis. *Meccanica*, **24** (1989) 36-41.
14. Rudnicki, J. W. & Rice, J. R., Conditions for Localization of Deformation in Pressure-Sensitive Dilatant Materials. *J. Mech. Phys. Solids*, **23** (1975) 371-394.
15. Rice, J. R. & Rudnicki, J. W., A Note on Some Features of the Theory of Localization of Deformation. *Int. J. Solids Struct.*, **16** (1980) 597-605.
16. Ortiz, M., Leroy, Y. & Needelman, A., A Finite Element Method for Localized Failure Analysis. *Comput. Meths Appl. Engrg.*, **61** (1987) 189-214.
17. Hild, F., Larsson, P.-L. & Leckie, F. A., Localization due to Damage in Fiber-Reinforced Composites. *Int. J. Solids Struct.*, **29** (24) (1992) 3221-3238.
18. Krajcinovic, D. & Silva, M. A. G., Statistical Aspects of the Continuous Damage Theory.

Int. J. Solids Structures, **18** (7) (1982) 551-562.

19. Hult, J. & Travnicek, L., Carrying Capacity of Fiber Bundles with Varying Strength and Stiffness. *Journal de Mécanique Théorique et Appliquée*, **2** (2) (1983) 643-657.
20. Weibull, W., The phenomenon of rupture in solids. Ing. Vetenskap. Akad., 153, (1939).
21. Curtin, W. A., Theory of Mechanical Properties of Ceramic Matrix Composites. *J. Am. Ceram. Soc.*, **74** (11) (1991) 2837–2845.
22. Cox, H. L., The elasticity and the strength of paper and other fibrous Materials. *Br. J. Appl. Phys.*, **3** (1952) 72-79.
23. Kelly, A. In *Strong Solids*Oxford University Press, 2nd edn., (1973) .
24. Henstenburg, R. B. & Phoenix, S. L., Interfacial Shear Strength Using Single-Filament-Composite Test. Part II: A Probability Model and Monte Carlo Simulations. *Polym. Comp.*, **10** (5) (1989) 389-406.
25. Curtin, W. A., Exact Theory of Fiber Fragmentation in Single-Filament Composite. *J. Mat. Sci.*, **26** (1991) 5239-5253.
26. Phoenix, S. L., Statstical Issues in the Fracture of Brittle Matrix Fibrous Composites. *Comp. Sci. Tech.*, (1992) submitted.
27. Hild, F., Domergue, J.-M., Evans, A. G. & Leckie, F. A., Tensile and Flexural Ultimate Strength of Fiber Reinforced Ceramic-Matrix Composites. *Int. J. Solids Struct.*, (1992) accepted.
28. Lemaitre, J., Micro-mechanics of crack initiation. *IntJ. Fract.*, **42** (1990) 87-99.
29. Hibbitt, H. D., Karlsson, B. I. & Sorensen, P., Abaqus, version 5.2. (1992).
30. Jansson, S. & Leckie, F. A., The Mechanics of Failure of Silicon Carbide Fiber–reinforced Glass–Matrix Composites. *Acta Metall.*, (1993) in press.
31. Hild, F., Billardon, R. & Marquis, D., Stress Heterogeneity Influence on Failure of Brittle Materials. *C. R. Acad. Sci. Paris*, **315** (II) (1992) 1293-1298.

Appendix 1

Model No. 0	Model No. 1
$$F_1 = \frac{E_\varphi}{k(1-\nu_{r\varphi}^2(1-D_\varphi)k)}$$ $$F_2 = \frac{E_\varphi \nu_{r\varphi}(\nu_{r\varphi}\varepsilon_{rr}+\varepsilon_{\varphi\varphi})}{(1-\nu_{r\varphi}^2(1-D_\varphi)k)^2}$$ $$F_4 = \frac{E_\varphi \nu_{r\varphi}(1-D_\varphi)}{1-\nu_{r\varphi}^2(1-D_\varphi)k}$$ $$F_5 = \frac{E_\varphi(\nu_{r\varphi}\varepsilon_{rr}+\varepsilon_{\varphi\varphi})}{(1-\nu_{r\varphi}^2(1-D_\varphi)k)^2}$$ $$F_6 = \frac{E_\varphi(1-D_\varphi)}{1-\nu_{r\varphi}^2(1-D_\varphi)k}$$	
$$F_3^{(0)} = \frac{\frac{m}{f\sigma_0}\left\{\frac{\sigma_{\varphi\varphi}}{(1-D_\varphi^{(0)})f\sigma_0}\right\}^{m-1}}{1-m\left\{\frac{\sigma_{\varphi\varphi}}{(1-D_\varphi^{(0)})f\sigma_0}\right\}^{m}}$$	$$F_3^{(1)} = \frac{\frac{m+1}{f\sigma_1}\left\{\frac{\sigma_{\varphi\varphi}}{(1-D_\varphi^{(1)})f\sigma_1}\right\}^{m}}{1-(m+1)\left\{\frac{\sigma_{\varphi\varphi}}{(1-D_\varphi^{(1)})f\sigma_1}\right\}^{m+1}}$$

Appendix 2

Material parameters for the ceramic matrix fiber composite analyzed in the finite element calculations are:

$E_r = 20.$ GPa

$E_\varphi = 140.$ GPa

$G_{r\varphi} = 13.$ GPa

$\nu_{r\varphi} = .0214$

$m = 4.$

$f\sigma_0 = 1450.$ MPa

$r_0 = .002$ m

$f\sigma_1 = 1300.$ MPa

$a = .3$ m, $b = .15$ m

Figure Caption

Figure 1: Localization mode.

Figure 2: Analyzed structures. The quantity ω represents the angular velocity.

(a) Coordinate system

(b) Spinning disk

(c) Spinning ring

Figure 3: Definition of the recovery length. Stress in the fiber against fiber axis x.

(a) Just before the break

(b) Just after the break

Figure 4: Localization angles θ for

(a) fibers parallel to the φ–axis ($\theta = \pi/2$)

(b) fibers parallel to the r–axis ($\theta = 0$)

Figure 5: Hoop stress $\sigma_{\varphi\varphi}(r)$ as a function of the radius obtained by a fully coupled computation and a decoupled computation at localization ($\rho\omega^2 = 2.26\ 10^{10}$ kg/m^3/s^2) for the ring with model No. 1. Note the stress redistribution.

Figure 6: Outer radial displacement as a function of the applied load ($\rho\omega^2$) obtained by a fully coupled computation and a decoupled computation up to localization ($\rho\omega^2 = 2.26\ 10^{10}$ kg/m^3/s^2) for the ring with model No. 1. Note the stiffness softening.

Figure 7a: Hoop stress $\sigma_{\varphi\varphi}(r)$ as a function of the radius intersecting (see the arrow) the r–dependent ultimate tensile strength $\sigma_u(r)$ at localization ($\rho\omega^2 = .59\ 10^{10}$ kg/m^3/s^2) for a fully coupled computation applied to the disk with model No. 0. Note the r–dependence of the ultimate tensile strength.

Figure 7b: Zoom around the radius at localization of the hoop stress $\sigma_{\varphi\varphi}(r)$ as a function of the radius intersecting (see the arrow) the r–dependent ultimate tensile strength $\sigma_u(r)$.

Figure 8a: Hoop stress $\sigma_{\varphi\varphi}(r)$ as a function of the radius intersecting (see the arrow) the r–independent ultimate tensile strength σ_u at localization ($\rho\omega^2 = 1.87\ 10^{10}$ kg/m^3/s^2) for a fully coupled computation applied to the disk with model No. 1. Note the r–independence of the ultimate tensile strength.

Figure 8b: Zoom around the radius at localization of the hoop stress $\sigma_{\varphi\varphi}(r)$ as a function of the radius intersecting (see the arrow) the r–independent ultimate tensile strength σ_u.

Figure 9: Damage variable $D_\varphi(r)$ as a function of the radius intersecting (see the arrow) the critical damage value at localization ($\rho\omega^2 = .59\ 10^{10}$ kg/m^3/s^2) for a fully coupled computation applied to the disk with model No. 0.

Figure 10: Damage variable $D_\varphi(r)$ as a function of the radius intersecting (see the arrow) the critical damage value at localization ($\rho\omega^2 = 1.87\ 10^{10}$ kg/m^3/s^2) for a fully coupled computation applied to the disk with model No. 1.

Figure 11: Localization radius as a function of the load level, for a fully coupled computation applied to the disk with model No. 1.

Figure 12: Maximum damage at localization as a function of the load level, for a fully coupled computation applied to the disk with model No. 1.

Figure 13: Maximum hoop stress at localization as a function of the load level, for a fully coupled computation applied to the disk with model No. 1.

Figure 14: Localization angle as a function of the load level, for a fully coupled computation applied to the disk with model No. 1.

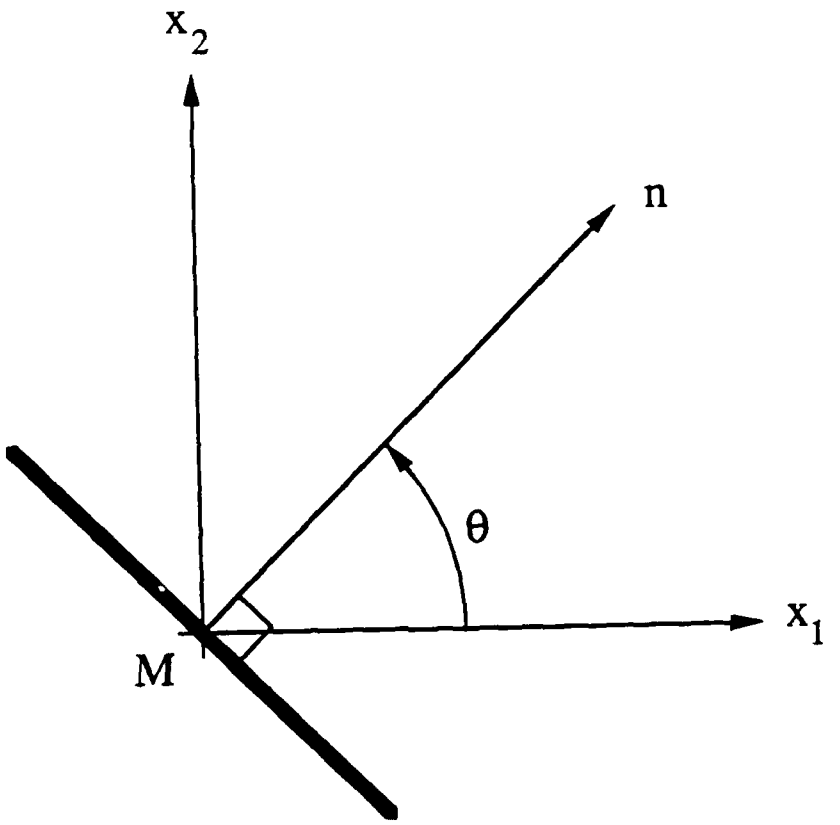

Fig. 1

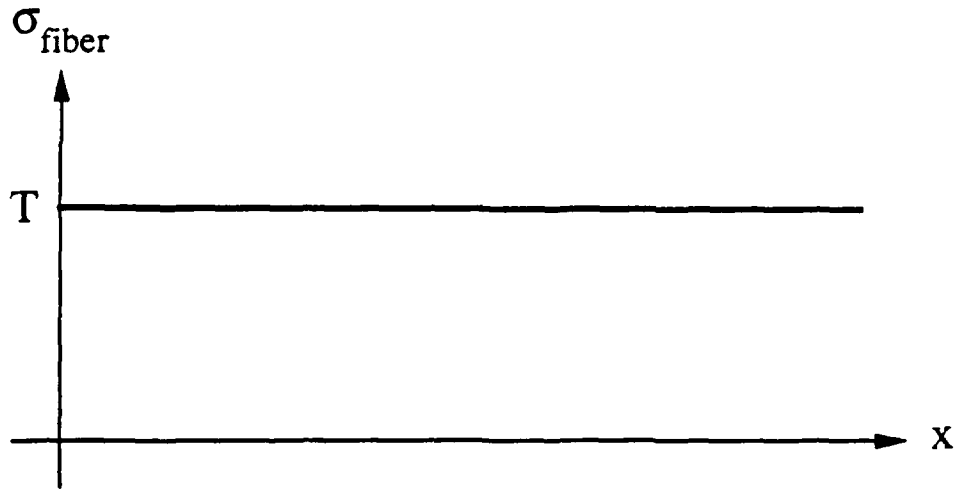

(a)

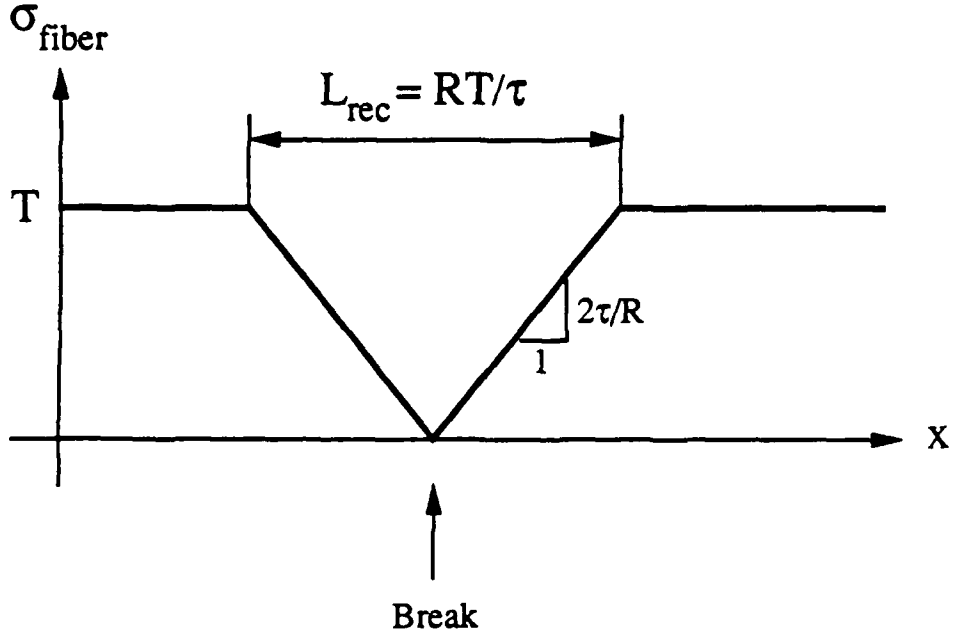

(b)

Fig 2

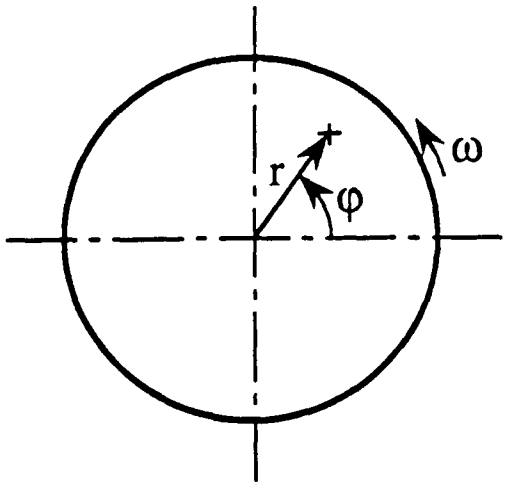

(a)

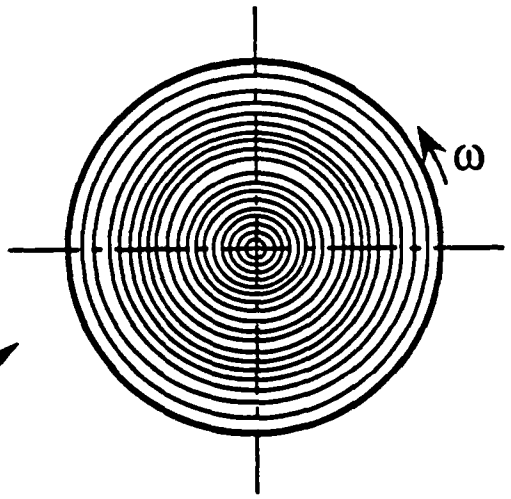

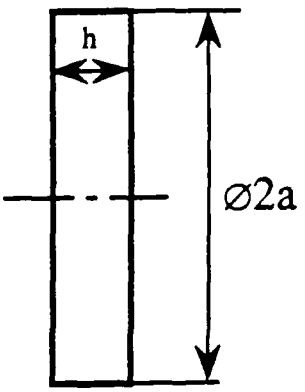

Fibers in the hoop direction

(b)

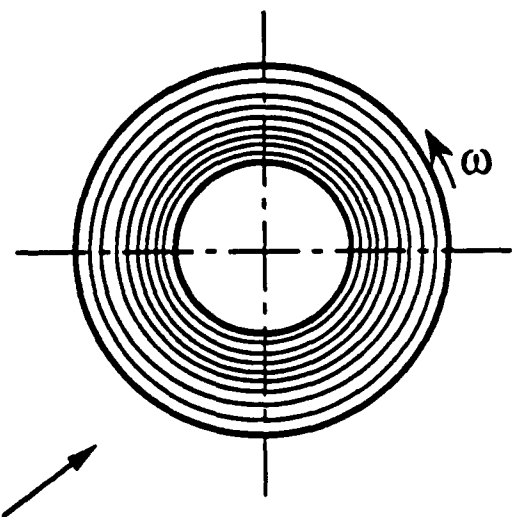

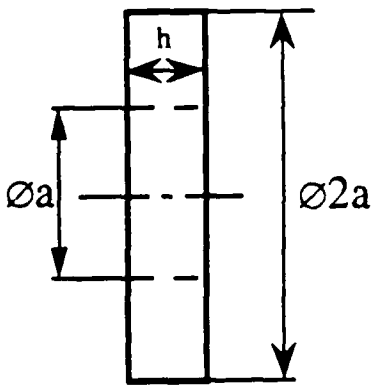

Fibers in the hoop direction

(c)

Fig 3

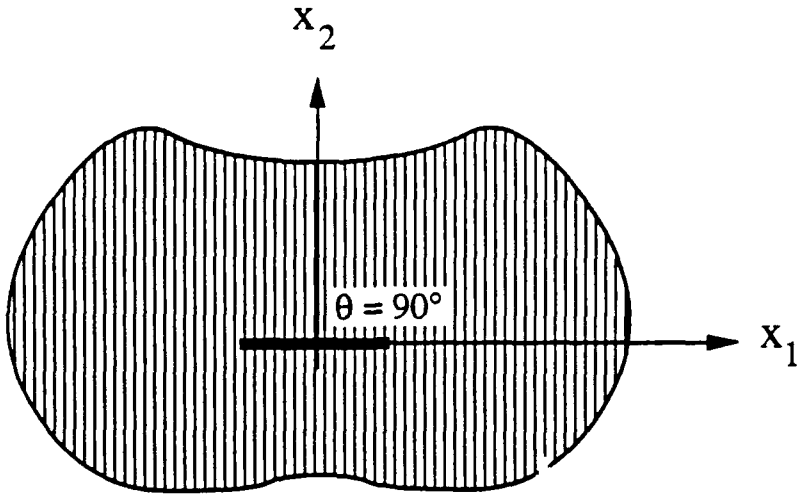

(a)

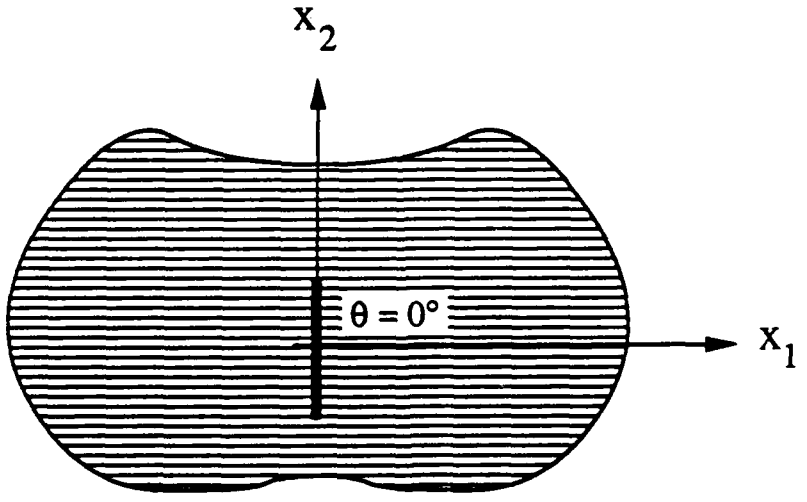

(b)

Fig. 4

Fig 4

Fig 5

Stress (MPa)
900
800
700
600
500
400
300
200
100
0.15
0.2
0.25
0.3
Radius, r (m)
Elasticity Coupled with Damage
Elasticity

Fig. 6

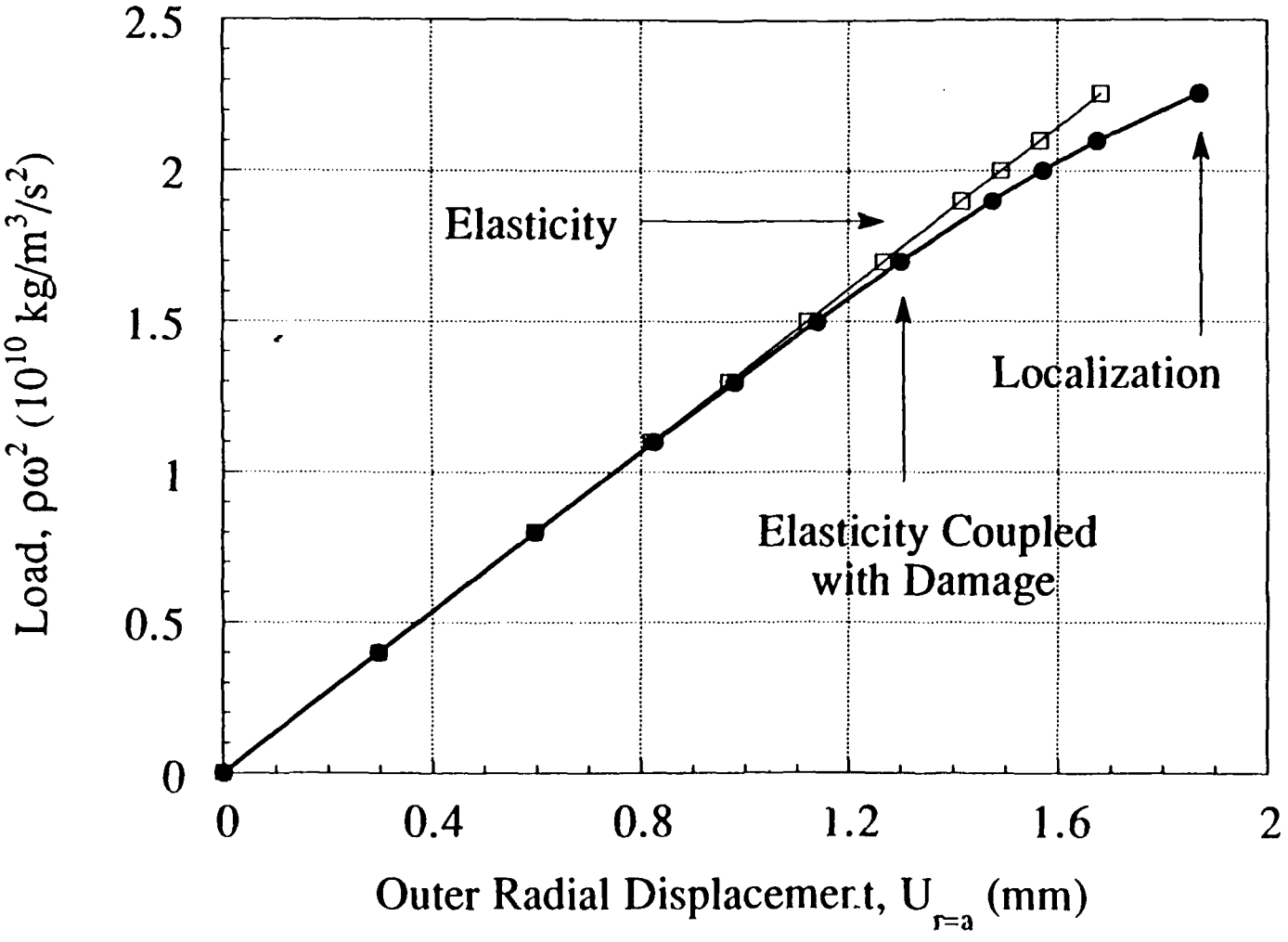
2.5
2
1.5
1
0.5
0
0
0.4
0.8
1.2
1.6
2
Load, $\rho\omega^2$ (10^{10} kg/m^3/s^2)
Outer Radial Displacement, $U_{r=a}$ (mm)
Elasticity
Localization
Elasticity Coupled
with Damage

Fig. 7a

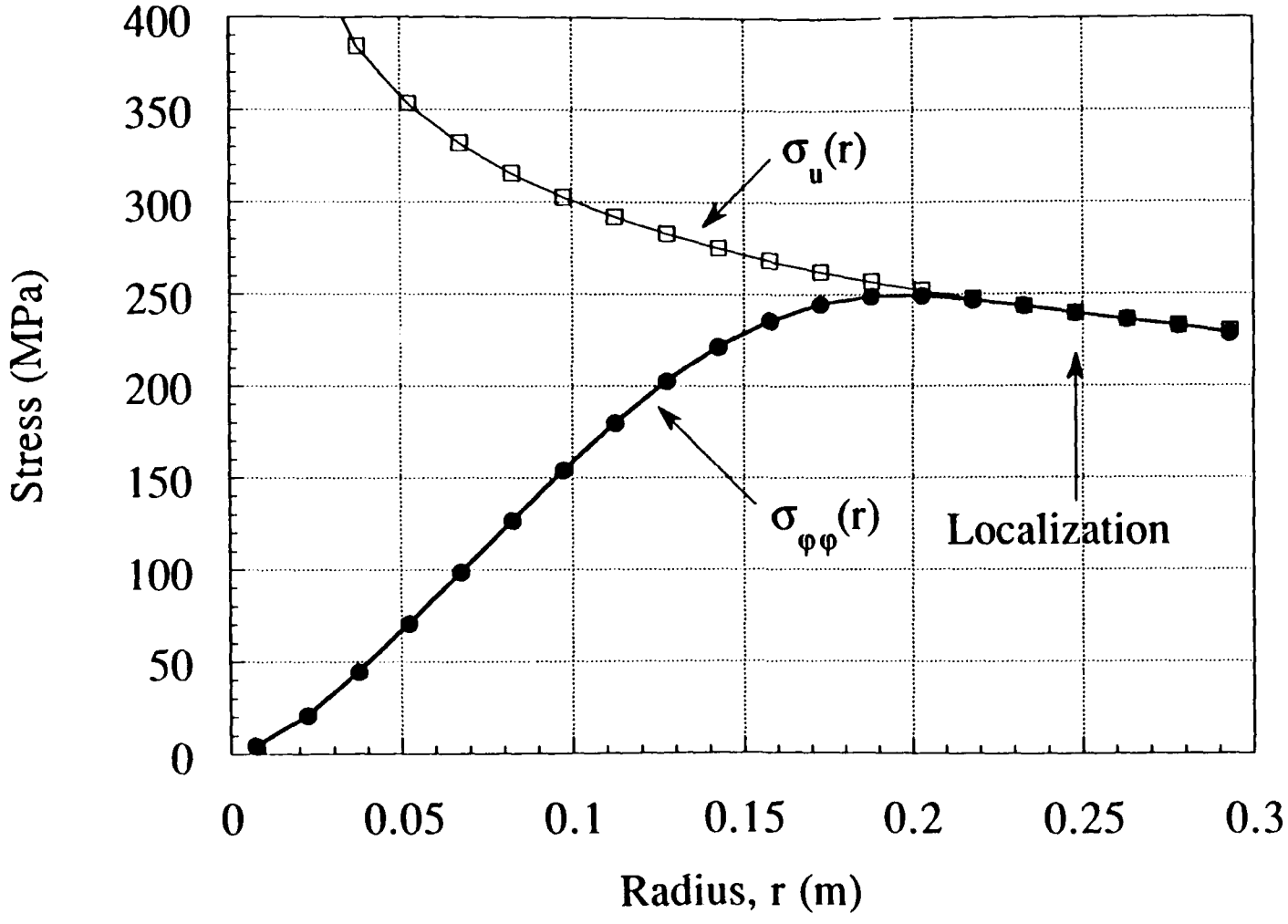
400
350
300
250
200
150
100
50
0
Stress (MPa)
0
0.05
0.1
0.15
0.2
0.25
0.3
Radius, r (m)
$\sigma_u(r)$
$\sigma_{\varphi\varphi}(r)$
Localization

Fig. 7b

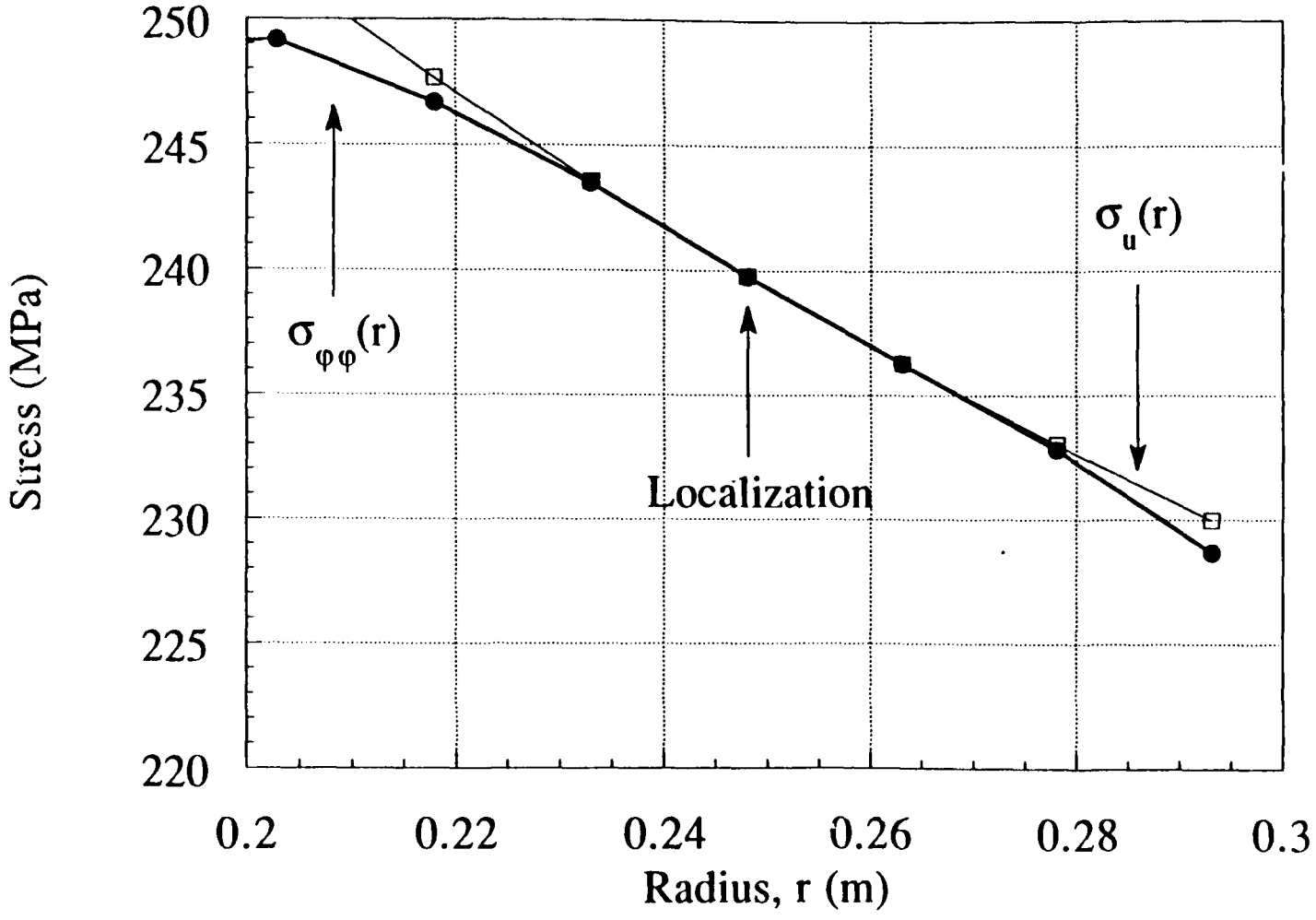
250
245
240
235
230
225
220
Stress (MPa)
0.2
0.22
0.24
0.26
0.28
0.3
Radius, r (m)
$\sigma_{\varphi\varphi}(r)$
$\sigma_u(r)$
Localization

Fig 3a

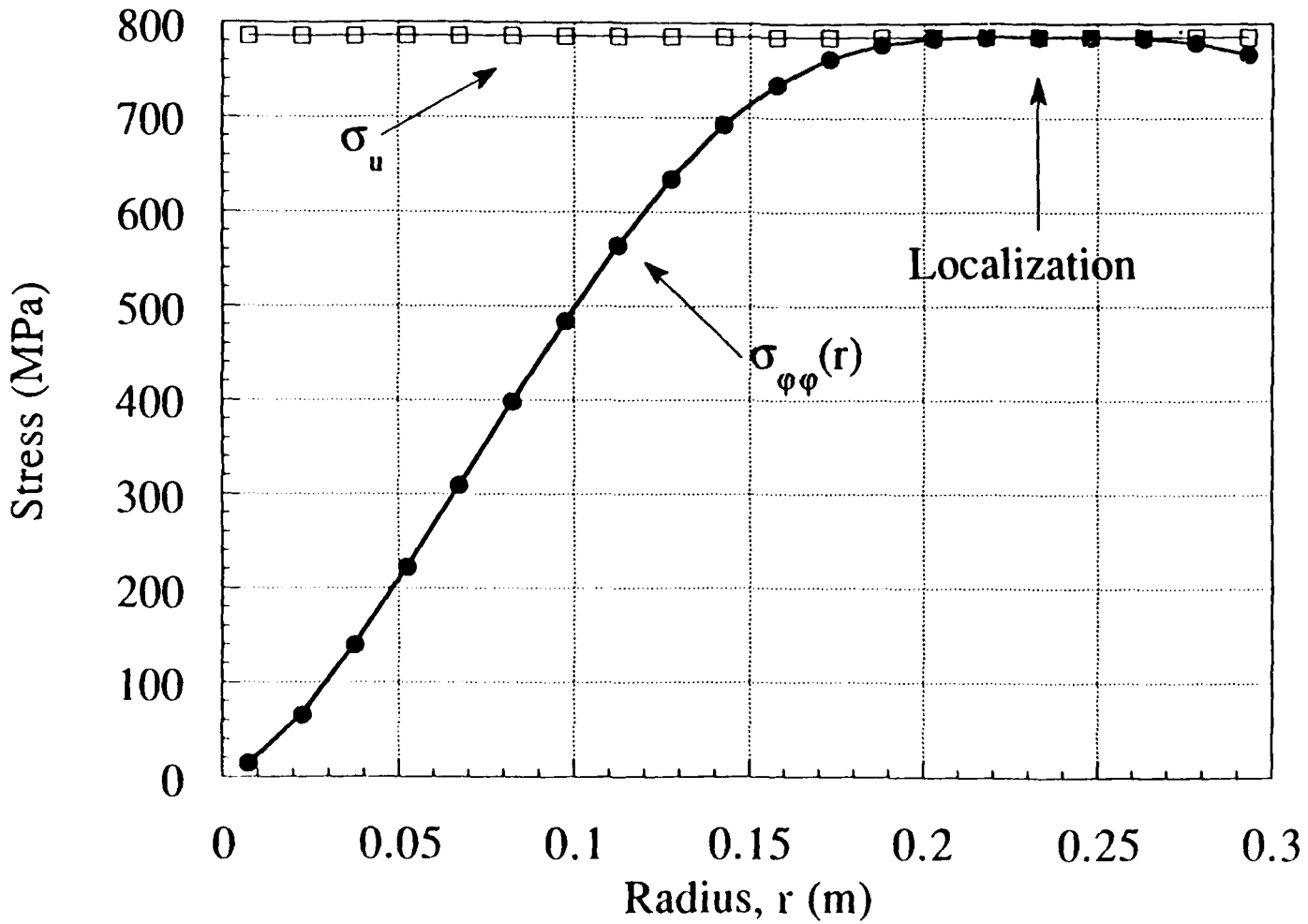
800
700
600
500
400
300
200
100
0
Stress (MPa)
σ_u
$\sigma_{\varphi\varphi}(r)$
Localization
0
0.05
0.1
0.15
0.2
0.25
0.3
Radius, r (m)

Fig. 16

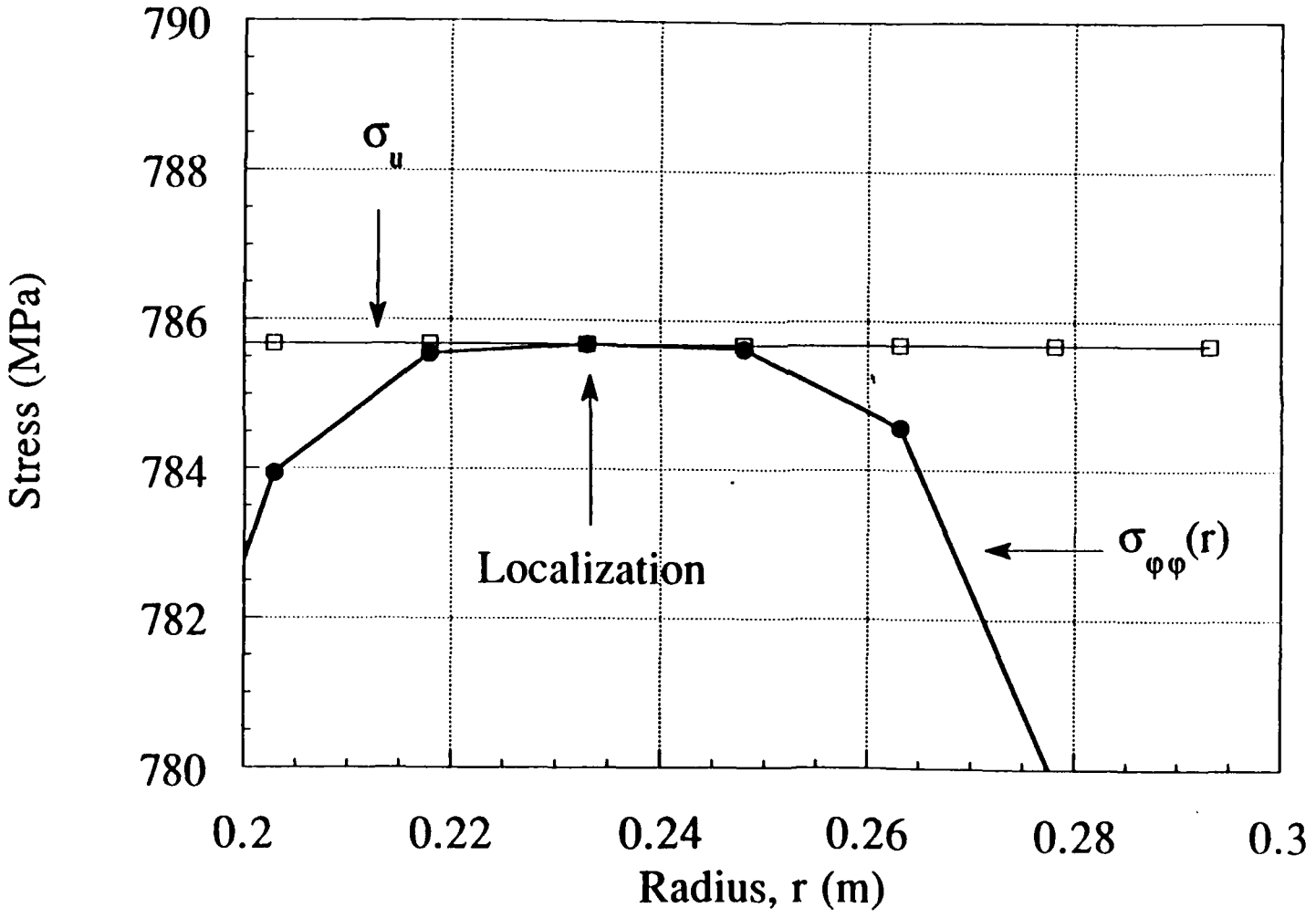
790
788
786
784
782
780
Stress (MPa)
σ_u
Localization
$\sigma_{\varphi\varphi}(r)$
0.2
0.22
0.24
0.26
0.28
0.3
Radius, r (m)

Fig. 3

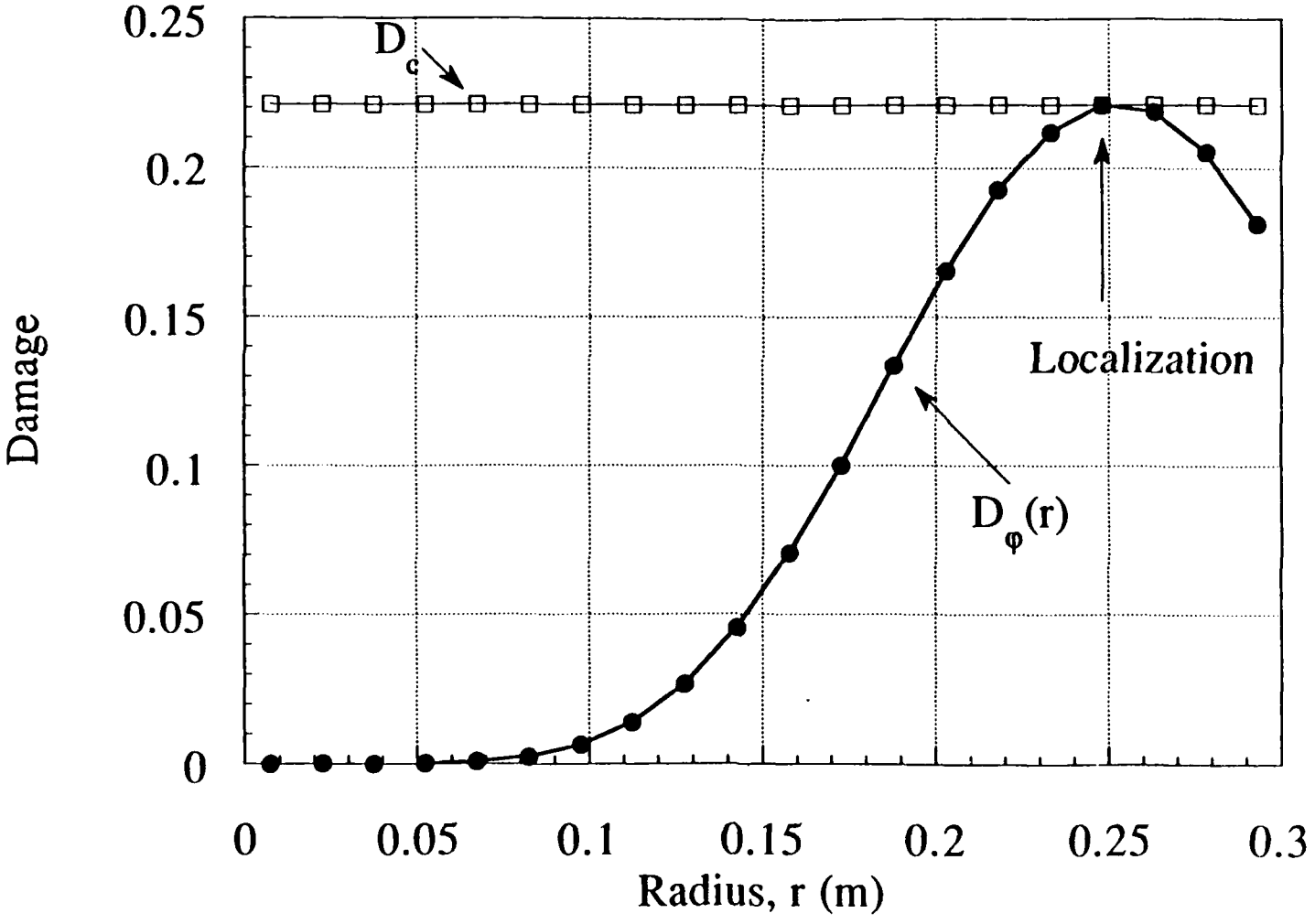
0.25
0.2
0.15
0.1
0.05
0
Damage
D_c
Localization
$D_\varphi(r)$
0
0.05
0.1
0.15
0.2
0.25
0.3
Radius, r (m)

Fig 10

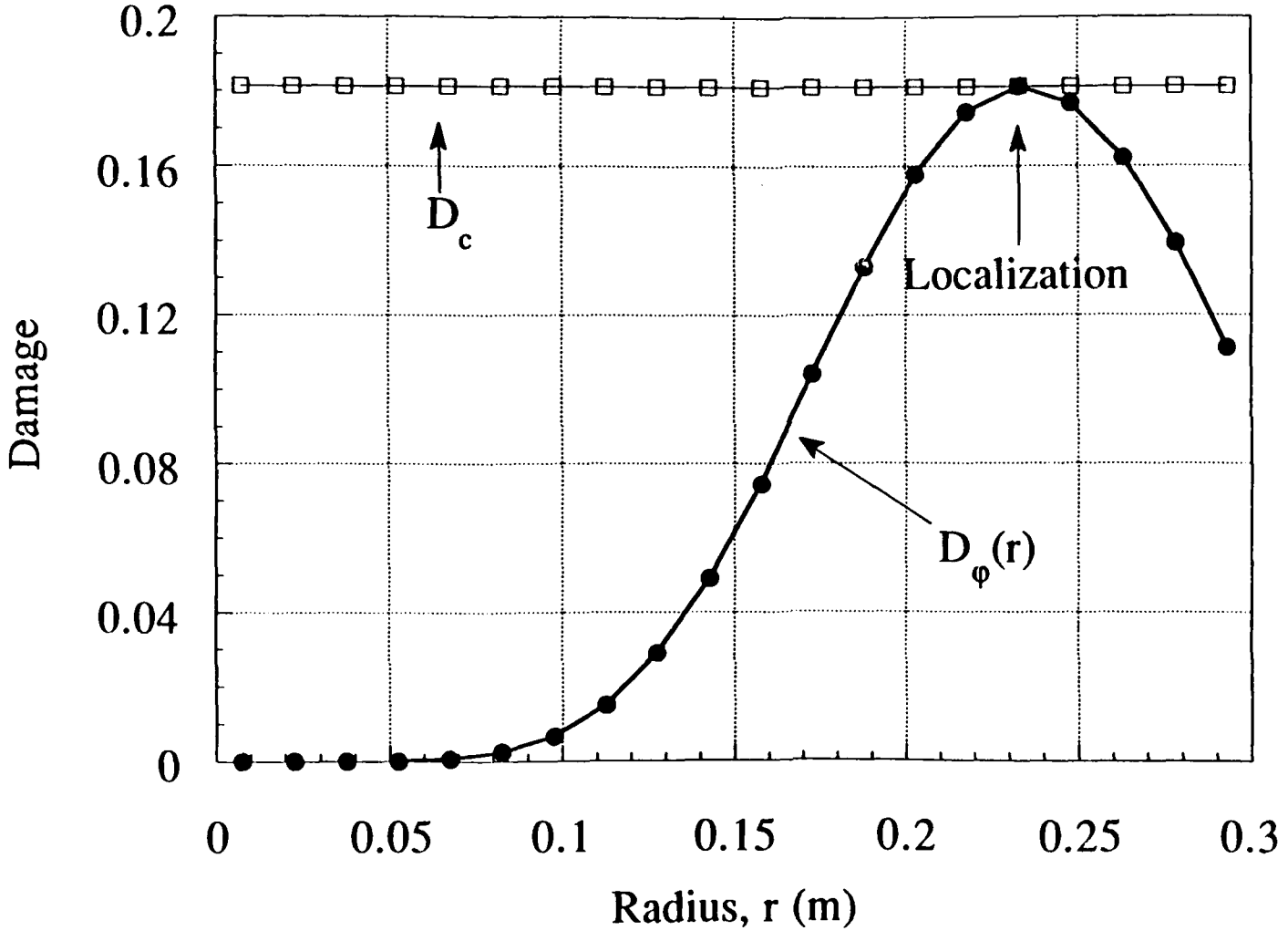
0.2
0.16
0.12
0.08
0.04
0
Damage
D_c
Localization
$D_\varphi(r)$
0
0.05
0.1
0.15
0.2
0.25
0.3
Radius, r (m)

Fig 11

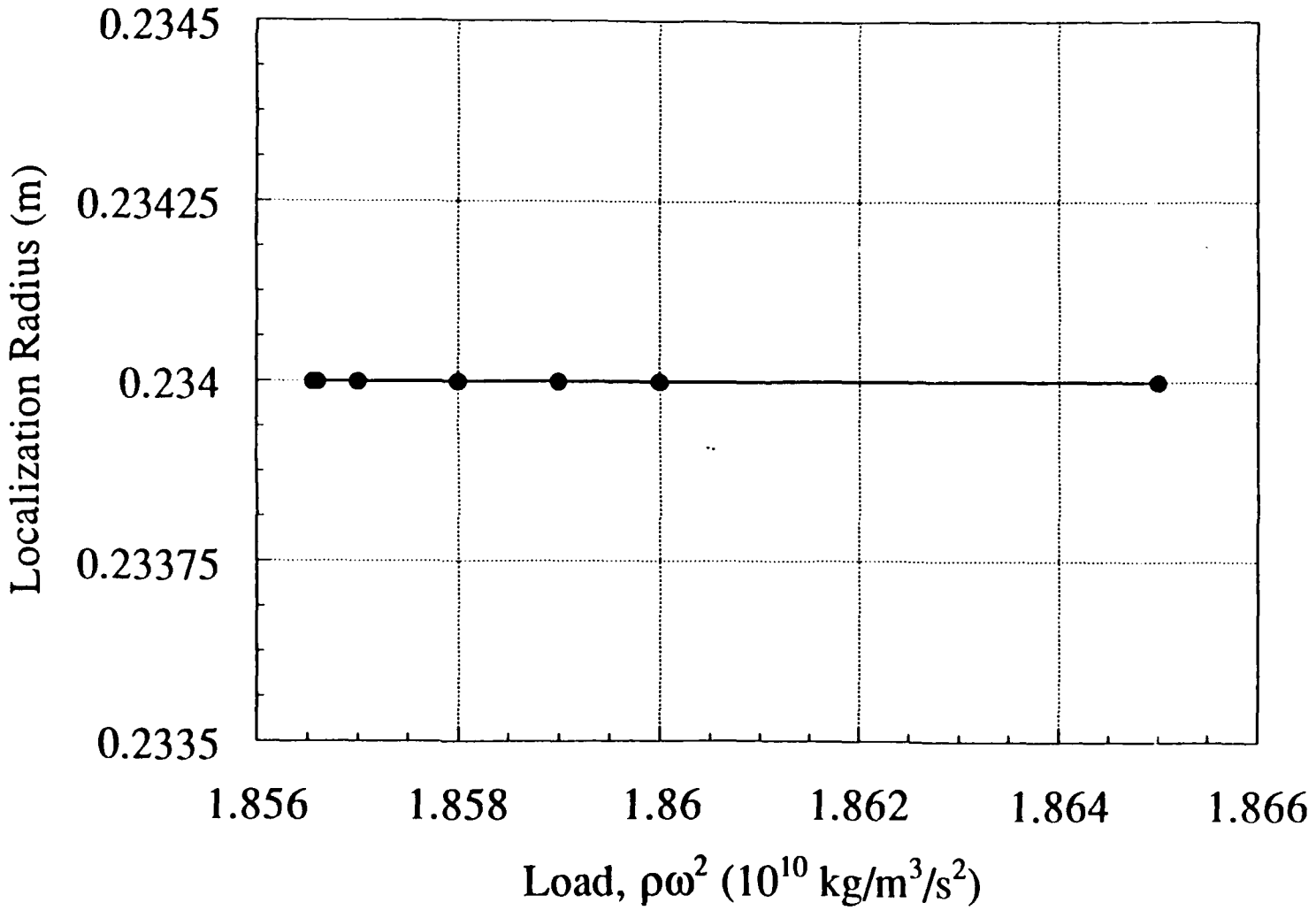
0.2345
0.23425
0.234
0.23375
0.2335
Localization Radius (m)
1.856
1.858
1.86
1.862
1.864
1.866
Load, ρω² (10¹⁰ kg/m³/s²)

Fig. 12

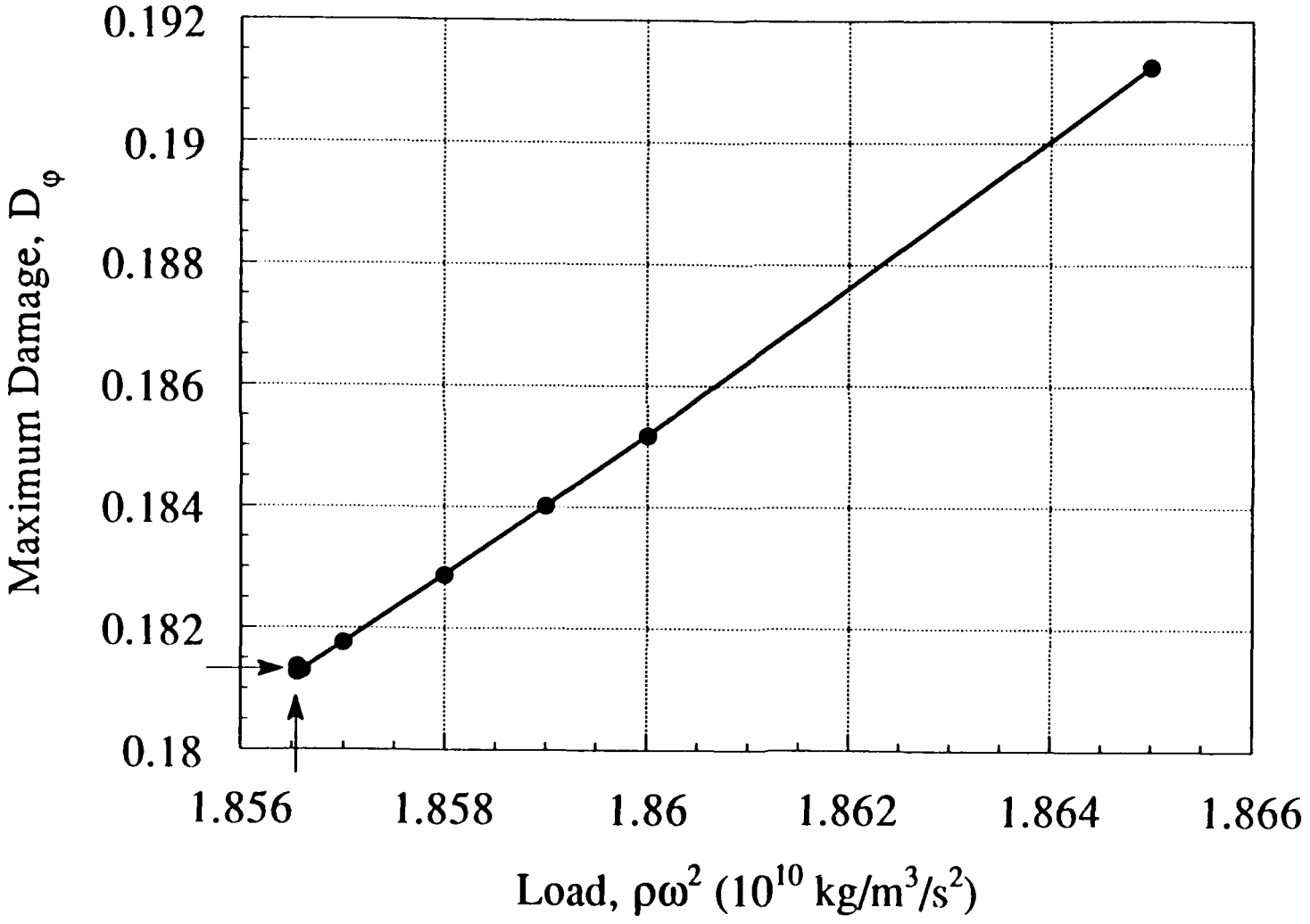
0.192
0.19
0.188
0.186
0.184
0.182
0.18
Maximum Damage, D_φ
1.856
1.858
1.86
1.862
1.864
1.866
Load, $\rho\omega^2$ (10^{10} kg/m^3/s^2)

Fig. 13

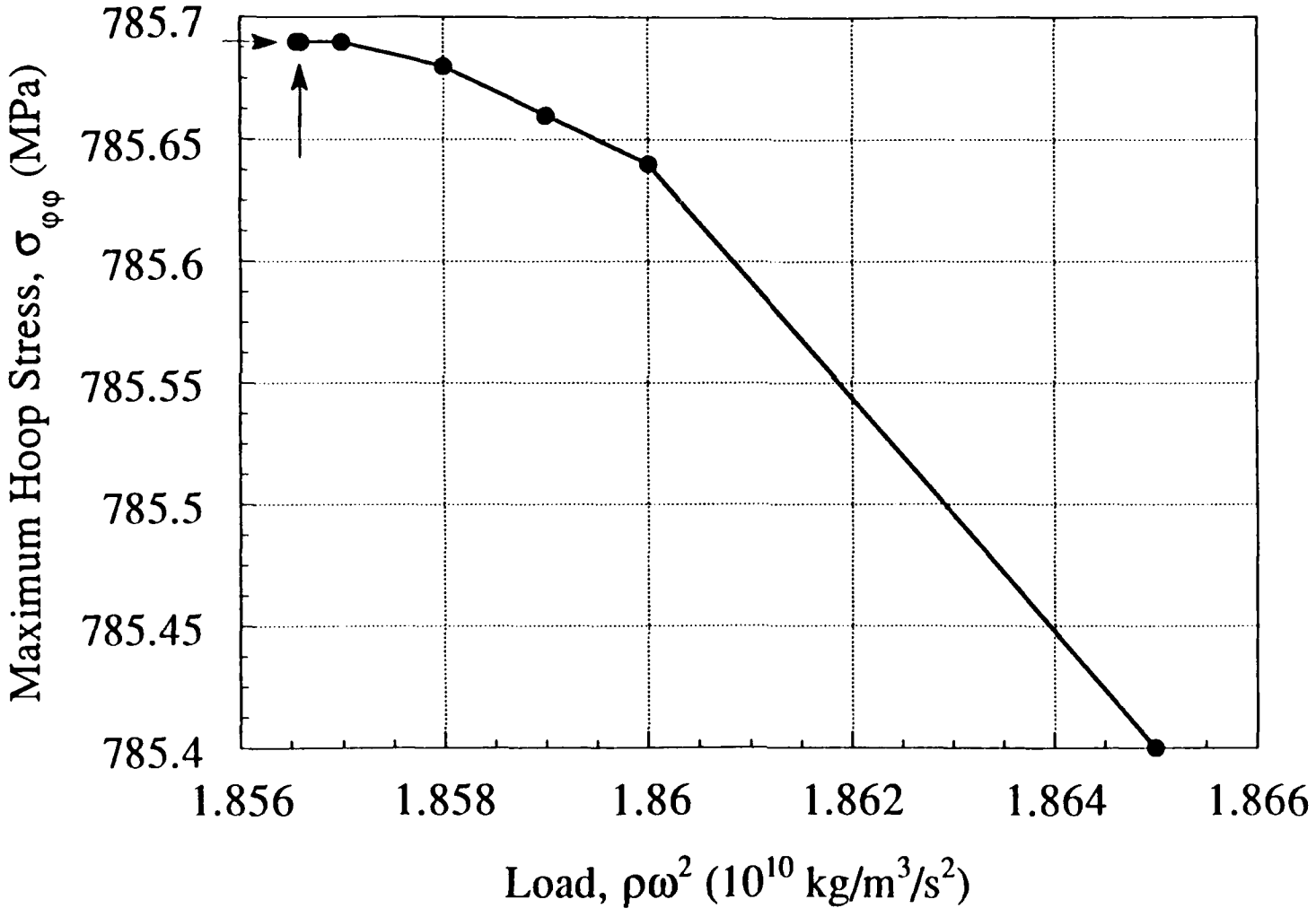
785.7
785.65
785.6
785.55
785.5
785.45
785.4
Maximum Hoop Stress, $\sigma_{\varphi\varphi}$ (MPa)
1.856
1.858
1.86
1.862
1.864
1.866
Load, $\rho\omega^2$ (10^{10} kg/m^3/s^2)

Fig. 14

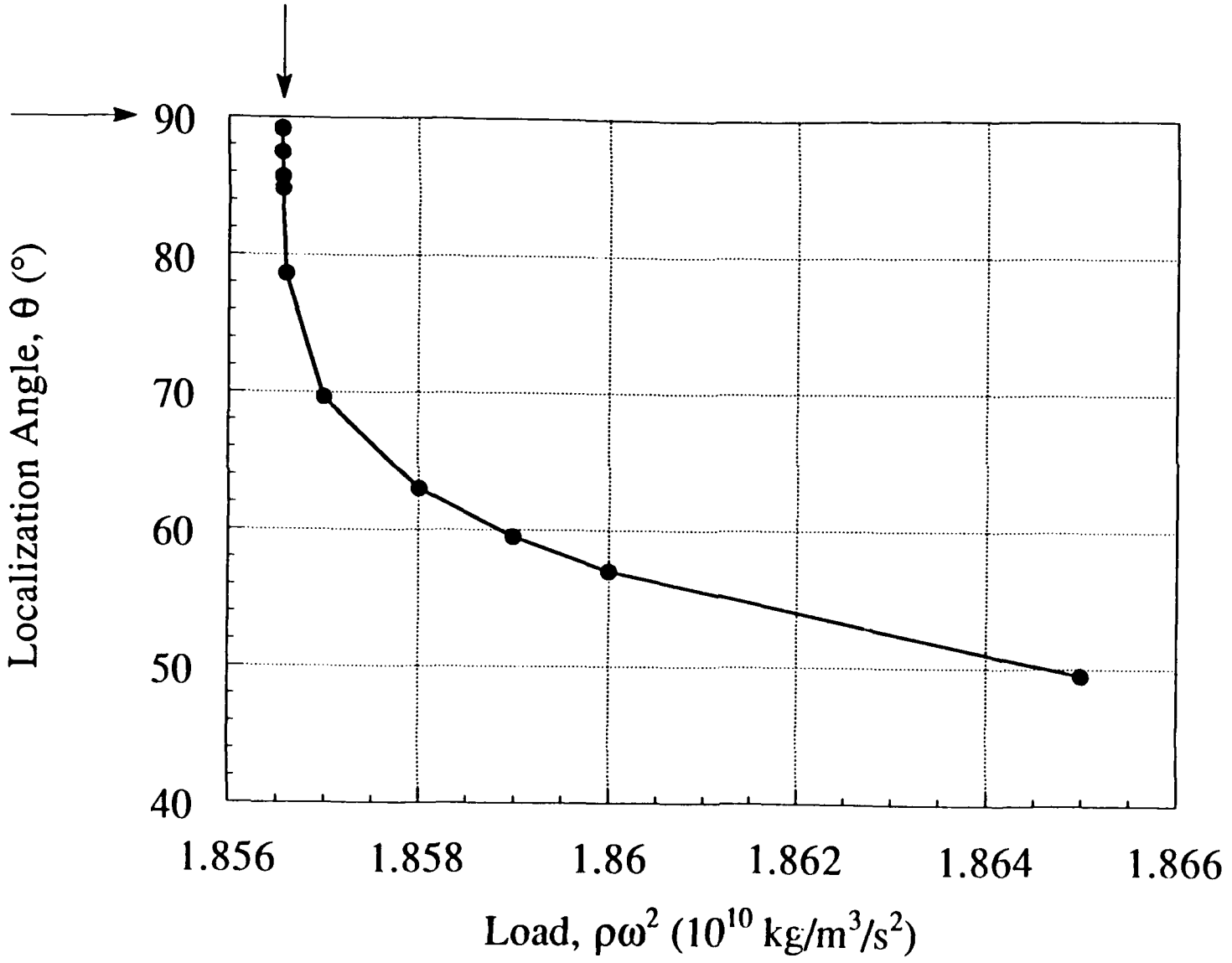
90
80
70
60
50
40
Localization Angle, θ (°)
1.856
1.858
1.86
1.862
1.864
1.866
Load, ρω² (10¹⁰ kg/m³/s²)

Table Caption

Table 1a: Load levels ($\rho\omega^2$) at localization for the two structures and the two models predicted by the fully coupled approach.

Table 1b: Normalized load levels ($\rho\omega^2 a^2/\sigma_u(\eta_{loc})$) at localization for the two structures and the two models predicted by the fully coupled approach.

Table 2a: Load levels ($\rho\omega^2$) at localization for the two structures and the two models predicted by the decoupled approach, in parenthesis () is the difference in terms of angular velocity with the fully coupled approach.

Table 2b: Normalized load levels ($\rho\omega^2 a^2/\sigma_u(\eta_{loc})$) at localization for the two structures and the two models predicted by the decoupled approach.

Table 3: Cumulative failure probability corresponding to the localization load levels obtained by the decoupled and fully approaches.

$\rho\omega^2$ (10^{10} kg/m^3/s^2)	Disc	Ring
Model No. 0	.59	.71
Model No. 1	1.87	2.26

Table 1a

$\rho\omega^2 a^2/\sigma_u(r_{loc})$	Disc	Ring
Model No. 0	2.2	2.7
Model No. 1	2.1	2.6

Table 1b

$\rho\omega^2$ (10^{10} kg/m^3/s^2)	Disc	Ring
Model No. 0	.53 (-4.6%)	.62 (-6.1%)
Model No. 1	1.75 (-3.1%)	2.05 (-4.5%)

Table 2a

$\rho\omega^2a^2/\sigma_u(r_{loc})$	Disc	Ring
Model No. 0	2.1	2.5
Model No. 1	2.1	2.5

Table 2b

P_F	Disc	Ring
Model No. 0	.60	.53
Model No. 1	1.00	1.00

Table 3

MATERIALS

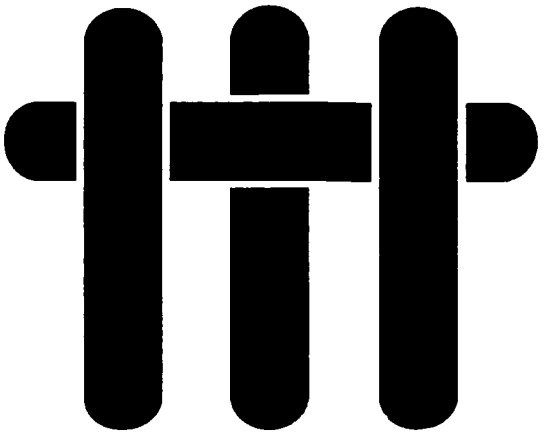

STRESS CORROSION CRACKING IN A UNIDIRECTIONAL CERAMIC-MATRIX COMPOSITE

by

S. M. Spearing*, F. W. Zok and A. G. Evans
Materials Department
College of Engineering
University of California
Santa Barbara, California 93106–5050

*Presently at BP Research Department
BP America Inc.
Cleveland, OH 44128-2837

Accepted for publication in the Journal of American Ceramic Society, August 1993

ABSTRACT

A study of matrix cracking in a unidirectional ceramic matrix composite under static loading conditions has been conducted. The evolution of crack density with time has been measured using both flexure and uniaxial tension tests. *Sub-critical cracking* has been observed at stresses below that required to develop matrix cracks in short duration, monotonic loading tests. Furthermore, a relatively high final crack density has been observed following extended periods (~10^6 s) under static load. A fracture mechanics analysis applicable to sub-critical crack growth has been developed and used successfully to model the evolution of matrix cracking with time and applied stress. The model incorporates the properties of the matrix, fibers and the interfaces, as well as the residual stress and the initial flaw distribution in the matrix.

1. INTRODUCTION

Unidirectional metal (MMC), intermetallic (IMC) and ceramic matrix composites (CMC) have been observed to undergo multiple matrix cracking during either monotonic or cyclic tensile loading[1-8]. All of these matrices are susceptible to either cycle or time dependent crack growth associated with either fatigue (MMC and IMC) or stress corrosion (CMC). Multiple cracking reduces the stiffness of the material, contributes to the inelastic strain and results in permanent deformations upon unloading[3,4].

The development of multiple matrix cracks upon *monotonic* loading has been extensively investigated on CMCs by analytical and experimental means[1,3,4,9-13]. It has also been found that significant degradation of the mechanical properties of CMCs occur upon cyclic loading[14-16]. However, the time-dependent behavior under static load has not been addressed. The aim of this paper is to present an experimental investigation of such behavior, in conjunction with the mechanics needed to predict matrix crack growth. The paper builds upon previous experimental studies of the SiC/CAS system[3,4] and associated modelling[3,4,10-12].

2. EXPERIMENTAL PROCEDURES

2.1 Mechanical Tests

All experiments were conducted on a unidirectional laminate of Nicalon/CAS material provided by Corning[17]. Relevant material properties are summarized in Table I. Tensile specimens were prepared by diamond machining coupons having dimensions 150 x 3 x 2.8 mm, followed by polishing. Similar procedures were used to prepare flexural specimens having dimensions 50 x 3 x 2.8 mm, with the fibers oriented along the beam axis.

Tensile tests were conducted in a servohydraulic machine, at constant load. For such tests, aluminum tabs were bonded to the specimen ends to ensure even load transfer from the hydraulic grips and also to avoid crushing of the specimen. Surface replicas were periodically made using a cellulose acetate tape. The replicas were subsequently examined in an optical microscope to determine the crack density. The flexure tests were conducted in four-point bending with inner and outer spans of 20 and 40 mm, respectively. The apparatus was situated within an optical microscope, allowing *in situ* observations to be made of the cracking process on the tensile face of the beam‡. A thermometer and humidity gauge were placed near the specimens during the tests. The temperature was consistently in the range 15 to 20°C and the relative humidity varied from 60 to 80%.

After the onset of matrix cracking, the stress distribution in a flexural beam becomes non-linear. Analysis of the errors associated with the non-linearity (Appendix) indicates that the stress on the tensile face is within ~10% of the *nominal* value calculated on the basis of linear-elasticity. In the subsequent presentation, only the *nominal* stress corresponding to each flexure test is reported. The following results validate that stress re-distribution does not influence the important trends in the damage evolution process.

2.2 Crack Density Measurements

Previous experience with unidirectional CMCs (including CAS/SiC) indicates that, during tensile loading, matrix cracks develop into more-or-less periodic arrays, with a characteristic crack spacing[3,4]. The cracks generally span a significant fraction of the specimen width and are bridged by fibers. One such example is shown in Fig. 1. Because of the periodic nature of the cracks, the average crack spacing can be related to changes in the composite modulus and the permanent strain following unloading using

‡ No particular effort was made to control the test environment.

relatively simple models based on shear lag[3,4]. This experience suggests that the relevant measure of damage in such composites is the *linear* crack density, measured parallel to the fiber direction[‡]. This approach was adopted in the present study. In all cases, the crack density was measured along a 20 mm gauge length parallel to the tensile axis. At the outset of each test, only one gauge length was examined. After longer durations (~ 30 minutes), measurements were made along three separate gauge lengths parallel to one another.

In making such measurements, two complicating features were encountered. In some instances, cracks were seen to bifurcate. Invariably, one of the branches arrested after propagating ~ 10-30 μm, whereas the other continued to propagate large distances. An example is indicated on Fig. 1. In other instances, cracks propagating in one direction arrested when they reached other cracks which were on nearly the same plane, but propagating in the opposite direction. In such cases, both sets of cracks arrested after propagating ~ 10-30 μm past one another. An example is again indicated on Fig. 1. These artefacts were excluded from the present crack density measurements. This was accomplished by counting only those cracks that traversed more than ~ 40 μm on both sides of the gauge line.

3. EXPERIMENTAL RESULTS

In situ observations of the flexure specimens indicated that matrix cracks evolve over time at constant load. Two types of cracking were observed (designated Type I and Type II) . At *low stresses* and *short times*, Type I cracking occurred. In this case, cracks appeared suddenly and grew rapidly across the specimen width. There was no

---

‡ The linear crack density is equivalent to the *inverse* of the average crack spacing.

evidence that visible cracks were subject to detectable growth*. This observation suggests that sub-critical* growth occurs at very short cracks which are invisible in the optical microscope. At larger lengths, the cracks propagated under sub-critical conditions at a sufficiently high velocity that they could not be followed in the optical microscope. Type I behavior coincides with low crack densities.

Type II behavior, at higher stresses or long times, involves the extension of existing, long cracks, between other closely-spaced cracks. One such example is shown in Fig. 2. This behavior arises at high crack density. This observation suggests that the cracks "shield" each other, thereby reducing the driving force for further growth, as shown schematically in Fig. 3.

In situ measurements of the crack density, ρ, in the flexure specimens revealed strong effects of the applied stress (Fig. 4(a)). This contrasts with the behavior of monolithic ceramics, for which time-dependent effects are only apparent at stresses close to the instantaneous failure stress. Two features of the damage evolution process are noteworthy: (i) At stresses below the matrix cracking stress measured in short duration, monotonic tests (130-150 MPa), no cracks were visible initially. However, appreciable cracking subsequently occurred over a period of ~ 10^6 s. Indeed, the final crack density, ρ_f, measured at 120 MPa reached a significant fraction of the *saturation* crack density, ρ_s*, found in short duration, monotonic tests ($\rho_f \approx 1/2\ \rho_s$)[4]. (ii) At either long times or high stress, ρ tends toward a constant value ($\rho \approx 12.5$ cracks/mm). This level is *higher* than ρ_s.

Measurements of crack density made from surface replicas of the tensile specimens are shown in Fig. 4(b). One of these tests was conducted at a stress close to

---

* Detectable crack growth is defined as the condition wherein the crack velocity is sufficiently low to allow crack growth to be followed in the microscope. In contrast, *sub-critical* crack growth refers *only* to conditions wherein the crack tip energy release rate is below the composite toughness. High crack growth rates (~ 10^{-3} m/s) have been measured in monolithic glass-ceramics under sub-critical conditions[18]. Such behavior would not result in detectable growth.

* $\rho_s \approx 10$ cracks/mm.

the initial matrix cracking stress (150 MPa) and the other at a higher stress (200 MPa). The results show trends similar to those found in flexure at comparable stress levels. The slight discrepancies may be attributed to differences in the stress states in the two types of tests, as well as variations in the testing environment (temperature and relative humidity). An assessment of the effects of flexure on matrix damage is given in the Appendix.

4. DAMAGE MECHANICS

The experimental observations affirm the existence of appreciable effects of time on matrix cracking. The modelling approach used to rationalize the experimental results has the following features*. (i) Crack growth in the matrix is governed by the crack tip energy release rate, $\mathcal{G}_{tip}$, in association with a stress corrosion law. (ii) Bridging of the crack by fibers occurs, subject to a sliding stress, τ. The magnitude of τ can change as a result of environmental interactions. However, in the following analysis, τ is assumed to be constant along the debonded interface. (iii) Fiber bridging is subject to two regimes. When the cracks are *short*, the tip energy release rate increases with crack length. When the cracks are *long*, the tip energy release rate is *independent* of crack length. (iv) Once the cracks became closely spaced, the slip lengths of neighboring cracks overlap, reducing the driving force for additional crack growth. Much of the relevant mechanics has been derived elsewhere[9-13]. In this section, adaptations of the existing mechanics suitable for sub-critical crack growth are presented.

*These features are suggested by the present consensus regarding the mechanisms of stress corrosion in ceramics[19].

4.1 Energy Release Rates

The effects of bridging fibers on the crack tip energy release rate $\mathcal{G}_{tip}$ or stress intensity K_{tip} for *single, isolated* cracks have been extensively analyzed[9-13]. Here, the numerical results of McMeeking and Evans[13] are presented and adapted to the problem of sub-critical crack growth. The trends in energy release rate with crack length (from Fig. 6 of Ref. 13) are shown in Fig. 5. These results are found to be well-approximated by two analytical expressions[‡]. When $2\xi\sigma_t R/\tau a \le \gamma$,

$$\frac{\mathcal{G}_{tip} E}{\sigma^2 \pi a\left(1-\nu^2\right)} = \frac{1}{25}\left(\frac{2\xi\sigma_t R}{\tau a}\right)^{2/3} \tag{1a}$$

and, when $2\xi\sigma_t R/\tau a > \gamma$

$$\frac{\mathcal{G}_{tip} E}{\sigma^2 \pi a\left(1-\nu^2\right)} = \frac{1}{12\pi}\left(\frac{2\xi\sigma_t R}{\tau a}\right) \tag{1b}$$

where R is the fiber radius; 2a is the crack length; E is the longitudinal composite modulus,

$$E = f E_f + (1\text{-}f) E_m \tag{2}$$

with E_m and E_f being the moduli of the matrix and the fibers; ν is Poisson's ratio, assumed to be the same for the matrix and the fibers; γ is a numerical coefficient

$$\gamma = (12\pi/25)^3 \approx 3.43 \tag{3}$$

---

‡ These features are suggested by the mechanisms of stress corrosion found in monolithic ceramics[19].

σ_t is the stress (applied plus residual),

$$\sigma_t = \sigma + q\,E/E_m \tag{4}$$

with q being the residual axial stress in the matrix; and ξ characterizes the elastic properties.

$$\xi = \frac{(1-f)^2 E_m^2}{f^2 E E_f \left(1-\nu^2\right)} \tag{5}$$

The expressions (1) and (2) are accurate to within 5% over the range $0 \le 2\xi\,\sigma R/\tau a \le 20$ (Fig. 5)‡.

For subsequent analysis, Eqns. (1a) and (1b) are re-written in terms of two fixed quantities, independent of stress and crack length. The first is the *steady state matrix cracking stress* in the *absence* of residual stress, σ_o. This stress is obtained by setting $\mathcal{G}_{tip}$ equal to the composite toughness,

$$\Gamma = \Gamma_m\,(1\text{-}f) \tag{6}$$

with Γ_m being the matrix toughness, whereupon[9,11]

$$\sigma_o = \left(\frac{6E_f f^2 E^2 \tau \Gamma_m}{E_m^2 (1-f) R}\right)^{1/3}. \tag{7}$$

---

‡ Note that the result of Eqn. (1a) corresponds to the short crack regime wherein the tip energy release rate increases with crack length. In contrast, the result of Eqn. (1b) corresponds to the steady-state regime wherein $\mathcal{G}_{tip}$ is independent of crack length.

This is the stress required to propagate a steady-state crack under monotonic tensile loading (in the absence of sub-critical behavior). The other quantity is the crack length, a_o, at which steady state conditions are attained at $\sigma = \sigma_o$. This length is obtained by equating the expressions for $\mathcal{G}_{tip}$ in Eqns. (1a) and (1b), yielding

$$a_o = \frac{2\xi R(\sigma_o + q E/E_m)}{\gamma \tau} . \tag{8}$$

Upon combining Eqns. (7) and (8) with Eqns. (1) and (2), the final results are:

$$\frac{\mathcal{G}_{tip}}{\Gamma_m (1-f)} = \left(\frac{\sigma_t}{\sigma_o}\right)^{8/3} \left(\frac{a}{a_o}\right)^{1/3} \qquad \left[\frac{a}{a_o} \le \frac{\sigma_t}{\sigma_o}\right] \tag{9a}$$

and

$$\frac{\mathcal{G}_{tip}}{\Gamma_m (1-f)} = \left(\frac{\sigma_t}{\sigma_o}\right)^{3} \qquad \left[\frac{a}{a_o} > \frac{\sigma_t}{\sigma_o}\right]. \tag{9b}$$

The predicted trends in energy release rate, $\mathcal{G}_{tip}/\Gamma_m$ (1-f), with crack length, a/a_o, for various values of stress, σ_t/σ_o, are presented in Fig. 6. Also shown by the dashed line is the boundary between the short crack and long crack regimes. These results predict three types of behavior, depending on the level of stress. (i) When $\sigma_t = \sigma_o$, the energy release rate initially increases with crack length, but reaches a steady state value equivalent to the composite toughness (Γ_m (1-f)) at a crack length $a = a_o$. (ii) When $\sigma_t > \sigma_o$, the energy release rate reaches the toughness at a crack length, $a/a_o = (\sigma/\sigma_o)^{-8}$. Crack growth beyond this point occurs subject to a constant energy release rate, equivalent to the toughness. The steady state conditions predicted by Eqn. (9b) are never attained. (iii) When $\sigma_t < \sigma_o$, the energy release rate reaches its

steady-state value, $(\sigma_t/\sigma_o)^3$, at a crack length, $a/a_o = \sigma/\sigma_o$. In this regime, the energy release rate never reaches the toughness. Consequently, the cracks extend *only under sub-critical conditions.*

When *multiple* matrix cracks occur and interact, an important quantity in the mechanics is the slip length, d, between matrix and fiber, given by[9,12],

$$d/R = 2E f \tau/(\sigma + qE/E_m) E_m (1-f) \tag{10}$$

When the slip zones between neighboring cracks overlap, $\mathcal{G}_{tip}$ for long cracks falls below the steady state value, $\mathcal{G}_o$, for a single, isolated crack, given by

$$\mathcal{G}_o = \frac{(\sigma + qE/E_m)^3 E_m^2 (1-f)^2 R}{6\tau f^2 E_f E^2} . \tag{11}$$

The relationship between $\mathcal{G}_{tip}$ and $\mathcal{G}_o$ is dictated by the spacing, ℓ, between neighboring cracks relative to d[12], and can be expressed as

$$\frac{\mathcal{G}_{tip}}{\mathcal{G}_o} = 1 \qquad \left[\frac{\ell}{d} \geq 2\right] \tag{12a}$$

$$\frac{\mathcal{G}_{tip}}{\mathcal{G}_o} = 1 - 4\left(1 - \frac{\ell}{2d}\right)^3 \qquad \left[1 \leq \frac{\ell}{d} \leq 2\right] \tag{12b}$$

$$\frac{\mathcal{G}_{tip}}{\mathcal{G}_o} = 4\left(\frac{\ell}{2d}\right)^3 \qquad \left[0 \leq \frac{\ell}{d} \leq 1\right]. \tag{12c}$$

Once again it is convenient to re-express these results in terms of two fixed quantities: the steady state matrix cracking stress, σ_o (defined in Eqn. 7), and the slip length, d_o, at $\sigma = \sigma_o$:

$$d_o / R = \frac{(\sigma_o + q E / E_m) E_m (1-f)}{2 E f \tau} . \qquad (13)$$

Combining Eqn. (9) with (4) and (10) yields the results

$$\frac{\mathcal{G}_{tip}}{\Gamma_m (1-f)} = \left(\frac{\sigma_t}{\sigma_o}\right)^3 \qquad \left[\frac{\ell}{d_o} \geq 2\frac{\sigma_t}{\sigma_o}\right] \qquad (14a)$$

$$\frac{\mathcal{G}_{tip}}{\Gamma_m (1-f)} = \left(\frac{\sigma_t}{\sigma_o}\right)^3 \left[1 - 4\left(1 - \frac{\ell}{2d_o}\frac{\sigma_o}{\sigma_t}\right)^3\right] \qquad \left[\frac{\sigma_t}{\sigma_o} \leq \frac{\ell}{d_o} \leq 2\frac{\sigma_t}{\sigma_o}\right] \qquad (14b)$$

$$\frac{\mathcal{G}_{tip}}{\Gamma_m (1-f)} = 4\left(\frac{\ell}{2d_o}\right)^3 \qquad \left[0 \leq \frac{\ell}{d_o} \leq \frac{\sigma_t}{\sigma_o}\right] . \qquad (14c)$$

The predicted trends in energy release rate, $\mathcal{G}_{tip}/\Gamma_m$ (1-f), with crack spacing, ℓ/d_o, for several values of stress, σ_t/σ_o, are shown in Fig. 7. These results also predict three types of behavior, depending on the level of stress. (i) When $\sigma_t < \sigma_o$, the energy release rate is independent of spacing, provided that $\ell/d_o > 2\,\sigma_t/\sigma_o$. In this regime, the slip lengths of adjacent crack do no overlap. When the crack spacing is in the range, $\sigma_t/\sigma_o \leq \ell/d_o \leq 2\,\sigma_t/\sigma_o$, the energy release rate decreases with decreasing ℓ at a rate that depends on the stress. Once the crack spacing reaches $\ell/d_o \leq \sigma_t/\sigma_o$, the energy release rate decreases with decreasing ℓ at a rate *independent* of stress. (ii) When the stress is in the range, $1 \leq \sigma_t/\sigma_o \leq 2^{1/3}$, the crack spacing immediately drops to

$$\frac{\ell}{d_o} = 2\frac{\sigma_t}{\sigma_o}\left\{1-\left[\frac{1}{4}\left(1-\left(\frac{\sigma_o}{\sigma_t}\right)^3\right)\right]^{1/3}\right\}. \qquad (15)$$

Further reductions in spacing lead to a decrease in $\mathcal{G}_{tip}$, first at a rate dependent on stress (over the range $\sigma_t/\sigma_o \le \ell/d_o \le 2\,\sigma_t/\sigma_o$), then at rate independent of stress (over the range $0 \le \ell/d_o \le \sigma_t/\sigma_o$). (iii) Finally, when the stress $\sigma_t/\sigma_o \ge 2^{1/3}$, the crack spacing diminishes to $\ell/d_o = 2^{1/3}$. Further reductions in crack spacing lead to a drop in $\mathcal{G}_{tip}$ independent of stress.

4.2 Crack Growth

The preceding energy release rates $\mathcal{G}_{tip}$ can be used in conjunction with a crack growth criterion to predict crack evolution. As noted above, stress corrosion is considered to be the mechanism that causes time-dependent matrix cracking. Consequently, crack growth can be described by the commonly-used power law,

$$\frac{da}{dt} = \dot{a}_o\left(K_{tip}/K_m\right)^n \equiv \dot{a}_o\left(\mathcal{G}_{tip}/\Gamma_m(1-f)\right)^{n/2} \qquad (16)$$

where $\dot{a}_o$ is a reference velocity, n is the power law exponent and K_m is the critical stress intensity factor for the matrix. For aluminosilicate glass ceramics[18], stress corrosion is caused by moisture and the power law exponent is, $n \approx 50$.

To provide a basis for further modeling, it is instructive to re-state the key experimental observations. The process of crack evolution exhibits three regimes. (i) At low stresses and small crack densities (Type I), damage evolution is governed by short, non-interacting cracks, with $\mathcal{G}_{tip}$ given by Eqn. (9). In this regime, because n is large, the behavior is dominated by stress corrosion occurring when the cracks are small and

invisible. (ii) At either high stresses or long times (Type II), multiple cracks are already present, and further crack growth occurs under steady-state conditions (independent of crack length), with $\mathcal{G}_{tip}$ given by Eqn. (14). Then, the new cracks should be continually visible and grow at a discernible, near-constant velocity across the specimen. (iii) An intermediate regime must exist which combines features of type I and II behaviors. The behavior in this regime is inherently difficult to analyze and is not considered in this study. Instead, interpolation between type I and type II could be used.

4.2.1 Short Cracks (Type I)

For short, non-interacting cracks, the time t_i required to grow a matrix crack of initial length a_i is evaluated by integrating the growth law (Eqn. (16)) between appropriate limits, yielding the result

$$t_i = \frac{1}{\dot{a}_o}\int_{a_i/a_o}^{a_f/a_o}\left(\frac{\Gamma_m(1-f)}{\mathcal{G}_{tip}}\right)^{n/2} d(a/a_o) \tag{17}$$

where a_f is an upper limit on the crack length, described below. Two cases are considered, defined by the level of stress. In the first, $\sigma_t/\sigma_o \geq 1$. In this regime, the appropriate upper limit on the integral is the crack length at which $\mathcal{G}_{tip}$ reaches the composite toughness. Beyond this point, the crack grows catastrophically. As noted earlier, this limit is, $a_f/a_o = (\sigma/\sigma_o)^{-8}$. Combining this result with Eqns. (9a) and (17) gives

$$\begin{aligned} t_i &= \frac{1}{\dot{a}_o}\left(\frac{\sigma_t}{\sigma_o}\right)^{-4n/3}\int_{a_i/a_o}^{(\sigma_t/\sigma_o)^{-8}}\left(\frac{a}{a_o}\right)^{-n/6} d\left(\frac{a}{a_o}\right) \\ &= \frac{1}{\dot{a}_o}\left(\frac{\sigma_t}{\sigma_o}\right)^{-4n/3}\left(\frac{6}{6-n}\right)\left[\left(\frac{\sigma_t}{\sigma_o}\right)^{-8(1-n/6)} - \left(\frac{a_i}{a_o}\right)^{(1-n/6)}\right]. \end{aligned} \tag{18}$$

For the material of present interest, n is large and thus $(\sigma/\sigma_o)^{-8(1-n/6)} << (a_i/a_o)^{(1-n/6)}$. Consequently, Eqn. (18) reduces to

$$t_i \approx \frac{1}{\dot{a}_o}\left(\frac{\sigma_t}{\sigma_o}\right)^{-4n/3}\left(\frac{6}{n-6}\right)\left(\frac{a_i}{a_o}\right)^{(1-n/6)} \tag{19}$$

The second regime is defined by $\sigma/\sigma_o < 1$. In this case, $\mathcal{G}_{tip}$ initially increases with crack length according to Eqn. (6), but then reaches a steady state level given by Eqn. (9b), at a crack length $a/a_o = \sigma/\sigma_o$. It is therefore convenient to separate the integral in Eqn. (15) into two parts. One is for condition wherein $\mathcal{G}_{tip}$ increases with a, and the other for $\mathcal{G}_{tip}$ independent of a. The result is

$$\begin{aligned} t_i &= \frac{1}{\dot{a}_o}\left\{\left(\frac{\sigma}{\sigma_o}\right)^{-8/3}\int_{a_i/a_o}^{\sigma/\sigma_o}\left(\frac{a}{a_o}\right)^{-2/n} d\left(\frac{a}{a_o}\right) + \left(\frac{\sigma_t}{\sigma_o}\right)^{-3/n}\int_{\sigma/\sigma_o}^{a_f/a_o} d\left(\frac{a}{a_o}\right)\right\} \\ &= \frac{1}{\dot{a}_o}\left\{\left(\frac{\sigma_t}{\sigma_o}\right)^{-4n/3}\left(\frac{6}{6-n}\right)\left[\left(\frac{\sigma_t}{\sigma_o}\right)^{(1-n/6)} - \left(\frac{a_i}{a_o}\right)^{(1-n/6)}\right] + \left(\frac{\sigma_t}{\sigma_o}\right)^{-3n/2}\left(\frac{a_f}{a_o} - \frac{\sigma_t}{\sigma_o}\right)\right\} \end{aligned} \tag{20}$$

where a_f is on the order of the specimen width.

Once again, because n is large, $(\sigma/\sigma_o)^{(1-n/6)} << (a_i/a_o)^{(1-n/6)}$. Furthermore, the experimental observations suggest that, once steady state conditions have been attained, the time required to grow the crack across the specimen width is relatively small. As a result, the last term in Eqn. (20) is neglected. With these approximations, Eqn. (20) reduces to

$$t_i \approx \frac{1}{\dot{a}_o}\left(\frac{\sigma_t}{\sigma_o}\right)^{-4n/3}\left(\frac{6}{n-6}\right)\left(\frac{a_i}{a_o}\right)^{(1-n/6)} \tag{21}$$

which is equivalent to the result in Eqn. (19). Consequently, the distinction between the two regimes is neglected in the subsequent analysis.

A representation for the matrix flaw distribution is now needed in order to predict damage evolution. For this purpose, an extreme value matrix flaw size distribution is assumed, given by,

$$F = 1 - \exp\left[-\frac{V}{V_*}\left(\frac{a_*}{a_i}\right)^{\alpha} \right] \tag{22}$$

where F is the fraction of flaws having size greater than a_i in a volume V, α is the shape parameter, and a_* and V_* are scale parameters. Consequently, if η_v is the total number of flaws per unit volume, the number η having size $a \geq a_i$ is

$$\eta = \eta_v \left[1 - \exp\left[-\frac{V}{V_*}\left(\frac{a_*}{a_i}\right)^{\alpha} \right] \right] \tag{23}$$

Assuming that only the largest flaws in the distribution evolve into *visible* matrix cracks, Eqn. (23) reduces to

$$\eta \approx \eta_v \left(V/V_*\right)\left(a_*/a_i\right)^{\alpha} \tag{24}$$

Combining this distribution with Eqn. (21) gives the number of flaws, η_s, that have developed into steady state cracks within a time, t:

$$\eta_s \approx \eta_v \left(\frac{V}{V_*}\right)\left(\frac{a_*}{a_o}\right)^{\alpha} \left(\frac{n-6}{6}\right)^{6\alpha/(n-6)} (t\dot{a}_o)^{6\alpha/(n-6)} \left(\frac{\sigma_t}{\sigma_o}\right)^{8n\alpha/(n-6)}$$

$$\equiv \lambda (t\dot{a}_o)^y \left(\frac{\sigma_t}{\sigma_o}\right)^x \qquad (25)$$

where

$$x \equiv \frac{8n\alpha}{n-6}, \qquad (26a)$$

and $$y \equiv \frac{6\alpha}{n-6} \qquad (26b)$$

while λ contains all of the parameters characterizing the flaw distribution. Furthermore, the linear density of cracks ρ measured parallel to the tensile axis, is related to η_s through

$$\rho = A \cdot \eta_s \qquad (27)$$

where A is the cross-sectional area of the composite.

Equations (25) and (27) suggest that the evolution of crack density can be described by a generic law of the form

$$\rho = \lambda' t^y \sigma^x \qquad (28)$$

where λ' embodies all the relevant material properties. However, many of the properties contributing to λ' are poorly characterized. Consequently, it is expedient to

use Eqn. (28) to fit data at one stress level and then *predict* crack growth rates at other stress levels.

4.2.2 Long Cracks

The evolution of crack density in the regime characterized by high stresses and high crack densities has been computed in a similar fashion. In this case, the governing relations for $\mathcal{G}_{tip}$ are given by Eqn. (14). Since the energy release rates are crack length *independent*, the crack density is computed by combining Eqn. (14) with Eqn. (16) and numerically integrating. Some predicted changes in crack density with time for a range of stresses are plotted on Fig. 8. In general, interpolation between these curves and the short crack results is needed to establish the overall behavior. An approach for such interpolation has not yet been established. However, it is important to note that, regardless of the initial state, the crack density eventually evolves with time in a manner *independent* of stress. This behavior arises because the strain energy release rates for multiple cracks converge to a single curve at high crack densities (Fig. 7), corresponding to the regime of closely-spaced cracks where Eqn. (14c) operates.

4.3. Comparison with Experiment

The approach used to compare experiment to theory involved two steps. (i) One set of experimental results was fitted to the model, in order to evaluate the unknown constants. (ii) By using the *same constants* the model was used to *predict* the behavior for other testing conditions. Comparisons of the constants inferred in this manner with values expected from corresponding phenomena occurring in monolithic material assess the consistency of the models. This procedure was applied separately to the low and high stress regimes.

The model was used to examine the data shown in Fig. 3(a). In the low stress regime (Type I), Eqn. (28) was fitted to the data at 120 MPa, using a stress corrosion exponent, $n = 50$[18] (Fig. 9). The best fit line corresponds to a value of the shape parameter, $\alpha = 1.5$. The value of α inferred from this comparison corresponds to a Weibull modulus*, $m \approx 3$. Values in this range are reasonable for ceramic matrix composites. Using the same constants, the model was used to *predict* the crack densities at other stress levels (Fig. 9). Evidently, the model predictions are in reasonable agreement with the experimental results for stresses $\sigma \leq 150$ MPa and for crack densities $\rho \lesssim 6$ mm. This model thus appears to provide a satisfactory description of damage evolution at low stresses and low crack densities.

The model predictions for type II behavior at high stresses and high crack densities was assessed by using the *same stress corrosion exponent* ($n = 50$). The curves were fitted to the measured crack density at 250 MPa after 10 s (9.7/mm), and then used to predict the behavior at other stresses and times. These predictions appear to be consistent with the data at stresses $\sigma \geq 180$ MPa at crack densities $\rho > 8$/mm.

5. CONCLUDING REMARKS

Matrix cracks have been shown to develop in a time-dependent manner in a unidirectional Nicalon fiber/CAS matrix composite. The phenomenon has been rationalized by a stress corrosion mechanism operating in the matrix. This process results in crack growth at stresses below that found in short duration monotonic tests. Furthermore, for most stress levels, the crack density ultimately evolves with time in a manner independent of the stress, and reaches values higher than those found in

*The shape parameter, α on flaw size (Eqn. 22) is half that for the tensile strength, via the Griffith relationship.

monotonic tests. Both of these observations have implications for the use of these materials in structural applications. The behavior of the composite contrasts with that of monolithic ceramics for which stress corrosion only occurs at stresses within a few percent of the failure stress. It is anticipated that ceramic matrix composites will be subjected to *localized* stresses well above the matrix cracking stress, in which case it will prove necessary to account for the effect of stress corrosion in the design process.

A fracture mechanics analysis has been used successfully to model the development of multiple matrix cracks with time and applied stress. The model has been developed separately for the regimes dominated by either non-interacting short cracks or interacting steady-state cracks. The approach is consistent with existing models for matrix cracking under monotonic loading conditions. However, a method for interpolating between the two regimes has yet to be developed.

ACKNOWLEDGMENTS

This work was supported by the Defense Advanced Research Projects Agency through the University Research Initiative under ONR contract N-0014-92-J-1808. The authors would like to thank Dr. K. Chyung for supplying the test material.

TABLE I

Properties of Unidirectional CAS/SiC Composite[4,20]

Property	Value
Fiber Radius, R (μm)	7.5
Fiber Volume Fraction, f	0.37*
Matrix Modulus, E_m (GPa)	97*
Fiber Modulus, E_f (GPa)	200
Thermal Expansion Coefficient of Matrix, α_m (K^{-1})	5×10^{-6}
Thermal Expansion Coefficient of Fibers, α_f (K^{-1})	4×10^{-6}
Sliding Stress, τ (MPa)	10 - 30
Residual Stress, q (MPa)	89
Matrix Fracture Energy, Γ_m (J/m^2)	25
Matrix Cracking Stress, $\sigma_o - q\,E/E_m$ (MPa)	130 - 150
Ultimate Tensile Strength, σ_u (MPa)	450
Ultimate Strain, ε_u	1.0%

* K. Chyung, Corning Labs

APPENDIX: An Assessment of the Effect of Flexure

During flexural loading of unidirectional CMCs, matrix cracks develop along the tensile face of the beam, leading to non-linearity in the stress-strain response. As a result, the nominal stress calculated from Euler-Bernoulli beam theory, assuming the material to be linear elastic, overestimates the true stress acting along the tensile face. The following analysis provides an estimate of the effects of such non-linearity on the maximum tensile stress in a flexural beam, both at the onset of loading and after an extended period under load.

The initial stress distribution (upon loading) is calculated assuming that: (i) the *compressive* stress-strain response of the composite is linear, with a modulus given by the rule of mixtures; (ii) the tensile response is that measured in a short-term uniaxial tensile test (Fig. A1), and (iii) the strain distribution across the beam remains linear. The analysis involves two steps. In the first, the sum of the forces acting parallel to the fiber direction is set equal to zero, enforcing static equilibrium. This condition can be expressed as

$$-\int_{\varepsilon_c}^{0} E\varepsilon\, d\varepsilon + \int_{0}^{\varepsilon_T} \sigma_T(\varepsilon)\, d\varepsilon = 0 \qquad \text{(A1)}$$

where $\sigma_T(\varepsilon)$ is the tensile stress-strain relation, and ε_c and ε_T are the maximum compressive and tensile strains, respectively. Solving the first integral in (A1) and re-arranging gives

$$\varepsilon_c = -\left[\frac{2}{E}\int_{0}^{\varepsilon_T} \sigma_T(\varepsilon)\, d\varepsilon\right]^{1/2}. \qquad \text{(A2)}$$

This equation relates ε_c to ε_T. In the second step, the applied bending moment, M, is equated to the moment supported by the beam. This condition can be written as

$$M = \frac{BD^2}{(\varepsilon_T - \varepsilon_c)^2}\left[\int_{\varepsilon_c}^{0} E\varepsilon(\varepsilon - \varepsilon_c)d\varepsilon + \int_{0}^{\varepsilon_T} \sigma_T(\varepsilon)(\varepsilon - \varepsilon_c)d\varepsilon\right] \quad \text{(A3)}$$

where B is the beam depth and D the height. The nominal stress, σ_{nom}, calculated on the assumption of linear elasticity, is related to M through

$$\sigma_{nom} = 6M/BD^2. \quad \text{(A4)}$$

Combining Eqns. (A3) and (A4) leads to the result

$$\sigma_{nom} = \frac{1}{(\varepsilon_T - \varepsilon_c)^2}\left[E\varepsilon_c^3 + 6\int_{0}^{\varepsilon_T} \sigma_T(\varepsilon)(\varepsilon - \varepsilon_c)d\varepsilon\right] \quad \text{(A5)}$$

To proceed further, an expression for $\sigma_T(\varepsilon)$ is required. For this purpose, the measured tensile stress-strain curve is fit by a polynominal of the form

$$\sigma_T(\varepsilon) = a\varepsilon + b\varepsilon^2 + c\varepsilon^3 + d\varepsilon^4 \quad \text{(A6)}$$

where the coefficients a, b, c and d are

$a = 1.4 \times 10^5$ MPa

$b = -1.12 \times 10^7$ MPa

$c = -3.89 \times 10^9$ MPa

$d = 5.51 \times 10^{11}$ MPa

This polynominal provides a good description of the experimental curve over the relevant range of stresses ($0 \leq \sigma_T \leq 300$ MPa), as shown in Fig. A1.

Equations (A2), (A5) and (A6) have been combined to determine the relation between the stress σ_T on the tensile face and the nominal applied stress, σ_{nom}. The results are presented in Fig. A2. Below the first matrix cracking stress (150 MPa), the two quantities are equal, since the composite is linear-elastic in both tension and compression. At higher nominal stresses, the true stress deviates from the nominal value, the difference increasing with increasing σ_{nom}. At the highest stress used in the present study (σ_{nom} = 250 MPa), the difference is ~11%.

Under sustained loading, additional matrix cracks are developed, leading to further stress re-distribution across the beam. A rigorous analysis of this problem is not presently feasible. However, it is instructive to consider a limiting case in which the stresses in the matrix on the tensile side of the beam are reduced to zero, such that the fibers support all the stress. In this case, the tensile response of the composite can be taken to be

$$\sigma_T(\varepsilon) \approx E_T \varepsilon \tag{A7}$$

where E_T is an effective (reduced) tensile modulus. A conservative estimate of E_T is σ_u/ε_u, where σ_u is the ultimate tensile strength and ε_u the corresponding tensile strain. This relation is plotted as the dashed line in Fig. A1. In this case, Eqns. (A2) and (A5) reduce to the simple analytical result

$$\sigma_T / \sigma_{nom} = \left(1 + \sqrt{\sigma_u / E\varepsilon_u}\right)/2. \tag{A8}$$

Using the experimentally measured values σ_u = 450 MPa and ε_u = 1.0% gives $\sigma_T/\sigma_{nom} \approx 0.80$. This result is plotted on Fig. A2. At most, there is a 20% reduction in the stress below the elastic value.

REFERENCES

[1] R.Y. Kim and N. Pagano, "Crack Initiation in Unidirectional Brittle Matrix Composites," *J. Am. Ceram. Soc.*, **74** [5], 1082-90 (1991).

[2] H.C. Cao, E. Bischoff, O. Sbaizero, M. Ruhle, A.G. Evans D.B. Marshall and J.J. Brennan, "Effect of Interfaces on the Properties of Fiber-Reinforced Ceramics" *J. Amer. Ceram., Soc.*, **73** (6), 1691-99 (1990).

[3] A. Pryce and P. Smith, "Modelling the Stress Strain Behaviour of Unidirectional Ceramic Matrix Composite Laminates" submitted to *J. Mater. Sci.*, (1991).

[4] D.S. Beyerle, S.M. Spearing, F.W. Zok and A.G. Evans, "Damage and Degradation of a Ceramic Matrix Composite," *J. Am. Ceram. Soc.*, **75** [10], 2719-25 (1992).

[5] A.G. Evans and D.B. Marshall, "The Mechanical Behavior of Ceramic Matrix Composites," *Acta Metall.*, **37** [10], 2567-83 (1989).

[6] D.M. Harmon and C.R. Saff "Damage Initiation and Growth in Fiber Reinforced Metal Matrix Composites" Metal Matrix Composites: Testing, Analysis and Failure Modes, ASTM STP 1032, W. S. Johnson, Editor, ASTM, Philadelphia, (1989).

[7] G. Rosenkranz, V. Gerold, K. Kromp, D. Stockel, L. Tillmann "Fatigue Behavior of Metallic Fibre-Reinforced Materials: A Study of Steel Fiber-Reinforced Silver, Part 2 Failure Mechanisms and High Cycle Fatigue Life" *J. Mat. Sci.*, **17**, 277-289 (1982).

[8] S.M. Jeng, C.J. Yang, J-M. Yang, D.G. Rosenthal and J. Goebel, "Mechanical Behavior and Failure Mechanisms of SCS6-Ti_3Al Composites" Mat. Res. Soc. Symp. Proc. **194**, 277-84 (1990).

[9] J. Aveston, G.A. Cooper and A. Kelly, "Single and Multiple Fracture in the Properties of Fiber Composites," *The Properties of Fiber Composites, IPC*, (1971).

[10] D.B. Marshall, B.N. Cox and A.G. Evans, "The Mechanics of Matrix Cracking in Brittle Matrix Fiber Composites," *Acta Metall.*, **33** [11], 2013-21 (1985).

[11] B. Budiansky, J.W. Hutchinson and A.G. Evans, "Matrix Fracture in Fiber-Reinforced Ceramics," *J. Mech. Phys. Solids*, **34** [2], 164-189 (1986).

[12] F.W. Zok and S.M. Spearing, "Matrix Crack Spacing in Brittle Matrix Composites," *Acta Metall. Mater.*, **40** [8], 2033-2043 (1992).

[13] R.M. McMeeking and A.G. Evans, "Matrix Fatigue Cracking in Fiber Reinforced Metal Matrix Composites," *Mech. Mater.*, **9**, 217 (1990).

[14] L.M. Butkus, L.P. Zawada and G.A. Hartman, "Fatigue Testing of Ceramic Matrix Composites at Room and Elevated Temperatures Matrix Composites," *J. Cyclic Deformation, Fracture and Nondestructive Evaluation of Advanced Materials, ASTM STP XXXX* (1990).

[15] T.J. Kotil, J.W. Holmes and M. Cominou, "Origin of Hysteresis Observed During Fatigue of Ceramic-Matrix Composites," *J. Am. Ceram. Soc.*, **73** [7], 1879-83 (1990).

[16] K.M. Prewo, "Fatigue and Stress rupture of Silicon Carbide Fibre-Reinforced Glass-Ceramics," *J. Mater. Sci.*, **22**, 2695-2701 (1987).

[17] K. Chyung, U.S. Patent 4,615,987 (7 Oct., 1986).

[18] B. Pletka and S.M. Wiederhorn, "Subcritical Crack Growth in Glass Ceramics," *Fracture Mechanics of Ceramics* (Ed. R.C. Bradt *et al.*) Plenum, NY, 745-59 (1983).

[19] S. Suresh, "Fatigue of Materials", *Cambridge Solid State Science Series*, Cambridge Univ. Press (1991).

[20] T.J. Mackin and F.W. Zok, *J. Amer. Ceram. Soc.*, **75**, (1993).

FIGURE CAPTIONS

Fig. 1 An optical micrograph showing matrix cracks in the CAS/SiC composite following a short duration, monotonic tensile test. The arrow labeled "A" indicates an example of a crack that had bifurcated and arrested. Arrow "B" indicates a crack that arrested as it approached another crack on nearly the same plane.

Fig. 2 (a) Micrograph of matrix cracks upon initial loading of a flexure specimen to 175 MPa. (b) Micrograph of the same region after 3 days at the same level of stress. Note the additional growth of matrix cracks in (b) (indicated by arrows).

Fig. 3 Schematic diagram showing the type of cracks observed either at high stress or long time, and the expected variation in energy release rate as the cracks interact.

Fig. 4 Evolution of crack density with time under static load: (a) flexure tests, (b) uniaxial tension tests. For comparison, the results of (b) have been superimposed onto (a) using dashed lines.

Fig. 5 Trends in crack tip energy release rate with crack length (adapted from [13]).

Fig. 6 Variation in energy release rate for single, isolated crack with crack length.

Fig. 7 Effects of crack spacing and stress on the steady state energy release rate.

Fig. 8 Predicted trends in crack density evolution, assuming existing long (steady-state) cracks based on Eqn. (9).

Fig. 9 Comparison of damage evolution predictions with experimental measurements. In the low stress regime, the model was fit to the data for $\sigma = 120$ MPa; in the high stress regime, it was fit to the datum for $\sigma = 250$ MPa at $t = 10$s.

Fig. A1 Tensile stress-strain response of the CAS/SiC composite.

Fig. A2 Variation in the stress, σ_T, acting along the tensile face of a flexure specimen with the nominal stress, σ_{nom}.

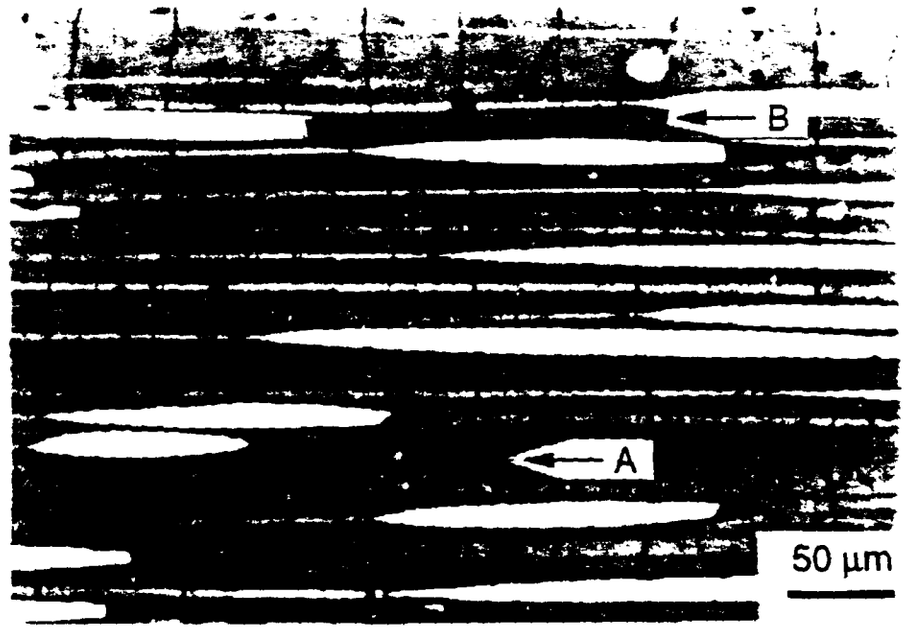

Fig. 1

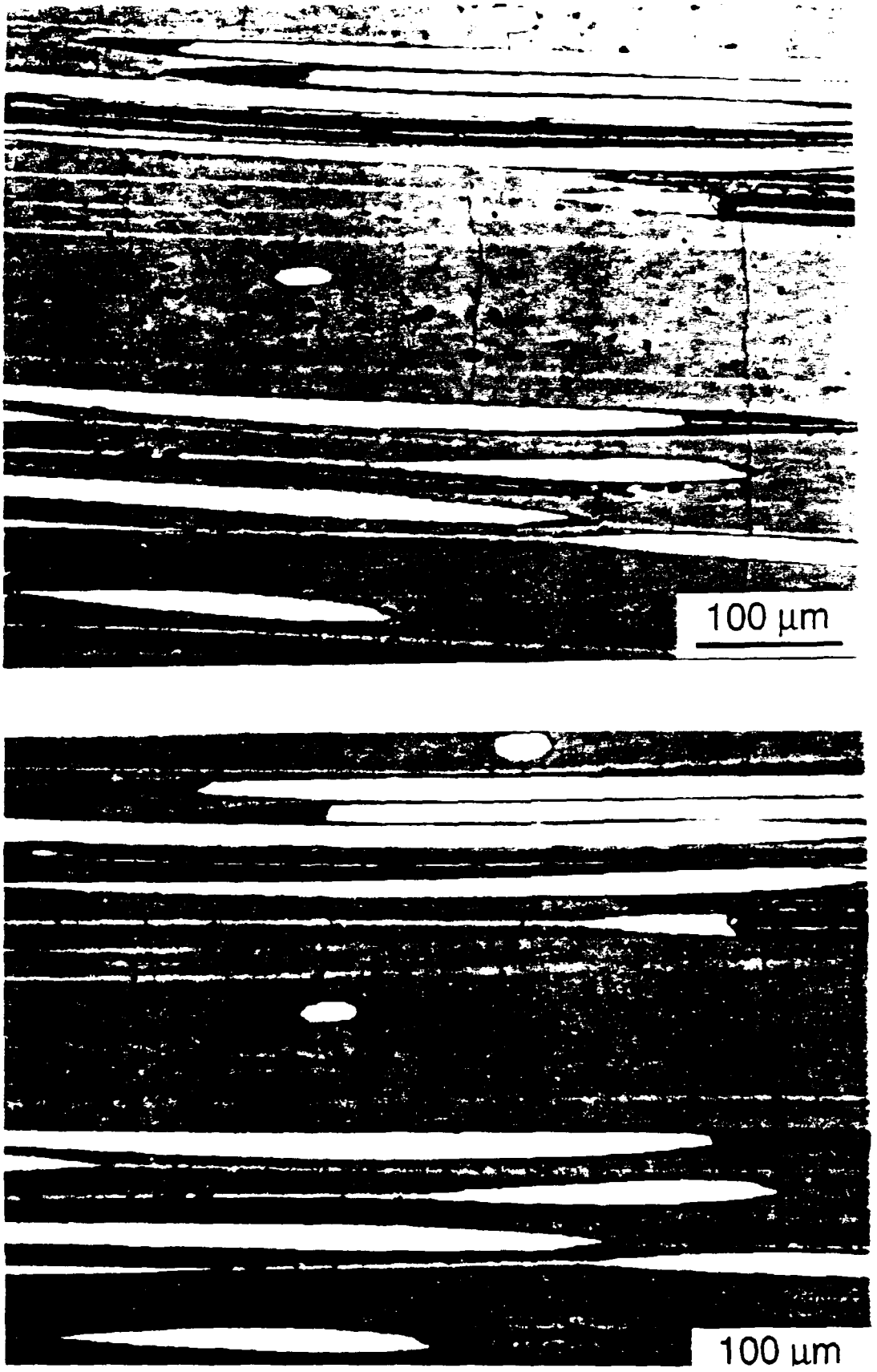

Fig. 2

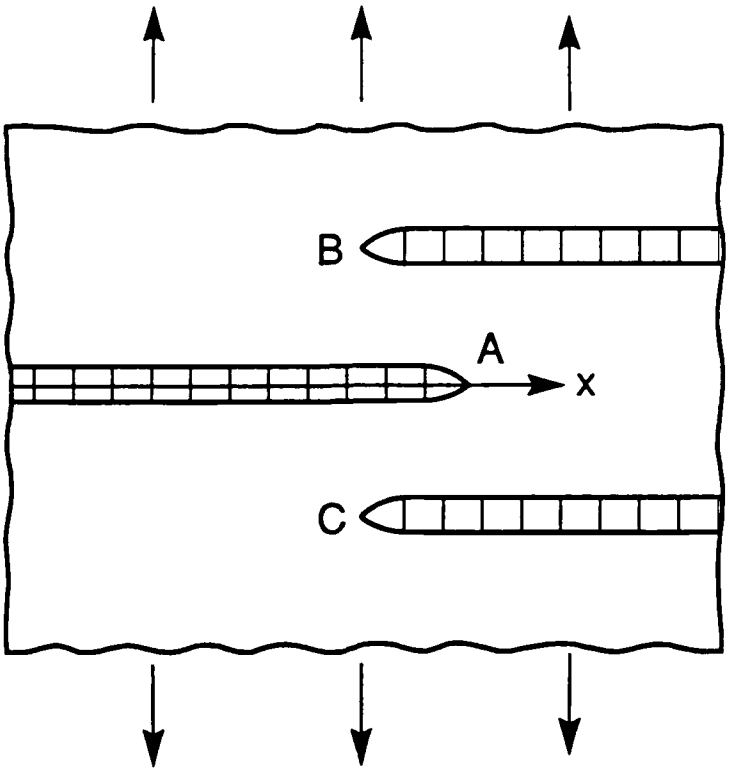
B
A
x
C

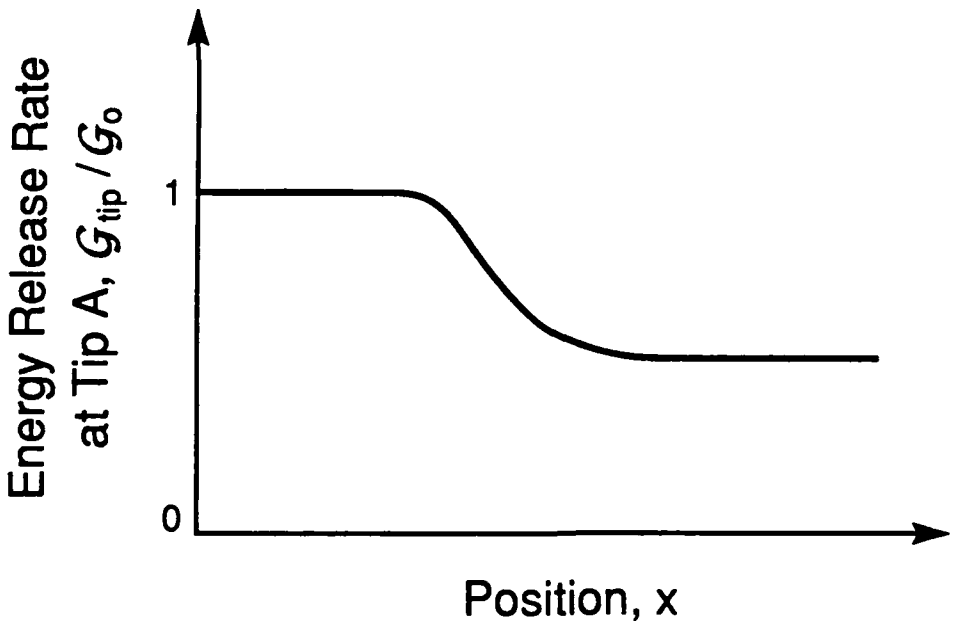
Energy Release Rate
at Tip A, $\mathcal{G}_{tip} / \mathcal{G}_o$
1
0
Position, x

Fig. 3

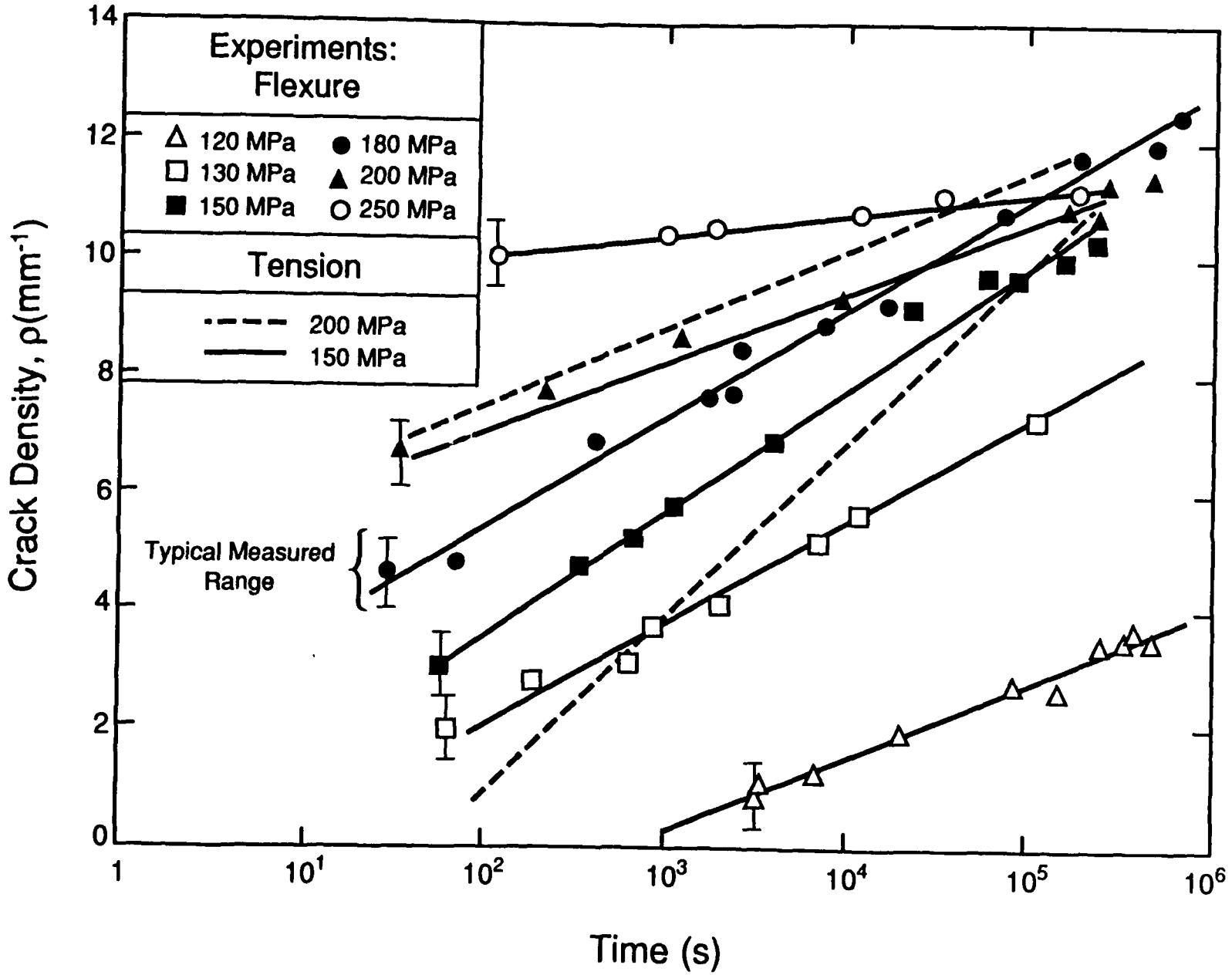
Experiments:
Flexure
120 MPa
130 MPa
150 MPa
180 MPa
200 MPa
250 MPa
Tension
200 MPa
150 MPa
Typical Measured Range
Crack Density, ρ(mm⁻¹)
Time (s)
0
2
4
6
8
10
12
14
1
10¹
10²
10³
10⁴
10⁵
10⁶

Fig. 4(a)

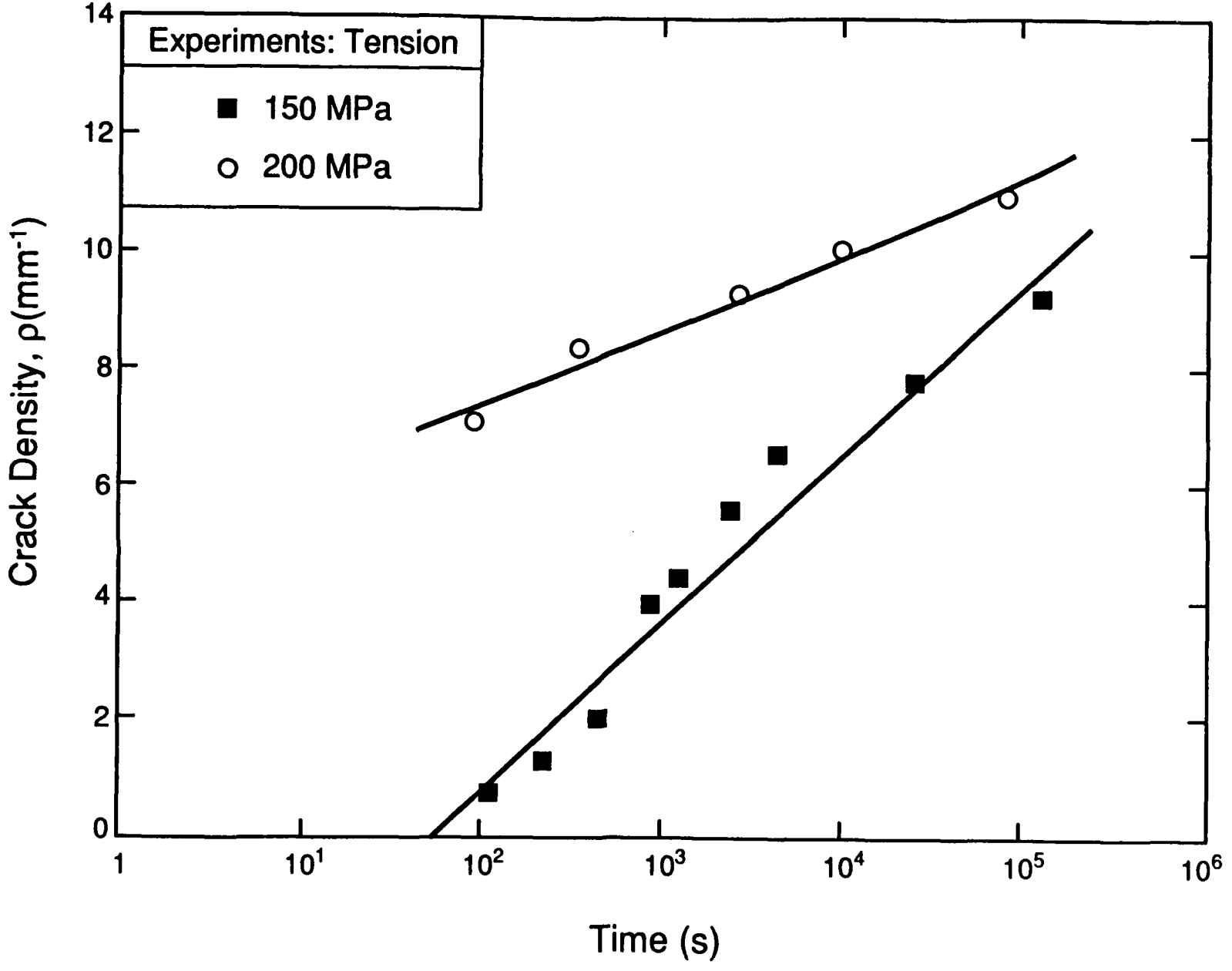
Experiments: Tension
150 MPa
200 MPa
Crack Density, ρ(mm⁻¹)
Time (s)
0
2
4
6
8
10
12
14
1
10¹
10²
10³
10⁴
10⁵
10⁶

Fig. 4(b)

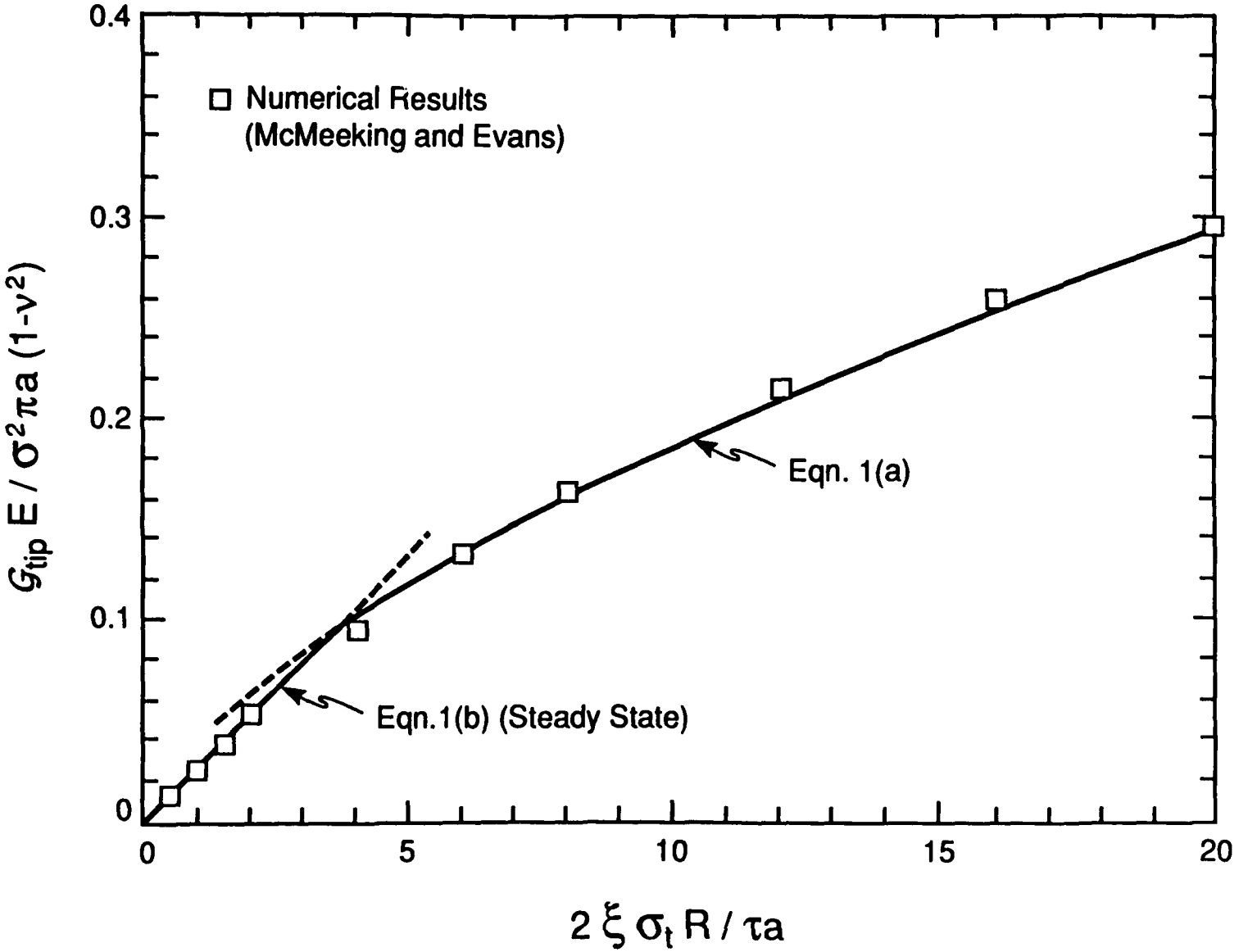
0.4
0.3
0.2
0.1
0
0
5
10
15
20
Numerical Results
(McMeeking and Evans)
Eqn. 1(a)
Eqn.1(b) (Steady State)
$\mathcal{G}_{tip} E / \sigma^2 \pi a (1-\nu^2)$
$2 \xi \sigma_t R / \tau a$

Fig. 5

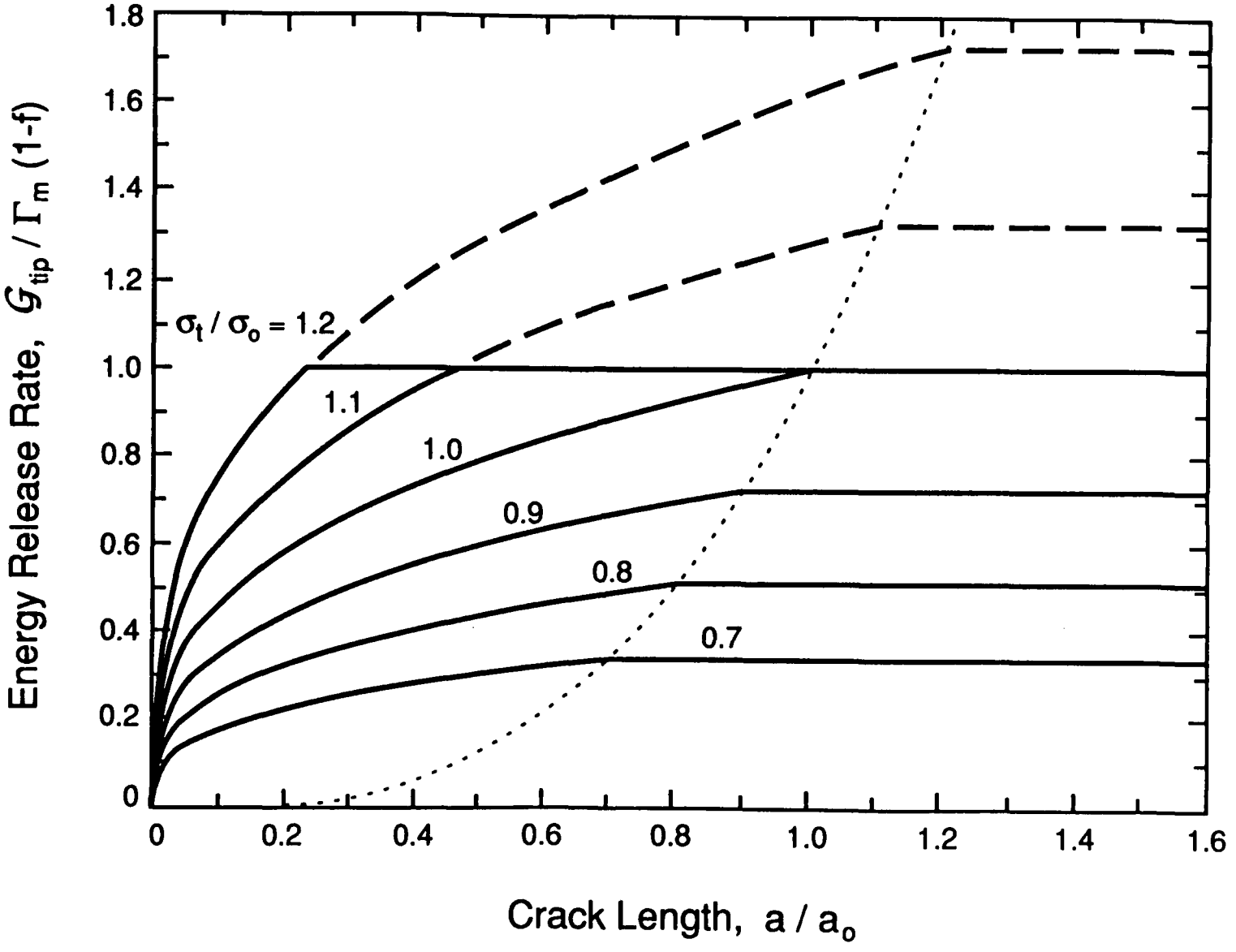
Energy Release Rate, $G_{tip} / \Gamma_m (1-f)$
Crack Length, a / a_o
$\sigma_t / \sigma_o = 1.2$
1.1
1.0
0.9
0.8
0.7
0
0.2
0.4
0.6
0.8
1.0
1.2
1.4
1.6
1.8

Fig. 6

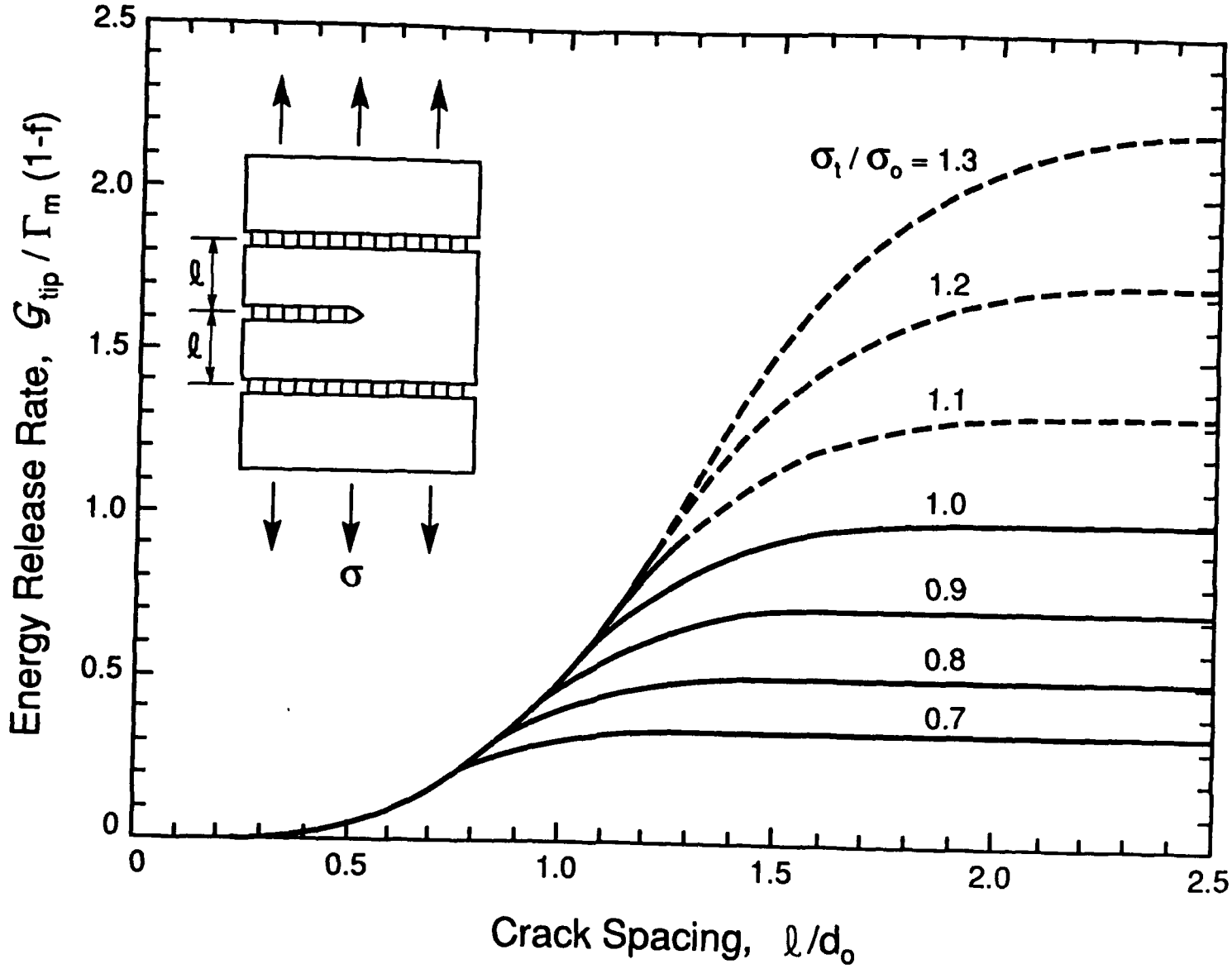
Energy Release Rate, $\mathcal{G}_{tip} / \Gamma_m (1-f)$
Crack Spacing, ℓ / d_o
$\sigma_t / \sigma_o = 1.3$
1.2
1.1
1.0
0.9
0.8
0.7
ℓ
ℓ
σ
0
0.5
1.0
1.5
2.0
2.5

Fig. 7

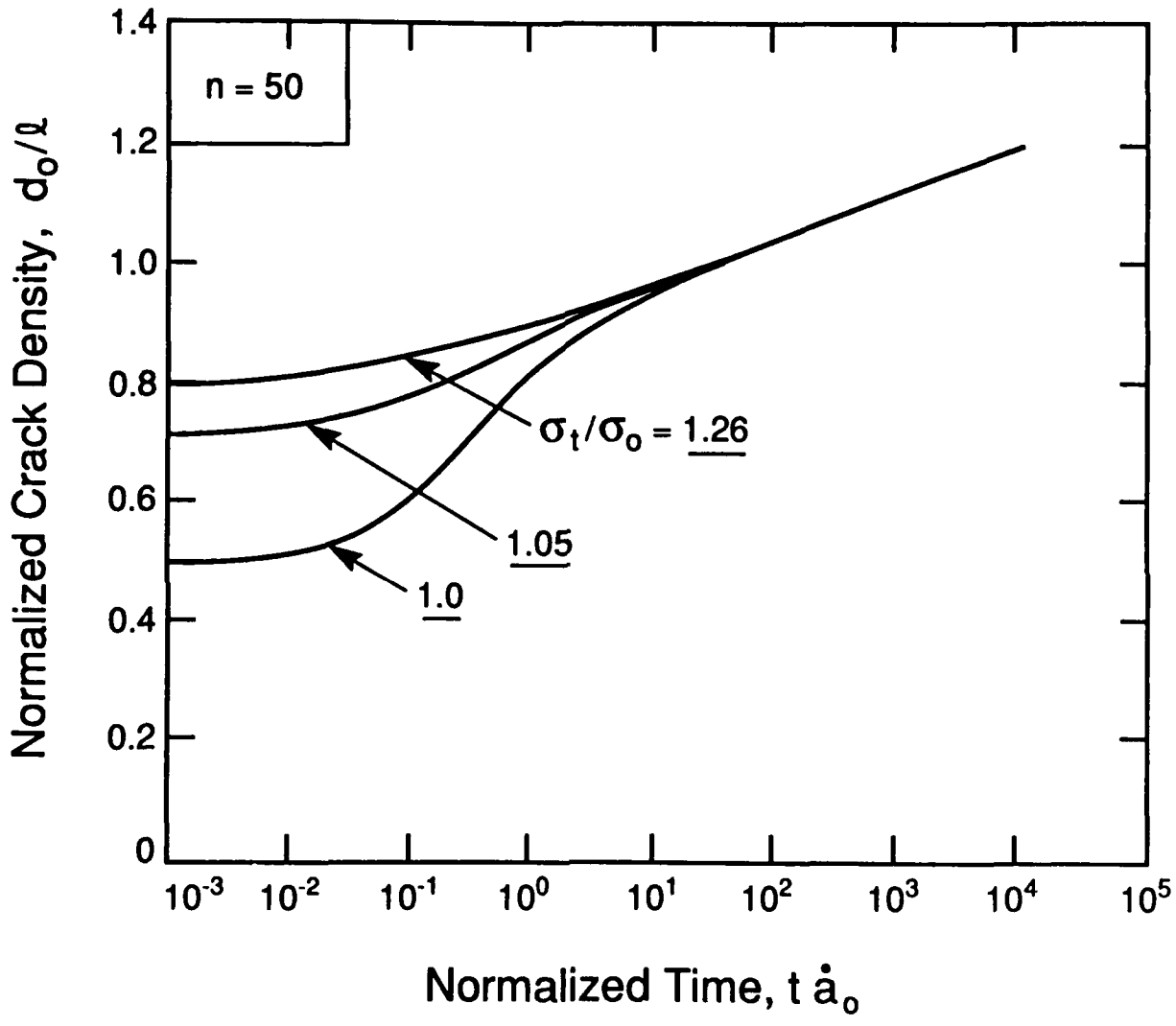
n = 50
σ_t/σ_o = 1.26
1.05
1.0
Normalized Crack Density, d_o/ℓ
Normalized Time, $t\,\dot{a}_o$
1.4
1.2
1.0
0.8
0.6
0.4
0.2
0
10^{-3} 10^{-2} 10^{-1} 10^{0} 10^{1} 10^{2} 10^{3} 10^{4} 10^{5}

Fig. 8

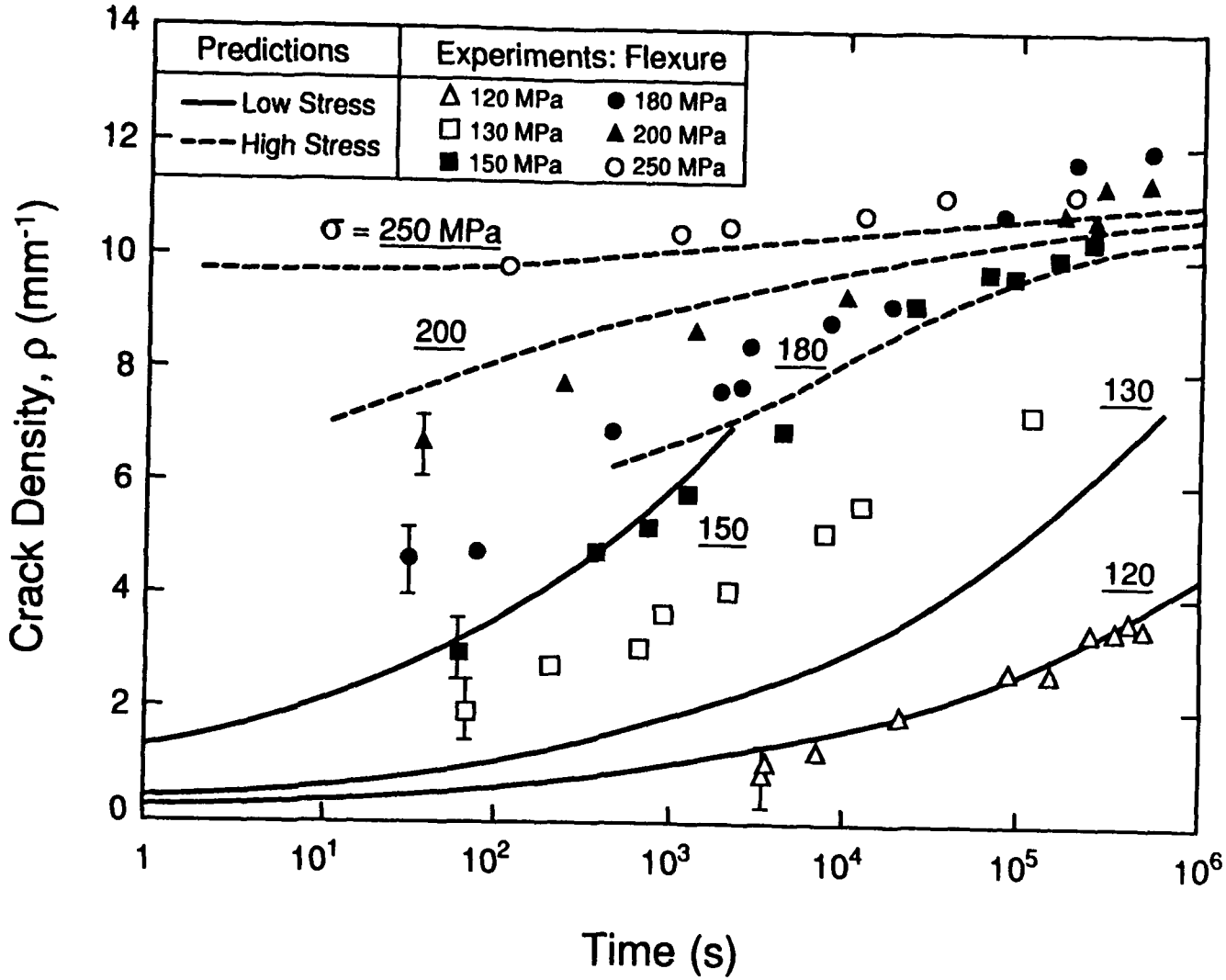
Predictions
Low Stress
High Stress
Experiments: Flexure
120 MPa
130 MPa
150 MPa
180 MPa
200 MPa
250 MPa
σ = 250 MPa
200
180
130
150
120
Crack Density, ρ (mm⁻¹)
Time (s)
0
2
4
6
8
10
12
14
1
10¹
10²
10³
10⁴
10⁵
10⁶

Fig. 9

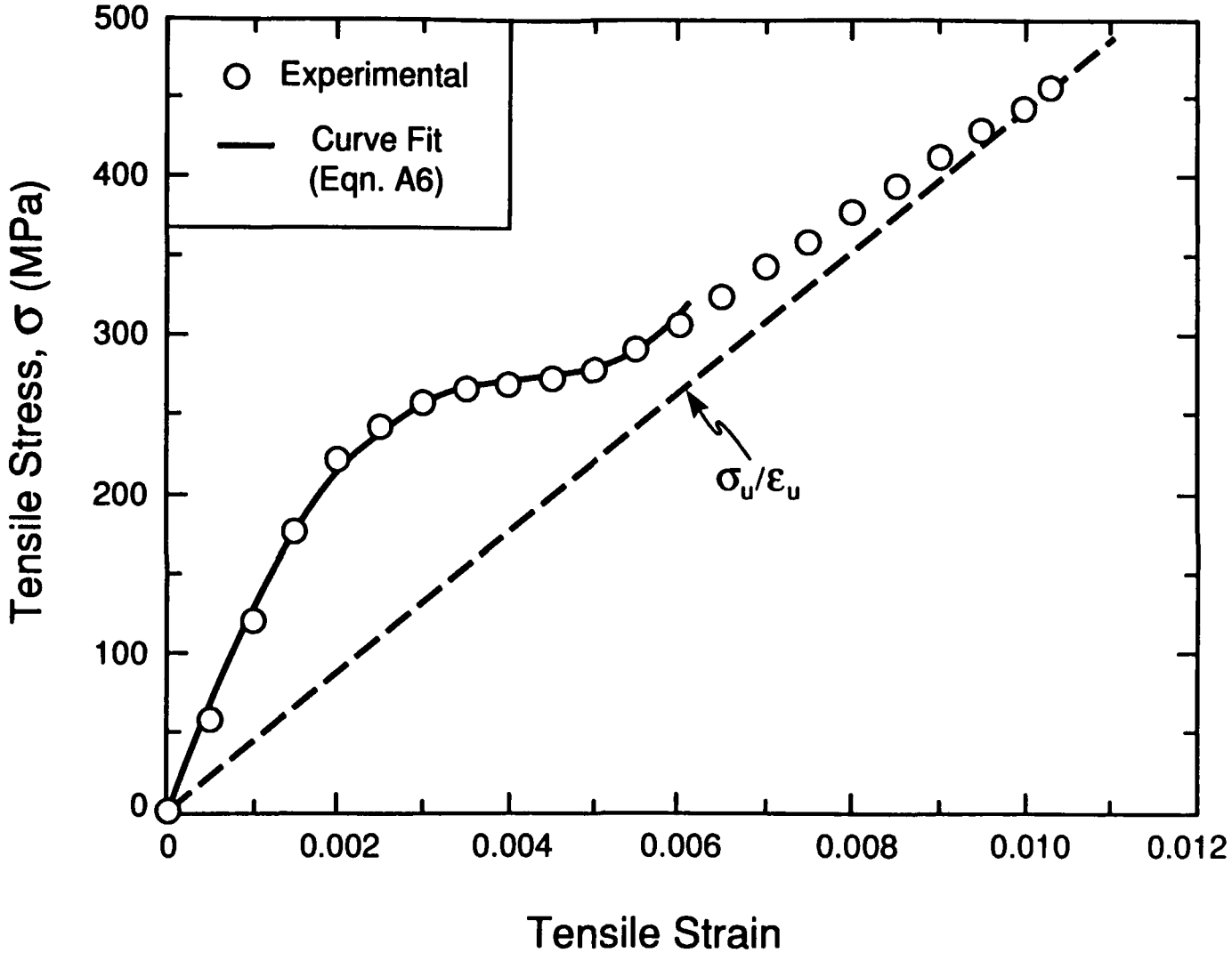

Fig. A1

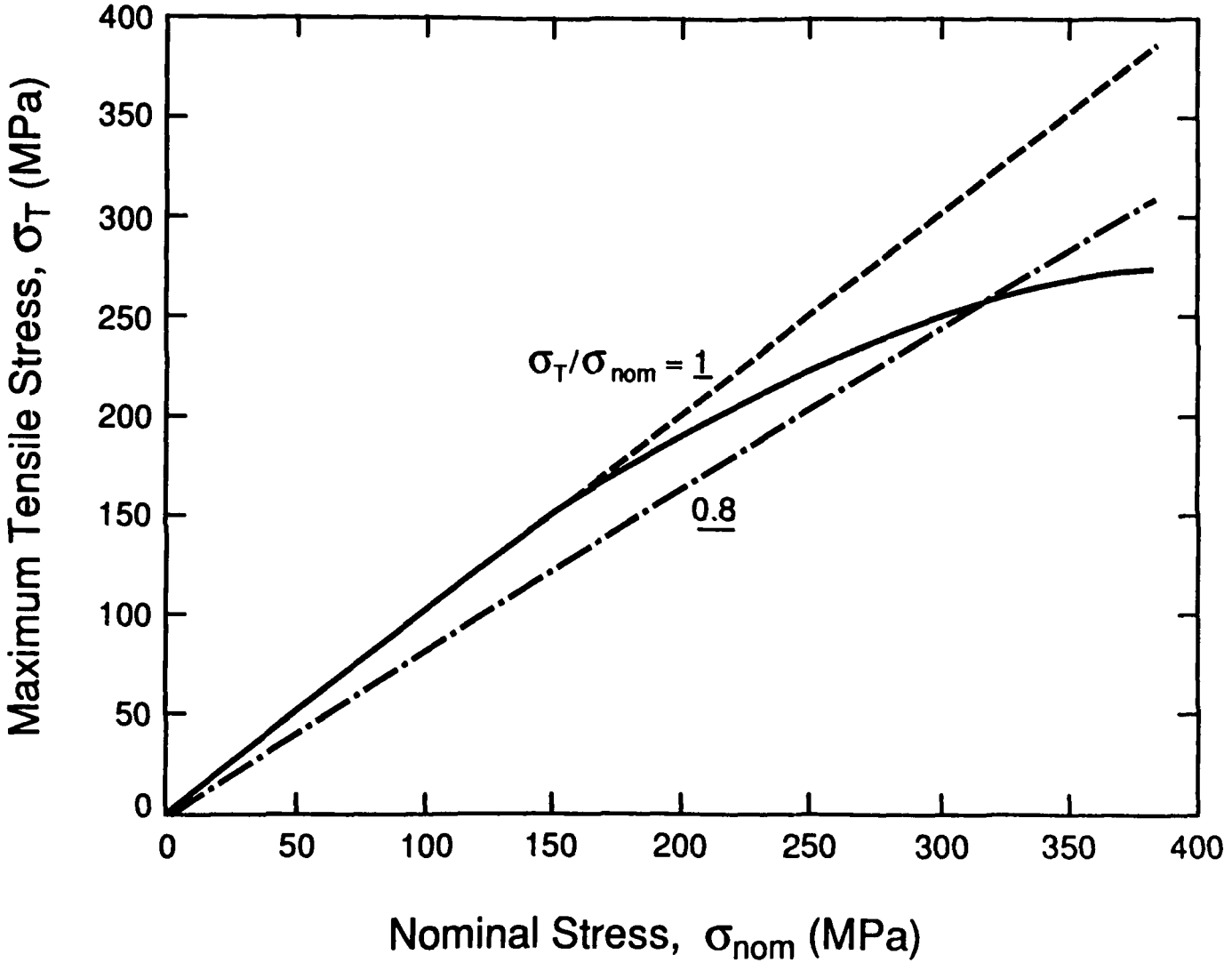
Maximum Tensile Stress, σ_T (MPa)
400
350
300
250
200
150
100
50
0
0
50
100
150
200
250
300
350
400
Nominal Stress, σ_{nom} (MPa)
$\sigma_T/\sigma_{nom} = 1$
0.8

Fig. A2

MATERIALS

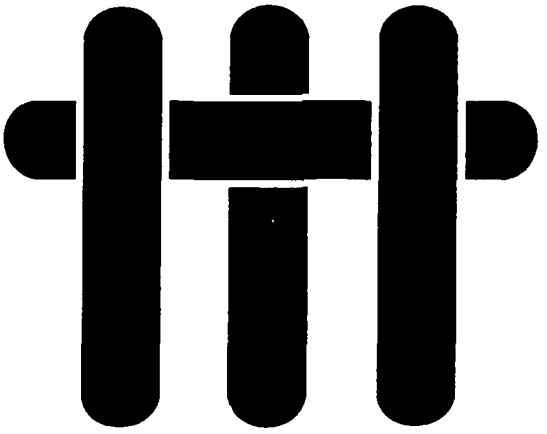

EFFECTS OF GAUGE LENGTH ON THE TENSILE STRENGTH OF SiC FIBERS

F.W. Zok, X. Chen and C.H. Weber

Materials Department
University of California
Santa Barbara, California 93106

Submitted to the Journal of the American Ceramic Society

December, 1993

71:MS36(December 2, 1993)1:59 PM/mef

ABSTRACT

An experimental investigation has been conducted on the effects of gauge length on the tensile strength of SiC fibers. Varying the fiber gauge length provides access to a broader range of strengths than that which is sampled with a single gauge length. The results show that the overall strength distribution cannot be described solely in terms of the two parameter Weibull function. It is demonstrated that such trends would not have been evident by only considering the strength distribution for a fixed fiber gauge length, a consequence of the relatively narrow range of strengths accessed by a single gauge length. The overall distribution is found to be consistent with two independent Weibull distributions: one of them being characteristic of the pristine fibers, and the other characteristic of the additional flaws introduced into the fiber during processing of the composite.

INTRODUCTION

The axial fracture, creep and fatigue properties of fiber-reinforced metal and ceramic matrix composites are dominated by the strength characteristics of the fibers. Several examples are noteworthy. (i) The ultimate tensile strength measured under *monotonic* loading is governed by the *in-situ* fiber bundle strength. Provided both the interface fracture energy and sliding resistance are sufficiently small (allowing global load sharing conditions to prevail[1]), the bundle strength can be described using weakest link statistics[2-5]. In this case, the relevant gauge length in the statistical description of the fiber failure probability depends on the sliding resistance of the fiber-matrix interface, coupled with the intrinsic fiber strength characteristics themselves[2-4]. Typically, these lengths are on the order of a few millimeters. (ii) Under *cyclic* loading, matrix cracks can initiate and propagate around the fibers, creating bridged cracks[6-8]. The life of the composite is then dominated by the number of loading cycles required to initiate fiber failure in the crack wake: a process which is also dictated by the fiber strength characteristics and the interfacial sliding resistance. (iii) Under *static* loading conditions at elevated temperatures (sufficient to cause matrix creep but below the fiber bundle strength), the axial strain asymptotically approaches a level that depends on the fraction of broken fibers[9,10]. Once again, the fiber strength characteristics appear as a dominant feature. Consequently, knowledge of the fiber strength characteristics is critical in understanding and predicting the performance of these composites.

The focus of the present study is on the strength characteristics of SiC fibers, extracted from a metal matrix composite. The study augments concurrent work on the creep, fatigue and fracture properties of the composite[10-12]. One of the main features of this study involves the effects of gauge length on the fiber strength distribution. Such effects are important in using experimental data obtained from a *fixed* gauge length (typically on the order of a few centimeters) in predicting the mechanical response of

the composite, particularly when the relevant gauge length in the composite is smaller than that used to characterize the fibers[13]. It is also demonstrated that conducting tests over a range of gauge lengths provides access to a broader range of strengths, yielding a more thorough description of the strength distribution. One of the key results emanating from this work is that the strength distribution of the SiC fibers cannot be described in terms of the two-parameter Weibull function, despite the fact that the data sets obtained from fixed gauge lengths appear to be consistent with this function. The implications of such effects in the use and interpretation of fiber tests are briefly discussed.

2. THEORETICAL BACKGROUND

The strength distribution of brittle ceramic fibers can be described using weakest link statistics. A convenient empirical description of this distribution is the Weibull functions,

$$P_f = 1 - \exp \frac{-L}{L_o}\left(\frac{\sigma}{\sigma_o}\right)^m \qquad (1)$$

where P_f is the cumulative failure probability up to a stress, σ; L is the length of the fiber; L_o is a reference length, taken to be 1m; σ_o is the reference strength; and m is the Weibull modulus. The radius, R, of all fibers is assumed to be the same. Physically, σ_o represents the stress at a failure probability of $P_f = 1 - e^{-1} \approx 0.632$ in a fiber of length, $L = L_o$. The Weibull modulus, m, is a measure of the dispersion in strengths: the coefficient of variation in the fiber strength scales roughly as 1/m. For convenience, Eqn. 1 can be re-written as

$$\ell n\ \ell n\,(1/P_s) = m\ \ell n\ \sigma + (\ell n\ L/L_o + m\,\ell n\,\sigma_o) \tag{2}$$

where P_s is the survival probability,

$$P_s = 1 - P_f \tag{3}$$

The parameters characterizing the strength distribution (σ_o and m) are usually obtained experimentally by conducting a series of N tensile tests on individual fibers with a fixed gauge length, L. The strength data are then sorted in ascending order and the failure probability corresponding to each strength obtained using the mean rank estimators[5]

$$P_f = \frac{i}{N+1} \tag{4}$$

where i is the ranking of the data. The parameters in Eqn. 1 are obtained by plotting $\ell n\ \ell n\,(1/P_s)$ vs. $\ell n\ \sigma$. In these coordinates, the slope of the data is equivalent to m; the intercept is given by the term in parentheses on the right side of Eqn. 2, from which σ_o is then obtained.

It should be recognized that, within such a series of tests, only a limited range of strengths from within the entire strength distribution is accessed. The range depends on the number of tests performed along with the fiber gauge length, and can be estimated in the following way[14]. On average, the *lowest* strength σ_L obtained in a series of N tests corresponds to a failure probability (following Eqn. 4) of ~ 1/N. Combining this result with Eqn. 1 gives

$$\frac{\sigma_L}{\sigma_o} \approx \left(\frac{-\ell n\left(1 - 1/N\right)}{L/L_o} \right)^{1/m} \tag{5}$$

Assuming that N is large compared with unity, the ℓn term can be well-approximated by the first two terms in a Taylor series expansion, whereupon Eqn. 5 becomes

$$\frac{\sigma_L}{\sigma_o} \approx \left(\frac{1}{NL/L_o} \right)^{1/m} \tag{6}$$

Following similar arguments, it can be shown that the *maximum* strength σ_u measured in the same series of tests corresponds to a failure probability of ~ 1/(1 + 1/N). Combining this result with Eqn. 1 yields the approximate relation

$$\frac{\sigma_u}{\sigma_o} \approx \left(\frac{\ell n\, N}{L/L_o} \right)^{1/m} \tag{7}$$

Trends in the upper and lower strengths with fiber gauge length for m = 3 and 9 are shown in Fig. 1. Here, the number of tests, N, is taken to be 20. It is evident from this figure that the range of strengths that is accessed can be changed dramatically by changing the fiber gauge length. In the present case (N = 20), changing the gauge length by an order of magnitude leads to a substantially different range of strengths.

The range of strengths accessible through a fixed gauge length can also be represented on a failure probability plot, as shown in Fig. 2. Here the ellipses represent the range of strengths that would be measured from 20 tests conducted at each of three different gauge lengths, each length differing from the next by an order of magnitude. As noted earlier, each of the three gauge lengths give access to different parts of the distribution, with some overlap between them.

An important conclusion to be drawn from the preceding analysis is that the range of strengths obtained from tests on a *fixed* fiber gauge length represents only a limited portion of the entire distribution. Consequently, the Weibull parameters determined from such tests are strictly valid only over the range of measured strengths. Evaluating failure probabilities outside this range requires extrapolation of the test results and implicitly assumes that the form of the strength distribution remains the same over the entire range of strengths.

Based on this insight, an experimental program to evaluate the strength characteristics of SiC fibers was developed. A central feature of the program was an assessment of the effects of fiber gauge length on the strength distribution. Comparisons have also been made with the results for pristine fibers (prior to composite consolidation).

3. EXPERIMENTS

The motivation for the experimental part of this program stems from concurrent studies on the tensile strength[11] and creep response[10,12] of fiber reinforced Ti matrix composites. In those studies, models that describe composite behavior in terms of various constituent properties are being developed and assessed. For this purpose, knowledge of the *in-situ* fiber strength characteristics is essential.

The composite system of interest is a Ti-6Al-4V alloy matrix reinforced unidirectionally with continuous SiC* fibers. Prior to composite consolidation, the fibers had a dual coating, consisting of an inner C layer, ~ 0.5 μm thick, and an outer TiB_2 layer, ~ 1 μm thick (Fig. 3(a)). During consolidation, the TiB_2 reacts with the Ti alloy to form a layer of TiB needles, ~ 0.7 μm thick. The fibers were extracted from the composite by dissolving the matrix in concentrated HF acid. Typically, the dissolution

* Sigma fibers, produced by British Petroleum.

was completed within ~ 45 to 60 mins. Extreme care was taken in handling the extracted fibers, such that no new flaws were introduced. Some of the extracted fibers were examined in a scanning electron microscope. Over much of the fiber surface, the C/TiB_2 coating was found to have completely spalled off (Fig. 3). Spalling is presumed to be a result of the residual stresses present in the coating coupled with the relaxation of these stresses following matrix dissolution. The effects of the HF acid on the fiber strength distribution were examined by allowing some of the fibers to soak in the acid following dissolution for a period of 60 hours. The diameter of the fibers was extremely uniform, with an average value, d = 100 μm.

Tensile tests were conducted on individual fibers using a dedicated fiber testing machine*. The fiber ends were attached to cardboard tabs (designed specifically for use with the fiber testing machine) using an epoxy adhesive. To ensure good alignment, the fiber ends were placed into straight shallow grooves that had been stamped along the center line of the tabs. The fibers were loaded using a computer-controlled linear stepper motor, and the load monitored using a 100 N load cell.

Four fiber gauge lengths were used: 5, 12.7, 25.4 and 265 mm. For each gauge length, 50 tests were performed. The parameters, σ_o and m, characterizing the Weibull distribution were evaluated using three different methods. In the first, the strength data for each gauge length were sorted and the failure probability evaluated using the mean rank estimator, given by Eqn. 4. The values of σ_o and m were then evaluated from a least-squares linear regression analysis of the data in the form $\ell n\ \ell n\ 1/P_s$ vs. $\ell n\ \sigma$. The second method was similar, except that the failure probability was estimated using[15],

$$P_f = (i - 0.5)/N \tag{8}$$

* Micropull Science.

Monte Carlo simulations of fiber fracture indicate that this estimator provides more accurate values of σ_o and m when the number of tests is relatively small[15]. The third method did not rely on estimating failure probabilities. Instead, the average strength, $\bar{\sigma}$, and standard deviation, s, for each data set were evaluated and related to σ_o and m through[5]

$$\mu = \frac{s}{\bar{\sigma}} = \frac{\left[\Gamma\left(1+\frac{2}{m}\right) - \Gamma^2\left(1+\frac{1}{m}\right)\right]^{1/2}}{\Gamma\left(1+\frac{1}{m}\right)} \tag{9}$$

and

$$\sigma_o = \frac{\bar{\sigma}(L/L_o)^{1/m}}{\Gamma\left(1+\frac{1}{m}\right)} \tag{10}$$

where μ is the variance and Γ is the gamma function. For convenience, Eqn. (9) is approximated by a power law of the form

$$\mu = m^{-0.913} \tag{11}$$

as shown in Fig. 4.

4. EXPERIMENTAL RESULTS

The strength distributions obtained from each of the four gauge lengths are shown in Fig. 5. In this case, the failure probabilities were evaluated using the mean rank estimator (Eqn. 4). For comparison, the results for pristine fibers with a 25 mm gauge length are also shown. The latter results were derived from > 1000 fiber tests

conducted by the fiber manufacturer. As expected, the strength decreases with increased gauge length. This trend is manifested as shifts in the failure probability curves. It should also be noted that the strength of the extracted fibers is substantially lower than that of the pristine fibers for the same gauge length, indicating that additional flaws are introduced into the fibers during processing of the composite.

The effects of the HF acid on the strength distribution for a 25 mm gauge length is shown in Fig. 5(b). Evidently, there is no significant change in the fiber strength following the additional ~ 59 h soak in HF. This result is consistent with fractographic examinations of the fibers which show that fracture generally originates from the tungsten core, not from the fiber surface[11].

The values of σ_o and m determined from each data set are shown in Fig. 6. The three methods used to determine m and σ_o yielded essentially the same results. Evidently, both of these parameters depend sensitively on the fiber gauge length: decreasing as length increases. The dependencies of σ_o and m on gauge length suggest that the measured distributions are *not* consistent with the two parameter Weibull function. In contrast, the high correlation coefficients obtained from the linear regression analyses for each data set (~ 0.96 to > 0.99) suggest that the individual data sets *are* consistent with a Weibull distribution.

To elucidate the origin of these seemingly contradictory conclusions, the data sets were combined in such a way that direct comparisons could be made between the results from various gauge lengths. For this purpose, it is useful to rewrite Eqn. 2 as

$$\ell n\, \ell n\, (1/P_s) - \ell n\, (L/L_o) = m\, \ell n\, \sigma - m\, \ell n\, \sigma_o \qquad (12)$$

The form of this equation suggests that the data corresponding to different gauge lengths should collapse onto a single curve when the results are plotted as $\ell n\, \ell n\, (1/P_s) - \ell n\, (L/L_o)$ vs. $\ell n\, \sigma$. Figure 7 shows such a plot. In this form, the data *do*

collapse onto a single curve, indicating that they are indeed derived from the same overall strength distribution. However, the overall distribution does *not* appear to be linear and thus cannot be described in terms of the two parameter Weibull distribution. Evidently, the observation that the data are consistent with the Weibull function for a *fixed* gauge length is a result of the limited range of strengths accessed by that gauge length. The variations in m and σ_0 with gauge length are manifestations of the various strength regimes accessed by the different gauge lengths, each giving values of m and σ_0 that represent a linear approximation to the distribution over a limited strength range.

One of the key conclusions derived from this work is that the two parameter Weibull function *cannot* be used to describe the strength distribution of the SiC fibers, though it may be consistent with a limited data set obtained using a fixed fiber gauge length. Consequently, evaluating failure probabilities by extrapolating the test results from a fixed gauge length to other parts of the distribution may lead to considerable errors in predicting fiber bundle properties. This effect would be particularly pronounced in calculating the fiber bundle strength within a composite, wherein the relevant gauge length may be considerably smaller than the gauge length typically used to characterize the fiber strength distribution. Conducting tests with varying gauge lengths provides access to a broader strength range and allows a more complete description of the strength distribution to be made.

5. ANALYSIS

The strength distribution in Fig. 7 can be rationalized in terms of a modified form of the Weibull function. For this purpose, it is assumed that there are two populations of flaws, each characterized by values of m and σ_0. The total survival probability at a

prescribed stress σ and gauge length L is then the product of the survival probabilities from each of the two distributions. This result can be expressed as

$$P_s = 1 - P_f = \left[\exp \frac{-L}{L_o}\left(\frac{\sigma}{\sigma_1}\right)^{m_1}\right]\left[\exp \frac{-L}{L_o}\left(\frac{\sigma}{\sigma_2}\right)^{m_2}\right] \tag{13}$$

where m_i and σ_i characterize the two distributions. Equation 10 can be simplified and re-written as

$$P_s = \exp \frac{-L}{L_o}\left(\left(\frac{\sigma}{\sigma_1}\right)^{m_1} + \left(\frac{\sigma}{\sigma_2}\right)^{m_2}\right) \tag{14}$$

Figure 8 shows an illustrative example of the prediction of Equation 11 for Weibull moduli of $m_1 = 3$ and $m_2 = 9$, along with the *individual* distributions, characterized by $m = 3$ and $m = 9$. For simplicity, it is assumed that $\sigma_1 = \sigma_2 = \sigma_o$. The figure demonstrates that, for low values of strength, the failure probability associated with the distribution with the higher Weibull modulus ($m_2 = 9$) is negligible compared with that of the lower value ($m_1 = 3$). Consequently, the strength distribution in this regime is linear, with a slope, $m = 3$. In contrast, for high values of strength, the failure probability is dominated by the distribution with the higher value of m, and thus the distribution is linear, with a slope, $m = 9$.

The utility of this approach in describing the strength distribution of the SiC fibers was assessed in the following way. In the high strength regime, the Weibull modulus and reference strength were taken to be equal to the values characteristic of the pristine fibers ($m = 18$ and $\sigma_o = 3.2$ GPa). The Weibull modulus and reference strength for the other flaw population were evaluated from the data at the low end of

the distribution* (m_2 = 4 and σ_2 = 1.4 GPa). The two distributions were combined using Eqn. 14 to produce the overall strength distribution, shown in Fig. 9. Also shown for comparison are the distributions corresponding to σ_2 = 1.2 and 1.6 GPa. The agreement between the calculated and experimentally measured curves suggests that the overall distribution is consistent with the two Weibull distributions, characterized by σ_1 = 3.2 GPa, m_1 = 18, σ_2 = 1.4 GPa and m_2 = 4.

As an additional comparison with the experimental data, the *apparent* Weibull modulus and reference strength corresponding to the modified Weibull function have also been calculated for a range of fiber gauge lengths. These parameters were evaluated by taking a "secant modulus" between the maximum strength, σ_u, evaluated at $P_f = N/(N+1)$, and the minimum strength, σ_L, evaluated at $P_f = 1/(N+1)$. In essence, this calculation gives estimates of the values of m and σ_0 that would be obtained from a series of experiments that probe only a limited portion of the entire strength distribution. Trends in the calculated apparent Weibull modulus and reference strength with gauge length are shown in Figs. 6(a) and (b), respectively. The calculated values appear to be broadly consistent with the experimental results.

6. CONCLUDING REMARKS

The present results indicate that the strength distribution of the SiC fibers extracted from the composite cannot be described solely in terms of the two parameter Weibull function. These conclusions would not have been reached by considering only the results for a fixed fiber gauge length, despite the relatively large number of tests performed at each gauge length. Performing tests over a range of gauge lengths provides access to a broader range of strengths and a more complete description of the overall distribution. In the present case, the distribution can be rationalized in terms of

* Excluding the 3 lowest strength values.

two Weibull distributions, one being characteristic of the flaws in the pristine fibers, and the other characteristic of new flaws introduced during processing of the composite*.

The results have implications concerning the development of testing procedures for characterizing fiber strength distributions. It is clear that results obtained from a single fiber gauge length may not be adequate for predicting fiber bundle properties when the selected gauge length is substantially different from the length governing fiber bundle behavior. This problem is exacerbated by the general observation that failure probability plots, in the coordinates of $\ell n\ \ell n\ 1/P_s$ vs. $\ell n\ \sigma$, usually appear nearly linear when the strength range is relatively small. This observation may lead to the erroneous conclusion that the data are consistent with a two parameter Weibull distribution and can thus be extrapolated to other parts of the distribution, as needed to evaluate fiber bundle behavior. Non-linearity in failure probability plots (indicating a breakdown in the two parameter Weibull distribution) only become evident when the strength range is sufficiently large, as obtained from tests on varying fiber gauge lengths.

Conducting tests over a range of gauge lengths may also prove to be an effective means of evaluating the strength parameters, even when the distribution is consistent with the two parameter Weibull function. It has been recognized that a substantial number of tests are usually required to accurately evaluate m and σ_0 from a single gauge length[15,16]. Conducting tests at two or more gauge lengths may be a more effective and accurate means of evaluating these parameters. The utility of this approach is presently being investigated[17].

---

* Conceivably, other variations on the two parameter Weibull function could be used to rationalize this strength distribution (see Ref. 13 for an alternate approach).

ACKNOWLEDGMENTS

This work was supported by the Defense Advanced Research Projects Agency through the University Research Initiative under ONR contract N-0014-92-J-1808. The authors gratefully acknowledge the assistance of J.R. Porter in the initial work on fiber testing.

REFERENCES

1. M.Y. He, A.G. Evans and W.A. Curtin, "The Ultimate Tensile Strength of Metal and Ceramic Matrix Composites," *Acta Metall. Mater.*, **41**, (1993), 871-78.

2. W.A. Curtin, "Theory of the Mechanical Properties of Ceramic-Matrix Composites," *J. Am. Ceram. Soc.*, **74**, (1991), 2837-45.

3. W.A. Curtin, "Exact Theory of Fiber Fragmentation in a Single Filament Composite," *J. Mater. Sci.*, **26**, (1991), 5239-53.

4. J. Neumeister, "A Constitution Law for Continuous Fiber Reinforced Brittle Matrix Composites with Fiber Fragmentation and Stress Recovery," *J. Mech. Phys. Solids*, **41**, (1993), 1383-1404.

5. G.J. DeSalvo, Theory and Structural Design Applications of Weibull Statistics, Chaps. 2-3, General Westinghouse, Pittsburgh, PA (1970).

6. D.P. Walls, G. Bao and F.W. Zok, "Mode I Fatigue Cracking in a Fiber Reinforced Metal Matrix Composite," *Acta Metall. Mater.*, **41** (1993) 2061-2071.

7. B.N. Cox and D.B. Marshall, *Fatigue Fracture Eng. Mater. Struct.*, **14** (1991), 847.

8. M.D. Sensmeier and P.K. Wright "The Effects of Fiber Bridging on Fatigue Crack Growth in Titanium Matrix Composites," in Fundamental Relationships Between Microstructure and Mechanical Properties of Metal Matrix Composites, P.K. Liaw and M.N. Gungor (Eds.), TMS, 1990, pp. 441-457.

9. McLean, M., "Creep Deformation of Metal-Matrix Composites," *Composites Sci. Tech.*, **23**, (1985), 37-52.

10. Z.Z. Du and R.M. McMeeking, to be published.

11. C.H. Weber, X. Chen, S.J. Connell and F.W. Zok, to be published.

12. C.H. Weber, Z.Z. Du, S.J. Connell and F.W. Zok, to be published.

13. K.K. Phani, "Strength Distribution and Gauge Length Extrapolation in Glass Fiber," *J. Mater. Sci.*, **23**, (1988), 1189-94.

14. R.F. Cook and D.R. Clarke, "Fracture Stability, R-Curves and Strength Variability," *Acta Metall. Mater.*, **36** (1988), 555-62.

15. J.R. Porter, "Statistical Analysis of the Properties of Advanced Fiber Designed for Titanium Alloy and Intermetallic Reinforcement," *Mat. Res. Symp. Proc.*, **273** (1992), 315-24.

16. C.A. Johnson and W.T. Tucker, "Weibull Estimates for Pooled Fracture Data" in Prediction Methodologies and Data for Ceramic Materials, ASTM STP 1201, C.R. Brinkman and S.F. Duffy (Eds.), ASTM, Philadelphia, PA (1993).

17. J.R. Porter and F.W. Zok, unpublished work.

FIGURES

Fig. 1 Effects of gauge length on the upper and lower strengths obtained from a series of 20 tensile tests.

Fig. 2 The strength distribution for fibers with a Weibull modulus of m = 3, showing the range of strengths that would be expected for various fiber gauge lengths.

Fig. 3 SEM micrographs showing (a) the C/TiB_2 coating in the composite, and (b) spalling of the coating following matrix dissolution.

Fig. 4 Relationships between the variance and the Weibull modulus for a two parameter Weibull distribution. The sold line represents the approximation of Eqn. 11.

Fig. 5 (a) Strength distributions obtained from fibers of different gauge lengths (dissolution time was ~ 1 h) (b) Effects of dissolution time on the fiber strength distribution (25 mm gauge length).

Fig. 6 Effects of fiber gauge length on (a) the Weibull modulus, m, and (b) the reference strength, σ_o.

Fig. 7 The strength distributions from Fig. 5(a), re-plotted using a parameter that combines the failure probability with the fiber gauge length (see Eqn. 12).

Fig. 8 An illustration of the predicted strength distribution obtained from two independent distributions, each characterized by the Weibull function.

Fig. 9 Comparisons between the experimental and predicted strength distributions.

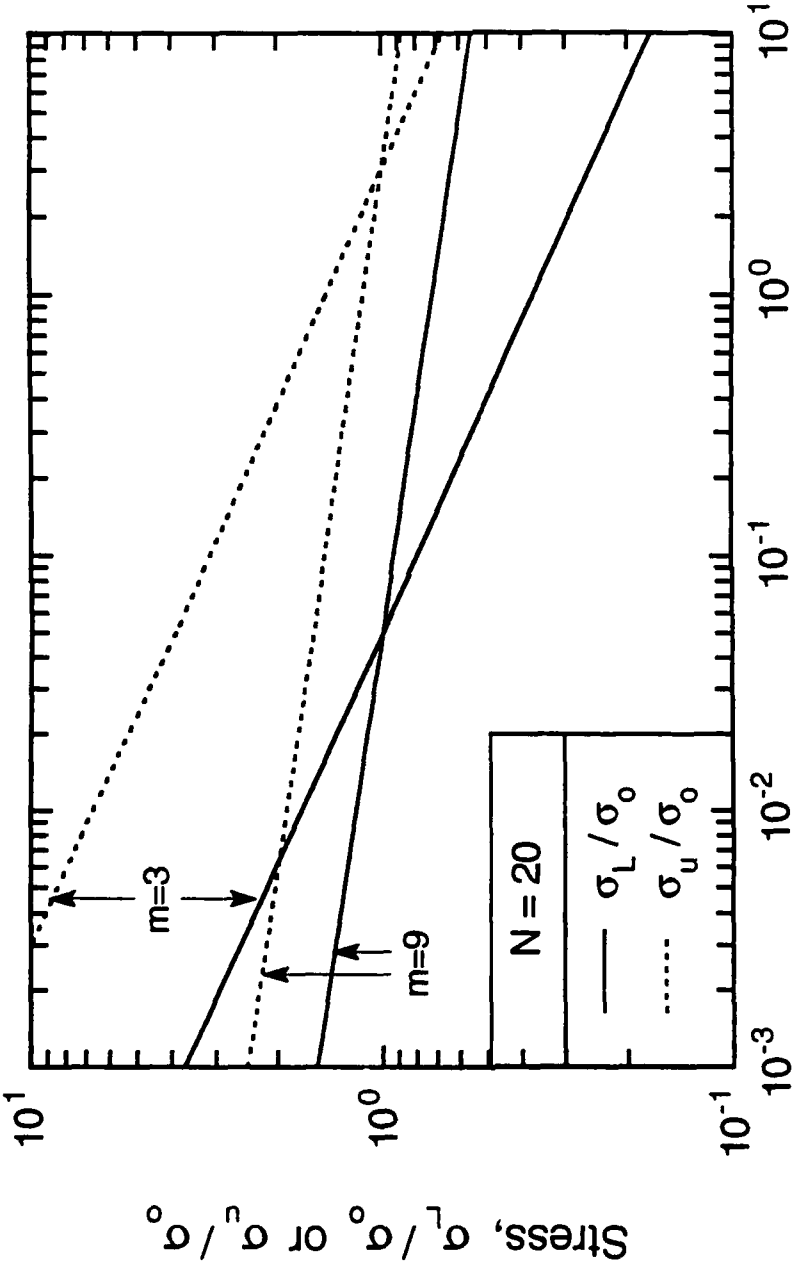
Stress, σ_L/σ_o or σ_u/σ_o
Gauge Length, L/L_o
10^{-1}
10^{0}
10^{-3}
10^{-2}
10^{-1}
10^{0}
10^{1}
m=3
m=9
N = 20
σ_L/σ_o
σ_u/σ_o

Figure 1

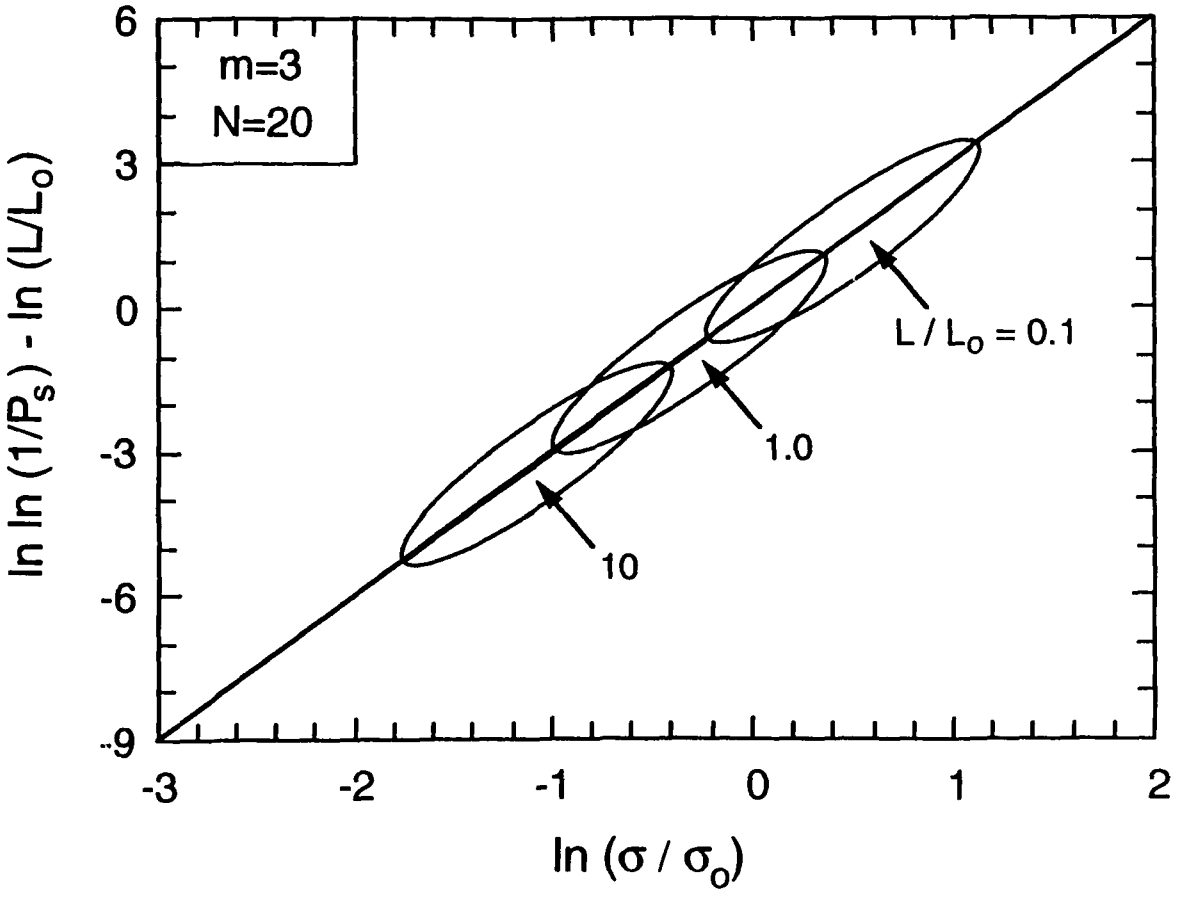

Figure 2

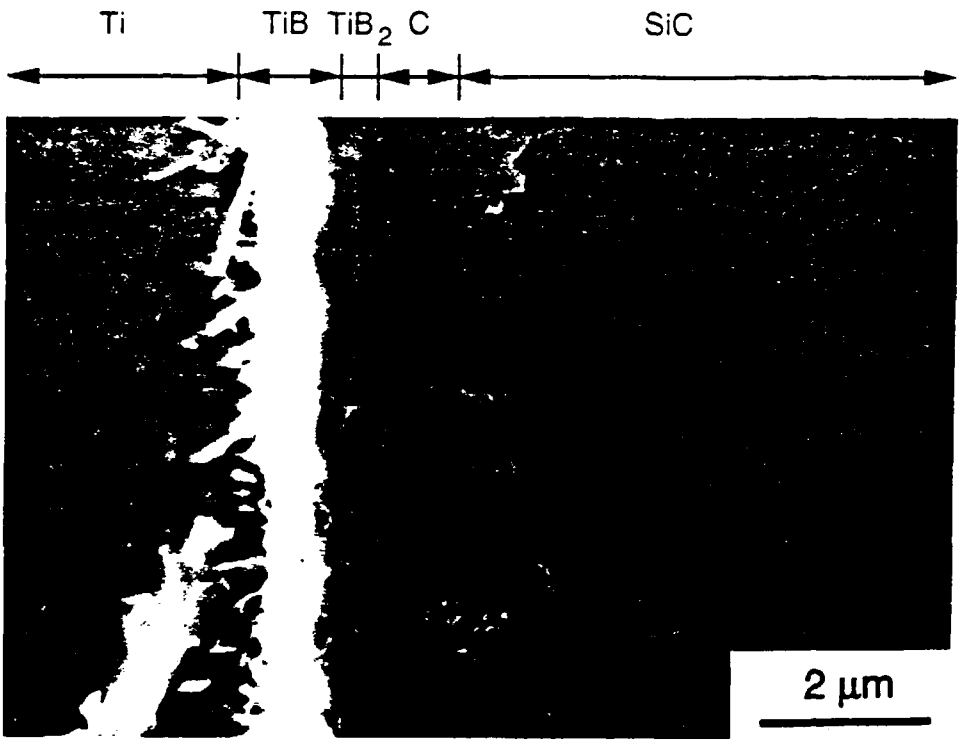

Figure 3(a)

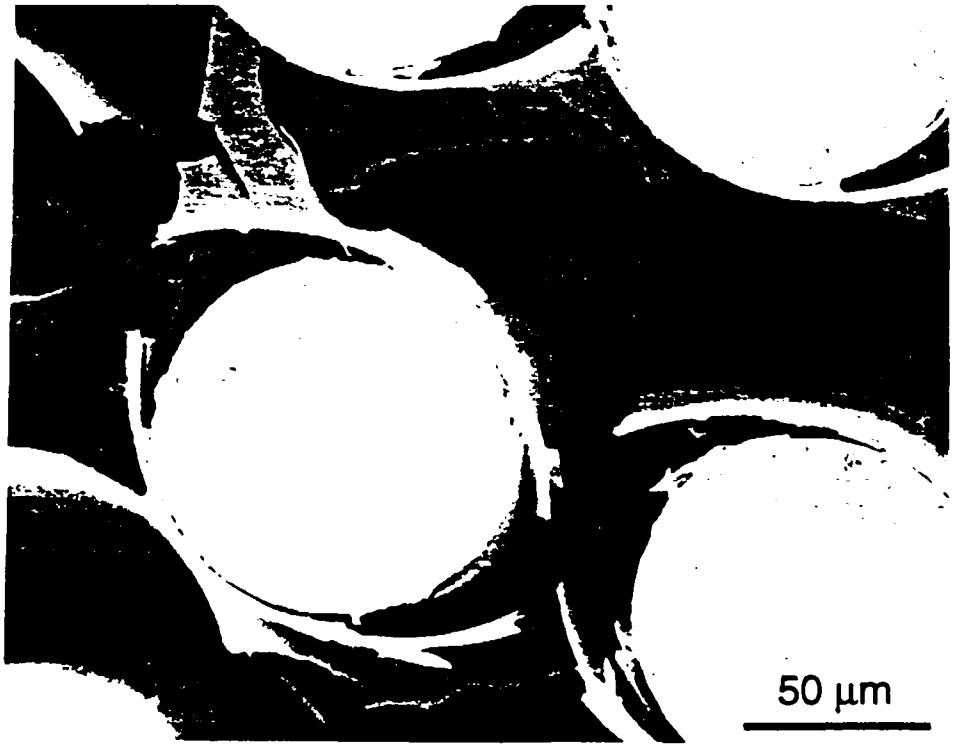

Figure 3(b)

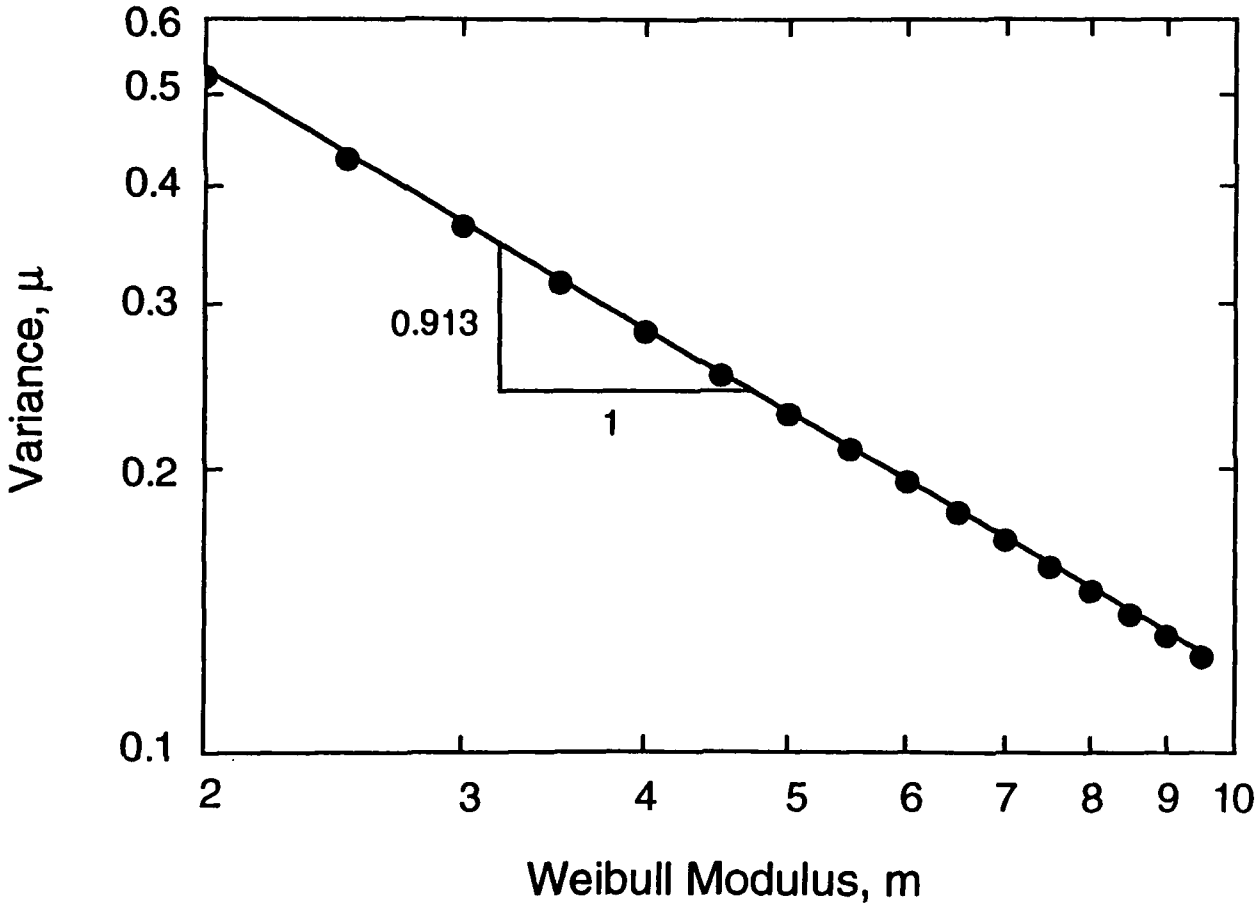
0.6
0.5
0.4
0.3
0.2
0.1
Variance, μ
0.913
1
2
3
4
5
6
7
8
9
10
Weibull Modulus, m

Figure 4

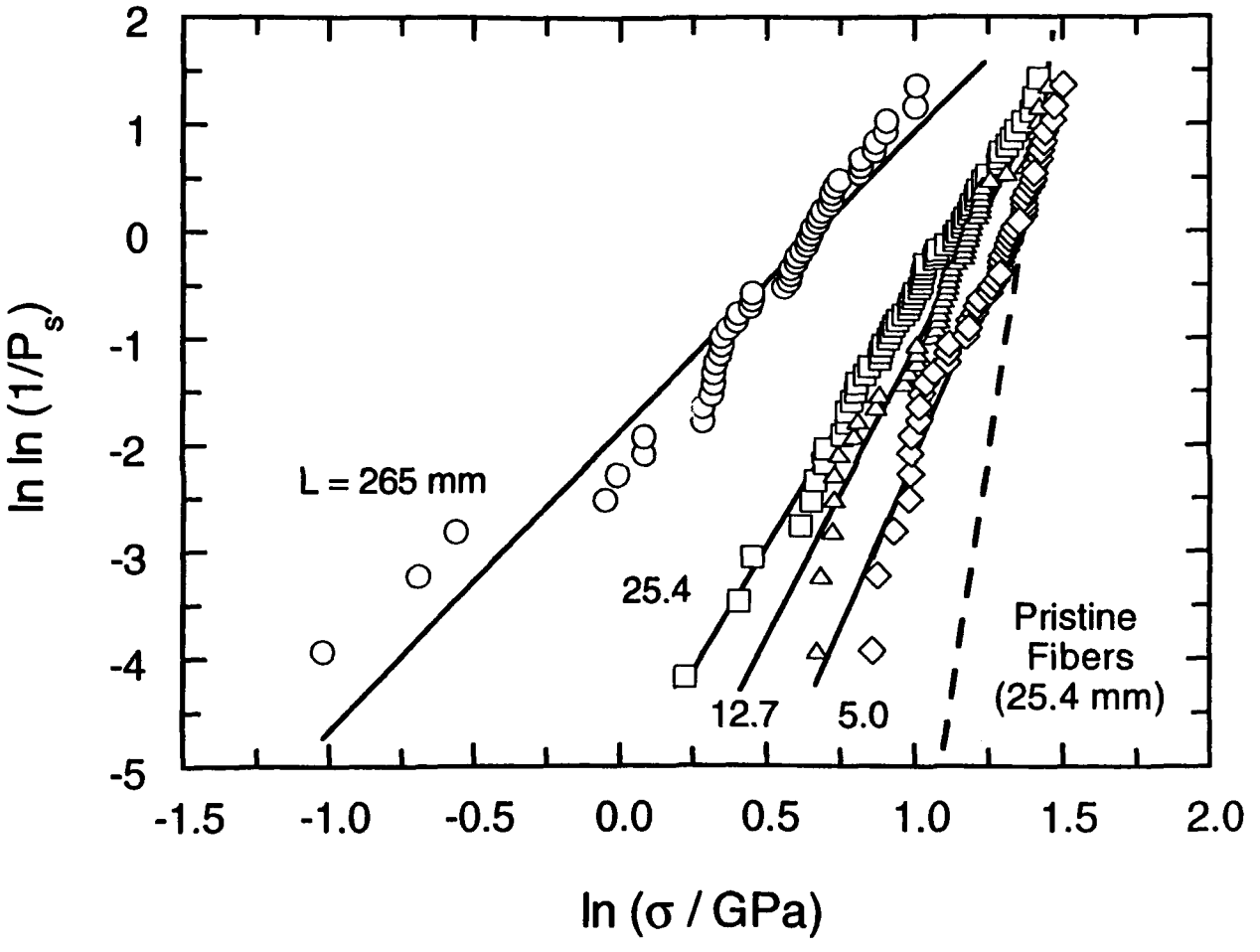
2
1
0
-1
-2
-3
-4
-5
-1.5
-1.0
-0.5
0.0
0.5
1.0
1.5
2.0
ln ln (1/P_s)
ln (σ / GPa)
L = 265 mm
25.4
12.7
5.0
Pristine
Fibers
(25.4 mm)

Figure 5(a)

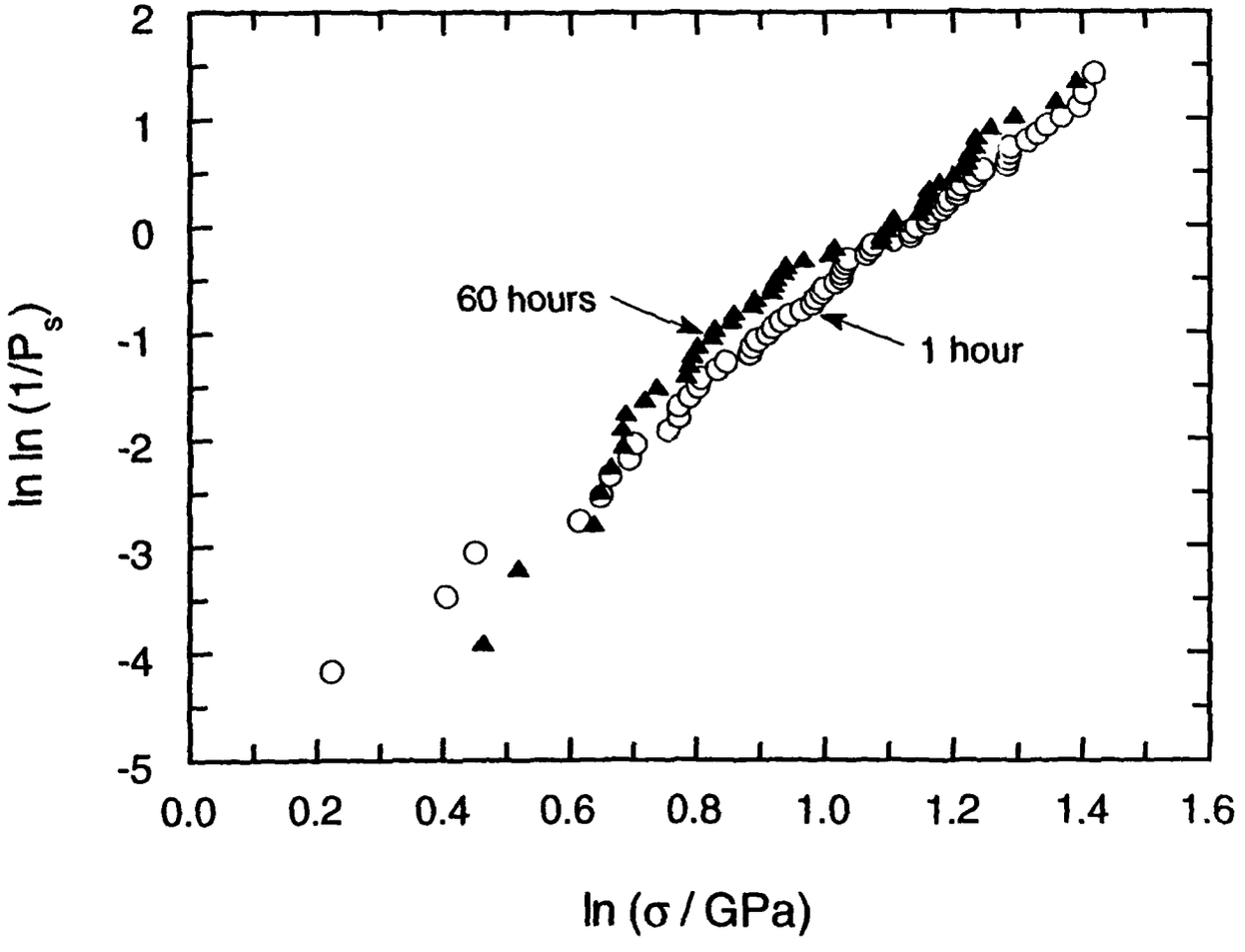
2
1
0
-1
-2
-3
-4
-5
0.0
0.2
0.4
0.6
0.8
1.0
1.2
1.4
1.6
ln ln (1/P_s)
ln (σ / GPa)
60 hours
1 hour

Figure 5(b)

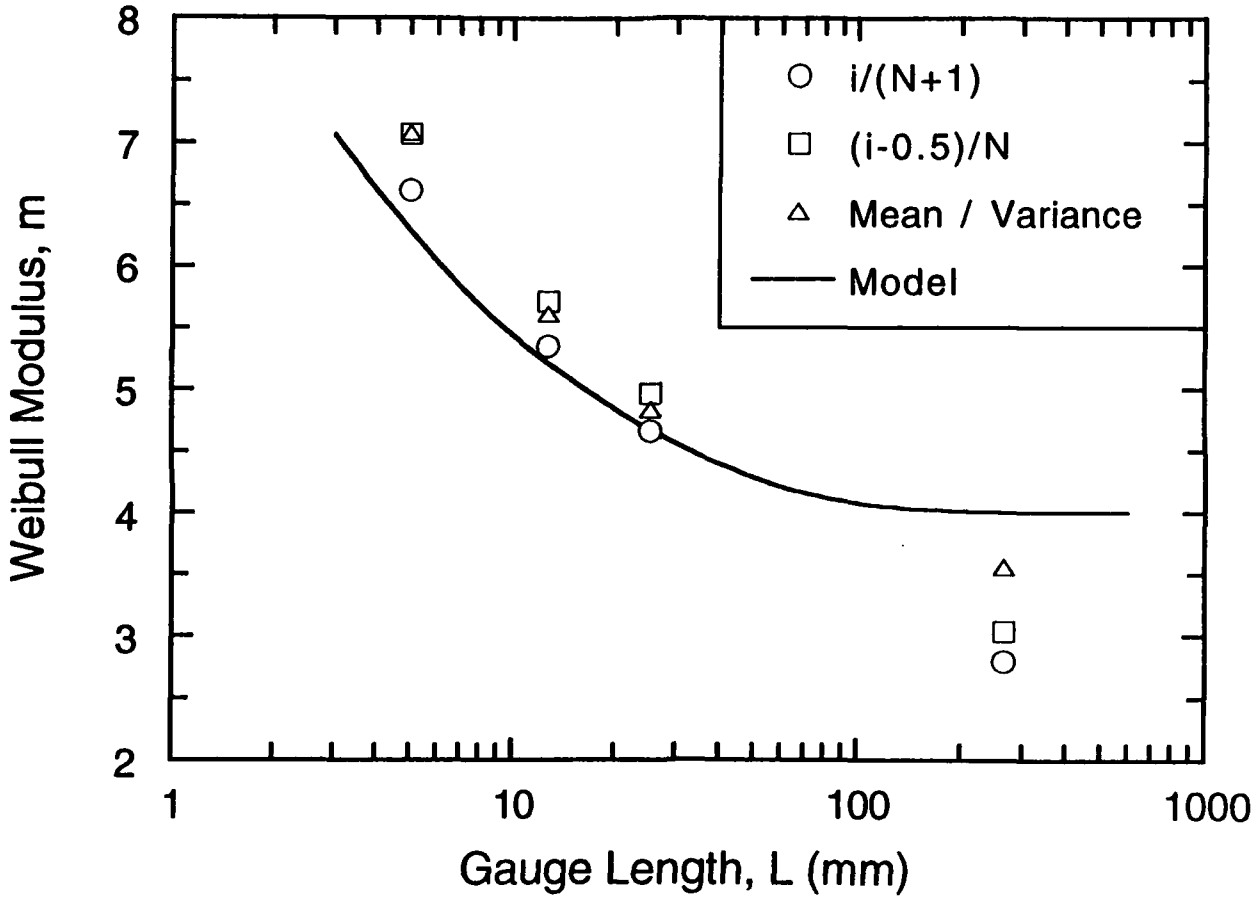
8
7
6
5
4
3
2
1
10
100
1000
Weibull Modulus, m
Gauge Length, L (mm)
i/(N+1)
(i-0.5)/N
Mean / Variance
Model

Figure 6(a)

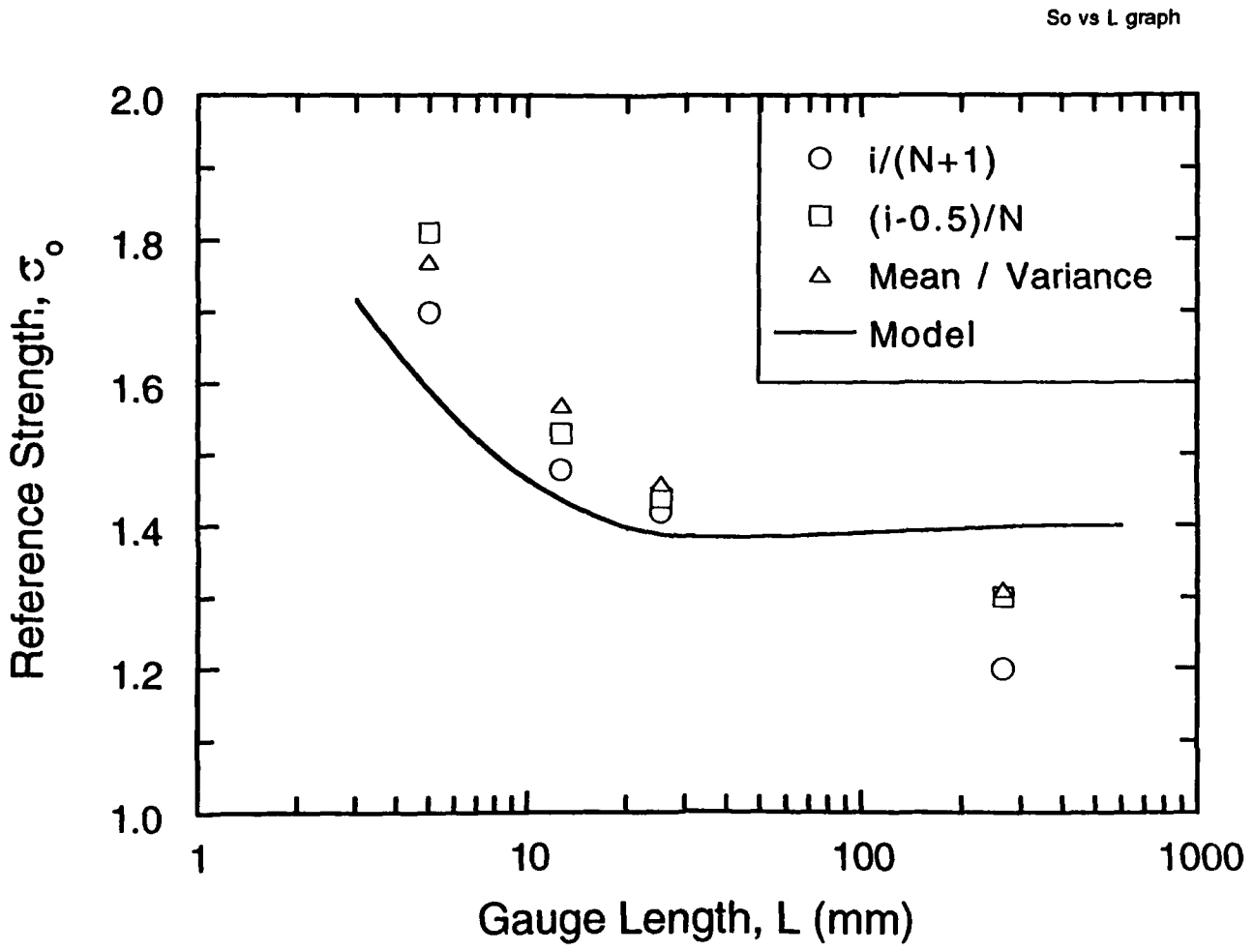
So vs L graph
2.0
1.8
1.6
1.4
1.2
1.0
Reference Strength, σ_o
1
10
100
1000
Gauge Length, L (mm)
i/(N+1)
(i-0.5)/N
Mean / Variance
Model

Figure 6(b)

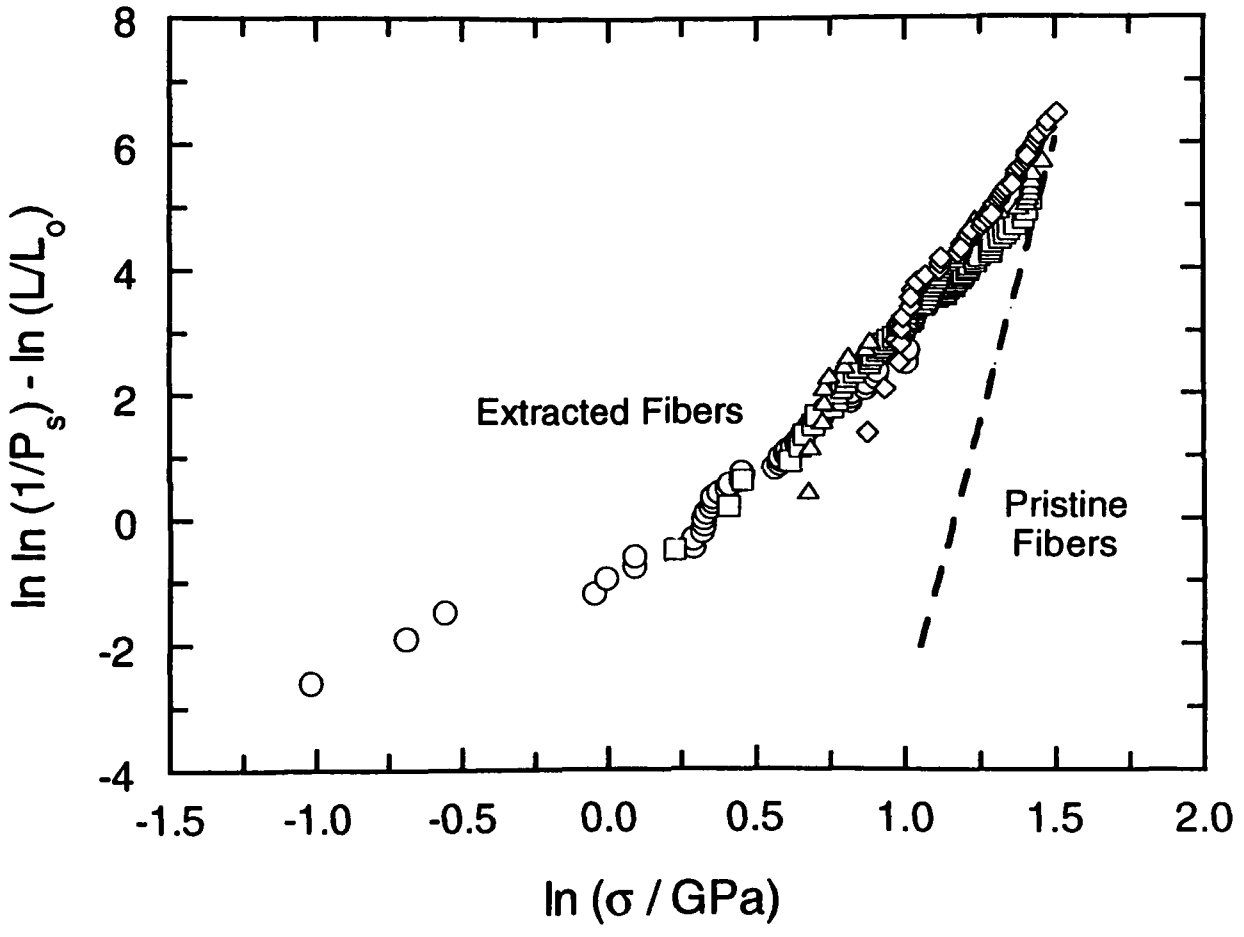
8
6
4
2
0
-2
-4
-1.5
-1.0
-0.5
0.0
0.5
1.0
1.5
2.0
ln ln (1/P$_s$) - ln (L/L$_o$)
ln (σ / GPa)
Extracted Fibers
Pristine
Fibers

Figure 7

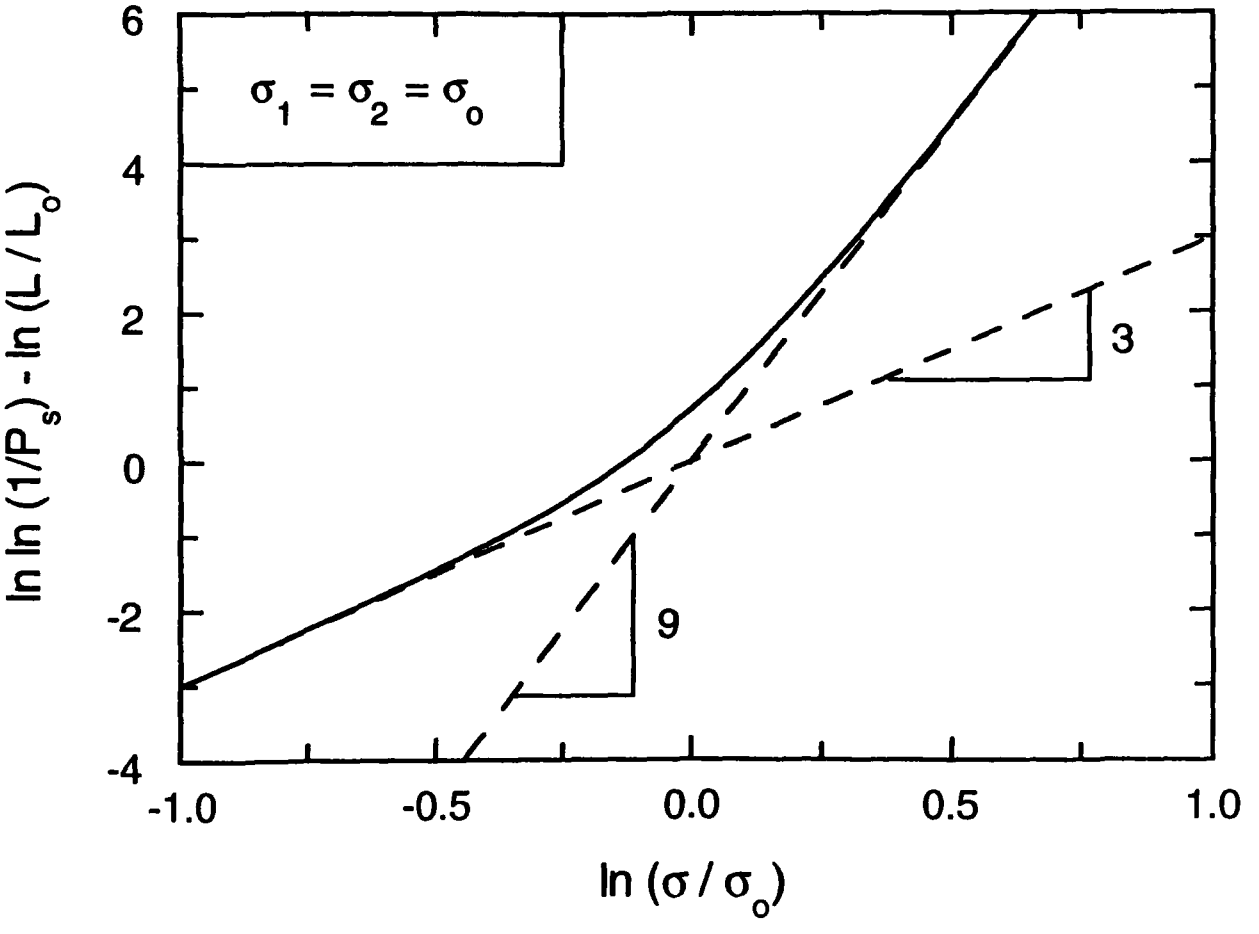
$\sigma_1 = \sigma_2 = \sigma_o$
3
9
6
4
2
0
-2
-4
-1.0
-0.5
0.0
0.5
1.0
ln ln (1/P$_s$) - ln (L / L$_o$)
ln (σ / σ$_o$)

Figure 8

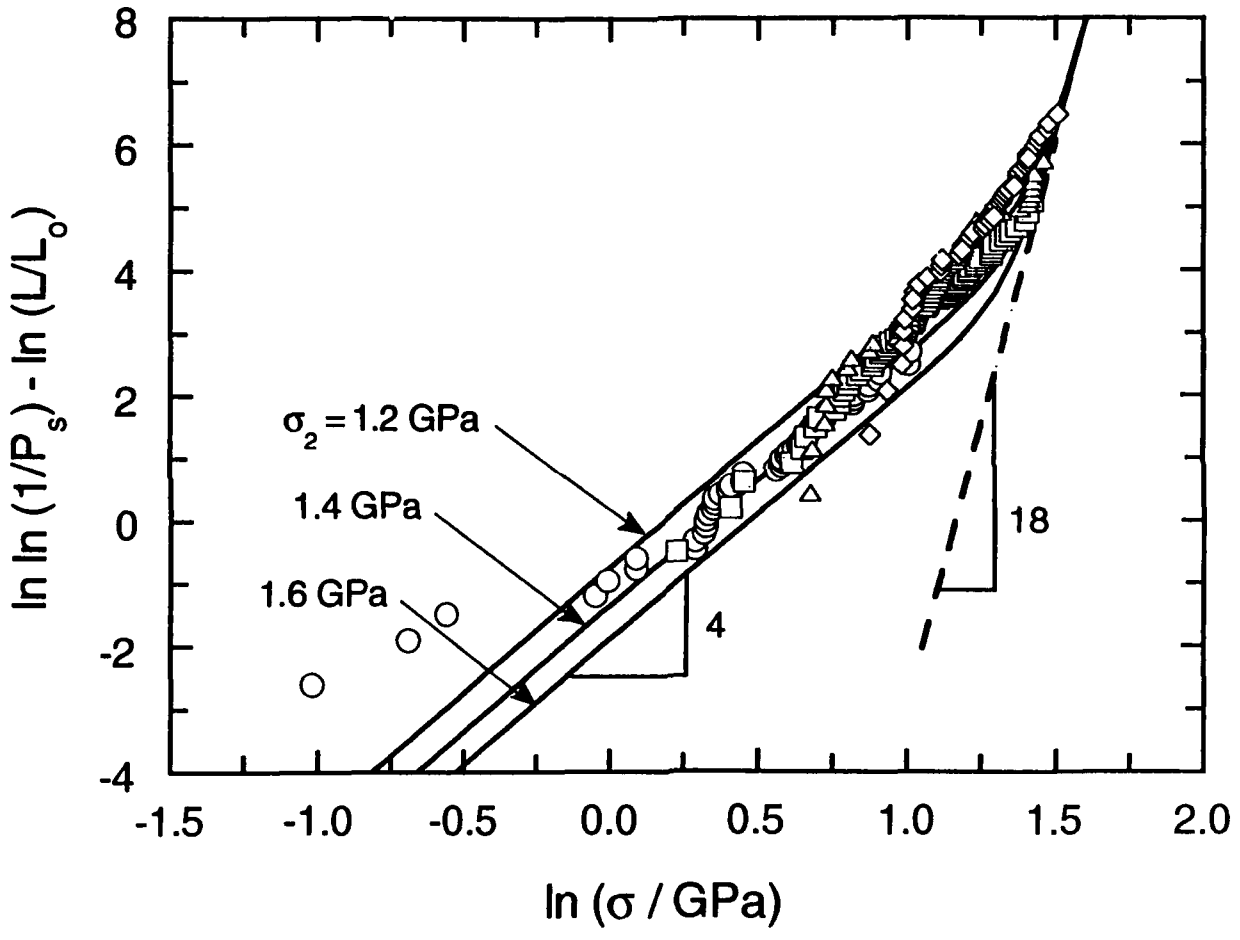
8
6
4
2
0
-2
-4
-1.5
-1.0
-0.5
0.0
0.5
1.0
1.5
2.0
ln ln (1/P_s) - ln (L/L_o)
ln (σ / GPa)
σ_2 = 1.2 GPa
1.4 GPa
1.6 GPa
4
18

Figure 9

Tunneling Cracks in Constrained Layers

S. Ho[1]

Z. Suo
Mem. ASME.

Mechanical Engineering Department,
University of California,
Santa Barbara, CA 93106-5070

A thin, brittle layer bonded between tougher substrates is susceptible to cracking under residual and applied stresses. Such a crack initiates from an equi-axed flaw, confined by the substrates, tunneling in the brittle layer. Although tunneling is a three-dimensional process, the energy release rate at the front of a steady-state tunnel can be computed using plane strain fields. Several technically important problems are analyzed, including tunnels in adhesive joints, shear fracture, and kinked tunnels in a reaction product layer. The concept is finally applied to microcracking in brittle matrix composites caused by thermal expansion mismatch.

Introduction

Layered materials subjected to residual and applied stresses are susceptible to cracking. Depending on the application, such cracks can either fail device or degrade material. For example, cracks in multilayer capacitors form easy conducting paths, leading to electrical leak. For metal matrix composites, microcracks in fiber coating can be the nucleation sites for fatigue cracks in the matrix. A commonly observed cracking process, tunneling, is examined in this paper.

Figure 1 illustrates a thin, brittle layer of thickness h, bonding two tougher substrates, subjected to both applied and residual stresses. If the net stress in the layer is tensile and sufficiently high, it drives pre-existing flaws to tunnel through the layer. The energy release rate at the *front*, G_F, varies from point to point, and depends on the tunnel length a. A long tunnel ($a/h \to \infty$) reaches a *steady-state*: the front self-adjusts to a shape such that G_F is the same at every point along the front, which no longer depends on the tunnel length, nor on the initial flaw geometry. This steady-state energy release rate is denoted as G_{ss} in Fig. 1.

Two facts, to be elaborated upon later suggest that G_{ss} is suitable for design of constrained thin layers. First, G_{ss} is relatively easy to compute (only plane-strain analyses are required). Second, the steady-state is readily reached if pre-existing flaw size is close to layer thickness. These concepts have evolved from studies of layered materials of many varieties: composite laminates (Parvizi et al., 1978; Wang, 1984; Dvorak and Laws, 1986; Fang et al., 1989), thin films (Gille, 1985; Hu et al., 1988; Bueth, 1992; Ye et al., 1992), and brittle adhesive layers (Suo, 1990).

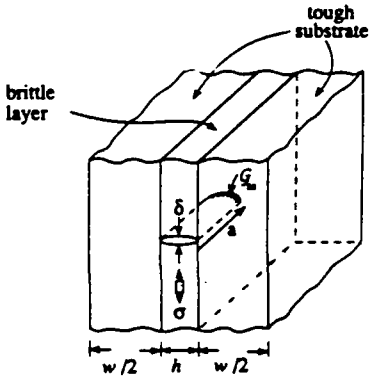

Fig. 1 A crack tunnels in a bonded layer

In this paper a new formula for G_{ss}, convenient for finite element analyses, is presented. We then discuss tunnel nucleation and the relevance of G_{ss} in design. The versatility of the concepts is demonstrated by several technically significant problems, including cracking in adhesive joints, shear fracture, and kinked cracks. The concepts are finally applied to microcracking in brittle matrix composites caused by thermal expansion mismatch.

Driving Force for Steady-State Tunneling

As sketched in Fig. 1, tunneling is a three-dimensional process. However, when the steady-state is reached, i.e., as $a/h \to \infty$, G_{ss} can be calculated using plane-strain elasticity solutions. Two alternative formulas are derived below. The tunnel is assumed to be perfectly constrained at the edges so that neither interface nor substrates crack. The significance of interface debonding and substrate cracking is reported elsewhere (Ye et al., 1992).

For such a semi-infinite tunnel the process that the front advances a unit distance is equivalent to (i) remove a unit thickness of material far ahead of the tunnel and, (ii) append a unit thickness of material in the wake. Let U be the difference in the strain energy stored in the two slices. By definition, it follows that

[1] Present address: Department of Theoretical and Applied Mechanics, University of Illinois, Urbana, IL 61801.

Contributed by the Applied Mechanics Division of THE AMERICAN SOCIETY OF MECHANICAL ENGINEERS for publication in the ASME JOURNAL OF APPLIED MECHANICS.

Discussion on this paper should be addressed to the Technical Editor, Professor Lewis T. Wheeler, Department of Mechanical Engineering, University of Houston, Houston, TX 77204-4792, and will be accepted until four months after final publication of the paper itself in the ASME JOURNAL OF APPLIED MECHANICS.

Manuscript received by the ASME Applied Mechanics Division, May 30, 1991; final revision, Aug. 17, 1992. Associate Technical Editor: F. Y. M. Wan.

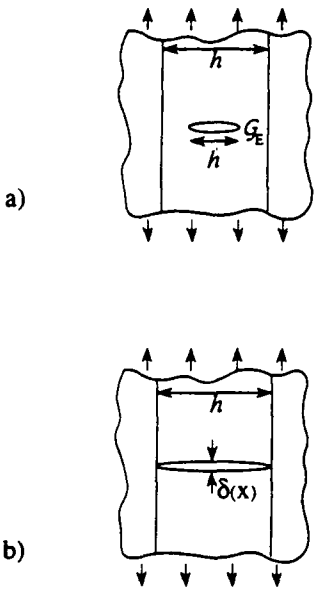

Fig. 2 (*a*) A plane-strain crack of size $h' < h$ used for formula (2); (*b*) a plane-strain crack of size h used for formula (3)

$$G_{ss} = U/h. \tag{1}$$

Observe that U equals the strain energy increase, at constant applied stress, due to introduction of a plane-strain crack in the unit slice. Let G_E be the energy release rate at the *edge* of a plane-strain crack of width $h' < h$ (Fig. 2(*a*)). It has been shown that (Gille, 1985; Dvorak and Laws, 1986)

$$G_{ss} = \frac{1}{h}\int_0^h G_E(h')dh'. \tag{2}$$

This formula requires G_E for plane-strain cracks of *various* width, $0 < h' < h$. As pointed out by these authors, such information is available in the literature only for a few inhomogeneous systems within limited parameter ranges, and finite element computation of G_E for various crack lengths is tedious.

Alternatively, U equals the work done by the stress through the crack opening (Fig. 2(*b*)), so that

$$G_{ss} = \frac{1}{2h}\int_0^h \sigma(x)\delta(x)dx. \tag{3}$$

Here $\sigma(x)$ is the stress distribution on the prospective crack plane prior to cracking; and $\delta(x)$ is the opening profile in the wake. Although (2) and (3) are equivalent, the latter is considerably more efficient in computation, since only two instead of many configurations need be analyzed: the stress in the uncracked body and the displacement for a plane-strain crack of *final width* h (Fig. 2(*b*)). Each of the two independent problems is under plane-strain conditions readily analyzed by commercial finite element codes.

Both (2) and (3) are valid for linear elastic systems uniform in geometry, material, and loading along the tunneling direction. In the following, (2) is used if G_E for the corresponding plane-strain cracks, with width varying from zero to the final tunnel size, is available in the literature; but (3) is used whenever finite element analysis is required.

Tunnel Nucleation

Tunnel nucleation is a complicated process. The nature of pre-existing flaws plays a predominant role—a gas bubble would behave differently from a microcrack. Several idealizations are invoked as follows. The pre-existing flaw is taken

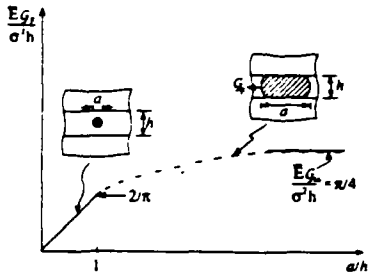

Fig. 3 The frontal energy release rate increases with the tunnel length, approaching quickly to an asymptote

to be a penny-shaped crack of initial diameter, a_0, less than layer thickness (Fig. 3). Some time-dependent subcritical cracking mechanism is assumed, so that the flaw grows slowly into a long tunnel under a constant applied stress, σ. The thin layer and the substrates are assumed to have identical elastic constants, and substrates are semi-infinite. The main objective of the following discussion is to provide a rough estimate of the tunnel length needed to attain the steady-state. None of the foregoing simplifications will change the conclusions qualitatively.

Let a be the current size of the crack (Fig. 3). When $a/h < 1$, the growing crack remains penny-shaped, since the energy release rate is the same at every point along the front. This energy release rate is given by (Tada et al., 1985)

$$G_F = \frac{2}{\pi}\sigma^2 a/\bar{E} \tag{4}$$

with $\bar{E} = E/(1-\nu^2)$, E and ν being Young's modulus and Poisson's ratio. Equation (4) is the straight line in Fig. 3, up to $a/h = 1$. After touching the interfaces, the crack is confined by the tough substrates and becomes noncircular, so that (4) is not valid when $a/h > 1$.

The crack will finally become a long tunnel and reach the steady-state. To compute G_{ss}, the classical solution is needed for G_E of a plane-strain crack of width h' (Fig. 2(*a*)):

$$G_E = \frac{\pi}{2}\sigma^2 h'/\bar{E}. \tag{5}$$

Integral (2) gives

$$G_{ss} = \frac{\pi}{4}\sigma^2 h/\bar{E}. \tag{6}$$

This result is indicated in Fig. 3 as the asymptotic value for $a/h \to \infty$.

Observe that the solutions for two limiting cases, $a/h = 1$ and $a/h \to \infty$, differ only by 23 percent. Consequently, for practical purposes, the tunnel attains the steady-state as soon as $a/h \sim 1$. The fact that the solution around $a/h \approx 1$ depends on the initial flaw geometry and the growth law of subcritical cracking discourages further elaboration in this region. The dashed line in Fig. 3 is the anticipated trend.

Now consider a brittle layer without subcritical cracking mechanism, but with a well-defined fracture energy Γ—that is, the crack will not grow if $G_F < \Gamma$. Following Dvorak and Laws (1986), we distinguish *thin* and *thick* layers by the ratio of the pre-existing flaw size to the layer thickness, a_0/h.

For a *thick* layer, where $a_0/h \ll$, the critical stress for the flaw to grow is governed by the flaw size

$$\sigma_c = (\pi\Gamma\bar{E}/2a_0)^{1/2}. \tag{7}$$

As suggested by Fig. 3, under a constant applied stress $\sigma = \sigma_c$, the flaw grows dynamically into a long tunnel. For example, the flaw size for a dense ceramic scales with grain diameter, typically $a_0 = 1 \sim 10$ μm. If the layer thickness is much larger than the grain diameter, the stress needed to nucleate a tunnel

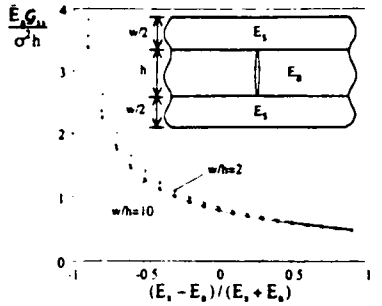

Fig. 4 Driving force for tunneling in an adhesive layer

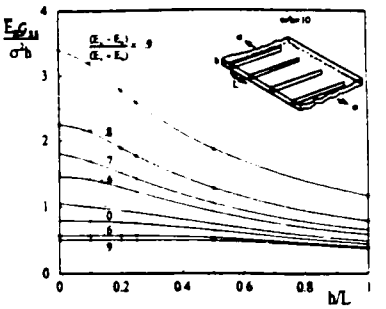

Fig. 5 Driving force for periodic tunnels

is given by (7). Consequently, the critical stress for a thick layer is identical to the strength of the material in bulk.

For a *thin* bonded layer, where the pre-existing flaws are on the other of layer thickness, i.e., $a_0/h \sim 1$, the steady-state energy release rate G_{ss} becomes relevant. From (6), one finds that the critical stress to maintain tunnel growth is

$$\sigma_c = (4\Gamma\bar{E}/\pi h)^{1/2}. \tag{8}$$

This critical stress is well defined: no knowledge of flaw geometry or microstructure is needed. It is conservative: any flaw, regardless of its initial size or shape, cannot grow into a long tunnel if the applied stress is below σ_c. Consequently, the critical stress derived from G_{ss} can serve as a well-defined, conservative design criterion for avoidance of tunnel cracks in brittle thin layers. It is clear from Fig. 3 that the criterion becomes overly conservative for very thick layers ($a_0/h \ll 1$).

Observe that the critical stress (8) is governed by layer thickness; the thinner the layer, the higher the strength, everything else being equal. This has motivated the conception of microlaminates, consisting of alternate metal and ceramic, each layer submicron thick, fabricated by a variety of thin film deposition techniques (Evans, private communication). Because cracks in a ceramic layer are confined by the adjacent metal layers, and dislocations in a metal layer is confined by the adjacent ceramic layers (Freund, 1990), the microlaminates can have very high elastic limit, unprecedented by bulk solids.

The rest of the paper will focus on applying tunneling concepts to a variety of technical problems, with nucleation stage ignored. Each individual application of the following results must be validated on the basis that the pre-existing flaw size is close to the layer thickness.

Adhesive Layer

Inserted in Fig. 4 is a cross-section of a tunnel wake. In finite element calculations, Poisson's ratios are taken to be $\nu_a = \nu_s = 1/3$, so that elastic mismatch is specified by $(E_s - E_a)/(E_s + E_a)$. The plane-strain conditions prevail in the tunnel wake. We analyze the plane-strain field using finite elements; the computed opening profile is integrated according to (3). The normalized G_{ss} is plotted in Fig. 4, varying the elastic mismatch and thickness ratio. Substrate thickness has little effect; the curve for semi-infinite substrates is nearly identical to the curve for $w/h = 10$ with the resolution of Fig. 4. Figure 4 is therefore sufficiently complete for practical purposes. The following illustrates an application.

In an experiment by Zdaniewski et al. (1987), different glasses were used to bond alumina substrates. Gas bubbles of size of layer thickness formed in the glass during bonding, acting as tunnel nuclei. The residual stresses for the four glasses used in the experiment were $\sigma_R = 63, 50, 131, 132$ MPa, respectively. Tunnels were observed to radiate from the bubbles in the last two glasses, but not the first two. Take $E_{glass} = 70$ GPa and $E_{alumina} = 350$ GPa. From Fig. 4, this elastic mismatch corresponds to $G_{ss}\bar{E}_a/\sigma^2 h = 0.6$. Given that $h = 50$ μm and $\Gamma_{glass} = 5$ Jm^{-2}, the predicted critical stress is $\sigma_c = 120$ MPa. The predicted critical stress indeed discriminates glass layers with and without tunnels.

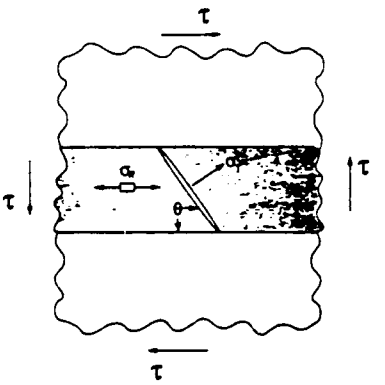

Fig. 6 Microcrack under combined residual stress and applied shear

Periodic Tunnels

Periodic tunnels can form under uniaxial tension (e.g., Parvizi et al., 1978; Laws and Dvorak, 1988). Figure 5 illustrates tunnels with spacing L. The opening profile, $\delta(x)$, is for one of the cracks which is computed using finite elements. The computed energy release rate G_{ss} is plotted in Fig. 5 for $w/h = 10$. Observe that, except for very compliant substrates, G_{ss} does not vary substantially with spacing L/h. Consequently, once the stress is sufficient to drive one tunnel, many tunnels will follow with a slightly higher stress, so long as the nucleation sites are readily available.

In Fig. 5, all the cracks are assumed to tunnel simultaneously. With a proper rearrangement of the results in Fig. 5, the driving force for new tunnels forming between existing tunnels can also be obtained (Hutchinson and Suo, 1992).

Shear Fracture

Upon closer examination of shear fracture in a laminate, one sees microcracks normal to the principal tensile stress nucleate and connect, causing macroscopic fracture (Chai, 1988). As an example consider a brittle thin layer bonded between tough substrates, subjected to shear stress τ and residual stress σ_R (Fig. 6). The larger principal stress, σ_1, and the angle between the interface and the plane of the principal stress, θ, are given by

$$\tan\theta = \sigma_1/\tau = \sigma_R/2\tau + \sqrt{(\sigma_R/2\tau)^2 + 1}. \tag{9}$$

Regardless of the sign of σ_R, σ_1 is always tensile; $\theta < 45$ deg if $\sigma_R < 0$, and $\theta > 45$ deg if $\sigma_R > 0$.

A tunnel is assumed to form perpendicular to σ_1. For simplicity, the elastic moduli of the substrates and the bonded

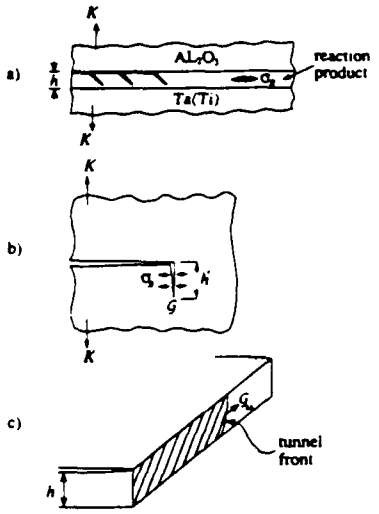

Fig. 7 Kinked tunnels

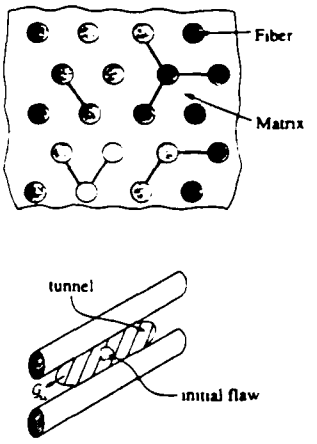

Fig. 8 Matrix cracking due to thermal mismatch

layer are taken to be identical and substrates are semi-infinite. The cross-section of the tunnel wake is a Griffith crack, so that (6) is applicable. Identifying the net stress σ_l and tunnel width $h/\sin\theta$, one obtains

$$G_{ss}\bar{E}/h\tau^2 = \frac{\pi}{4}\sin\theta/\cos^2\theta. \tag{10}$$

For layers with different elastic constants, the tunnel angle should still be determined by (9), but finite element analysis is needed to calculate G_{ss}. Judged from Fig. 4, however, the results should be insensitive to elastic mismatch if substrates are stiffer than the layer.

Kinked Tunnels

When a Al_2O_3 plate is diffusion bonded to a Ta(Ti) alloy, a reaction product layer (RPL) of thickness 2 μm forms (He et al., 1991). The system debonds along the Al_2O_3-RPL interface upon loading, leaving behind a trail of microcracks in the RPL (Fig. 7(*a*)).

The tunnel is driven by the stress intensity at the parent crack front, K, and by the residual stress in the layer, σ_R. For simplicity the remote load is assumed to be mode I, and the microcracks are taken to be perpendicular to the interface. The system is taken to be elastically homogeneous and the two substrates are semi-infinite. None of these assumptions will affect the conclusions qualitatively.

For a kink of depth h' under the plane-strain conditions (Fig. 7(*b*)), the stress intensity factor is (He et al., 1991)

$$K_I = 0.374K + 1.766\sigma_R\sqrt{h'},\quad K_{II} = -0.347K + 0.201\sigma_R\sqrt{h'}. \tag{11}$$

The energy release rate at the kink tip can be computed from Irwin's relation

$$G_{\mathcal{L}} = (K_I^2 + K_{II}^2)/\bar{E}. \tag{12}$$

The energy release rate at the tunnel front G_{ss} (Fig. 7(*c*)) can be integrated according to (2), giving

$$\bar{E}G_{ss}/K^2 = 0.260 + 0.788\eta + 1.58\eta^2,\quad \eta = \sigma_R\sqrt{h}/K. \tag{13}$$

The parameter η reflects the effect of the residual stress. When a tunnel forms, the residual tension is locally relieved. As the interface crack grows further, the residual tension recovers, driving a new tunnel.

Kinked tunnels were also observed by Chai (1987) in an epoxy bonded between aluminum substrates. He observed that the main crack ran alternating on the two interfaces, leaving behind a wavy fracture surface. This did not happen in the system of He et al. (1991), presumably because the Ta(Ti)-RPL interface is much tougher.

Thermal Cracking in Brittle Matrix Composites

All previous examples are related to layered materials. But tunneling is more prevalent. To illustrate, consider matrix cracking caused by thermal mismatch. An intermetallic reinforced by ceramic fibers, such as $MoSi_2$-SiC, usually has higher thermal expansion coefficient in the matrix than in the fibers. Upon cooling from the processing temperature, the matrix is subjected to tensile hoop stress and susceptible to cracking (Lu et al., 1991). One experimental finding is that cracking is more likely to occur in the matrix reinforced by fibers of larger radius, so that a critical fiber radius exists, below which matrix cracking is suppressed.

Focus on the radial crack in Fig.8. The thermal mismatch strain is

$$\epsilon_0 = \int_{T_r}^{T_p}(\alpha_m - \alpha_f)dT, \tag{14}$$

where α_m and α_f are thermal expansion coefficients of the matrix and fiber, and T_p and T_r are the processing temperature and room temperature. The residual stress estimated from the mismatch strain for $MoSi_2$-SiC is high (~ 2 GPa), well in excess of the bulk strength of $MoSi_2$. Also note that the residual stress is *independent* of fiber radius for a fixed fiber volume. These two facts eliminate the possibility of explaining the experimental finding on the basis of bulk strength.

We assume porosity exists, of size limited only by the fiber spacing, which tunnels through the matrix under sufficiently high thermal stress (Fig. 8). On dimensional grounds, the steady-state energy release rate takes the form

$$G_{ss} = \Omega\epsilon_0^2 E_m R, \tag{15}$$

where R is fiber radius and E_m is the Young's modulus of the matrix. The dimensionless prefactor, Ω, depends on fiber volume fraction, fiber arrangement, elastic mismatch, and interface properties, which has been computed using finite elements on the basis of the tunneling crack concepts developed in the previous sections (Ho and Suo, 1992).

The tunnel will not form if $G_{ss} < \Gamma_m$, Γ_m being the fracture energy of the matrix. Thus (15) gives

$$\Gamma_m/\epsilon_0^2 E_m R > \Omega. \tag{16}$$

The dimensionless group on the left-hand side consists of measurable parameters and predicts, among other things, that the larger the fiber radius, the more likely will the matrix crack, which is in agreement with the experimental findings.

Concluding Remarks

Cracks tunnel in confined geometries. The steady-state tunneling defines a conservative design limit. The energy release rate at the tunnel front is computed for a number of cases. To demonstrate the versatility of the concepts without going into technical details we have treated each problem in its simplest form. Many more computations are needed to take key variables into account, so that rigorous design criteria will emerge. Nevertheless, results presented here can be used as a base line for such purposes. Although this paper has focused on cracking in brittle layers, tunnels can form in ductile metal or polymer layers under cyclic loading. The fatigue life is dictated by the steady-state energy release rate, provided large flaws are available and tunnels do not take many cycles to nucleate.

Acknowledgment

Support is provided by ONR/URI contract N-0014-92-J-1808, and by NSF Young Investigator Award MSS-9258115. Finite element analyses are carried out using ABAQUS.

References

Beuth, J. L., 1992, "Cracking of Thin Bonded Films in Residual Tension," *Int. J. Solids and Structures*, Vol. 29, pp. 1657-1675.

Chai, H., 1987, "A Note on Crack Trajectory in an Elastic Strip Bounded by Rigid Substrates," *Int. J. Fracture*, Vol. 32, pp. 211-213.

Chai, H., 1988, "Shear Fracture," *Int. J. Fracture*, Vol. 37, pp. 137-159.

Dvorak, G. J., and Laws, N., 1986, "Analysis of First Ply Failure in Composite Laminates," *Engng. Fracture Mech.*, Vol. 25, pp. 763-770.

Dvorak, G. J., and Laws, N., 1988, "Progressive Transverse Cracking in Composite Laminates," *J. Composite Materials*, Vol. 22, pp. 900-916.

Fang, G. P., Schapery, R. A., and Weitsman, Y., 1989, "Thermally-Induced Fracture in Composites," *Engng. Fracture Mech.*, Vol. 33, pp. 619-623.

Freund, L. B., 1990, "The Driving Force for Gliding of a Threading Dislocation in a Strained Epitaxial Layer on a Substrate," *J. Mech. Phys. Solids*, Vol. 38, pp. 657-679.

Gille, G., 1985, "Strength of Thin Films and Coatings," *Current Topics in Materials Science*, Vol. 12, E. Kaldis, ed., North Holland, Amsterdam.

He, M.-Y., Bartlett, A., Evans, A. G., and Hutchinson, J. W., 1991, "Kinking of a Crack Out of an Interface: Role of In-Plane Stress," *J. Am. Ceram. Soc.*, Vol. 74, pp. 767-771.

Ho, S., and Suo, Z., 1992, "Microcracks Tunneling in Brittle Matrix Composites Driven by Thermal Expansion Mismatch," *Acta. Mer. Mater.*, Vol. 40, pp. 1685-1690.

Hu, M. S., Thouless, M. D., and Evans A. G., 1988, "The Decohesion of Thin Films from Brittle Substrates," *Acta Met.*, Vol. 36, pp. 1301-1307.

Hutchinson, J. W., and Suo, Z., 1992, "Mixed-Mode Cracking in Layered Materials," *Advances in Applied Mechanics*, Vol. 29, pp. 63-191.

Lu, T. C., Yang, J., Suo, Z., Evans, A. G., Hecht, R., and Mehrabian, R., 1991, "Matrix Cracking in Intermetallic Composites Caused by Thermal Expansion Mismatch," *Acta. Metall. Mater.*, Vol. 39, pp. 1883-1890.

Parvizi, A., Garrett, K. W., and Bailet J. E., 1978, "Constrained Cracking in Glass Fiber-Reinforced Epoxy Cross-Ply Laminates," *J. Matter Sci.*, Vol. 13, pp. 195-201.

Suo, Z., 1990, "Failure of Brittle Adhesive Joints," ASME *Applied Mechanics Reviews*, Vol. 43, pp. S276-S279.

Tada, H., Paris, P. C., and Irwin, G. R., 1985, *The Stress Analysis of Cracks Handbook*, Del Research, St. Louis, MO.

Wang, A. S. D., 1984, "Fracture Mechanics of Sublaminate Cracks in Composite Materials," *Composite Tech. Rev.*, Vol. 6, pp. 45-62.

Ye, T., Suo, Z., and Evans, A. G., 1992, "Thin Film Cracking and the Roles of Interface and Substrate," *Int. J. Solids Structures*, Vol. 29, pp. 2639-2648.

Zdaniewski, W. A., Conway, J. C., and Kirchner, H. P., 1987, "Effects of Joint Thickness and Residual Stresses on the Properties of Ceramic Adhesive Joints," *J. Am. Ceram. Soc.*, Vol. 70, pp. 104-109.

The Effect of Interfacial Properties on the Flow Strength of Discontinuous Reinforced Metal Matrix Composites

D. B. Zahl[†] and R. M. McMeeking

Mechanical Engineering Department

University of California, Santa Barbara, CA 93106

[†]Current Address:

Max-Planck-Institut für Metallforschung

Institut für Werkstoffwissenschaft

Seestraße 92, D-70174 Stuttgart

October 1993

Submitted to Mechanics of Composite Materials and Structures

ABSTRACT

The effect of interfacial properties on the strength of discontinuous reinforced metal matrix composites is systematically studied by theoretical modeling. The calculations were carried out within the framework of continuum plasticity theory using cell models and the finite element method. A wide range of inclusion aspect ratios, volume fractions, and interfacial strengths were investigated for perfectly plastic and hardening matrices. Interfaces were modeled as either strongly bonded, as shearable but strong normal to the inclusions, or as debonding at the reinforcement ends but strong on the sides. Additionally, the effects of reinforcement arrangement and extensive damage to continuous fiber composites were addressed. Debonding at the ends of the inclusions was found to be the most deleterious effect to the strength of the composite. When debonding did not occur but interface sliding takes place freely, an amount of strengthening is seen which is a function of inclusion volume fraction but is primarily independent of inclusion aspect ratio. For extensively damaged continuous fiber composites a weak interface yields a steady state composite flow strength slightly higher than the volume fraction of the matrix times the yield strength of the matrix. This increases linearly with the interfacial shear strength up to the level for strongly bonded composites and can be estimated from the intact fiber aspect ratio, the matrix yield stress the volume fraction, and the interfacial strength.

1. INTRODUCTION

Previous studies on metal matrix composites have dealt with continuous fiber composites and with discontinuous reinforced composites with a uniform array of aligned inclusions. These geometries lend themselves to axisymmetric models for the study of the longitudinal behavior of these composites. Using the axisymmetric formulation the effects of volume fraction of inclusions [1], inclusion shape [1], debonding [2], and residual stresses due to mismatch in the thermal expansion of the constituents [3] have been investigated. Plane strain calculations have been used to examine the transverse properties of continuous fiber composites [4] and, by note of similarities in the development of field quantities between the axisymmetric and plane strain models, the effect of clustering in discontinuous reinforced composites has been investigated [5,6]. Three dimensional calculations have been used to investigate the effect of volume fraction in particulate composites [7], and have validated the use of the axisymmetric model. Three dimensional calculations have also been used to study the transverse properties of discontinuous reinforced composites [8]. Constitutive equations for multiaxial loading of weakly bonded and strongly bonded transversely isotropic continuous fiber composites have been developed by Gunawardena [9] for the former and by Herath [10] for the latter. Jansson and Leckie [11] investigated the behavior of a transversely loaded continuous fiber composite subjected to thermal cycling.

In this work the behavior of metal matrix composites is further investigated. The role that interfacial strength plays with regard to the axial composite strength of these materials is systematically studied with the use of the axisymmetric cell model for a variety of interfacial behavior including strong interfaces, sliding interfaces, and debonding interfaces. A wide range of volume fractions, inclusion aspect ratios, and interfacial strengths are examined for composites with cylindrical shaped

inclusions. In addition, the role of interfacial sliding in continuous fiber composites is studied for the situation in which the fibers have experienced extensive cracking.

2. CONSTITUENT BEHAVIOR AND CELL FORMULATION

Composite materials can be viewed as having three distinct components: the matrix, the reinforcement, and the interface. In metal matrix composites the inclusions are generally ceramic and therefore much stiffer than the matrix and do not exhibit significant plastic behavior. For these reasons the inclusions are assumed to be rigid relative to the matrix material in this study.

The matrix and the interface are modeled as elastic-plastic with uniaxial behavior characterized by

$$\sigma = \sigma_o\left(\frac{\varepsilon}{\varepsilon_o}\right) = E\varepsilon \qquad \varepsilon \le \varepsilon_o \qquad (1)$$

$$\sigma = \sigma_o \qquad \varepsilon > \varepsilon_o$$

for elastic-perfectly plastic behavior, and by

$$\sigma = \sigma_o\left(\frac{\varepsilon}{\varepsilon_o}\right)^{1/n} \qquad \varepsilon > \varepsilon_o \qquad (2)$$

for power law hardening material, where σ_o is the yield uniaxial stress, $\varepsilon_o = \sigma_o/E$ is the yield strain, E is Young's modulus, and n is the strain hardening exponent.

The J_2 flow theory of plasticity is used to characterize the rate-independent material. With the von Mises yield criterion the condition for plastic flow is given by

$$F=3s_{ij}s_{ij}+2\sigma_f^2=0 \qquad (3)$$

where s_{ij} is the deviatoric stress, and σ_f is the current value of the yield stress in tension.

The solutions were calculated incrementally with the stress increment related to the strain increment through

$$\dot{\sigma}_{ij} = \frac{E}{1+\nu}\left\{\dot{\varepsilon}_{ij} + \frac{\nu}{1-2\nu}\dot{\varepsilon}_{kk}\delta_{ij} - \frac{3}{2\sigma_e^2}\frac{s_{ij}s_{kl}\dot{\varepsilon}_{kl}}{\left[1+\frac{2}{3}(1+\nu)\frac{E_t}{E-E_t}\right]}\right\} \qquad (4)$$

where σ_{ij} is the stress, ε_{ij} is the strain, $\sigma_e = (3s_{ij}s_{ij}/2)^{1/2}$ is the effective stress, ν is Poisson's ratio, and E_t is the current tangent modulus of the uniaxial stress-strain curve. For an elastic increment the last term in (4) is zero. Young's modulus is taken to be 1000 times the yield stress in tension. For the cases of a work hardening matrix material, values of n=5 and n=10 were used. Poisson's ratio was given the value of ν=0.25. The matrix stress-strain behavior is shown in figure 1.

The results are based on a widely used axisymmetric cell model. This model represents a uniform array of aligned inclusions, which have the arrangement shown in figure 2a. To evaluate the behavior of this arrangement subject to axial stress, only one of the hexagonal cells, figure 2b, need be analyzed. As a further simplification, the axisymmetric cell, figure 2c, is used. This has been shown to be a good representation of the 3-dimensional cell [7]. The cell is subject to an overall stress $\bar{\sigma}$ parallel to the cylindrical axis. Based on symmetry and periodicity requirements, the cell must remain a right circular cylinder with zero shear tractions on all surfaces and zero average normal traction on the lateral surface. The

end faces of the cell must remain planar. The inclusions are modeled as rigid circular cylinders with an aspect ratio λ defined as the ratio of the height of the cylinder to its diameter, $\lambda=H/D$, and can be fiber shaped, equiaxed, or disk shaped. Due to the rigidity, the purely elastic results and the transition from elastic behavior to fully plastic matrix flow do not represent exactly the phenomena which occur in materials with elastic inclusions. However, the fully plastic flow is captured accurately in an approach in which rigid inclusions are used. The focus in this paper is exclusively on the results related to fully plastic flow. The volume fraction f is taken as the ratio of the inclusion volume to the cell volume. The cell is constructed such that the thickness of matrix material between fibers laterally is the same as it is axially.

The axisymmetric formulation does not allow the study of reinforcements which are aligned but located randomly. To properly address this issue a three dimensional model is required. However, Christman et al. [7] noted similarities in the development of field quantities between the axisymmetric formulation and a plane strain formulation. The assumption that the development of these fields would remain similar if clustering or random placement of aligned reinforcements took place allowed them to examine these effects. As the axisymmetric and plane strain models do not relate to each other on a one to one basis, results in this paper for staggered inclusions are calculated using plane strain and are compared with results for non-staggered inclusions also using the plane strain model. The configuration of these plane strain cells is depicted in figures 3 and 4 for the aligned and staggered models respectively. The cell geometry is such that the spacing between reinforcements in the plane strain case is identical to the spacing between inclusions for the axisymmetric formulation for a volume fraction $f=0.4$. As with the axisymmetric model, the reinforcements are modeled as rigid.

Additional calculations for axial strength were carried out for a model representing continuous fiber reinforcement after the fibers have broken but the matrix remains intact. The cell for this is depicted in figure 5. Calculations were carried out for a material with a volume fraction of fibers equal to 0.4. It was assumed that the distance between breaks was 10 times the diameter of the fiber and that breaks were present in all fibers. The fractures in the fibers were all in the same plane, representing a situation where one broken fiber leads to a stress concentration in neighboring fibers causing them to fail as well. However, all fiber breaks were assumed to exist in the material prior to the application of stress.

The calculations were carried out with the ABAQUS finite element code [12] using 8-noded 2-dimensional axisymmetric biquadrilateral elements. With the use of an FPS500EA computer having 2 scalar and 2 vector processors plus 128 Mbytes of memory, the calculation of a single stress-strain curve would take from 30 minutes to 5 hours. The longer computation times were associated with low values of interfacial strength.

3. PERFECTLY BONDED INTERFACES

Most analytic work with regard to metal matrix composites has assumed that the matrix is strongly bonded to the inclusions. This is a good model for some composites, such as Al reinforced with Al_2O_3. In developing a model for this case the selection of the aspect ratio for the axisymmetric cell is a matter of concern. Bao et al. [1] have shown that the predicted strength from these cell calculations depends on the cell aspect ratio which need not be the same as the reinforcement aspect ratio. Bao et al. [1], as well as Dragone [2] and Christman et al. [7], used cells which had the same aspect ratio as that of the inclusion. However, this results in excessive spacing

between fibers end to end as compared to the spacing side to side. The converse occurs for disk shaped reinforcements. The strategy of using cells in which the end to end spacing is the same as the side to side spacing in all cases is more likely to represent typical practical situations. However, it must not be forgotten that all the results depend on the cell aspect ratio and in that sense the results presented here are special and not general.

Results for Perfectly Bonded Composites

Stress-strain curves for composites with an elastic-perfectly plastic matrix are plotted in figure 6 for fiber aspect ratios ranging from 0.1 to 10 and a volume fraction of 0.4. These results are computed with the axisymmetric cell and therefore represent the arrangement in figure 2. A transient stage from elastic to fully plastic flow exists which increases in extent as the inclusion aspect ratio deviates from 1. Disk shaped inclusions cause a larger transient region than fiber shaped inclusions. Calculations for various volume fractions of reinforcements show that the transient stage also increases with increasing volume fraction. In figure 6, it can be seen when the matrix has perfectly plastic behavior that at large macroscopic strains the flow stress of the composite does not increase with further strain. The resulting steady state flow stress, Σ, is defined as the composite flow stress. This is demonstrated in the inset in figure 7. Figure 7 is a plot of this steady state flow stress versus reinforcement aspect ratio for inclusion volume fractions of 0.2, 0.3, 0.4 and 0.5. This demonstrates the strengthening effect of adding well bonded rigid inclusions to a ductile matrix.

In comparing these results to equivalent calculations of Bao et al. [1], we note that the stresses computed here for fibers and plates are somewhat less than computed by Bao et al. However, the difference can be attributed to the shapes of the unit cell, since Bao et al. [1] used a cell aspect ratio equal to the reinforcement aspect

ratio, whereas the results shown in figure 7 are based on a cell with the same distance between fibers end to end and side to side. The results in figure 7 show that Σ=6.1 for fibers with a volume fraction of 0.4 and an aspect ratio of 10 and Σ=3.3 for disks with aspect ratio of 0.1. The corresponding values computed by Bao et al. [1] are Σ=7.6 for fibers and Σ=5.7 for disks. This indicates a relaxation in constraint in the current model caused by the increase of the distance between fibers side to side or between disks end to end compared to the cells used by Bao et al. [1]. The constraint is relaxed more for disk shaped inclusions than for fiber shaped inclusions. However, the overall conclusions here are the same as for Bao et al. [1]. Fiber shaped inclusions provide the greatest strengthening and the strengthening increases with increasing fiber aspect ratio. Disks provide strengthening to a lesser degree than fibers. It is interesting to note that the lowest level of strengthening is not given by unit cylinders (H=D), but rather by slightly squat cylinders. This is in contrast to the results of Bao et al. [1] in which unit cylinders resulted in the least strengthening. At an inclusion aspect ratio of 1 the current model is identical to the model used by Bao et al. [1] and gives the same results.

The influence of a power law hardening matrix material is shown in figure 8. These calculations were also carried out using the axisymmetric cell and so represent the configuration in figure 2. In figure 8 the stress is normalized by the matrix yield stress at the same strain. This has been used by Bao et al. [1] to give an indication of the extent in terms of strain of the transition stage to pure power law behavior in the composite. This then allows some comparison with the transition to perfectly plastic composite behavior which occurs when the matrix is perfectly plastic. Figure 8 presents stress-strain curves in which the matrix is hardening with strain hardening exponents of n=5 and 10 and for volume fractions of 0.3 and 0.4 for fibers with aspect ratios of 5 and 10. The transient stage increases with increasing hardening. This effect was also observed by Bao et al. [1]. For a given level of matrix

hardening the transient stage increases with increasing volume fraction and increasing fiber aspect ratio, as seen for composites with a perfectly plastic matrix. After the transient stage, the normalized stress-strain curves as shown in figure 8 are flat. At this stage, the composite strength $\bar{\sigma}$ is equal to a fixed pure number multiplied by $\sigma_o\left(\frac{\bar{\varepsilon}}{\varepsilon_o}\right)^{1/n}$ where $\bar{\varepsilon}$ is the axial strain for the composite material. This shows clearly that, after the transient stage, the composite material exhibits power law hardening with the same exponent as the matrix.

The influence of staggered inclusions with strong interfaces is studied using the plane strain model described in section 2. These were carried out with the plane strain cell depicted in figure 4. The dimensions of the cell are chosen to be identical to that for an axisymmetric problem with a volume fraction of f=0.4. The volume fraction of the plane strain cell is then a function of the reinforcement thickness, and comparisons between the plane strain and axisymmetric results are made with respect to the cell geometry and not the reinforcement volume fraction. However, comparison with the results for the axisymmetric case indicates that the axial strength for the plane strain case is comparable to the strength when there are 50% by volume of fibers. All results for the plane strain calculations are for perfect plasticity. The steady state flow stress is plotted versus reinforcement aspect ratio in figure 9 for both the case of regular inclusions as shown in figure 3 and the case of staggered inclusions as shown in figure 4. These results are denoted the "strong interface" results. With reference to the results for strong interfaces in figure 9, there is a reduction in the composite flow stress when inclusions are staggered as compared to the regular case of aligned inclusions for all reinforcement aspect ratios considered. This is in accord with the calculations of Christman et al. [5]. In fact, they found that any deviation from the idealized uniform array of aligned inclusions will have an adverse effect on the composite strength. We infer from

our results that in a fibrous composite with staggered fibers with a high volume fraction around 50%, the axial strength would be about 75% of that arising when the fibers are fully aligned in the regular arrangement shown in figure 2.

4. SLIDING INTERFACES

Strengthening of metal matrices with aligned short fibers is thought to be largely due to load transfer between the fibers and the matrix through shear stress on the side of the fibers with the normal load transfer at the fiber ends being secondary. As a result, the strength of the interface in shear is an important issue with regard to the strength of these composites. Dragone and Nix [6] allowed frictional sliding to occur in their model. The condition for interfacial sliding is then dependent on the local normal stress on the interface. Their results show that compared to the strength associated with a perfect interface, there is a reduction in the composite flow strength and initial composite yield strength with the effect becoming more marked with decreasing friction coefficient. Some reduction occurred even when the friction coefficient was assigned the high value of 1. In our work the condition for sliding is considered to be dependent only on the level of shear stress at the interface. If the shear stress exceeds a specified value, sliding will occur. This model can represent an unbonded interface subject to friction controlled by a large residual compression caused by thermal strains compared to which the stresses due to elastic and plastic strains are negligible. This is a common situation in composites. In addition, the model can represent the effect of a ductile interphase with a low yield stress in shear. In this situation, the sliding is controlled by the plastic straining of the interphase which is considered to be perfectly plastic. The

interfaces investigated have shear strengths ranging from zero up to the shear yield strength of the matrix.

Interface Model

For the case of zero interfacial strength the condition is modeled with a boundary condition on the reinforcement surface. In other cases, the interface is modeled as a thin bonded layer of perfectly plastic material between the matrix and the inclusion. The thickness of the interfacial layer is taken as 0.5% of the thickness of the matrix ligament between inclusions. The thickness of the layer is held constant throughout the composite stress-strain history. The thin layer is assigned a tensile yield stress σ_i. The yield stress of this layer in shear is then $\tau_i = \sigma_i / \sqrt{3}$. When the shear stress in the interfacial layer exceeds τ_i extensive straining in shear will occur. This strain simulates sliding of the matrix relative to the fiber. The interface can transmit any level of normal stress between the fiber and the matrix without debonding and constraint then eliminates the possibility of plastic strain which thickens the interphase. The ratio of σ_i/σ_o is the same as the ratio τ_i/τ_o where σ_o and τ_o are the matrix yield stress in tension and the matrix yield stress in shear respectively. The interface is assumed to have values of τ_i/τ_o ranging from 0 to 1.4 in these calculations. When τ_i/τ_o has a value of 0 the interface can slide freely. If the matrix does not harden, setting $\tau_i \geq \tau_o$ will represent a strong interface. When the matrix is hardening it is useful to assign τ_i values greater than τ_o as the interface is assumed not to have any hardening behavior. Therefore when τ_i exceeds τ_o, slip will occur after some initial hardening takes place in the matrix near the interface. It should be reemphasized that while the interface is modelled as a thin layer of ductile material, the layer is so thin that the model is capable of

representing frictional slip of a debonded interface in compression caused by a large thermal residual stress.

Results for Interfacial Sliding

Stress-strain curves are plotted in figure 10 for composites with a fiber aspect ratio of λ=10 and a volume fraction f=0.4 as computed with the axisymmetric cell. These results, therefore, represent the arrangement depicted in figure 2. The matrix flow behavior is perfectly plastic and curves are given for interfacial strengths ranging from τ_i/τ_o=0 to 1. When interfacial sliding takes place, there is a reduction in the composite flow strength relative to the case of a strongly bonded non-shearing interface. The composite strength decreases with decreasing interfacial shear strength. However, even when the interface is allowed to slide freely the composite is still seen to be strengthened relative to the matrix material alone. Note that the transient stage is influenced by the strength of the interface with extensive strain occurring prior to steady state flow when the interface is weak. In some cases, the flow strength of the composite is still rising after a strain equal to 20 times the matrix yield strain. However, the calculations were terminated at this strain level and the result for flow strength at that strain will be used as an approximation to the steady state flow strength for the material.

The flow stress of the composite at 20 times the matrix yield strain is plotted versus interfacial strength in figure 11 for composites with a perfectly plastic matrix. The volume fraction of reinforcement is 0.4 in each case. Inclusions which are particulate shaped, with aspect ratios ranging from λ=0.5 to λ=2, are not significantly affected by interfacial sliding when the fiber ends are strongly bonded and the strength in the sliding case is only a little lower than the strength of the composite with the non-sliding interface. On the other hand, composites with fiber and disk shaped inclusions are more seriously affected by slip with the material with fiber

shaped reinforcements weakened considerably. A factor of 3 is involved in the strength range for the material with fibers with an aspect ratio of 10. When slip is allowed to take place freely, with $\tau_i/\tau_o=0$, the strengthening that does exist is essentially independent of reinforcement aspect ratio. This suggests that the strength which does arise in this case is due to constraint and load transfer only near the ends of the fibers extending over an extent similar in each case independent of total fiber length.

Also shown on figure 11 are some results for the limit flow stress when slip is allowed to occur freely for a volume fraction of 0.2 and the results for the same case when the interface is strong. It can be seen that composites with a weak interface and a higher volume fraction are less sensitive to variation in reinforcement aspect ratio. At the lower volume fraction of f=0.2, the composite retains more of its strength for both the disk shaped and fiber shaped inclusions, but more so for disks. On the other hand, the particulate materials lose almost all strength in excess of the matrix when the interface is weak. The results for a sliding interface with $\tau_i=0$ when the fibers are in the regular arrangment depicted in figure 2 are summarized in figure 7.

The influence of matrix hardening is presented in figures 12 and 13. These show stress-strain curves for hardening matrices with n=10 in figure 12 and n=5 in figure 13. The volume fraction is f=0.4 and the fiber aspect ratio is $\lambda=10$ in both cases. The results are computed with the axisymmetric cell and so represent the configuration shown in figure 2. Curves for interfacial strengths ranging from $\tau_i/\tau_o=0$ to 1.4 are given. In this case τ_o is the initial matrix yield strength in shear. Also included in these plots is the stress-strain curve for the appropriate composite in which the interface is strongly bonded. For these curves no sliding takes place. When the interface is strong, no sliding or debonding takes place. When sliding is occurring, the interface is nonhardening even though the matrix strain hardens. It

can be seen that the flow stress of the composite remains below the curve for the strongly bonded composite, and deviates further from that case as straining goes on and the matrix continues to harden. The degree of hardening when the interface is subject to slip is less than that of the composite when it is strongly bonded, presumably reflecting the nonhardening behavior of the interface. For comparison, the stress-strain curve for the pure matrix is shown in figures 12 and 13. With increased matrix hardening (n=5) the reduction in strength relative to the case of a strongly bonded composite becomes more pronounced. It can be inferred that the composite strength is controlled more dominantly by the interface strength than by the matrix properties.

The influence of staggered reinforcement when there is a weak interface is studied using the plane strain model as before. The calculations are carried out with the cell shown in figure 4. The geometry for the plane strain cell is chosen to be the same as used for the axisymmetric model for a volume fraction of f=0.4. As noted previously, the strength levels from the plane strain calculation are comparable, however, with the axisymmetric results with a volume fraction of 0.5. The calculations were carried out with a perfectly plastic matrix. The results for the limit flow stress versus reinforcement aspect ratio for both the regular and staggered cases are plotted in figure 9 when the interface has no strength (τ_i=0). The regular case is the arrangement in figure 3 whereas the staggered case is shown in figure 4. These results are denoted the "sliding interfaces" case in figure 9. The composite flow stress is almost independent of aspect ratio. In addition, staggering of inclusions has little effect on the composite strength compared to the regular case. This finding seems to confirm the hypothesis that when there is no interface shear strength, elevation of the flow strength of the composite material is due only to constrained flow and load transfer at the reinforcement ends. It follows that the strength is substantially independent of aspect ratio and depends little on whether the

reinforcements are staggered or aligned. Thus, an arrangement of staggered fbers with drag free interfaces between the fibers and the matrix would have the same strength as found for a regular arrangement (as shown in figure 2) of the same fibers.

5. DEBONDED INTERFACES

High tensile stresses are typically present at the fiber ends for aligned short fiber reinforced composites. This indicates a potential site for fiber-matrix debonding, which has been observed experimentally with cavitation near fiber ends by Nutt and Duva [13] and Chokshi and Mukherjee [14]. Dragone [6] allowed debonding at the fiber ends to occur in his calculations when the normal stress across the interface reached a critical value. Values for the critical stress chosen by Dragone [6] ranged from 0.3 to 3 times the matrix yield stress. When the interface strength was 3 times the matrix yield stress, debonding was not seen to occur, effectively representing a strong interface in his model. His results indicate a rather sharp break in the stress-strain curve for a strongly bonded composite when debonding occurred, indicating that the debonding spreads rapidly across fiber ends. When debonding occurred in Dragone's [6] calculations, the effective hardening of the composite was drastically reduced compared to the case where no debonding occurred.

Debond Model

The configuration of the fibers is shown in figure 2. The unit cell is axisymmetric. In our work, the fiber ends are assumed to be initially debonded. While this may not reflect the true sequence of events occurring during stressing of

the pristine composite, the composite flow stress calculated at large composite strain will be valid as a model for materials in which the fiber end bond breaks during stressing. In addition, the periodic nature of the material represented by the unit cells means that the debonding occurs simultaneously at both ends of every fiber in the composite and this is reflected in the resulting stress-strain curve. Instead, in reality debonding can be expected to occur over a range of strain, with weak fiber ends failing first and strong ones later. Such effects cannot be captured in a single cell model. Thus, this investigation is not concerned with the initial portion of the stress-strain curve prevailing prior to and during debonding, but rather the focus is on the macroscopic flow behavior of the composite after extensive debonding has occurred. It should be noted that only the very end of the fiber debonds and the lateral surface of the fiber remains strongly bonded to the matrix. A further point is that there may be materials in which the fiber ends are never bonded to the matrix. This would occur if the matrix does not wet the fiber end (as opposed to the lateral surface of the fiber) and so processing fails to make any bond at the fiber end. This could occur even when strong bonds can form on the lateral surface of the fiber which often have differing chemistries from the fiber interior. A wide range of inclusion aspect ratios are considered in this work for reinforcement volume fractions of 0.2 and 0.4.

Results for Debonded Ends

Stress-strain curves are plotted in figure 14 for composites which have fibers with debonded ends, but which remain strongly bonded without sliding on their lateral surfaces. Curves are given for reinforcement aspect ratios ranging from 0.1 to 10. The volume fraction in all cases is f=0.4 and the matrix flow is perfectly plastic. As noted above, the details of the stress-strain curve are not relevant to a material which is initially bonded. However, the stress-strain curves are meaningful for

materials which are initially debonded at the end, perhaps due to processing and the limit flow stress is relevant to the strength of a heavily damaged fibrous composite. The transient stage to fully plastic flow occurs over less strain in this case than for the strongly end bonded composite. Indeed, the transition from elastic to fully plastic behavior in the end debonded case is rather abrupt. The limit stress is plotted versus inclusion aspect ratio in figure 7 for volume fractions of 0.2 and 0.4. Not surprisingly, the limit flow stress is very low for disk shaped reinforcements, since the plastic constraint between the disks end to end that normally provides the strengthening in these composites is relieved by the debonding. In fact, the composite is then weaker than the matrix for all disk shaped reinforcements. There is some strengthening for inclusion aspect ratios higher than 2, but it is only significant for the larger aspect ratios of 5 and 10. However, with debonded ends, the strength in these cases is only 1/2 and 1/3 of the strength of the fully bonded material respectively. This indicates a very significant influence of end debonding. It should be noted that the strength of the strongly end bonded composite with particulates of aspect ratio λ=2 is 50% greater than the matrix for f=0.2. Thus, the end debonding eliminates 1/3 of the composite strength for this case and the result is no stronger than the matrix. It is interesting to note that when the inclusions are disk shaped the composite with a lower volume fraction is stronger. For short fibers of aspect ratio 2 to 5, the strength is independent of volume fraction and when the aspect ratio is 10, the material with the lower volume fraction of fibers has the higher strength.

If one recognizes that the composite material with end debonded reinforcements has many penny shaped cracks, the behavior described above can be rationalized. The number of cracks per unit volume is $2f/\lambda D^3$ and so there will be the highest density of cracks when there is a high volume fraction or a low aspect ratio (i.e. disks). The density of microcracks will affect the limit strength of the

composite. Therefore, when the aspect ratio of the reinforcement is fixed, increasing the volume fraction should decrease the strength. In addition, at fixed volume fraction, decreasing the aspect ratio of the reinforcements will decrease the strength. These trends generally are seen to occur in the results depicted in figure 7 for the end debonded case.

The issue of staggered reinforcement is again addressed using the plane strain model with a perfectly plastic matrix. As before, the spacing between reinforcements is the same as the spacing for the axisymmetric model with a volume fraction of f=0.4. The limit flow stress versus reinforcement aspect ratio for both the regular (figure 3) and staggered (figure 4) cases when there is no end bond is plotted in figure 9. At low aspect ratio there is no difference in composite strength between the regular and staggered cases. However, when end debonding has occurred, increasing the aspect ratio causes the composite with staggered inclusions to be stronger than the composite with reinforcements aligned in the regular fashion. It should be noted that, although this staggering improves the strength of the composite when debonding has taken place compared to the fully aligned regular case, the composite strength remains lower than calculated for composites with freely sliding interfaces which have strongly bonded ends, which is in turn lower than the strength of the case with strongly bonded non-sliding interfaces.

The behavior of the plane strain system with reinforcements with debonded ends is somewhat different from the axisymmetric system. With reinforcements aligned in the regular arrangement in plane strain, the strength is insensitive to the aspect ratio of the reinforcements and in all cases studied strength is below that of the matrix. This seems to arise because deformation can be concentrated near the ends of the reinforcements and so the length of the reinforcements is irrelevant to the strength. In contrast, when the axisymmetric cell is used with end debonded inclusions, there is a weak dependence on aspect ratio of the inclusion.

Furthermore, if the aspect ratio is greater than 2, the composite is stronger than the matrix. An additional point is that when the reinforcements are staggered, significant deformation can only occur if neighboring reinforcements move relatively in opposite directions causing shearing deformation between them. This mode of deformation has been discussed by Mileiko [15] in the context of creep. The strength can be estimated, based on the stress necessary to allow shearing to occur in the matrix which will be the yield strength in shear of the matrix. This shear stress will transfer load to the fibers in a shear lag fashion. As a result, for the staggered end debonded inclusions in the plane strain perfectly plastic matrix case, the composite strength can be estimated to be $f\lambda\sigma_0 / 2\sqrt{3}$ over and above the strength arising from end effects of the reinforcements. The slope of the plot for the composite material with staggered end debonded reinforcements in figure 9 is approximately $f / 2\sqrt{3}$, so the Mileiko [15] model for the effect is quite reasonable.

6. DAMAGED CONTINUOUS FIBER COMPOSITES

Continuous fiber composites with strong fibers provide the greatest strengthening of metal matrices when the composite is loaded parallel to the direction of the fibers. The strain to failure is typically low in these composites, due to low fiber failure strain. In order to improve the ductility of these composites, the fiber-matrix interface is often tailored with coatings to allow sliding to occur. This weakened interface is then expected to spread the load transfer between the matrix and fibers as the fibers begin to fail. This effect will limit the extent of nearby fiber and matrix failure emanating from an initial fiber failure. In some cases significant fiber cracking can take place while the composite and matrix remain intact. If fibers are cracked throughout the specimen, the matrix will be the only continuous

constituent. Strength arising from the fibers can only be maintained by load transfer between the fibers and the matrix. However, extensive plastic flow will be possible, and a composite steady state flow strength will exist. Whether this steady state stress is achieved in practice will depend on the propagation of the fiber cracks into the matrix and the tendency of the matrix to fail. However, with a low strength ductile matrix, the strength may be determined by the limit stress of the composite when plastic flow occurs.

Model for Extensive Damage in a Continuous Fiber Composite

In this work an extensively damaged continuous fiber composite is modeled as a uniform array of fibers in which all fibers in the composite are cracked in a periodic manner and in which all cracks in one fiber are aligned with the cracks in all other fibers. This is shown in figure 5 along with the repeating cell. The intact length of the fiber is assumed to be 10 times the fiber diameter. The fibers in the calculations were modeled as elastic with Young's modulus set at 10 times the Young's modulus for the matrix. This is perhaps extreme for a metal matrix composite with ceramic fibers which will generally have a lower ratio of fiber to matrix modulus. The calculations were carried out using the axisymmetric formulation. One notable difference between this model and the previous axisymmetric model is that here there is no matrix material between adjacent ends of the pieces of the fiber. The fibers are initially touching end to end and are allowed to separate on loading. This is clearly appropriate for fibers which have broken after processing has been completed so that the matrix cannot intrude into the fiber breaks. The interfacial properties used for the calculations in this section are identical to those developed for interfacial sliding. That is, the interface is modeled as a thin layer of perfectly plastic material with a yield stress σ_i. The layer has a

thickness of 0.5% of the matrix thickness between fibers and is constrained in the radial direction, resulting in a shearable interface capable of transmitting any level of stress normal to the fiber surface effectively without yielding or debonding. The interface then has a yield strength in shear of $\tau_i = \sigma_i / \sqrt{3}$. Sliding will occur when the shear stress in the interface reaches this level. The matrix used for all these calculations for broken continuous fibers has a perfectly plastic flow behavior. The interface is assumed to have strengths ranging from τ_i/τ_o=0 to 1 where $\tau_o = \sigma_o / \sqrt{3}$ is the yield stress in shear of the matrix material. The value τ_i/τ_o=0 means sliding can take place freely whereas τ_i/τ_o=1 means the composite is strongly bonded.

Results for Damaged Continuous Fiber Composites with Sliding Interfaces

The stress-strain curve for an undamaged continuous fiber composite with volume fraction f=0.4 is plotted in figure 15. The curve exhibits a bilinear behavior with the barely visible knee occurring at the matrix yield strain. This behavior for longitudinal strain is well known. Also plotted in this figure are stress-strain curves for damaged continuous fiber composites. These composites also have a volume fraction of f=0.4 and are for interface strengths τ_i/τ_o ranging from 0 to 1. The existence of extensive cracking in the fibers results in a qualitatively different behavior and a substantial reduction in the composite strength. The damaged composites exhibit a limit flow stress not seen in the undamaged composite. A transient stage between elastic and fully plastic behavior is seen which decreases in extent with decreasing interfacial strength. When the interface can slip freely the composite experiences an essentially elastic-perfectly plastic behavior with a limit stress of Σ/σ_o=0.638. This is slightly higher than would be predicted by assuming the fiber plays no part in the strength so that the composite strength is obtained by multiplying the matrix volume fraction by the matrix yield stress to get

$$\Sigma_0=(1-f)\sigma_o \tag{5}$$

This results in $\Sigma_0/\sigma_o=0.6$ for the case of a volume fraction equal to 0.4. Thus, the inclusions do not play an important role in strengthening of the composite when the interface can slip freely, but instead have the opposite effect since their presence serves to eliminate matrix material.

When the interface is strong there is a rather long transient stage leading up to the limit stress. The limit stress has a value of $\Sigma/\sigma_o=2.87$ in this case. This limit stress can be estimated in the following way, based on the work of McMeeking [16] and Kim and McMeeking [17]. In the geometry of figure 5, plastic deformation takes place by the opening of the cracks or by the squeezing of material from between the fibers at the same time that the cracks open. If it is assumed that the latter mechanism occurs, the flow of material must be accommodated by a shear stress on the fiber surface equal to τ_i so that slip can occur there. As a result, for $z>0$ (the upper half of the reinforcement), the shear stress in the matrix is equal to

$$\sigma_{rz}=\frac{\tau_i}{1-f}\left(\frac{D}{2r}-\frac{2rf}{D}\right) \tag{6}$$

where the coordinate system is shown in figure 2. This form is such that $\sigma_{rz}=\tau_i$ on $r=D/2$ which is the reinforcement surface and $\sigma_{rz}=0$ at the outer lateral surface of the unit cell. In addition, σ_{rz} is in equilibrium with a hydrostatic stress

$$\sigma=\frac{4\tau_i f}{D(1-f)}\left(z-\frac{H}{4}\right) \tag{7}$$

for z>0 where this hydrostatic stress level has been selected to ensure that the average transverse stress is zero to the neglect of a deviatoric transverse stress. The axial deviatoric stress is independent of z and so need not be considered in the balancing of the shear stress against the axial stress. The axial deviatoric stress must be chosen so that it agrees with the flow of material as it stretches parallel to the fiber and is constrained by the yield criterion. The result is rather complicated. On the other hand, a reasonable, albeit high estimate is that the axial deviatoric stress is σ_o everywhere in the matrix. As a consequence, the axial stress in the matrix is

$$\sigma_{zz} = \sigma_o + \frac{4\tau_i f}{D(1-f)}\left(z - \frac{H}{4}\right) \tag{8}$$

As long as H/D is large compared to 1, this estimate is reasonably good in comparison with more exact numerical results, except that it neglects the details of the stress distribution near the fiber breaks and near the center of the reinforcement. However, it can be used to estimate the limit flow strength of the composite material. At the fiber breaks, all of the composite stress is sustained by the matrix since the fiber stress there is zero. Therefore the limit flow stress is estimated to be 1-f times σ_{zz} at z=H/2. Thus

$$\Sigma = (1-f)\sigma_o + \lambda f \tau_i \tag{9}$$

which predicts a value of Σ/σ_o=2.91 for the strong interface when $\tau_i=\tau_o$. This should be compared with a numerical result of Σ/σ_o=2.87 for this case as depictedin figure 15 at $\bar{\varepsilon}/\varepsilon_o = 8$. As noted before, when τ_i=0, the limit flow stress is predicted well by $\Sigma = (1-f)\sigma_o$ so equation (9) works well for that case as well. Comparison of equation (9) with the numerical results shown in figure 15 shows that the agreement is excellent when Σ is taken to be the value of $\bar{\sigma}$ when $\bar{\varepsilon}/\varepsilon_o = 8$. That is, the

numerical results show that Σ is almost linear in τ_i ranging from the strengthless interface (τ_i=0) to the full strength interface (τ_i=τ_o).

7. DISCUSSION

The influence of interfacial properties on the flow strength of metal matrix composites has been analytically investigated with the finite element method. Interfacial behavior examined included strong interfaces, interfaces which could shear but were strong normal to the inclusion surface, and interfaces which were debonded at the ends of the inclusions but strong on the sides of the inclusions. The effect of staggered inclusions was investigated for each of these interfacial behaviors. In addition a study was done on extensively damaged continuous fiber composites.

Strong Interfaces

The calculated strength of composites reinforced with a uniform array of discontinuous inclusions using an axisymmetric cell model depends on the aspect ratio of the cell used. A cell in which the spacing between reinforcements end to end is the same as the spacing side to side was used to represent typical or average situations. The calculated composite strengths for inclusion aspect ratios other than 1 using these cells is less than calculated by Bao et al. [1] who used cells in which the cell aspect ratio was equal to the inclusion aspect ratio. This difference arises because the distance between inclusions for the cells of Bao et al. is smaller parallel to the smallest inclusion dimension. That is, fibers are closer together side to side and disks are closer together end to end. This closer spacing in the cells of Bao et al. leads to a higher level of constraint in their model, and thus higher calculated composite strengths. The reduction in constraint resulting from the cells used in our work,

which have the same spacing side to side as end to end, is greater for disk shaped inclusions than for fiber shaped inclusions. This means a greater reduction in strength is seen for disk reinforced composites than for fiber reinforced composites, as compared to the results of Bao et al.,. Surprisingly, the inclusion shape providing the least strengthening in our calculations is not a unit cylinder, but a slightly flattened cylinder with aspect ratio 0.5. This demonstrates the importance of constraint between reinforcements side to side in these composites. When the matrix is strongly bonded to the inclusions, staggered placement of the reinforcements in the matrix results in a reduction in the strength of the composite. Again, this emphasizes the importance of constraint between fibers side to side, as the staggered arrangement relieves some of the constraint.

Sliding Interfaces

Composites which have interfaces which are allowed to shear, but remain strongly bonded in the direction normal to the fiber surfaces, experience a reduction in strength relative to their strongly bonded counterparts. Composites with fiber shaped inclusions are more seriously affected by interfacial sliding than disk shaped inclusions. However the fibers continue to provide more strengthening than disks. It is not too surprising that interfacial sliding does not strongly affect the strength of composites with disks since the largest fiber surface in these composites is normal to the loading direction. However, even particulate shaped inclusions, with aspect ratios up to 2, show little sensitivity to interfacial sliding. This indicates that the constraint between fiber ends remains important for these aspect ratios. Only with the higher reinforcement aspect ratios does the constraint between fibers side to side take on a dominant role. When $\tau_i/\tau_0=0$ and therefore interfacial sliding takes place freely, the strength of the composite is due primarily to the difficulty of flow around the fiber corners. When the matrix hardens but the shearable interface does not, the

resulting composite hardening behavior reflects the latter feature with a lower hardening exponent than seen for the strongly bonded composite. With increasing matrix hardening the composite strength shows little improvement. This indicates that the strength of matrix hardening composites with nonhardening interfaces is dominated by the interfacial behavior, and not the matrix behavior. Staggered arrangement of reinforcements when the interfaces are free to slip has little effect on the composite strength. As indicated previously, the strength of these composites is linked to the flow around inclusion corners. The domain of influence of inclusion corners does not change with staggered reinforcements for a given volume fraction.

Debonded Interfaces

Calculations for reinforcements with debonded interfaces were done with an axisymmetric cell model. The repeating nature of these cells in this model means that all fibers in the composite are debonded at both ends. As a result, the composite can be viewed as having an extensive array of cracks which are aligned. Not surprisingly, the resulting composite strength is very low. Composites with fiber shaped inclusions are somewhat stronger than with disk shaped inclusions. This can be attributed to the effective density of cracks which increases with the aspect ratio of the diameter to the height for axisymmetric reinforcements. In addition, the effective density of cracks increases with the volume fraction of reinforcements. Thus, the weakest cases when the reinforcement ends are debonded are all high volume fractions and cases with disks with a large diameter to thickness ratio.

Damaged Continuous Fibers

Extensively damaged continuous fiber composites result in a steady state flow stress for the composite. The limit strength of the damaged composite when there is no interfacial shear strength and thus when slip can occur freely is given

approximately by the rule of mixtures with the assumption that the fibers provide zero strength contribution to the composite. The composite limit strength increases linearly with interfacial strength as long as the interfacial shear strength is below the matrix yield strength in shear. Increase of interfacial strength beyond that level has no effect on composite strength when the matrix is perfectly plastic. The composite limit strength increases linearly also with the volume fraction of fibers and the aspect ratio of the broken pieces of fiber, as given by eq. (9).

Closing Comments

Discontinuous reinforced composites are strongest when the interface is strong. Composites which have an interface that can shear but are strongly bonded normal to the fiber surface are stronger than composites with debonding at inclusion ends and a strong interface at the inclusion sides. The strength of composites with shearable interfaces is controlled primarily by the interfacial strength. Composites with debonding ends, on the other hand, are dominated primarily by the matrix properties. The strength of damaged continuous fiber composites also depend strongly on the matrix behavior. These composites are similar to short fiber composites with debonding ends, and therefore it is likely that debonded short fiber composites with shearable interfaces would behave in a similar way as the damaged continuous fiber composites with shearable interfaces. Staggered arrangement of the reinforcements reduces the strength of strongly bonded composites. However, staggering can be beneficial in the case of end debonded fiber composites provided the fiber aspect ratio is sufficiently large. Fiber shaped inclusions provide the greatest strengthening, both for strongly bonded composites and composites with weakened interfaces.

It should be noted that the limit flow strength of a composite material with brittle reinforcements may not be achieved if the reinforcements fail or if the matrix

ruptures before the applied stress reaches the limit flow strength. Therefore, the concept of the limit flow strength would not be relevant to such materials. However, the limit flow strength determines the level of stress which can be achieved without fiber failure and without matrix rupture in those materials and therefore governs the transition from elastic response to elastic-plastic behavior. Consequently, the limit flow strength provides valuable insights even for materials in which reinforcement failure or matrix rupture occurs during the transition from elastic to plastic response. In addition, the limit flow strength is a valuable concept for all metal matrix composite materials at high temperature where the reduction of the yield stress will make fully plastic flow possible without fiber failure. Furthermore, the limit flow strength provides a guidance on the creep strength of reinforced composites since the creep strength is closely related to constraint in fully plastic flow.

ACKNOWLEDGMENT

This research was supported by the DARPA University Research Initiative at the University of California, Santa Barbara (ONR Prime Contract N00014-92-J-1808). The ABAQUS code was provided by Hibbitt, Karlsson and Sorensen Inc., Pawtucket, R.I. through an academic license.

REFERENCES

[1] G. Bao, J. W. Hutchinson, and R. M. McMeeking, "Particle Reinforcement of Ductile Matrixes against Plastic Flow and Creep", *Acta Metall. Mat.*, V39 N8:1871 (1991)

[2] T. L. Dragone, "Effects of Interface Properties on the Mechanical Behavior of Short Fiber Metal Matrix Composites", AIAA-91-0981 (1991)

[3] D. B. Zahl and R. M. McMeeking, "The Influence of Residual Stress on the Yielding of Metal Matrix Composits", *Acta Metall. Mat.*, V39 N6:1117 (1991)

[4] D. B. Zahl, S. Schmauder and R. M. McMeeking, "Transverse Strength of Metal Matrix Composites Reinforced with Strongly Bonded Continuous Fibers", to be published (1993)

[5] T. Christman, A. Needleman, and S. Suresh, "An Experimental and Numerical Study of Deformation in Metal and Ceramic Composites", *Acta Metall. Mat.*, V37 N11:3029 (1989)

[6] T. L. Dragone and W. D. Nix, "Geometric Factors Affecting the Internal Stress Distribution and High Temperature Creep Rate of Discontinuous Metal Matrix Composites", *Acta Metall. Mat.*, V38 N10:1942 (1990)

[7] C. Hom and R. M. McMeeking, "Plastic Flow in Ductile Materials Containing a Cubic Array of Rigid Spheres", *Int. J. Plast.*, V7 N4:255 (1991)

[8] G. Bao and R. M. McMeeking, unpublished work

[9] S. Gunawardena, "Constitutive Equations for Weakly Bonded Metal Matrix Composites", Ph.D. Dissertation, Department of Mechanical and Environmental Engineering, University of California, Santa Barbara (1992)

[10] K. Herath, "Constitutive Equations for Fully Bonded Metal Matrix Composites", Ph.D. Dissertation, Department of Mechanical and Environmental Engineering, University of California, Santa Barbara (1992)

[11] S. Jansson and F. A. Leckie, "Mechanical Behavior of a Continuous Fiber-reinforced Aluminum Matrix Composite Subjected to Transverse and Thermal Loading", *J. Mech. Phys. Sol.*, V40 N3:593 (1992)

[12] ABAQUS Finite Element Program, Version 4.7, c1988, Hibbitt, Karlsson, and Sorensen, Inc., Pawtucket, R.I.

[13] S. R. Nutt and J. M. Duva, "A Failure Mechanism in Al-SiC Composites", *Scripta Metall.*, V20:1055 (1986)

[14] A. H. Chokshi and A. K. Mukherjee, *Proc. Superplast. Aero.* (1988)

[15] S. T. Mileiko, "Steady State Creep of a Composite Material with Short Fibers", *J. Mater. Sci.*, V45:254 (1970)

[16] R. M. McMeeking, "Power Law Creep of a Composite Material Containing Discontinuous Rigid Aligned Fibers", to appear in *Int J. Sol. Struct.*, (1993)

[17] K. T. Kim and R. M. McMeeking, "Power Law Creep with Interface Slip and Diffusion in a Composite Material", to be published, (1993)

FIGURE CAPTIONS

Figure 1: Matrix stress-strain behavior.

Figure 2: a) Hexagonal array of aligned fibers; b) hexagonal cell; c) axisymmetric cell.

Figure 3: Plane strain cell for inclusions aligned in the regular arrangrement.

Figure 4: Plane strain cell for staggered inclusions.

Figure 5: Configuration and unit cell for damaged continuous fiber composites.

Figure 6: Composite stress-strain curves for strong interfaces and a perfectly plastic matrix as computed with the axisymmetric cell. Inclusion aspect ratios range from 0.1 to 10 and the volume fraction is 0.4.

Figure 7: Limit flow stress versus inclusion aspect ratio for volume fractions ranging from 0.2 to 0.5 as computed with the axisymmetric cell and perfectly plastic matrix.

Figure 8: Stress-strain curves for composites with strong interfaces in a strain hardening matrix with n=10 as computed with the axisymmetric cell.

Figure 9: Limit flow stress versus aspect ratio for aligned and staggered reinforcements with a strong interface as computed with plane strain cells and a perfectly plastic matrix.

Figure 10: Stress-strain curves for composites with shearing interfaces with interfacial strengths ranging from zero to strong as computed with the axisymmetric cell. The matrix is perfectly plastic. The volume fraction is 0.4 and the inclusion aspect ratio is 10.

Figure 11: Composite stress versus interfacial strength as computed with the axisymmetric cell. Inclusionspect ratios λ range from 0.1 to 10. The matrix is perfectly plastic and the volume fraction of fibers f is 0.4.

Figure 12: Stress-strain curves for composites with shearing interfaces with interfacial strengths ranging from zero to strong computed with the axisymmetric cell. The matrix is hardening with n=10. The volume fraction of fibers is 0.4 and the inclusion aspect ratio is 10.

Figure 13: Stress-strain curves for composites with shearing interfaces with interfacial strengths ranging from zero to strong computed with the axisymmetric cell. The matrix is hardening with n=5. The volume fraction of fibers is 0.4 and the inclusion aspect ratio is 10.

Figure 14: Stress-strain curves for composites with inclusions which have debonds at the ends computed with the axisymmetric cell. Reinforcement aspect ratios range from 0.1 to 10. The matrix is perfectly plastic and the volume fraction of fibers is 0.4.

Figure 15: Stress-strain curves for an undamaged continuous fiber composites and for damaged fiber composites with shearable interfaces computed with the axisymmetric cell. Interfacial strengths range from zero to strong. The matrix is perfectly plastic, the aspect ratio of the broken fiber pieces is 10, and the volume fraction of fibers is 0.4.

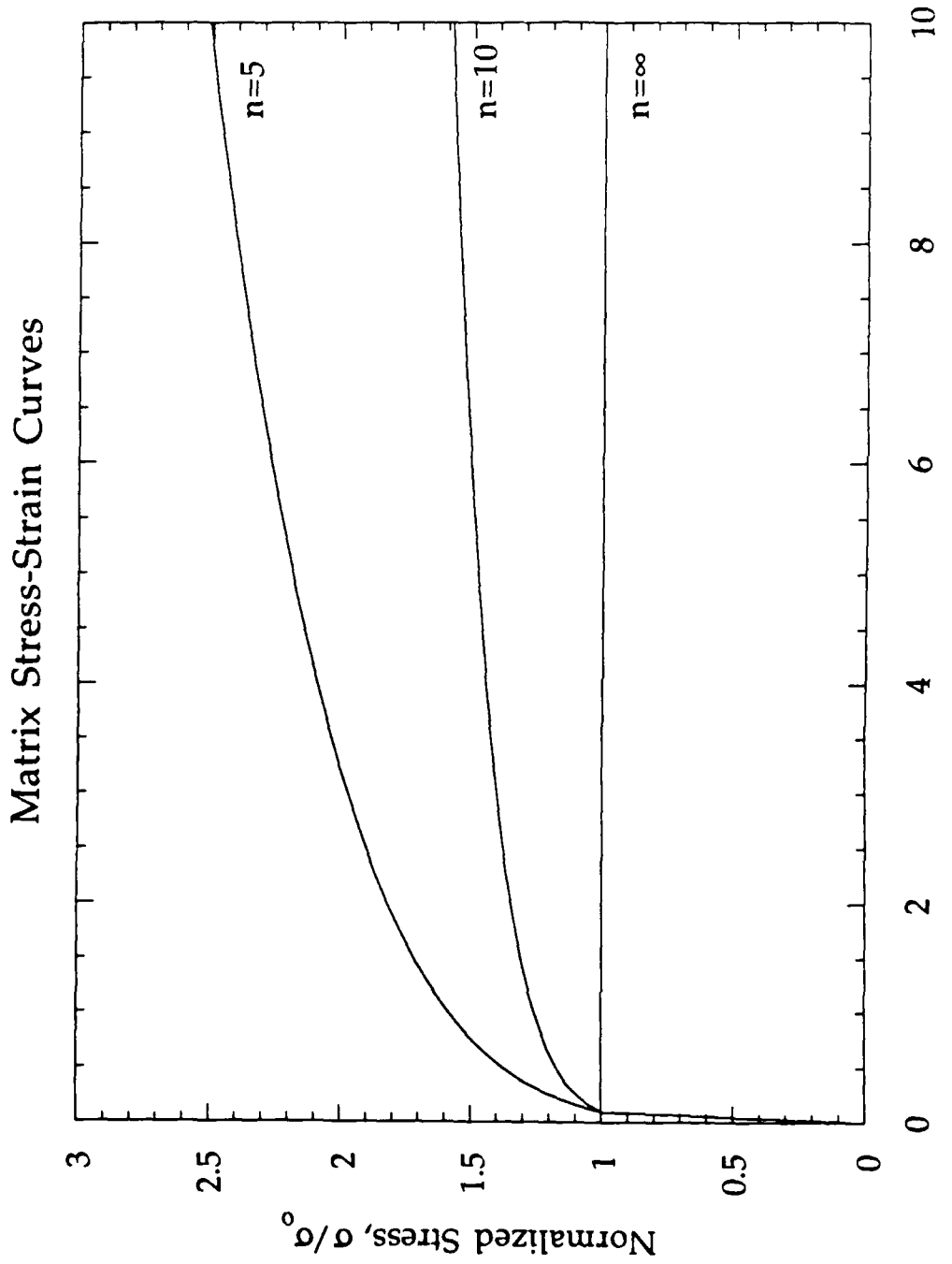
Matrix Stress-Strain Curves
n=5
n=10
n=∞
Normalized Stress, σ/σ_o
Normalized Strain, ε/ε_o
0
0.5
1
1.5
2
2.5
3
0
2
4
6
8
10

Figure 1

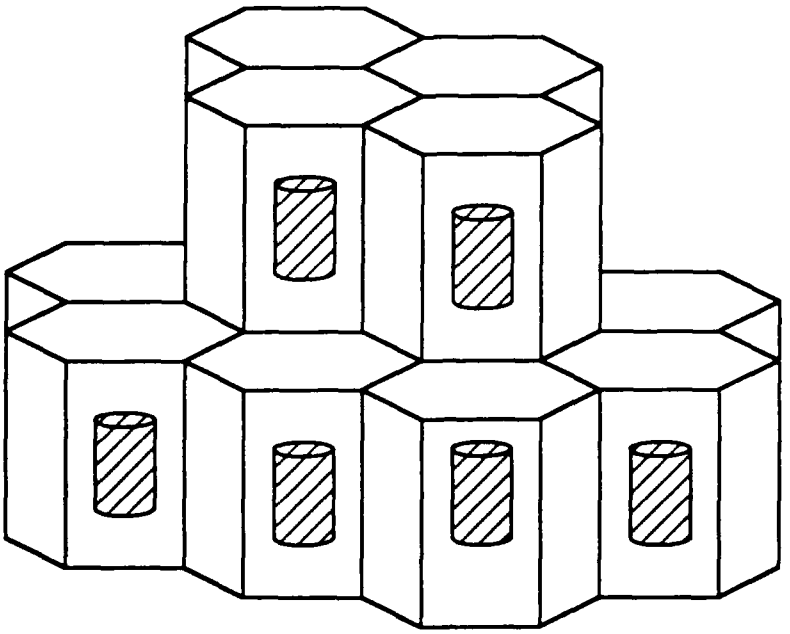

(a)

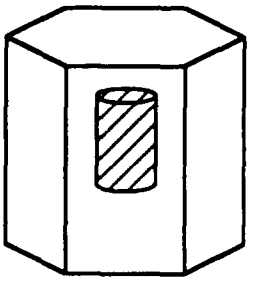

(b)

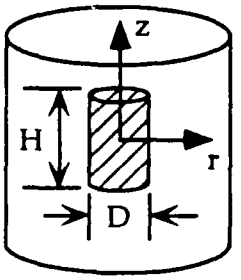

(c)

Figure 2

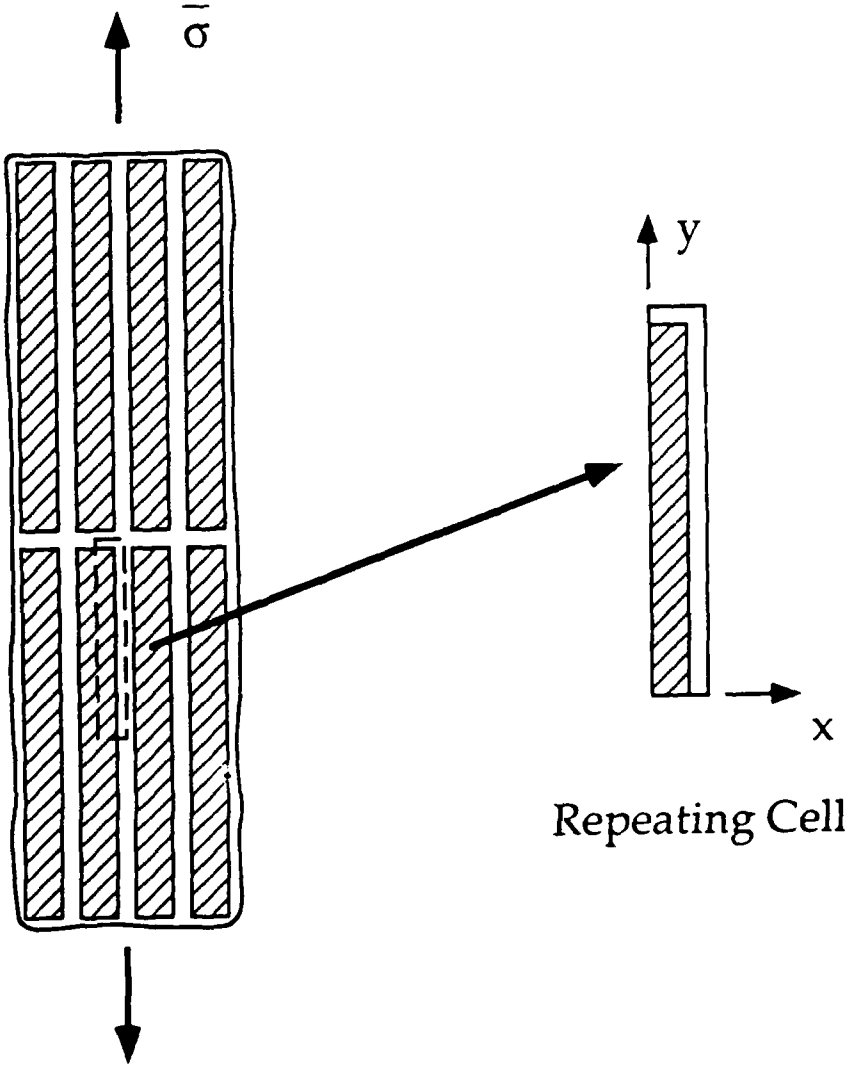

Figure 3

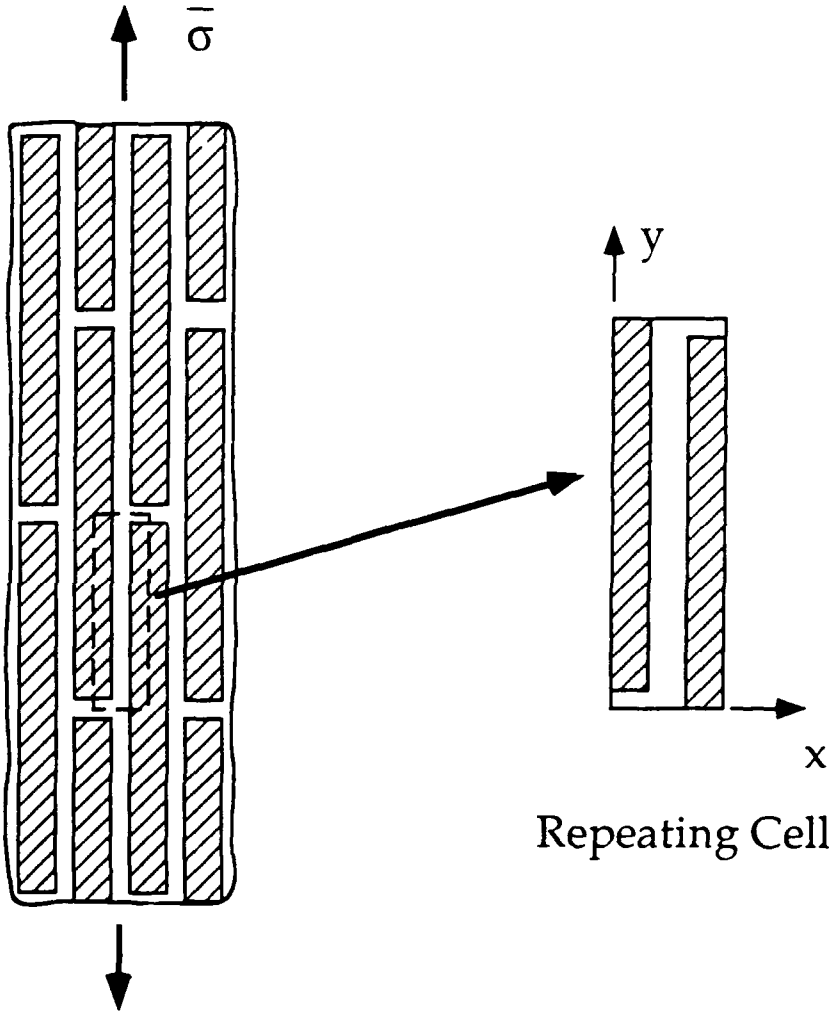

Repeating Cell

Reinforcement Configuration

Figure 4

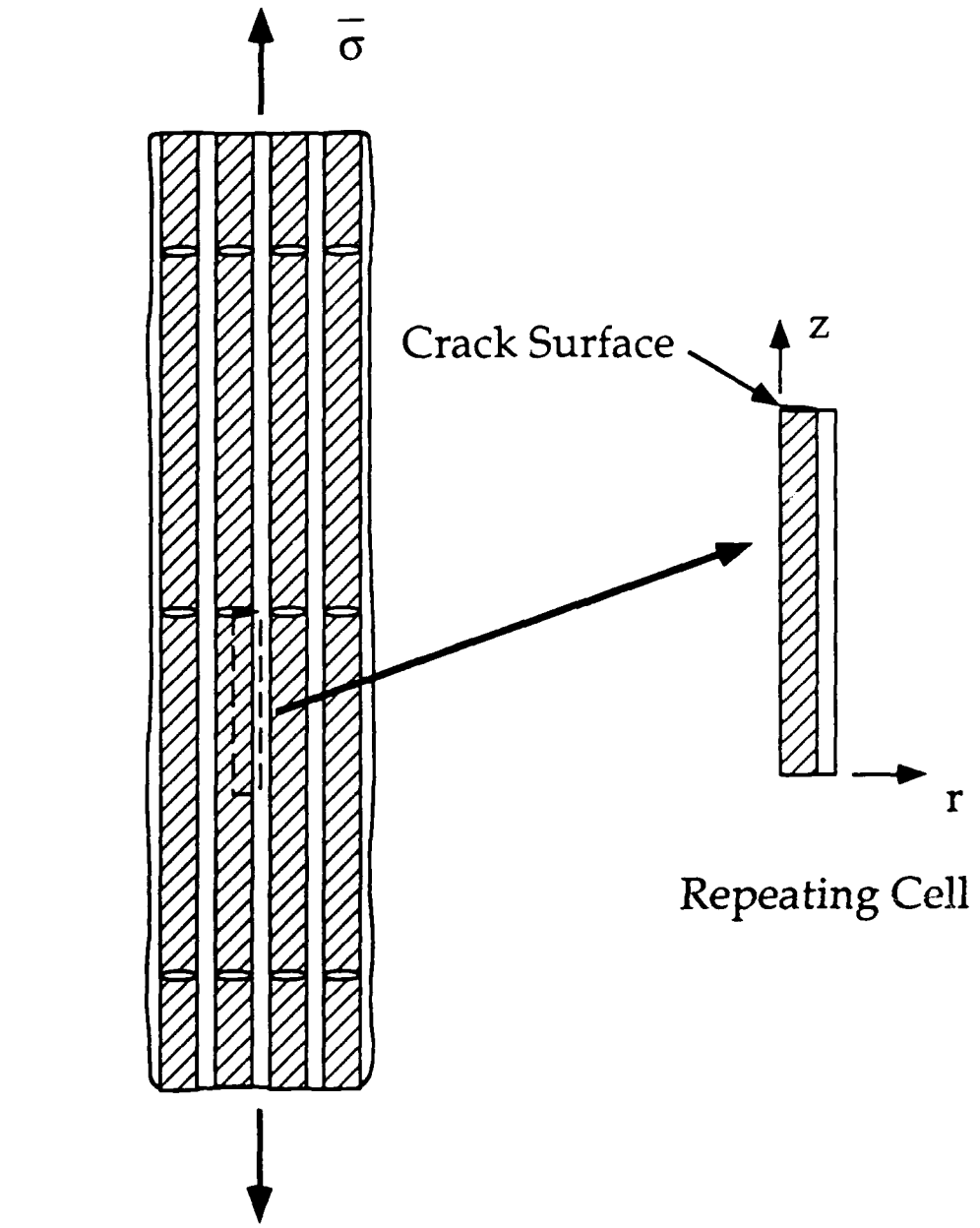
$\bar{\sigma}$
Crack Surface
z
r
Repeating Cell
Reinforcement Configuration

Figure 5

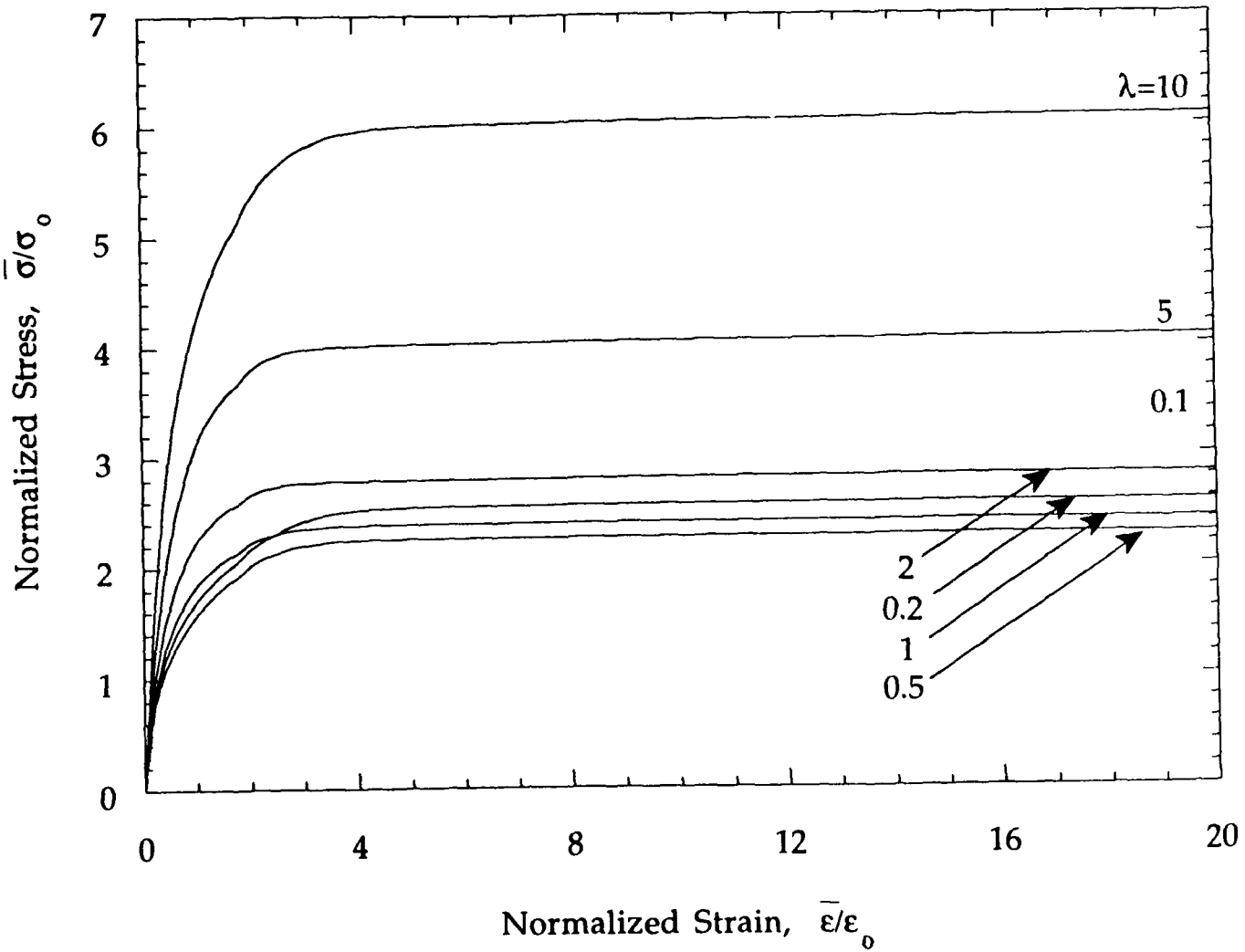
Normalized Stress, $\bar{\sigma}/\sigma_o$
Normalized Strain, $\bar{\varepsilon}/\varepsilon_o$
λ=10
5
0.1
2
0.2
1
0.5
0
1
2
3
4
5
6
7
0
4
8
12
16
20

Figure 6

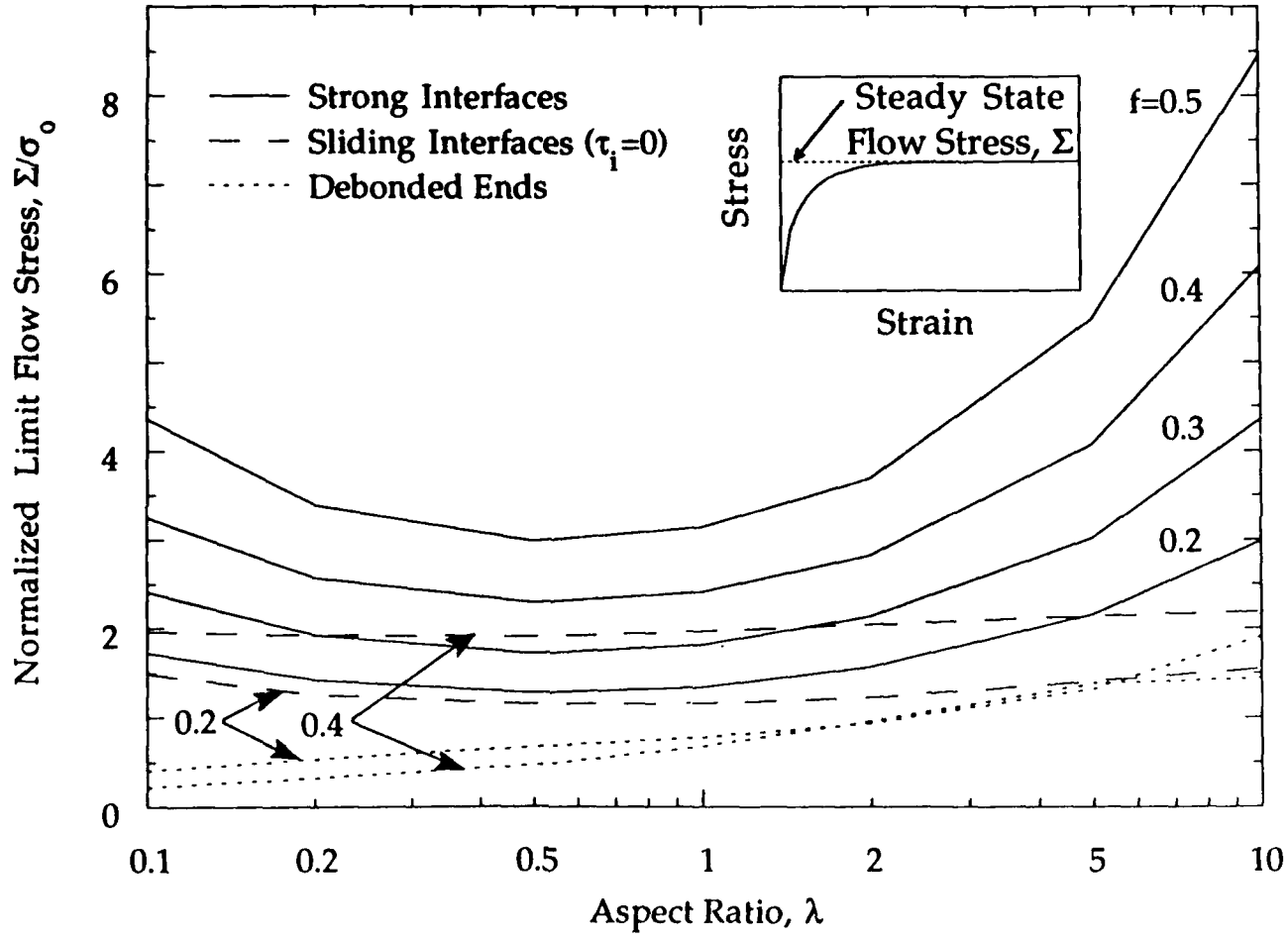
Strong Interfaces
Sliding Interfaces (τ_i=0)
Debonded Ends
Steady State
Flow Stress, Σ
Stress
Strain
f=0.5
0.4
0.3
0.2
0.2
0.4
Normalized Limit Flow Stress, Σ/σ_o
Aspect Ratio, λ
0
2
4
6
8
0.1
0.2
0.5
1
2
5
10

Figure 7

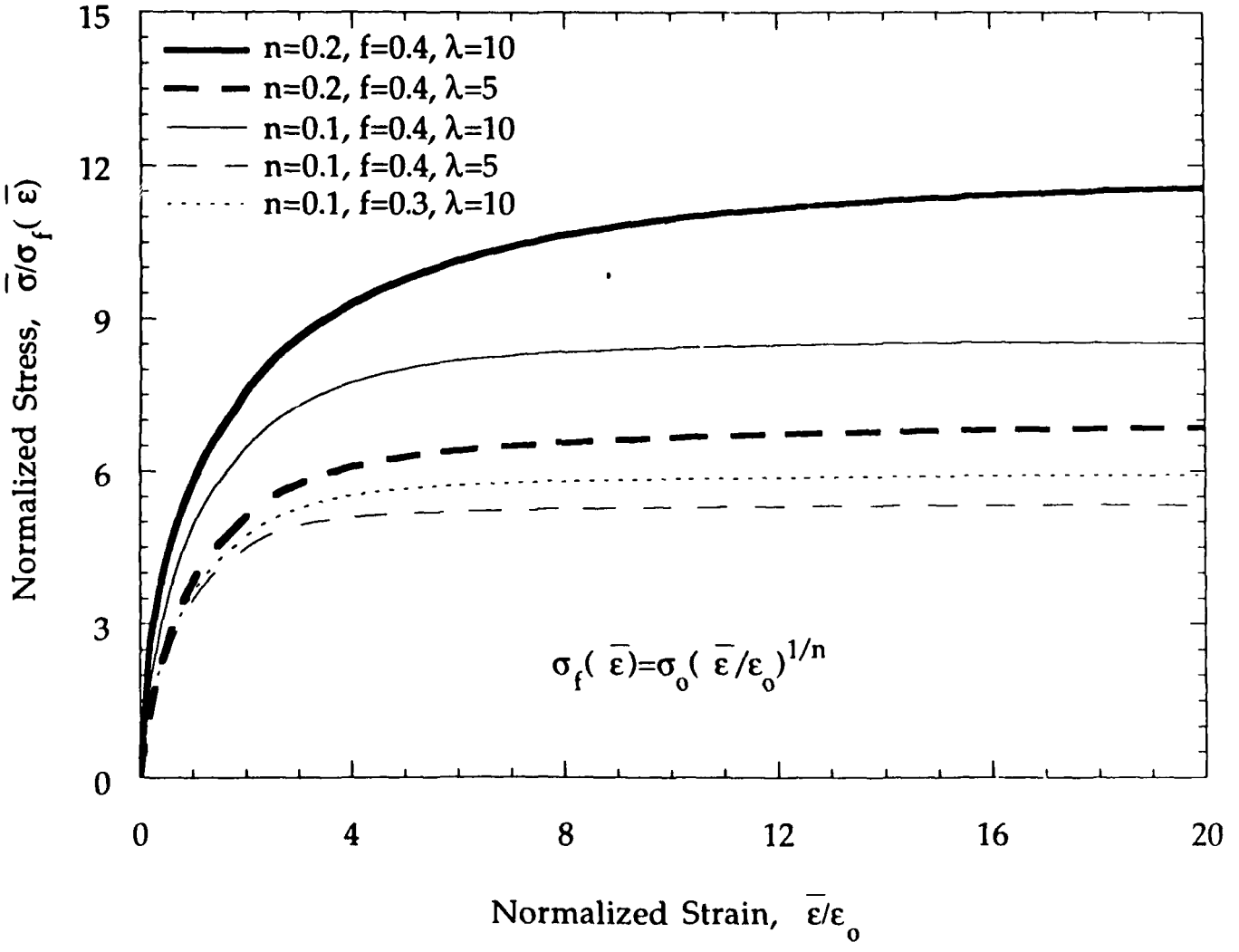
n=0.2, f=0.4, λ=10
n=0.2, f=0.4, λ=5
n=0.1, f=0.4, λ=10
n=0.1, f=0.4, λ=5
n=0.1, f=0.3, λ=10
$\sigma_f(\bar{\varepsilon})=\sigma_o(\bar{\varepsilon}/\varepsilon_o)^{1/n}$
Normalized Stress, $\bar{\sigma}/\sigma_f(\bar{\varepsilon})$
Normalized Strain, $\bar{\varepsilon}/\varepsilon_o$
0
3
6
9
12
15
0
4
8
12
16
20

Figure 8

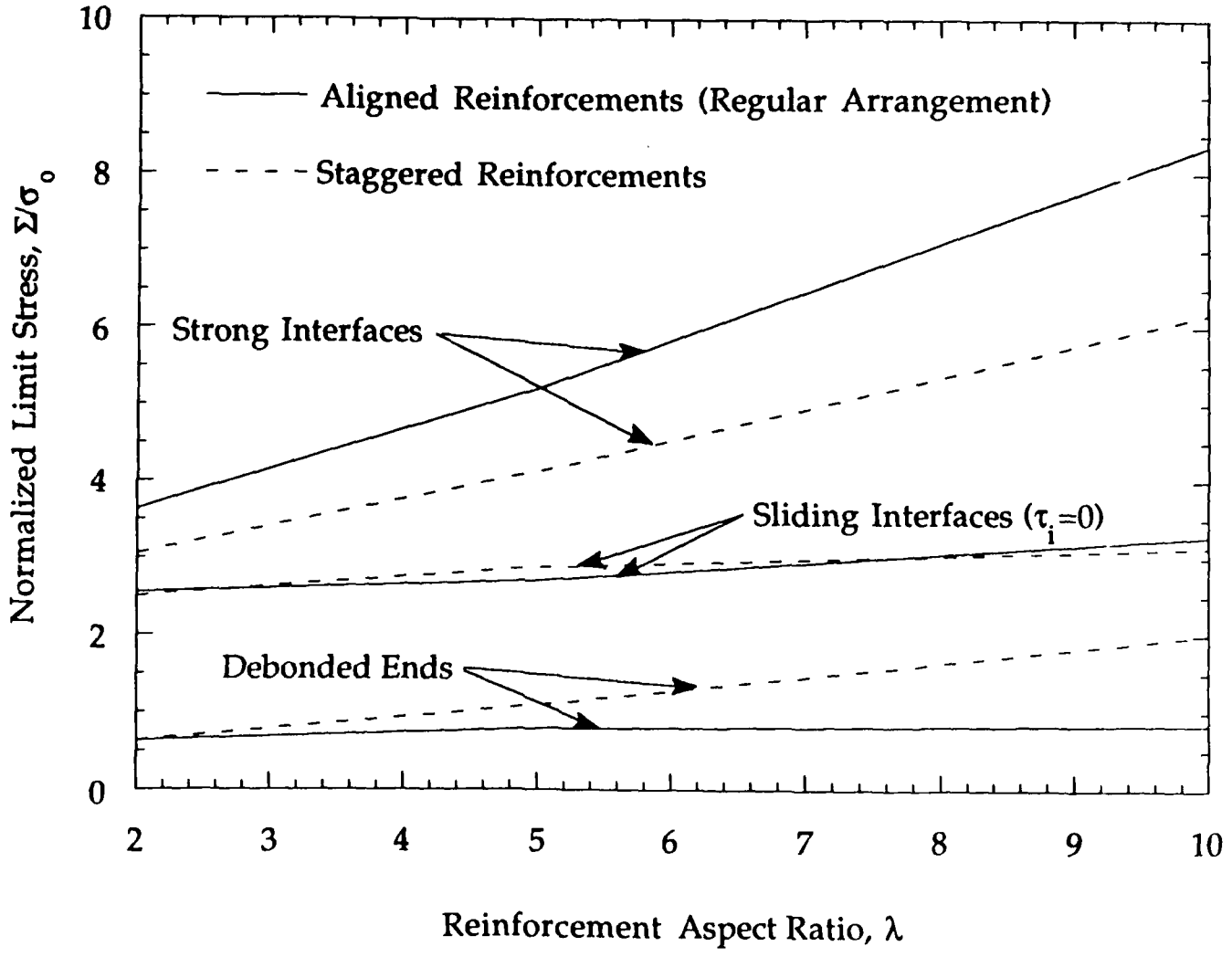
Aligned Reinforcements (Regular Arrangement)
Staggered Reinforcements
Strong Interfaces
Sliding Interfaces (τ_i=0)
Debonded Ends
Normalized Limit Stress, Σ/σ_o
Reinforcement Aspect Ratio, λ
0
2
4
6
8
10
2
3
4
5
6
7
8
9
10

Figure 9

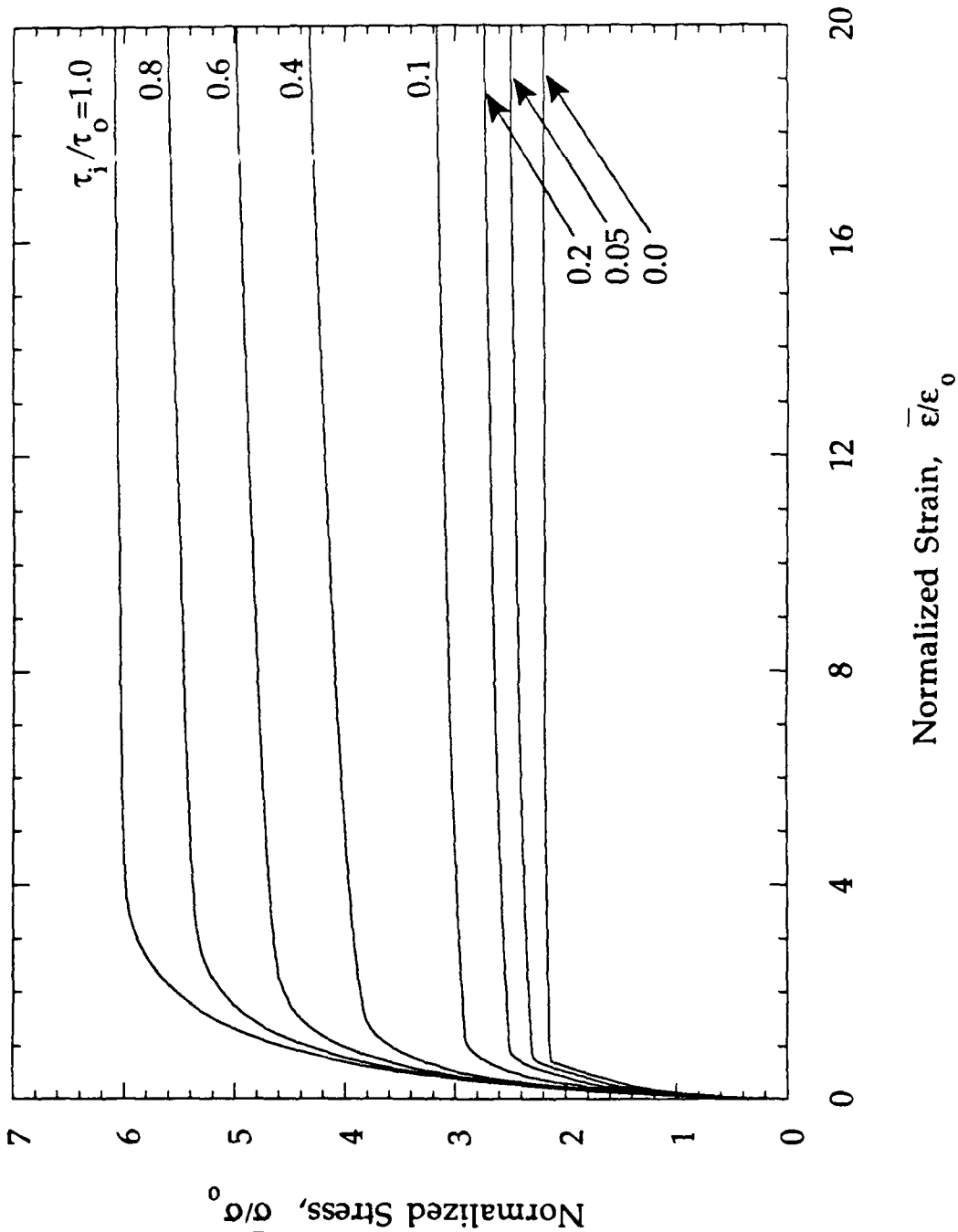
Normalized Stress, $\bar{\sigma}/\sigma_o$
Normalized Strain, $\bar{\varepsilon}/\varepsilon_o$
τ_i/τ_o=1.0
0.8
0.6
0.4
0.1
0.2
0.05
0.0
0
1
2
3
4
5
6
7
0
4
8
12
16
20

Figure 10

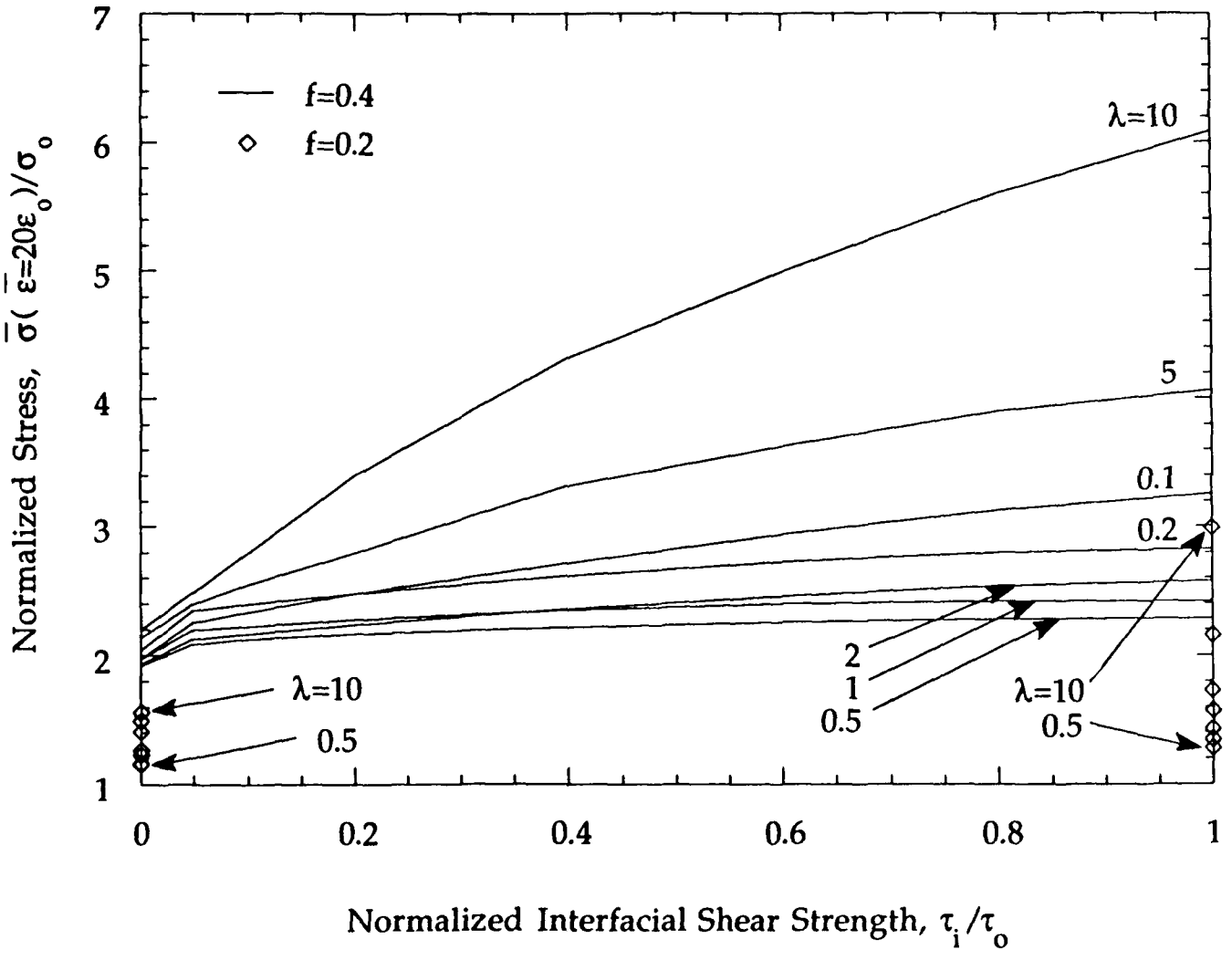
f=0.4
f=0.2
λ=10
5
0.1
0.2
2
1
0.5
λ=10
0.5
λ=10
0.5
Normalized Stress, $\bar{\sigma}(\bar{\varepsilon}=20\varepsilon_o)/\sigma_o$
Normalized Interfacial Shear Strength, τ_i/τ_o
1
2
3
4
5
6
7
0
0.2
0.4
0.6
0.8
1

Figure 11

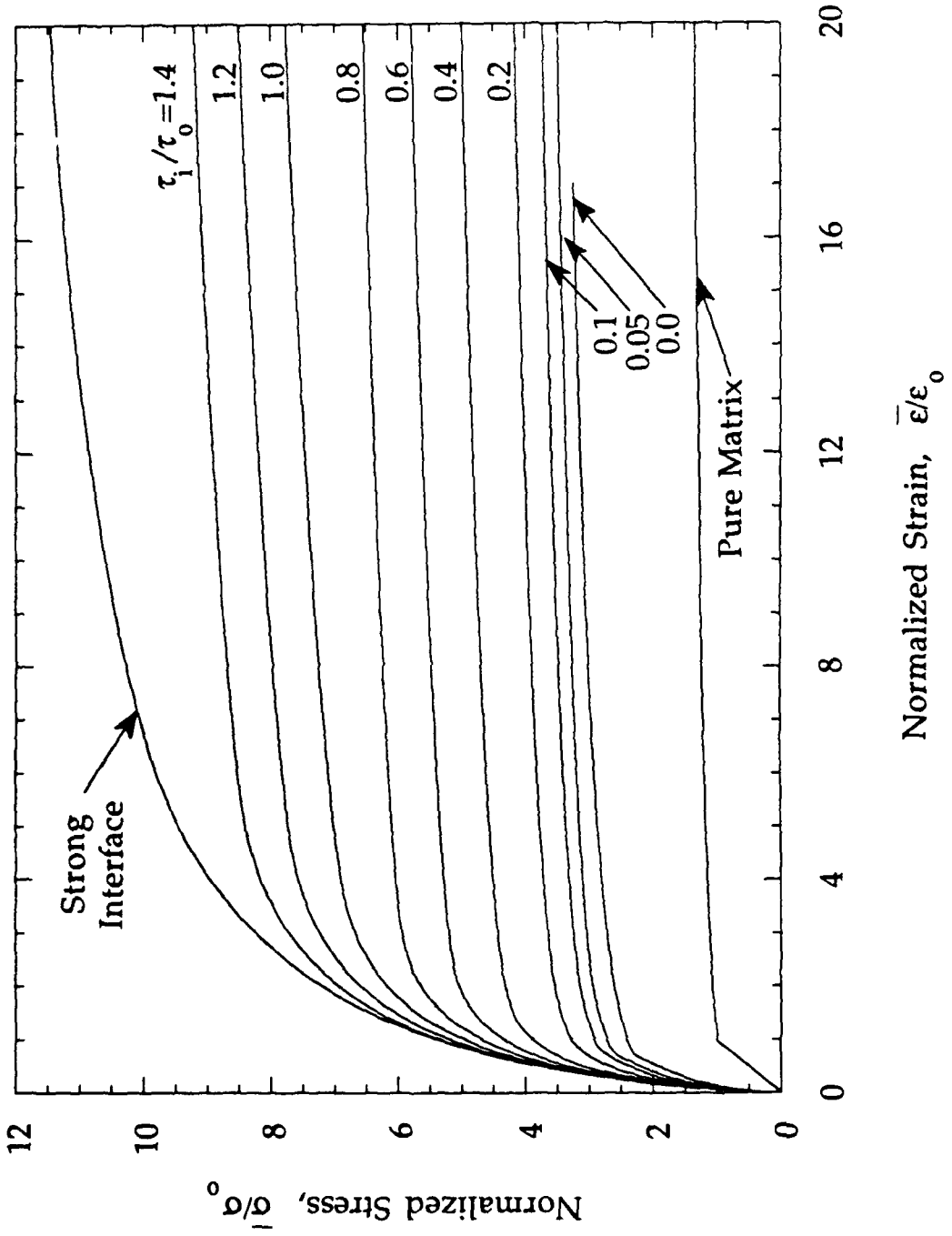
Normalized Stress, $\bar{\sigma}/\sigma_o$
Normalized Strain, $\bar{\epsilon}/\epsilon_o$
0
2
4
6
8
10
12
0
4
8
12
16
20
Strong Interface
τ_i/τ_o=1.4
1.2
1.0
0.8
0.6
0.4
0.2
0.1
0.05
0.0
Pure Matrix

Figure 12

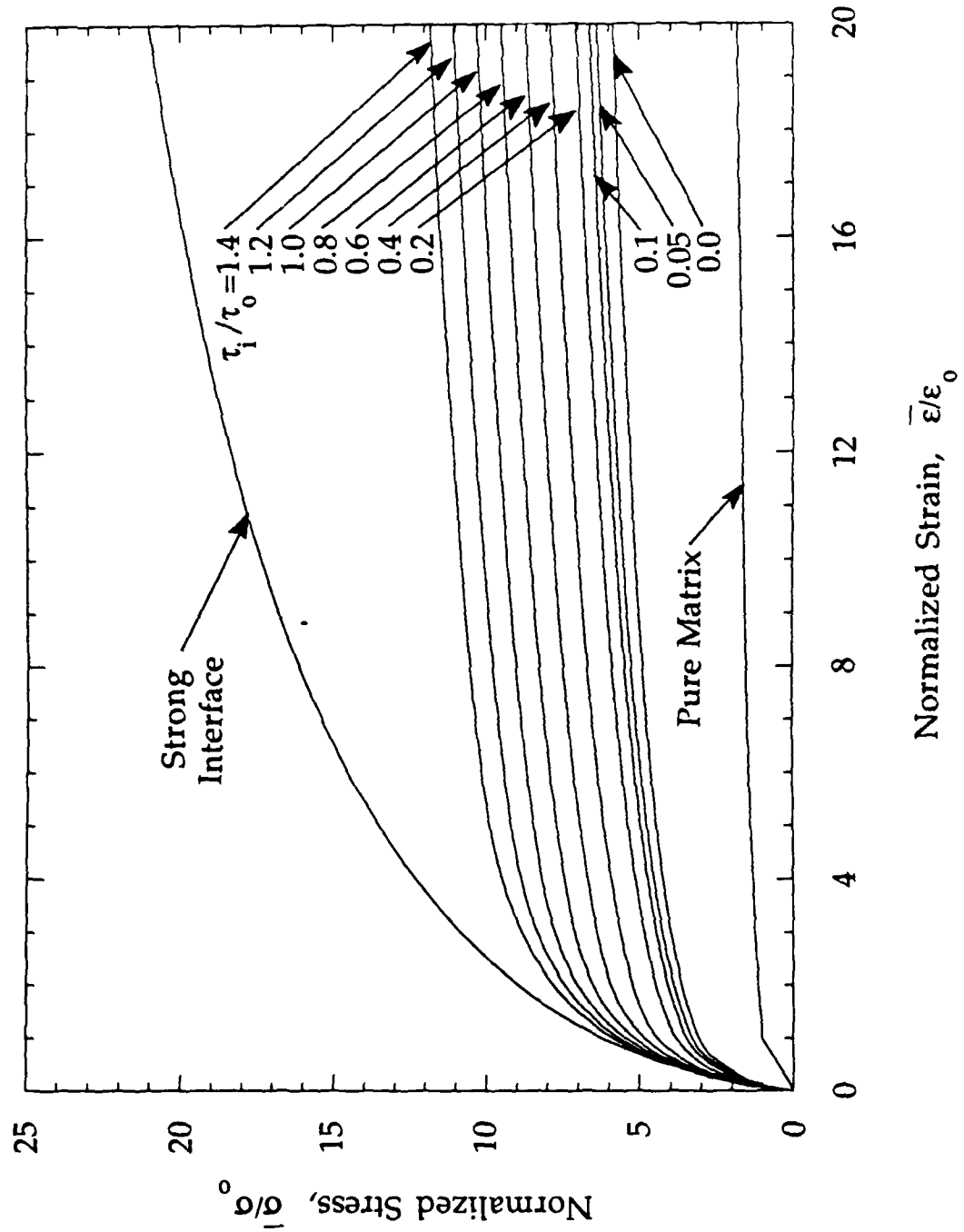
Normalized Stress, $\bar{\sigma}/\sigma_o$
Normalized Strain, $\bar{\varepsilon}/\varepsilon_o$
τ_i/τ_o=1.4
1.2
1.0
0.8
0.6
0.4
0.2
0.1
0.05
0.0
Strong Interface
Pure Matrix
0
5
10
15
20
25
0
4
8
12
16
20

Figure 13

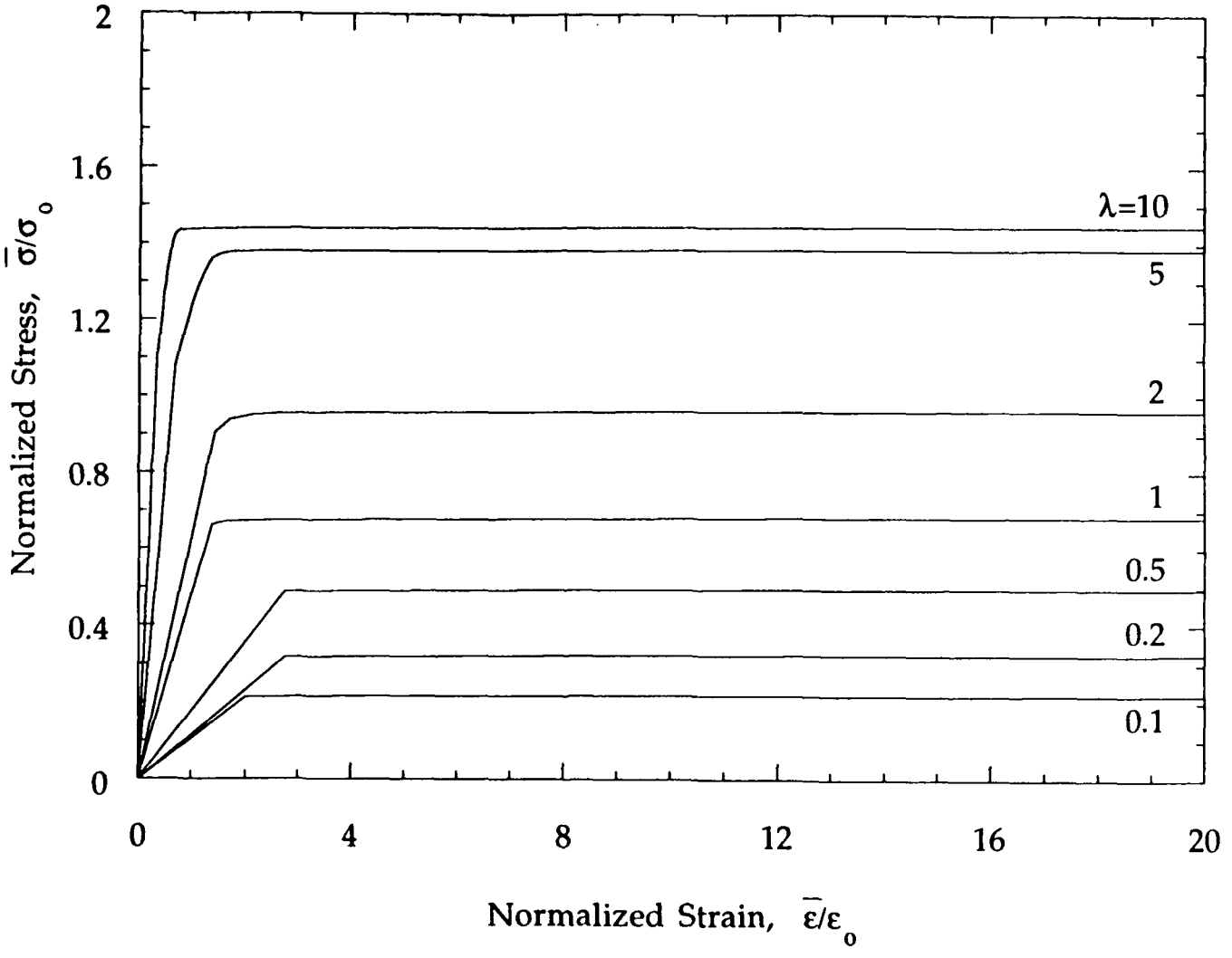
2
1.6
1.2
0.8
0.4
0
Normalized Stress, $\bar{\sigma}/\sigma_o$
λ=10
5
2
1
0.5
0.2
0.1
0
4
8
12
16
20
Normalized Strain, $\bar{\varepsilon}/\varepsilon_o$

Figure 14

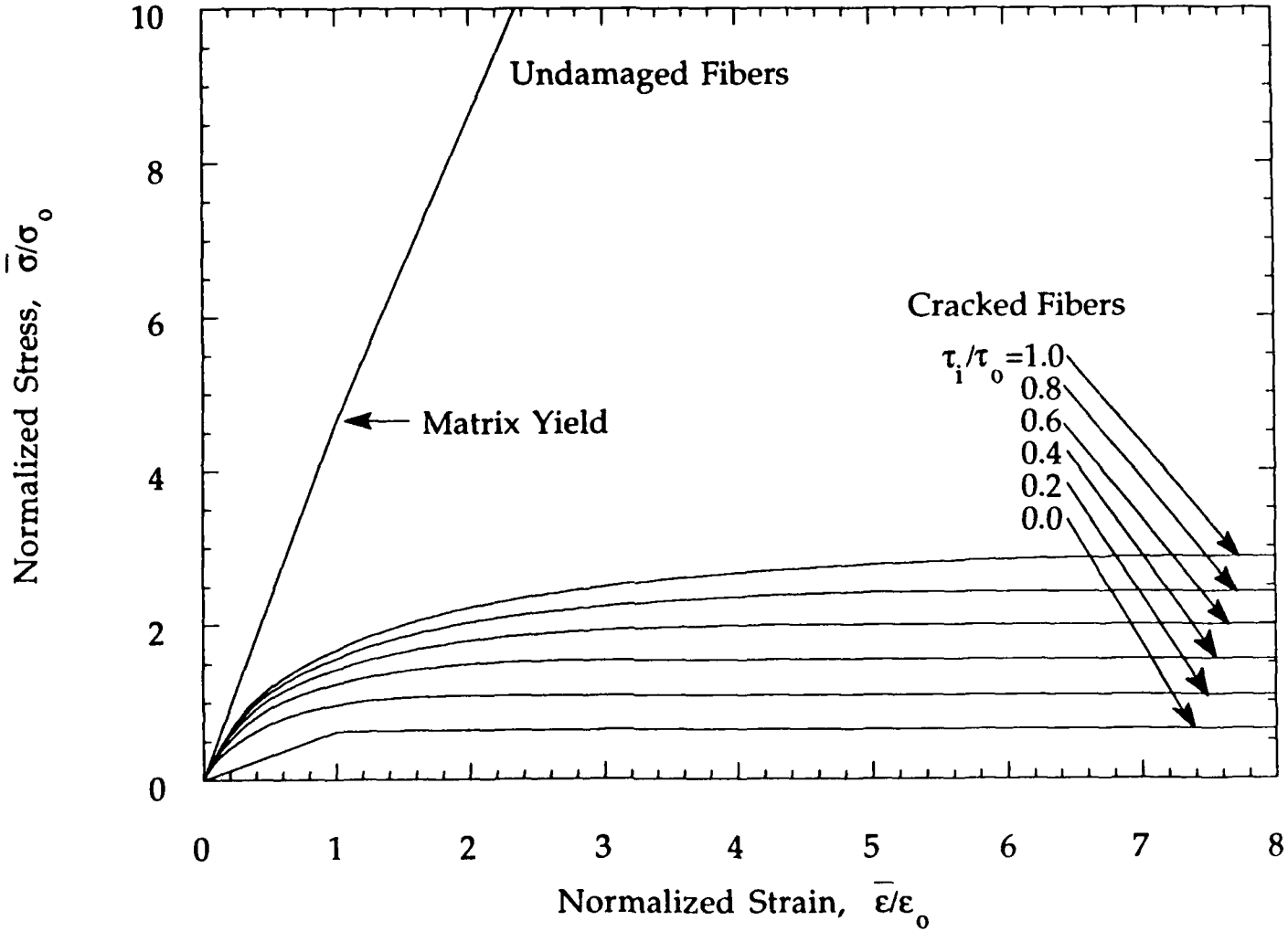
Undamaged Fibers
Matrix Yield
Cracked Fibers
τ_i/τ_o =1.0
0.8
0.6
0.4
0.2
0.0
Normalized Stress, $\bar{\sigma}/\sigma_o$
Normalized Strain, $\bar{\varepsilon}/\varepsilon_o$
0
2
4
6
8
10
0
1
2
3
4
5
6
7
8

Figure 15

ON DISLOCATION STORAGE AND THE MECHANICAL RESPONSE OF FINE SCALE MICROSTRUCTURES

J.D. Embury[1] and J.P. Hirth[2]

[1] Department of Materials Science,McMaster University, Hamilton, Ontaric L8S 4H3 Canada

[2] Department of Mechanical and Materials Engineering, Washington State University, Pullman, Washington, 99164-2920

ABSTRACT

For lamellar aggregates, a small size scale is attained where flow in a ductile layer occurs by the motion of single dislocations rather than dislocation arrays. Analysis of such a case indicates that the flow stress should follow an Orowan-type relation accompanied by rapid effective work hardening. Consequences for flow instability and fracture are considered.

INTRODUCTION

Currently there is much interest in the plasticity of fine scale microstructures including nanocrystalline materials [1] and structures produced either by the imposition of large plastic strains such as composites subjected to wire drawing [2] or materials produced by sputtering or evaporation [3]. There is extensive literature which describes the application of various strengthening mechanisms to these structures.

However both the scale of the structure and the strength levels attained invite consideration of some basic issues in crystal plasticity and comparison of the events occurring in fine scale microstructures with those occurring in work hardening and fatigue of pure metals.

There are in essence two aspects of the problem which arise from the scale of the microstructure. The first is that alternative processes of relaxation and plasticity may arise due to the density of high diffusivity paths. These processes effectively translate the mechanisms of deformation operative at high reduced temperature, T/T_m vaiues to lower temperature regimes and in addition the fine scale structures may provide alternative relaxation and fracture modes. There is a variety of experimental data available which demonstrate these effects for fine grain size materials [4-6].

The second aspect of the problem, the one with which this communication is concerned, is that pertaining to low temperature plasticity where the flow stresses of the fine scale microstructures can approach to within a fraction of 1/2 or 1/3 of the theoretical strength of order $\mu/30$, where μ is the shear modulus. In this regime we can consider the following problems: a) what processes may limit the accumulated local dislocation density?; b) in two phase material what factors permits the flow stress to attain such high values?; c) as the theoretical stress is approached does the character of plasticity and its spatial organization change from that operative during more usual descriptions of plasticity and work hardening?

Format

It is appropriate to consider a simplified view of microstructures in order to draw some analogies between single phase and two phase material. Consider first that the structure can be divided into lamellar regions α and β. β may represent either regions of very high dislocation density as in a single phase material subject to fatigue or a second phase which differs in elastic modulus from the regime α.

If we now consider the deformation process operative in such a structure we can consider in essence a hierarchy of events: a) the imposition of an appropriate scaling law to describe the change in dislocation configuration, b) the storage and annihilation of dislocations as a consequence of flow and c) the geometrical aspects of the spread of plasticity in such structures.

Single Phase Structures

Crystals deformed at low temperatures in general form rough cells and tangles with local misorientations of 1 or 2° and many dislocations of opposite sign, i. e. with dipole character [6,7]. With either static or dynamic recovery, these cells convert to narrower, well-defined cell walls [8]. The detailed mechanisms of interaction between the mobile dislocations and the cell walls or regions of high dislocation density are difficult to elucidate in structures produced by uniaxial deformation. In contrast, in single phase structures produced in fatigue, persistent slip bands develop that have a regular ladder structure consisting of walls of high dislocation density separated by channels in which dislocation motion occurs. The seminal work of Basinski and Basinski [9] has shown that at low temperatures the walls contain dislocation densities of the order 10^{17} m/m^3, i.e., on the average the dislocations are approximately 3 nm apart. In these structures, some annihilation of dislocations occurs in a form of local recovery to preserve the constancy of structure and mechanical response.

Hence, these fatigue structures with the largest local dislocation densities can sustain

very large flow stresses. In nanoscale systems with barriers, such as dispersed or lamellar second phase particles, similar large densities of dislocations can occur. The attendant higher stresses can result in the shearing of obstacles that are usually impenetrable in mesoscale microstructures. This shearing relieves local stress concentrations and permits the annihilation of edge dislocations as an alternative recovery process to climb or to cross-slip of screw dislocations.

In the following, we present an explicit derivation of a flow relation for the case of a lamellar structure and demonstrate the effects of the scale of the microstructure.

Dislocation Models

The scaling law for dislocation spacing λ_0 in a single phase material is

$$\lambda_0 \equiv \frac{\mu b}{3\tau} \tag{1}$$

applicable for cell structures or random arrays of dislocations, where b is Burgers vector magnitude, μ is shear modulus and τ is the resolved shear stress on the glide system. When this distance becomes small compared to the layer thickness h, the concept of pileups and slip bands becomes meaningless. Instead single dislocation loops form in the α phase and are deposited at or near the interface at a spacing λ. The process is illustrated in Fig. 1. The structure is akin to those formed in persistent slip bands in fatigue [9] and in partially relaxed strained layered structures [10] (strained superlattices). The essential point is that the fine scale plasticity may not occur by groups of dislocations moving on slip planes separated by distances of the order of a micrometer but instead by single dislocations moving on closely spaced glide planes from one boundary to the next. Two issues of importance are the role of image stresses in any possible standoff distance of the dislocations from the interface and an expression for the flow stress of the structure.

The image arrays are represented in Fig. 2. For a single screw dislocation in α, for example,the image repulsion from ß produces a standoff distance w given by [11]

$$w = \frac{\mu b \lambda \eta}{4\pi\tau} \tag{2}$$

where

$$\gamma = \frac{\mu_\beta - \mu_\alpha}{\mu_\beta + \mu_\alpha} \tag{3}$$

and η is a factor representing the multiple interface image correction [12]. Any other interface will tend to weaken the image repulsion force on the α dislocations, as can be perceived qualitatively from Fig. 2. Another ß interface to the right of that in Fig. 2 would produce a repulsive force acting to the left which would tend to decrease w. Another α interface to the left of that shown would decrease the repulsive force acting to the right and again tend to decrease w.

Typical values [12] of the factor η are ~0.5 for $w/\lambda = 0.1$ and the η values decrease with increasing w/λ. With $\eta = 0.5$, and $\lambda = h$, Eqs. (1) and (2) give

$$w \equiv \frac{h\gamma}{8} \tag{4}$$

An extreme case of large γ is provided by the example of alumina ß layers and niobium α layers; giving $\gamma = 0.72$ and $w = 0.09h$ (the upper bound on γ is 1; which would give $w = 0.12\lambda$). Even in this extreme case, to first order one can neglect the standoff distance w compared to the dimension h. For many considerations w is much smaller: e.g. TiC and Ni where $\gamma = 0.14$ and $w = 0.018h$. The uncertainty in h introduced by neglecting w in such a case is very small compared to the uncertainty associated with the assumptions of isotropic elasticity, the magnitude of the core energy of dislocations and effects associated with dislocation curvature.

For multiple dislocation arrays, the stress field becomes limited [13] by the dislocation spacing λ, the image forces are further reduced, and w becomes even smaller than for the case discussed above. Hence, to a good approximation, w can also be neglected for this case.

Koehler [14] considered the single interface case where $\eta = 1$ and suggested that the limiting strength in a two-phase structure would be reached when the distance w attained the core

size ~b, whereupon the dislocations could in principle penetrate into the harder ß phase. In many cases, such penetration would be limited by other factors such as the Peierls stress of the harder phase or interactions with intrinsic interface dislocations. Lehoczky [15,16] has used the Koehler model to estimate the value of h where dislocations penetrate the hard phase and produce general yielding in a composite, so that stress no longer varies with h. He found reasonable agreement with experimental results for Al-Cu and Al-Ag laminates. We regard this agreement as somewhat fortuitous in view of the above discussions, and note that strength increases accompanying size decreases into the nm structure scale have been observed for nanostructures.

For an explicit example, we suppose that the interface dislocations in Fig. 1a are pure edge so that the moving segments in Fig. 1b are screw in character. With the neglect of w, the Orowan stress to move the dislocation segments in Fig. 1c is then

$$\tau = \left[\frac{\mu b}{2\pi h}\ell n\left(\frac{h}{b}\right)\right]\cos\phi \tag{5}$$

where the core cutoff radius is set equal to b. The angle ϕ is determined by a balance between the line tension of the moving screw segment, S_S and that of the edge imbedded in the interface array, S_e

$$\cos\phi = \frac{S_e}{S_s} = \frac{4\pi S_e}{\mu b^2}\cdot\frac{h}{\ell n(h/b)} \tag{6}$$

If we assume that the array in Fig. 1a is uniform, the energy S_e is just the interaction energy when a dislocation is brought from a distance h/2 into the boundary, given by Eq. (19-85) in ref. 18 as

$$S_e = \frac{\mu b^2}{4\pi(1-\nu)}\left\{\frac{\pi b}{\lambda}\coth\frac{\pi b}{\lambda} - \ell n\sinh\frac{\pi b}{\lambda} - \frac{\pi h}{\lambda}\coth\frac{\pi h}{\lambda} + \ell n\sinh\frac{\pi h}{\gamma}\right\} \tag{7}$$

In the limit of large (h/λ) the bracket term becomes $\ell n(\lambda/2\pi b)$, and hence

$$\cos\phi = \frac{2}{(1-\nu)}\frac{\ell n(e\lambda/2\pi b)}{\ell n(h/b)} \tag{8}$$

Together, Eqs. (5) and (8) give

$$\tau = \frac{\mu b}{\pi h(1-\nu)} \ell n\left(\frac{\lambda}{2\pi b}\right) \tag{9}$$

In this limit, the τ and h values are related by a pure Orowan relation $\tau \propto h^{-1}$. For smaller (h/λ) values, the result is, instead,

$$\tau = \frac{2S_e}{bh} \ell n\left(\frac{\lambda}{2\pi b}\right) \tag{10}$$

This gives an Orowan type relation but not of the simple h^{-1} form because of the weak h dependence of S_e; a situation analogous to the dispersion hardening case [18].

For a layer structure, the plastic strain is related to λ by

$$\varepsilon = \frac{m}{X_\alpha} \frac{b}{\lambda} \tag{11}$$

where X_α is the volume fraction of the α phase and m is a strain resolution factor of the order of 0.5 for the active slip systems. Hence, the λ dependence in Eq. (10) would appear to give strain softening. This is not the case, however. Instead, the constraint of the undeforming, or less-deforming, ß phase produces a stress transfer to ß and an overall stress elevation that in turn yields an effective large work hardening of the composite in the sense of an increased load carried by the composite even though the resolved shear stress for flow of the α phase is unchanged.

Stress Strain Relations

Stress strain relations can be constructed for two cases. We first consider macroscopic loading parallel to the interface of a lamellar aggregate.

As discussed in the Introduction, once the α-phase begins deforming, it soon develops a symmetric, plane plastic strain deformation mode. Moreover, with reference to Fig. 1a, once the value $<\lambda>$ is less than h, the stress distribution in the two phases essentially becomes that of a

continuum plastic model with the phase flow relation of the form of Eq. (10). The constraint in the x direction is such that $\varepsilon_{xx}^{\alpha p} = -\varepsilon_{yy}^{\alpha p}, \varepsilon_{zz}^{\alpha p} = 0$ where the superscripts α and p denote the α phase and plastic strain respectively. The elastic stresses and strains are constrained to obey the relations $\varepsilon_{xx}^{\alpha} = \varepsilon_{xx}^{\beta} = 0, \varepsilon_{yy}^{\beta} = \varepsilon_{yy}^{\alpha p} + \varepsilon_{yy}^{\alpha}$; and $\sigma_{yy}^{\alpha} = \tau / m$. Since the major effect is the compensation of the plastic strain $\varepsilon_{yy}^{\alpha p}$ by the elastic strain $\varepsilon_{yy}^{\alpha}$, we make the simplifying assumption that α and ß have the same elastic constants μ and ν, which greatly reduces the complexity of the results. The above conditions together with Hooke's law give the result, derived in Appendix A,

$$\sigma_{yy}^{\beta} = \frac{2\mu}{(1-\nu)}\varepsilon_{yy}^{\alpha p} + \frac{\tau}{m} = \frac{2\mu}{(1-\nu)}\varepsilon_{yy}^{\beta}$$
$$\sigma_{yy}^{\beta} = \frac{\tau}{m} \tag{12}$$

where m is the Schmidt factor for the operating slip system and the overall strain ε_{yy} is equal to ε_{yy}^{β}. The mean stress σ_{yy} is given by

$$\begin{aligned}\sigma_{yy} &= X_{\alpha}\sigma_{yy}^{\alpha} + X_{\beta}\sigma_{yy}^{\beta} \\ &= \frac{\tau}{m} + X_{\beta}\frac{2\mu}{(1-\nu)}\varepsilon_{yy}^{\alpha p}\end{aligned} \tag{13}$$

This case closely resembles the continuum plasticity result [19,20] for a lamellar aggregate, the difference being that the slip systems depicted in Fig. 1 result in plane strain deformation and that m would equal 0.5 for the continuum case. Like that case, work hardening is rapid for small strains, Eq. (13). In the present case, the rapid hardening persists until one of two events occurs, whereupon the hardening rate drops precipitously. First, σ_{yy} can reach the fracture stress σ_{yy}^{*}, resulting in the breakup of the ß phase into segments of length ~2h. In this case, the stress distribution in the ß phase is that of Fig. 3 with an average stress $<\sigma_{yy}^{\beta}> = \sigma_{yy}^{*} / 2$. This situation again closely parallels the continuum result. Second, σ_{yy}^{β} can reach the flow stress of the ß phase locally, resulting in a slip band or shear band penetrating the ß phase over lengths

of ~2h. The stress distribution in the ß phase again resembles that in Fig. 3 but σ^{*}_{yy} is now the flow stress in the ß phase. Of course, the yield stress τ/m is related to h through Eq. (9) or (10).

Once penetration of the β phase occurs, a variety of processes can occur which influence the mechanical stability of the α/β composites. The flow stress of the microscale composites is high. As a consequence, geometrical stability can only be sustained either by the apparent high work hardening caused by the stress transfer to the β phase or by the prevention of geometric instability by means of imposed compressive isostatic stress states such as those in wire drawing.

Thus, codeformation of α and β may occur by the transfer of individual dislocations from interface to interface, resulting in uniform deformation of the two-phases, even at very large strains. Examples of such behavior can be found in the drawing of two-phase systems such as Cu-Ag or Cu-Nb [21]. However, alternative processes may also occur. If dislocation motion in the β phase is difficult because of high lattice friction, as is true for many compounds such as oxides, the β phase may fracture. In such a case, if the crack length, equal to the width of the β phase, is sufficiently large, the local value of the stress intensity at the crack tip can exceed the critical value K_{Ic} for the α phase and fracture of the entire composite would ensue. Secondly, the crack tip can blunt and initiate a growing void in the α phase, eventually leading to ductile fracture of the composite. In the case that the β phase deforms, stable subsequent deformation behavior can follow.

For smaller values of h, cracking of α becomes less likely because of the attendant smaller thickness of the β layers and consequent lower stress intensity at the crack tip. Also, hole growth at the crack tip is less likely because of the lower stress intensity. Indeed, the size scale may be in a range where capillary constraints could arise because of the small crack tip curvature [22]. Delamination at the crack tip would also tend to suppress crack propagation For the case that the β phase deforms, assisted by the compressive isostatic stress elevation arising from load transfer, large elongations can be sustained before fracture because of the stable symmetrical

texture that evolves (which eliminates geometrical softening) and the continued effective work hardening of the composite, both effects tending to suppress necking or macroscopic shear instability. Such large elongations are found for heavily drawn steel wires [7] and in tensile tests of nanoscale lamellar aggregates of Al and Al_2O_3 [23].

Finally, we emphasize that any local dilatency may trigger a shear localization instability that may be noncrystallographic in form at the large stress levels attained in the microcomposites, Such a localization results in a macroscopic shear failure that extends across the α and β regions [23].

The second situation again would correspond to Fig 1a, but with loading in the z-direction and with the dislocations of opposite sign. The continuum plastic analog for this case has been developed by Drucker [24]. In this case, the plastic strains are $\varepsilon_{zz}^{\alpha p}$ and $\varepsilon_{xx}^{\alpha p} = \varepsilon_{yy}^{\alpha p} = -\frac{1}{2}\varepsilon_{zz}^{\alpha p}$. The elastic strains are $\varepsilon_{xx}^{\beta} = \varepsilon_{yy}^{\beta} = \varepsilon_{xx}^{\alpha} - \frac{1}{2}\varepsilon_{yy}^{\alpha p} = \varepsilon_{yy}^{\alpha} - \frac{1}{2}\varepsilon_{yy^p}$, and both $\varepsilon_{zz}^{\alpha}$ and ε_{zz}^{β} are non-zero. The stress conditions are $\sigma_{xx}^{\beta} = \sigma_{xx}^{\alpha}(X_\alpha / X_\beta), \sigma_{yy}^{\beta} = \sigma_{yy}^{\alpha}(X_\alpha / X_\beta), \sigma_{zz}^{\alpha} = \sigma_{zz}^{\beta}$ and $\sigma_{zz}^{\alpha} = \sigma_{xx}^{\alpha} + (\tau / m)$. Considerable manipulation of these conditions together with Hooke's law yields, as shown in Appendix B,

$$\begin{aligned}
\sigma_{yy}^{\alpha} &= \sigma_{zz}^{\beta} + \frac{\mu(1+\nu)}{(1-\nu)} X_\beta \sigma_{yy}^{\alpha p} \frac{\tau}{m} \\
\sigma_{yy}^{\alpha} &= \sigma_{xx}^{\alpha} = \frac{\mu(1+\nu)}{(1-\nu)} X_\beta \varepsilon_{yy}^{\alpha p} \\
\sigma_{ii}^{\alpha} &= \frac{\mu(1+\nu)}{(1-\nu)} X_\beta \varepsilon_{yy}^{\alpha p} \frac{\tau}{3m}
\end{aligned} \tag{14}$$

The form of the stress-strain relation for this case closely resembles that of Eq. (13). The yield stress is again related to h by the Orowan-like Eqs. (9) or (10). Rapid work hardening occurs and is terminated by one of several events. First the hydrostatic tensile stress σ_{ii}^{α} can lead to cavitation in the α-phase. Second, $(\sigma_{zz}^{\beta} - \sigma_{xx}^{\beta}) / m_\beta$ can reach the resolved shear stress for flow in

the ß-phase, whereupon both phases deform together. Third, σ^{β}_{zz} can reach the fracture stress of the ß-phase, leading to fragmentation and subsequently to hole growth and fracture or brittle crack propagation. Fourth, interface glide can initiate at the edge of the crystal, Fig. 4. The latter process will initiate when

$$\sigma^{\alpha}_{xx} = \sigma_P h + \gamma_\beta - \gamma_i \qquad (15)$$

where σ_P is the Peierls stress resisting interface dislocation motion (interface sliding), γ_β is the surface energy of the ß-phase, and γ_i is the α-ß interfacial free energy.

All of the above processes require resistance to flow of the α-phase at the edge. Failure to satisfy Eq. (15) ensures that such flow will not occur by interface sliding. The necking type flow of the α-phase, as would occur for macroscopic layers, Fig. 5, will not occur initially because the most favourable dislocation motion is governed by Eqs. (9) or (10) and the other systems, which would give flow of the type in Fig. 5, require larger stresses and nucleation at the free surface. For macroscopic layers, where Eq. (1) governs flow, necking would occur, and the stress build-up in α would be much less, the flow following the Drucker process [24,25].

Discussion

The plastic properties of fine scale structures are of increasing importance. In the current work we have considered some idealized lamellar structures. In these materials it is important to consider that the scale of the structure may be reduced to a level where it is inappropriate to consider that the scale of the structure is such to permit the spread of plasticity via the operation of Frank-Read sources. The interfaces become both the sources and sinks of distortion and the structure can store energy during plastic flow by the accumulation of dislocations at interfaces, thereby causing their extension, rather than by the storage of discrete lattice dislocations. The energy is manifested macroscopically as elastic energy in the harder phase and as increased interfacial energy. The present work indicates that the flow stress should scale inversely with layer spacing and that large effective work hardening should occur for such

flow. Ancillary features are that dislocations in the interface should lead to symmetric plane-strain tensile textures and to uniform distributions of dislocations in the interfaces, tantamount to misfit dislocation arrays.

Here, the flow problem is treated for elastically homogeneous layer structures. More generally, the incorporation of dislocations into the interface between two solids of differing elastic constants may be more complex because the interface may cease to be in local equilibrium. That is, there may be a standoff distance of the dislocations from the interface.

There is also a problem of the inherent stability of flow. As the scale of the structure is decreased, the flow stress increases but the energy storing (or work hardening) ability of the structure is decreased. Thus, fine scale structures may either suffer localized shear or may deform in a very homogeneous manner by dislocations eventually traversing every atomic plane. Both the scaling laws relating structure dimensions to critical strains and the detailed mechanism of storage present further areas for study for such instability events.

Summary

For nanometer-scale lamellar structures, flow is controlled in the softer α phase by motion of screw dislocations obeying an Orowan type relation, with stress roughly related to the reciprocal of the ductile layer thickness. This process plates edge dislocations at the α-ß interface which in turn sheds load from the α to the ß phase. For uniaxial loading either parallel or perpendicular to the α-ß interfaces, this process leads to rapid effective work hardening followed by flow or fracture of the ß phase or, for the perpendicular loading case, to cavitation in the α phase. These latter processes lead to a subsequent very low work hardening rate. Hence, overall, fine scale lamellar aggregates are characterized by a large yield stress and rapid effective work hardening at small strains, followed by low effective work hardening and attendant plastic instability or fracture.

Acknowledgements

This research was supported in part through the Summer Research Group at the Materials Science Center at Los Alamos National Laboratory, in part by the ARPA University Research Initiative through ONR Contract 00014-93-I-0213 with the University of California, Santa Barbara (JPH), and in part by NSERC, Canada.

References

1. M. Nastasi, D. Parkin and H. Gleiter, Mechanical Properties and Deformation Behavior of Materials Having Ultra-Fine Microstructures, Kluwer, Dortrecht, 1993.
2. A. Kelly and N. H. MacMillan, Strong Solids, 3rd ed., Oxford University Press, 1987.
3. J. D. Embury, Scripta Met. 1993, **26**, 1211.
4. X. Zhu, R. Birringer, U. Herr and H. Gleiter, Phys. Rev. **B35,** 9085 (1987).
5. R. W. Siegel, Mater. Sci. Forum, **37**, 299 (1989).
6. A. S. Keh and S. Weissman, in Electron Microscopy and Strength of Crystals, G. Thomas and J. Washburn (eds.), Interscience, New York, 1963, p. 131.
7. J. D. Embury, A. S. Keh, A.S. and R. M. Fisher, Metall. Trans. **12**, 478 (1967).
8. J. T. Fourie, P.J. Jackson, D. Kuhlmann-Wilsdorf, D. A. Rigney, J. H. van der Merwe and H. G. F. Wilsdorf, Scripta Metall., **16**, 157 (1982).
9. Z. S. Basinski and S. J. Basinski, Acta Metall., **37**, 3255, 3263, 3275 (1989).
10. R. Hull and J. C. Bean, J. Vac. Sci. Tech. **A7**, 2580 (1989).
11. A. K. Head, Philos. Mag. **44**, 92 (1953).
12. S. V. Kamat, J. P. Hirth, and B. Carnahan, Scripta Metall. **21**, 1587 (1987); Mater. Res. Soc. Symp. Proc. **103**, 55 (1988).
13. J. P. Hirth and J. Lothe, Theory of Dislocations, 2nd ed., Wiley, New York, 1982, p. 740.
14. J. S. Koehler, Phys. Rev. **B2**, 547 (1970).
15. S. L. Lehoczky, Phys. Rev. Lett. **41**, 1814 (1978).
16. S. L. Lehoczky, J. Appl. Phys. **49**, 5479 (1978).
17. J. P. Hirth and J. Lothe, Theory of Dislocations, 2nd Ed., Wiley, New York, 1982.
18. M. F. Ashby, Acta Metall. **14**, 679 (1966).
19. D. K. Hale and A. Kelly, Ann. Rev. Mater. Sci., **2**, 405 (1972).

20. G. Bao, J. W. Hutchinson and R. M. McMeeking, Acta Metall. et Mater., **39**, 1871 (1991).

21. W. A. Spitzig, Acta Metall. et Mater., **38**, 1085 (1990).

22. A. K. Vasudevan, O. Richmond, F. Zok and J. D. Embury, Mater. Sci. Engin., **A107**, 63 (1989).

23. A. T. Alpas, J. D. Embury, D. A. Hardwick and R. W. Springer, J. Mater. Sci., **25**, 1603 (1990).

24. D. C. Drucker, in High Strength Materials, V. Zackay (ed.), Wiley, New York, 1965, p. 795.

25. T. Christman, A. Needleman and S. Suresh, Acta Metall., **37**, 3029 (1989).

Appendix A - Derivation of Eq. (12)

The boundary conditions from Fig. 1 are

$$\varepsilon_{ss}^{\alpha} = \varepsilon_{ss}^{\beta} = 0; \varepsilon_{yy}^{\beta} = \varepsilon_{yy}^{\alpha p} + \varepsilon_{yy}^{\alpha}; \sigma_{zz}^{\alpha} = \sigma_{zz}^{\beta} 0 = \tag{A1}$$

and the flow condition gives

$$\sigma_{yy}^{\alpha} = \tau / m \tag{A2}$$

Since $\varepsilon_{xx} = 0$, Hooke's law gives

$$\begin{aligned} \sigma_{xx}^{\alpha} &= \nu(\sigma_{yy}^{\alpha} + \sigma_{zz}^{\alpha}) = \nu\sigma_{yy}^{\alpha} \\ \sigma_{xx}^{\beta} &= \nu\sigma_{yy}^{\beta} \end{aligned} \tag{A3}$$

Hooke's law also gives the relation

$$\varepsilon_{yy}^{\beta} = \frac{1}{E}\sigma_{yy}^{\beta} - \frac{\nu^2}{E}\sigma_{yy}^{\beta} \tag{A4}$$

where $E = 2\mu(1+\nu)$ is Young's modulus. Hence

$$\sigma_{yy}^{\beta} = \frac{2\mu}{(1-\nu)}\varepsilon_{yy}^{\beta}; \quad \sigma_{yy}^{\alpha} = \frac{2\mu}{(1-\nu)}\varepsilon_{yy}^{\alpha} \tag{A5}$$

Substitution of eqs. (A1) and (A2) into (A5) gives

$$\sigma_{yy}^{\beta} = \frac{2\mu}{(1-\nu)}\varepsilon_{yy}^{\alpha p} + \frac{\tau}{m} \tag{A6}$$

Appendix B - Derivation of Eq. (14)

The boundary conditions from Fig. 1 are

$$\varepsilon_{xx}^{\beta} = \varepsilon_{yy}^{\beta} = \varepsilon_{xx}^{\alpha} - \frac{1}{2}\varepsilon_{yy}^{\alpha p} = \varepsilon_{yy}^{\alpha} - \frac{1}{2}\varepsilon_{yy}^{\alpha}$$
$$\varepsilon_{xx}^{\alpha p} = \varepsilon_{yy}^{\alpha p} = -\frac{1}{2}\varepsilon_{zz}^{\alpha p} \tag{E 1}$$

The requirement of zero net force at the surfaces normal to x and z, and equilibrium in the z direction give

$$\sigma_{xx}^{\beta} = -\sigma_{xx}^{\alpha}(X_{\alpha} / X_{\beta});\ \ \sigma_{yy}^{\beta} = -\sigma_{yy}^{\alpha}(X_{\alpha} / X_{\beta})$$
$$\sigma_{zz}^{\alpha} = \sigma_{zz}^{\beta} \tag{B2}$$

The flow law yields

$$\sigma_{zz}^{\alpha} = \sigma_{xx}^{\alpha} + \tau / m = \sigma_{yy}^{\alpha} + \tau / m \tag{B3}$$

Substitution of these relations into Hooke's law gives

$$\sigma_{xx}^{\alpha} = (\mu + \lambda)(2\varepsilon_{xx}^{\beta} + \varepsilon_{yy}^{\alpha p}) + \lambda\varepsilon_{zz}^{\alpha} \tag{B4}$$

$$\sigma_{zz}^{\alpha} = (2\mu + \lambda)\varepsilon_{zz}^{\alpha} + \lambda(2\varepsilon_{xx}^{\beta} + \varepsilon_{yy}^{\alpha p}) = \sigma_{xx}^{\alpha} + \tau / m \tag{B5}$$

$$\sigma_{xx}^{\beta} = (\mu + \lambda)2\varepsilon_{xx}^{\beta} + \lambda\varepsilon_{zz}^{\beta} = -\sigma_{xx}^{\alpha}(X_a / X_{\beta}) \tag{B6}$$

$$\sigma_{zz}^{\beta} = (2\mu + \lambda)\varepsilon_{zz}^{\beta} + 2\lambda\varepsilon_{xx}^{\beta} = \sigma_{zz}^{\beta} \tag{B7}$$

where _ is Lame's constant, $\lambda = 2\ \mu\nu/(1-2\nu)$.

Solving eqs. (B4) to (B7) simultaneously leads to the result

$$\sigma_{xx}^{\alpha} = \mu\frac{(1+\nu)}{(1-\nu)}X_{\beta}\varepsilon_{yy}^{\alpha p}$$
$$\sigma_{zz}^{\alpha} = \mu\frac{(1+\nu)}{(1-\nu)}X_{\beta}\varepsilon_{yy}^{\alpha p} + \frac{\tau}{m} \tag{B8}$$

Figure Captions

Fig. 1. Dislocation arrays at interfaces of an imbedded layer: views parallel to the interface, (a) along dislocation line direction, (b) normal to (a), and (c) detail of end of loop in (b).

Fig.2. Dislocations and image dislocations near interface.

Fig. 3. Stress distribution in segmented β phase.

Fig. 4. Interface sliding at laminate edge with slipped area $\approx$ h.

Fig. 5. Deformation at edge for macroscopic layer structure.

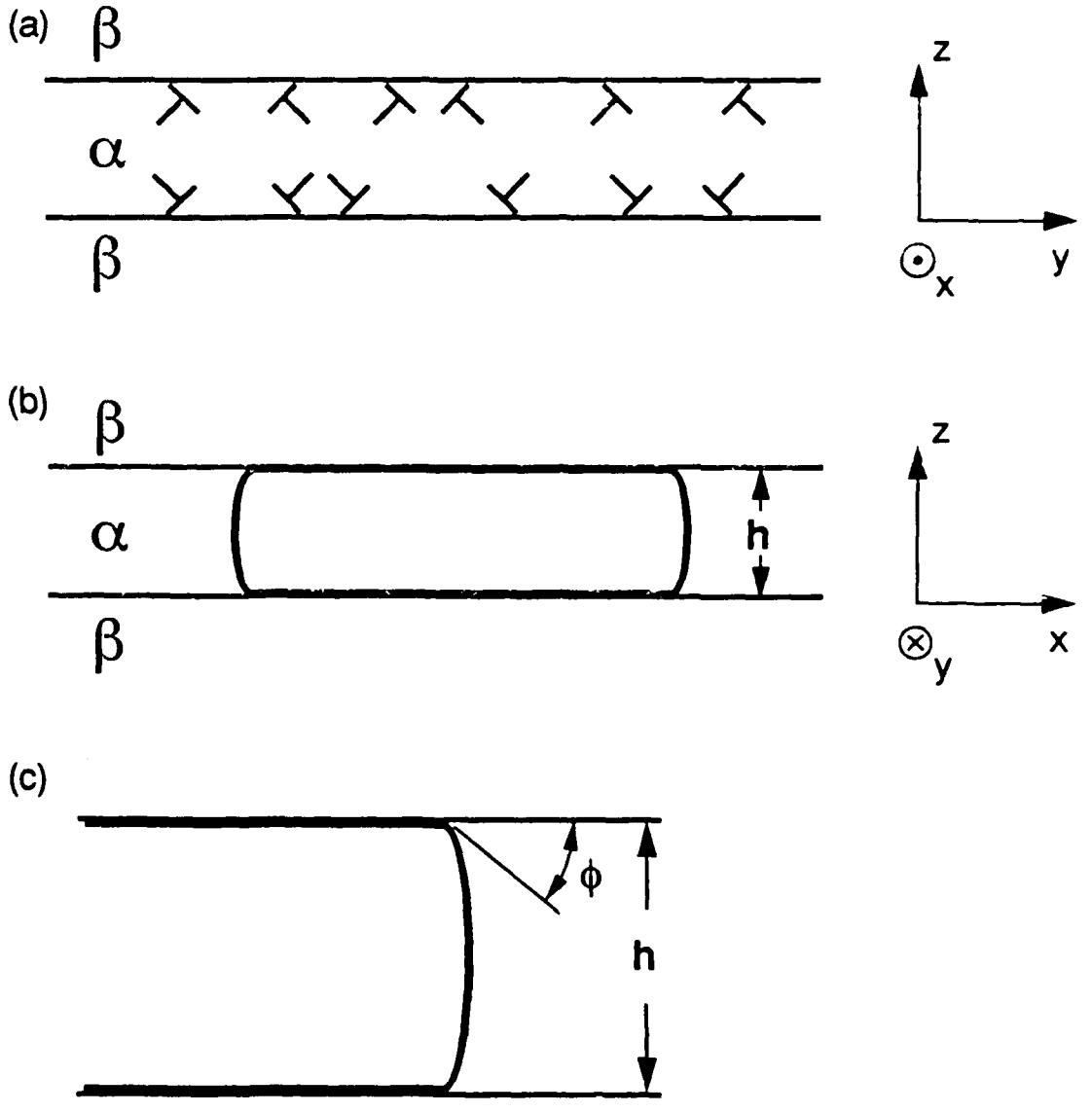

Fig. 1. Dislocation arrays at interfaces of an imbedded layer: views parallel to the interface, (a) along dislocation line direction, (b) normal to (a), and (c) detail of end of loop in (b).

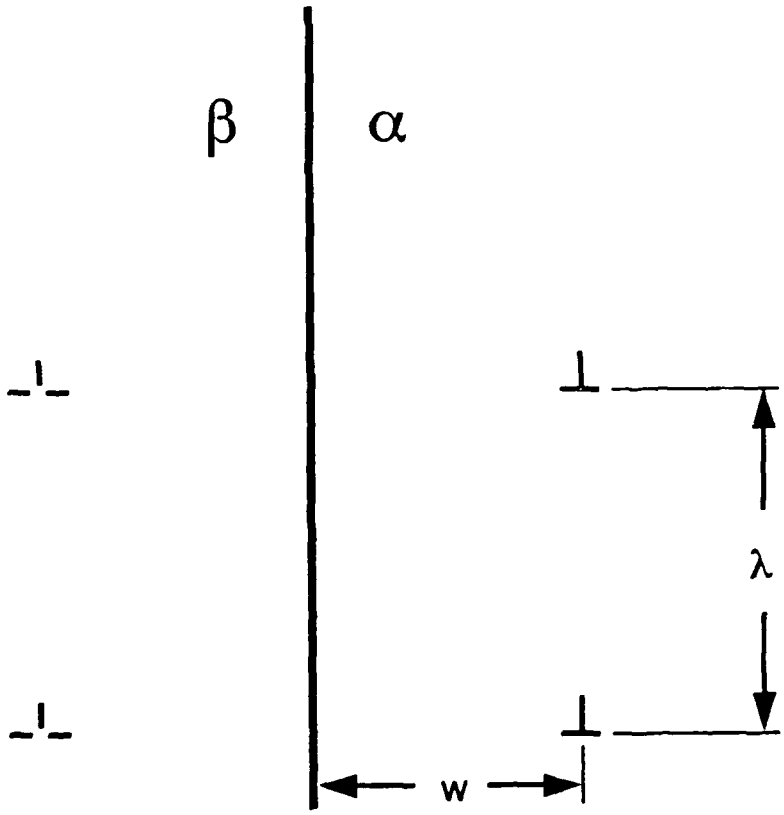

Fig. 2. Dislocations and image dislocations near interface.

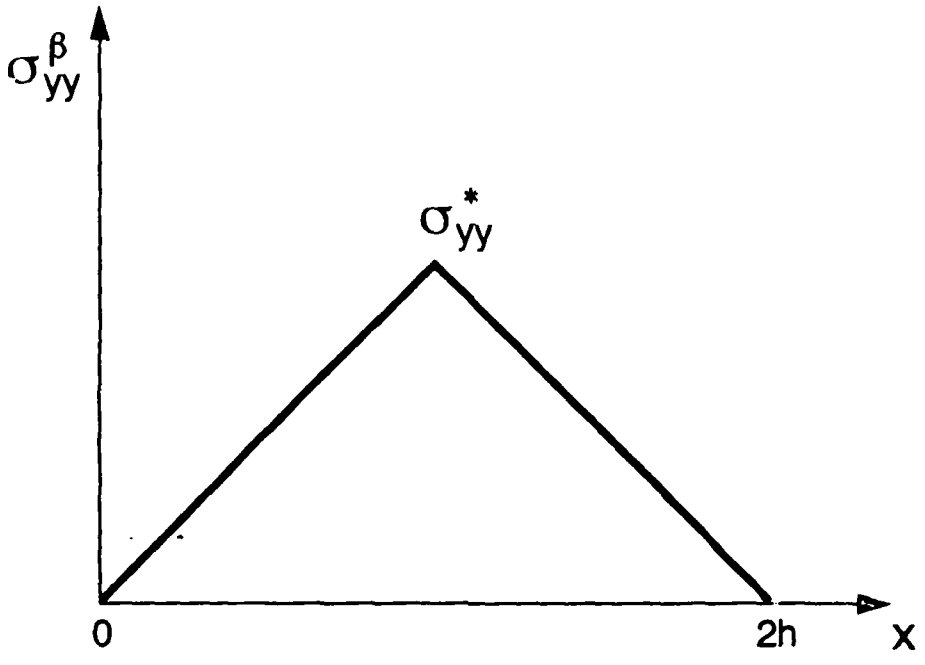

Fig. 3. Stress distribution in segmented β phase.

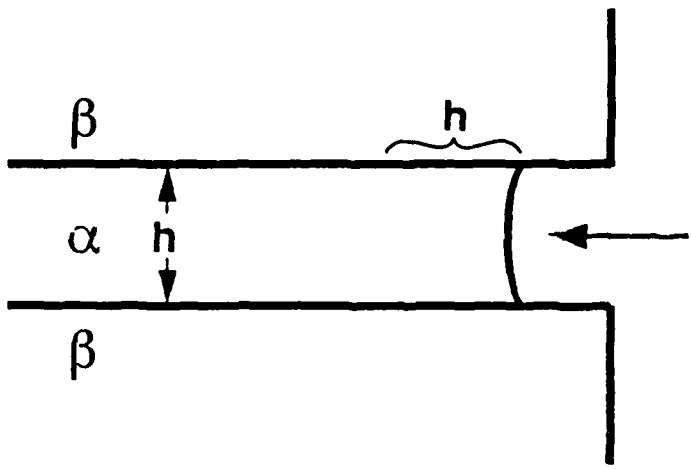

Fig. 4. Interface sliding at laminate edge with slipped area ≈ h.

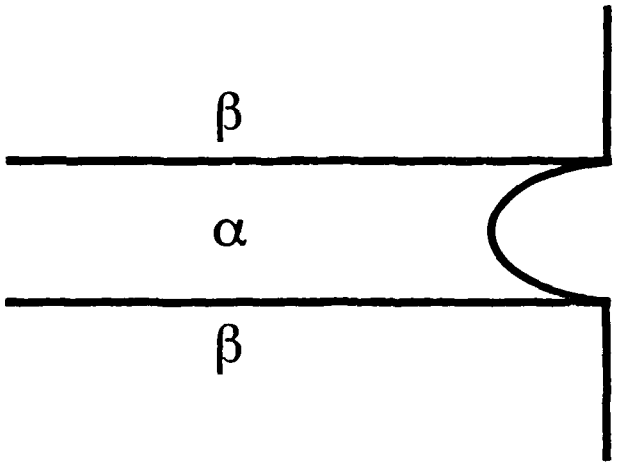

Fig. 5. Deformation at edge for macroscopic layer structure.

EFFECT OF MICROSTRUCTURAL PARAMETERS ON THE YIELD STRENGTH OF Al-4%Mg/Al_2O_3p COMPOSITES

R.H. Pestes*, S.V. Kamat** and J.P. Hirth**

*Hewlett-Packard, Camus, WA 98607
**Mechanical and Materials Engineering Department, Washington State University, Pullman, WA 99164-2920

Introduction

The quest for materials with high specific strengths and stiffness has been the impetus for the development of metal-matrix composites (MMC's) in recent years. MMC's containing continuous reinforcements possess the highest strengths and stiffnesses in the direction of the reinforcement. However, such composites have poor transverse properties and are extremely expensive for most applications. In contrast, MMC's with particulate reinforcements, while not achieving the strengths and stiffness levels of continuous fiber-reinforced MMC's, exhibit greater isotropy in their properties. Furthermore, they can be processed by conventional means and are much less expensive.

Active research has led to considerable advances in an understanding of particulate reinforced MMC's. In particular, substantial experimental and theoretical work [1-20] has been done on the effect of microstructural parameters such as volume fraction, particulate size and interparticle spacing on the yield strength of such composites. However, most of the experimental studies have been restricted to composites containing a single uniform particulate size and volume fractions less than 0.3. In cases where a range of these parameters were studied, the flow stress was found to vary with the edge-edge particle spacing rather than with volume fraction alone, as would be expected from simple elastic-plastic models.

The objective of this present investigation was to study the effect of microstructural parameters on the yield strength of Al-4%Mg/Al_2O_3p composites containing volume fractions greater than 0.45 and with a bimodal mixture of particle sizes in order to further discriminate among the effects of particulate size and interparticle spacing variables.

Experimental

The composite materials were obtained from the University of California at Santa Barbara in the form of 50mm x 50mm x 12mm blocks. The matrix for all the composites was an aluminum alloyed with 4wt% magnesium and the reinforcements were alumina particulates with an aspect ratio (L/t) of about 2. The composites contained alumina particulates varying from 3 to 165μm in size, and the volume fraction of the reinforcement was in the range 0.45 to 0.54. Two of the composites had a bimodal mixture of two particulate sizes. Lists of the composites studied in this investigation and of the particulate characteristics are given in Table 1. The composites contain a nominally homogeneous distribution of alumina particulates, although there are a few clustered regions. The composites also have an excellent bonding between the alumina particulates and the aluminum alloy matrix because of the formation of $MgAl_2O_4$ spinel at the interface [21,22].

Tension and compression tests were performed on these composites with the matrix in the annealed condition. Round-bar specimens with a gage length of 25mm and a gage diameter of 3.2mm were used for tension tests, whereas

cylindrical specimens with a height of 12.7mm and a diameter of 6.35mm were used for compression tests. The tests were carried out on an Instron 1361 testing machine at a constant cross-head speed of 0.5mm/min.

Results and Discussion

The experimentally obtained yield strengths in tension and compression are enumerated in Table 2. Evidently, there is considerable scatter in the tensile yield strength data. This could be attributed to the greater effect for the large volume fraction material of particle-particle interactions [23], particle clustering [24] and fracture [25] on plastic deformation in tension than in compression. Consequently, only compressive yield strength data for the composites have been considered for correlation with the microstructural parameters and comparison with theoretical predictions.

Dislocation-crystal plasticity based models for strengthening in particulate reinforced MMC's predict a yield strength dependence roughly with the inverse of interparticle spacing (λ^{-1}) for a superdislocation model [26] or on inverse square root of interparticle spacing ($\lambda^{-1/2}$) [19,20] in a model consistent with a geometrically necessary dislocation description. In turn, such relations imply an indirect dependence on both volume fraction and particle size via the dependence of λ on these parameters. On the other hand, simple elastic-plastic continuum-mechanics based models [10-17] predict a yield strength dependence on only volume fraction for a given particle shape, which implies the independence of yield strength from particle size. More refined continuum-mechanics based models that include strain gradient terms [27,28] contain an explicit dependence on both volume fraction and particle size. The variation of compressive yield strength with λ^{-1}, $\lambda^{-1/2}$ and volume fraction are shown in Figs. 1,2 and 3, respectively. Clearly, the compressive yield strength does not exhibit any correlation with either λ^{-1} or $\lambda^{-1/2}$. In contrast, the correlation with volume fraction is good. In addition, Table 2 shows that the yield strength is independent of particle size. The correlations in Fig. 3 show that the magnitude of the observed strengthening far exceeds that predicted by the elastic-plastic modified shear-lag theory [10]. However, the magnitude of the strengthening is comparable to the predictions based on finite element calculations [17]. These observations imply that the strengthening behavior in these composites obey the simple elastic-plastic continuum-mechanics description. This behavior is in marked contrast to a number of observations on the tensile yield strength of Al matrix, particulate MMC's [3-9], wherein the yield strength was found to vary explicitly as a function of λ and thus obey a crystal plasticity description.

The discrepancy in the strengthening behavior in the two cases can be attributed to both the difference in loading and to the large volume fraction of the alumina particulates. The volume fraction of alumina was greater than 0.45 in the present study, whereas it was less than 0.20 in the other cases [3-9]. Large particles and high volume fractions are known to accelerate particle fracture because of the increased attendant particle-particle interaction of strain incompatibility fields [23]. Also, particle clustering should enhance early fracture [24]. Both effects would in turn provide defects that would enhance shear localization and trigger further particle cracking. These instability events observed, as well at lower volume fractions [20,25] in tension, would lead to a lowered flow stress in tension and, because of the statistical nature of the particle-particle interactions and clustering effects, to a greater scatter in macroscopic yield events, both effects as observed here. Voids are known to enhance shear localization in tension [29], and the superdislocation model that provides a fair correlation with yield strengths at lower volume fractions [26] is in essence a shear microband localization model: both observations are consistent with the above view.

In contrast, compressive loading perforce suppresses the propagation of shear localization events (although voids would still enhance the initiation of recent localization events) [30]. Thus, the picture that emerges is that testing of these large volume fraction composites in compression results in the suppression of shear localization and a correlation of flow stress with volume fraction only, as expected from simple elastic-plastic continuum models. In tension, shear microband propagation introduces a superdislocation bowing dependence on particle spacing, roughly of the Orowan type. For large volume fractions, particle interaction effects lead to particle cracking, and a large statistical variation in these events obscures correlation of the yield strength with microstructural parameters.

Conclusion

The compressive yield strength of the Al-4%Mg/Al_2O_3p composition is a function only of volume fraction of alumina and is independent of particle size or interparticle spacing, in the volume fraction range of 0.45 to 0.54. The strengthening behavior obeys a simple elastic-plastic continuum-mechanics microstructural parameteric description in this volume fraction range. In contrast, the tensile yield strengths are lower and do not correlate well with any microstructural modes.

Acknowledgment

The authors are grateful for the support of this research by the Office of Naval Research under ONR contract No. 0014-93-I-0213 with the University of California, Santa Barbara. They are also grateful to Dr. R. Mehrahian for supplying the composites.

References

1. D.L. McDanels, *Metall. Trans.*, **16A**, 1105 (1985).
2. WC. Harrigan Jr., G. Gaebler, E. Davis and E.J. Levin, in Mechanical Behavior of Metal Matrix Composites, J.E. Hack and M.F. Amateau eds., TMS-AIME Publication, 167 (1982).
3. J.J. Stephens, J.P. Lucas and F.M. Hosking, *Scripta Metall.*, **22**, 1307 (1988).
4. S.V. Kamat, J.P. Hirth and R. Mehrabian, *Acta Metall.*, 37, 2395 (1989).
5. M. Manoharan, C. Liu and J.J. Lewandowski, in International Conference on Fracture, K. Salama *et al.* eds, Pergamon, 2977 (1989).
6. W.S. Miller and F.J. Humphreys, in Fundamental Relationships between Microstructure and Mechanical Properties of Metal Matrix Composites, P.K. Liaw *et al.* eds., TMS-AIME, Warrendale, PA, 517 (1990).
7. R.M. Aikin Jr. and L. Christodoulou, *Scripta Metall. Mater.*, **25**, 9 (1991).
8. W.S. Miller and F.J. Humphreys, *Scripta Metall.*, **25**, 33 (1991).
9. R J. Arsenault, L. Wang and C.R. Feng, *Acta Metall. Mater.*, **39**, 47 (1991).
10. V.C. Nardone and K.M. Prewo, *Scripta Metall.*, **20**, 42 (1986).
11. H. Lilholt, *Mater. Sci and Engng.*, **A135**, 161 (1991).
12. H. Lilholt, in Mechanical and Physical Behavior of Metallic and Ceramic Composites, S.I. Andersen *et al.* eds., Riso National Laboratory, Roskilde, Denmark, 89 (1988).
13. T. Christman, A. Needleman and S. Suresh, *Acta Metall.*, **37**, 3029 (1989).
14. J.M. Papazian and P.N. Adler, *Metall. Trans.*, **21A**, 401 (1990).
15. A. Levi and J.M. Papazian, *Metall. Trans.*, **21A**, 411 (1990).
16. V. Tvergaard, *Acta Metall.*, **38**, 192 (1990).
17. A.G. Evans, J.W. Hutchinson and R.M. McMeeking, *Scripta Metall. Mater.*, **25**, 3 (1991).
18. R.J. Arsenault and N. Shi, *Mater. Sci. and Engng.*, **81**, 175 (1986).
19. M.F. Ashby, in Strengthening Methods in Crystals, A. Kelly and R.B. Nicholson eds., Elseiver, Amsterdam, 184 (1971).
20. S.V. Kamat, A.D. Rollet and J.P. Hirth, *Scripta Metall. Mater.*, **25**, 27 (1991).
21. C.G. Levi, G.J. Abbaschian and R. Mehrabian, *Metall. Trans.*, **9A**, 697 (1978).
22. B.F. Quiglcy, G.J. Abbaschian, R. Wunderlin and R. Mehrabian, *Metall. Trans.*, **13A**, 93 (1982).
23. A.S. Argon and J. Im, *Metall. Trans.*, **6A**, 839 (1975).
24. A.K. Vasudevan, O. Richmond, F. Zok and J.P. Embury, *Mater. Sci. Engng.*, **A107**, 63 (1989).
25. W.H. Hunt, Jr., J.R. Brockenbrough and P.E. Magnusen, *Scripta Metall. Mater.*, **25**, 15 (1991).
26. J.P. Hirth, *Appl Mech. Rev.*, **45**, 575 (1992).
27. N.A. Fleck, J.W. Hutchinson and M.F. Ashby, *Acta Metall. Mater.*, in press.
28. H.M. Zbib, in Modelling of Plastic Deformation and its Engineering Applications, S.I. Andersen *et al.* eds., Riso National Lab., Roskilde, Denmark, 525 (1992).
29. J.W. Hutchinson and V. Tvergaard, *Int. J. Mech. Sci.*, **22**, 339 (1980).
30. V.B. Ruian and J.P. Hirth, *Metall. Trans.*, **18A**, 335 (1987).

Table 1: List of Composites Investigated (The matrix is A1-4%Mg and the reinforcement is alumina particulates). Two data sets (1,2) listed for bimodal case.

Composite No	Total Vol. Fraction	1		2		Interparticle spacing μm
		Part. Size μm	Vol. fract.	Part. Size μm	Vol. fract.	
Matrix	0	-	-	-	-	∞
1	0.45	3	0.45	-	-	1.33
2	0.46	3	0.41	30	0.05	2.32
3	0.47	3	0.26	30	0.21	3.13
4	0.47	45	0.47	-	-	18.80
5	0.50	9	-	-	-	3.50
6	0.53	30	0.53	-	-	10.70
7	0.54	165	0.54	-	-	57.40

Table 2: Yield Strengths in Tension and Compression for the Composites Investigated.

Composite No.	Yield Strength (Tension) MPa	Yield Strength (Compression) MPa
Matrix	77	83
1	163	210
2	205	214
3	148	217
4	150	221
5	203	227
6	169	247
7	176	245

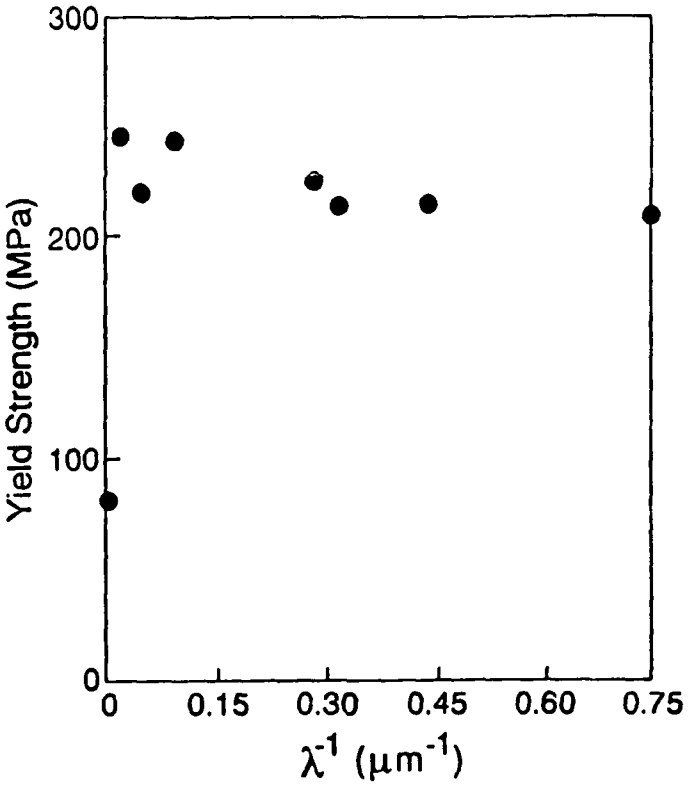

Figure 1. Compressive yield strength versus inverse of interparticle spacing

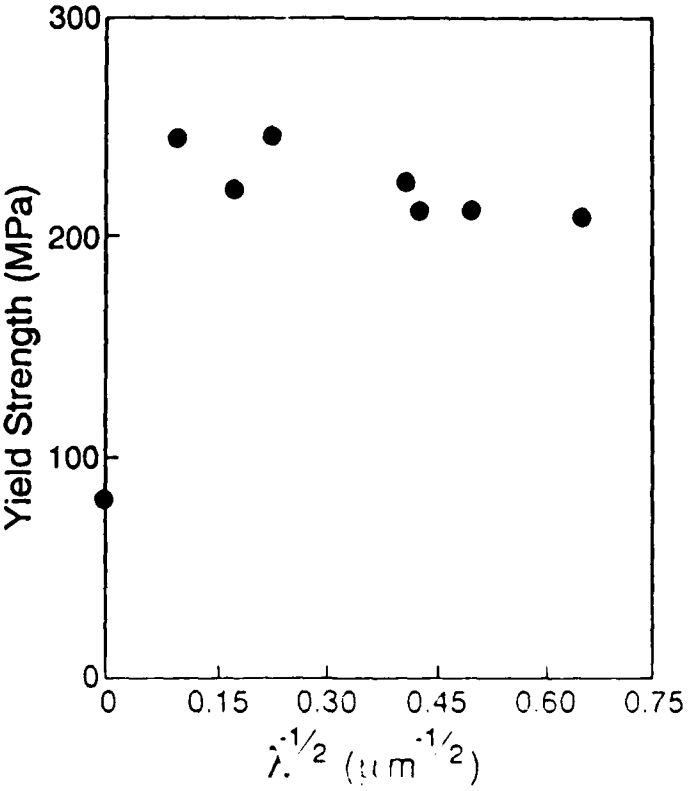

Figure 2. Compressive yield strength versus inverse square root of interparticle spacing

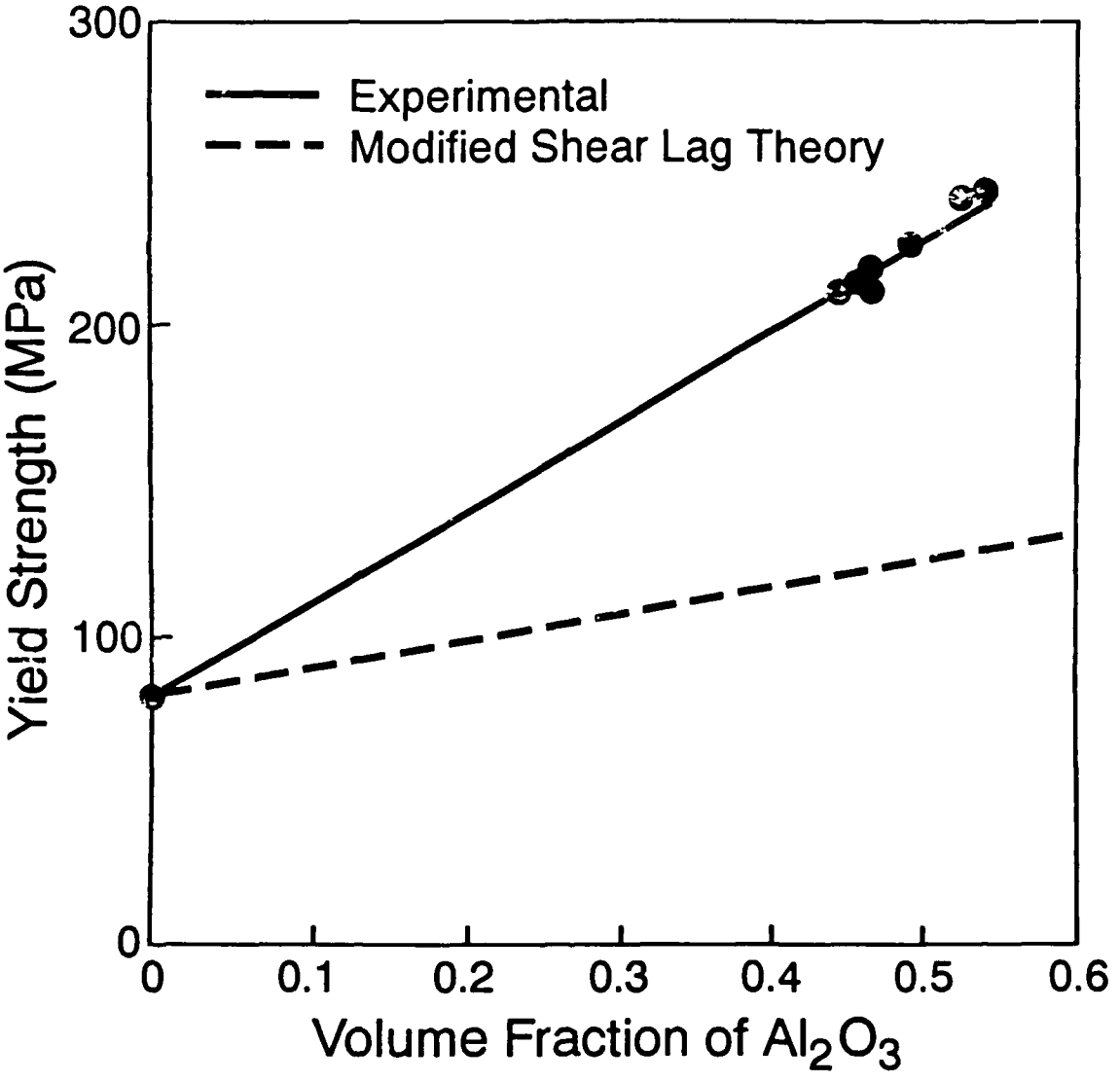

Figure 3. Compressive yield strength versus volume fraction of alumina.